DESIGN AND SYNTHESIS OF CHIRAL AND ACHIRAL α2, 3 AND 5 SUBTYPE SELECTIVE GABA(A)REGIC LIGANDS FOR TREATMENT OF CENTRAL NERVOUS SYSTEM DISORDERS AND DIFFERENT TYPES OF CANCERS

by

Sepideh Rezvanian

A Dissertation Submitted in

Partial Fulfillment of the

Requirements for the Degree of

Doctor of Philosophy

in Chemistry

at

The University of Wisconsin-Milwaukee

December 2023

ABSTRACT

DESIGN AND SYNTHESIS OF CHIRAL AND ACHIRAL α2, 3 AND 5 SUBTYPE SELECTIVE GABA(A)REGIC LIGANDS FOR TREATMENT OF CENTRAL NERVOUS SYSTEM DISORDERS AND DIFFERENT TYPES OF CANCERS

by

Sepideh Rezvanian

The University of Wisconsin-Milwaukee, 2023
Under the Supervision of Professor James M. Cook

Part I: Design and Synthesis of Chiral α5 Subtype Selective GABA(A)ergic Ligands for Schizophrenia, Depression and Alzheimer's Disease

Gamma (γ)-amino butyric acid, a naturally occurring amino acid, serves as a proteinogenic amino acid and acts as the principal inhibitory neurotransmitter in the central nervous system (CNS), including the cerebrum of the mammalian brain. The benzodiazepines (BZDs) bind at the extracellular interface of the α+γ2-subunits of $GABA_AR$, influencing various brain functions. The α1-subtypes are linked to anxiolytic sedative, ataxic, amnesic, anticonvulsant, and addictive effects, while the α2/3-subtypes contribute to anxiolytic, anticonvulsant, and antinociceptive activities. α5-containing $GABA_ARs$ in the CNS play a role in cognition, learning, and memory processes. Dysfunctions in these receptors in the CNS are implicated in various CNS disorders.

There is an urgent need for improved medications to treat anxiety and depression, especially considering their comorbidity. Presently, no drugs on the market for depression or schizophrenia address cognition problems, representing an unmet medical need. Leveraging the "privileged

imidazodiazepine (IMZD) structure," over 150 novel α5-preferring ligands have been synthesized in Milwaukee for evaluation of pro-cognitive, anxiolytic, and antidepressant activity. The lead compounds, GL-II-73 and GL-I-54 (developed by Guanguan Li) were identified as anxiolytic, antidepressant, and pro-cognitive—a significant discovery. GL-I-54 was resynthesized and evaluated for additional biological activity. The ligand showed symptomatic, disease-modifying, and neurotrophic effects in a mouse model of chronic stress, reversing stress-induced and age-related working memory deficits in both old and young mice. DAMONA PHARMACEUTICALS is currently conducting further studies to advance GL-I-54 towards clinical applications for depression and potentially Alzheimer's disease.

Additionally, some other novel α5-subtype selective ligands were synthesized based on the structure of GL-I-54 and evaluated for pro-cognitive and anxiolytic. Among these ligands, the amide analog SRE-II-11 showed pro-cognitive effects in primary and secondary screenings using the Y-maze assay. This ligand will undergo further testing in the forced-swim test and elevated plus maze to determine their anti-depressive and anxiolytic behavioral profile. Furthermore, the 1,2,4-oxadiazoles SRE-II-42 and SRE-III-07 demonstrated strong pro-cognitive profiles in the Y-maze assay, suggesting their potential as key backups for ligand GL-I-54, pending further assessments in tests such as the forced-swim test, UCMS, elevated plus maze, metabolism, etc.

Part II: Design and Synthesis of Achiral α2/3 Ligands for Anxiety, Epilepsy, and Pain: Large scale Synthesis of Hz-166 and Analogs

Epilepsy, a prevalent neurological condition, is a leading cause of neurological disability, affecting approximately 1-2% of the global population, with about 33% of patients experiencing refractory epilepsy. Various drugs, including the widely prescribed benzodiazepine class (e.g., Valium and Xanax), are available for treatment of neurological disorders such as epilepsy and anxiety.

Unfortunately, patients often develop tolerance to benzodiazepines, and mostly they are effective for only around 3 days in status epilepticus. These drugs, known to bind non-selectively at the subtypes to the α and γ interface of the gamma-aminobutyric acid type A ($GABA_A$) receptor, lead to adverse effects, encompassing tolerance, addiction, sedation, ataxia, somnolence, and confusion.

The novel imidazodiazepine agent HZ-166 was developed in Milwaukee and it was identified as α2/α3 receptor subtype-selective ligands, demonstrating anxiolytic and anticonvulsive activities without undesirable side effects like sedation and ataxia. However, the ester function in HZ-166 (6) was prone to metabolism into the less active corresponding carboxylic acid, resulting in poor exposure, high clearance, and limited blood-brain barrier penetration. The strategic replacement of the ester with heterocycles, specifically oxazoles, significantly enhanced metabolic stability and pharmacokinetics. This improvement led to the development of the clinically advancing non-sedating anticonvulsant, KRM-II-81. As part of ongoing efforts, analogs based on the structure of KRM-II-81 were designed and synthesized. Utilizing docking procedures in the human full-length heteromeric α1β3γ2 $GABA_A$ receptor subtype CryoEM structure (6HUO), following the protocols outlined by Masiulis et al. in Nature, 2019, their biological activities were tested. Crucially, several novel analogs of oxazole and oxazoline have demonstrated potent anticonvulsant activity, showcasing improved in-vivo and in-vitro stability without inducing cytotoxicity, sedation, ataxia, or loss of righting response. Among all the novel KRM-II-81 bioisosteres designed and synthesized, ZK-III-58 featuring an 8-bromo substituted imidazodiazepine as well as ZK-IV-07 exhibited enhanced exposure at the target site (brain) and improved metabolic stability in both plasma and brain. This translated to improved oral bioavailability, aligning precisely with the requirements for pre-clinical studies.

ZK-III-58 demonstrated great efficacy in various epilepsy models such as pentylenetetrazole (metrazole) induced clonic and tonic seizure models. Significantly, ZK-III-58 exhibited full potency in therapy-resistant seizure models, non-convulsive status epilepticus models, and chronic seizure models. Its anticonvulsant activity remained potent through intraperitoneal (i.p.) or oral administration in both mice and rats. Remarkably, this 1,4-oxazole displayed a favorable toxicity profile and selectively bound to the rat brain benzodiazepine receptor site without undesired binding to other receptors, including HERG.

ZK-III-58 did not induce sedation, ataxia, or loss of righting response, even at doses up to 120 mg/kg, and showed non-toxicity in the HEK-293 cell line. The synthesis of ZK-III-58 was successfully executed without employing column chromatography in any synthetic step and without the need for toxic and expensive palladium. Undoubtedly, as a $GABA_A$ potentiator and potentially α2/α3 receptor subtype-selective compound, ZK-III-58 and ZK-IV-07 serve as potent and safe backup anticonvulsant agents to the clinically advancing KRM-II-81 for the treatment of epilepsy.

Part III: Design and Synthesis of α5 Subtype Selective GABA(A)ergic Ligands for Treatment of Different Types of Cancer

Gamma-aminobutyric acid type A receptors ($GABA_ARs$) are transmembrane pentameric ligan-gated ion channel in the central nervous system, responding to GABA as the principal inhibitory neurotransmitter. This study focuses on designing ligands for the extracellular interface of $GABA_AR$ α and γ2-subunits, aiming to selectively modulate subtypes for therapeutic benefits. Specifically, α5 plays a crucial *role* in CNS disorders, such as schizophrenia and major depressive disorders.

Medulloblastoma, the most prevalent pediatric brain tumor, is classified into four subgroups: WNT, SHH, Group 3, and Group 4. Among these, Group 3 exhibits the highest morbidity, relapse, and metastasis rates. Conventional treatment involves surgical tumor removal, followed by radiation and chemotherapy, leading to adverse effects like hearing impairment, permanent damage to the endocrine system, neurocognitive function impairment, and secondary tumors. Due to these issues, medulloblastoma needs better treatment. Notably, Group 3 tumors display elevated expression of the α5 subunit of ligand-gated ionotropic γ-aminobutyric acid type A receptors.

Positive allosteric modulators like KRM-II-008 and QH-II-066 targeting α5 $GABA_AR$ subunits exhibit promising results against Group 3 medulloblastoma. Analogs of KRM-II-008 and QH-II-066, synthesized and assayed, demonstrate potent anti-cancer effects, suggesting their potential as efficient drugs.

Melanoma, a deadly skin cancer, shows high expression of α5 $GABA_AR$ subunits. QH-II-66, a benzodiazepine, proves effective in sensitizing melanoma cells to radiation and immune checkpoint inhibitors. Additionally, testing in H1792 lung cancer cell lines reveal their activity, and a novel compound, SRE-III-35, emerges with enhanced efficacy and improved synthesis.

These benzodiazepine-based anticancer drugs exhibit rapid blood-brain barrier penetration, enhancing their therapeutic potential. Furthermore, their non-toxic nature for normal cells, coupled with anxiolytic effects, could offer clinical significance, especially in combination therapies. The study concludes with the potential clinical relevance of these promising anticancer agents.

To

My beloved family

And

Woman-Life-Freedom

TABLE OF CONTENTS

LIST OF FIGURES xx

LIST OF TABLES xxxvi

LIST OF SCHEMES xxxix

LIST OF ABBREVIATIONS xli

ACKNOWLEDGMENTS xlvi

Chapter 1. Introduction 1

1.1. The $GABA_A$ receptors 1

1.3. Modulation of BZDs on the Pharmacological Effects of $GABA_AR$ 7

1.4. Molecular Modeling 11

1.4.1. Early pharmacophore Model 11

1.4.2. Modern pharmacophore model 18

1.5. Research Objectives 29

Chapter 2. Design and Synthesis of Chiral α5 Subtype Selective GABA(A)ergic Ligands for Schizophrenia, Depression and Alzheimer's Disease 30

2.1. Introduction and Background 30

2.2 Chemistry: Results and Discussion 48

2.2.1 The synthetic route to SH-053-2'F-S-CH_3, original done on small scale by Huang and Li 48

2.2.4 Improved synthesis of GL-I-54 55

2.2.5 Synthesis of analogs of GL-I-54 for SAR 65

2.3. Results and Discussion: Biological Evaluation of GL-I-54 and is Analogs 75

2.3.1. Comparative study of electrophysiological profiles of GL-II-73 and its enantiomer, GL-I-54 with Ashley Bernardo, Dr Prevot and coworkers[1] 76

2.3.2 Study of anxiety-like behavior of GL-II-73 and GL-I-54, respectively, in the elevated plus-maze with Dr Felipe V. Gomes, Adriana Jesus Souza, Dr Prevot, Dr Sibille, and coworkers..... 82

2.3.3. Anti-depressant efficacy study of GL-II-73 and GL-I-54 in the force swim test with Dr Felipe V. Gomes, Adriana Jesus Souza, Dr Prevot, Dr Sibille, and coworkers 86

2.3.4. Motor impairment coordination study of GL-II-73 and GL-I-54 in the rotarod with Dr Felipe V. Gomes, Adriana Jesus Souza, Dr Prevot, Dr Sibille, and coworkers 89

2.3.5. Metabolic stability of GL-II-73 and GL-I-54 with Ashley Bernardo, Dr Prevot and coworkers..... 90

2.3.6. Reversal of stress-induced working memory deficits by the S enantiomer of GL-II-73; GL-I-54 on Ymaze task with Michael Marcotte, Dr. Prevot , Etienne Sibille and coworkers. 91

2.3.7. Evaluation of anxiolytic activity of acute administration of GL-RM (racemic mixture of GL-I-54 and GL-II-73) with Ashley Bernardo, Dr Prevot and coworkers..... 92

2.3.8. Evaluation of depressive-like behaviors of acute administration of GL-RM (racemic mixture of GL-I-54 and GL-II-73) with Ashley Bernardo, Dr Prevot and coworkers 98

2.3.10. Evaluation of anxiolytic behaviors of chronic treatment with GL-RM with Ashley Bernardo, Dr Prevot and coworkers 101

2.3.11. Evaluation of chronic treatment of GL-RM on emotionality with Ashley Bernardo, Dr Prevot and coworkers 105

2.3.12. Evaluation of chronic treatment of GL-RM on Y-maze with Ashley Bernardo, Dr. Prevot and coworkers 107

2.3.14. Correlation of spine density in the PFC and CA1 with spatial working memory and emotionality by GL-RM with Ashley Bernardo, Dr. Prevot and coworkers 111

2.3.15. Evaluation of reversal of stress-induced working memory deficits by SRE-II-11 on the Y-maze task with Michael Marcotte, Dr. Prevot, Etienne Sibille and coworkers.....113

2.3.16. Evaluation of reversal of stress-induced working memory deficits by SRE-II-42 on the Y-maze task with Michael Marcotte, Dr. Prevot, Etienne Sibille and coworkers.....116

2.3.17. Evaluation of reversal of stress-induced working memory deficits by SRE-II-44 on the Y-maze task with Michael Marcotte, Dr. Prevot, Etienne Sibille and coworkers..... 120

2.3.18. Evaluation of reversal of stress-induced working memory deficits by SRE-III-07 on the Y-maze task with Michael Marcotte, Dr. Prevot, Etienne Sibille and coworkers..... 123

2.3.19. Biological Activity: Metabolism, Cytotoxicity and Rotarod Studies with Mechelle Meyer and Anika Tylek, Dr. Arnold's group 125

2.3.20. Receptor binding studies 127

2.3.21. Conclusion 135

2.4. Methods 136

2.4.1. Elevated plus maze assay with Dr Felipe V. Gomes, Adriana Jesus Souza, and coworkers..... 136

2.4.2. Forced swim test (FST) with Dr Felipe V. Gomes, Adriana Jesus Souza, and coworkers 137

2.4.3. Electrophysiology with Ashley Bernardo, Dr Tom Prevot, Dr Etienne Sibille and coworkers 137

2.4.4. Y-maze assay with Ashley Bernardo, Dr Tom Prevot, Dr Etienne Sibille and coworkers 138

2.4.5. Liver microsomal assay with Ashley Bernardo, Dr Tom Prevot, Dr Etienne Sibille and coworkers 139

2.4.6. PhenoTyper™ (PT) Test with Ashley Bernardo, Dr Tom Prevot, Dr Etienne Sibille and coworkers 139

2.4.7. Golgi Staining Analysis of mice brain with Ashley Bernardo, Dr Tom Prevot, Dr Etienne Sibille and coworkers 142

2.4.8. Radioligand binding assays on rat brain homogenates with the National Institute of Mental Health's Psychoactive Drug Screening Program (NIMH PDSP) at UNC with Dr Bryan Roth 143

2.5. Experimental 144

2.5.2. (S)-7-Bromo-5-(2-fluorophenyl)-3-methyl-1,3-dihydro-2H-benzo[e][1,4]diazepin-2-one (4) 146

2.5.3. Tert-butyl (S)-(1-((4-bromo-2-(2-fluorobenzoyl) phenyl) amino)-1-oxopropan-2-yl) carbamate (3) 148

2.5.4. (S)-7-Bromo-5-(2-fluorophenyl)-3-methyl-1,3-dihydro-2H-benzo[e][1,4]diazepin-2-one (4) 149

2.5.5. Ethyl (S)-8-bromo-6-(2-fluorophenyl)-4-methyl-4H-benzo[f]imidazo[1,5-a][1,4]diazepine-3-carboxylate (5) 150

2.5.6. Tert-butyl-(R)-(1-((4-bromo-2-(2-fluorobenzoyl)phenyl)amino)-1-oxopropan-2-yl) carbamate (10) 152

2.5.7. (*R*)-7-Bromo-5-(2'fluorophenyl)-3-methyl-1,3-dihydro-2*H*-benzo[*e*][1,4]diazepin-2-one (11) 153

2.5.8. Ethyl (*R*)-8-bromo-6-(2-fluorophenyl)-4-methyl-4*H*-benzo[*f*]imidazo[1,5-*a*][1,4] diazepine-3-carboxylate (12) 155

2.5.9. Ethyl(S)-6-(2'fluorophenyl)-4-methyl-8-((triisopropylsilyl)ethynyl)-4H benzo [f] imidazo [1,5-a][1,4]diazepine-3-carboxylate (6) 156

2.5.10. Ethyl (S)-8-ethynyl-6-(2'fluorophenyl)-4-methyl-4H-benzo[f]imidazo[1,5-a] [1,4] diazepine-3-carboxylate (7) 158

2.5.11. (S)-8-Ethynyl-6-(2'fluorophenyl)-4-methyl-4H-benzo[f]imidazo[1,5-a][1,4]diazepine-3-carboxylic acid (13) 160

2.5.12. (S)-8-Ethynyl-6-(2'fluorophenyl)-N,N,4-trimethyl-4H-benzo[f]imidazo[1,5-a] [1,4] diazepine-3-carboxamide (GL-I-54, 14) 161

2.5.13. Tert-butyl (S)-(1-((4-bromo-2-(2'chlorobenzoyl)phenyl)amino)-1-oxopropan-2-yl)carbamate (17) 163

2.5.14. (S)-7-Bromo-5-(2'chlorophenyl)-3-methyl-1,3-dihydro-2H-benzo[e][1,4]diazepin-2-one (18) 164

2.5.15. Ethyl (S)-8-bromo-6-(2'chlorophenyl)-4-methyl-4H-benzo[f]imidazo[1,5-a] [1,4] diazepine-3-carboxylate (19) 165

2.5.16. Ethyl (S)-8-cyclopropyl-6-(2'fluorophenyl)-4-methyl-4H-benzo[f]imidazo[1,5-a][1,4]diazepine-3-carboxylate (20) 167

2.5.17. (S)-8-Cyclopropyl-6-(2'fluorophenyl)-4-methyl-4H-benzo[f]imidazo[1,5-a] [1,4] diazepine-3-carboxylic acid (21) 169

2.5.18. (S)-5-(8-Cyclopropyl-6-(2-fluorophenyl)-4-methyl-4H-benzo[f]imidazo[1,5-a] [1,4] diazepin-3-yl)-3-ethyl-1,2,4-oxadiazole (22) 170

2.5.19. (S)-5-(8-Cyclopropyl-6-(2-fluorophenyl)-4-methyl-4H-benzo[f]imidazo[1,5-a] [1,4] diazepin-3-yl)-3-methyl-1,2,4-oxadiazole (23) 172

2.5.20. Ethyl 8-bromo-6-(2'fluorophenyl)-4-methyl-6H-benzo[f]imidazo[1,5-a] [1,4] diazepine-3-carboxylate (26) 173

2.5.21. (S)-8-Bromo-6-(2'fluorophenyl)-N-((R)-1-hydroxypropan-2-yl)-4-methyl-4H-benzo [f] imidazo[1,5-a] [1,4]diazepine-3-carboxamide (27) 174

2.5.22. (S)-8-Bromo-6-(2'fluorophenyl)-N-((S)-1-hydroxypropan-2-yl)-4-methyl-4H-benzo [f] imidazo[1,5-a][1,4]diazepine-3-carboxamide (28) 175

2.5.23. (4S)-8-Bromo-6-(2'fluorophenyl)-N-(1-hydroxybutan-2-yl)-4-methyl-4H-benzo [f] imidazo [1,5-a][1,4]diazepine-3-carboxamide (33) 176

2.5.24. (4R)-8-Bromo-6-(2'fluorophenyl)-N-(1-hydroxybutan-2-yl)-4-methyl-4H-benzo [f] imidazo[1,5-a][1,4]diazepine-3-carboxamide (34) 178

2.5.25. (S)-8-Bromo-6-(2'fluorophenyl)-4-methyl-N-((R)-1-oxopropan-2-yl)-4H-benzo[f] imidazo [1,5-a][1,4]diazepine-3-carboxamide (29) 179

2.5.26. (S)-8-Bromo-6-(2'fluorophenyl)-4-methyl-N-((S)-1-oxopropan-2-yl)-4H-benzo [f] imidazo [1,5-a][1,4]diazepine-3-carboxamide (30) 180

2.5.27. (S)-8-Cyclopropyl-6-(2'fluorophenyl)-N,N,4-trimethyl-4H-benzo[f]imidazo[1,5-a] [1,4] diazepine-3-carboxamide (24) 182

2.5.28. (S)-8-Cyclopropyl-N-ethyl-6-(2'fluorophenyl)-4-methyl-4H-benzo[f]imidazo[1,5-a] [1,4] diazepine-3-carboxamide (25) 183

Chapter 3: Design and Synthesis of Achiral α2/3 Ligands for Anxiety, Epilepsy, and Pain: Large Scale Synthesis of Hz-166 and Analogs 185

3.1. Introduction 185

3.2. Chemistry 205

3.2.1. Synthesis of α2/3-$GABA_AR$ Subtype-selective Imidazodiazepines 205

3.2.2. Synthesis of the ZK oxazolines analogs 219

3.2.3. Synthesis of the ZK oxazole analogs 220

3.3 Biology of KRM-II-81 analogs 223

3.3.1. Rotarod studies of novel compounds in female CFW mice via oral administration at various doses 223

3.3.3. Summary of the primary and secondary binding affinity of novel ligands in the Psychoactive Drug Screening Program (PDSP) of NIMH run by Dr. Bryan Roth (UNC) in the 46 receptor and HERG assays and over seen by Dr. Jamie Driscoll (Po) at NIMH. 227

3.3.4. Effects of ZK series in the pentylenetetrazol (PTZ) seizure model by Dr. Witkin, and Dr. Ping (Indiana University School of Medicine). 230

3.3.5. Protection against lethality by oral administration of KRM-II-81 analogs against PTZ (s.c) (75 mg/kg) induced seizures in mice (data source: Dr. Jeffrey Witkin and coworker, Indiana University School of Medicine). 232

3.3.6. In-vivo pharmacokinetic (PK) study of KRM-II-81 analogs 233

3.4. Discussion and Conclusion 240

3.5. Methods 242

3.5.1. Rotarod studies carried out by Nick Zahn and Michelle Meyer (Dr. Arnold's laboratory, MIDD). 242

3.5.2. Cytotoxicity studies by Michelle Meyer and coworkers in Dr. Arnold's lab, University of Wisconsin-Milwaukee and MIDD. 243

3.5.3. Analysis of ligands in the pentylenetetrazol seizure model (PTZ) by Dr. Jeffery Witkin and Dr. Xingjie at Indiana University, School of Medicine. 243

3.5.4. Methods of molecular docking with the help of Dr. Lalit Golani (UWM). 244

3.5.5. Neuropharmacokinetic in vivo evaluation of ligands in plasma and brain (Source: Dr. Savic and coworkers, University of Belgrade, Serbia) 244

3.6. Experimental 246

3.6.1. General experimental conditions 246

3.6.2. N-(4-Bromo-2-picolinoylphenyl)-2-chloroacetamide (11) 247

3.6.3. 7-Bromo-5-(pyridin-2-yl)-1,3-dihydro-2H-benzo[e][1,4]diazepin-2-one (12) 248

3.6.4. Ethyl 8-bromo-6- (pyridin-2-yl)-4H-benzo[f]imidazo[1,5-a][1,4]diazepine-carboxylate (13) 250

3.6.5. Ethyl 6-(pyridin-2-yl)-8-((triisopropylsilyl)ethynyl) 4H benzo[f]imidazo[1,5a][1,4] diazepine-3-carboxylate (14) 251

3.6.6. Ethyl-6-(pyridin-2-yl)-8-((trimethylsilyl)ethynyl)-4H-benzo[f] imidazo[1,5a]-[1,4]dia zepine-3-carboxylate (21) 253

3.6.7. Ethyl 8-ethynyl-6-(pyridin-2-yl)-4H-benzo[f]imidazo[1,5-a][1,4]diazepine-3-carboxylate (1, Hz-166) 254

3.6.8. (R)-8-Bromo-N-(1-hydroxypropan-2-yl)-6-(pyridin-2-yl)-4H-benzo[f]imidazo[1,5-a][1,4]diazepine-3-carboxamide (14) 256

3.6.9. (S)-8-Bromo-N-(1-hydroxypropan-2-yl)-6-(pyridin-2-yl)-4H-benzo[f]imidazo[1,5-a][1,4]diazepine-3-carboxamide (15) 257

3.6.10. 2-(8-Bromo-6-(pyridin-2-yl)-4H-benzo[f]imidazo[1,5-a][1,4]diazepin-3-yl)-4-methyl-4,5-dihydrooxazole (4, ZK-III-51) 258

3.6.11. (R)-2-(8-Bromo-6-(pyridin-2-yl)-4H-benzo[f]imidazo[1,5-a][1,4]diazepin-3-yl)-4-methyl-4,5-dihydrooxazole (5, ZK-III-56) 260

3.6.12. (R)-8-Bromo-N-(1-oxopropan-2-yl)-6-(pyridin-2-yl)-4H-benzo[f]imidazo[1,5-a][1,4]diazepine-3-carboxamide (18) 261

3.6.13. (S)-8-Bromo-N-(1-oxopropan-2-yl)-6-(pyridin-2-yl)-4H-benzo[f]imidazo[1,5-a][1,4]diazepine-3-carboxamide (19) 262

3.6.14. 2-(8-Bromo-6-(pyridin-2-yl)-4H-benzo[f]imidazo[1,5-a][1,4]diazepin-3-yl)-4-methyloxazole (6, ZK-III-58) 264

3.6.15. 2-(8-ethynyl-6-(pyridin-2-yl)-4H-benzo[f]imidazo[1,5-a][1,4]diazepin-3-yl)-4-methyloxazole (9, ZK-IV-07) 265

Chapter 4: Design and Synthesis of α5 Subtype Selective GABA(A)ergic Ligands for Treatment of Different Types of Cancer 267

4.1. Introduction 267

4.2. Cytotoxicity 277

4.3. IC_{50} value of lead compounds with their nor-analogs 279

4.4. Gene expression of Medulloblastoma 281

4.5. Chemistry 287

4.5.1. Synthesis of the QH-II-066 and KRM-II-008 287

4.5.2. Synthetic route to make 7-cyclopropyl analogs. 290

4.5.3. Synthetic route to make deuterated analogs. 292

4.6. Result and Discussion 294

4.6.1. Lung adenocarcinomas express GABA(A) receptor subunits by Drs. Bhattacharya, Krummel, Sengupta and coworkers 294

4.6.2. Activation of GABA(A) receptors is depolarizing and triggers cancer cell death by Drs. Bhattacharya, Krummel, Sengupta and coworkers. The ley mechanism of action. 296

4.6.3. GABA(A) receptor activation potentiates radiation by Drs. Bhattacharya,Krummel, Sengupta and coworkers2 300

4.6.4. Increased survival of mice bearing a lung brain metastatic tumor by Drs. Bhattacharya, Krummel, Sengupta and coworkers 306

4.6.5. Depolarization of cancer cells by different benzodiazepines, by Drs. Toukam, Krummel and coworkers 308

4.6.6. Cytotoxicity of different benzodiazepine analogs by Drs. Toukam, Krummel and coworkers..... 310

4.6.7. In vivo effectiveness of benzodiazepine analogs on Lewis Lung Carcinoma (LLC) tumors by Drs. Toukam, Krummel and coworkers.....311

4.6.8. MTS cytotoxicity assay by Drs. Toukam, Krummel and coworkers..... 313

4.6.9. Receptor binding studies 316

4.7. Conclusion..... 321

4.8. Methods..... 322

4.8.1. Radioligand binding assays on rat brain homogenates with the National Institute of Mental Health's Psychoactive Drug Screening Program (NIMH PDSP) at UNC with Dr Bryan Roth..... 322

4.8.2. Mitochondrial depolarization by Drs. Bhattacharya, Krummel, Sengupta and coworkers[2] 323

4.8.3. Lung cancer-chips by Drs. Bhattacharya, Krummel, Sengupta and coworkers[2]..... 323

4.8.4. Viability assays by Drs. Bhattacharya, Krummel, Sengupta and coworkers[2] 325

4.9. Experimental 327

4.9.1. General experimental conditions..... 327

4.9.2. N-(2-Benzoyl-4-bromophenyl)-3-bromopropanamide (11) 328

4.9.3. 3-Bromo-N-(4-bromo-2-(2-fluorobenzoyl)phenyl)propenamide (12) 329

4.9.4. 7-Bromo-5-phenyl-1,3-dihydro-2H-benzo[e][1,4]diazepin-2-one (13) 330

4.9.5. 7-Bromo-5-(2-fluorophenyl)-1,3-dihydro-2H-benzo[e][1,4]diazepin-2-one (14) 331

4.9.6. 7-Cyclopropyl-5-phenyl-1,3-dihydro-2H-benzo[e][1,4]diazepin-2-one (17) 332

4.9.7. 7-Cyclopropyl-5-(2'fluorophenyl)-1,3-dihydro-2H-benzo[e][1,4]diazepin-2-one (18) 333

4.9.8. 7-Bromo-1-methyl-5-phenyl-1,3-dihydro-2H-benzo[e][1,4]diazepin-2-one (16) 334

4.9.9. 7-Cyclopropyl-1-methyl-5-phenyl-1,3-dihydro-2H-benzo[e][1,4]diazepin-2-one (19, TA-IV-74) 336

4.9.10. 7-Ethynyl-5-(2'fluorophenyl)-1-methyl-1,3-dihydro-2H-benzo[e][1,4]diazepin-2-one-3,3-d2 (25) 337

4.9.11. 7-Cyclopropyl-5-phenyl-1,3-dihydro-2H-benzo[e][1,4]diazepin-2-one-3,3-d2 (21) 338

4.9.12. 7-Cyclopropyl-1-(methyl-d3)-5-phenyl-1,3-dihydro-2H-benzo[e][1,4]diazepin-2-one (22)..... 339

4.9.13. 7-Ethynyl-1-(methyl-d3)-5-phenyl-1,3-dihydro-2H-benzo[e][1,4]diazepin-2-one (24) 340

4.9.13. 7-Cyclopropyl-1-(methyl-d3)-5-phenyl-1,3-dihydro-2H-benzo[e] [1,4] diazepin-2-one-3,3-d2..... 342

REFERENCES 343

Appendix..... 379

LIST OF FIGURES

Chapter 1. Introduction

Figure 1. A proposed $GABA_AR$ subunit topology. The extracellular domain starts with the N-terminal end, and the M1-M4 are regions within the membrane. (Modified from the Figure in Burt, et al. [16] and Clayton, et al.)…….2

Figure 2. The schematic representations of $GABA_AR$, the ligand-gated chlorine ion channel in longitudinal vision (A) and cross-sectional vision (B). The number 1-4 represents the M1-M4 transmembrane domains. The domain M2 contributes to most of the pore lining within the lipid bilayer membrane. (Modified from the Figure in Keramidas et al.[18], and Clayton et al.)…….3

Figure 3. The arrangement of the $\alpha1\beta3\gamma2$ $GABA_AR$ subtype as viewed from the synaptic cleft. The binding sites of GABA are located at the interfaces between β^+ and α^- subunits and the BZD binding site is located at the interface of the $\alpha^+\gamma^-$ subunits. The + represents the loop C of each subunit. (Modified from the Figure in Clayton, et al.[18] and Ernst, et al.)……4

Figure 4. The structures of common BZDs: diazepam, chlordiazepoxide, imidazodiazepine (IMDZ) midazolam and flumazenil (antagonist). The atoms are labeled for both BZDs and IMDZs. Diazepam, chlordiazepoxide, and midazolam can bind only to the DS sites, whereas flumazenil can bind to both the DS and DI sites……5

Figure 5. The membrane potential over time when a depolarizing stimulus initiates a nerve signal. A hyperpolarized state indicates a potential further away from the threshold potential. (Modified from the Figure in the Ph.D. thesis of Terry Clayton)[3] ……..……10

Figure 6. The locations of the descriptors and areas of the Milwaukee-Unified Pharmacophore/Receptor Model for BZD at $GABA_AR$ BzR. Depicted here is pyrazolo[3,4-c]quinolin-3-one CGS-9896 as a dotted line, a diazadiindole template as a thin line, and diazepam as a thick line aligned within the unified pharmacophore/receptor model for the BzR. H_1 and H_2 stand for the hydrogen bond donor sites within the BzR, while A_2 stands for a hydrogen bond acceptor site that may be necessary for potent inverse agonist activity in vivo. L_1, L_2, L_3, and L_{Di} represent the four lipophilic regions and S_1, S_2, and S_3 represent the regions of negative steric repulsion. LP stands for the lone pair of electrons on the nitrogen (N) or oxygen (O) atoms of the ligands. (Modified from the Figure in Clayton et al.)[3] ……..13

Figure 7. Overlap images between the included volumes derived from receptor subtype selective ligands: a) α1 and α2 subtypes; b) α2 and α3 subtypes; c) α4 and α6 subtypes; d) α1 and α6 subtypes; e) α1 and α5 subtypes; f) diazepam and the descriptors of the unified pharmacophore model in the included volume of the α1 subtype. The yellow color represents overlapping induced volumes, and each grid measures 4 Å in width and height. This was taken from Clayton et al.[3] ...15

Figure 8. Bz/$GABA_AR$ in vitro binding data of diazepam and the anticancer compound QH-II-066. (Modified from the Figure in the Ph. D. thesis of M. Poe and T. Clayton)[3] …….16

Figure 9. The structures of enantiotropic chiral imidazodiazepine (IMDZ) ligands 1 and 2…...16

Figure 10: Ligand occupation of SH-053-2'F-R-CH_3 (1) and SH-053-2'F-S-CH_3 (2) in the α5 and α2 pharmacophore/receptor models. (Modified and reproduced from that reported by Clayton et al.)[3]……...16

Figure 11. The complex of diazepam (yellow) with the α1 (aquamarine) and γ2 (orchid) subunits of α1β3γ2L GABAA receptor 6HUP. The dashed lines (- - -) indicate π–π interactions, hydrogen

bonding interactions, and a halogen bonding interaction. The image is modified from Golani et. al. 2022[4] which originates from the classic work in Nature Neuroscience (2019)[5]……19

Figure 12. The complex of alprazolam (orange) with α1 (aquamarine) and γ2 (orchid) subunits of α1β3γ2L GABAA receptor 6HUO. The dashed lines (- - -) indicate π–π interactions, hydrogen bonding interactions, and a halogen bonding interaction. The image is modified from Golani et. al. 2022.[4] …….20

Figure 13. The overlay diagram of flumazenil (grey) and diazepam (yellow) in the ion complex with α1 (aquamarine) and γ2 (orchid) subunits of α1β3γ2L GABAAR (6D6U and 6HUP). The image is modified from Golani et. al. 2022 [4] which originates from the classic work in Nature Neuroscience (2019)[5] ……22

Figure 14. The docking pose of QH-II-066 5 (deep sky blue) with the α1 (aquamarine) and γ2 (orchid) subunits of α1β3γ2L GABAA receptor 6HUP. No halogen bond is observed in case of the ethynyl group. The image is modified from Golani et. al. 2022.[4] ……..28

Chapter 2. Design and Synthesis of Chiral α5 Subtype Selective GABA(A)ergic Ligands for Schizophrenia, Depression and Alzheimer's Disease

Figure 1. The α5β3γ2 subtype $GABA_AR$. IBDZs like SH-053-2'F-RCH_3 and GL-II-73 exert their effects at the α5+γ2- interface as positive allosteric modulators (PAMs). Image was modified from Jacob et al., Nature Reviews Neuroscience, 2008……..34

Figure 2. Lead α2/3 and α5-selective ligands in this research……..35

Figure 3. The potentiation of GL-II-73 at α1, α2, and α3 subtypes were lower than at theα5 subtype at 1 μM, which indicated that this ligand is more α5 preferred. The Figure is modified from the PhD thesis, Guanguan Li, University of Wisconsin – Milwaukee, 2019……39

Figure 4. Verification of placements and response to pilocarpine. (A, Left) Representative brain slice containing an electrode track in the ventral tegmental area (VTA; black arrow) and cannula track in the ventral hippocampus (vHipp; white arrow) with a corresponding schematic of the brain section (right, −5.40 mm posterior to bregma). (B) Pilocarpine-treated rats exhibited significantly higher average Racine ratings (seizures) as compared to saline-treated controls, **** $p < 0.0001$, $n = 6–16$/group; circles denote male subjects and squares denote females.[6] ……..42

Figure 5. GL-II-73 reverses pilocarpine-induced increases in VTA dopamine neuronal activity. (A) Intra-ventral hippocampal (vHipp) pilocarpine significantly increased the number of spontaneously active dopamine cells per track (population activity), which was reversed by intra-vHipp administration of GL-II-73 (100 ng/μL; 0.75 μL). Average firing rate (B) and percent burst firing (C) were not changed by pilocarpine or drug treatment. (D) Representative trace of dopamine neuronal firing and action potential for saline-treated (left) and pilocarpine-treated (right) rats. ** $p < 0.005$, $n = 6–13$/group; circles denote male subjects and squares denote females.[6] ……..45

Figure 6. Pilocarpine does not alter total or synaptic α5 protein. There were no differences in total α5 protein expression. (A) Co-immunoprecipitation of α5 and gephyrin was used to measure synaptic α5 protein (B) between saline- and pilocarpine-treated rats. Representative bands from saline- (left) and pilocarpine-treated rats (right) are below graphs. n = 5 rats/group, circles denote male subjects and squares denote female rats. [6] ……47

Figure 7. Estimate maximum free brain concentrations of 5 mg/kg of GL-I-54 and 5 mg/kg of GL-II-73……80

Figure 8. Potentiation of GL-I-54 at α1-5-containing receptors in the presence of GABA. Figures were modified from Ashely et al. 2021 Electrophysiological of GL-I-54 and GL-II-73.

Electrophysiological recordings were obtained from HEK-293T cells transfected with full-length cDNA for human $GABA_A$ receptor subtypes α1β3γ2, α2β3γ2, α3β3γ2, α4β3γ2 or α5β3γ2, in presence of GL-I-54 (A) or GL-II-73 (B), and in the presence of GABA in the medium (5 μM)….81

Figure 9. The electrophysiological profile of GL-I-54 and GL-II-73 at α1-5-containing receptors in absence of GABA in the media Agonist effect or the lack thereof, GL-I-54 (A) and GL-II-73 (B) were tested in HEK-296. The cells expressing recombinant α1-5-$GABA_A$ receptors, in absence of GABA in the media, in order to test a potential agonist effect. As expected, neither GL-I-54 nor GL-II-73 induced potentiation at any of the receptors, confirming their role as allosteric modulators and not agonists. ……82

Figure 10. (A) The percentage of entries into open arms increased by GL-II-73, at 10 mg/kg in male mice and (B) at 5 and 10 mg/kg, the number of entries into enclosed arms of the elevated plus-maze (EPM; n=7-8/group). (C) In females, GL-II-73 increased the exploration of the open arms of the EPM at 10 mg/kg, (D) There was no change in the number of entries into enclosed arms (n=10/group). *$p<0.05$ vs. vehicle; EPM: one-way ANOVA followed by Tukey's test. Figures were modified from Souza et al. 2022[7] ……84

Figure 11. Male mice treated with GL-II-73 at 5 and 10 mg/kg, no correlation was found between the percentage of entries into the open arms and the number of entries into the enclosed arms of the EPM. Figures were modified from Souza et al. 2022. [7] ……85

Figure 12. GL-I-54 and GL-II-73 were then tested in the elevated plus maze and forced swim test at the dose of 5 mg/kg, in mice previously exposed to chronic restraint stress (CRS). Drugs were administered IP, 30 min prior to testing. Percent time spent in the open arms (A) and percent entries

into open arm (B) showed no difference between groups. Examination of the data on GL-II-73 versus GL-I-54 and vehicle, clearly showed anxiolytic active.[1] …….86

Figure 13. Forced swim test of GL-II-73……..87

Figure 14. Effect of GL-I-54 on time spent immobile in the FST. The ligand GL-I-54 at 5 mg/kg i.p. administered (24, 20, 1 h before testing) induced a significant antidepressant-like action when compared to the vehicle group (n = 9). ***p<0.001……..88

Figure 15. Time immobile showed more time spent immobile in the CRS-Vehicle group, and less time immobile in animals receiving GL-I-54, compared to CRS-Vehicle. ……88

Figure 16. Results of rotarod. The latency to fall was decreased by diazepam in the rotarod in (A) males and (B) females (n=5-10/group). No such effects were produced by GL-II-73. *p<0.05 vs. vehicle; Rotarod: Kruskal-Wallis test……89

Figure 17. independent mice were tested in the rotarod (H; N = 5 Control Vehicle and N = 6 GL-I-54). Mice were trained to maintain themselves on a rotating rod (rotarod) for 3 trials. Then, they were injected with GL-I-54 at 10 mg/kg, and tested 5 min, 20 min and 60 min past injection time. Latency to fall from the rod was recorded and showed significant reductions in latency to fall in mice receiving GL-I-54…….90

Figure 18. In the Y-maze, CRS induced an alternation rate deficit that was reversed by GL-I-54 at 10 mg/kg but not 5 mg/kg, suggesting the capacity of reversing spatial working memory deficits.92

Figure 19. Effect of acute treatment of GL-RM on anxiety. Time spent (A) and entries (B) in the open arms in the elevated plus maze. Figures were modified from Ashely et al. 2021[1] …….93

Figure 20. Effect of acute treatment of GL-RM on latency to approach (A) and latency to bite (B) in novelty suppressed feeding. Statistical analyses showed that acute GLRM treatment reduces latency to approach in mice subjected to UCMS. Figures were modified from Ashely et al. 2021.[1] ……95

Figure 21. Before initiating chronic stress and treatment, time spent in the food zone (A-B) and shelter zone (C-D) in the Phenotyper Boxes were recorded. In order to create an aversive stimulus, a light challenge was applied from 11pm to 12am, above the food zone. *p<0.05, **p<0.01, ***p<0.001 effect of UCMS, #p<0.05, ##p<0.01, effect of GL-RM. Figures were modified from Ashely et al. 2021.[1]……96

Figure 22. Residual avoidance score, UCMS subjected mice showed a significant increase in residual avoidance on statistical analyses. *p<0.05, **p<0.01, ***p<0.001 effect of UCMS, #p<0.05, ##p<0.01, effect of GL-RM. Figures were modified from Ashely et al. 2021……..97

Figure 23. Forced swim test and sucrose consumption paradigm to evaluate depressive-like and anhedonia-like behaviors. Statistical analyses did not reveal significant differences between groups in the force swim test (B). Chronic GL-RM treated group showed a significant increase in preference to sucrose in sucrose paradigm test (A). The impact of UCMS at increasing emotionality was significant that was confirmed by statistical analyses while combining the individual score into a global z-score (C), the chronic treatment of GLRM reduced emotionality. *p<0.05, **p<0.01, ***p<0.001 effect of UCMS, #p<0.05, ##p<0.01, effect of GL-RM. Figures were modified from Ashely et al. 2021[1]…….98

Figure 24. Evaluation of cognitive activity in the Y maze. UCMS altered the alteration rate in mice which was reversed by acute GL-RM treatment. *p<0.05, **p<0.01, ***p<0.001 effect of UCMS, #p<0.05, ##p<0.01, effect of GL-RM. Figures were modified from Ashely et al. 2021.[1]…….101

Figure 25. Prior to being subjected to 6 weeks of UCMS, the mice (both male and female) were tested at baseline in the Y-Maze, the phenotyper and the sucrose consumption test. Chronic treatment with GL-RM was initiated after 3 weeks of UCMS and the treatment was continued for a total of 4 weeks. The weight and coat state of the mice were measured weekly and mice were tested in the phenotyper test and the sucrose consumption assay weekly. *p<0.05, **p<0.01, ***p<0.001 effect of UCMS, #p<0.05, ##p<0.01, effect of GL-RM. Figures were modified from Ashely et al. 2021[1]……..102

Figure 26. Testing of mice in the elevated plus maze after 6 weeks of UCMS and 3 weeks of treatment. No significant statistical difference was observed in the time spent in open arms (A) and number of entries in the open arms (B), and the time spent (C) in the open field. *p<0.05, **p<0.01, ***p<0.001 effect of UCMS, #p<0.05, ##p<0.01, effect of GL-RM. Figures were modified from Ashely et al. 2021.[1]……..……..103

Figure 27. The number of entries in the inner zone (A). Mice were evaluated for latency to approach (B) and latency to bite (C) in the novelty suppress feeding test. *p<0.05, **p<0.01, ***p<0.001 effect of UCMS, #p<0.05, ##p<0.01, effect of GL-RM. Figures were modified from Ashely et al. 2021[1]……..104

Figure 28. The residual avoidance scores from week 3 to 6 in the Phenotyper test. UCMS showed a significant effect and a trend level of effect was observed by treatment. *p<0.05,

**p<0.01, ***p<0.001 effect of UCMS, #p<0.05, ##p<0.01, effect of GL-RM. Figures were modified from Ashely et al. 2021.[1]……..105

Figure 29. No significant differences between groups was revealed on statistical analyses in the forced swim test. *p<0.05, **p<0.01, ***p<0.001 effect of UCMS, #p<0.05, ##p<0.01, effect of GL-RM. Figures were modified from Ashely et al. 2021.[1]……106

Figure 30. A significant increase in preference to sucrose was observed in mice receiving chronic GL-RM in the sucrose consumption test (A). A significant impact of UCMS at increasing emotionality was observed while chronic GL-RM reduced emotionality (B). *p<0.05, **p<0.01, ***p<0.001 effect of UCMS, #p<0.05, ##p<0.01, effect of GL-RM. Figures were modified from Ashely et al. 2021.[1]……..……..107

Figure 31. GL-RM treatment reversed altered alternation with UCMS in the Y-maze task. *p<0.05, **p<0.01, ***p<0.001 effect of UCMS, #p<0.05, ##p<0.01, effect of GL-RM. Figures were modified from Ashely et al. 2021.[1] …….……..108

Figure 32. Spine densities of the basal and apical segment in the PFC of the hippocampus. Significant differences between groups in the basal and apical segments of PFC were revealed on ANOVA analysis. UCMS subjected mice showed decrease in spine densities, as compared to control mice that was partially reversed by chronic treatment with GL-RM. *p<0.05, **p<0.01, ***p<0.001 compared to “UCMS”; +p<0.05, ++p<0.01, +++p<0.001 compared to “Control”. Figures were modified from Ashely et al. 2021.[1] ……..109

Figure 33. Staining of brains with Golgi-Cox solution. Analysis of dendritic length, spine counts and spine density of pyramidal neurons (N=6 per mouse) from 4 mice (A-C). Scale bar in (A-C) represents 50µm.Figures were modified from Ashely et al. 2021.[1]……..110

Figure 34. Spine densities of basal and apical segments in the CA1 of the hippocampus. Significant differences between groups in the basal and apical segments of PFC was revealed on ANOVA analysis. UCMS subjected mice showed a decrease in spine density, as compared to control mice that was partially reversed by chronic treatment with GL-RM. *p<0.05, **p<0.01, ***p<0.001 compared to "UCMS"; +p<0.05, ++p<0.01, +++p<0.001 compared to "Control". Figures were modified from Ashely et al. 2021[1] ……..……..111

Figure 35. Correlation between morphological features from the PFC and the CA1 with the alternation rate (A-D). The positive correlation of basal (A) and apical (B) spines with the alternation rate, where higher density correlated with higher memory performances. Similar findings were also observed at basal and apical spine density from the CA1 (C-D)[1]……112

Figure 36. Maximum tolerated dose of SRE-II-11 in mice (Unpublished data) ……....114

Figure 37. Effect of 10mg/kg SRE-II-11 on percent alternation rate in the Y-maze spatial alternation task assessing working memory in mice. (Unpublished data) ……..115

Figure 38. Effect of 10 mg/kg SRE-II-11 on percent alternation rate in the Y-maze spatial alternation task assessing working memory in mice. (Unpublished data)……...116

Figure 39. Maximum tolerated dose of SRE-II-42 in mice (Unpublished data)……..118

Figure 40. Effect of 10 mg/kg SRE-II-42 on percent alternation rate in the Y-maze spatial alternation task assessing working memory in mice. (Unpublished data)…….……..119

Figure 41. Effect of 3 mg/kg SRE-II-42 on percent alternation rate in the Y-maze spatial alternation task assessing working memory in mice. (Unpublished data)……...120

Figure 42. Maximum tolerated dose of SRE-II-59 in mice (Unpublished data)……..122

Figure 43. Effect of SRE-II-44 on percent alternation rate in the Y-maze spatial alternation task assessing working memory in mice. (Unpublished data)……123

Figure 44. Maximum tolerated dose of SRE-III-07 in mice (Unpublished data)……...125

Figure 45. Effect of analogs of GL-I-54 on sensorimotor coordination. Mice were placed on the rotarod at three separate time points of 10, 30, and 60 minutes after each oral gavage drug administration at 40 mg/kg. Their performance on the rotarod for 3 minutes was recorded and analyzed. After a second fall, it would be considered a fail, and that time point would be recorded. (Unpublished data)……...……126

Chapter 3: Design and Synthesis of Achiral α2/3 Ligands for Anxiety, Epilepsy, and Pain: Large Scale Synthesis of Hz-166 and Analogs

Figure 1. Structures of HZ-166, KRM-II-81, and MP-III-080……...……186

Figure 2. The $GABA_AR$ α2/3β3γ2 subtypes are pentameric ligand-gated chloride channels. IBDZs (HZ-166 and KRM-II-81) mediate their effects at the DS-Bz site (α2/3+γ2- interface) as positive allosteric modulators (PAMs). Image modified from Jacob et al., Nature Reviews Neuroscience, 2008.[8]……..187

Figure 3. Average enhancement of the current evoked to GABA EC3 by 0.1 μM (α1, α2, α3, α5) or 1 μM (α4, α6) of either diazepam or KRM-II-81. This figure was redrawn from Cerne et al. 2021.[9]……...……188

Figure 4. Alprazolam vs KRM-II-81 at the α+γ- interface of the GABAA receptor. (A) Alprazolam (orange) in the complex with the α1β3γ2L GABAA receptor 6HUO. (B) KRMII-81

docked (sandy brown) in the complex with the α1β3γ2L GABAA receptor 6HUO. α1 (aquamarine); γ2 (orchid) subunit. Dashed lines indicate π-π, hydrogen bond and halogen bond interactions. Data are modified from (Witkin et al., 2020, Golani, Mian et al 2021)[4,10]…....189

Figure 5. Structures of ZK-III-51, ZK-III-56 and ZK-III-58 made by MdZubair Ahmed Khan...198

Figure 6. Enlarged cryoEM structure of the human full-length α1β3γ2L $GABA_A$ receptor ion complex with Diazepam (yellow) using AutoDock Vina……..201

Figure 7. Overlay of the docked conformations of [A. Alprazolam (gold) and 4 (cadet blue) and B. Alprazolam(gold) and 5 (cadet blue)], in the complex with the α1β3γ2L $GABA_A$ receptor 6HUO at the α+β- interface BZ binding site [α1 (represented as chain D, color: aquamriane) and γ2 (represented as chain C, color: orchid)], dashed lines indicate hydrogen bonds……..202

Figure 8. Structures of ZK-IV-04, ZK-IV-05 and ZK-IV-07 made by Md Zubair Ahmed Khan.204

Figure 9. Structures of potential ZK series compounds, which were resynthesized in the present work…….205

Figure 10. Effect of ligands ZK-III-51 (4), ZK-III-56 (5) and ZK-III-58 (7) on sensorimotor coordination. Mice were placed on the rotarod at three separate time points of 10, 30, and 60 minutes after each oral gavage drug administration at 40 mg/kg. Their performance on the rotarod for 3 minutes was recorded and analyzed. After a second fall, it would be considered a failure, and that time point would be recorded. ZK-III-58 (7) shows sedation…….224

Figure 11. Rotarod studies ZK-III-51 (4), ZK-III-56 (5) and ZK-III-58 (6) at 120, 120, and 40 mg/kg dose respectively. Diazepam is the control. Confidential and unpublished data……..225

Figure 12. Relationship of potencies of compounds to bind benzodiazepine receptors vs. kappa opioid receptors. Direct structural analogs are shown in matching colors; non-structurally

related analogs are in black. Bold = Bromine analog; non-Bold = Ethynyl analog. Only the 9 compounds shown on the regression line were used for computing the linear regression. (Unpublished data)……...230

Figure 13. Effects of compounds (p.o., 2 h prior) on clonic (left) and tonic (right) seizures induced by PTZ (75 mg/kg, s.c.). The latency to exhibit convulsions are shown for each animal tested. Means and S.E.M. of those data are shown for each compound as a horizontal red line and error bars. * $P < 0.05$; ** $P < 0.01$; *** $P < 0.001$ compared to vehicle values by Dunnett's test. (Unpublished data)……...231

Figure 14. Pharmacokinetics of ZK-III-58 in plasma and brain after oral administration of 2.0 mg/kg in rats. Each point represents the mean $\pm$ standard error of the mean in three rats. AUC: area under the curve from 0 -24 h; C_{max}: maximal concentration achieved; T_{max}: time of maximum concentration; $t_{1/2}$ - terminal elimination half-life. (Unpublished data)……234

Figure 15. Pharmacokinetics of ZK-IV-07 in plasma and brain after oral administration of 2.0 mg/kg in rats. Each point represents the mean $\pm$ standard error of the mean in three rats. AUC: area under the curve from 0 -24 h; C_{max}: maximal concentration achieved; T_{max}: time of maximum concentration; $t_{1/2}$ - terminal elimination half-life. (Unpublished data)……235

Figure 16. Pharmacokinetics of ZK-III-56 in plasma and brain after oral administration of 2.0 mg/kg in rats. Each point represents the mean $\pm$ standard error of the mean in three rats. AUC: area under the curve from 0 -24 h; C_{max}: maximal concentration achieved; T_{max}: time of maximum concentration; $t_{1/2}$ - terminal elimination half-life. (Unpublished data)……236

Figure 17. Pharmacokinetics of ZK-III-51 in plasma and brain after oral administration of 2.0 mg/kg in rats. Each point represents the mean $\pm$ standard error of the mean in three rats. AUC:

area under the curve from 0 -24 h; C_{max}: maximal concentration achieved; T_{max}: time of maximum concentration; $t_{1/2}$ - terminal elimination half-life. (Unpublished data)…….237

Figure 18. Relationship of plasma and brain concentrations of compounds. Dotted lines show boundaries of compounds with relatively low vs. high plasma and brain levels. Direct structural analogs are shown in matching colors; non-structurally related analogs are in black. Bold = Bromine analog; non-Bold = ethynyl analog. (Unpublished data)……..……..239

Figure 19. Relationships of compound parameters to antiseizure efficacy. Top panels: linear regression analysis of the two parameters that were associated with tonic seizure latency. Bottom panel: tonic seizure latency as a function of the brain concentration of compounds as assessed over 24 h (AUC)…….240

Chapter 4: Design and Synthesis of α5 Subtype Selective GABA(A)ergic Ligands for Treatment of Different Types of Cancer

Figure 1. Comparison of the various subgroups of medulloblastoma including their affiliations with previously published papers on medulloblastoma molecular subgrouping……..…..269

Figure 2. Structures of the lead compounds, QH-II-066 and KRM-II-008……...…….274

Figure 3. QH-II-066 at α+ γ - Interface of $GABA_A$ Receptor in the α1β3γ2 em cryostructure (Nature 2019)……..……275

Figure 4. KRM-II-008 (19) at the α + γ - Interface of $GABA_A$ Receptor…….……..276

Figure 5. The efficacy of ligands expressed in HEK, α1-6,β3γ2 GABA ion channels with EC3 GABA. ……..……..……277

Figure 6. The potency of the ligands……...……279

Figure 7. GABR expression MYC and in medulloblastoma and evidence for a functional α5-GABAA receptor in patient cell lines Daoy, D283, and D425 a. qRT-PCR of N-MYC (left) and MYC (right). b. in D283 qRT-PCR of GABR expression……..……..283

Figure 8. The structures of compounds for comparison in treatment of medulloblastoma (A) Structurally α5 subtype selective benzodiazepine(B) The structures of the standard-of case treatment compounds. JQ1 shares a similar structural similarity as the ligand SH-I-75……...284

Figure 9. Representative images of D425 and DAOY tumor sections removed 24 hours after exposure to a microdose of each drug from the device, showing distinct regions of apoptosis assessed by cleaved-caspase-3 expression (brown) after 24 hours. Scale bars, 250 μm. (B) Apoptotic index (%apoptotic cells/all cells in drug-affected tissue region) for human D425 and DAOY tumors exposed to KRM-II-08, SH-I-75, QH-II-066, JQ1, mebendazole and cisplatin (all 35% drug in PEG1450). Averages are taken from 6 spatially distinct reservoirs from at least 3 tumors please give ($p < 0.01$)……..285

Figure 10. The molecular imaging of compound distribution in MALDI FTICR mass spectrometry. The distribution of three drugs in sections of a mouse flank tumor with an implanted device via Matrix-assisted laser desorption/ionization Fourier-transform ion cyclotron resonance (MALDI FTICR) mass spectrometric imaging (MSI): (A) KRM-II-008 (m/z 293.1084); (B) QH-II-066 (m/z 275.1178); and (C) a fragment of JQ1 (m/z 401.0834)…...286

Figure 11. GABA(A) receptor subunit gene expression in lung cancers.[2]……..……..295

Figure 12. AM-101 or QH-II-066 (1) (left and single cell patch clamp electrophysiology trace of patient-derived adenocarcinoma lung cell line H1793 (right) ……..…..……..296

Figure 13. Lung adenocarcinoma (H1792) cells incubated with QH-II-066 are depolarized, as assessed by the TMRE assay and Fluorescence Activated Cell Sorting (FACS) analysis. Shown is the degree of depolarization relative to treatment with DMSO alone treatment and FCCP, which provide negative and positive controls in this experiment, respectively.[2]……..……..297

Figure 14. Effect of AM-101 and diazepam on survival of non-small cell lung cancer cells

4.6.3. GABA(A) receptor activation potentiates radiation by Drs. Bhattacharya,Krummel, Sengupta and coworkers[2]……..……...300

Figure 15. GABA(A) receptor activation potentiates radiation.[2]……..……...303

Figure 16. Human-relevant ex vivo 'lung-on-chip' data. [2]…….....304

Figure 17. Mouse xenograft experiments[2]……...305

Figure 18. GABA(A) receptor activation increases survival of mice bearing lung brain metastatic tumors.[2]…….……...308

Figure 19. Benzodiazepines depolarize cancer cells. (Unpublished data)……..…….309

Figure 20. In vivo test for different benzodiazepine analogs in LLC tumor growth. (Unpublished data) ……..……...312

Figure 21. MTS cell proliferation/cytotoxicity assays. A375 = Human melanoma, H1792 = Human Lung cancer, LN18 = Human glioblastoma, and LLC = mouse lung carcinoma cell lines. (Unpublished data)……...…314

LIST OF TABLES

Chapter 1. Introduction

Table 1. The CNS effects at $GABA_A$ $\alpha_{1-6}\beta_{1-3}\gamma_2$ receptor subtypes.[18, 46-58] Presented at the Mona Symposium (2014), University of the West Indies.[59] Earlier reported, in part, by Mckernan et al. (ACNP)……8

Table 2. Binding Affinities at α1-3 and α5 human $GABA_A$ R subtypes……23

Table 3. Binding Affinities at α1-3 and α5 human $GABA_A$ R subtypes……24

Table 4. The sequence alignment of α1-6 subunits. ……..……26

Chapter 2. Design and Synthesis of Chiral α5 Subtype Selective GABA(A)ergic Ligands for Schizophrenia, Depression and Alzheimer's Disease

Table 1. Binding affinity of SH-053-2'F-R-CH3 at αxβ3γ2 GABAA/benzodiazepine site subtypes. Measurements were made in duplicate. Ki values are reported in nM……..36

Table 2. Efficacy of SH-053-2'F-R-CH3 at αxβ3γ2GABAA receptor subtypes as % of control current at 100 nM and 1 μM concentrations……..37

Table 3. Binding affinity of GL-II-73 at αxβ3γ2 GABAA/benzodiazepine site subtypes……38

Table 4. Comparison of cost of benzodiazepine produced by NCA route and Boc route……63

Table 5. Statistical significance of potentiation between the different α-subunits; EC3……..…77

Table 6. Statistical significance of potentiation between the different α-subunits; EC3…..……78

Table 7. Comparative metabolic stability of GL-II-73 and GL-I-54 in a liver microsomal assay(C57BL6 mouse)……...……91

Table 8. Binding affinities at hERG, only the C-8 cyclopropyl compounds among the entire compound library have slight affinity to hERG (PDSP). Unpublished data…….…….128

Table 9. Binding affinities at peripheral benzodiazepine receptor (PBR) for the novel compounds (PDSP). Unpublished data……130

Table 10. KOR binding affinity from the primary binding assay. Unpublished data. (PDSP)...132

Table 11. BZR binding affinity from the primary binding assay. Unpublished data. (PDSP) ..133

Chapter 3: Design and Synthesis of Achiral α2/3 Ligands for Anxiety, Epilepsy, and Pain: Large Scale Synthesis of Hz-166 and Analogs

Table 1. Effect of KRM-II-81 and it's analogs in different pain model……..191

Table 2. Effects of KRM-II-81 and it's analogs in different models of epilepsy……..193

Table 3. Docking score (computed binding affinity) of bioisosteric ligands……..199

Table 4. Cytotoxicity studies of ligands in HEK 293 cell lines. (Unpublished data)…….…226

Table 5. Receptor binding profile of KRM-II-81 analogs. (Unpublished data)……..228

Table 6. Protection against lethality induced by 75 mg/kg PTZ (s.c.) after oral administration (60 min prior) of test compounds in male, C57BL/6N mice. (Unpublished data)……..232

Table 7. Plasma and brain concentrations of compounds at C_{max} and brain/plasma ratios. (Unpublished data)……...238

Chapter 4: Design and Synthesis of α5 Subtype Selective GABA(A)ergic Ligands for Treatment of Different Types of Cancer

Table1. Cytotoxicity data of the lead ligands in HEK293T and HEPG2 cells……....278

Table 2. The IC50 value of the ligands in D283 cell line. ……..…....279

Table 3. Viability of lung adenocarcinoma cells……...…....299

Table 4. IC_{50} (μM) ……..……....310

Table 5. Binding affinities at hERG (PDSP). Unpublished data. ……....……....317

Table 6. Binding affinities at PBR (PDSP). Unpublished data. ……....318

Table 7. Binding affinities at KOR (PDSP). Unpublished data. ……..…..……....319

Table 8. Binding affinities at BZR (PDSP). (Rat brain homogenates are sysnaptosomal membranes containing all 6 benzodiazepine / GABA(A) subtypes) Unpublished data. ……..……....320

LIST OF SCHEMES

Chapter 2. Design and Synthesis of Chiral α5 Subtype Selective GABA(A)ergic Ligands for Schizophrenia, Depression and Alzheimer's Disease

Scheme 1. Synthesis of SH-05-2'F-S-CH_3…….50

Scheme 2. Synthesis of SH-I-47……...…….52

Scheme 3. Synthesis of GL-I-54……...…….54

Scheme 4: Possible mechanism of chlorination of SH-053-2'F-S-CH_3 acid…….55

Scheme 5. Cyclization of free amine to form benzodiazepine 4……..…….56

Scheme 6. Possible mechanism of racemization of benzodiazepine, 3…….56

Scheme 7. Improved synthesis of GL-I-54…….58

Scheme 8. Synthesis of benzodiazepine intermediate by NCA route……..…….59

Scheme 9: Possible mechanism of imidazole top installation on benzodiazepine 4……..60

Scheme 10. Peptide coupling and cyclization for formation of benzodiazepine, 4……..62

Scheme 11. Synthesis of GL-I-54 with Boc route…….....64

Scheme 12: Synthesis of analogs of SH-I-48B…….66

Scheme 13. Synthesis of the 2'Cl imidazodiazepine intermediate ……..……..68

Scheme 14. Synthesis of 8-cyclopropyl analogs……..……..70

Scheme 15. Amide analogs of GL-I-54……..…….……..71

Scheme 16. Synthesis of amide analogs ……..…….……..72

Scheme 17. Synthesis of SRE-II-48……..……..…….……..73

Scheme 18. Synthesis of the oxazole analog, SRE-II-07……..……..74

Scheme 19. Synthesis of the enantiomer of MYM-V-28, SRE-III-07…….…..……..75

Chapter 3: Design and Synthesis of Achiral α2/3 Ligands for Anxiety, Epilepsy, and Pain: Large Scale Synthesis of Hz-166 and Analogs

Scheme 1. Synthesis of the key intermidate by Li et al. 2018[11]…….206

Scheme 2. Possible Route to Bromoacetamide via the Pyridium Salt……..….207

Scheme 3. Route for the formation of the imidate impurity…….……208

Scheme 4. Synthetic route of the key imidazodiazapine. …….210

Scheme 5. Formation of Benzodiazepine by the Delepine- related Reaction[12–14]…….211

Scheme 6. Possible mechanism of the Delepine reaction…….213

Scheme 7. Probable mechanism of installation of imidazole top on benzodiazepine…….215

Scheme 8. Synthesis of Hz-166……216

Scheme 9: Possible mechanism for copper free Sonogashira coupling……..…..217

Scheme 10. Possible mechanism for fluoride mediated deprotection of the TIPS group…...…218

Scheme 11. Synthetic route to make oxazolines ZK series…….220

Scheme 12. Synthetic route to make oxazoles in the ZK series……..……221

Scheme 13. Proposed mechanism for the oxazole forming reaction for ZK-III-58……....222

Chapter 4: Design and Synthesis of α5 Subtype Selective GABA(A)ergic Ligands for Treatment of Different Types of Cancer

Scheme1. Synthesis of the key intermediate for the lead compounds 1 and 2……..…….288

Scheme2. Synthetic route to make the lead compounds QH-II-066 (1) and KRM-II-008 (2)…...290

Scheme 3. Structure of analogs of QH-II-066……..291

Scheme 4. Synthesis of cyclopropyl analogs to replace a 7-ethynyl group ...……..……..292

Scheme 5. Synthetic route to make D3-analogs……..293

Scheme 6. Synthetic route to make the D3 and D5 analogs……..……293

LIST OF ABBREVIATIONS

ACh	acetylcholine
AHR	airway hyperresponsiveness
AP-4	4-Aminopyridine
ASM	airway smooth muscle
BALF	bronchoalveolar lavage fluid
BBB	blood-brain-barrier
BQL	below the quantification limit
BZD	benzodiazepine
BzR	benzodiazepine receptor
CFA	complete Freund's adjuvant
CDAP	chlordiazepoxide
CINP	Chemotherapy-induced neuropathic pain
CMC	carboxymethyl cellulose
CNS	central nervous system
COPD	chronic obstructive pulmonary disease
CRS	chronic restraint stress
DI	diazepam-insensitive
DLM	dog liver microsomes
DNP-KLH	dinitrophenyl hapten-keyhole limpet hemocyanin
DS	diazepam-sensitive
ETSP	Epilepsy Therapy Screening Program
FDA	Food and Drug Administration

FST	forced swim test
GABA	gamma-aminobutyric acid
$GABA_AR$	gamma-aminobutyric acid type A receptors
$GABA_BR$	gamma-aminobutyric acid type B receptors
GINA	Global Initiative for Asthma
hERG	human Ether-à-go-go-Related Gene
HEK	human embryonic kidney cells
HDM	house dust mite
HLM	human liver microsomes
HPLC	high-performance liquid chromatography
ICSS	ICSS
IMDZ	imidazodiazepine
IgG	immunoglobulin G
IP	intraperitoneal
IV	intravenously
KA	kainic acid
KOR	kappa opioid receptors
LABA	long-acting β_2 agonist
LR	Lawesson's reagent
LTG	lamotrigine
MAM	methylazoxymethanol acetate
MCh	methacholine
MDD	major depressive disorder

MED	minimal effective dose
MES	maximal electroshock
MLM	mouse liver microsomes
MOE	Molecular Operating Environment
MPE	maximum possible effect
MRM	multiple reaction monitoring
MTD	minimal toxic dose
mTLE	mesial temporal lobe epilepsy
MW	molecular weight
NAM	negative allosteric modulator
NIMH	National Institute of Mental Health
NO	nitric oxide
NMDA	*N*-methyl-D-aspartate
Ova s/c	ovalbumin sensitized challenged
PAM	positive allosteric modulator
PBR	peripheral benzodiazepine receptor
PCLS	precision-cut lung slice
PCP	phencyclidine
PDSP	Psychoactive Drug Screening Program
PEG	polyethylene glycol
PFC	mouse prefrontal cortex
PI	protective indices
PK	pharmacokinetics

PPI	prepulse inhibition
PTZ	pentylenetetrazole
PWT	paw withdrawal threshold
PO	oral administration
RLM	rat liver microsomes
SABA	short-acting β_2 agonist
SAR	structure-activity relationship
scMET	subcutaneous pentylenetetrazole
SE	severe epilepsy
SEM	standard error of the mean
SLA	spontaneous locomotor activity
SNL	sciatic nerve ligation
SSRI	selective serotonin reuptake inhibitors
sRaw	specific airway resistance
SST	somatostatin
TLC	thin-layer chromatography
TLE	temporal lobe epilepsy
TPE	time of peak effect
TSPO	translocator protein
UCMS	unpredictable chronic mild stress

ACKNOWLEDGMENTS

I am profoundly grateful to my esteemed advisor, Professor James M. Cook, for his exceptional guidance, unwavering support, and invaluable mentorship throughout my marvelous doctoral journey. His expertise, insightful feedback, and commitment to excellence have been instrumental in shaping this dissertation as well as my papers and patents. I would also like to thank the members in my doctoral committee, Professor's Alan W Schwabacher, Arsenio Andy Pacheco, Mark Dietz and Xiaohua Peng for their guidance, valuable suggestions, instructive discussions, and constructive criticism. I extend my gratitude to our numerous collaborators, from whom I have gained extensive knowledge and substantial insights in the fields of pharmacology and medicinal chemistry. Special appreciation goes to Dr. Jeff Witkin (Ascension St. Vincent Hospital, Indianapolis, IN), Dr. Etienne Sibille (CAHM, University of Toronto, Canada), Dr. Tom Prevot (CAHM, University of Toronto, Canada), Soma Sengupta (University of North Carolina), Daniel A. Pomeranz Krummel (University of North Carolina), Donatien Kamdem Toukam (University of Cincinnati College of Medicine) Miroslav M Savić (University of Belgrade, Serbia), , Dr. Donna M. Platt (Mississippi Medical School, USA), Dr. Charles W. Emala (Columbia University, USA), Dr. LC Chiou (Taiwan University, Taiwan), Dr. Kiyoshi Egawa (Hokkaido University, Japan), Dr. Bradford Fisher (Cooper Medical School of Rowan University, USA), Dr. Katarzyna Kuter (Polish Academy of Sciences, Poland), and Dr. David White (NIH). Their collaborative efforts have significantly contributed to my personal and professional development in these research areas.

I am thankful for the past and present members of the Cook group. It has been a great pleasure to be a part of this excellent group. I thank the former members in the group, Dr. Guanguan Li, Dr. Daniel Knutson, Dr. V. V. N. Phani Babu Tiruveedhula, Dr. Tofique Rahman,

Dr. Rajwana Jahan, Dr. Md Zubair Ahmed Khan, Dr. Farjana Rashid, Dr. Lalit Golani, Dr. Md Yeunus Mian, Dr. Kamal Pandey and Dr.Taukir Ahmed; for their great help on introducing me to many research techniques, modeling and skills in organic chemistry, which benefited me throughout my Ph.D. years here. I would like to thank all the current group members Dr. Dishary Sharmin, Prithu Mondal and Morteza Panahzadeh for creating an awesome environment in helping each other as much as one can in this group and for bringing extra fun (FOOD) for our Saturday group meetings. I would also like to thank Michelle Meyer (Arnold group, for cytotoxicity and rotarod), Anika Tylek (Arnold group, for rotarod).

I would like to acknowledge the financial and academic support of the Department of Chemistry at UW-Milwaukee, the UW-Milwaukee Graduate School. I express deep gratitude to Dr. Frank H Holger for his invaluable help for NMR, and Mr. Neal Korfhage for the design and fabrication of very specialized glassware. I greatly appreciate Dr. Anna Benko for her outstanding expertise and support during the last couple of years for help with mass spectroscopy. I would also like to thank Dr. Shama Mirza and Dr. Vilashini Rajaratnam for their help in the analysis of mass spectra. I would also like to thank Mr. Kevin Blackburn, Ms. Elise D. Nicks, Ms. Wendy Grober, Ms. Shelley Hagen, Ms. Bailey Hewitt for their unwavering support and willingness to assist whenever I needed help.

I express my heartfelt gratitude to my parents, sisters, friends and my dog, Twix, for all their unconditional love, invaluable support and encouragement throughout my life from day one. I would never be able to accomplish this hard task without their help, support, respect, blessing, and trust.

And last but not least, I would like to express my deepest gratitude to my husband, Mohammad Khamechian, whose unwavering support and understanding have been the cornerstone of my

journey through the challenges and triumphs of pursuing a Ph.D. His encouragement, patience, and belief in my abilities have been a constant source of inspiration, providing the emotional fortitude needed to navigate the demands of academic life.

Chapter 1. Introduction

1.1. The $GABA_A$ receptors

Gamma-aminobutyric acid (GABA) is an amino acid that functions as an inhibitory neurotransmitter in the human brain by decreasing neuronal signals in the Central Nervous System (CNS) and decreasing overall neuronal activity. It occurs naturally in the human body [151]. Gamma-aminobutyric acid (GABA) produces a calming effect when it attaches to a protein ion channel in the brain (GABA receptor). There are two main classes of GABA receptors: $GABA_A$ receptors ($GABA_AR$) and $GABA_B$ receptors ($GABA_BR$). The latter is not discussed in this thesis. $GABA_A$-rho receptors ($GABA_CR$) are now considered to be a subtype of $GABA_ARs$[216]. The $GABA_A$ receptors ($GABA_ARs$) are found in the chloride channels of integral membrane proteins known as ligand-gated ion channels (LGICs). These channels enable fast synaptic transmission in the nervous system and somatic neuromuscular junction, taking place in milliseconds (0.001s) and are considered as fast-acting transmembrane receptors[173]. When activated, $GABA_A$ receptors ($GABA_ARs$) cause a suppression of neuronal transmission by hyperpolarizing the electrochemical gradient in the chlorine channel[184]. In contrast, the $GABA_BRs$ are slow-acting receptors that modulate the activity of potassium and calcium channels[195]. The available literature suggests that the $GABA_ARs$ in the central nervous system are involved in a variety of neurological disorders, including schizophrenia,[206] anxiety disorders,[217] epilepsy[22],[8] Angelman syndrome, autism, cognition, neuropathic pain disorders,[239] and clinical depression. Numerous researchers have reported a potential relationship between the $GABA_AR$ and CNS diseases and attribute its pharmacological benefits to the specific combination of $GABA_AR$ subunits found in the CNS.[2410] Of the total nineteen subunit isoforms found in mammals (α1-6, β1-3, γ1-3, δ, ε, π, θ, ρ1-3),[11] $GABA_ARs$ typically consist of α, β and γ2 subunits (α1-6β1-3γ2) in a stoichiometric ratio of 2:2:1.[2]

This stoichiometry is necessary for complete allosteric function by benzodiazepines at the α-γ2 interface.

Immunocytochemistry combination of the α, β and γ subunits in rodents have shown that there are different distributions of $GABA_AR$ assemblies in the central nervous system of these animals.[12] The $GABA_AR$ subunits are highly abundant throughout the rodent brain, both as synaptic and extra synaptic receptors.[13] Of all the $GABA_A$ receptors in the rat brain, about 50-60% consist of the α1β2γ2 subunit combination, while other subunits are present in lower percentages.[13-15] For example, α2 and α3 subunits are present at around 20-30% and the α5 subunit at around 5%.[13-15] In addition to the brain, there is also evidence of the presence of $GABA_A$ receptors in other bodily tissues such as the sinoatrial node of the heart, intestines, lungs, stomach, etc. The β2 and β3 subunits can be interchanged without loss of efficacy and binding affinity, to date.

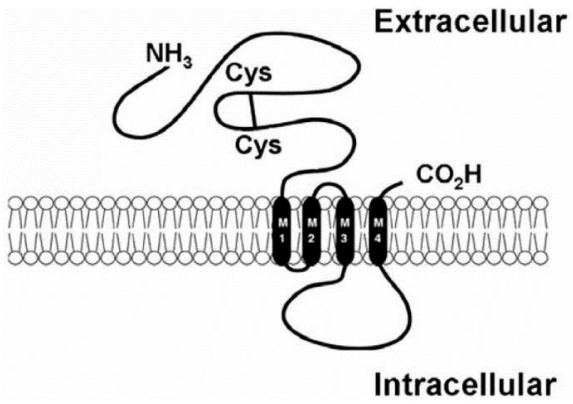


Figure 11. A proposed $GABA_AR$ subunit topology. The extracellular domain starts with the N-terminal end, and the M1-M4 are regions within the membrane. (Modified from the Figure in Burt, et al. [16] and Clayton, et al.)[17]

A $GABA_AR$ subunit has a molecular mass of about 50 kD and is a receptor structure characterized by high homology. As shown in Figure 1, a suggested $GABA_AR$ subunit topology starts with the extracellular domain at the N-terminal end, and the M1-M4 regions are within the membrane. (Adapted from the Figure in Burt[25], et al. and Clayton, et al[26].), Each receptor subunit of the $GABA_AR$ has four transmembrane domains (M1-M4) in the lipid bilayer of the neuron. The N- and C-terminals of the $GABA_ARs$ are situated outside the cell membrane and may include possible glycosylation sites. Additionally, there is a Cys-loop enabled by a disulfide bond at the N-terminal end. Beneath the membrane, there is a large intracellular region between M3 and M4 that is mainly responsible for regulating $GABA_AR$ activity at phosphorylation sites. Five monomeric $GABA_AR$ subunits arranged in a ring shape form a hetero- or homo-pentameric chloride channel.[17-18]

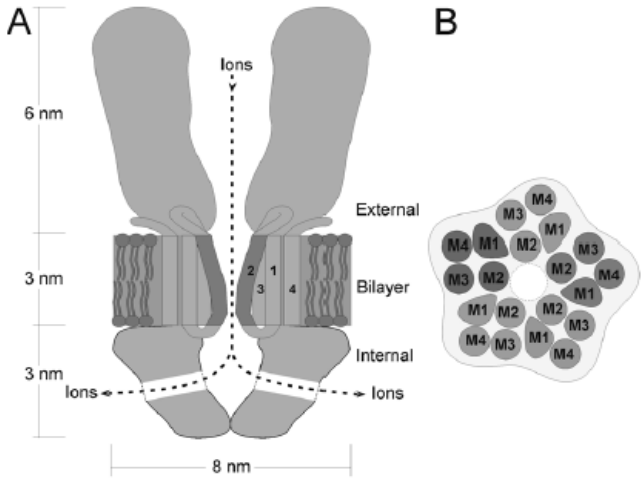


Figure 12. The schematic representations of $GABA_AR$, the ligand-gated chlorine ion channel in longitudinal vision (A) and cross-sectional vision (B). The number 1-4 represents the M1-M4 transmembrane domains. The domain M2 contributes to most of the pore lining within the lipid bilayer membrane. (Modified from the Figure in Keramidas et al.[18], and Clayton et al.)[17]

It is well established in the literature that $GABA_AR$s have multiple binding sites for psychoactive compounds such as benzodiazepines, anesthetics, barbiturates, neurosteroids, ethanol, etc. at the synapse and synaptic ion channels.[1-2, 10, 14, 17] Illustrated in **Figure 3** is the clockwise arrangement of the αβαβγ subunits in the extracellular region. This view clearly shows the binding sites of the $GABA_AR$.[1, 2, 7, 17] While benzodiazepines bind at the γ-α+ interface,[1, 2, 7, 17] GABA binds at the two α-β+ interfaces. Another interface of interest is the β-α+ interface, which has been recently reported as a binding site for the subtype-selective compound CGS 9895 (PQ).[17,19,20] Moreover, the receptor at this site has been found to be α6-selective.[21-23] Additionally, barbiturates[1-2, 15] and ethanol[24-25] can also bind in the intra-channel region to enhance the response, which can also open the pores directly. This increases the risk of addiction and death.[1-2, 14-16]

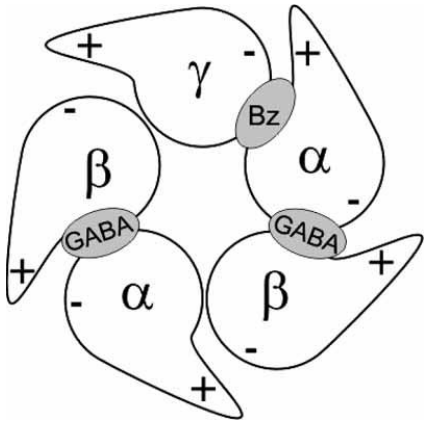
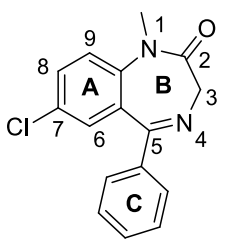


Figure 13. The arrangement of the α1β3γ2 $GABA_AR$ subtype as viewed from the synaptic cleft. The binding sites of GABA are located at the interfaces between β^+ and α^- subunits and the BZD binding site is located at the interface of the $\alpha^+\gamma^-$ subunits. The + represents the loop C of each subunit. (Modified from the Figure in Clayton, et al.[18] and Ernst, et al.)

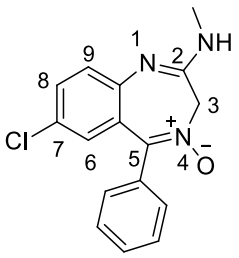
1.2. Benzodiazepines (BZDs)

Benzodiazepines (BZDs) are a class of drugs that are commonly prescribed by doctors to treat a variety of conditions. In the United States, the Food and Drug Administration (FDA) has approved benzodiazepines for the treatment of insomnia, anxiety disorders (generalized and social), seizure disorders (e.g., epilepsy) and panic disorder. These drugs have been used to treat these conditions for over 50 years in the US. Other uses of benzodiazepines include treatment of sleep disorders, bipolar disorder, and management of alcohol withdrawal.

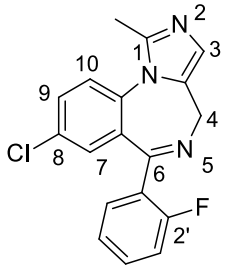
BZDs were first discovered by Leo Sternbach in 1955. One of the most well-known, widely used, and commercially successful BZD drugs is diazepam or Valium, which was first marketed in 1963. The commercial success of diazepam can be attributed to its potency and low toxicity. and its fast and efficient penetration of the blood-brain barrier, minimal drug-drug interactions within the liver, rapid absorption in the gastrointestinal tract and efficient distribution within the brain. Some common BZD structures are illustrated in **Figure 4**, all of which share common features: a core of a benzene ring attached to a diazepine ring, which is attached to a pendant C ring.



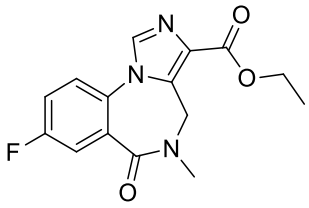
diazepam (Valium)



chlordiazepoxide (Librium)



midazolam (Versed)



flumazenil (Romazicon)

Figure 14. The structures of common BZDs: diazepam, chlordiazepoxide, imidazodiazepine (IMDZ) midazolam and flumazenil (antagonist). The atoms are labeled for both BZDs and IMDZs. Diazepam, chlordiazepoxide, and midazolam can bind only to the DS sites, whereas flumazenil can bind to both the DS and DI sites.

Generally, benzodiazepines including those shown in **Figure 4**, as well as alprazolam have high, non-selective affinity for the $GABA_AR$ at the BZR binding site at the γ-α+ interface. Thus, the pharmacological properties of the BZDs are primarily dependent on the α and γ subunits rather than the β subunits. The current evidence suggests that BZDs interact most prominently with the α1-3,5β2/3γ2 subtypes of the $GABA_ARs$ and less effectively with the γ1,3 subtypes. The α4 and α6 subtypes are not highly sensitive to BZDs. These subtypes do not bind well with diazepam (1,4-benzodiazepine) and midazolam (imidazodiazepine), but readily bind with drugs like flumazenil. This is due to the absence of the pendent phenyl C ring in the flumazenil structure (**Figure 4**) and are called diazepam-insensitive (DI) sites. In the α4 and α6 ligands the lipophilic pocket in those ion channels is too small to accommodate the c-ring.

A BZD cannot modulate the $GABA_AR$ by itself without the presence of GABA. Instead, the binding of a BZD to the $GABA_AR$ ion channel enhances the affinity of GABA to the receptor, resulting in hyperpolarization of the neuronal membrane electric potential. This is how BZDs are able to reduce neuronal firing frequency, which leads to various pharmacological effects such as anticonvulsant effects, ataxia, anxiolytic effects, as well as ataxia, sedation, and amnesia. These properties have made BZDs the preferred drug for various CNS disorders, such as GAD, SAD, PTSD, status epilepticus, and panic disorders. However, BZDs also have undesirable effects on the human body, some of which can be attributed to their non-selective binding and efficacy at

other $GABA_ARs$. Common adverse effects of BZDs include sedation, amnesia, ataxia, addiction, dependence, fatigue, withdrawal, muscle-relaxation, and the development of tolerance to the anticonvulsant and antinociceptive effects. Therefore, there is a need for research and improvements in BZD drugs. The goal is to design better drugs for CNS disorders with similar or better pharmacological effects to BZDs but with minimal side effects.

1.3. Modulation of BZDs on the Pharmacological Effects of $GABA_AR$

Over the years, strong evidence has emerged confirming that the pharmacological effects of $GABA_ARs$ are dependent upon the modulation of different receptor subtypes, primarily the alpha (α) subunits. The pharmacological effects associated with each subunit have been determined by receptor binding, pharmacological methods, and a molecular genetic procedures by introducing a point mutation into the respective α subunits. This groundbreaking work was carried out by Mohler, Sieghart, McKernan, Sigel, Seeburg, Squires, and Haefely. This process involves replacing the histidine amino acid with an arginine amino acid in the subunit: (α1His101Arg, α2His101Arg, α3His126Arg, and α5His105Arg). Animals with these mutations were administered diazepam and the behavioral response was ablated. Any changes in the response compared to untreated animals were attributed to the mutated subunits. This is the classic “knock” in genetic mouse models of Mohler and coworkers.

Table 1. The CNS effects at $GABA_A$ $\alpha_{1-6}\beta_{1-3}\gamma_2$ receptor subtypes.[18, 46-58] Presented at the Mona Symposium (2014), University of the West Indies.[59] Earlier reported, in part, by Mckernan et al. (ACNP).

Subtype	Associated Effect
α1	Sedation, anterograde amnesia, ataxia, some **anticonvulsant** action, **anxiolysis**, addiction, dependence, as well as involved in the development of tolerance, and **muscle relaxation**
α2	**Anxiolytic**, **anticonvulsant action**, **antihyperalgesic effects**
α3	Some **anxiolytic action**, **some antinociceptive effects,** anticonvulsant action at higher doses, some muscle relaxation at higher doses
α4	Diazepam-insensitive (DI) site, important in lung disorders in the periphery
α5	**Cognition**, learning, temporal and spatial memory (maybe memory component of anxiety); schizophrenia, **depression** and in the **peripheral-asthma**
α6	Diazepam-insensitive (DI) site, important in **Tic disorders**, **Tourette's syndrome**, migraine, **trigerminal orofacial pain** and perhaps schizophrenia

Pharmacology indicated in red was discovered by pharmacologists in collaboration with the Milwaukee group. Presented by J. Cook at the BBC meeting, San Antonio, March 2018.

The α1 subunits with $GABA_A$Rs are associated with the mediation of various conditions, such as **anxiolytic** and sedative effects, ataxia, anterograde amnesia, the development of tolerance, dependence, addiction, **anticonvulsant actions**, and **muscle relaxation**. On the other hand, the α2 subunit of $GABA_A$Rs is mainly associated with anxiolytic, antinociceptive, and anticonvulsant

effects, as well as occasional muscle relaxation and hypnotic effects. Studies with triple-point mutations and the work of Zeilhofer, Cook et al. have already confirmed that the antihyperalgesic effects of the $GABA_AR$ mainly take place in the spinal cord mediated principally by α2β2/3γ2 ion channels. The α3 subunits containing $GABA_ARs$ are responsible for potential anxiolytic, anticonvulsant, antinociception, and muscle relaxation effects. The α5 subunits containing $GABA_ARs$ play a role in cognition, such as memory, spatial learning, and possibly in a memory component of anxiety. They are antidepressant and appear to be involved in Autism and Angelman syndrome in the CNS, while in the periphery with asthma. The α4 and α6 subunits containing $GABA_ARs$ do not exhibit any significant ataxic or sedative CNS effects due to the lack of a large binding pocket for the pendant C ring of BZDs. Recently, it has been shown that the α4 and α5 subunit-containing $GABA_ARs$ are expressed in the peripheral nervous system (PNS) of the lungs as well, which opens up the possibility of treating asthma with IMBZDs. Savic et al. have just reported that GABA(A) BZR are located in blood vessels. Moreover, Knutson et al. reported that the α6 Bz/GABAergic subtypes are associated with diseases such as migraine, trigeminal pain, tic disorders (e.g. Tourette's syndrome), OCD, and possibly schizophrenia.

The influx of chloride ions into membrane ion channels is capable of causing pharmacological effects due to the $GABA_ARs$ enabled by the allosteric modulation of GABA in the central nervous system. On the chloride channel, a BZD binds to the $GABA_AR$ BZD allosteric site, increasing the orthosteric binding of GABA to the chloride channel and holding the ion channel open longer. After the $GABA_AR$ is bound to GABA, it changes its conformation, causing the frequency and duration of opening of the chloride channel to increase and the membrane potential to decrease. (**Figure 5**) This process further reduces neuronal transmission, causing pharmacological effects in the CNS. Although BZR ligands in the absence of GABA are incapable of acting on the chloride

channels, they can still modulate the influx of chloride ions and the opening frequencies of other allosteric complex modulators in the presence of GABA. The three types of BZDs that interact with GABAA/BzR are agonists (positive allosteric modulators or PAMs), inverse agonists (negative allosteric modulators or NAMs), and antagonists. Agonists enhance the activity of GABA and increase chloride ion influx, while inverse agonists (negative modulators, NAM's) reduce both the activity of GABA and chloride ion influx, leading to depolarization of the neuronal membrane and increased neuronal firing. Antagonists do not affect the functions of GABA and have no pharmacological effects. They block both PAMs and NAMs from binding to the BzR site by having high binding affinity but no allosteric modulation. In addition, these antagonists have been used to investigate the role of specific subunits in the pharmacological effects of BZDs. For example, flumazenil, which has a high binding affinity for the α6 subunit, has been used to study the contribution of this subunit to the effects of BZDs in various CNS disorders. This highlights the potential of subtype-selective antagonists in the development of more targeted and effective BZD drugs with fewer side effects. Flumazenil also antagonizes all benzodiazepine receptors and is used clinically to reverse benzodiazepine overdose.

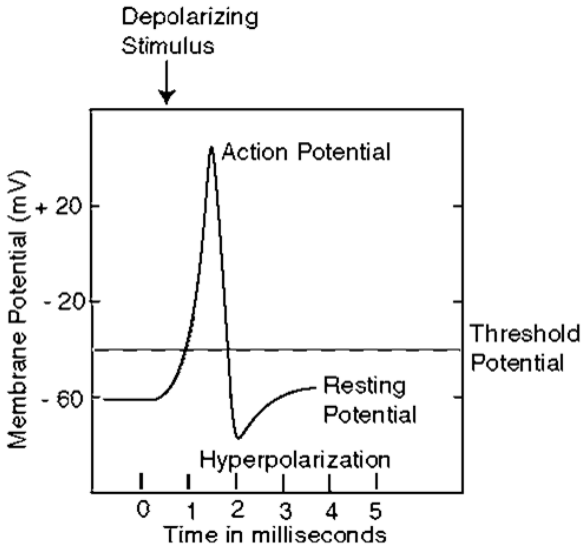


Figure 15. The membrane potential over time when a depolarizing stimulus initiates a nerve signal. A hyperpolarized state indicates a potential further away from the threshold potential. (Modified from the Figure in the Ph.D. thesis of Terry Clayton)[3]

In order to make progress towards better ligand design for the treatment of various CNS disorders, it is important to understand the pharmacological effects of $GABA_AR$s. The BZD allosteric modulation and the multiplicity of $GABA_AR$ subtypes play a central role in this concept. For example, α1-subtype selective antagonists are able to reverse effects induced by BZDs such as ataxia, hypnosis, amnesia, sedation, respiratory depression, etc. whereas α1-subtype selective agonists can induce these effects. Ligands that are α2/3/5 or α2/3-subtype selective agonists or partial agonists with α1-subtype antagonist effects (inverse agonists) or no effects at all have been found to effectively treat convulsions, anxiety disorders, diabetic neuropathy, inflammatory pain, neuropathic pain and in animal models with minimal sedative effects. Furthermore, α-5 subtype selective inverse agonists can improve learning and memory deficiencies specifically when it binds only to the α-5 subtype. A proper understanding of these features is crucial in the development of a range of pharmacological effects.

1.4. Molecular Modeling

1.4.1. Early pharmacophore Model

In conclusion, the development of new and improved BZDs for the treatment of various CNS disorders is a very important goal in the field of pharmacology. Understanding the pharmacological effects of $GABA_AR$s, particularly the BZD allosteric modulation, and multiplicity of $GABA_AR$ subtypes, is crucial in this endeavor. Advances in technology such as the crystallization of the transmembrane protein $GABA_AR$ and the use of electron microscopy have greatly improved our

understanding of BZD binding and pharmacology. This knowledge can be used to develop new drugs with improved efficacy and fewer side effects.

The initial Unified Pharmacophore/Receptor Model was a valuable tool for understanding the binding and pharmacological effects of BZDs on $GABA_A$Rs. It is based on in vitro binding affinities of >100 rigid ligands at BzR subtypes and has been developed over several decades to include over 150 different agonists, antagonists, and inverse agonists. The model has been used to generate approximate binding pockets by overlaying subtype selective ligands for α1-6β2/3γ2 $GABA_A$Rs on planar template ligands within the BZD binding site. This approach has been used to study ligands from various structural families, including BZDs, triazolopyrimidines, β-carbolines, pyridodiindoles, imidazodiazepines, pyrazoloquinolines and imidazopyridines. The unified pharmacophore/receptor model is a useful tool for understanding the binding of BZDs to $GABA_A$Rs and for the development of new drugs. It is based on in vitro binding affinities of 150 different ligands, as mentioned, at BzR subtypes and includes data from 15 different structural families. The model uses four important descriptors as anchor points: H1 and H2 as the donor sites of the two hydrogen bonds, A2 as the acceptor site of one hydrogen bond, and L1 as the lipophilic pocket. Additionally, the model includes other lipophilic regions, where ligand-protein interactions are mediated by van der Waals interactions and p-π and π-π stackings, as well as negative steric repulsive regions that represent the proteins. The are lipophilic interactions with the receptor at L_2, L_3 and L_{Di}.

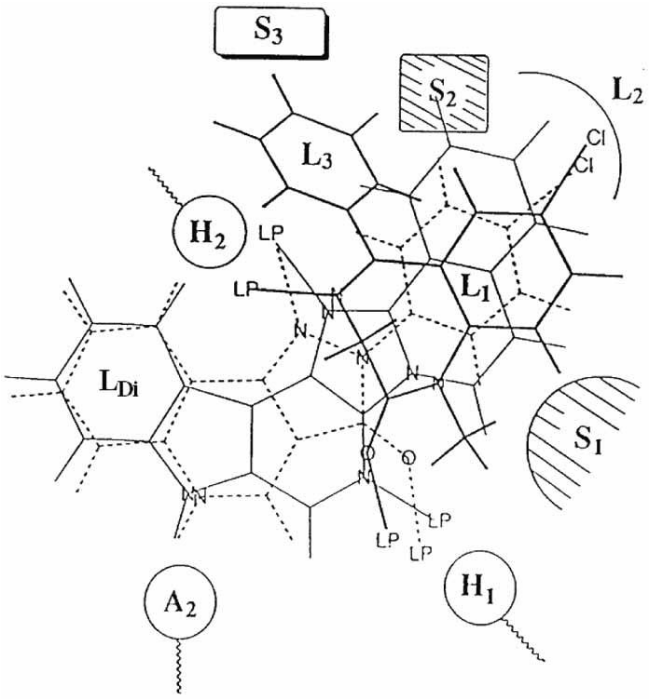


Figure 16. The locations of the descriptors and areas of the Milwaukee-Unified Pharmacophore/Receptor Model for BZD at GABA$_A$R BzR. Depicted here is pyrazolo[3,4-c]quinolin-3-one CGS-9896 as a dotted line, a diazadiindole template as a thin line, and diazepam as a thick line aligned within the unified pharmacophore/receptor model for the BzR. H_1 and H_2 stand for the hydrogen bond donor sites within the BzR, while A_2 stands for a hydrogen bond acceptor site that may be necessary for potent inverse agonist activity in vivo. L_1, L_2, L_3, and L_{Di} represent the four lipophilic regions and S_1, S_2, and S_3 represent the regions of negative steric repulsion. LP stands for the lone pair of electrons on the nitrogen (N) or oxygen (O) atoms of the ligands. (Modified from the Figure in Clayton et al.)[3]

The pharmacophore model and the studies based on it have provided valuable insights into the binding of BZDs to the different GABAAR subtypes and have helped in the ongoing efforts to design and modify ligands for the treatment of CNS disorders. The model has highlighted the differences in the size, lipophilicity and shape of the binding pockets of the various subtypes,

which can be used to increase selectivity for specific subtypes. For example, the larger L2 region in the α5 subtype can be targeted to increase selectivity for this subtype while reducing binding to the α1 subtype. The use of different chemical groups, such as the Cl atom in diazepam or the ethynyl group in QH-II-066, can also greatly increase the α5/α1 ratio and further increase selectivity. Overall, the pharmacophore model and the studies based on it have advanced our understanding of BZD binding to $GABA_ARs$ and have provided a valuable tool for the development of new and improved BZDs for the treatment of CNS disorders. This breakthrough has led to the development of QH-II-066, a potential treatment for cancer. Additionally, it was found that tolerance to the pain-relieving effects of traditional benzodiazepines (BZDs) is caused by the interaction of certain subtypes (α2, α3), leading to the creation of new antinociceptive compounds that do not cause tolerance. This is also a significant achievement for the treatment of status epilepticus, as conventional BZDs lose effectiveness after just a few days, but KRM-II-81(2) and HZ-I-66(1) do not in animal models.

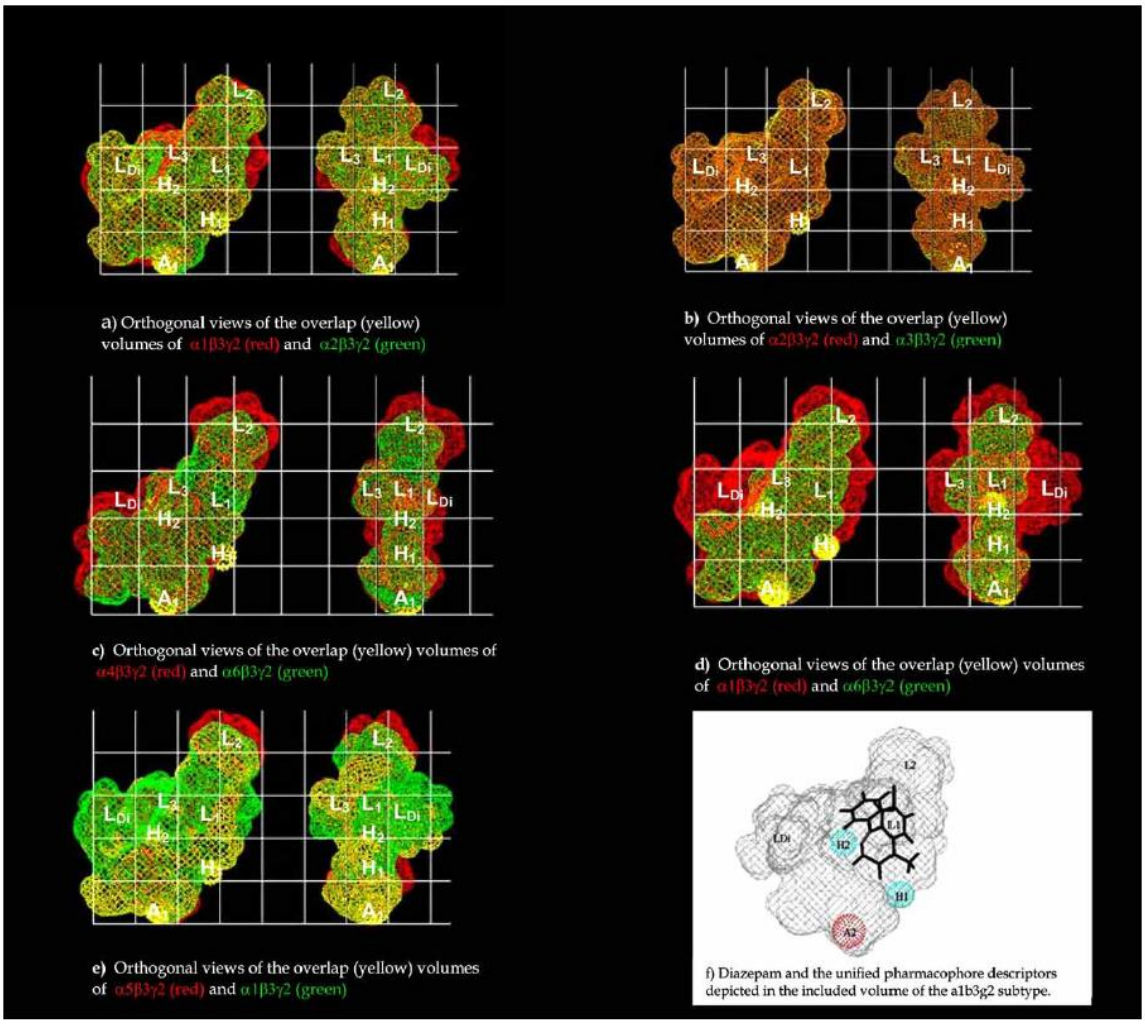
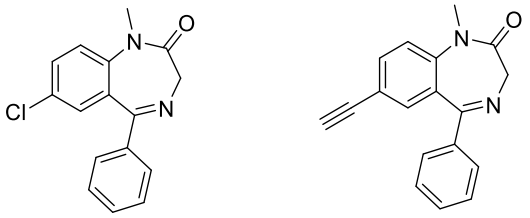


Figure 17. Overlap images between the included volumes derived from receptor subtype selective ligands: a) α1 and α2 subtypes; b) α2 and α3 subtypes; c) α4 and α6 subtypes; d) α1 and α6 subtypes; e) α1 and α5 subtypes; f) diazepam and the descriptors of the unified pharmacophore model in the included volume of the α1 subtype. The yellow color represents overlapping induced volumes, and each grid measures 4 Å in width and height. This was taken from Clayton et al.[3]



Bz/GABA$_A$ receptor binding data (K_i = nM)

	α1	α2	α3	α5	α1/α5	Change in Selectivity
diazepam	14	20	15	11	1.27	8.83
QH-II-066	76.3	42.1	47.4	6.8	11.22	

Figure 18. Bz/GABA$_A$R in vitro binding data of diazepam and the anticancer compound QH-II-066. (Modified from the Figure in the Ph. D. thesis of M. Poe and T. Clayton)[3]

Recent developments in this research include updated pharmacophore models and homology models, as well as the discovery of a new lipophilic region (L4) at the C(4) position in two chiral methyl enantiomers of the IMDZ class. This region for the R enantiomer was found to be specific in the α5 subtype, and not in the α2 or α3 subtypes. The R-isomer did not fit in the binding pockets of the α2, α3 subtypes and thus had no efficacy, while the S-isomer was a non-sedating anxiolytic in rhesus monkeys. In this case the S-isomer bound in the receptor pocket of α5, α2 and α3 subtypes**.** These findings support the use of pharmacophore receptor models and the potential for an α2/3/5 subtype-selective ligand as a nonsedating anxiolytic.

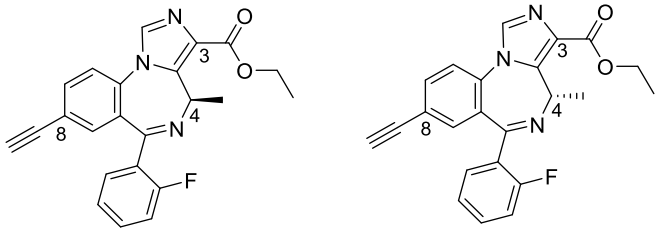
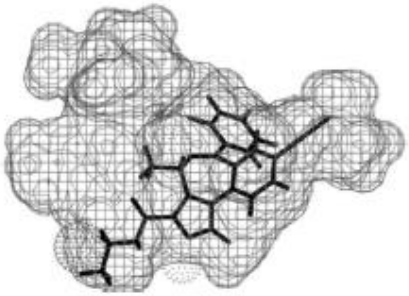
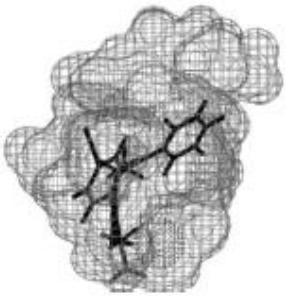


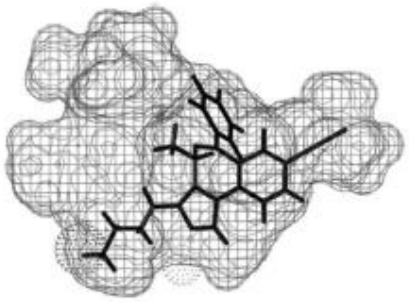
Figure 19. The structures of enantiotopic chiral imidazodiazepine (IMDZ) ligands 1 and 2.



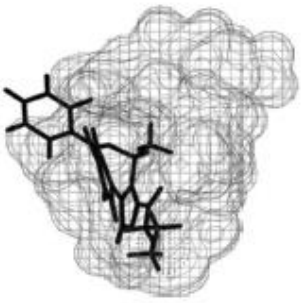
SH-053-2′F-S-CH_3 **2** fits the pharmacophore in the included volume of the alpha 2 subtype



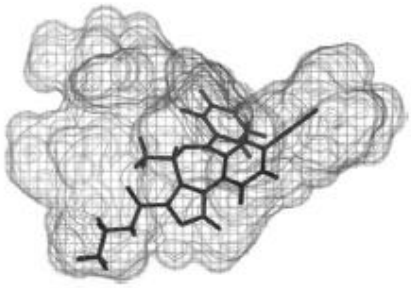
The left image of figure rotated 90°. It can be clearly seen that **2** fits within the included volume



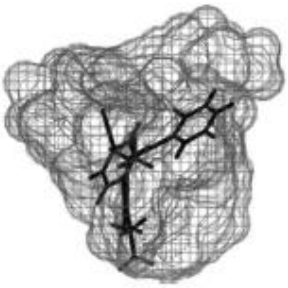
SH-053-2′F-R-CH_3 **1** does not fit the pharmacophore in the included volume of the alpha 2 subtype



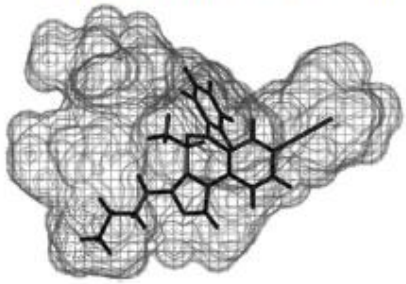
The left image of figure rotated 90°. It can be clearly seen that the conformation of **1** is such that the pendant 6-phenyl sticks outside the included volume



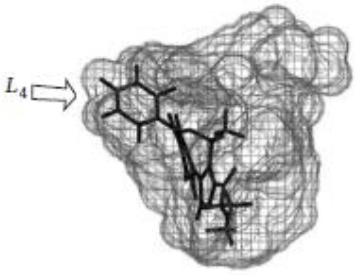
SH-053-2′F-S-CH_3 **2** fits the pharmacophore in the included volume of the alpha 5 subtype



The left image of figure rotated 90°. It can be clearly seen that **2** fits within the included volume



SH-053-2′F-R-CH_3 **1** fits the pharmacophore in the included volume of the alpha 5 subtype



The left image of figure rotated 90°. It can be clearly seen that **1** fits within the included volume

Figure 20: Ligand occupation of SH-053-2'F-R-CH_3 (1) and SH-053-2'F-S-CH_3 (2) in the α5

and α2 pharmacophore/receptor models. (Modified and reproduced from that reported by Clayton et al.)[3]

1.4.2. Modern pharmacophore model

Various cryo-EM investigations have offered significant insights into the configuration of heteropentameric $GABA_A$ Rs. These studies have revealed the comprehensive layout of these receptors and the protein interactions involving various agents such as the GABA agonist and positive allosteric modulators (PAMs) like diazepam and alprazolam. The signaling mechanism of the GABAA receptor is known as the "lock and pull" mechanism. Binding of GABA at the β3+/α1- interface triggers the movement of loop-C, resulting in a coordinated global counterclockwise motion in the extracellular domain (ECD) caused by this loop movement. This action is facilitated by BZDs binding at the α1+/γ2- ECD interface. The examination of cryo-EM structures (6HUP and 6HUO) of the α1β3γ2L GABAA R highlights the active conformations of diazepam (DZP) and alprazolam (ALP). These structures underscore three crucial interactions necessary for BZDs to operate as PAMs.

The first interaction involves the formation of a bifurcated hydrogen bond with α1Ser205. The second feature is a halogen bonding interaction with the backbone of α1His102. Notably, flunitrazepam and clonazepam, containing nitro groups at the C7 position, participate in hydrogen bonding interactions with the histidine side chain, compensating for the absence of the C7 halogen bond interaction present in diazepam. The third feature essential for BZDs to act as PAMs is pi-pi stacking with α1Tyr210 and α1Phe100, as depicted in **Figures 1** and **2**.

Diazepam displays different binding sites within the GABAAR complex. Classical benzodiazepines like DZP and ALP interact via halogen bonding interactions with the backbone

carbonyl group of α1His102. In the DZP-bound cryo-EM structure (6HUP), the distance between the chlorine atom and carbonyl oxygen of α1His102 is 3.8 Å, while in the ALP-bound cryo-EM structure (6HUO), this distance is 2.9 Å. Both structures exhibit a σ-hole angle of 165-167°.

The bifurcated hydrogen bond formed by DZP with α1Ser205 is larger than the corresponding bond formed with bound ALP. ALP's stronger binding affinity towards α1 compared to DZP, owing to the shorter halogen bond and bifurcated hydrogen bond interactions, results in increased sedation, making it more potent than diazepam. Nevertheless, both ligands effectively modulate the α1β3γ2 ion channel.

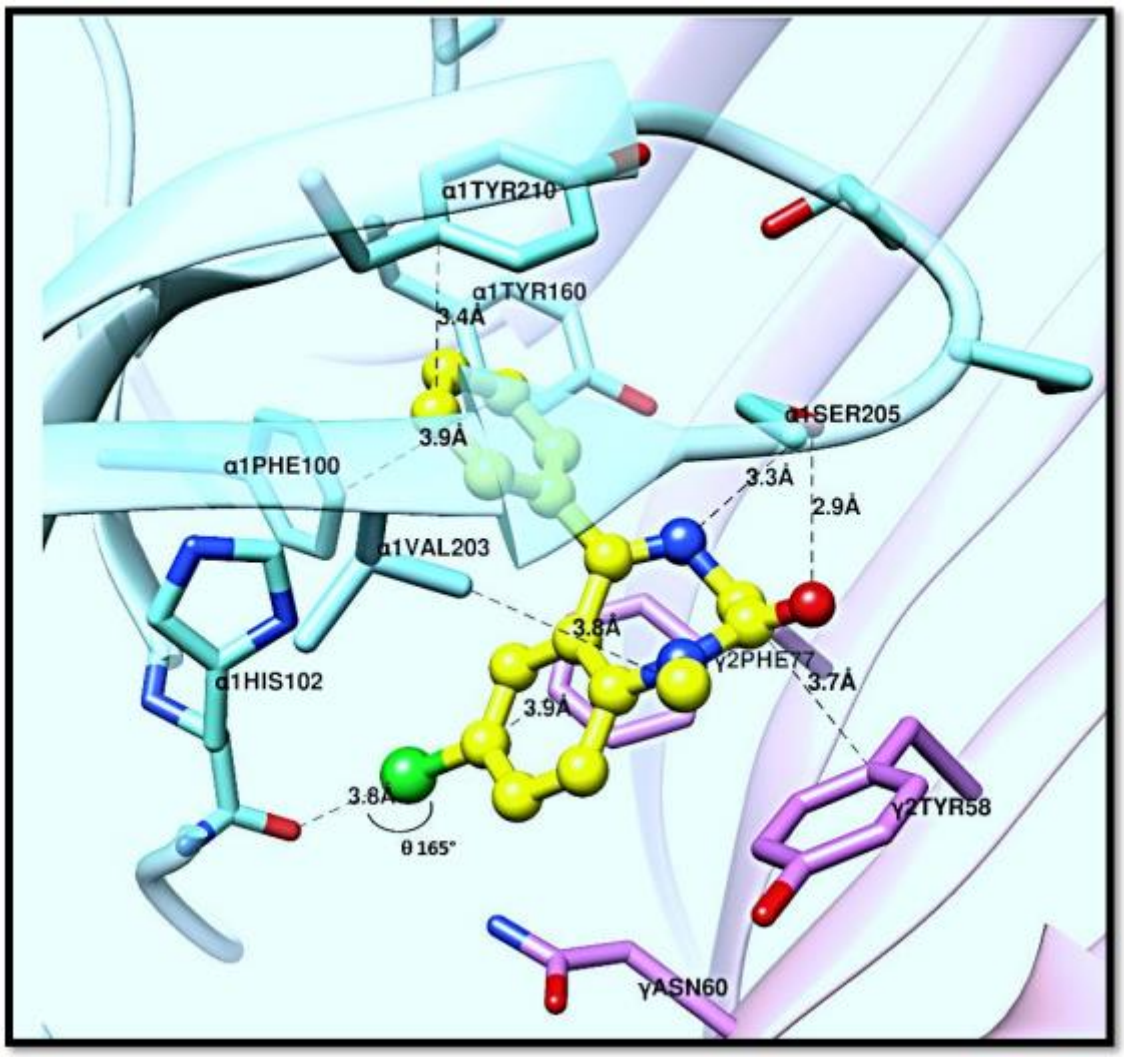


Figure 11. The complex of diazepam (yellow) with the α1 (aquamarine) and γ2 (orchid) subunits of α1β3γ2L GABAA receptor 6HUP. The dashed lines (- - -) indicate π–π interactions, hydrogen bonding interactions, and a halogen bonding interaction. The image is modified from Golani et. al. 2022[4] which originates from the classic work in Nature Neuroscience (2019)[5]

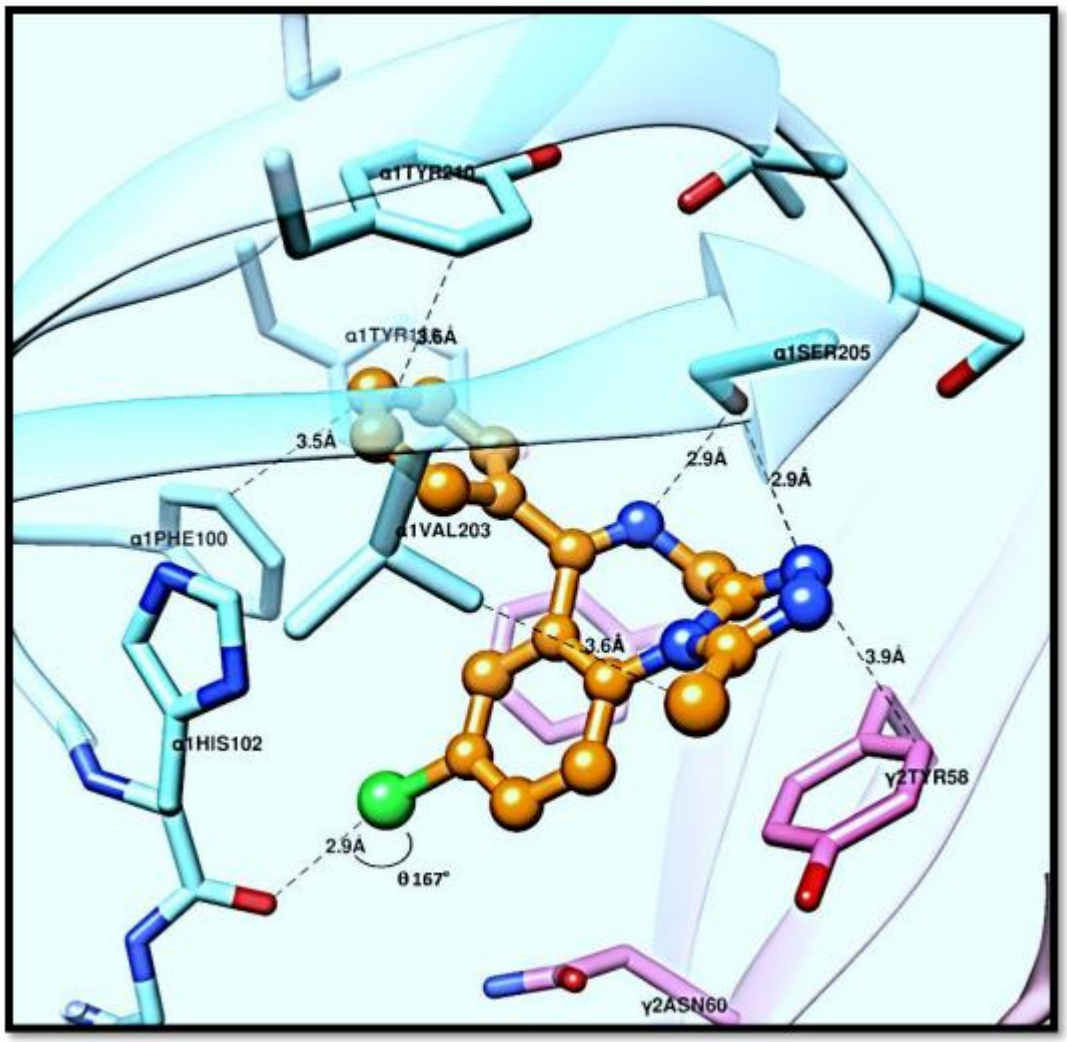


Figure 12. The complex of alprazolam (orange) with α1 (aquamarine) and γ2 (orchid) subunits of α1β3γ2L GABAA receptor 6HUO. The dashed lines (- - -) indicate π–π

interactions, hydrogen bonding interactions, and a halogen bonding interaction. The image is modified from Golani et. al. 2022.[4]

Flumazenil, utilized as an antagonist for BZDs, serves as an antidote in the management of benzodiazepine overdose. The cryo-EM structure of flumazenil (6D6U) in conjunction with the $GABA_A$ R indicates a distinct binding conformation compared to DZP or ALP, particularly at the α+/γ- interface (**Figure 3**). In this structure, the two principal interactions - the bifurcated hydrogen bond and the halogen bond interaction with the protein - are notably absent (in the cryo-EM structure 6D6U). This absence suggests that flumazenil does not engage in the bifurcated hydrogen bond or the halogen bond with the protein side chain. As a consequence of these lacking interactions, flumazenil fails to induce the movement of loop-C at the α+/γ- interface of the $GABA_A$ R. Consequently, flumazenil functions as a competitive antagonist at this particular site (**Figure 12**), where it only partially aligns with the structure of the BZDs and blocks the ion channel to exclude some of the benzodiazepines from entering, thus antagonist.

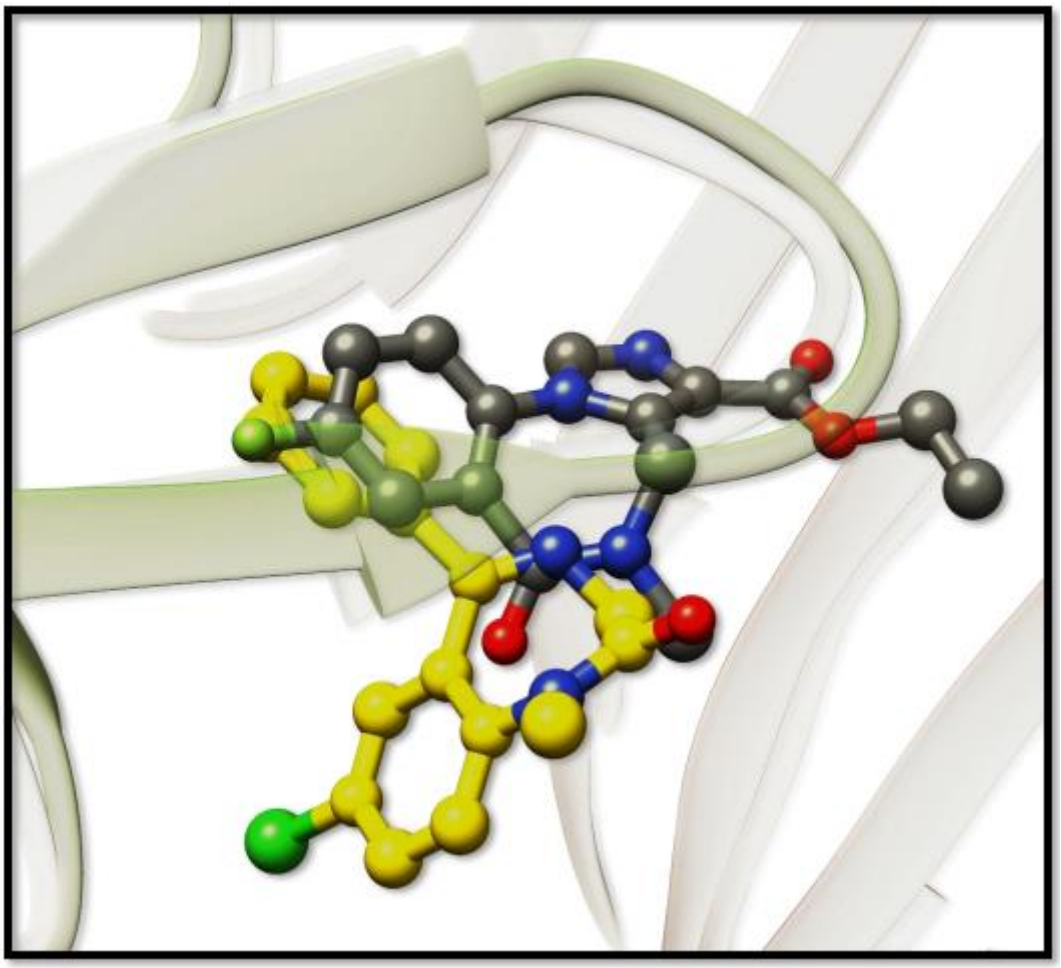


Figure 13. The overlay diagram of flumazenil (grey) and diazepam (yellow) in the ion complex with α1 (aquamarine) and γ2 (orchid) subunits of α1β3γ2L GABAAR (6D6U and 6HUP). The image is modified from Golani et. al. 2022 [4] which originates from the classic work in Nature Neuroscience (2019)[5]

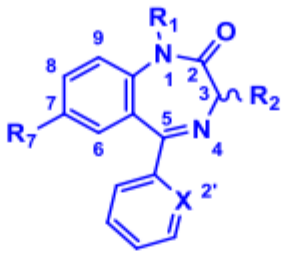


Table 2. Binding affinities at α1-3 and α5 human $GABA_A$ R subtypes									
Comp	**Code**	**R_1**	**R_2**	**R_7**	**X**	**K_i (nM)**			
						α1	**α2**	**α3**	**α5**
1.	Diazepam	CH_3	H	Cl	C-H	14	20	15	11
2.	QH-II-059	CH_3	H	H	C-H	81	138	318	98
3.	QH-II-063	CH_3	H	Br	C-H	9.4	9.3	31	7.7
4.	QH-II-058b	H	H	H	C-H	288	233	350	140
5.	QH-II-066	CH_3	H	C≡CH	C-H	76.3	42.1	47.4	6.8
6.	XLi-352	CH_3	H	C≡CH	C-Cl	1.6	0.99	ND	1.96
7.	KRM-II-08	CH_3	H	C≡CH	C-F	3.9	1.2	3.4	0.8
8.	XLI-286	H	H	Br	C-Cl	0.05	0.06	0.12	0.68
9.	JYI-42	H	H	Br	C-F	0.26	0.15	0.28	0.26
10.	flunitrazepam[36]	CH_3	H	NO_2	C-F	2.2	2.5	4.5	2.1
11.	SH-I-030	H	*S*-CH_3	Br	C-H	14.4	11	19.1	1.89
12.	SH-I-035B	H	*R*-CH_3	Br	C-H	>3000	>3000	>3000	>3000

The affinity of compounds at $GABA_A$ recombinant subtypes was measured by competition of [^{3}H] flunitrazepam binding to HEK cell membranes expressing human $\alpha x\beta 2\gamma 2$ receptors. Data represent the average of at least three determinations with a SEM of ±5%. ND: not determined. [276]

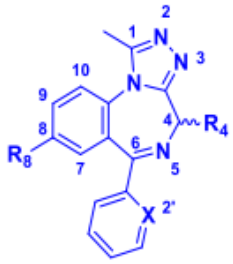


Table 3. Binding affinities at α1-3 and α5 human GABA$_A$ R subtypes

Comp.	Code	R_4	R_8	X	K_i (nM)			
					α1	α2	α3	α5
1.	alprazolam[36]	H	Cl	C-H	0.8	0.6	1.4	1.5
2.	Xli-2TC	H	Br	C-H	2.8	0.7	ND	0.6
3.	DM-II-90	H	Br	C-Cl	0.5	1	0.6	0.4
4.	SH-I-04	H	Br	N	7.3	6.1	5.1	7.7
5.	XLi-270	H	C≡CH	C-H	36.4	25.8	ND	5.3
6.	XLi-296	H	C≡CH	C-Cl	3.3	0.6	1.9	4.4
7.	JYI-70	H	C≡CH	C-F	6.3	2.1	ND	0.6
8.	SH-TRI-108	H	C≡CH	N	143.9	81.3	103.9	45.6
9.	SH-TS-CH3	*S*-CH_3	C≡CH	C-H	107.2	50.1	20.9	8.1

The affinity of compounds at GABA$_A$ recombinant subtypes was measured by competition of [^{3}H] flunitrazepam binding to HEK cell membranes expressing human *αxβ2γ2* receptors. Data represent the average of at least three determinations with a SEM of ±5%. ND: not determined. [16]

Comparison studies of the sequence alignment among α1-6 subunits demonstrate that α1His102 is not present in the α4 and α6 peptides. Instead, this residue is substituted with an arginine residue in the α4 and α6 subtypes (as shown in **Table 4**). It is worth noting that the arginine residue is

larger in size compared to the histidine residue. This larger size causes a steric clash with ALP and DZP. Consequently, classical 1,4-benzodiazepines like DZP and ALP do not effectively bind to GABAA R subtypes that contain the α4 or α6 subunits.

However, it's important to mention that the His102 residue is conserved in the α1-3 and α5 subunits, as mentioned earlier. The amino acid residues that remain conserved in α1-3 and α5 subunits and interact with the pendant ring of DZP and ALP are outlined in Table 4. Notably, the amino acid residues within the loop-C region in the BZD binding site of the α subunits show subtle differences among them (as listed in **Table 4**). For instance, while the α5 subunits have Thr205, the α1 subunit features a Ser205 residue in this position. Furthermore, Ile203 is found in α2-3 and α5 subunits, whereas the α1 subunit has this residue replaced with Val203. These subtle differences in amino acids result in unique 3-dimensional shapes of the BZD R binding pockets. These differences significantly contribute to subtype selectivity, shaping the topography of the lipophilic pockets termed H1, H2, L1, L2, L3, and LDi in earlier homology models.

Table 4. The sequence alignment of α1-6 subunits.

α subunits	Halogen bond interaction with αHis102	Pendent ring pi-pi stacking interactions region	Bifurcated hydrogen bond interaction region (Loop-C)
α1	FFHN	GSYAY	GIVQSSTGEYV
α2	FFHN	GSYAY	ETIKSSTGEYT
α3	FFHN	GSYAY	EIIRSSTGEYV
α4	FFRN	GSYAY	ETIKSITGEYI
α5	FFHN	GSYAY	ENISTSTGEYT
α6	FFRN	GSYAY	ETIKSNTGEYV

Each single letter represents an amino acid residue. The red colored amino acids are involved in the interaction with ligand. [27]

Several novel subtype-selective Positive Allosteric Modulators (PAMs) have been developed in Milwaukee, and the interactions between these compounds and GABAA Rs have been detailed. Our research group also crafted and synthesized similar analogs of DZP (refer to Table 2, entry 1) and ALP (refer to Table 3, entry 1) to further delve into the molecular interactions and binding affinities at the α1-3+/γ- and α5+/γ- interfaces of GABAA Rs. Various compounds were designed to investigate the impact of the halogen atom at C7, leading to the design of different molecules (listed in Table 2, entries 2, 3, and 5). Some ligands were specifically created to explore the molecular interactions of the 2-substituent on the pendant phenyl ring of DZP (Table 2, entries 6-9). Additionally, Ligands 11 and 12 were devised to discern the role of a chiral methyl group in the seven-membered ring of DZP.

The significance of the halogen bond with the α1His102 backbone group in the binding of DZP and ALP, as well as the movement of loop-C (acting as a PAM), was highlighted. This loop-C movement can prolong the opening of the chlorine ion channel, which results, in increased sedation and ataxia. However, substituting the halogen group at C-7 or C-8 with an ethynyl group brings about an important change. The halogen participates in a halogen bonding interaction, whereas the ethynyl group does not exhibit such interaction. Consequently, compounds with an ethynyl group at C-7 result in less sedation and ataxia compared to chlorine compounds. The C7 chlorine atom of DZP was substituted with an ethynyl group (as observed in Table 2, entry 5). The docking pose of ligand 5 (QH-II-066) in the α1β3γ2L cryo-EM structure 6HUP was depicted in **Figure 14**. The docking position clearly mirrors a similar pose to that of DZP, allowing it to overlap as a PAM at the α1 $GABA_A$ R subtype with significantly reduced sedation and ataxia compared to diazepam.

The investigation of the C7 nitro group (refer to Table 2, entry 10) demonstrated that ligand 10 adopts a similar conformation to DZP. Two hydrogen bonding interactions were observed between the nitro group at C7 and the side chains of α1His102 and γ21Asn60. Due to the ability of this nitro ligand to interact with α1His102 through hydrogen bonding, it displays strong sedation in vivo.

Docking studies of compounds 11 and 12 at the α1β3γ2L $GABA_A$ R (6HUP and 6HUO) unveiled sufficient space for the (S)-methyl group in the alpha 2,3,5 subtypes but not for the (R)-methyl group (as seen in compound 12). This discrepancy in subtype selectivity between the (S) and (R) enantiomers has been documented. Nonetheless, the R-enantiomer displays binding affinity and efficacy at the alpha 5 subtype.

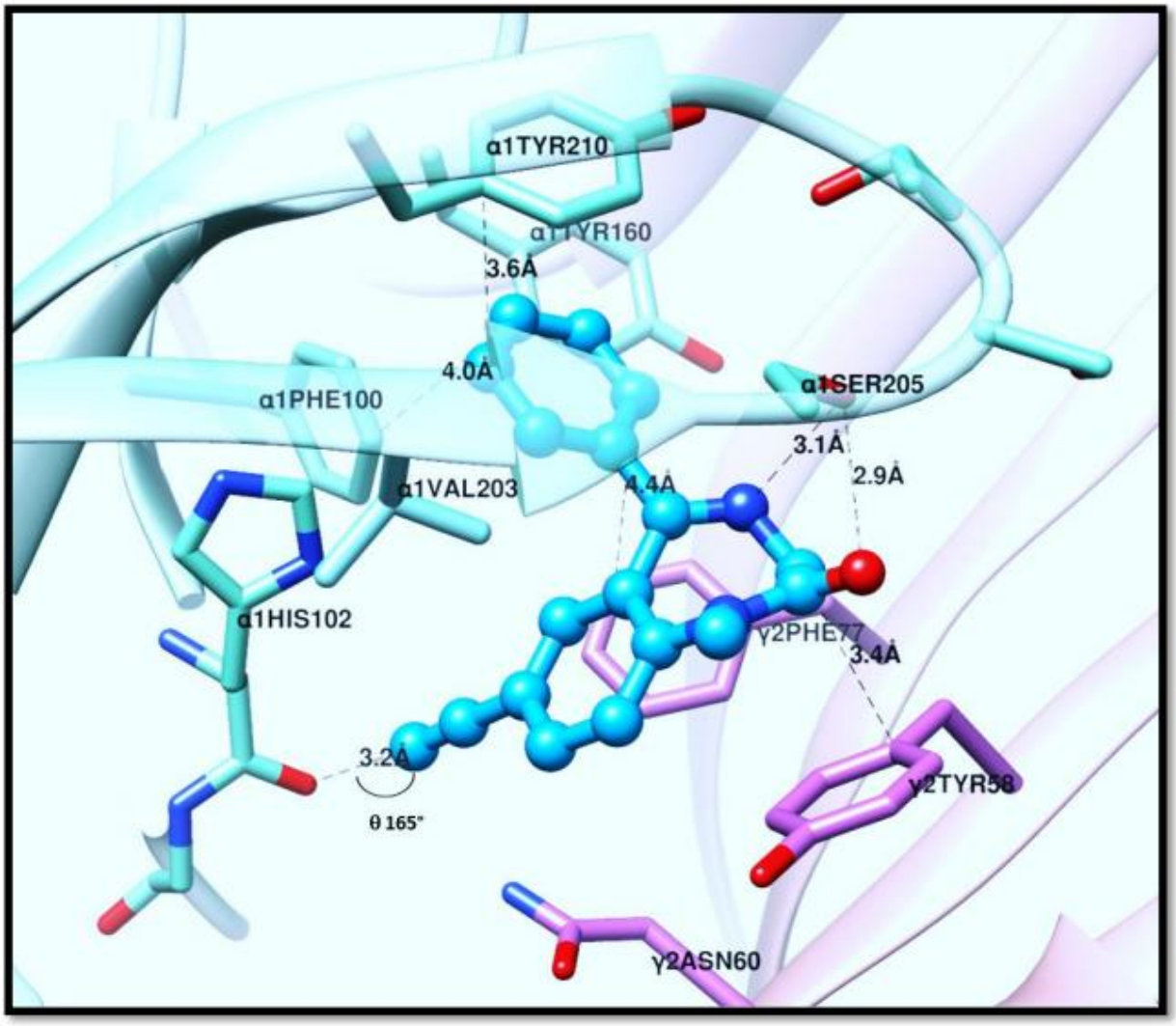


Figure 14. The docking pose of QH-II-066 5 (deep sky blue) with the α1 (aquamarine) and γ2 (orchid) subunits of α1β3γ2L GABAA receptor 6HUP. No halogen bond is observed in case of the ethynyl group. The image is modified from Golani et. al. 2022.[4]

1.5. Research Objectives

Using a unified pharmacophore model as a guide, the primary aim of this study was to create and produce a range of innovative optically active BZD compounds that exhibit superior binding affinity and effectiveness at BzR while avoiding the side effects associated with BZDs. This was achieved by diminishing their efficacy or affinity at the α1 subtypes. Additionally, in some cases it was desirable to reduce their efficacy at both α1 and α5 subtypes to minimize the development of tolerance. These newly developed ligands were not only utilized to explore the Structure-Activity Relationships (SAR) but also to assess the pharmacological effects of potential drugs on various GABAAR subtypes, either individually or in combination.

To determine their suitability for treating conditions like asthma, schizophrenia, major depressive disorder (MDD), anxiety, epilepsy, and pain disorders, these ligands had to undergo evaluation through different in vitro tests and in vivo animal models. Beyond advancing potential drug candidates, the secondary objective of the research was to enhance the synthesis of key compounds on a larger scale, resulting in improved yields, as compared to previous methods. This step was crucial to ensure a reliable and efficient supply of these ligands for investigations into their pharmacology in larger animal models, with the ultimate goal of addressing a range of central nervous system (CNS) disorders.

Chapter 2. Design and Synthesis of Chiral α5 Subtype Selective GABA(A)ergic Ligands for Schizophrenia, Depression and Alzheimer's Disease

2.1. Introduction and Background

Numerous mental health conditions are linked to disruptions in GABAergic neurotransmission within the brain. [27] For instance, in post-mortem examinations of schizophrenia patients, deficiencies in GABAergic interneurons and reduced levels of the GABA synthesizing enzyme GAD67[28] have been observed. [29] Changes in GABA levels and signaling are also associated with depression and anxiety. [30,31] Moreover, benzodiazepines, commonly used to manage anxiety disorders, frequently result in undesirable side effects like sedation and ataxia due to their lack of specificity at $GABA_AR$ with varying subunits[32] However, targeting specific $GABA_AR$, particularly those containing α2, α3, and α5 subunits, can yield the desired therapeutic effects while circumventing the benzodiazepine-related side effects.

Schizophrenia, a mental disorder, displays positive symptoms such as disorganized thought, hallucinations, delusions, and psychosis, alongside negative symptoms such as reduced emotional expression, anhedonia, and social withdrawal. Additionally, cognitive impairments such as deficits in working memory, learning reversal, and executive function are key characteristics of schizophrenia [33,34] .The pathophysiology of schizophrenia is intricate, and various hypotheses have been proposed over time regarding its origins. One longstanding hypothesis involves the hyperactivity of the mesolimbic dopamine system, which mediates positive symptoms (e.g., hallucinations and delusions) in affected individuals. [35,36] Despite this, there is no definitive mechanism established. Consequently, any disturbances in the brain's upstream regions might lead to abnormal dopamine system activity. The hippocampus, responsible for regulating the activity

of dopamine neurons, undergoes structural and functional alterations in schizophrenia. [37,38] The heightened baseline activity in the hippocampus is thought to be associated with the positive symptoms observed in affected individuals.

Several reports derived from rodent studies across different models indicate pathophysiological aspects linked to schizophrenia. [39–43] These studies demonstrate multiple mechanisms in rodent models revealing a multi-synaptic pathway involving the nucleus accumbens (NAc), ventral pallidum (VP), and ventral tegmental area (VTA), which contributes to hippocampal hyperactivity responsible for aberrant dopamine system function. [39–43] Furthermore, investigations in rodent models have successfully restored aberrant dopamine system function using pharmacological, neurosurgical, and cell-based approaches. [41–44] The collective evidence suggests that hippocampal hyperactivity likely plays a pivotal role in the pathophysiology of schizophrenia, and reducing this hyperactivity could be a beneficial aspect for the treatment of schizophrenia.

Post-traumatic stress disorder (PTSD) is a stress-induced mental disorder that emerges following exposure to traumatic events like assault or combat. Evidence suggests a significant portion of the United States population (approximately 8% of the general population and 20% of US combat veterans) suffers from PTSD. [45,46] The core symptoms of PTSD include hyperarousal, cognitive deficits, avoidance of trauma-related stimuli, and sleep disturbances. [47,48]

PTSD also shows a relatively high occurrence of coexisting symptoms of psychosis such as hallucinations and delusions[47] The management of PTSD has encountered challenges due to the unfavorable side effects and the restricted effectiveness of antipsychotic medications, leading to treatment withdrawal or discontinuation[49]. To devise and create effective therapies for PTSD, it's imperative to comprehend the pathophysiology of psychosis linked to PTSD. Major Depressive

Disorder (MDD), categorized as one of the primary causes of disability globally, affects over 322 million individuals[50]. Patients with MDD exhibit a range of symptoms encompassing anxiety, low mood, anhedonia, and cognitive dysfunctions, and current therapies often prove inadequate[51–53]. Dysfunctions in the GABAergic system[54], the monoaminergic system[55], reduced neuronal complexity[56], and neuroendocrinology dysfunctions [57] contribute to the underlying pathologies of MDD. Despite the complex nature of MDD's pathology, the current treatment mainly revolves around rectifying the imbalance in the monoaminergic system. However, addressing this imbalance has limited efficacy on mood symptoms and no impact on cognitive symptoms, neglecting other encountered pathologies in MDD, such as anxiety. Even when mood symptoms improve, cognitive dysfunctions often persist [58] . There is a suggested link between mood and cognitive symptoms, where the relapse of mood symptoms can be foreseen from enduring cognitive symptoms [59–62] . Understanding the molecular pathology of MDD is crucial for developing novel therapies aimed at the disorder. Crafting such therapies for psychiatric conditions is incredibly challenging, yet it presents significant opportunities to aid millions of patients, globally. Connectivity between neurons is diminished in individuals affected by depression, which may intensify the severity of the condition. [63] Several postmortem studies have reported a reduced number of synapses and the expression of genes associated with synaptic function in individuals with MDD in the dorsolateral prefrontal cortex (PFC). Long-term stress-related disorders exhibit a similar impact in animal models[64–70] Chronic stress induces diverse alterations in dendritic length, spine density, and inter-neuronal connections in several brain regions within the limbic system, including the prefrontal cortex (PFC), the hippocampus (HPC), and the amygdala [71]. Specifically, chronic stress reduces dendritic length and spine density in the PFC and the HPC, while it elevates various subnuclei within the amygdala [72]. The influence of chronic stress on the

neuronal structure in the PFC and HPC regions contributes partly to cognitive deficits, while the amplified connectivity in the amygdala is associated with heightened anxiety episodes observed in chronic stress-related disorders. Dysregulated GABAergic (inhibitory) functions contribute to an altered balance between excitation and inhibition in individuals with MDD [54]. Research reports indicate decreased levels of GABA in cerebrospinal fluid[72], plasma[73–77], and specific brain regions like the occipital cortex[78–82] in untreated depressed patients[83,84]. Reductions in GABA levels are observed in brain areas such as the PFC[85] and anterior cingulate cortex (ACC)[76,85–87] of individuals with depression. Presently, there are no available treatment options to address this imbalance in MDD patients. Targeting the modulation of α2/3 $GABA_A$-Rs is proposed as beneficial in managing mood and anxiety[88], whereas α5 $GABA_A$-Rs are believed to be useful in addressing anxiety and cognitive performance. The hippocampus serves as the primary location of α5-$GABA_AR$ subtypes within the central nervous system, constituting around 5% of all $GABA_AR$ α-subtypes in the brain. [89,90] Notably, these α2/3, which make up 30% in the CNS, and α5-containing $GABA_ARs$ are notably concentrated in the hippocampus, accounting for nearly a quarter of all $GABA_ARs$ in this region.[91] Specifically, higher expression of α5 is observed in the ventral compared to the dorsal subregions within the hippocampus, making it an attractive target for modulating hippocampal activity. [92,93]

Positive modulation of $GABA_AR$ has been associated with anxiolytic effects. Studies have shown that reducing α5-$GABA_ARs$ in healthy animals induces deficits like psychosis in sensorimotor gating, as demonstrated by pre-pulse inhibition (PPI).[94] Conversely, boosting the expression of the α5 subunit ion channelsin the ventral hippocampus reversed dysfunction in the dopamine system and behavioral deficits in a rodent model of psychosis[95]. Selective ligands targeting the α5-$GABA_AR$ subtype have displayed promising effects in various cognitive assessments, such as

memory and spatial learning.[96] These cognitive disorders include Alzheimer's disease, Huntington's disease, Down syndrome, schizophrenia, and depression,[87,97–100] all of which present cognitive impairments.

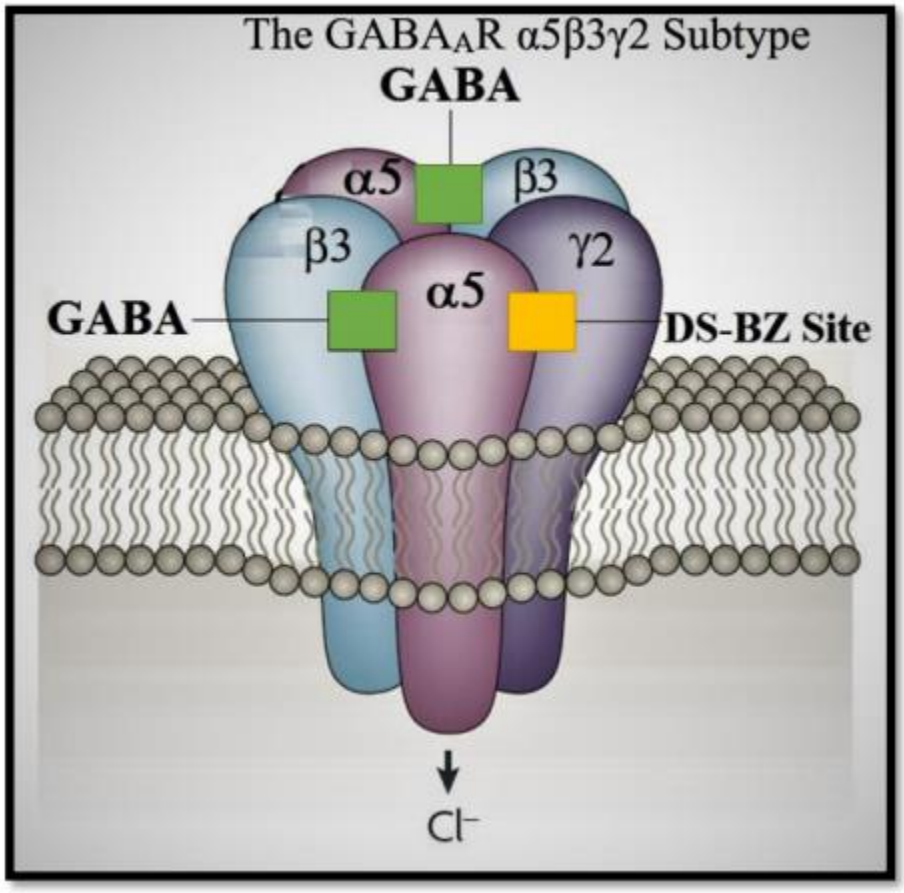


Figure 1: The α5β3γ2 subtype GABA$_A$R. IBDZs like SH-053-2'F-RCH$_3$ and GL-II-73 exert their effects at the α5+γ2- interface as positive allosteric modulators (PAMs). Image was modified from Jacob et al., Nature Reviews Neuroscience, 2008.

The Cook research group in Milwaukee created several innovative α2/3 and α5-selective ligands (Figure 2). Among these ligands, SH-053-2'F-R-CH$_3$, GL-II-73, and GL-I-54 demonstrated

significant efficacy in models related to memory loss, cognitive disorders, depression, Angelman's syndrome, and schizophrenia by various investigations.

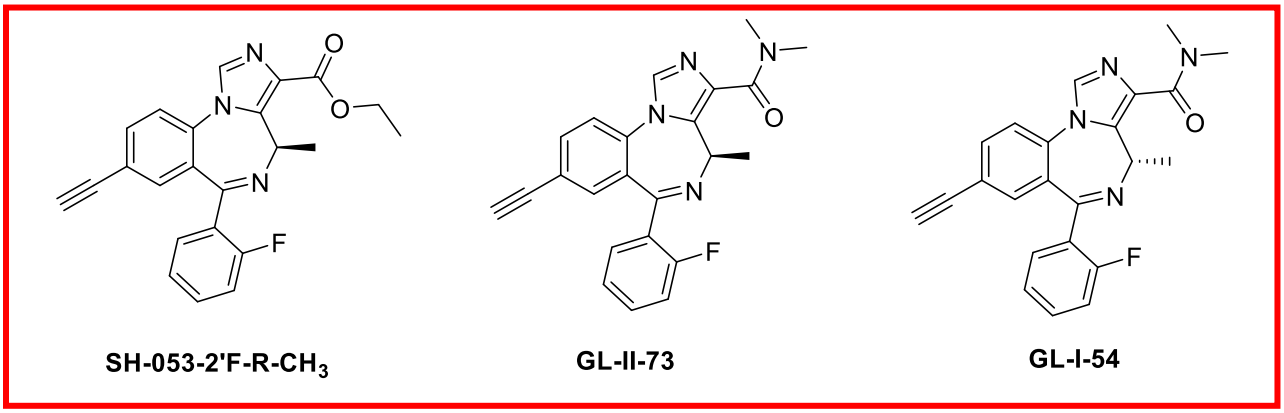


Figure 2: Lead α2/3 and α5-selective ligands in this research

The highly specific $GABA_AR$ α5-subtype selective positive allosteric modulator (PAM), known as SH-053-2'F-R-CH_3, exhibited enhanced potency at α5 GAB_AA receptor subtypes, along with a simultaneous decrease at the α1, α2, and α3 subtypes. The in vitro binding affinity of SH-053-2'F-R-CH_3, detailed in **Table 1**, demonstrates its greater selectivity for α5 GAB_AA receptors compared to other $GABA_A$ receptor subtypes [101]. Outlined in **Table 2** is the in vitro efficacy data, showing the increased efficacy values for α5 GAB_AA receptors with varying concentrations of SH-053-2'F-R-CH_3 [101].

In experimental models, SH-053-2'F-R-CH_3 displayed a reduction in amphetamine-induced hyperactivity of the dopamine system in the MAM model of schizophrenia[102]. Additionally, this compound exhibited anxiolytic and antidepressant effects in a sex-dependent manner in a chronic stress mouse model[103,104].

Table 1: Binding affinity of SH-053-2'F-R-CH_3 at αxβ3γ2 $GABA_A$/benzodiazepine site subtypes. Measurements were made in duplicate. Ki values are reported in nM	
Subtype	Ki (nM)
α1	759.1
α2	948.2
α3	768.8
α4	ND[a,b]
α5	95.2
α6	ND[a,b]

[a]ND, not determined. [b]Binding at α4$GABA_A$A and α6$GABA_A$A receptors have not been determined. because ligands which contain pendent phenyl ring do not bind to α4 and α6 diazepam insensitive BzR. The Table is modified from Fisher et al. 2010[104]

The cognitive benefits of the enantiomer, SH-053-2'F-S-CH_3 enantiomer were assessed through a spatial-recognition working-memory test conducted in the Y-maze, induced by prenatal immune activation. While the distance traveled in the Y-maze test remained unaffected by prenatal exposure to poly (I:C), the total distance covered significantly increased following the administration of SH-053-2'F-S-CH_3[105]. This compound effectively alleviated the amphetamine hypersensitivity caused by poly (I:C) without generating side effects in the control offspring. [105] Additionally, SH-053-2'F-S-CH_3 exhibited anxiolytic-like effects in the Elevated Plus Maze (EPM) and facilitated the extinction of fear memory in male mice. [105] Moreover, this compound reduced the hyperactive movement caused by MK-801 and prevented PPI disruption in female mice, though it did not exhibit the same effect in male mice.[105]

Table 2: Efficacy of SH-053-2'F-R-CH3 at αxβ3γ2GABAA receptor subtypes as % of control current at 100 nM and 1 μM concentrations.	
Subtype	% of control current
α1	111/154
α2	124/185
α3	125/220
α4	
α5	183/387
α6	ND [a]

Data were presented as 100 nM/ 1mM. The table is adopted from Fischer et al. 2010[104]

a. **Not determined.**

As previously mentioned, the α5-subunit is notably present exclusively in key brain regions the hippocampus and prefrontal cortex both significantly involved in cognitive processes.[106] Analysis of both preclinical and postmortem data, [107–109] indicates a downregulation of the α5-subunit during aging. Furthermore, a recent study demonstrated that synaptic localization of $GABA_A$ receptors containing the α5-subunit contributed to dendritic outgrowth and spine maturation.[110] This evidence strongly suggests the crucial involvement of this specific α5-containing $GABA_A$ receptor subunit in regulating cognitive function through the GABAergic system. Reversing the reduced receptor activity during aging, either directly or indirectly through dendritic growth, is intricately associated with this regulation. The lead compound, GL-II-73 (**Figure 3**), identified as an α5-positive allosteric modulator (α5-PAM), was developed in Milwaukee, and exhibited enhanced

working memory in a mouse model simulating chronic stress and aging.[111] GL-II-73 shows a preference for binding to α5-containing GABAA receptors. Its binding affinity is notably 6 times stronger than for the α2 subtype, 11 times stronger for the α1 subtype, and 12.5 times stronger for the α3 subtype ion channels (**Table 3**). Significantly, the effectiveness of GL-II-73 is notably more potent at the α5 subtypes compared to any other BZR subtypes (**Figure 3**). As a result, the observed biological impact stems from these α5 subtype-selective or preferring ligands rather than other subtypes. Furthermore, a comprehensive 47-panel PDSP screen (PDSP, ROTH, UNC; taken from Guanguan Li's PhD thesis) indicates the exclusion of involvement of other CNS receptors, including HERG channels.

In comparison with various α5-PAMs, GL-II-73, tested in old rats[112] (in collaboration with Etienne Sibille and Thomas Prevot), demonstrated improved cognitive functions. Furthermore, when evaluated in vivo in aged mice, this compound enhanced cognitive deficits and reversed dendritic shrinkage. [113]These findings are pivotal for Major Depressive Disorder (MDD), schizophrenia, and Alzheimer's disease.

Table 3: Binding affinity of GL-II-73 at αxβ3γ2 $GABA_A$/benzodiazepine site subtypes

Subtype	Ki (μM)
α1	55 ± 4
α2	30 ± 5
α3	63 ± 7
α4	ND[a]
α5	5 ± 2
α6	ND

Ki values are reported in µM. This table is adopted from Fisher et al. 2010 and Prevot et al. 2019. [111] [a]**ND=Not reported**

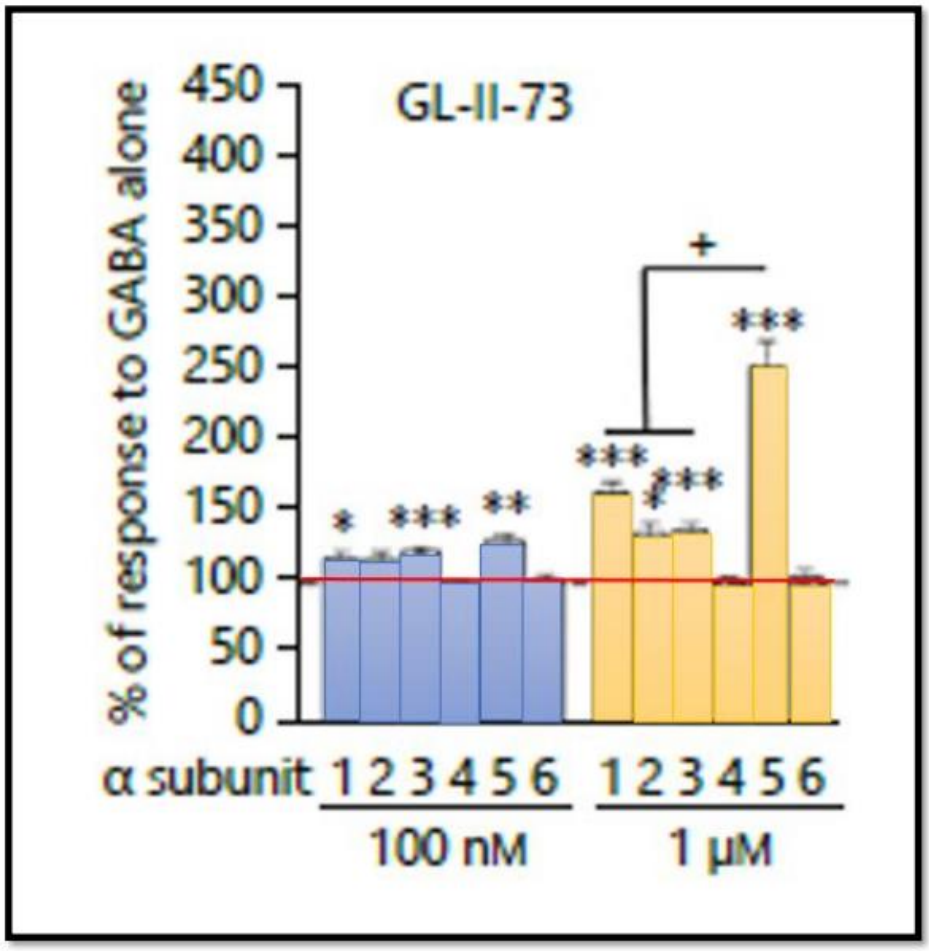


Figure 3: The potentiation of GL-II-73 at α1, α2, and α3 subtypes were lower than at theα5 subtype at 1 µM, which indicated that this ligand is more α5 preferred. The Figure is modified from the PhD thesis, Guanguan Li, University of Wisconsin – Milwaukee, 2019.

The GABAergic system significantly impacts the aging process, and diminished GABAergic functions play a critical role in aging-related changes. Research has shown that GL-II-73 specifically targets the α5-$GABA_A$ receptors, offering a means to counteract these deficits and potentially reverse the decline in cognitive abilities associated with aging.[111] Chronic

administration of GL-II-73 reversed cognitive decline, dendritic shrinkage, and spine atrophy in both the prefrontal cortex and the CA region of the brain in aged mice. Notably, the chronic treatment with GL-II-73 led to increased dendritic length, spine count, and spine density in these crucial brain regions in older mice.

Of note, GL-II-73 is the first known GABAergic drug that has demonstrated neurotrophic effects. In contrast, commonly used benzodiazepines have been observed to decrease spine density in cortical pyramidal neurons.[114] Recent reports have suggested that ketamine exerts its antidepressant effects by acting through the NMDA receptor of GABA neurons.[115,116] Several ongoing studies aim to unravel the mechanism behind the neurotrophic effects of GL-II-73 and to explore any potential connection with the mechanism of action of ketamine.

Significant neurotrophic effects of GL-II-73 were notably more prominent in the apical segment of pyramidal neuron dendrites than in the basal segment. It is worth noting that the apical segment of pyramidal neurons represents one of the locations where α5 $GABA_A$ receptors are situated.[117] These findings strongly indicate that the neurotrophic effects of GL-II-73 are likely mediated through α5 $GABA_A$ receptors. Additionally, GL-II-73 increased both spine counts and spine density in the basal segment of pyramidal neurons in the CA1 region.

Interestingly, when the administration of GL-II-73 was discontinued, the cognitive effects diminished, while the neurotrophic effects persisted. This suggests that even with a robust neurotrophic effect, continuous presence of GL-II-73 is necessary in patients to sustain continuous improvement in cognitive performance.

Temporal lobe epilepsy (TLE) is a condition distinguished by the occurrence of spontaneous seizures or uncontrolled neural activity within the temporal lobe, specifically affecting the hippocampal formation.[118–121]

In a study aimed at creating a rodent model for temporal lobe epilepsy (TLE)[122,123], pilocarpine was administered directly into the ventral hippocampus (vHipp) through unilateral injection. Illustrated in **Figure 4A** is a representative brain slice indicating the path of the cannula. Rats subjected to intra-vHipp pilocarpine injection exhibited a notably higher Racine rating in comparison to control rats treated with saline. (**Figure 4B**, t test; $t = 11.29$, $p < 0.0001$). [124]

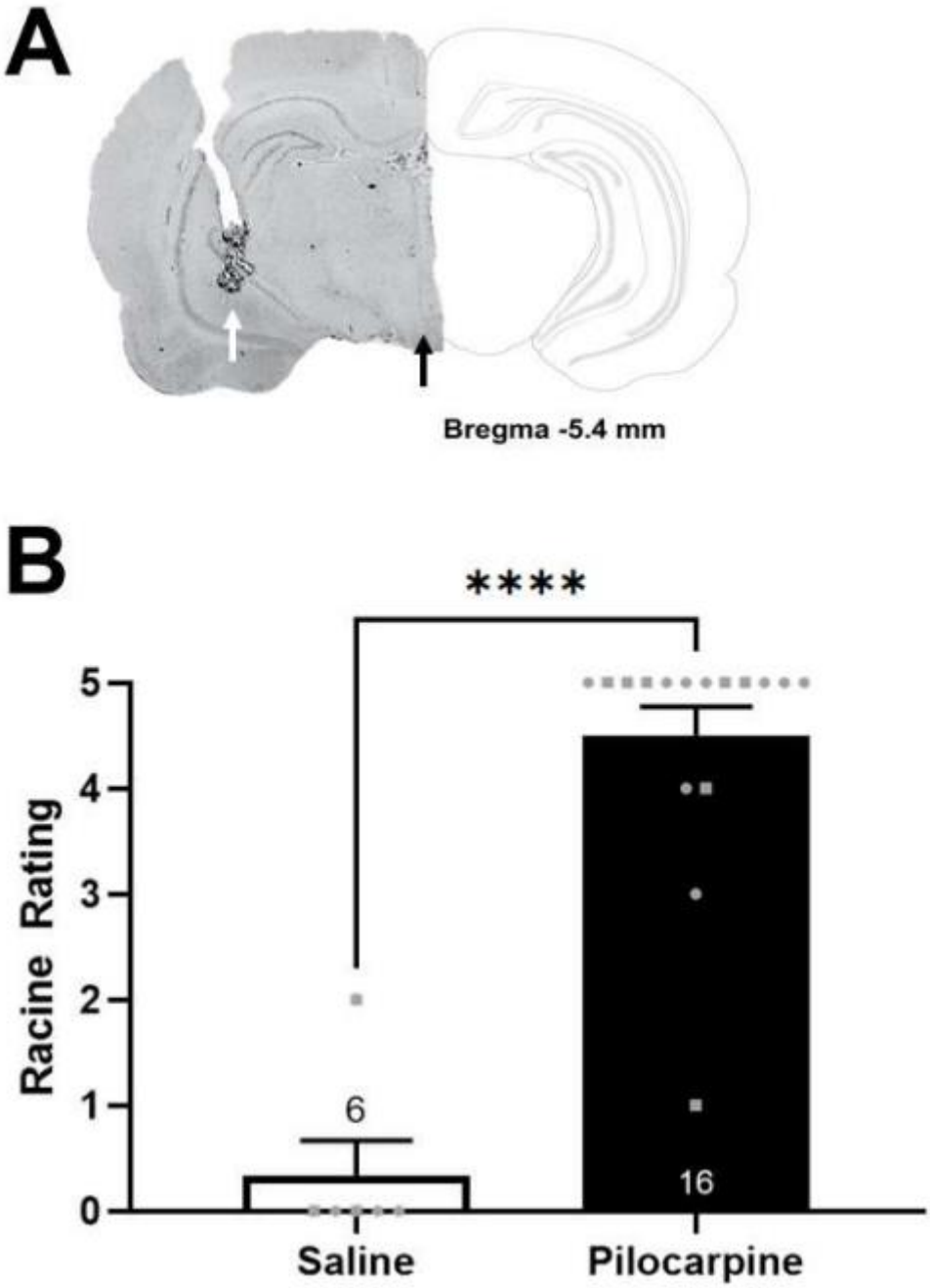


Figure 4. Verification of placements and response to pilocarpine. (A, Left) Representative brain slice containing an electrode track in the ventral tegmental area (VTA; black arrow) and cannula track in the ventral hippocampus (vHipp; white arrow) with a corresponding schematic of the brain section (right, −5.40 mm posterior to bregma). (B) Pilocarpine-treated

rats exhibited significantly higher average Racine ratings (seizures) as compared to saline-treated controls, **** $p < 0.0001$, n = 6– 16/group; circles denote male subjects and squares denote females.[6]

The functionality of the dopamine system is recognized to undergo changes in individuals with psychosis and in rodent models designed for psychosis research, including rats treated with pilocarpine.

The functioning of the dopamine system is recognized to undergo changes in individuals with psychosis[125–127] and in rodent models designed for studying psychosis[128–131] , including rats treated with pilocarpine[129]. In line with prior findings, a notable elevation in dopamine neuronal activity was observed in pilocarpine-treated rats that received intra-ventral hippocampus (vHipp) vehicle (**Figure 5A**, n = 13 rats; 1.88 ± 0.10 cells per track; two-way ANOVA; Pilocarpine (1,33) = 15.370; $p < 0.001$; FDrug (1,33) = 7.121; $p = 0.012$; Holm–Sidak; $t = 3.977$, $p = 0.002$) compared to saline-treated rats that received intra-vHipp vehicle (n = 6 rats; 1.13 ± 0.13 cells per track). Intriguingly, the pilocarpine-induced increase in dopamine neuronal activity was entirely reversed by the intra-vHipp administration of GL-II-73 (n = 12 rats; 1.30 ± 0.13 cells per track; Holm–Sidak; $t = 3.800$, $p = 0.002$), with no effect observed in saline-treated rats (n = 6 rats; 1.00 ± 0.09 cells per track). Consistent with a prior observation[129], a subgroup of rats (4 out of 17) did not exhibit a hyperdopaminergic phenotype (n = 4 rats; 1.05 ± 0.13 cells per track) and were classified as non-responders (defined as >1.5 cells per track) and were excluded from this dataset. As expected, no significant differences were noted in the average firing rate (**Figure 5B**; Pilocarpine (1,228) = 0.140; $p = 0.709$; Drug (1,228) = 0.039; $p = 0.844$) or bursting pattern (**Figure 5C**; Pilocarpine (1,228) < 0.001; $p = 0.989$; Drug (1,228) = 0.034; $p = 0.853$). It is noteworthy that while both male

(circles) and female (squares) subjects were represented, the study may not have sufficient power to detect any sex differences.

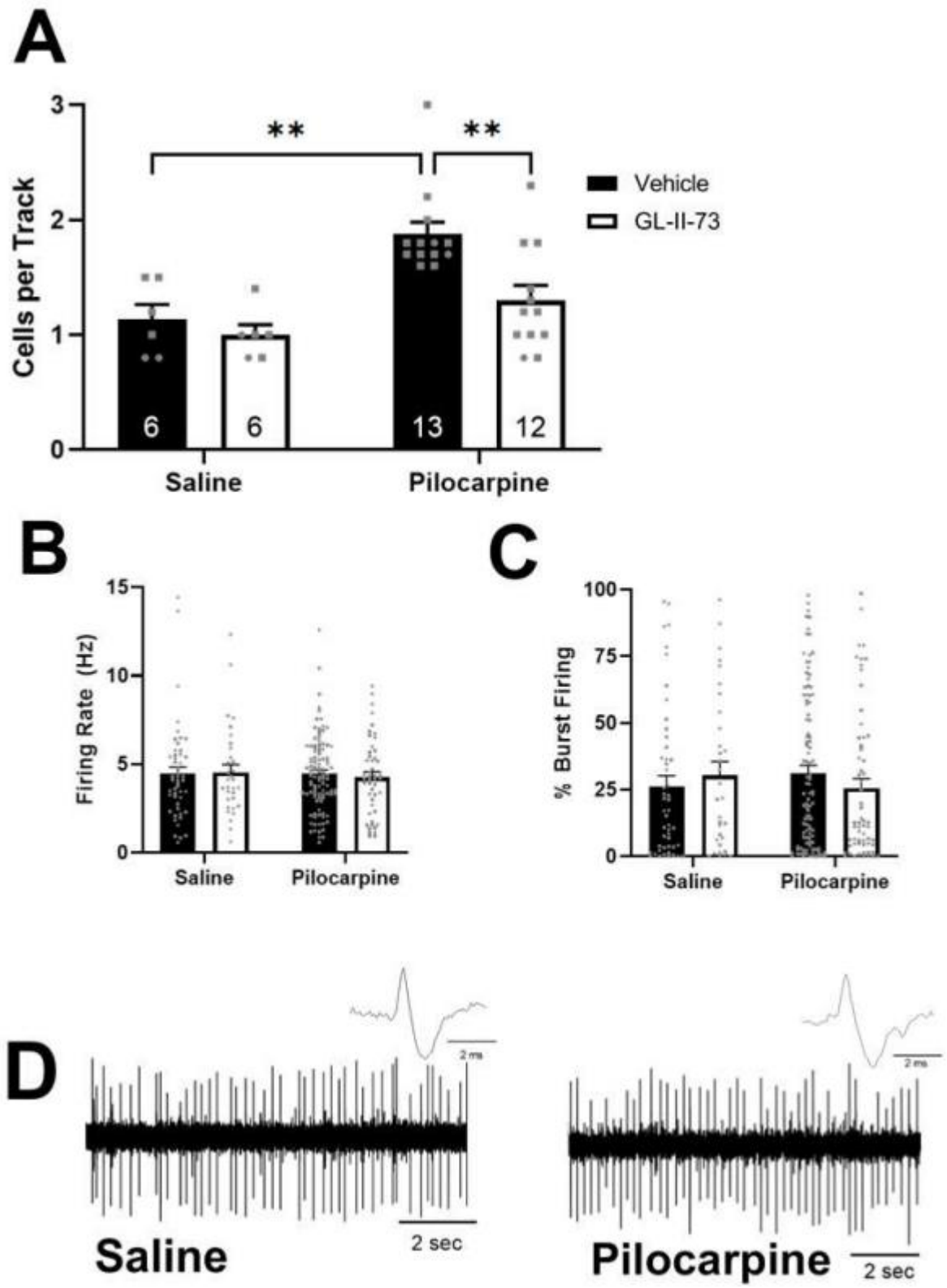

A
Cells per Track
3
2
1
0
**
**
Vehicle
GL-II-73
6
6
13
12
Saline
Pilocarpine
B
Firing Rate (Hz)
15
10
5
0
Saline
Pilocarpine
C
% Burst Firing
100
75
50
25
0
Saline
Pilocarpine
D
2 ms
2 sec
Saline
2 ms
Pilocarpine
2 sec

Figure 5. GL-II-73 reverses pilocarpine-induced increases in VTA dopamine neuronal activity. (A) Intra-ventral hippocampal (vHipp) pilocarpine significantly increased the number of spontaneously active dopamine cells per track (population activity), which was reversed by intra-vHipp administration of GL-II-73 (100 ng/µL; 0.75 µL). Average firing rate (B) and percent burst firing (C) were not changed by pilocarpine or drug treatment. (D) Representative trace of dopamine neuronal firing and action potential for saline-treated (left) and pilocarpine-treated (right) rats. ** $p < 0.005$, n = 6–13/group; circles denote male subjects and squares denote females.[6]

The specific localization of α5 $GABA_A$Rs, whether extra synaptic or synaptic, plays a pivotal role in modulating dopamine neuronal activity in the hippocampus[132], with known activity-dependent changes in α5$GABA_A$R localization[133]. Consequently, the expression and localization of α5 $GABA_A$Rs in rats treated with saline and pilocarpine was verified. To investigate synaptic localization, gephyrin-associated α5 $GABA_A$Rs has been measured, by using coimmunoprecipitation. The results indicated no discernible differences in total α5 protein levels (**Figure 5A**, t test; $t = 1.075$, $p = 0.314$) or gephyrin-pulldown α5 protein levels (**Figure 5B**, t test; $t = 1.631$, $p = 0.142$) between rats treated with pilocarpine and those treated with saline.[6]

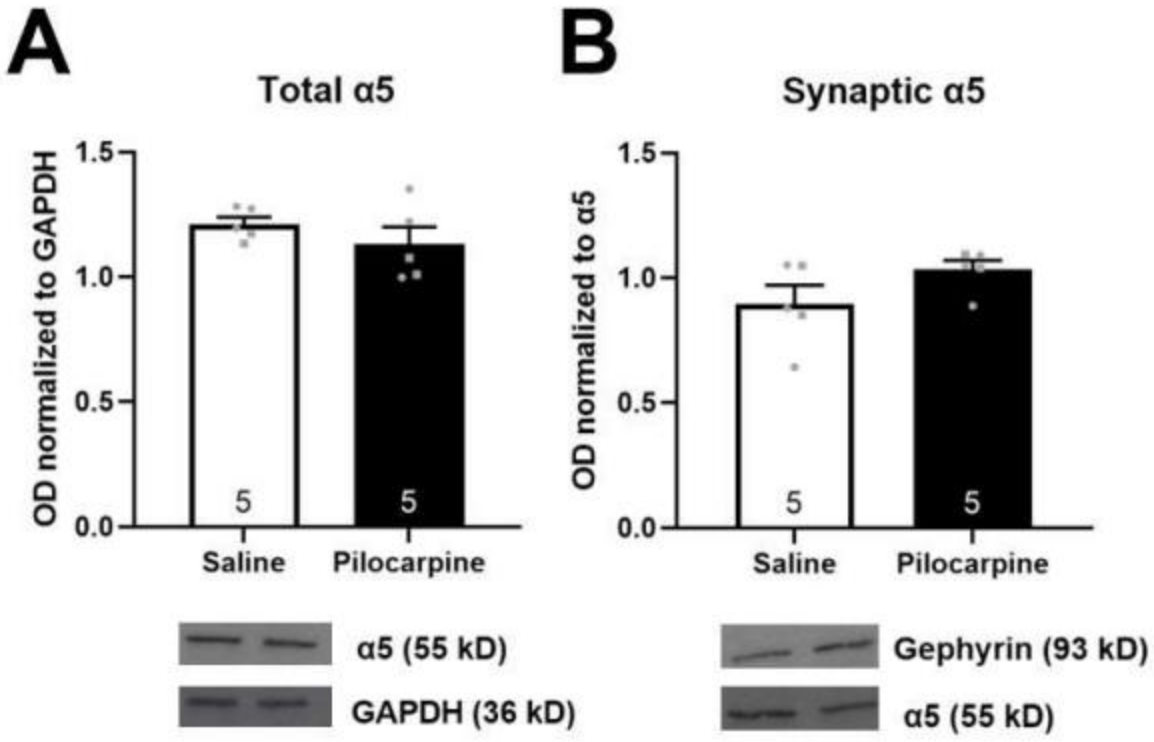


Figure 6. Pilocarpine does not alter total or synaptic α5 protein. There were no differences in total α5 protein expression. (A) Co-immunoprecipitation of α5 and gephyrin was used to measure synaptic α5 protein (B) between saline- and pilocarpine-treated rats. Representative bands from saline- (left) and pilocarpine-treated rats (right) are below graphs. n = 5 rats/group, circles denote male subjects and squares denote female rats. [6]

As mentioned earlier, GL-II-73 stands as the lead agent that induces neurotrophic effects targeting an inhibitory system to alleviate symptoms associated with depression and cognitive deficits. It has the potential to serve as a promising intervention for patients experiencing cognitive decline due to GABAergic downregulation, presenting anxiolytic and antidepressant effects.[111] Considering the promising results of these α5-$GABA_AR$ subtype selective ligands in animal

models, synthesizing the enantiomer of GL-II-73 would be crucial to transition this technology into clinical trials for GL-I-54 (enantiomer) has very similar effects as GL-II-73.[1]

Resynthesizing GL-I-54 has been undertaken to manufacture more of this drug for further biological studies related to its absorption, distribution, metabolism, excretion, and toxicity (For ADME toxicity studies).

2.2 Chemistry: Results and Discussion

2.2.1 The synthetic route to SH-053-2'F-S-CH_3, originally done on small scale by Huang and Li.

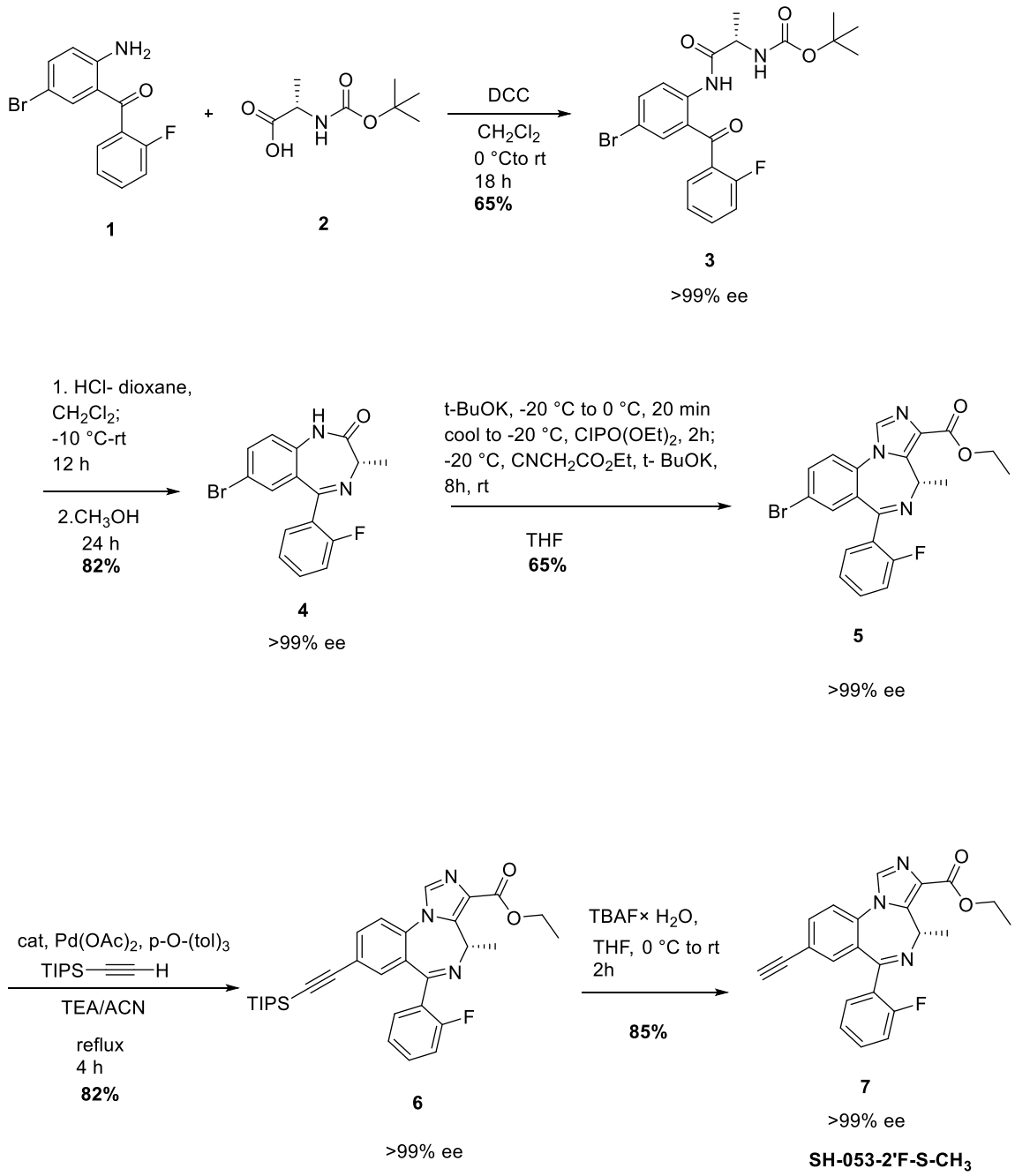
The (S) ethyl ester, ethyl (S)-8-ethynyl-6-(2-fluorophenyl)-4-methyl-4H-benzo[f]imidazo[1,5-a][1,4]diazepine-3-carboxylate, known as SH-053-2'F-S-CH_3 was produced on a relatively large scale to facilitate synthesis of additional analogs for structure-activity relationship (SAR) analysis. This synthesis followed a previously established synthetic route. As illustrated in **Scheme 1,** SH-053- 2'F-S-CH_3 originated from using the S-amino acid, (tert-butoxycarbonyl)-L-alanine.

The peptide coupling reaction involving the initial amine; 2-amino-5-bromophenyl)(2'-fluorophenyl)methanone (**1**), and the chiral amino acid was conducted utilizing the peptide coupling reagent N,N'-dicyclohexylcarbodiimide (DCC). The synthesis of amide (**3)** was achieved by reacting the amine with the S amino acid, N-Boc-L-alanine, in the presence of DCC, which resulted in a 65% yield on a 50-gram scale.

It is noteworthy that DCC, dissolved in dichloromethane (DCM), should be slowly added dropwise to the mixture of alanine and the initial benzophenone (**1**) in DCM at 0 °C. It is essential to avoid adding DCC in one portion at rt to prevent dimerization into a DCC urea dimer due to its concentration. The deprotection of the Boc-group was carried out using 4M HCl in dioxane. The

acid solution was gradually added to the mixture of amides (**3**) in dichloromethane (DCM) while maintaining the temperature between -10 and 0 °C for an hour. Subsequently, the mixture was stirred for 12 hours at rt. The 4M HCl in dioxane was effective for Boc-deprotection. The concentration of acid appeared to contribute to the enhanced deprotection of the Boc-group. The acidic solution was neutralized with an aqueous sodium bicarbonate ($NaHCO_3$) solution, which resultedin a mild exothermic reaction upon addition of the solution. The cyclization of the deprotected amine was achieved by dissolving the amine in methanol under neutral conditions and stirring for 24 hours. The desired 1,4-benzodiazepine intermediate (**4**) was purified by washing with a 10% ethyl acetate-hexane solvent mixture. The yield for the S-benzodiazepine intermediate (**4**) was 82%. The installation of the imidazole ring was excecuted using potassium t-butoxide, diethyl chlorophosphate, and ethyl isocyanoacetate. To ensure a successful reaction, it is crucial to add the reagents in a systematic manner and carefully monitor the temperature throughout the process. In the synthesis, potassium t-butoxide was introduced to the solution of benzodiazepine (**4**) in tetrahydrofuran (THF) at -20˚C, and this was followed by the addition of diethyl chlorophosphate at the same temperature after the formation of the anions. Subsequently, ethyl isocyanoacetate and a second portion of potassium t-butoxide were added at -20 ˚C. The reaction mixture was allowed to stir for 12 hours, which resulted in the formation of the desired imidazodiazepine (**5**) in 65% yield. The imidazodiazepine was purified by washing with t-butyl methyl ether. Copper-free Sonogashira coupling was then carried out to the imidazodiazepines to obtain TIPS-protected imidazodiazepine. The deprotection of the TIPS-protected imidazodiazepine (**6**) through fluoride-mediated methods resulted in the synthesis of SH-053-2'F-S-CH_3. The TIPS deprotection of the imidazodiazepine was carried out using tetra-n-butylammonium fluoride (1M solution in THF), to yield 85% of SH-053-2'F-S-CH_3.

Scheme 1. Synthesis of SH-05-2'F-S-CH_3



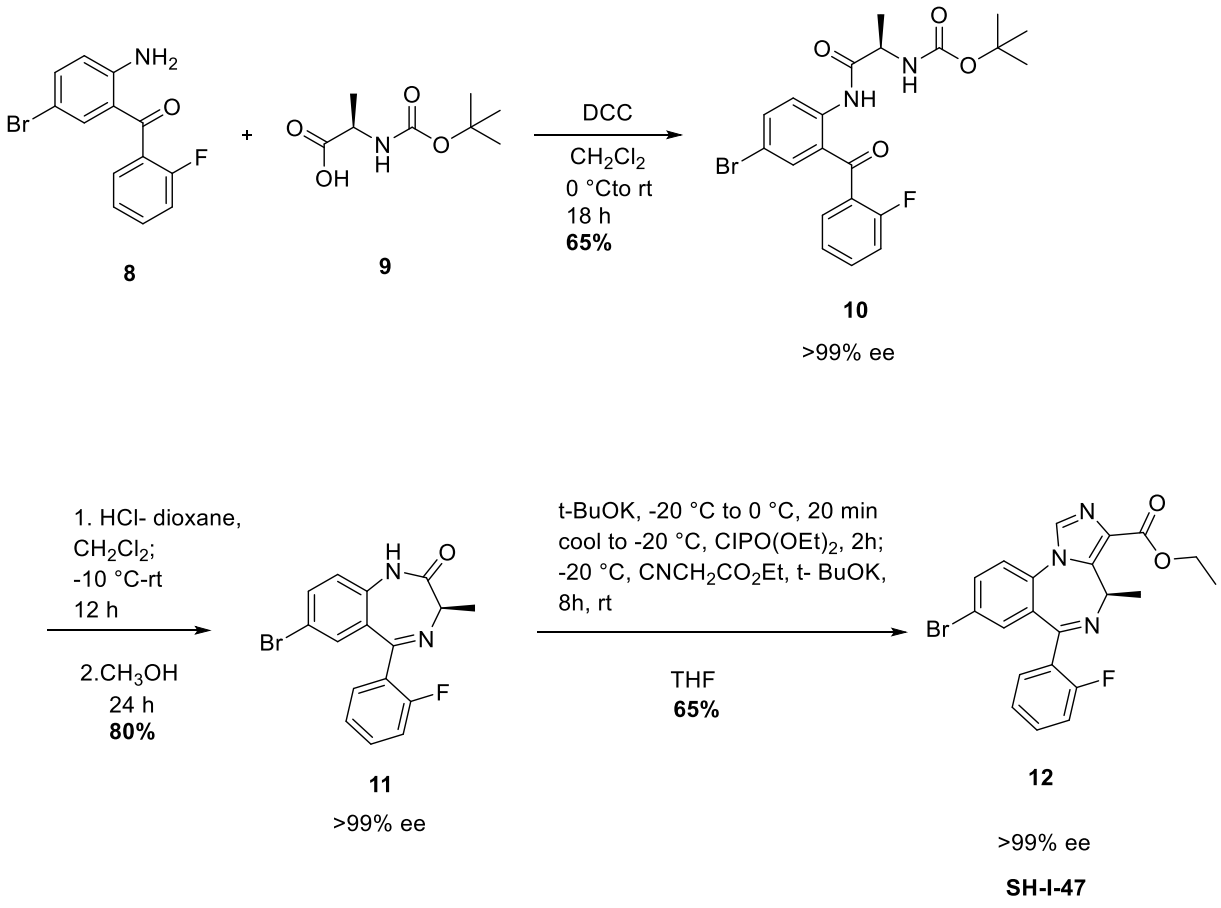
2.2.2 Synthesis of SH-I-47

A similar synthetic approach was followed to produce the R-amide, tert-butyl (R)-(1-((4-bromo-2-(2'fluorobenzoyl) phenyl)amino)-1-oxopropan-2-yl)carbamate (**10**), with N-Boc-L-alanine. The reaction yield for the R-enantiomer was comparable to that of the S-enantiomer. The synthesis involved coupling Boc-D-alanine with 2-amino-5-bromophenyl)(2'-fluorophenyl)methanone (**8**), utilizing the peptide coupling reagent N,N'-dicyclohexylcarbodiimide (DCC). The synthesis of amide (**10**) was achieved by reacting the amine with the R amino acid, N-Boc-D-alanine, in the presence of DCC, which resulted in a 67% yield on a 50-gram scale. **It is imperative to create a homogenous mixture by dissolving DCC in dry DCM before adding it to the mixture of Boc-L-alanine and the starting material in this coupling reaction. DCC was then added dropwise at 0°C to prevent the formation of the DCC urea dimer**.[134] The subsequent step involved Boc group deprotection, accomplished by dissolving the amide in dry DCM and adding 4M HCl in ether dropwise at 0°C. The mixture was stirred for 12 hours at rt. To ensure safety and quantify HCl, 4M HCl in dioxane was used instead of gaseous HCl. After consumption of the starting material, the reaction was quenched and washed with an aqueous $NaHCO_3$ solution.

For cyclization into the seven-membered ring, a neutral path was chosen. No strong base was used to maintain a pH of 8.5 and prevent racemization of the chiral R-CH_3 group. Dry MeOH at rt was exclusively used for cyclization, resulting in an 80% yield. The optical purity, confirmed by chiral HPLC, indicated that (**11**) was 99% optically pure. The installation of the imidazole ring was facilitated using potassium t-butoxide, diethyl chlorophosphate, and ethyl isocyanoacetate. To ensure a successful reaction, it is crucial to add the reagents in a systematic manner and carefully monitor the temperature throughout the process. In the synthesis, potassium t-butoxide was introduced to the solution of benzodiazepine (**11**) in tetrahydrofuran (THF) at -20˚C, and this was followed by the addition of diethyl chlorophosphate at the same temperature for the formation of

the anion. Subsequently, ethyl isocyanoacetate and a second portion of potassium t-butoxide were added at -20 ˚C. The reaction mixture was stirred for 12 hours, resulting in the formation of the desired imidazodiazepine (**12**) in 65% yield. The imidazodiazepine was purified through washing with t-methyl ether.

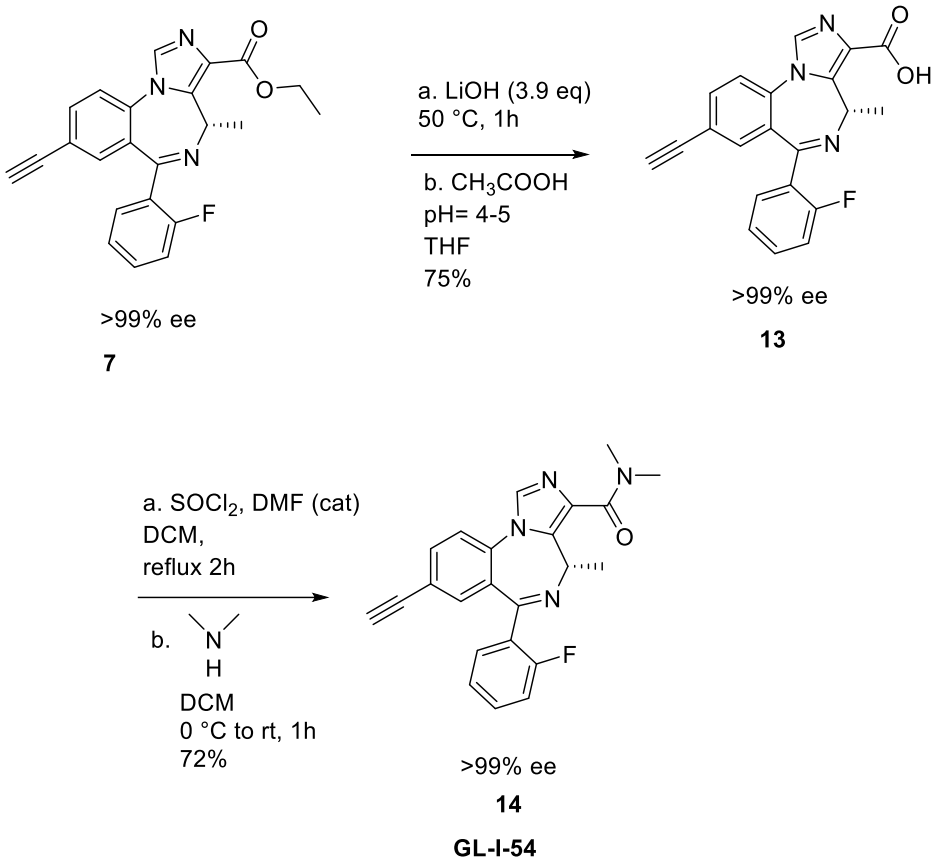
Scheme 2. Synthesis of SH-I-47



2.2.3 Synthesis of GL-I-54

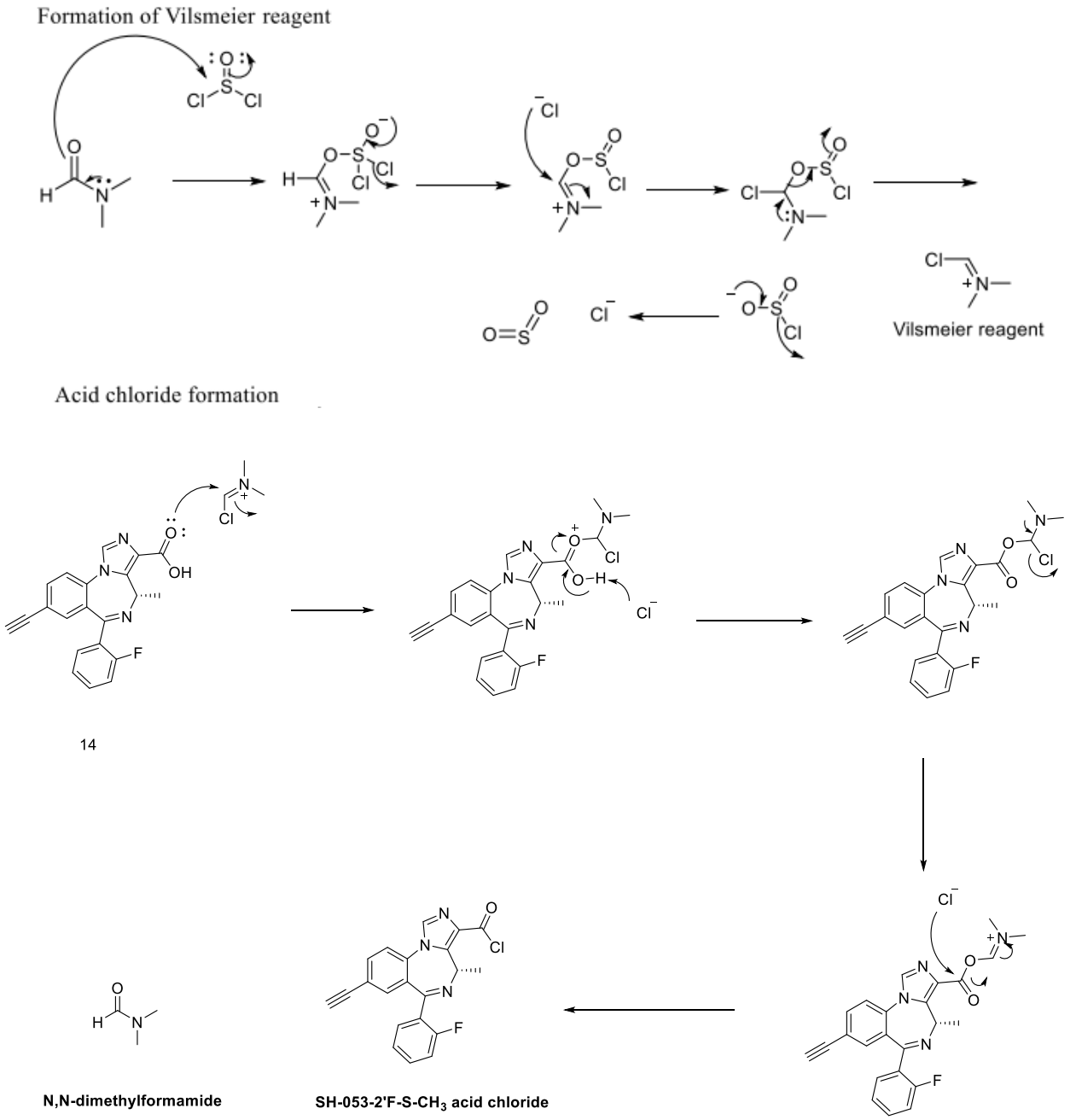
The synthesis of GL-I-54 (**Scheme 3**) was carried out starting from the ethyl ester SH-053-2'F-S-CH_3 (**7**). Initially, the ethyl ester was transformed into SH-053-2'F-S-CH_3 acid through base catalyzed hydrolysis. A solution of aqueous LiOH was gradually added to the THF solution of SH-053-2'F-S-CH_3. Following the completion of the ester hydrolysis reaction, the mixture was diluted with water before introducing acetic acid to neutralize the excess base. The dilution step with water played a crucial role, preventing the formation of a jelly-like thick mass during the evaporation of the THF. Acetic acid was employed to adjust the pH to 4-5, facilitating the precipitation of the acid (**13**) from the acidic water solution. The acid (**13**) by recrystallization from hot methanol recrystallization was purified.

Scheme 3. Synthesis of GL-I-54



GL-I-54 was synthesized through the Vilsmeier chlorination of SH-053-2'F-S-CH_3 acid (**13**), and this was followed by the addition of dimethylamine (2M solution in THF). The conversion of the acid into the acid chloride was achieved using anhydrous DCM and thionyl chloride. The thionyl chloride reacted with the catalytic N,N-dimethylformamide, to generate the Vilsmeier reagent, N,N-dimethyliminium chloride, a crucial reactive species in the Vilsmeier chlorination (**Scheme 4**). The GL-I-54 was formed through the nucleophilic attack of N,N-dimethylamine on the SH-053-2'F-S-CH_3 acid chloride. The purification of GL-I-54 was conducted via column chromatography (silica gel, EtOAc with 1% methanol), which resulted in a 72% yield.

Scheme 4: Possible mechanism of chlorination of SH-053-2'F-S-CH$_3$ acid



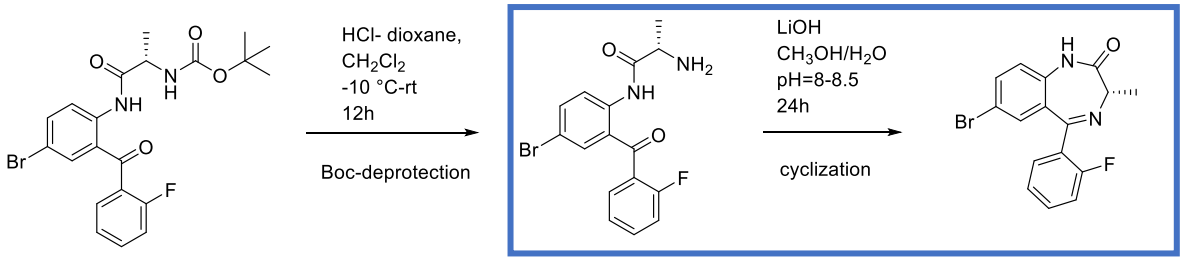
2.2.4 Improved synthesis of GL-I-54

The amide coupling reaction yield (**Scheme 1**), required development during the scale-up process to achieve a more effective generation of the Boc-protected β-amino amide intermediate (**3**).

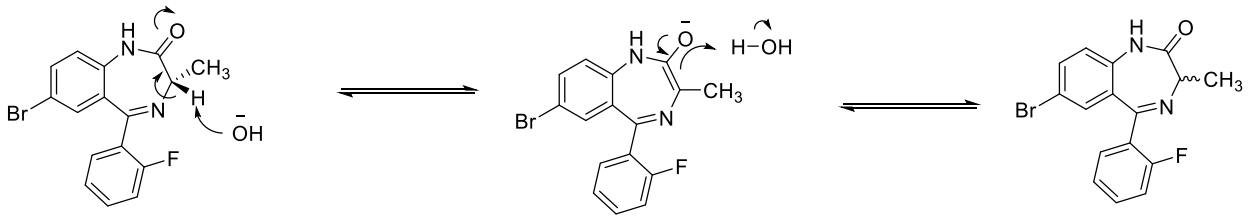
Although the reaction was stirred for a long time, the consumption of amino benzophenone was not completed. Knutson et al. attempted various strategies in 2020 to improve the yield, but unfortunately, no successful outcome was achieved.[135]

Epimerization of the chiral methyl group was also noted during the previous closure of the benzodiazepine ring (**Scheme 5, highlighted by a blue box**) under basic condensation conditions. Initially, 0.1 eq of aq. NaOH (1N) was utilized to adjust the pH to 8-8.5. To enhance the reaction rate, the equivalent of NaOH was increased to 1eq, which resulted completion in the reaction in 12 hours instead of 24 hours. While the intensified basic conditions improved the reaction rate, they concurrently induced epimerization of the chiral methyl group (Knutson et al.). Considering both the reaction yield of the peptide coupling reaction and the issues related to epimerization in the cyclization reaction, a new synthetic method was devised for the synthesis of GL-I-54 (**Scheme 7**).

Scheme 5. Cyclization of free amine to form benzodiazepine 4

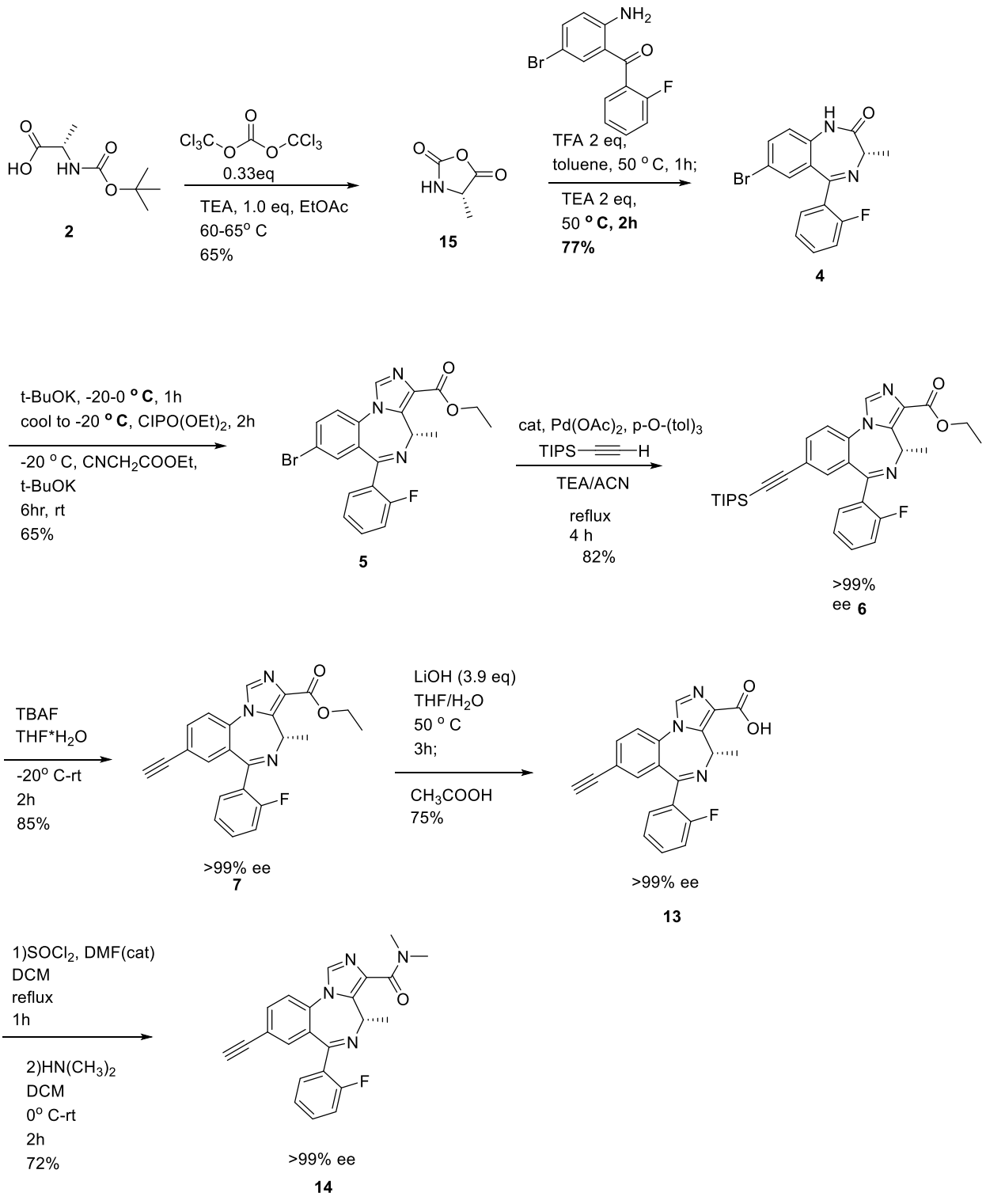


Scheme 6. Possible mechanism of racemization of benzodiazepine, 3

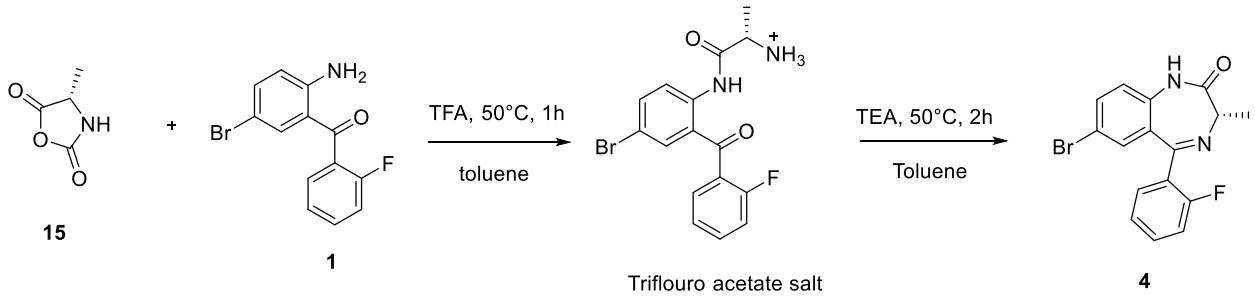


A novel procedure was developed, inspired by the method employed by Fier and Whitakker[136] at Merck and Co, wherein N-carboxyanhydrides (NCAs) were synthesized from optically pure amino acids. In non-polar solvents under neutral conditions, the condensation portion of the synthesis was conducted. A literature-based synthetic approach for N-carboxy-D-alanine anhydride (**17**) was utilized, which involved, the reaction of the amino acid with either phosgene [137,138] or triphosgene[139]. Considering safety concerns associated with phosgene, our group used triphosgene. The Boc-protected amino acid, N-carboxy-D-alanine (1 eq), was treated with triphosgene in the presence of 1 equivalent of triethylamine to yield N-carboxy-D-alanine anhydride (**17**). This method resulted in a moderate yield (65%) on a 60 g scale. The NCA was purified by the precipitation of the crude oily mass in a DCM: hexane (1:1) mixture. Subsequently, amino benzophenone (**1**) was reacted with the Boc-D-Alanine NCA in toluene in the presence of trifluoroacetic acid (2 eq) to produce the amide intermediate as the trifluoroacetate salt (**Scheme 8**). Trifluoroacetic acid was employed to provide the trifluoroacetate salt of the amide intermediate, preventing oligomer formation. Triethylamine (2 equivalents) was then added to facilitate condensation of the primary amine with the benzophenone carbonyl group, yielding the optically pure (>99 %ee) benzodiazepine (**3**) in 77% yield. The benzodiazepine solid was easily purified by washing with the ethyl acetate / hexanes mixture (1:9).

Scheme 7. Improved synthesis of GL-I-54

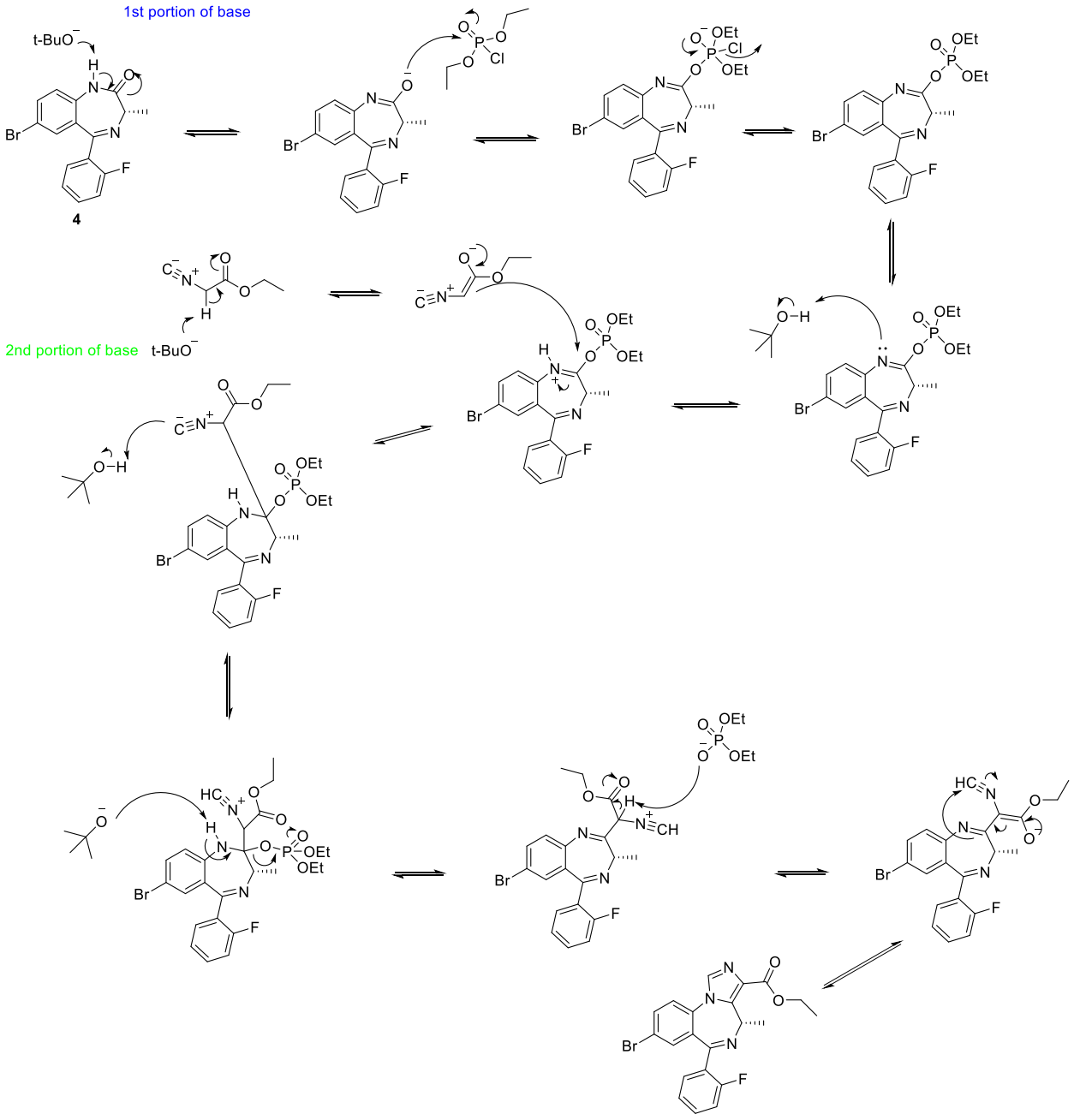


Scheme 8: Synthesis of benzodiazepine intermediate by NCA route



The third step involved the synthesis of the imidazodiazepine (**12**) by introducing the imidazole ring onto the seven-membered ring of benzodiazepines[140]. Several modifications were implemented to enhance the overall reaction conditions. In the previous procedure, 1.5 equivalents of solid potassium t-butoxide were added once to deprotonate the benzodiazepine, whereas in this procedure, a solution of potassium t-butoxide (1.3 eq) in THF was utilized to achieve the same effect. Deprotonation was effectively achieved under these basic conditions. Diethylchlorophosphate was then added to form the iminophosphate (**Scheme 9**). As indicated by TLC. Once all starting materials were consumed the second portion of base and ethyl isocyanoacetate were added. A smaller amount of ethyl isocyanoacetate (1.3 eq) was used as compared to the previous procedure, and no chromatography was necessary to purify the product. Pure imidazodiazepine (**12**) was obtained by washing the crude solid with t-butyl methyl ether. The hot t-butyl methyl ether effectively removed any traces of byproducts related to the phosphate byproducts. The subsequent step in the reaction sequence involved converting aryl bromide **12** into the silyl-protected acetylene through a copper-free Sonogashira coupling[141,142]. Palladium played a crucial role in both cycles of the reaction. The copper-free Sonogashira coupling of the imidazodiazepine intermediate with TIPS-acetylene resulted in the formation of TIPS-protected SH-053-2'F-S-CH_3 in 85% yield.

Scheme 9: Possible mechanism of imidazole top installation on benzodiazepine 4



The final step involved the fluoride-mediated deprotection of the silyl protecting group. By carefully adding TBAF (1M solution in THF) at a temperature of -10°C, successful deprotection of the TIPS group was achieved, which resulted in SH-053-2'F-S-CH_3 with 99% ee. Unlike the previous method that relied on chromatographic purification of this R-enantiomer, the newly developed method utilized a methanol-water mixture to eliminate impurities related to tetrabutylammonium salts. **It is much more efficient.**

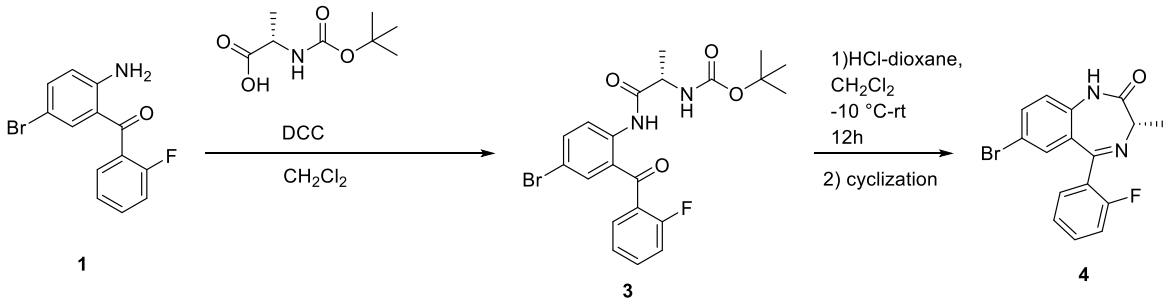
Subsequently, the ethyl ester (SH-053-2'F-S-CH_3) was hydrolyzed to SH-053-2'F-S-CH_3 acid using a base. Previously, NaOH was employed for this purpose, exhibiting no issues with hydrolytic capacity but, which caused, gel formation during the reaction workup. Acetic acid was required to neutralize the excess base and precipitate the acidic product, but the gel formation made stirring almost impossible. In the new method, LiOH was used as the base, successfully resolving the gel formation problem; it did not form.

The SH-053-2'F-S-CH_3 was purified from hot ethanol through precipitation. The acid (**13**) underwent the Vilsmeier chlorination to form the acid chloride, and this was followed by nucleophilic addition of dimethylamine to the acid chloride to provide the desired GL-I-54 in 99%ee. The yield of this step closely resembled that of the previous method (70%). Unlike the prior approach, which involved purification of GL-I-54 through silica gel column chromatography, this method employed a t-butyl methyl ether wash to remove impurities, which resulted, in GL-I-54 in similar purity to the product purified by column chromatography. However, the amount obtained, was higher.

This novel approach is robust and demonstrates a relatively higher yield, as compared to the prior method. Moreover, the initial two steps (NCA formation and cyclization, **Scheme 10**) demand stringent anhydrous conditions, involving anhydrous reagents, dry flasks, and meticulous

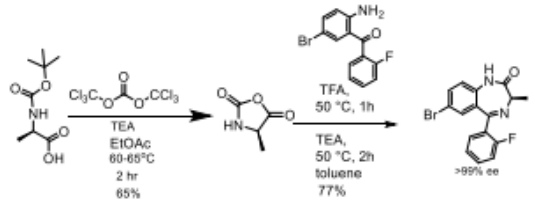
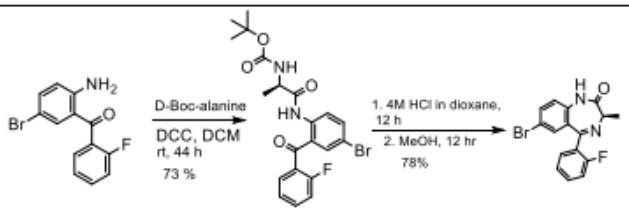
monitoring, as even trace amounts of moisture can compromise the reaction. These steps can be somewhat challenging, especially during warmer seasons. Additionally, the anhydrous solvents and reagents utilized are more costly than ACS-grade reagents.

Scheme 10: Peptide coupling and cyclization for formation of benzodiazepine, 4

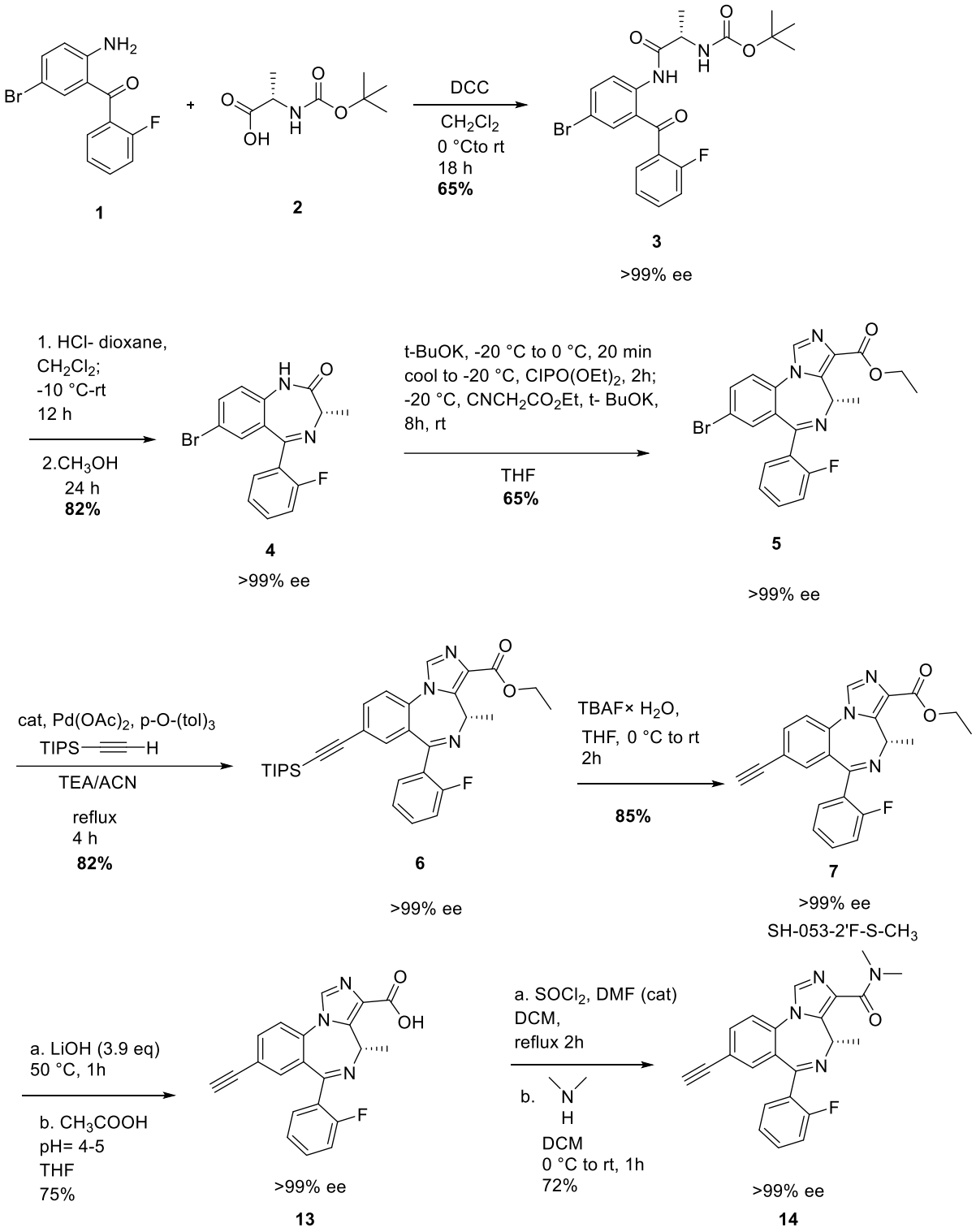


The cost analysis (**Table 4**) comparing the production of benzodiazepine (**3**) through both routes (NCA route and Boc-route) revealed that the Boc-route incurred slightly lower costs than the NCA route. However, despite the cost advantage of the Boc-route, the NCA route demonstrated a better yield and proved to be relatively less time-consuming. It is noteworthy that both routes yielded optically pure benzodiazepine (**4**). **The Boc-route was favored for all chiral benzodiazepines due to its robust and straightforward nature** with less need stringent anhydrous monitoring. This material was sent to Domana pharmaceuticals for preclinical toxicology and bioavailability.

Table 4. Comparison of cost of benzodiazepine produced by NCA route and Boc route

NCA route			**Boc route**		
					
Chemicals	Amount	Cost($)	Chemicals	Amount	Cost
Benzophenone	140 g	350	Benzophenone	120 g	300
Boc-D-Ala-OH	100 g	76	Boc-D-Ala-OH	105 g	80
Ethyl acetate (anhydrous)	4200 mL	270.9	Dichloromethane	2500 mL	128
Triethylamine (anhydrous)	214 ml	197	4M HCl in dioxane	323 mL	88
Dichloromethane (anhydrous)	400 mL	27.6	$NaHCO_3$	50 g	76
Hexane (anhydrous)	900 mL	98.1	Methanol	1200 mL	74
Toluene (anhydrous)	2200 mL	106.59	Ethyl acetate	100 mL	14
Trifluoro acetic acid (anhydrous)	73 mL	60	Hexane	900 mL	65
Ethyl acetate	170 mL	24			
Heptane	1500 mL	95			
Total cost		1350	Total cost		825
Time		28 hr	Time		65 hr
Yield	127 g	10.27$/g	Yield	93 g	8.87 $/g

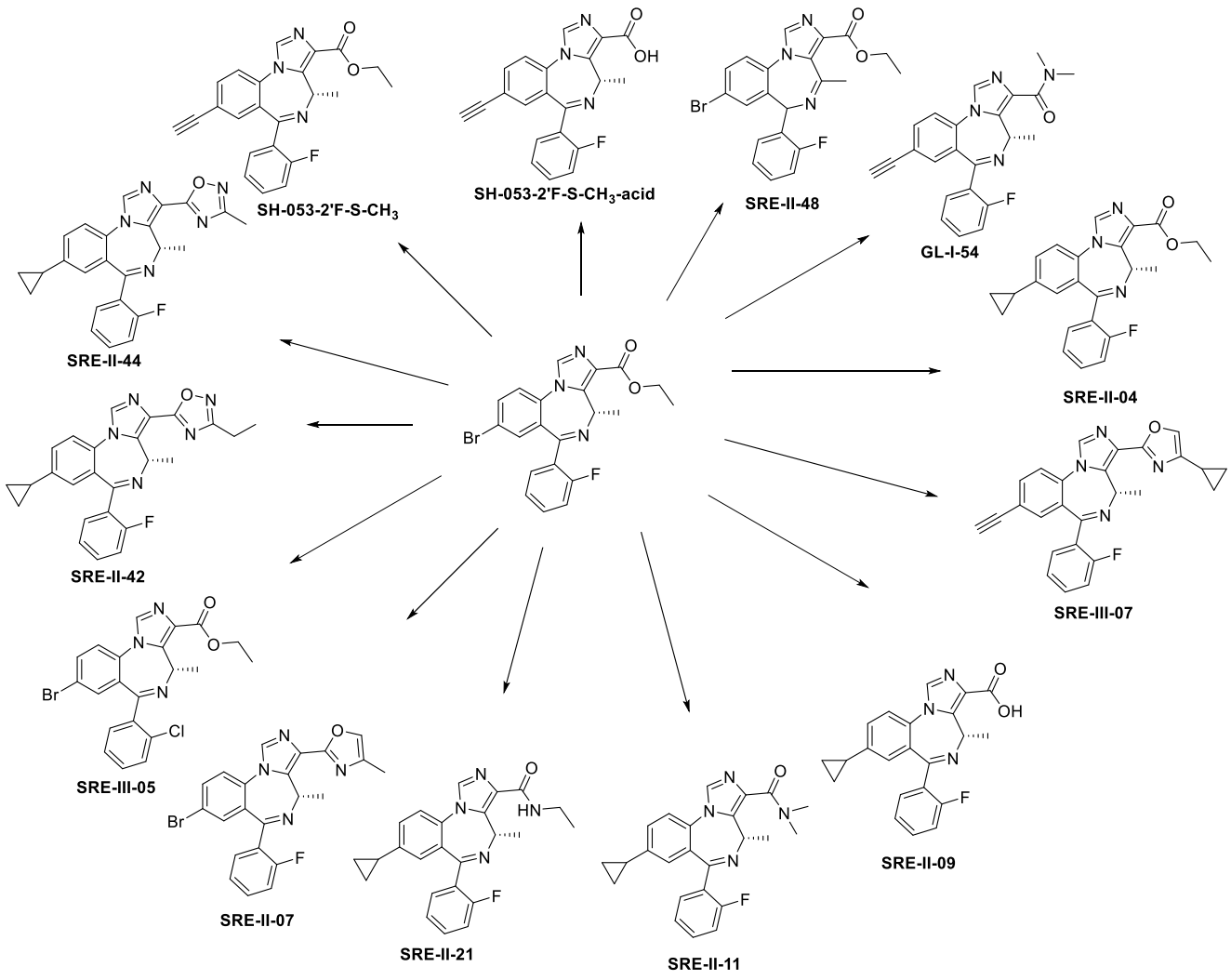
Scheme 11. Synthesis of GL-I-54 with Boc route



2.2.5 Synthesis of analogs of GL-I-54 for SAR

Evidence suggests that even subtle alterations in the structure of IMDZ substituents can significantly impact the subtype selectivity of BzR/GABA(A)R.[143] For instance, the α5-subtype selectivity experiences a decrease when the chiral methyl group at the C(4) position of imidazodiazepines is lost. Additionally, altering the lipophilic groups at the C(8) position influences α5 selectivity. To improve active ligands with a more favorable antipsychotic or procognitive profile, several modifications were introduced into the structure of GL-I-54 (**Scheme 12**). These newly synthesized analogs demonstrated increased affinity and potency at α5[144] or α2/3-subtypes, leading to enhanced and prolonged physiological effects. These novel analogs were systematically characterized and evaluated in various animal models to assess their bioactivity and structure-activity relationships (SAR). As previously noted, the C(8)-ethynyl and C(4) methyl function of imidazodiazepines were identified as crucial positions for enhancing α5-subtype selectivity. Consequently, to replace the ethynyl group, a cyclopropyl group was introduced at the C-8 position of GL-I-54. The incorporation of a cyclopropyl group is a common strategy employed in various biologically active molecules to achieve improved pharmacological properties. This cyclopropyl group is expected to engage in similar interactions within the lipophilic binding pocket (L2, see **Figure 6**) as the cyclopropyl group, leading to parallel physiological effects and enhanced subtype selectivity.[145]

Scheme 12: Synthesis of analogs of SH-I-48B



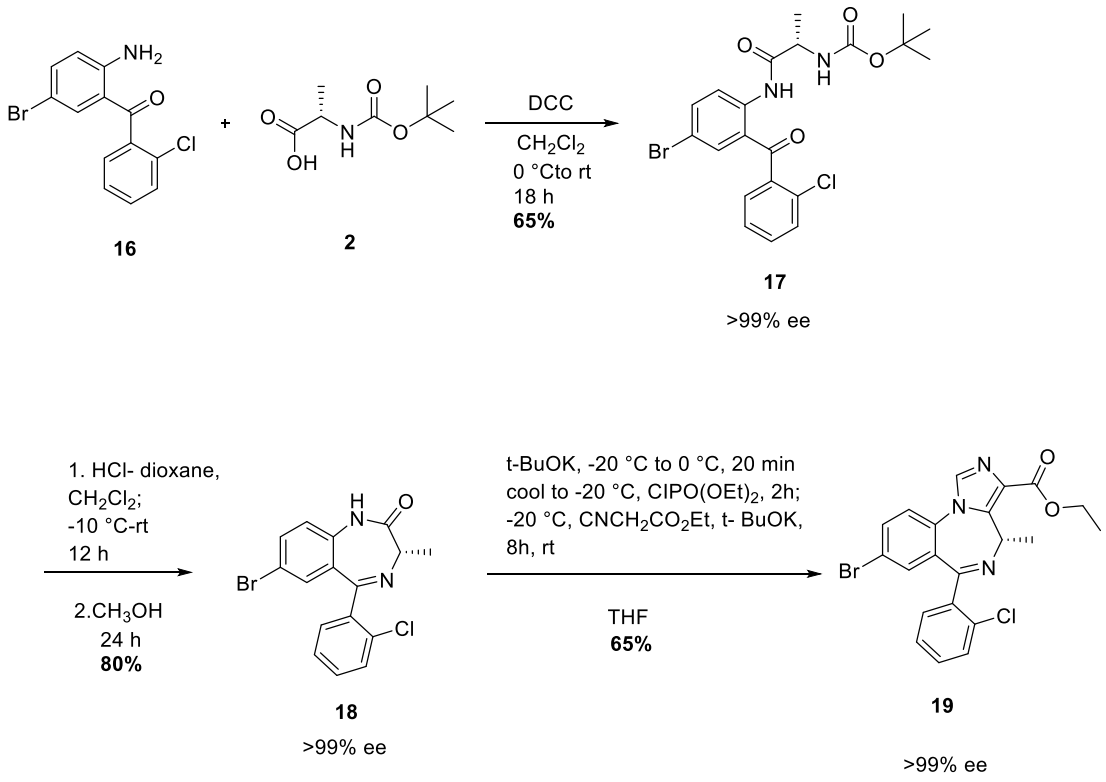
A similar synthetic approach was followed to produce the 2'Cl imidazodiazapine (**19**), with N-Boc-D-alanine. The synthesis involved coupling Boc-D-alanine with 2-amino-5-bromophenyl)(2'-chlorophenyl)methanone (**16**), utilizing the peptide coupling reagent N,N'-dicyclohexylcarbodiimide (DCC). The synthesis of amide (**17**) was achieved by reacting the amine with the S amino acid, N-Boc-D-alanine, in the presence of DCC, which resulted in a 67% yield on a scale of 100-grams.

It's imperative to create a homogenous mixture by dissolving DCC in dry DCM before adding it to the mixture of Boc-D-alanine and the starting material in this coupling reaction. DCC was then added dropwise at 0°C to prevent the formation of DCC urea dimer byproduct.

The subsequent step involved Boc group deprotection, accomplished by dissolving the amide in dry DCM and adding 4M HCl in ether dropwise at 0°C. The mixture was stirred for 12 hours at rt. To ensure safety and quantify HCl, 4M HCl in dioxane was used instead of gaseous HCl. After consumption of the starting material, the reaction was quenched and washed with an aqueous solution of $NaHCO_3$.

For cyclization into the seven-membered ring, a neutral path was chosen. No strong base was used to maintain a pH of 8.5 and prevent racemization of the chiral R-CH_3 group. Dry MeOH at rtwas exclusively used for the cyclization, resulting in an 80% yield. The optical purity, as confirmed by HPLC, indicated that (**18**) was 99% optically pure. The installation of the imidazole ring was accomplished using potassium t-butoxide, diethyl chlorophosphate, and ethyl isocyanoacetate. To ensure a successful reaction, it is crucial to add the reagents in a systematic manner and carefully monitor the temperature throughout the process. In the synthesis, potassium t-butoxide was introduced into a solution of benzodiazepine (**18**) in tetrahydrofuran (THF) at -20˚C and this was followed by the addition of diethyl chlorophosphate at the same temperature after the formation of anion. Subsequently, ethyl isocyanoacetate and a second portion of potassium t-butoxide were added at -20 ˚C. The reaction mixture was allowed to stir for 12 hours, which resulted in the formation of the desired imidazodiazepine (**19**) in 65% yield. The imidazodiazepine was purified by washing away the impurities witht-methyl ether.

Scheme 13. Synthesis of the 2'Cl imidazodiazepine intermediate



The 8-cyclopropyl ester intermediate, SRE-II-04 (**20**), was synthesized using the 8-bromo imidazodiazepine ester (**5**) through a sequence followed by Suzuki coupling with cyclopropyl boronic acid. The Vilsmeier chlorination was applied on 8-cyclopropyl ester (**20**) to synthesis 8-cyclopropyl, acid (**21**). The substitution of the ester functions with bioisosteric replacement has been utilized in drug discovery and medicinal chemistry to promote increased metabolic stability, minimize side effects, and collectively enhance the development of a superior clinical candidates. The replacement of ester functions in ligand SH-053-2'F-S-CH_3 with substituted 1,2,4-oxadiazoles resulted in improved hydrophilicity of the ligands and enhanced in vitro and in vivo stability. This

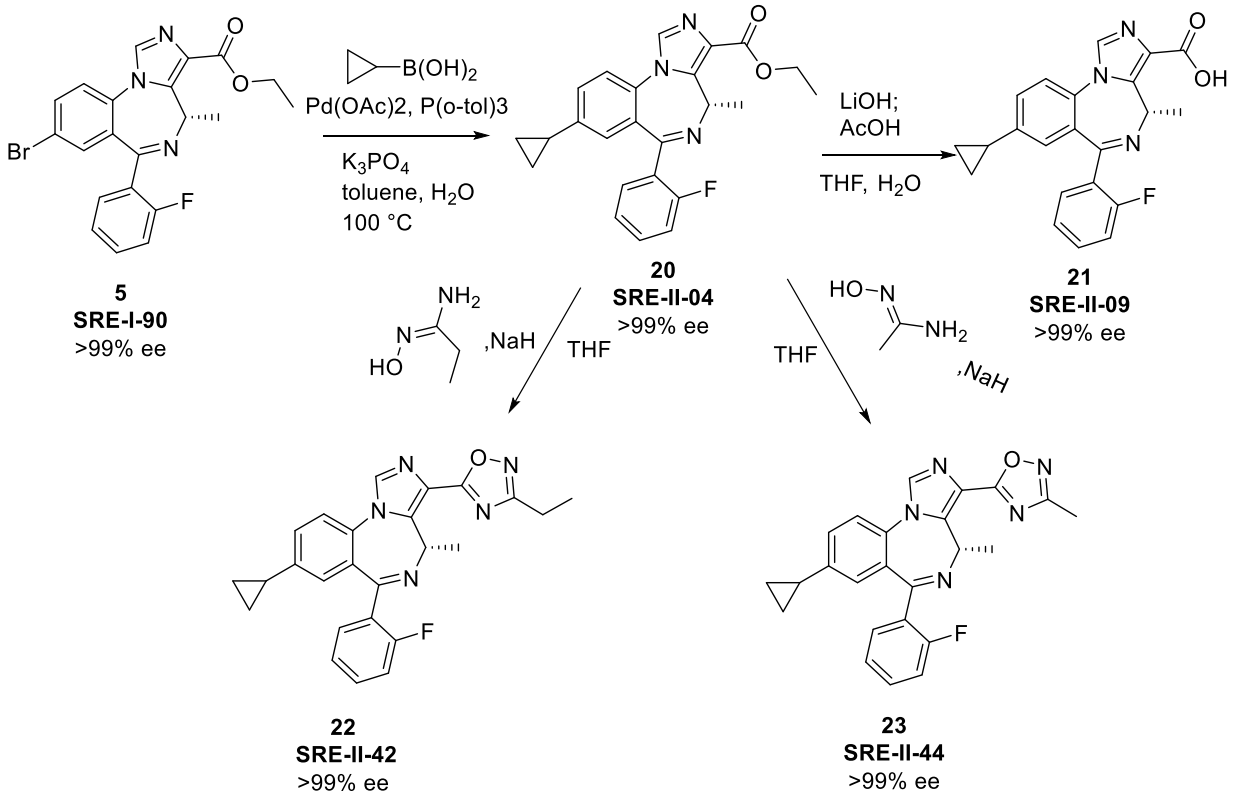
substitution also selectively elevated the efficacy of ligands at BZD receptors, as compared to their ester counterparts. Oxadiazole rings play a crucial role in drug discovery, contributing to ligand binding as an essential part of the pharmacophore. In various cases, these rings act as flat, aromatic-like linkers with strategically placed substituents. By modifying molecular properties, oxadiazoles can modulate them into the periphery of the molecule. Additionally, oxadiazoles serve as bioisosteric replacements for carbonyl-containing compounds such as esters and amides. Various regioisomeric forms of oxadiazole rings exist, including two 1,2,4-isomers, a 1,3,4-isomer, and a less common 1,2,5-regioisomer. Oxadiazoles exhibit hydrogen bond acceptor properties, and the regioisomers display different hydrogen bonding potentials. Considering these factors, several 1,2,4-oxadiazole analogs related to the structure of SH-053-2'F-S-CH_3 and GL-I-54 were synthesized. The synthesis of 1,2,4-oxadiazole analogs of GL-I-54 involved treating different imidazodiazepine ethyl esters with various oximes (methyl, ethyl and cyclopropyl) in the presence of sodium hydride. This approach is particularly significant for the synthesis of bioisosteric replacements in the context of drug development.

The required oximes were reacted with sodium hydride in THF for one hour, and this was followed by the addition of a THF solution containing the ethyl ester (**20**). **Caution is advised regarding the quantity of sodium hydride used, if the quality of hydride is not of sufficient purity** an incomplete reaction may occur. When the hydride is effective and the equivalents exceed 1.3, there is a risk of forming a non-polar olefinic migrated byproduct. This byproduct tends to accumulate at the top of the corresponding oxadiazole products on silica gel (TLC). The final compounds **22** and **23** were produced in yields ranging from 73 to 80%.

Remarkably, the 8-cyclopropyl analogs demonstrated promising pro-cognitive activity in the Y-maze assay (data not published). The oxadiazole emerged as a pivotal factor in the observed

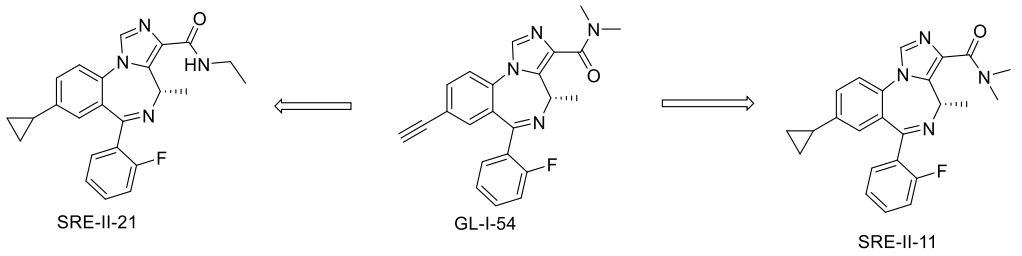
procognitive activity, challenging the conventional expectation that ligands with a chiral substituent at C-4 are requisite for precognitive activity.

Scheme 14. Synthesis of 8-cyclopropyl analogs



Since GL-I-54 and the 8-cyclopropyl analog were effective in precognitive assay at low doses. Analogs for Angelman's syndrome, and neuropathic pain, the other amide analog of GL-I-54 was also synthesized to test in the model of cognition and Angelman's syndrome. On the other hand, the S enantiomer of GL-III-68 was also synthesized for further SAR studies.

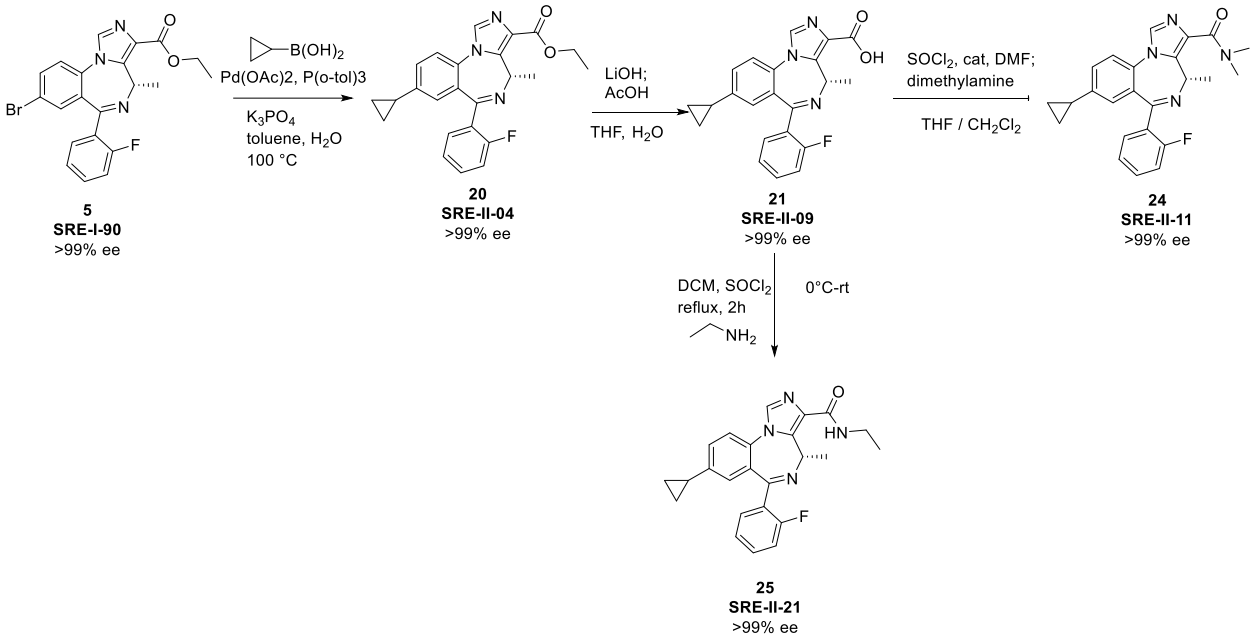
Scheme 15: Amide analogs of GL-I-54



The synthesis of SRE-II-11 (**Scheme 16**) was carried out starting from the 8-cyclopropyl, ethyl ester SRE-II-04 (**20**). Initially, the ethyl ester was transformed into SRE-II-09 acid through base hydrolysis. A solution of aqueous LiOH was gradually added to the THF solution of SRE-II-09. Following the completion of the ester hydrolysis, the mixture, which resulted, catalyzed was diluted with water before introducing acetic acid to neutralize the excess base. The dilution step with water played a crucial role, preventing the formation of a jelly-like thick mass during the removal of THF under reduced pressure. Acetic acid was employed to adjust the pH to 4-5, to facilitate the precipitation of the acid (**21**) from the acidic water solution. The acid (**21**) was purified by recrystallization from hot methanol. GL-I-54 was synthesized through the Vilsmeier chlorination of SRE-II-09 acid (**21**) and this was followed by the addition of dimethylamine or ethyl amine (2M solution in THF). The conversion of the acid into the acid chloride was achieved using anhydrous DCM and thionyl chloride. Thionyl chloride reacted with catalytic N, N-dimethylformamide, generating the Vilsmeier reagent, N,N-dimethyliminium chloride, a crucial reactive species in the Vilsmeier chlorination (**Scheme 16**). SRE-II-11 and SRE-II-21 were formed through the nucleophilic attack of N, N-dimethylamine or ethylamine on the SRE-II-09 acid chloride, respectively. The purification of both amides was conducted via column

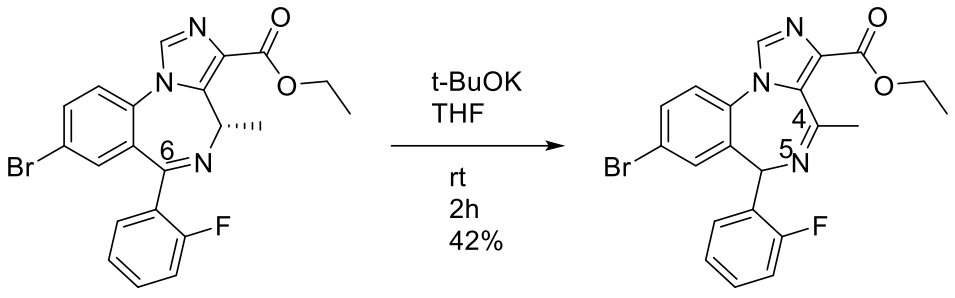
chromatography (silica gel, EtOAc with 1% methanol), which resulted in a 72% yield for both amides.

Scheme 16. Synthesis of amide analogs



The significance of the chiral methyl group in conferring selectivity for the α5-$GABA_AR$ subtype has been highlighted earlier. Investigations indicate that both chiral configurations (R and S) exhibit promising outcomes in various anxiety, depression, and asthma models [1,146]. The seven-membered ring of imidazodiazepines is capable of transitioning between two conformations, major and minor. Fixing the chiral methyl group and stabilizing the rotation of the seven-membered ring could result in the exclusive preparation of one SH-I-48B conformer, potentially the active conformation for receptor interactions. To test this hypothesis, isomerizing the olefinic bond (C=N) to the C-5 and N-5 positions was explored, leading to the development of a more rigid analog of SH-I-48B referred to as SRE-II-48 (**Scheme 17**).

Scheme 17. Synthesis of SRE-II-48



5 **26**

SH-I-48B underwent treatment with potassium t-butoxide in THF to facilitate olefinic migration, which resulted in the production of olefinic isomeer **26**. In this process, potassium t-butoxide abstracted the chiral proton, inducing migration of the imine bond, as outlined in **Scheme 17**.

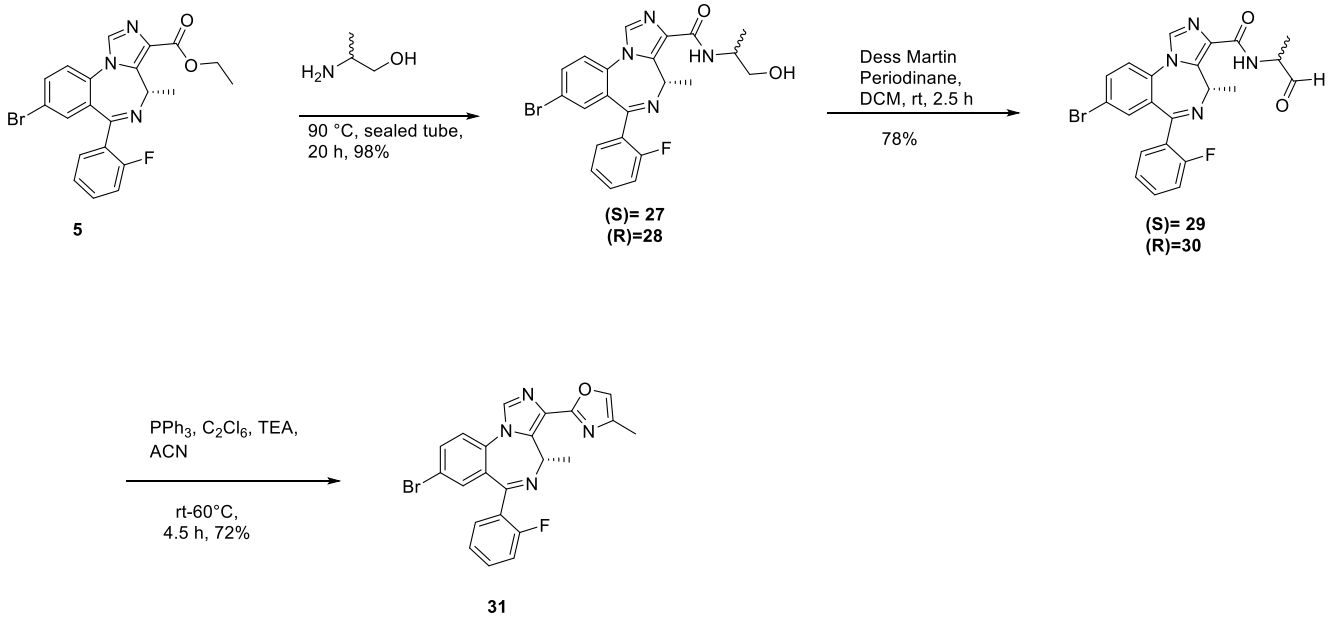
The procedure for synthesizing oxazoles was disclosed by Pandey et, al[147]. Following the completion of the large-scale synthesis of the ethyl ester intermediate **5**, it was heated in a sealed tube at 90 °C with either a substituted chiral or racemic methanolamine, individually, which resulted in the corresponding β-hydroxy amides. These amides were then purified through flash column chromatography, achieving yields between 80% and 98% [147]. Notably, this method employed only 6 equivalents of methanolamines to produce β-hydroxy amides (**27** and **28**), as depicted in **Scheme 18**. This represented an improvement over previous syntheses of β-hydroxy amides, which required a substantial excess (>40 equivalents) of methanolamine[147]. Most of the amino alcohols **27** and **28** were obtained by adding cold water after completion of the reaction.

Furthermore, the purification of these β-hydroxy amides (**27** and **28**) involved precipitation from 10-20% MeOH in EtOAc.

The oxidation of the hydroxy functional group in the formed β-hydroxy amides (**27** and **28**) was accomplished using the Dess-Martin reagent (1.2 equivalents), to yieldthe corresponding α-acylaminoaldehydes (**29** and **30**). These aldehydes underwent purification through precipitation from 10-20% MeOH in EtOAc.[147]

Ultimately, after several attempts, the reaction conditions were chosen triphenylphosphine and hexachloroethane. The optimal conditions involved the use of triphenylphosphine (3 equivalents), hexachloroethane (3 equivalents), and triethylamine (6 equivalents), with stirring for 2 hours at a temperature ranging from 0 °C to rt. This resulted in a yield of 71-74%. Employing this method, SRE-II-07 (**31**) was successfully synthesized and purified by precipitation and then by flash column chromatography, to yield an off-white colored solid, as illustrated in **Scheme 18**.

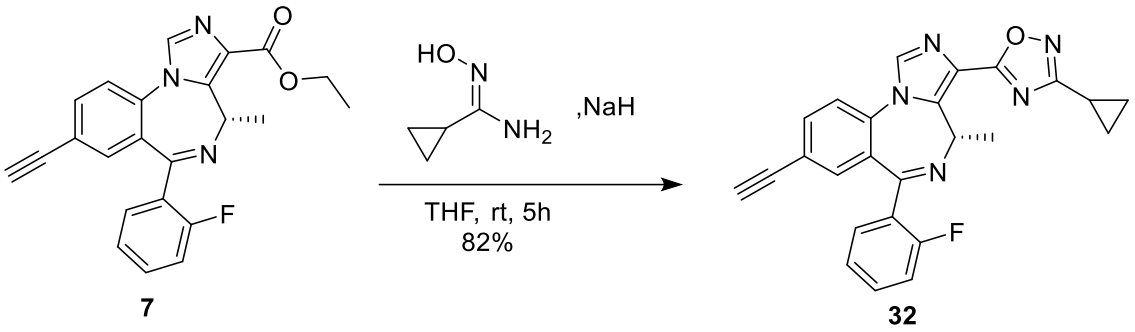
Scheme 18. Synthesis of the oxazole analog, SRE-II-07



Previously, we found the importance of the synthesis of different bioisosterics. As the cyclopropyl oxadiazole MYM-V-28, made by Md Yeunus Mian, demonstrated potentioal great activity in different studies. The S enantiomer of this compound, SRE-III-07 was made for further screening.

The cyclopropyl oxime reacted with sodium hydride in THF for one hour and this was followed by the addition of a THF solution, which continued, the ethyl ester (**7**). Caution is advised regarding the quantity of sodium hydride employed in this sequence. If the quality of hydride is not of sufficient purity, as an incomplete reaction may occur. When the hydride is effective and the equivalents exceed 1.3, there is a risk of forming a non-polar olefinic migrated byproduct. This byproduct tends to accumulate at the top of the corresponding oxadiazole products on silica gel (TLC). The final compound **32** was produced in yield 82%.

Scheme 19. Synthesis of the enantiomer of MYM-V-28, SRE-III-07



2.3. Results and Discussion: Biological Evaluation of GL-I-54 and is Analogs

A series of biological assays, such as cytotoxicity assays, rotarod tests, receptor binding studies, electrophysiology recording assays as well as PK studies, were performed with the lead compounds (GL-II-73 and GL-I-54), as well as all newly designed IMDZs. GL-II-73 was

resynthesized by my colleagues, Dishary Sharmin and Md Yeunus Mian, and GL-I-54 was resynthesized by me.

2.3.1. Comparative study of electrophysiological profiles of GL-II-73 and its enantiomer, GL-I-54 with Ashley Bernardo, Dr Prevot and coworkers[1]

The electrophysiological characteristics of each compound were separately investigated to assess their effects on human recombinant α1-5 $GABA_A$-Rs. The HEK- 293T cell line was transfected with full-length cDNAs for the human $GABA_A$ receptor subtypes (α1β3γ2, α2β3γ2, α3β3γ2, α4β3γ2 or α5β3γ2) for this study. The electrophysiological data was recorded using a standard method. [1] Confirming their roles as allosteric modulators and not agonists, when GABA was absent from the media, neither GL-II-73 nor GL-I-54 exhibited potentiation at any of the receptors on their own. (**Figure 7**)

In the presence of GABA, GL-I-54 was tested, revealing increased potentiation at α2 (beginning at 0.03μM and above), α3 (starting from 0.33μM and above), α1 (from 1μM and above), and α5 (at 0.03, 0.33, and 3.33 μM) as depicted in **Figure 7A**. However, preferences among α1-5 were discerned through repeated measurements of ANOVA. Significant subunit differences ($F(4;105)=81.19$; $p<0.0001$) were identified, and concentration-dependent effects ($F(6;105)=19.4$; $p<0.0001$) were noted for GL-I-54 (**Table 5**). An interaction between subunit and concentration was also observed ($F(24;105)=5.201$; $p<0.0001$; **Figure 7A**). In the case of GL-I-54, α2 exhibited preferential activity over α1, α3, α4, and α5 at various concentrations, while α3 demonstrated preference over α1, α4, and α5. α4 subtype exhibited less potentiation than α5 and α1, with no discernible preference between α5 and α1. In summary, α2 was significantly targeted over α1 at a concentration of 0.3μM ($p<0.01$), aligning with the findings reported by Fischer, Rowlett et al. (2010).[104]

Table 5. Statistical significance of potentiation between the different α-subunits; EC3

n=4		GL-I-54									
		α1vα2	α1vα3	α1vα4	**α1vα5**	α2vα3	α2vα4	**α2vα5**	α3vα4	**α3vα5**	**α4vα5**
Concentration (μM)	0.03	ns	ns	ns	ns	ns	ns	ns	ns	ns	ns
	0.1	ns	p<0.05	ns	ns	ns	ns	ns	p<0.05	ns	ns
	0.33	p<0.01	p<0.001	ns	ns	ns	p<0.001	ns	p<0.001	ns	ns
	1	ns	p<0.001	ns	ns	ns	p<0.001	ns	p<0.001	p<0.05	p<0.01
	3.33	ns	p<0.001	p<0.01	ns	p<0.001	p<0.001	p<0.01	p<0.001	p<0.001	ns
	10	ns	p<0.001	p<0.01	ns	p<0.001	p<0.001	ns	p<0.001	p<0.001	p<0.01
	33.3	ns	p<0.001	p<0.01	ns	p<0.001	p<0.001	p<0.05	p<0.001	p<0.001	ns

GL-II-73 demonstrated a significant increase in potentiation at $GABA_AR$s, specifically at α5 (starting from 1μM and above), α2 (starting from 3.33μM and above), and α1 (at 33.33μM) in the presence of GABA. Through a repeated measure of ANOVA (**Figure 7B**), the preferential selectivity of GL-II-73 for one subunit type over others was observed. Notably, GL-II-73 exhibited α5 selectivity over α1, α2, α3, and α4 at various concentrations, including 0.3μM ($p<0.05$), 3.33μM ($p<0.001$), 10μM ($p<0.001$), and 33μM ($p<0.001$). These findings, summarized in **Table 6,** lead to the conclusion that GL-II-73 behaves as a selective α5 positive allosteric modulator (PAM) of $GABA_AR$ at concentrations below 10 μM.[1]

Table 6. Statistical significance of potentiation between the different α-subunits; EC3

n=4		GL-II-73									
		α1vα2	α1vα3	α1vα4	**α1vα5**	α2vα3	α2vα4	**α2vα5**	α3vα4	**α3vα5**	**α4vα5**
Concentration (μM)	0.03	ns	ns	ns	**ns**	ns	ns	**ns**	ns	**ns**	**ns**
	0.1	ns	ns	ns	**ns**	ns	ns	**ns**	ns	**ns**	**ns**
	0.33	ns	ns	ns	**p<0.05**	ns	ns	**ns**	ns	**ns**	**ns**
	1	ns	ns	ns	**p<0.05**	ns	ns	**ns**	ns	**p<0.05**	**ns**
	3.33	ns	ns	ns	**p<0.001**	ns	ns	**p<0.01**	ns	**p<0.01**	**p<0.001**
	10	ns	ns	ns	**p<0.001**	ns	ns	**p<0.001**	ns	**p<0.001**	**p<0.001**
	33.3	p<0.05	p<0.05	ns	**p<0.001**	ns	p<0.001	**ns**	p<0.001	**ns**	**p<0.001**

A stepwise approach to estimate the maximum free brain concentrations of 5 mg/kg of GL-I-54 and 5 mg/kg of GL-II-73 (doses used in acute behavioral testing) and associate them with the range of corresponding $GABA_A$ receptor potentiation values (obtained in electrophysiological experiments) was carried out. Maximum brain concentrations were achieved around 20 min after dosing (**Figure 7C** and Prevot et al.[9]). Blue content (color) refers to GL-I-54 and green to GL-II-73. White and nuances of the grey and black color at the right bottom graph refer to the particular α subunit of $GABA_A$ receptors, as indicated in the upper right table. **Step 1** – brain concentrations (ng/g) determined 20 minutes after intraperitoneal dosing of 3 mg/kg GL-I-54 or GL-II-73 to male mice, respectively (n = 3 per compound); **Step 2** – estimation of maximum brain concentrations (ng/g) for 5 mg/kg of GL-I-54 and 5mg/kg of GL-II-73, obtained by multiplying Step 1 concentrations with the factor 5/3 (=1.67), based on an assumption that both GL-I-54 and GL-II-73 display first-order pharmacokinetics (pharmacokinetics of GL-II-73 was not saturated at 3 and 10 mg/kg, since the increase in the concentration of the compound is proportionate); **Step 3** – free brain concentrations (ng/g) obtained by multiplying Step 2 concentrations with the free fractions

in the brain determined by rapid equilibrium dialysis (0.1149 for GL-I-54 and 0.1214 for GL-II-73); **Step 4** – adjusting the Step 3 concentrations (ng/g) for the brain density (1.04 g/ml) and converting the units to ng/ml; **Step 5** – further conversion of units to nmol/l (unit used in electrophysiological experiments) by multiplying Step 4 concentrations with 1000/386.42 (386.42 g/mol is a molecular weight of GL-I-54 and GL-II-73) – the comparable estimated maximum free brain concentrations (nmol/l) of 5 mg/kg GL-I-54 and 5 mg/kg of GL-II-73 were then obtained; **Step 6** – association of Step 5 concentrations with the electrophysiological results – the estimated concentrations closely correspond to 100 nmol/l or, to a lesser extent, to 330 nmol/l of a compound administered in an electrophysiological experiment. This implies that, in acute behavioral experiments with 5 mg/kg dose, GL-I-54 likely potentiates α_1, α_2, α_3 and α_5 $GABA_A$ receptors, however, α_1 potentiation is weak; however, 5 mg/kg of GL-II-73, on the other hand, is fairly silent on all $GABA_A$ receptors, with the potential to mildly activate α_2 and α_5 receptors; on α_1 and α_3 receptors, nevertheless, it behaves as a null modulator. Due to such properties, the racemic mixture of 5 mg/kg of GL-I-54 and 5 mg/kg of GL-II-73 might display an advantageous pharmacological profile in vivo. By complete attenuation of activity at α1 $GABA_A$ receptors with GL-II-73, the potentiation of α2, α3 and α5 $GABA_A$ receptors by GL-I-54 might become predominant, exhibiting favorable behavioral effects. Ø – potentiation < 120% (null), + – potentiation < 200% (mild), ++ – potentiation < 250% (moderate), +++ – potentiation ≥ 250 % (strong). For exact values of potentiation at $GABA_A$ receptors containing distinct α subunits, please refer to **Figure 7.**

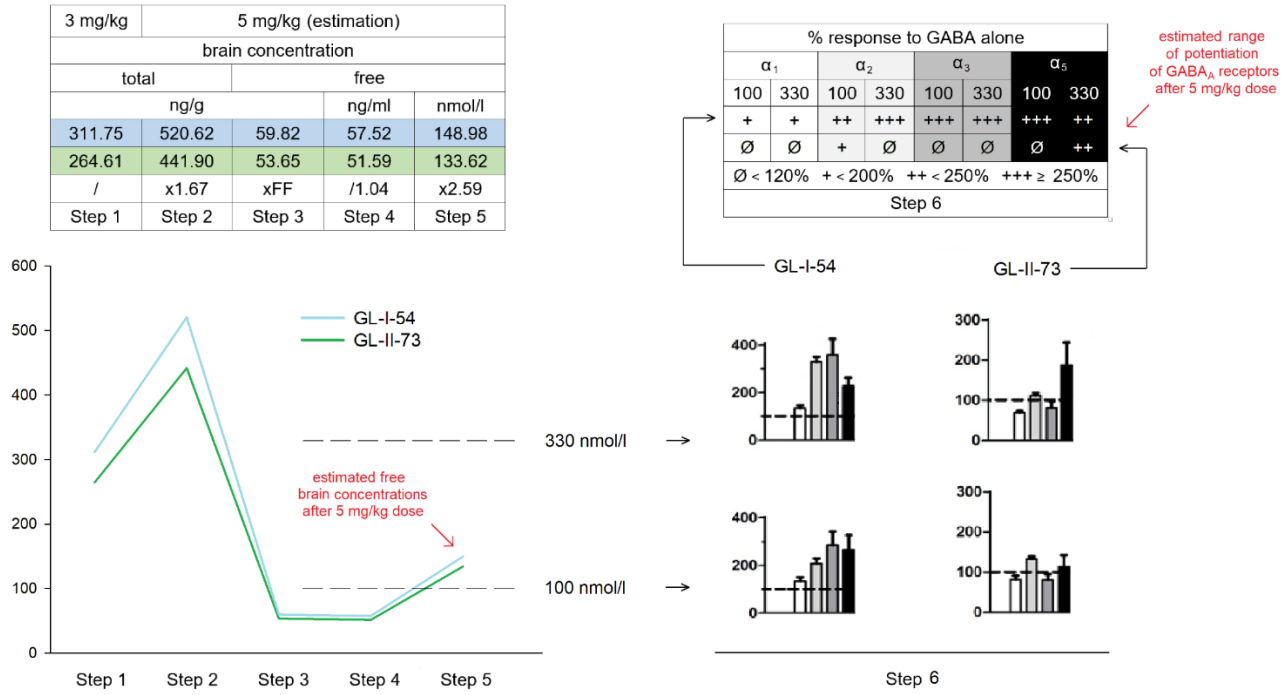


Figure 7. Estimate maximum free brain concentrations of 5 mg/kg of GL-I-54 and 5 mg/kg of GL-II-73

Examination of the results indicated neither GL-II-73 (**Figure 8B**) nor GL-I-54(**Figure 8A**) produced any potentiation at any of the receptors in the absence of GABA in the media. This evidence suggested that both GL-II-73 and GL-I-54 acted as allosteric modulators of GABAAR but not as an orthostatic agonist.

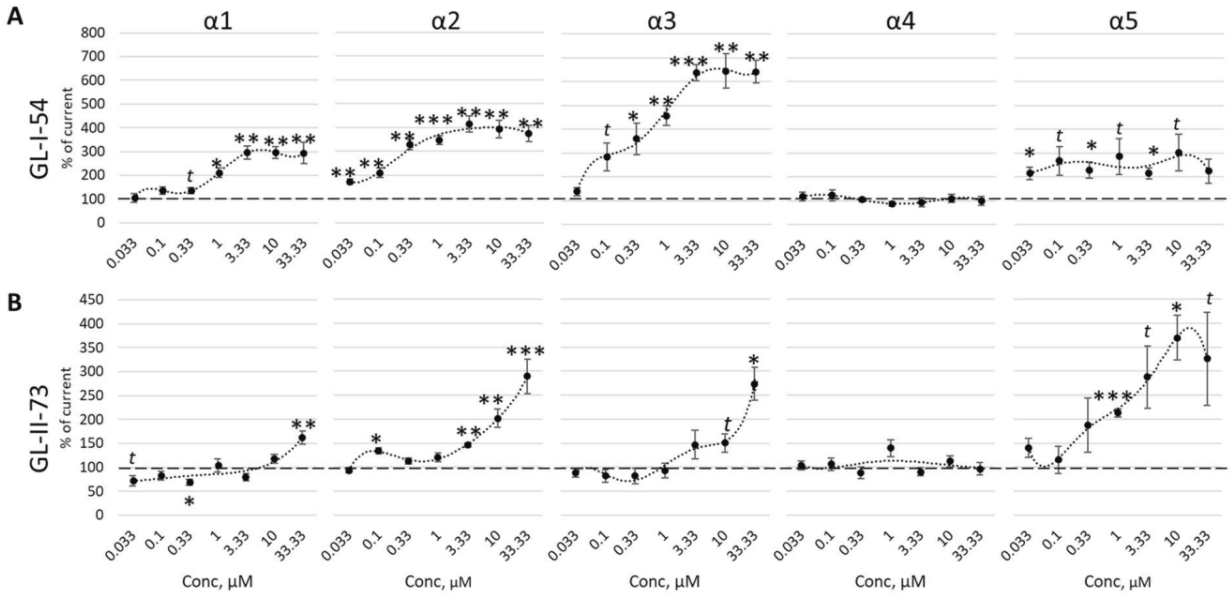


Figure 8. Potentiation of GL-I-54 at α1-5-containing receptors in the presence of GABA. Figures were modified from Ashely et al. 2021 Electrophysiological of GL-I-54 and GL-II-73. Electrophysiological recordings were obtained from HEK-293T cells transfected with full-length cDNA for human $GABA_A$ receptor subtypes α1β3γ2, α2β3γ2, α3β3γ2, α4β3γ2 or α5β3γ2, in presence of GL-I-54 (A) or GL-II-73 (B), and in the presence of GABA in the medium (5 μM).

Both enantiomers were verified as positive allosteric modulators (PAMs) rather than orthostatic agonists, functioning exclusively in the presence of GABA. GL-I-54 demonstrated a significant increase in potentiation at α2-$GABA_A$-Rs (>0.03 μM), α3-$GABA_A$-Rs (>0.33 μM), α1-GABAA-Rs (>1 μM), and α5-$GABA_A$-Rs (0.03, 0.33, and 3.33 μM; **Figure 9A**). This effect exhibited preferential activity at α3- and α2-$GABA_A$-Rs over α1-, α4-, and α5-$GABA_A$-Rs.

On the other hand, GL-II-73 displayed a significant increase in potentiation at α5-GABAA-Rs (>1 μM), α2-$GABA_A$-Rs (3.33 μM), α3-$GABA_A$-Rs (33.33 μM), and α1-$GABA_A$-Rs (33.33 μM; **Figure 9B**). Notably, it showed preferential activity at α5-$GABA_A$-Rs over α1-$GABA_A$-Rs (>0.3

μM), α2-$GABA_A$-Rs (between 3.3 and 10 μM), α3-GABAA-Rs (between 1 and 10 μM), and α4-$GABA_A$-Rs (>0.33 μM), confirming previously published data[1].

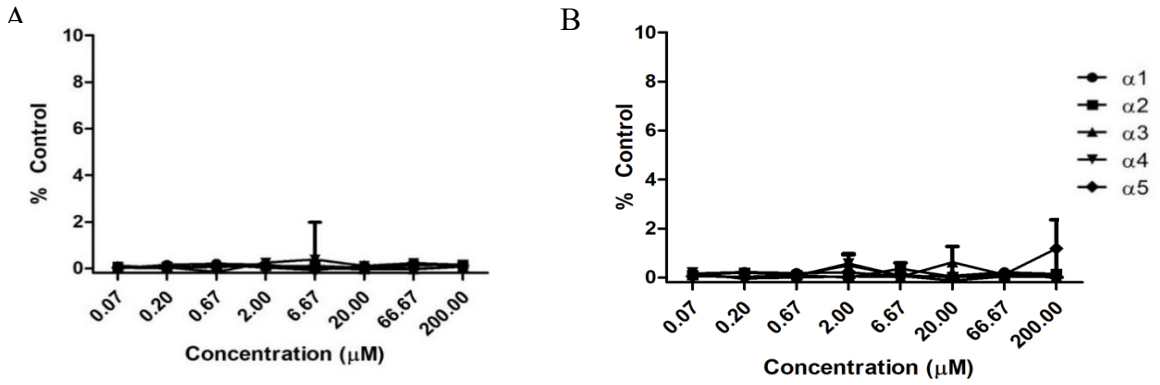


Figure 9. The electrophysiological profile of GL-I-54 and GL-II-73 at α1-5-containing receptors in absence of GABA in the media Agonist effect or the lack thereof, GL-I-54 (A) and GL-II-73 (B) were tested in HEK-296. The cells expressing recombinant α1-5-$GABA_A$ receptors, in absence of GABA in the media, in order to test a potential agonist effect. As expected, neither GL-I-54 nor GL-II-73 induced potentiation at any of the receptors, confirming their role as allosteric modulators and not agonists.

2.3.2 Study of anxiety-like behavior of GL-II-73 and GL-I-54, respectively, in the elevated plus-maze with Dr Felipe V. Gomes, Adriana Jesus Souza, Dr Prevot, Dr Sibille, and coworkers

Anxiety-like behaviors in rodents were studied using the elevated plus maze (EPM). Both male and female C57BL/6 mice received the test compounds (GL-II-73 or GL-I-54) 30 minutes before the behavioral tests at doses of 1, 5, and 10 mg/kg. Subsequently, the mice were individually placed

on the central platform of the EP maze, which consisted of four white Plexiglas arms (two open arms measuring 29x7 cm and two enclosed arms measuring 29x7x17 cm), facing an open arm. The mice were allowed to explore the maze for 5 minutes. A digital camera and the ANY-maze Video Tracking System recorded and analyzed the percentage of open arm entries and time spent in these arms (indicators of an anxiolytic response), as well as the number of enclosed arm entries (an indicator of locomotor activity).

Both male ($F_{3,25}=3.14$, $p<0.05$) and female ($F_{3,36}=4.60$, $p<0.05$) mice exhibited elevated exploration of the open arms in the elevated plus maze at doses of 10 mg/kg GL-II-73 (**Figure 10**, **A** and **C**). Furthermore, GL-II-73, at 5 and 10 mg/kg, raised the number of entries into the closed arms of the EPM ($F_{3,25}=23.38$, $p<0.05$) in males but not in females. This data suggests that the exploration of the open arms may be influenced by increased locomotor activity (**Figure 10**, **B** and **D**).

Nevertheless, upon further analysis, no correlation was observed between the percentage of entries into the open arms and the number of entries into the enclosed arms for male mice treated with GL-II-73 at 5 and 10 mg/kg (**Figure 10**), but in this system GL-II-73 was trending toward anxiolytic activity.

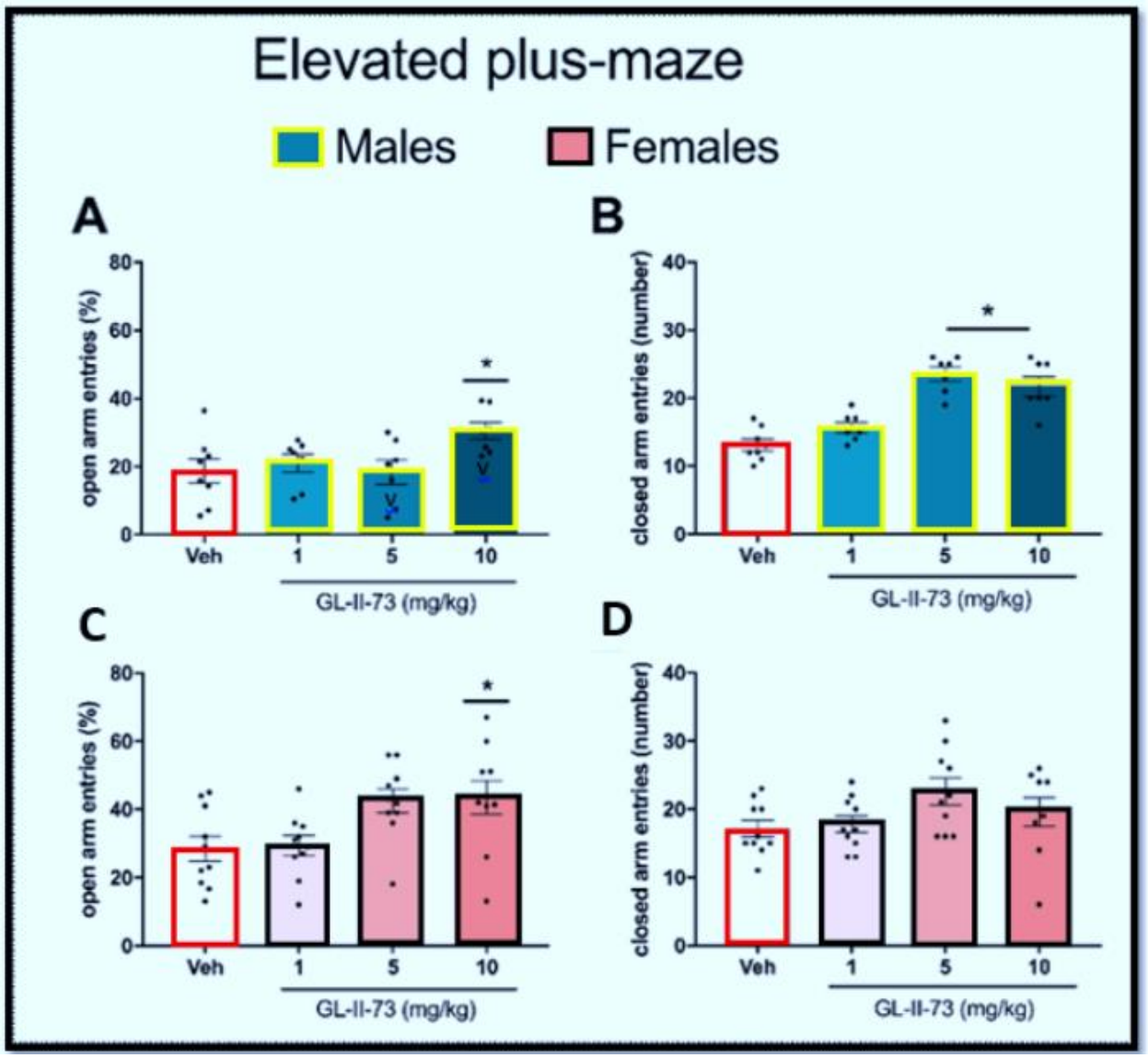


Figure 10: (A) The percentage of entries into open arms increased by GL-II-73, at 10 mg/kg in male mice and (B) at 5 and 10 mg/kg, the number of entries into enclosed arms of the elevated plus-maze (EPM; n=7-8/group). (C) In females, GL-II-73 increased the exploration of the open arms of the EPM at 10 mg/kg, (D) There was no change in the number of entries into enclosed arms (n=10/group). *p<0.05 vs. vehicle; EPM: one-way ANOVA followed by Tukey's test. Figures were modified from Souza et al. 2022[7]

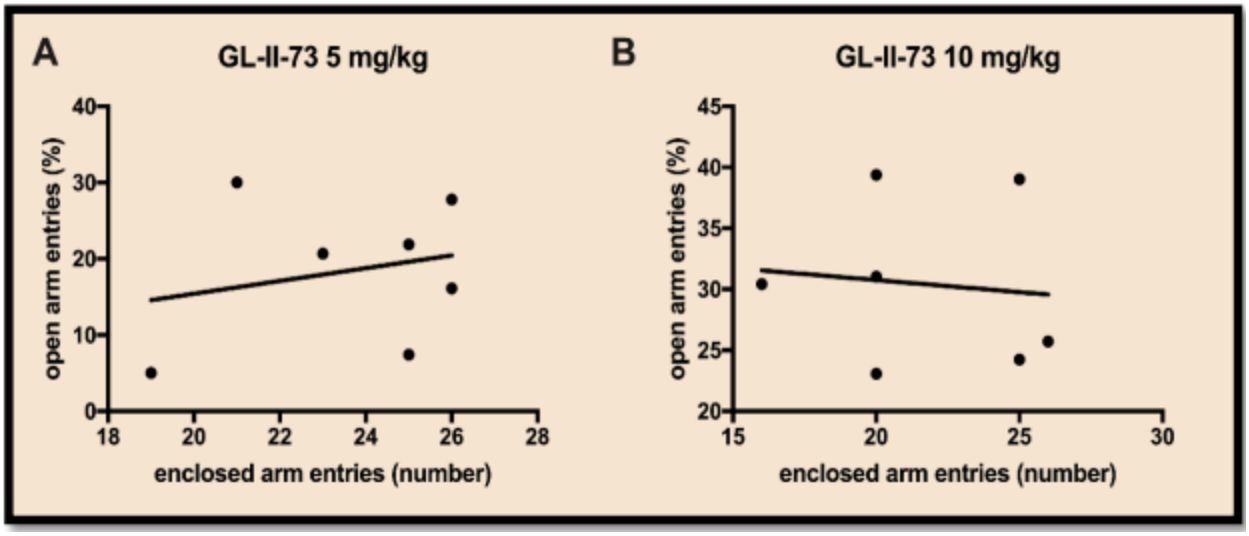


Figure 11: Male mice treated with GL-II-73 at 5 and 10 mg/kg, no correlation was found between the percentage of entries into the open arms and the number of entries into the enclosed arms of the EPM. Figures were modified from Souza et al. 2022. [7]

Chronic stress serves as a contributing factor to psychiatric conditions, such as Major Depressive Disorder (MDD), characterized by mood and cognitive manifestations. [148–150] Current interventions for depression and other stress-related mental health issues have primarily targeted the monoaminergic system[151], demonstrating restricted effectiveness on mood symptoms and no impact on cognitive symptoms. This underscores the existing clinical gaps. Recent research has shifted attention to the glutamatergic system[152] , revealing encouraging outcomes in terms of mood improvement, cognitive enhancement, and cellular structure. [153,154] Comparable positive effects have been observed with substances aimed at the GABAergic system.[1]

In mice exposed to chronic restraint stress (CRS), the impact of GL-I-54 (5 mg/kg) and GL-II-73 (5 mg/kg) was evaluated in terms of their influence on anxiety-related avoidance using the elevated plus maze (EPM).

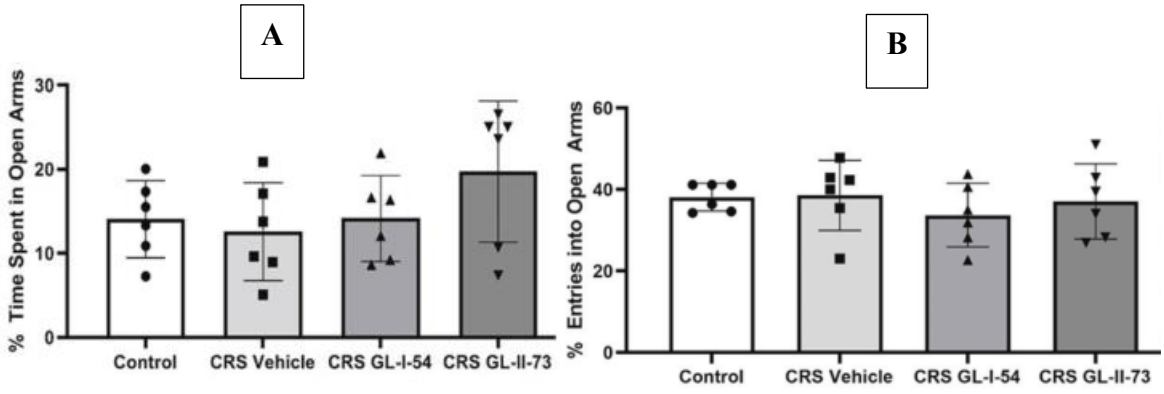


Figure 12. GL-I-54 and GL-II-73 were then tested in the elevated plus maze and forced swim test at the dose of 5 mg/kg, in mice previously exposed to chronic restraint stress (CRS). Drugs were administered IP, 30 min prior to testing. Percent time spent in the open arms (A) and percent entries into open arm (B) showed no difference between groups. Examination of the data on GL-II-73 versus GL-I-54 and vehicle, clearly showed anxiolytic active.[1]

2.3.3. Anti-depressant efficacy study of GL-II-73 and GL-I-54 in the force swim test with Dr Felipe V. Gomes, Adriana Jesus Souza, Dr Prevot, Dr Sibille, and coworkers

The impact of GL-II-73 and GL-I-54 was assessed in the force swim test, where both male and female mice were placed in a water-filled glass cylinder and forced to swim for 6 minutes at a temperature of 23–25 °C. Immobility time was measured during the last four minutes, considering minor movements such as those required to keep the head above water as immobility. The findings revealed that GL-II-73, at a dose of 10mg/kg, reduced immobility time in the force swim test for both male ($F_{3,25}=4.64$, $p<0.05$) and female ($F_{3,36}=4.60$, $p<0.05$) mice (**Figure 13, A** and **B**).

Further investigation into the sustainability of these effects up to 72 hours indicated a decrease in immobility time 24 hours after the administration of GL-II-73 (10mg/kg) for both male and female mice. However, no such change in immobility time was observed 72 hours after GL-II-73 administration (**Figure 13, C, D, E,** and **F**).

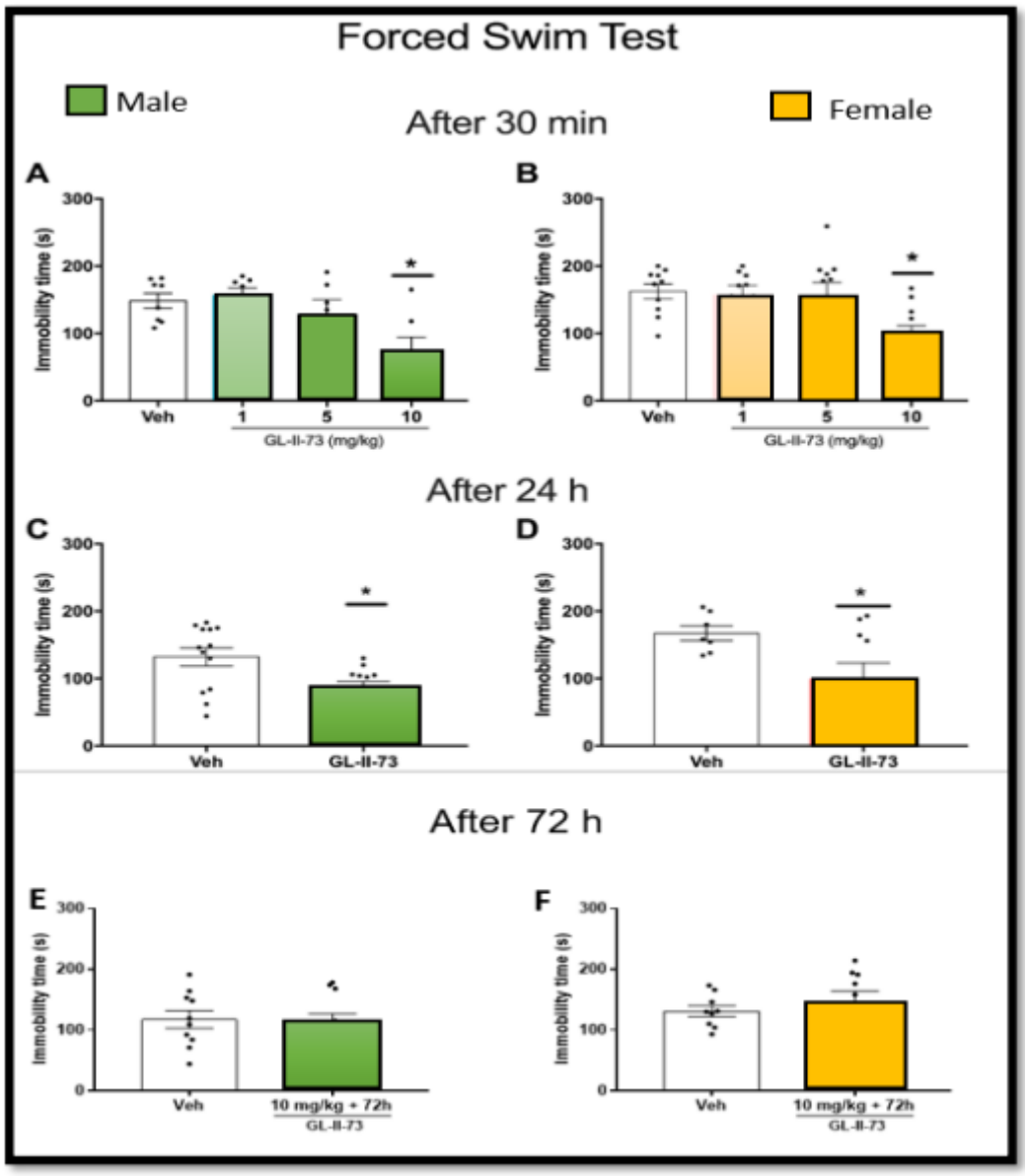


Figure 13. Forced swim test of GL-II-73

The enantiomer of GL-II-73, the dimethyl amide in the *S* series (GL-I-54), significantly reduced the time spent immobile at a lower dose, 5 mg/kg, as compared to the control vehicle, as shown in **Figure 14**.

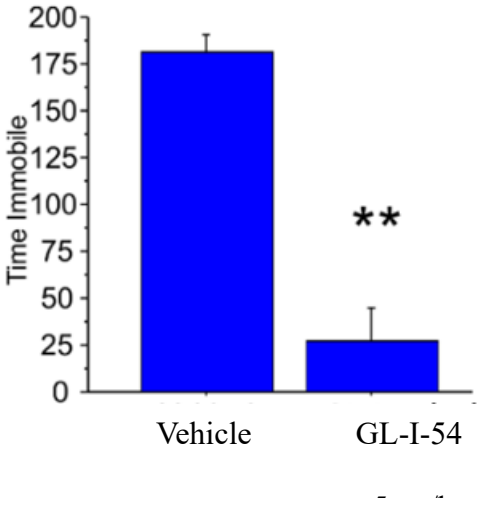


Figure 14. Effect of GL-I-54 on time spent immobile in the FST. The ligand GL-I-54 at 5 mg/kg i.p. administered (24, 20, 1 h before testing) induced a significant antidepressant-like action when compared to the vehicle group (n = 9). ***p<0.001.

In another test, the mice exposed to chronic restraint stress (CRS), the impact of GL-I-54 (5 mg/kg) and GL-II-73 (5 mg/kg) was evaluated on immobility in the forced swim test (FST). In Figure 9, the FST, CRS increased time spent immobile, which was significantly reversed by GL-I-54, suggesting GL-I-54 reverses stress induced increase in immobility in this test.

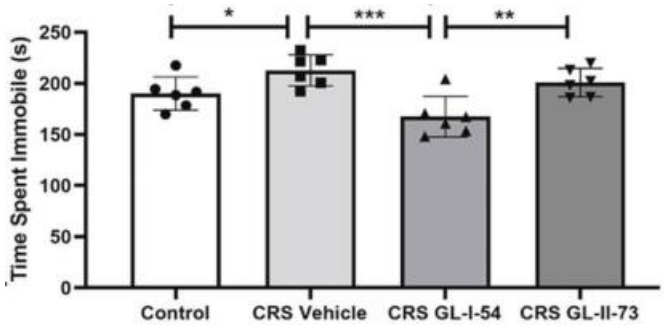


Figure 15. Time immobile showed more time spent immobile in the CRS-Vehicle group, and less time immobile in animals receiving GL-I-54, compared to CRS-Vehicle.

2.3.4. Motor impairment coordination study of GL-II-73 and GL-I-54 in the rotarod with Dr Felipe V. Gomes, Adriana Jesus Souza, Dr Prevot, Dr Sibille, and coworkers

GL-II-73 or GL-I-54 underwent evaluation in the rotarod test to determine their impact on motor coordination and assess their potential rewarding effects in the conditioned place preference assay. The findings revealed that these ligands did not induce any motor coordination impairments in the rotarod test, as illustrated in **Figure 16** and **17**, unlike diazepam. Additionally, there were no indications of rewarding-like effects in the conditioned place preference assay for both GL-II-73 and GL-I-54, as depicted in **Figure 16** and **17**. This study shows no sedation or ataxia, as well as a significantly reduction in the risk of dependence compared to the control.

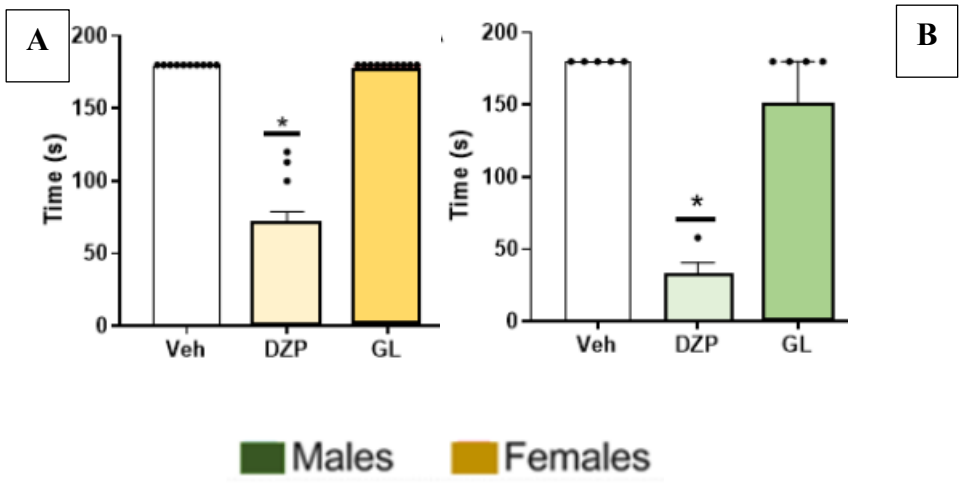


Figure 16*:* Results of rotarod. The latency to fall was decreased by diazepam in the rotarod in (A) males and (B) females (n=5-10/group). No such effects were produced by GL-II-73. *p<0.05 vs. vehicle; Rotarod: Kruskal-Wallis test.

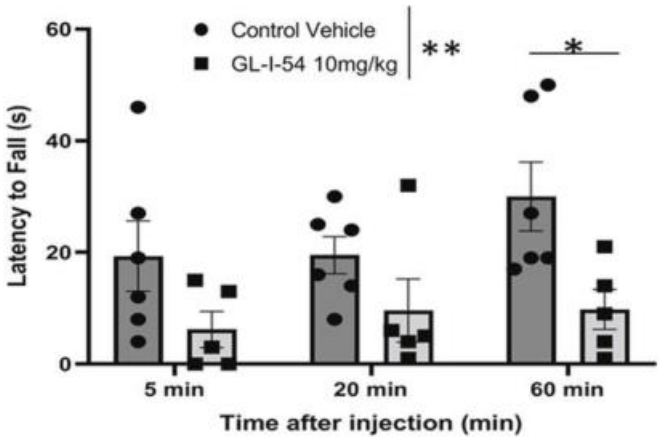


Figure 17. independent mice were tested in the rotarod (H; N = 5 Control Vehicle and N = 6 GL-I-54). Mice were trained to maintain themselves on a rotating rod (rotarod) for 3 trials. Then, they were injected with GL-I-54 at 10 mg/kg, and tested 5 min, 20 min and 60 min past injection time. Latency to fall from the rod was recorded and showed significant reductions in latency to fall in mice receiving GL-I-54.

2.3.5. Metabolic stability of GL-II-73 and GL-I-54 with Ashley Bernardo, Dr Prevot and coworkers.

The liver microsomal assay was employed to assess the metabolism and stability of GL-II-73 and GL-I-54. The outcomes are outlined in **Table 7**, revealing that the half-life of GL-II-73 exceeded that of GL-I-54. Conversely, the intrinsic hepatic clearance for GL-I-54 was greater than that for GL-II-73, as indicated in **Table 7.**

Table 7. Comparative metabolic stability of GL-II-73 and GL-I-54 in a liver microsomal assay(C57BL6 mouse)

Parameter	GL-II-73	GL-I-54
Half-life ($t_{1/2}$ in min)	256	198
% remaining after 2 hours	75.6%	70%
Intrinsic hepatic clearance (mL/min/kg)	21.3	27.6

2.3.6. Reversal of stress-induced working memory deficits by the S enantiomer of GL-II-73; GL-I-54 on Ymaze task with Michael Marcotte, Dr. Prevot , Etienne Sibille and coworkers.

Groups of C57BL/6J mice, aged 9 weeks, were administered a compound in the maximum tolerated dose (MTD) assay. The mice received a low dose of the twocompounds (1mg/kg) and were observed for signs of sedation or ataxia for up to 3 hours post-injection. The dosage was incrementally raised each day, reaching 90mg/kg on day 5. No sedation nor ataxia was observed.

In the subsequent week, the mice underwent Y maze training to evaluate their baseline performance in the alternation task. Eight mice were maintained under control conditions, while 18 mice were relocated to a separate housing room and exposed to chronic restraint stress to induce working memory impairment. This impairment was assessed through the spontaneous alternation Y-maze task. The mice experienced chronic restraint stress (CRS) for one hour, twice daily, over the course of one week. Following this, they were placed in a Falcon™ Tube with perforations at the tip and lid for airflow. The mice were then returned to their home cage for one hour.

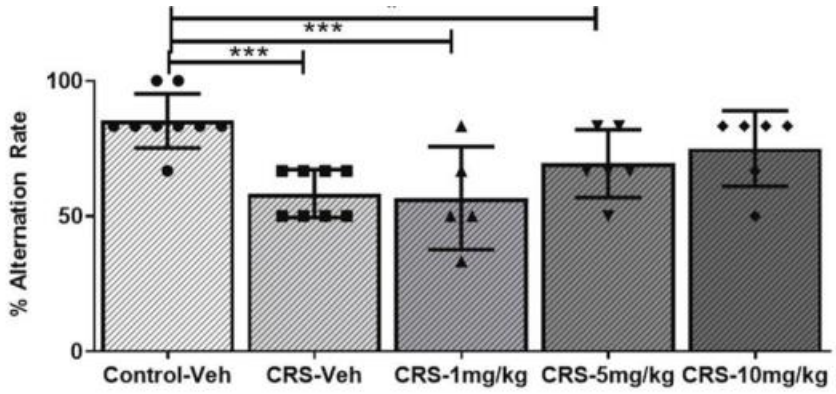


Figure 18. In the Y-maze, CRS induced an alternation rate deficit that was reversed by GL-I-54 at 10 mg/kg but not 5 mg/kg, suggesting the capacity of reversing spatial working memory deficits.

2.3.7. Evaluation of anxiolytic activity of acute administration of GL-RM (racemic mixture of GL-I-54 and GL-II-73) with Ashley Bernardo, Dr Prevot and coworkers

GL-RM, which is the racemic mixture of both enantiomers of GL-II-73 and GL-I-54 was synthesized and investigated for its anxiolytic effects and efficacy in enhancing working memory. The Unpredictable Chronic Mild Stress (UCMS) model was employed to assess the impact of acute administration of GL-RM on symptoms induced by prolonged stress. Chronic restraint stress (CRS) was induced in mice using a Falcon™ tube with a hole at the conical tip and a hole in the lid, where mice were placed for one hour, twice daily with a one-hour interval, over the course of a week. A variety of mild stressors, randomly applied 1-2 times daily over 6 weeks, were introduced for the UCMS paradigm. UCMS-exposed animals were housed in a separate room without environmental enrichment to magnify the impact of other stressors. The evaluation of UCMS effects and the gradual decline in self-care was determined by monitoring the coat

condition of each animal weekly, following a published protocol.[155]A coat state scoring system ranging from 0 to 1 was used for seven anatomical areas, with 0 indicating a well-groomed, smooth coat and 1 representing a soiled coat or bald patches. The degradation of coat condition induced by UCMS was not reversed by acute treatment.

Subsequently, animals were studied in the elevated maze plus (EPM) to evaluate the anxiolytic behavior of GL-RM. The anxiolytic effects of GL-RM were screened in the elevated maze plus following acute administration. The percentage of time spent in the open arms remained unaffected by UCMS (F (1;42) = 0.0791; p = 0.379) and treatment alone (F(1;42) = 1.377; p = 0.2472) according to ANOVA analysis (**Figure 19A**). No significant impact of sex differences was observed (F (1;38) = 0.508; p = 0.4802). UCMS did not alter the number of entries into open arms (F (1;42) = 0.29; p = 0.5929), but there was a significant increase induced by GL-RM (F(1;42) = 7.317; p = 0.0098; **Figure 19 B**). The interaction between UCMS and treatment (F(1;42) = 1.972; p = 0.1684) did not demonstrate any significant effects.

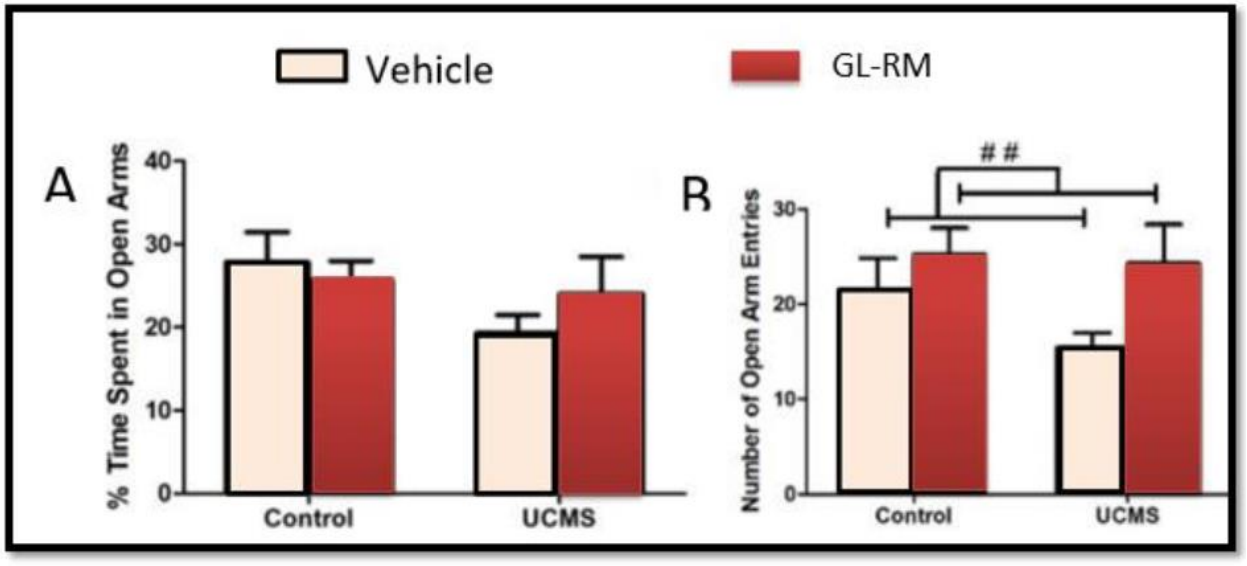


Figure 19. Effect of acute treatment of GL-RM on anxiety. Time spent (A) and entries (B) in the open arms in the elevated plus maze. Figures were modified from Ashely et al. 2021[1]

No effect of GL-RM ($F(1;37) = 0.003$; $p = 0.9538$) observed on latency to approach in the Novelty-Suppressed Feeding (NSF) test in trend-level effect of UCMS ($F(1;41) = 2.927$; $p = 0.0947$). Two-way ANOVA revealed a significant interaction for UCMS treatment ($F(1;41) = 5.477$; $p = 0.0242$). Animals exposed to UCMS and treated with GL-RM exhibited reduced approach latencies compared to control GL-RM treated animals ($p = 0.0284$), and GL-RM reduced approach latency in animals exposed to UCMS compared to vehicle-treated mice ($p = 0.0113$) (**Figure 20 A**). No significant effects of sex were identified ($F(1;37) = 1.912$; $p = 0.175$). There was no significant effect of UCMS ($F(1;41) = 0.671$; $p = 0.4175$), drug ($F(1;41) = 0.588$; $p = 0.4475$), or interaction between UCMS treatment ($F(1;41) = 0.981$; $p = 0.3277$) for latency to bite (**Figure 20 B**).

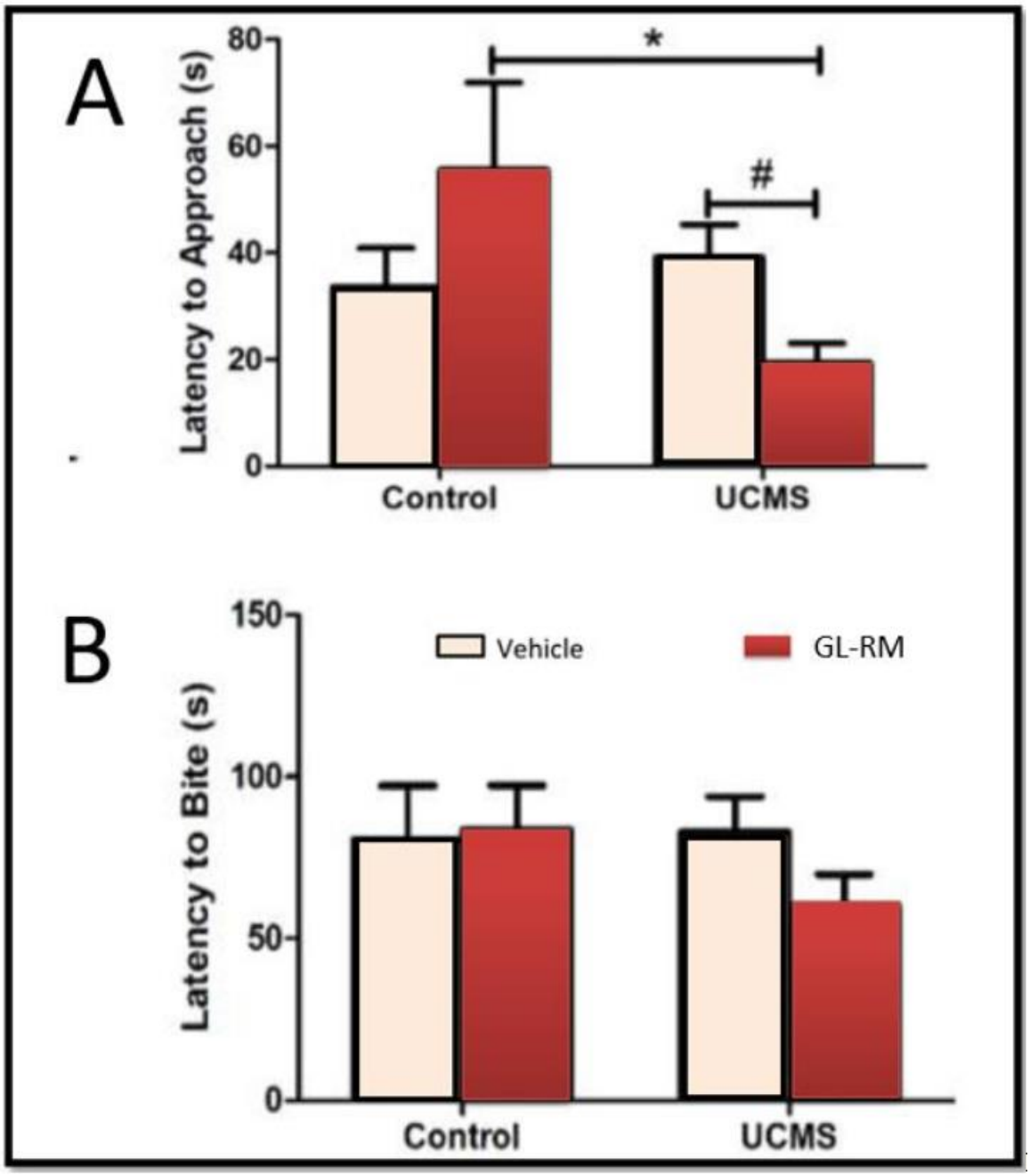


Figure 20. Effect of acute treatment of GL-RM on latency to approach (A) and latency to bite (B) in novelty suppressed feeding. Statistical analyses showed that acute GLRM treatment reduces latency to approach in mice subjected to UCMS. Figures were modified from Ashely et al. 2021.[1]

Anxiety-like behavior was evaluated weekly using a Phenotyper test. To eliminate any potential artificial distinctions between groups before UCMS or treatment, baseline activity was documented before the onset of UCMS. (**Figure 21**)

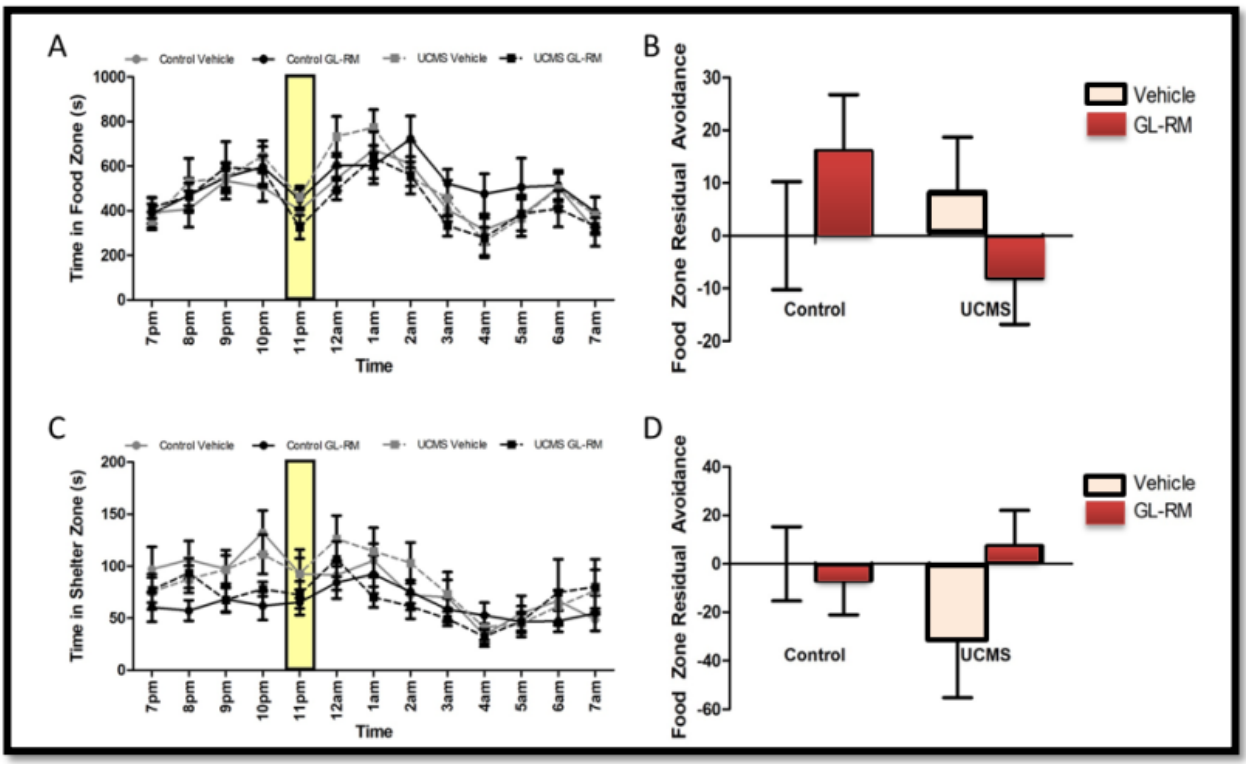


Figure 21. Before initiating chronic stress and treatment, time spent in the food zone (A-B) and shelter zone (C-D) in the Phenotyper Boxes were recorded. In order to create an aversive stimulus, a light challenge was applied from 11pm to 12am, above the food zone. *p<0.05, **p<0.01, ***p<0.001 effect of UCMS, #p<0.05, ##p<0.01, effect of GL-RM. Figures were modified from Ashely et al. 2021.[1]

The total time spent in the food and shelter zones was evaluated following the initiation of UCMS. One-way ANOVA indicated an impact of UCMS ($F(1;44)=37.715$; $p=<0.001$) on the time spent in the shelter by week 6, but no influence of treatment ($F(1;44)=1.519$; $p=0.2243$) or interaction ($F(1;44)=0.202$; $p=0.6557$). Notably, a significant sex effect was observed ($F(1;40)=16.061$;

p=0.0003), with males spending more time in the shelter zone than females. In terms of residual avoidance, Two-way ANOVA revealed a substantial effect of UCMS ($F(1;44)=23.964$; $p<0.0001$) in the shelter zone by week 6. No interaction ($F(1;44)=0.499$; $p=0.4835$) or treatment effect was identified ($F(1;44)=0.182$; $p=0.6714$) at week 6 (**Figure 22**). Males exhibited greater residual avoidance compared to females based on the sex effect ($F(1;46)=16.046$; $p=0.0002$).

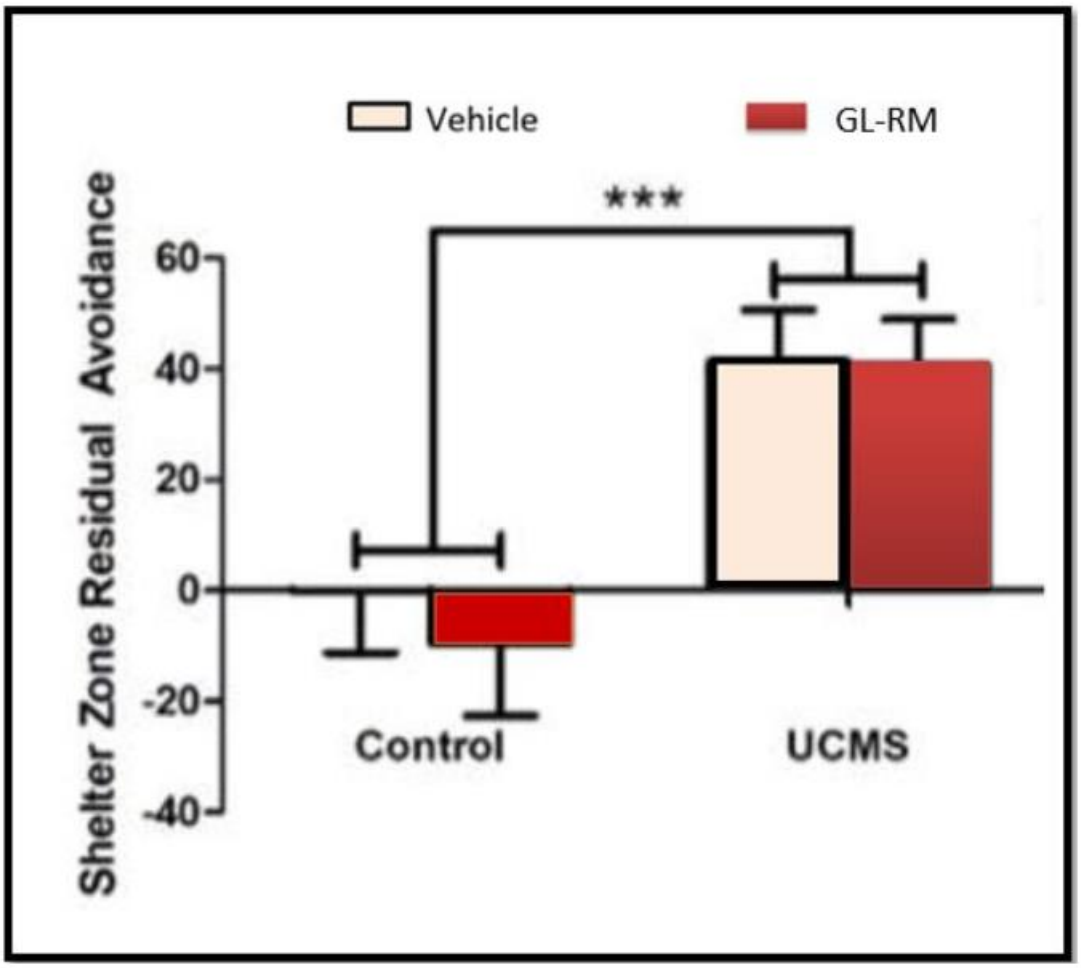


Figure 22. Residual avoidance score, UCMS subjected mice showed a significant increase in residual avoidance on statistical analyses. *p<0.05, **p<0.01, ***p<0.001 effect of UCMS, #p<0.05, ##p<0.01, effect of GL-RM. Figures were modified from Ashely et al. 2021.

2.3.8. Evaluation of depressive-like behaviors of acute administration of GL-RM (racemic mixture of GL-I-54 and GL-II-73) with Ashley Bernardo, Dr Prevot and coworkers

By using the forced swim test and sucrose consumption paradigms, mice were tested for behaviors indicative of depression and anhedonia, respectively. In the sucrose consumption paradigm, UCMS led to a notable reduction in sucrose consumption by week 6 ($F(1;42)=4.230$; $p=0.0460$), whereas GL-RM exhibited no effect ($F(1;42)=0.256$; $p=0.6714$) (**Figure 23A**). No interaction was observed between UCMS and treatment ($F(1;42)=1.971$; $p=0.48535$). In week 8, the forced swim test was conducted. Both UCMS ($F(1;42)=11.060$; $p=0.0018$) and treatment ($F(1;42)=12.313$; $p=0.001$) significantly influenced the time spent immobile according to one-way ANOVA analysis. However, there was no interaction between UCMS and treatment ($F(1;42)=0.164$; $p=0.6879$).

A significantly longer duration of immobility was observed in the vehicle treated UCMS animals compared to the control group treated with the vehicle ($p=0.0341$). However, the administration of GL-RM led to a reduction in immobility time in UCMS animals when compared to the vehicle-treated UCMS group ($p=0.0094$). No significant differences were observed between groups based on sex ($F(1;38)=1.492$; $p=0.2295$) (Figure **23 B**). A comprehensive effect of UCMS ($F(1;40)=45.937$; $p<0.0001$) was identified in the two-way ANOVA. Additionally, two-way ANOVA indicated no significant impact of treatment ($F(1;40)=2.491$; $p=0.1224$) and no interaction ($F(1;40)=0.324$; $p=0.5723$) (Figure **23 C**). The influence of sex was found to be insignificant ($F(1;36)=0.652$; $p=0.4248$). This evidence suggests the potential of GL-RM in reversing some of the behavioral changes induced by chronic stress. This highlights the possible role of GL-RM in ameliorating certain behavioral alterations caused by prolonged stress.

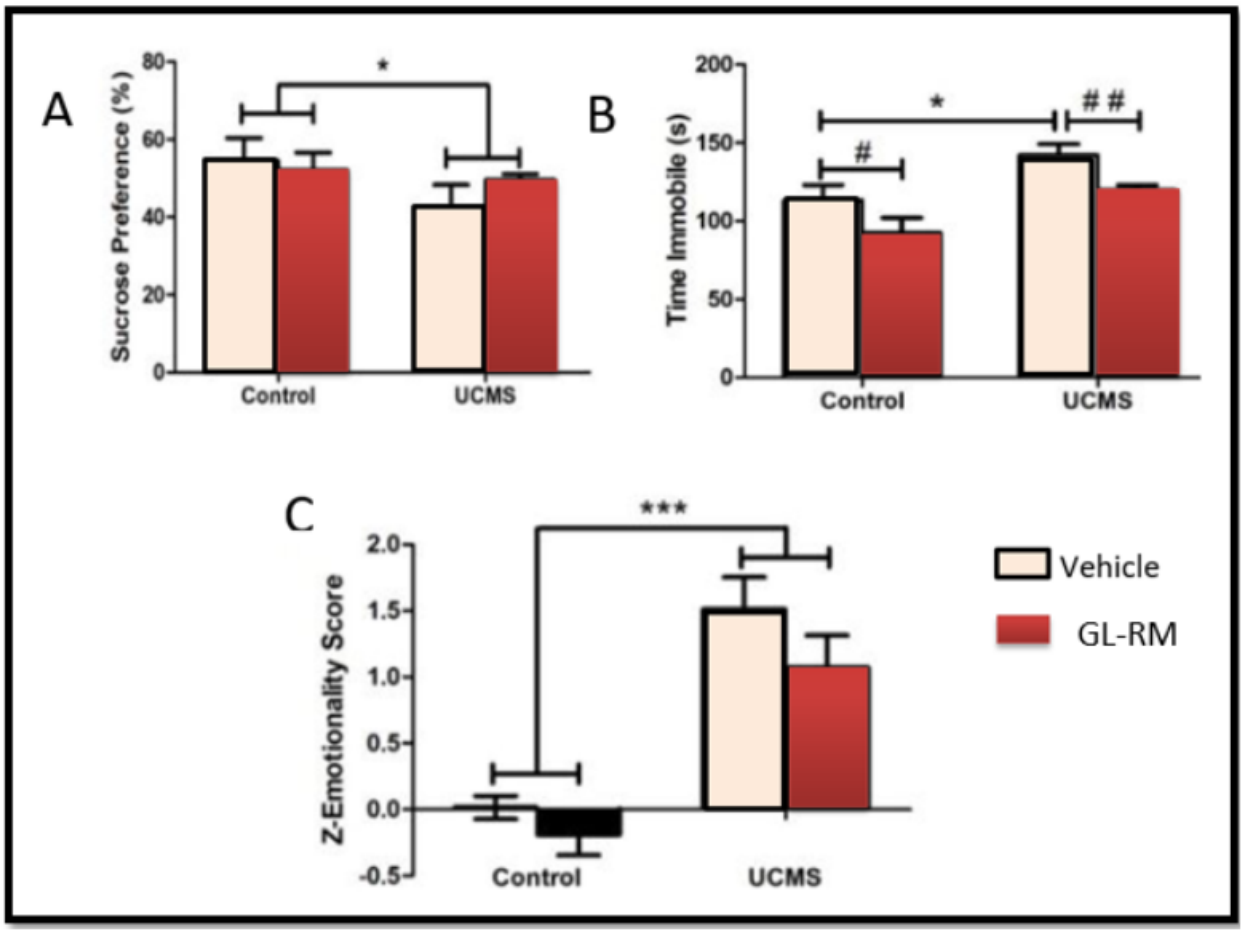


Figure 23. Forced swim test and sucrose consumption paradigm to evaluate depressive-like and anhedonia-like behaviors. Statistical analyses did not reveal significant differences between groups in the force swim test (B). Chronic GL-RM treated group showed a significant increase in preference to sucrose in sucrose paradigm test (A). The impact of UCMS at increasing emotionality was significant that was confirmed by statistical analyses while combining the individual score into a global z-score (C), the chronic treatment of GLRM reduced emotionality. *p<0.05, **p<0.01, ***p<0.001 effect of UCMS, #p<0.05, ##p<0.01, effect of GL-RM. Figures were modified from Ashely et al. 2021[1]

2.3.9. Evaluation of spatial working memory of acute treatment of GL-RM on Y-maze with Ashley Bernardo, Dr Prevot and coworkers

The spatial working memory following acute administration of GL-RM was assessed using the Y-maze task, specifically focusing on spontaneous alternation. In this spatial working memory paradigm derived from the T-maze described by Faucher et al.[156], mice were subjected to the Y-maze with a 90-second inter-trial interval (ITI) after becoming accustomed to the maze. The trials commenced from a 'start box,' allowing the mouse to choose between the left or right arm in each trial. The chosen arm was then explored for 30 seconds before the mouse returned to the start box for a 90-second ITI. This process was repeated up to seven times, with the maze being lightly wiped down with 70% ethanol between each trial to eliminate olfactory cues. On the eighth trial, a short ITI (10 seconds) was introduced to evaluate the animal's motivation to alternate. Animals failing to alternate on the eighth trial were excluded from analysis, as their results would be influenced more by a lack of motivation than cognitive performance. The mean alternation rate, expressed as a percentage, was calculated using the following formula: Mean Alternation % = [(Number of alternations/number of trials)*100].

Upon two-way ANOVA analysis, a notable effect of UCMS ($F(1;18)=11.62$; $p=0.003$) on the alternation rate was observed. The analysis also indicated no impact of treatment ($F(1;18)=1.748$; $p=0.2027$), but a significant interaction for UCMS*treatment ($F(1;18)=16.85$; $p=0.0007$). UCMS led to a significant reduction in the alternation rate of vehicle-treated animals ($p=0.0013$), while GL-RM-treated animals exhibited an increased alternation rate under UCMS conditions ($p=0.0022$; **Figure 24**). The assay did not show any effect related to sex ($F(1;14)=0.034$; $p=0.8567$). Based on this evidence, **it can be inferred that GL-RM was able to mitigate the cognitive deficit induced by UCMS.**

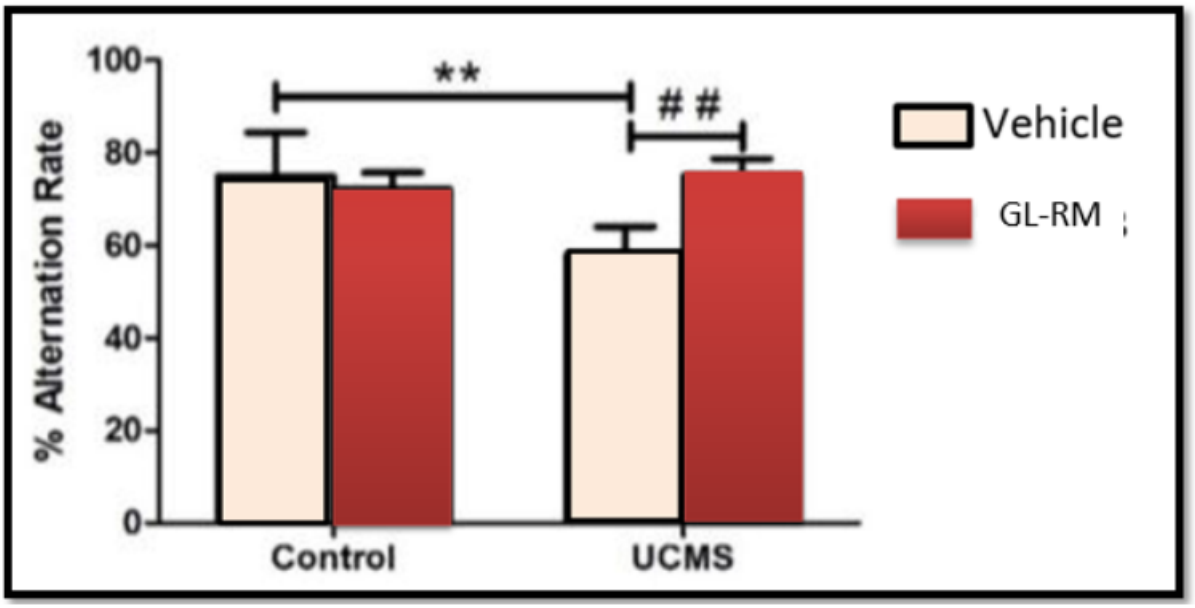


Figure 24. Evaluation of cognitive activity in the Y maze. UCMS altered the alteration rate in mice which was reversed by acute GL-RM treatment. *p<0.05, **p<0.01, ***p<0.001 effect of UCMS, #p<0.05, ##p<0.01, effect of GL-RM. Figures were modified from Ashely et al. 2021.[1]

2.3.10. Evaluation of anxiolytic behaviors of chronic treatment with GL-RM with Ashley Bernardo, Dr Prevot and coworkers

Building on the positive outcomes observed with the acute administration of GL-RM, the effects of chronic administration of GL-RM were also explored in the same UCMS model. It's crucial to emphasize that the chronic administration commenced in week 3 of the UCMS protocol (**Figure 25).** Weekly assessments were conducted for coat condition and weight gain, revealing a consistent pattern of increased coat deterioration associated with UCMS, aligning with previous observations.

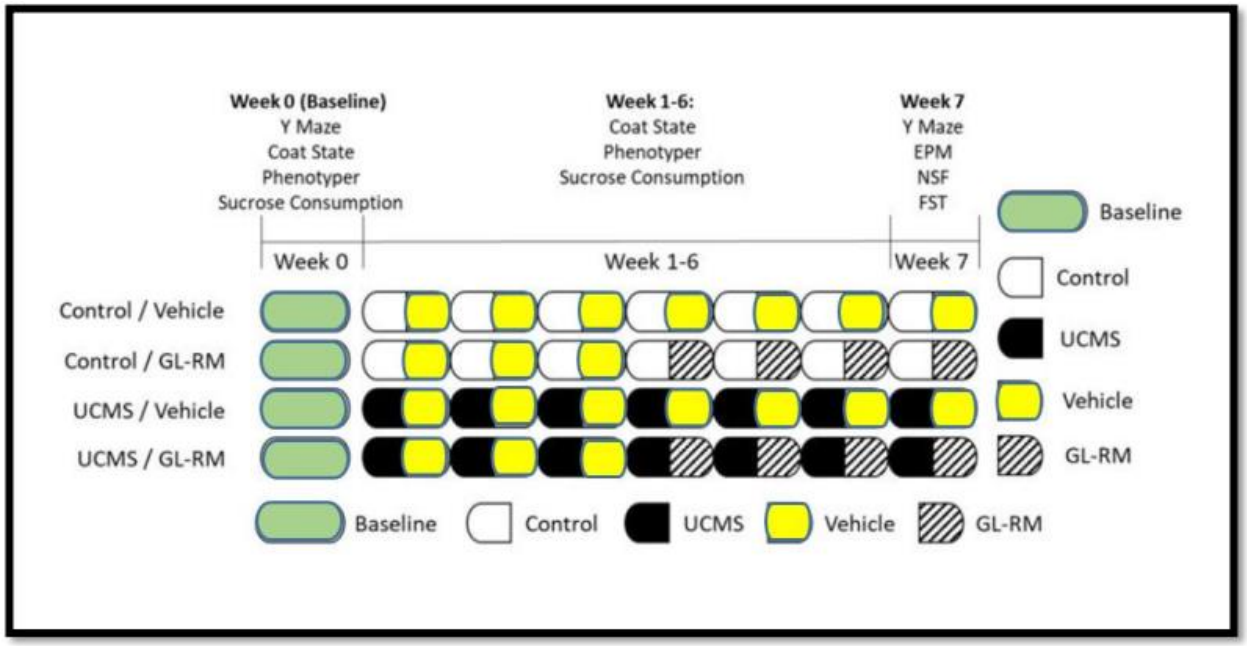


Figure 25. Prior to being subjected to 6 weeks of UCMS, the mice (both male and female) were tested at baseline in the Y-Maze, the phenotyper and the sucrose consumption test. Chronic treatment with GL-RM was initiated after 3 weeks of UCMS and the treatment was continued for a total of 4 weeks. The weight and coat state of the mice were measured weekly and mice were tested in the phenotyper test and the sucrose consumption assay weekly. *p<0.05, **p<0.01, ***p<0.001 effect of UCMS, #p<0.05, ##p<0.01, effect of GL-RM. Figures were modified from Ashely et al. 2021[1]

Two-way ANOVA analyses did not reveal any impact of UCMS, treatment, interaction, or sex on the percentage of time spent in the open arms in the elevated plus maze (**Figure 26 A**) or the number of entries into open arms (**Figure 26 B**). Additionally, ANOVA analysis did not show any effect of UCMS ($F(1;44)=0.055$; $p=0.8160$), treatment ($F(1;44)=0.706$; $p=0.4053$), or interaction ($F(1;44)=1.046$; $p=0.3121$) on the time spent in the inner zone in the open field test (**Figure 26 C**). There were no detected sex effects either ($F(1;40)=0.122$; $p=0.7288$).

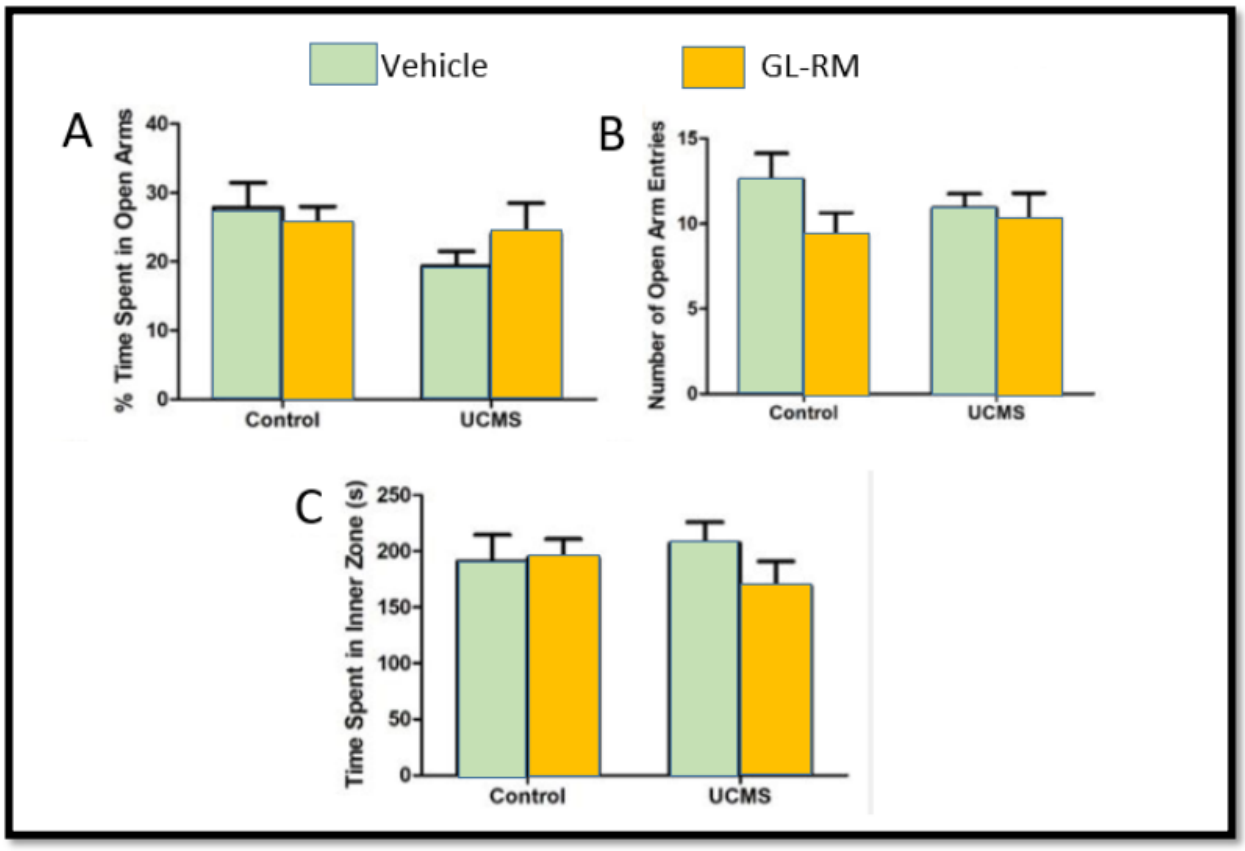


Figure 26. Testing of mice in the elevated plus maze after 6 weeks of UCMS and 3 weeks of treatment. No significant statistical difference was observed in the time spent in open arms (A) and number of entries in the open arms (B), and the time spent (C) in the open field. *p<0.05, **p<0.01, ***p<0.001 effect of UCMS, #p<0.05, ##p<0.01, effect of GL-RM. Figures were modified from Ashely et al. 2021.[1]

The number of entries into the inner zone remained unaffected by UCMS. However, chronic treatment with GL-RM demonstrated a significant effect, and no interaction was observed between UCMS and treatment (F(1;44)=0.777; p=0.3828) (**Figure 27 A**). There were non-significant sex effects detected (F(1;40)=3.287; p=0.0773). In the analysis of latency to approach in the novelty-suppressed feeding test during week 6, no effects of UCMS (F(1;44)=0.496; p=0.4851), treatment (F(1;44)=0.410; p=0.5255), or interaction (F(1;44)=0.542; p=0.542) were identified (**Figure 27**

B). However, latency to bite exhibited a significant effect of UCMS (F(1;44)=6.871; p=0.0120) (**Figure 27 C**), as well as a significant effect of drug treatment (F(1;44)=6.723; p=0.0129), with no significant interaction (F(1;44)=1.256; p=0.2685).

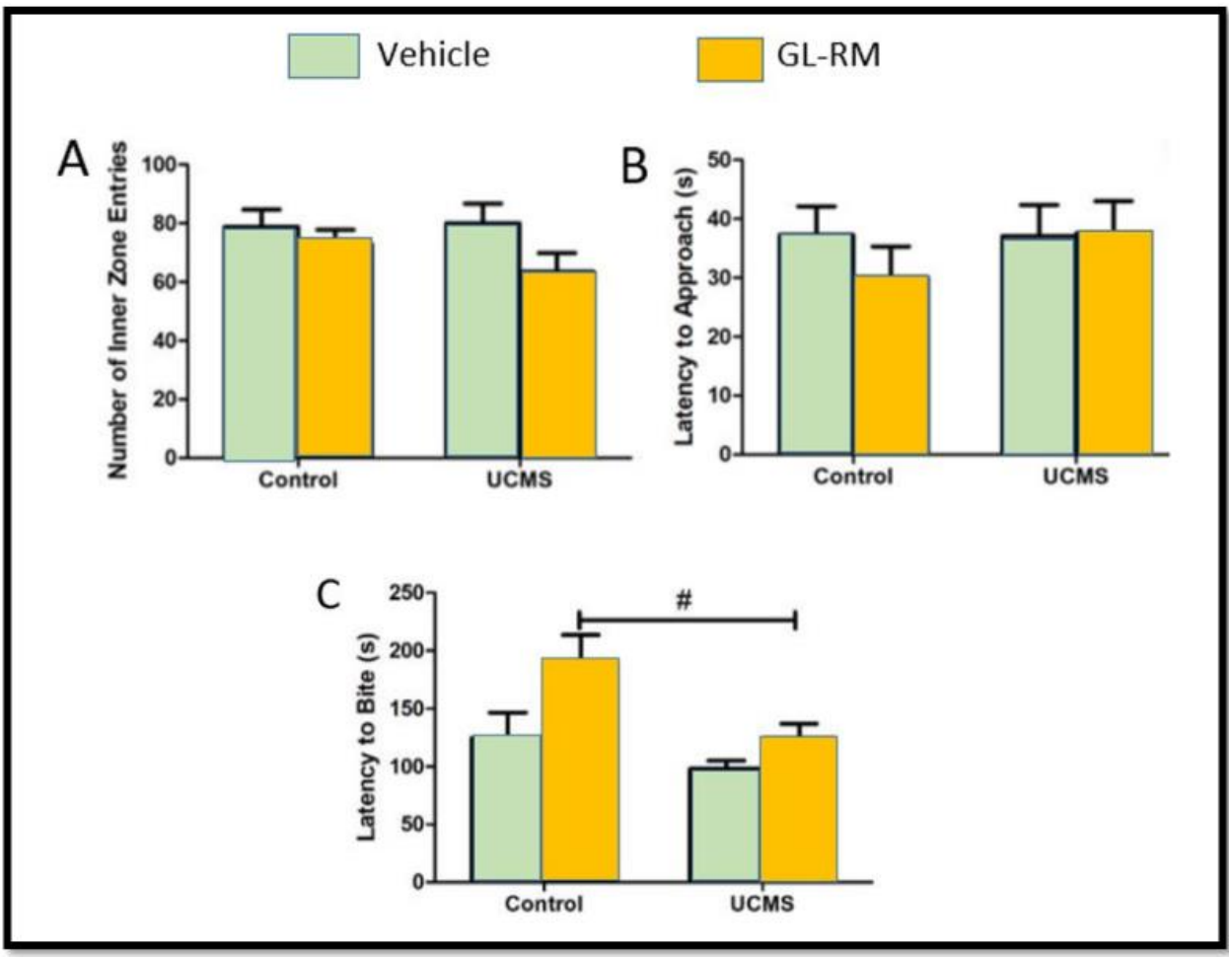


Figure 27. The number of entries in the inner zone (A). Mice were evaluated for latency to approach (B) and latency to bite (C) in the novelty suppress feeding test. *p<0.05, **p<0.01, ***p<0.001 effect of UCMS, #p<0.05, ##p<0.01, effect of GL-RM. Figures were modified from Ashely et al. 2021[1]

A repeated measures ANOVA on the residual avoidance scores for the shelter zone in the Phenotyper test revealed a significant effect of UCMS (F(1;44)=60.082; p=<0.0001), a trend-level

effect of treatment (F(1;44)=2.819; p=0.09), and no significant interaction (F(1;44)=2.377; p=0.1303; **Figure 28**). **All these data collectively indicate the potential anxiolytic effects of chronic treatment with GL-RM.**

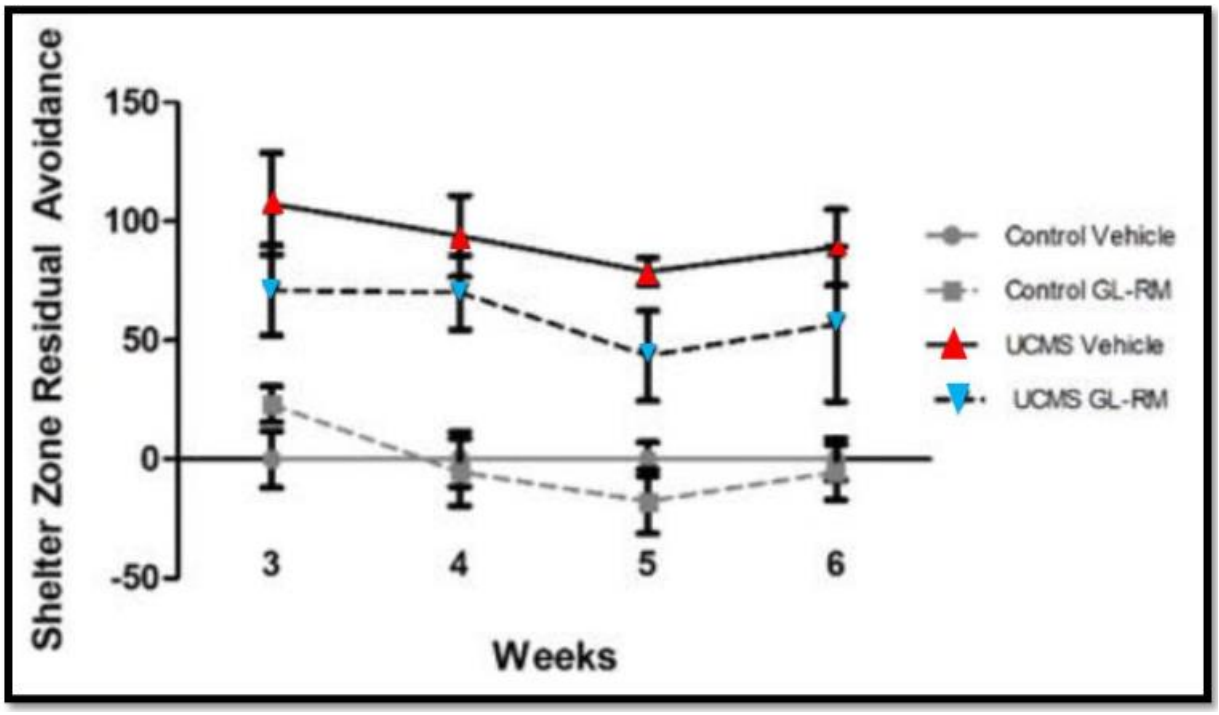


Figure 28. The residual avoidance scores from week 3 to 6 in the Phenotyper test. UCMS showed a significant effect and a trend level of effect was observed by treatment. *p<0.05, **p<0.01, ***p<0.001 effect of UCMS, #p<0.05, ##p<0.01, effect of GL-RM. Figures were modified from Ashely et al. 2021.[1]

2.3.11. Evaluation of chronic treatment of GL-RM on emotionality with Ashley Bernardo, Dr Prevot and coworkers

The impact of chronic GL-RM treatment was also assessed in the forced-swim test. Two-way ANOVA analysis on the time spent immobile revealed no effect of UCMS (F(1;44)=0.025;

p=0.8759), treatment (F(1;44)=0.034; p=0.8542), and no significant interaction (F(1;44)=1.206; p=0.2781) (**Figure 29**).

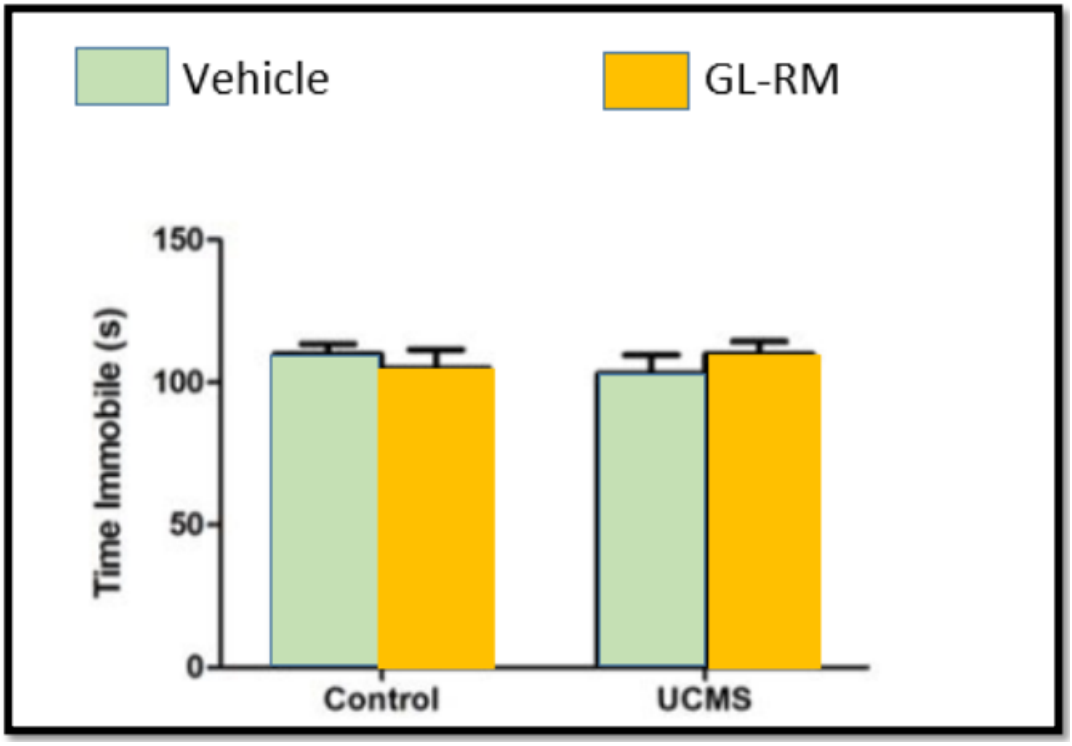


Figure 29. No significant differences between groups was revealed on statistical analyses in the forced swim test. *p<0.05, **p<0.01, ***p<0.001 effect of UCMS, #p<0.05, ##p<0.01, effect of GL-RM. Figures were modified from Ashely et al. 2021.[1]

The sucrose consumption test was subjected to a two-way ANOVA analysis, revealing a non-significant effect of UCMS but a significant impact of GL-RM (F(1;44)=6.294; p=0.0159). No significant interaction between UCMS and GL-RM treatment was observed (F(1;44)=0.67; p=0.7968) (**Figure 30 A**). Regarding Z-emotionality, both UCMS and treatment significantly influenced the scores, with no significant interaction detected (F(1;44)=0.34; p=0.56) in Z-score analysis for Z-emotionality (**Figure 30 B**). Post hoc analysis did not reveal specific group

differences responsible for these overall effects. **Therefore, it can be inferred that chronic treatment with GL-RM demonstrated a beneficial influence on emotionality scores.**

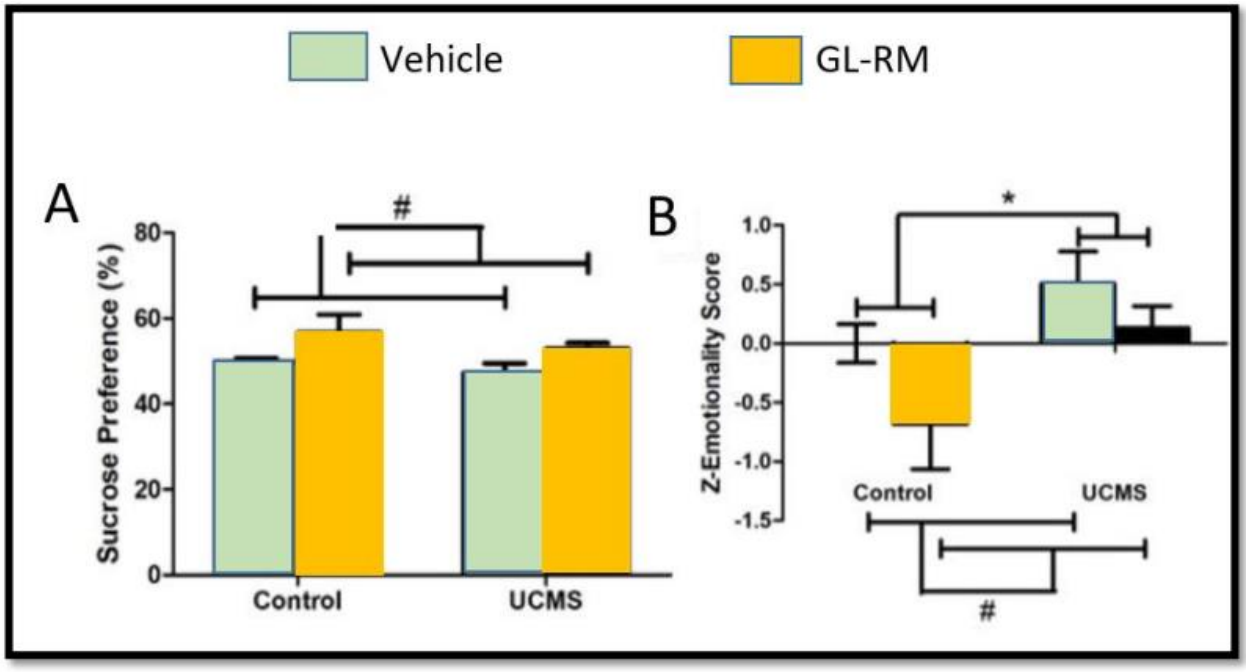


Figure 30. A significant increase in preference to sucrose was observed in mice receiving chronic GL-RM in the sucrose consumption test (A). A significant impact of UCMS at increasing emotionality was observed while chronic GL-RM reduced emotionality (B). *p<0.05, **p<0.01, ***p<0.001 effect of UCMS, #p<0.05, ##p<0.01, effect of GL-RM. Figures were modified from Ashely et al. 2021.[1]

2.3.12. Evaluation of chronic treatment of GL-RM on Y-maze with Ashley Bernardo, Dr. Prevot and coworkers

The impact of chronic administration of GL-RM was examined using the Y-maze, revealing remedial cognitive effects in mice under chronic GL-RM treatment. These outcomes in the Y-maze

closely resembled those observed with acute GL-RM treatment. UCMS had an adverse effect on the alternation rate, but this effect was mitigated by GL-RM treatment, with a significant interaction observed between UCMS and treatment. Furthermore, animals treated with GL-RM (exposed to UCMS) demonstrated significantly improved performance compared to vehicle-treated animals, irrespective of sex (**Figure 31**).

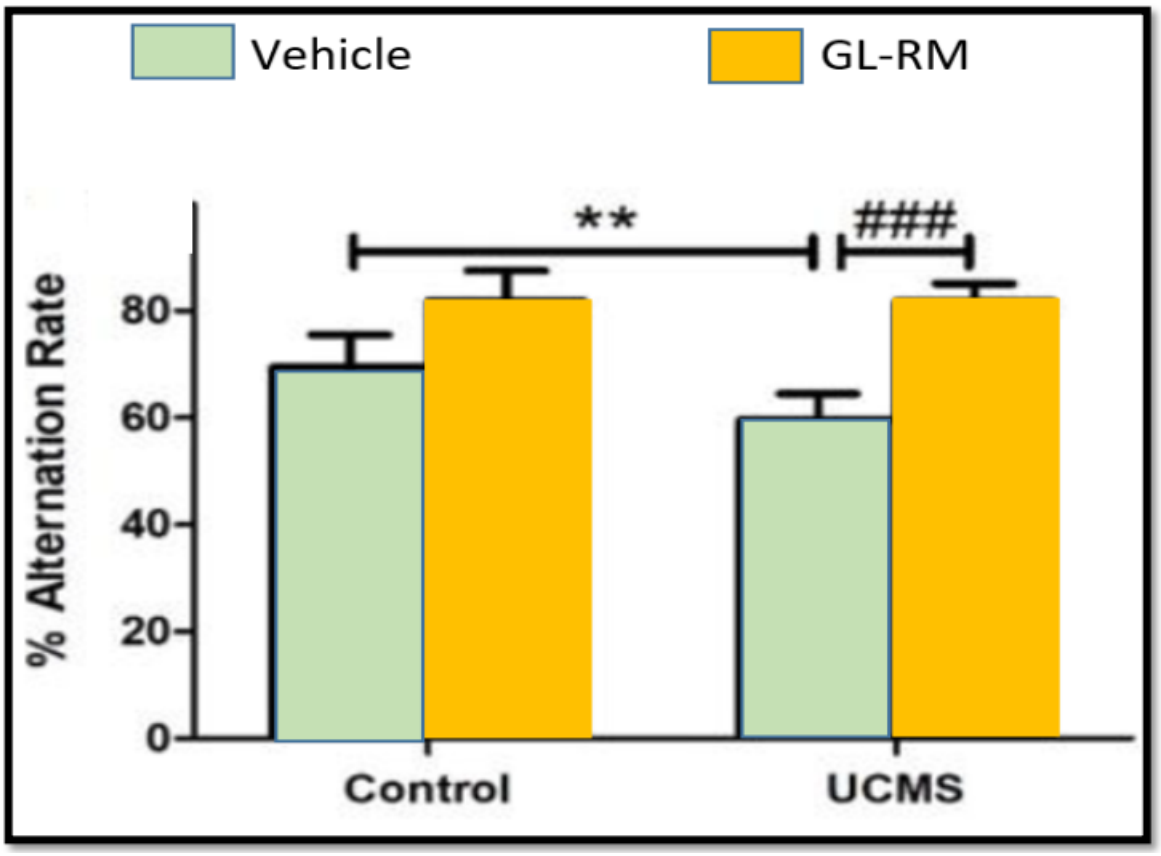


Figure 31. GL-RM treatment reversed altered alternation with UCMS in the Y-maze task. *p<0.05, **p<0.01, ***p<0.001 effect of UCMS, #p<0.05, ##p<0.01, effect of GL-RM. Figures were modified from Ashely et al. 2021.[1]

2.3.13. Evaluation of effects of GL-RM treatment on neuronal morphology deficits induced by UCMS with Ashley Bernardo, Dr. Prevot and coworkers

The impact of GL-RM treatment on deficits in neuronal morphology was evaluated. A Golgi staining approach combined with neuron tracing was utilized to quantify the morphological changes in the apical and basal dendrites of pyramidal neurons in the prefrontal cortex (PFC) (**Figure 32**). The analysis involved examining dendritic length and spine count in both the basal and apical segments of pyramidal neurons from the PFC. Additionally, spine densities for the basal and apical segments of PFC neurons were assessed (**Figure 33**). **The analysis confirmed a reduction in spine density induced by UCMS in both basal and apical segments. Importantly, the administration of GL-RM reversed these morphology deficits induced by UCMS.**

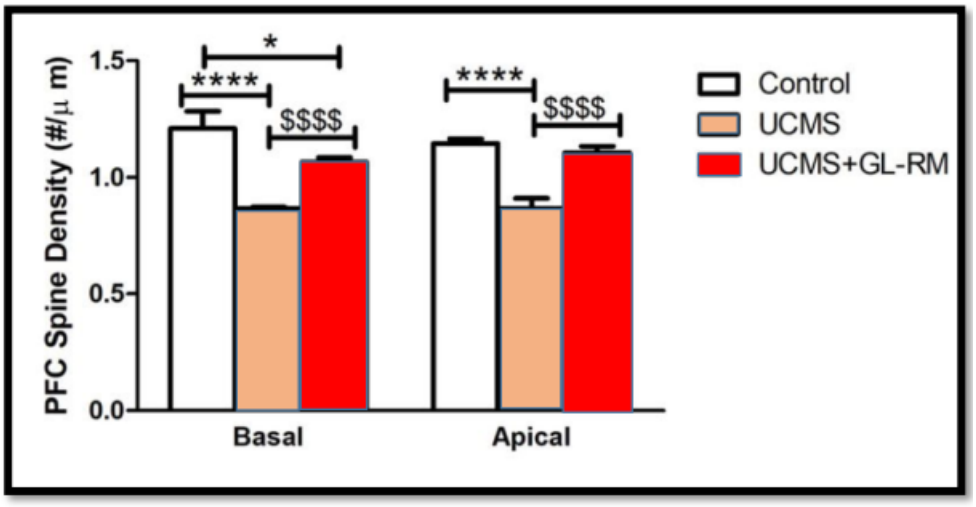


Figure 32. Spine densities of the basal and apical segment in the PFC of the hippocampus. Significant differences between groups in the basal and apical segments of PFC were revealed on ANOVA analysis. UCMS subjected mice showed decrease in spine densities, as compared to control mice that was partially reversed by chronic treatment with GL-RM. *p<0.05, **p<0.01, ***p<0.001 compared to "UCMS"; +p<0.05, ++p<0.01, +++p<0.001 compared to "Control". Figures were modified from Ashely et al. 2021.[1]

Mice exposed to UCMS exhibited a reduction in spine density compared to control mice, and this decrease was partially ameliorated by chronic administration of GL-RM.

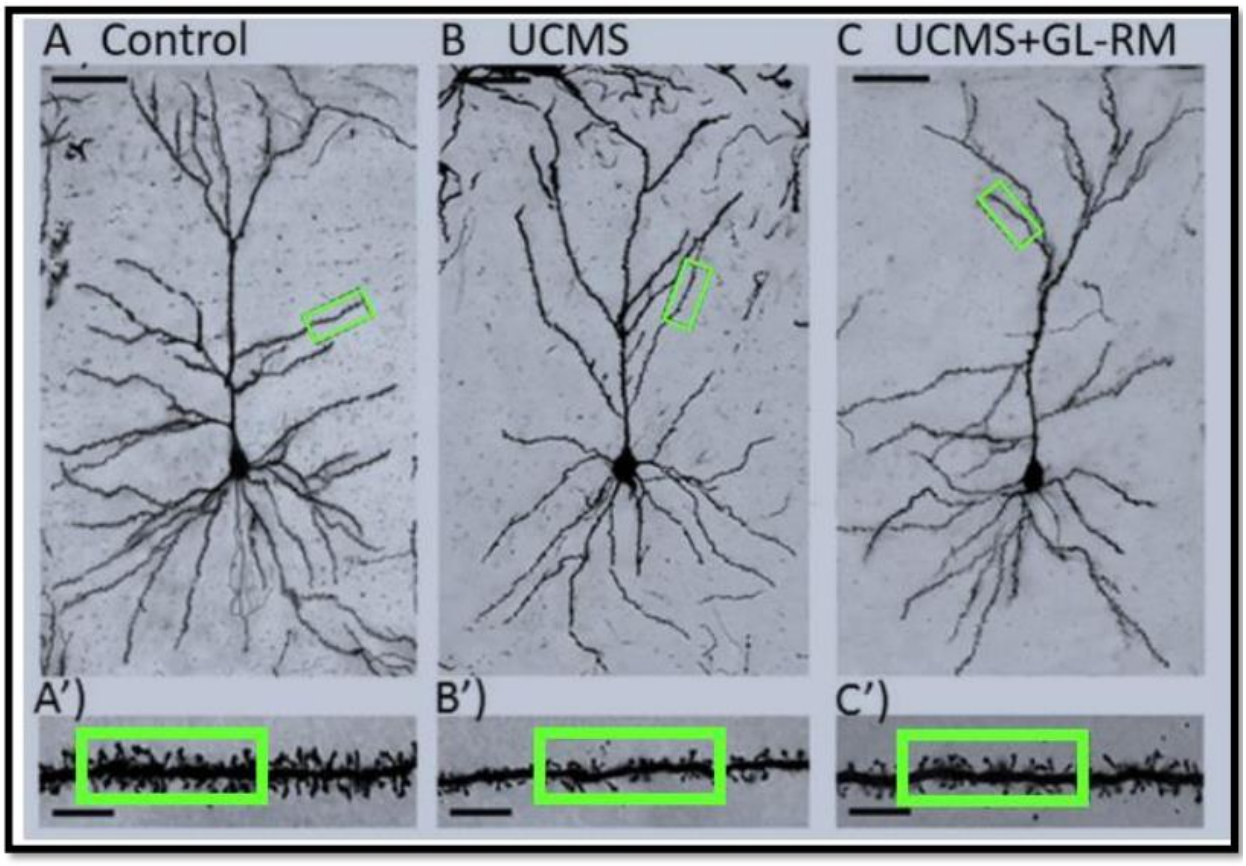


Figure 33. Staining of brains with Golgi-Cox solution. Analysis of dendritic length, spine counts and spine density of pyramidal neurons (N=6 per mouse) from 4 mice (A-C). Scale bar in (A-C) represents 50µm.Figures were modified from Ashely et al. 2021.[1]

The principal neurons of the CA1 were also examined in a similar manner. Spine density was diminished in UCMS-exposed animals, as compared to control animals (both basal and apical, $p<0.0001$). **However, the administration of GL-RM to UCMS-exposed animals significantly elevated spine density compared to UCMS vehicle-treated mice in both basal ($p<0.001$) and apical ($p<0.01$) dendrites.**

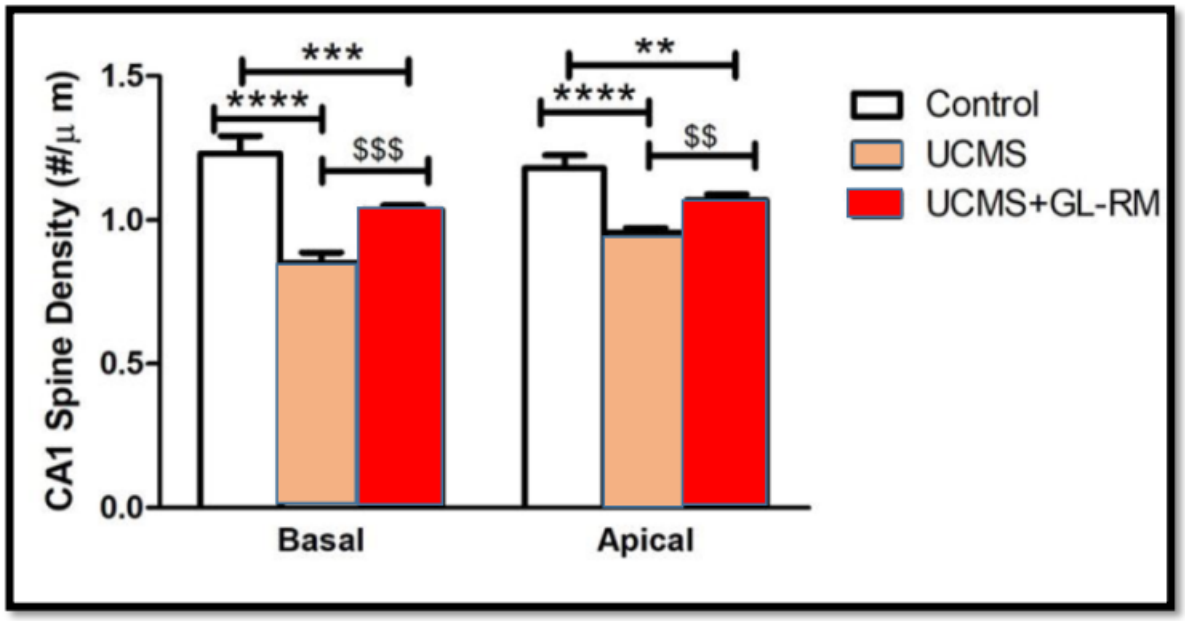


Figure 34. Spine densities of basal and apical segments in the CA1 of the hippocampus. Significant differences between groups in the basal and apical segments of PFC was revealed on ANOVA analysis. UCMS subjected mice showed a decrease in spine density, as compared to control mice that was partially reversed by chronic treatment with GL-RM. *p<0.05, **p<0.01, ***p<0.001 compared to "UCMS"; +p<0.05, ++p<0.01, +++p<0.001 compared to "Control". Figures were modified from Ashely et al. 2021[1]

2.3.14. Correlation of spine density in the PFC and CA1 with spatial working memory and emotionality by GL-RM with Ashley Bernardo, Dr. Prevot and coworkers

The performance in spatial working memory, as assessed by the Y maze task, was correlated with spine density in both the PFC and CA1. A direct relationship was observed at both apical and basal segments for both brain regions. Lower spine densities in the PFC were associated with reduced alternation rates (basal Spearman r=0.7616; p=0.004, apical Spearman r=0.6217; p=0.0309, **Figure 35 A** and **B**). Similar associations were identified in the CA1 region (basal Spearman r=0.6615; p=0.0191, apical Spearman r=0.7496; p=0.005; **Figure 35 C** and **D**).

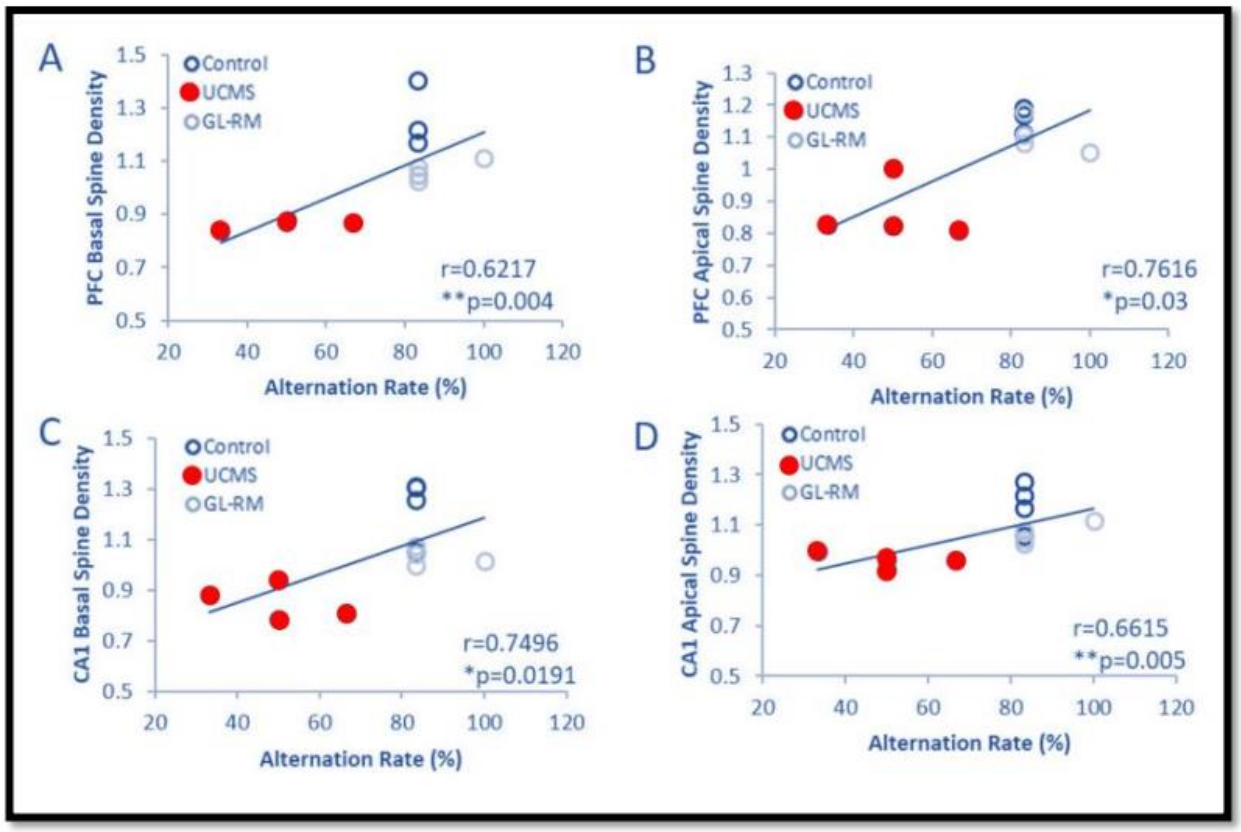
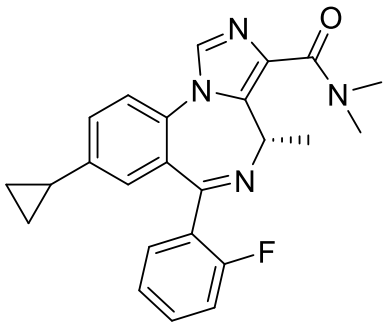


Figure 35. Correlation between morphological features from the PFC and the CA1 with the alternation rate (A-D). The positive correlation of basal (A) and apical (B) spines with the alternation rate, where higher density correlated with higher memory performances. Similar findings were also observed at basal and apical spine density from the CA1 (C-D)[1]

2.3.15. Evaluation of reversal of stress-induced working memory deficits by SRE-II-11 on the Y-maze task with Michael Marcotte, Dr. Prevot, Etienne Sibille and coworkers



SRE-II-11
24

A CNS-MPO score greater than 4.0 suggests SRE-II-11 **is likely brain penetrant**; the observation of ataxia in the maximum tolerated dose study supports this conclusion. In the Y-maze spatial alternation task for working memory, this shows a moderate but non-significant increase in alternation rate. Given that repeated testing produced similar results there is a possible effect on working memory. Additionally, given the rate of ataxia at 30mg/kg it is possible that elevated doses activate α1 $GABA_A$ receptors, which may interfere with any procognitive effect due to activity at α5 $GABA_A$ receptors. Testing in the Y-Maze at 3 mg/kg will proceed at a future date, but may not elicit procognitive efficacy.

CNS-MPO score: 4.36

A Central nervous system multi=parametric optimization (CNS-MPO) score greater than 4 suggests this compound is likely to penetrate the blood brain barrier.

Maximum Tolerated Dose

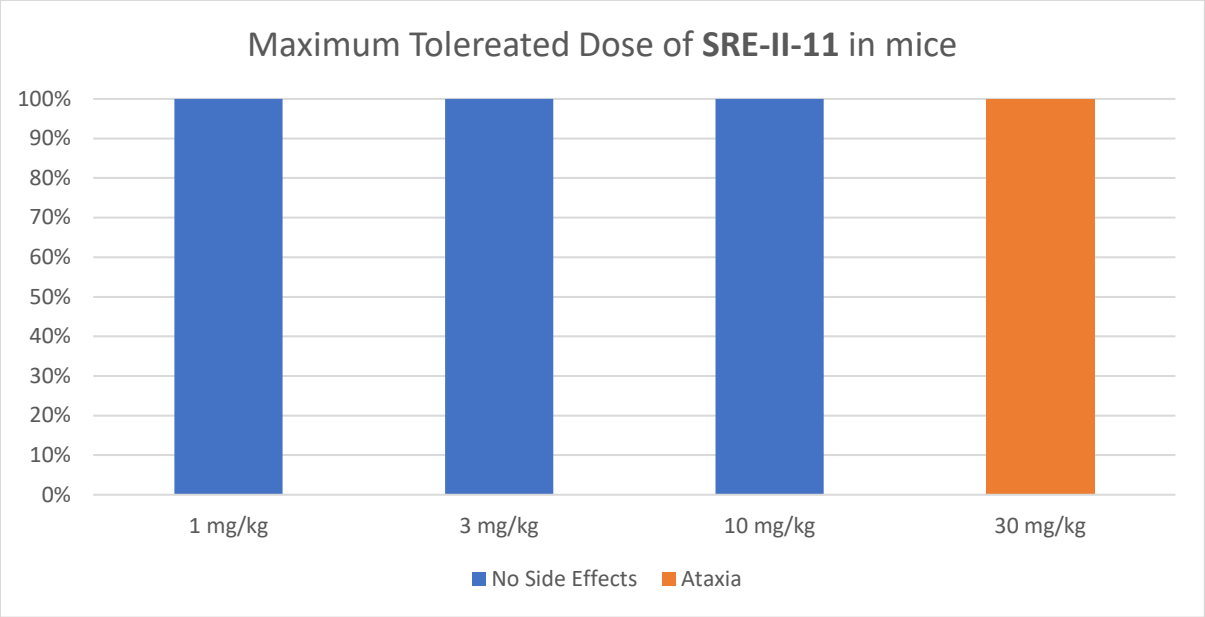


Figure 36. Maximum tolerated dose of SRE-II-11 in mice (Unpublished data)

Mice were administered SRE-II-11 by intraperitoneal (I.P.) injection at increasing doses (1mg/kg, 3mg/kg, 10mg/kg, 30mg/kg) and monitored for adverse events at 5, 20, 60, 120 and 180 minutes. Administration of each dose was separated by a minimum of 24 hours. No side effects were observed at 1 mg/kg, 3 mg/kg or 10 mg/kg. At 30 mg/kg all mice displayed some level of ataxia. N = 6

Y-Maze results (Pro-cognitive efficacy)

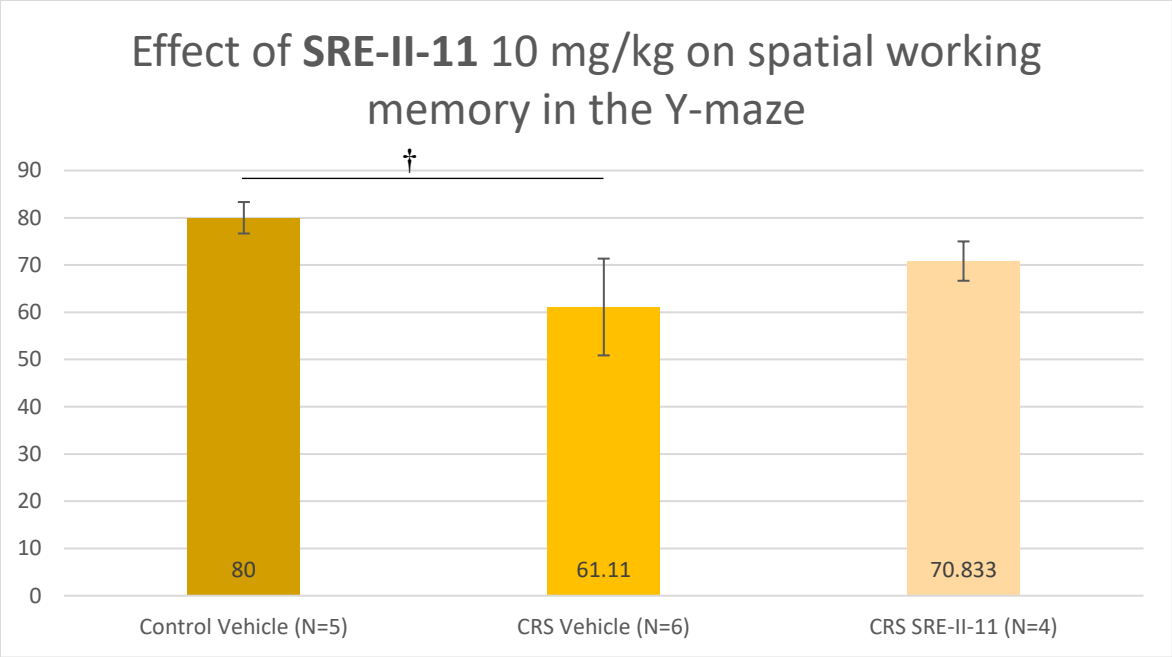


Figure 37. Effect of 10mg/kg SRE-II-11 on percent alternation rate in the Y-maze spatial alternation task assessing working memory in mice. (Unpublished data)

Mice subjected to chronic restraint stress (CRS) were injected with SRE-II-11 (10 mg/kg, i.p., 30 min before testing) and tested for spatial working memory in the Y-maze (YM). Analysis of variance found no overall effect of treatment; however, post hoc analysis revealed a trend level effect of stress in reducing alternation rate in comparison to non-stressed controls († $p < 0.10$), **treatment with 10 mg/kg of SRE-II-11 produced a non-significant increase in alternation.**

Due to the high variability of the CRS-Vehicle Controls and the promising nature of the increase in alternation, this experiment was repeated in a subsequent cohort of animals.

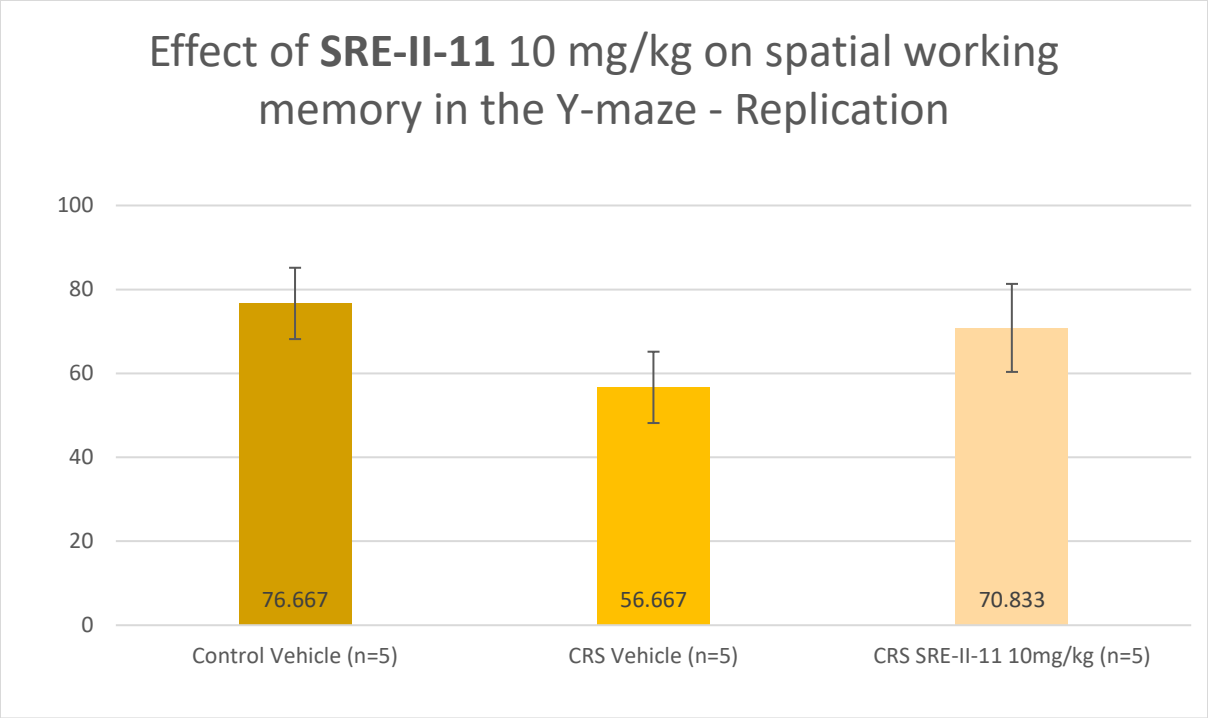
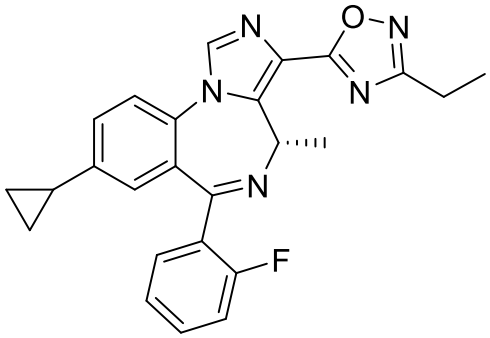


Figure 38. Effect of 10 mg/kg SRE-II-11 on percent alternation rate in the Y-maze spatial alternation task assessing working memory in mice. (Unpublished data)

Mice subjected to chronic restraint stress were injected with SRE-II-11 (10 mg/kg, i.p., 30 min before testing) and tested for spatial working memory in the Y-maze. **Analysis of variance did not find an overall effect.**

2.3.16. Evaluation of reversal of stress-induced working memory deficits by SRE-II-42 on the Y-maze task with Michael Marcotte, Dr. Prevot, Etienne Sibille and coworkers



22
SRE-II-42

A CNS-MPO score between 3-4 suggests SRE-II-42 may be brain penetrant. In the Y-maze spatial **alternation task for working memory SRE-II-42 shows a strong procognitive effect at 3mg/kg and 10mg/kg, confirming brain penetration**. In the maximum tolerated dose studies with SRE-II-42 no side effects were observed in the expected dose range. Further testing will proceed at 30 mg/kg in the Y-maze and in behavioral paradigms for anxiety and depressive like behaviors.

CNS-MPO score: 3.2

A CNS-MPO score of 3-4 suggests a compound is possibly brain penetrant. The ideal range would be >4.

Maximum Tolerated Dose

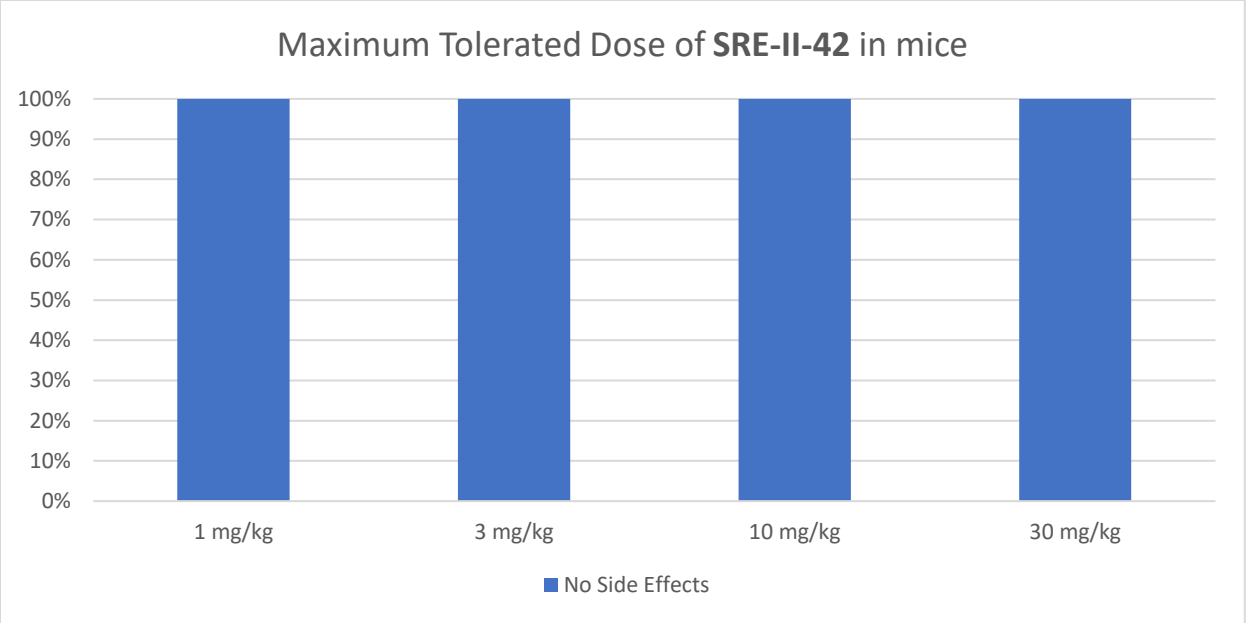


Figure 39. Maximum tolerated dose of SRE-II-42 in mice (Unpublished data)

Mice were administered SRE-II-42 by I.P. injection at increasing doses (1mg/kg, 3mg/kg, 10mg/kg, 30mg/kg) and monitored for adverse events at 5, 20, 60, 120 and 180 minutes. Administration of each dose was separated by a minimum of 24 hours. **No side effects were observed at the administered doses. (n=6)**

Y-Maze results (Pro-cognitive efficacy)

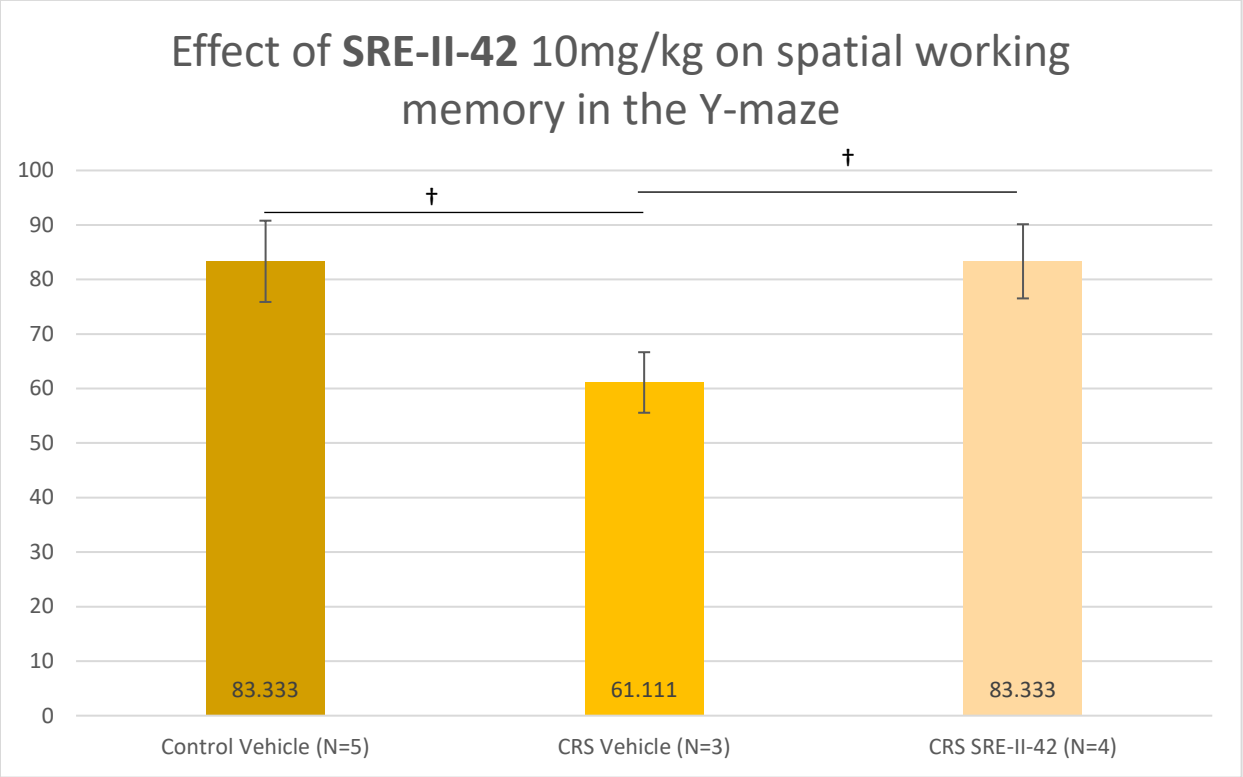


Figure 40. Effect of 10 mg/kg SRE-II-42 on percent alternation rate in the Y-maze spatial alternation task assessing working memory in mice. (Unpublished data)

Mice subjected to chronic restraint stress were injected with SRE-II-42 (10 mg/kg, i.p., 30 min before testing) and tested for spatial working memory in the y-maze. Analysis of variance found no overall effect **however post hoc analysis revealed that stress marginally reduced alternation rate at a level († $p < 0.10$), treatment with 10 mg/kg of SRE-II-42 improved alternation rate at a trend level († $p < 0.10$) in comparison to the stressed controls.**

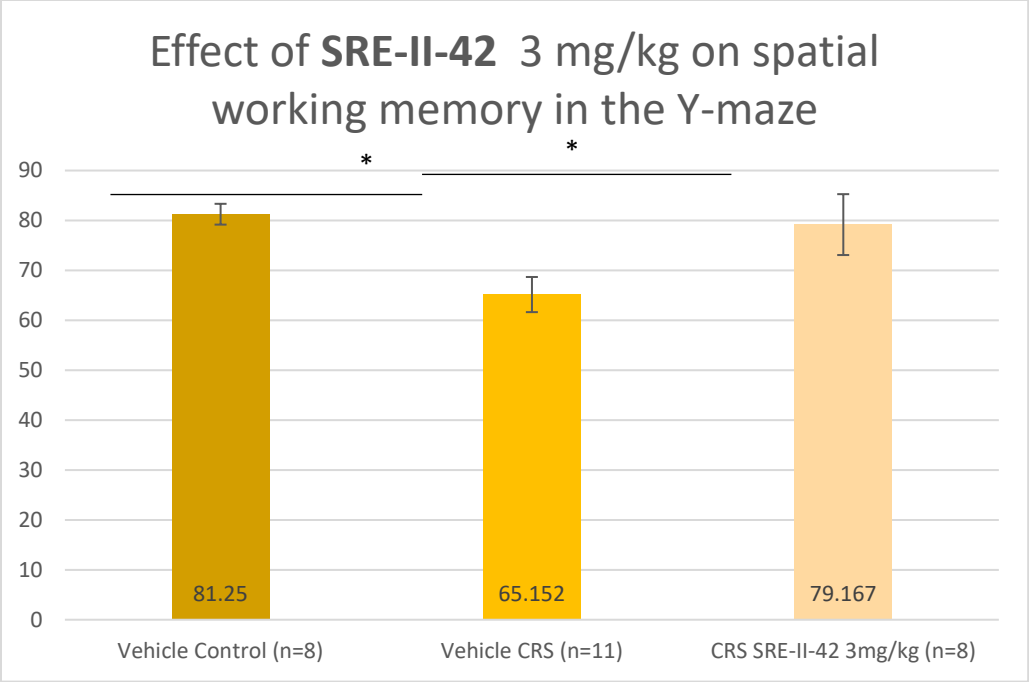
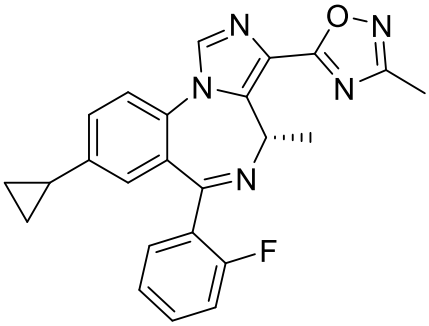


Figure 41. Effect of 3 mg/kg SRE-II-42 on percent alternation rate in the Y-maze spatial alternation task assessing working memory in mice. (Unpublished data)

Mice subjected to chronic restraint stress were injected with SRE-II-42 (3 mg/kg, i.p., 30 min before testing) and tested for spatial working memory in the Y-maze. Analysis of variance found an overall effect of ($p < 0.5$); however, post hoc analysis revealed that stress significantly reduced alternation rate at a level (* $p < 0.05$), treatment with 3 mg/kg of SRE-II-42 improved alternation rate at a marginal level (*$p < 0.05$) in comparison to the stressed controls.

2.3.17. Evaluation of reversal of stress-induced working memory deficits by SRE-II-44 on the Y-maze task with Michael Marcotte, Dr. Prevot, Etienne Sibille and coworkers



23
SRE-II-44

A CNS-MPO score between 3-4 suggests SRE-II-44 may be brain penetrant. In the maximum tolerated dose studies of SRE-II-59 no side effects were observed in the expected dose range. In the Y-maze spatial alternation task for working memory SRE-II-44 showed no effect on alternation rate. There is no testing currently planned for SRE-II-44.

CNS-MPO score: 3.56

A CNS-MPO score of 3-4 suggests a compound is possibly brain penetrant.

Maximum Tolerated Dose

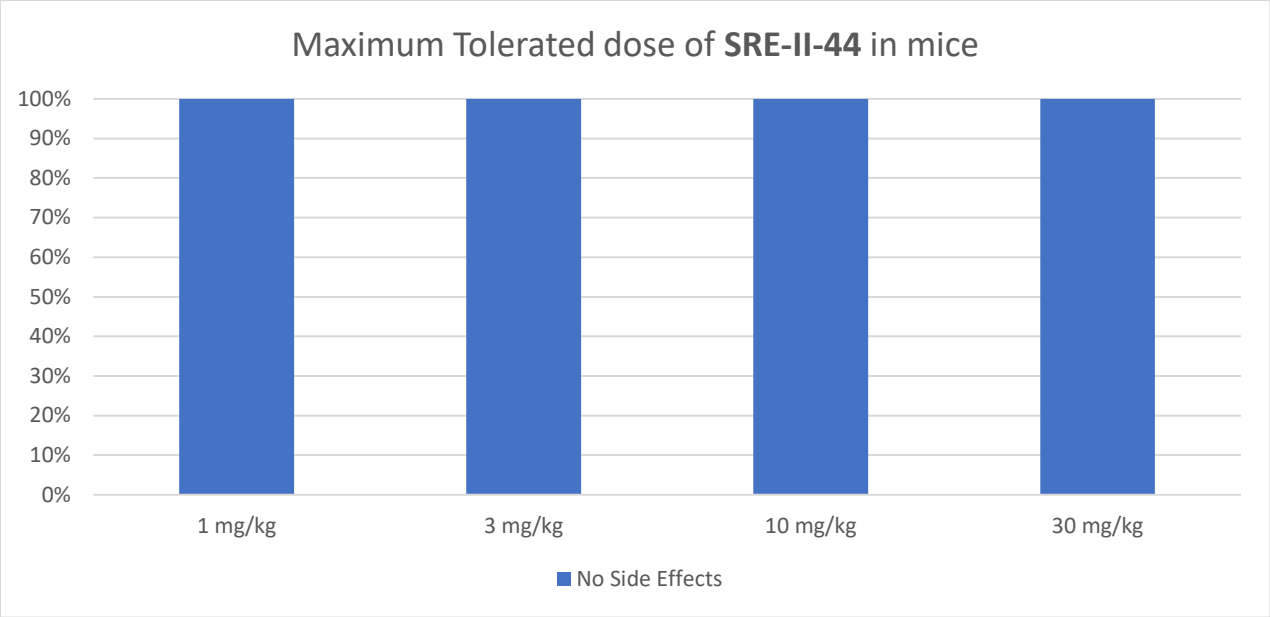


Figure 42. Maximum tolerated dose of SRE-II-59 in mice (Unpublished data)

Mice were administered SRE-II-44 by I.P. Injection at increasing doses (1mg/kg, 3mg/kg, 10mg/kg, 30mg/kg) and monitored for adverse events at 5, 20, 60, 120 and 180 minutes. Administration of each dose was separated by a minimum of 24 hours. **No side effects were observed at any dose administered. (n=6)**

Y-Maze results (Pro-cognitive efficacy)

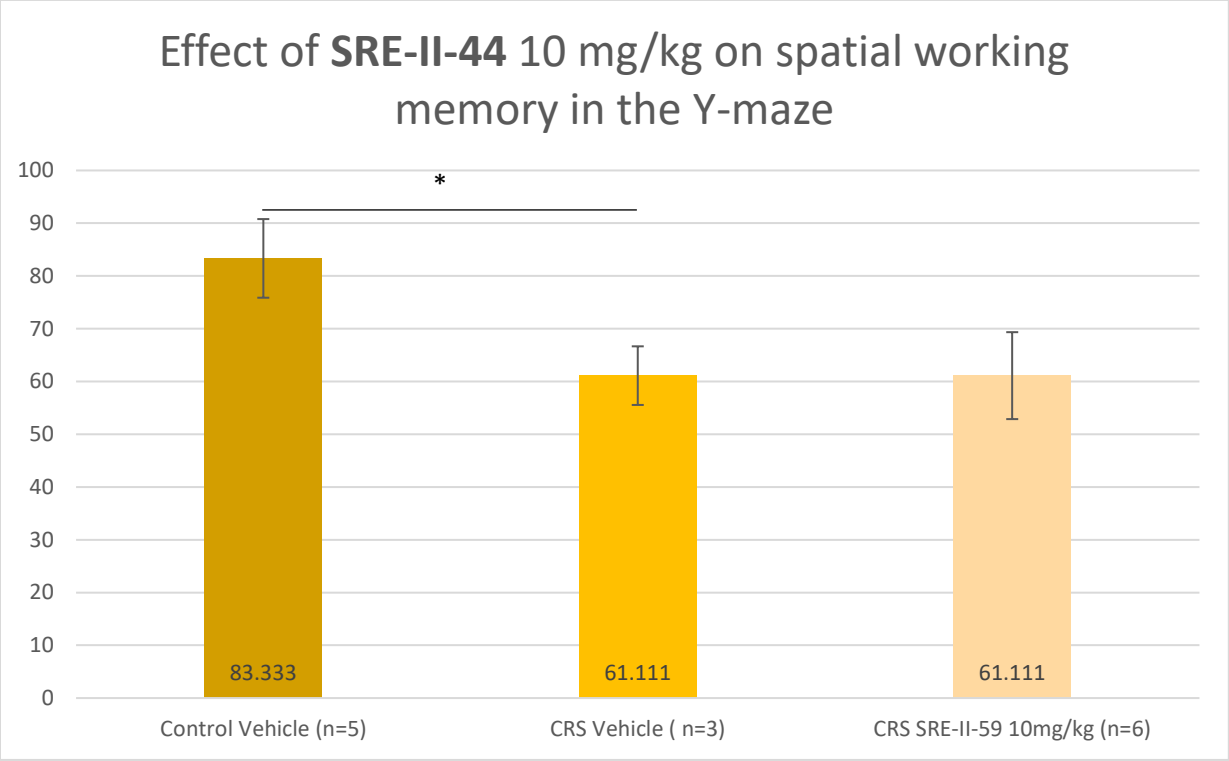
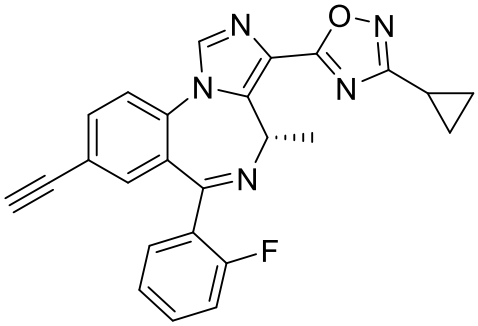


Figure 43. Effect of SRE-II-44 on percent alternation rate in the Y-maze spatial alternation task assessing working memory in mice. (Unpublished data)

Mice subjected to chronic restraint stress were injected with SRE-II-44 (10 mg/kg, i.p., 30 min before testing) and tested for spatial working memory in the Y-maze. Analysis of variance found an overall effect ($p < 0.05$) and post hoc analysis revealed that stress significantly reduced alternation rate in comparison to non-stressed controls (* $p < 0.05$). **Treatment with 10 mg/kg of SRE-II-44 had no effect on alternation rate.**

2.3.18. Evaluation of reversal of stress-induced working memory deficits by SRE-III-07 on the Y-maze task with Michael Marcotte, Dr. Prevot, Etienne Sibille and coworkers



SRE-III-07

Mice were administered SRE-III-07 by I.P. Injection at increasing doses (1mg/kg, 3mg/kg, 10mg/kg, 30mg/kg) and monitored for adverse events at 5, 20, 60, 120 and 180 minutes. Administration of each dose was separated by a minimum of 24 hours. **No side effects were observed at any dose administered. (n=6)**

CNS-MPO score: 4.1

A CNS-MPO score of greater than 4.0 suggests a compound is likely brain penetrant.

Maximum Tolerated Dose

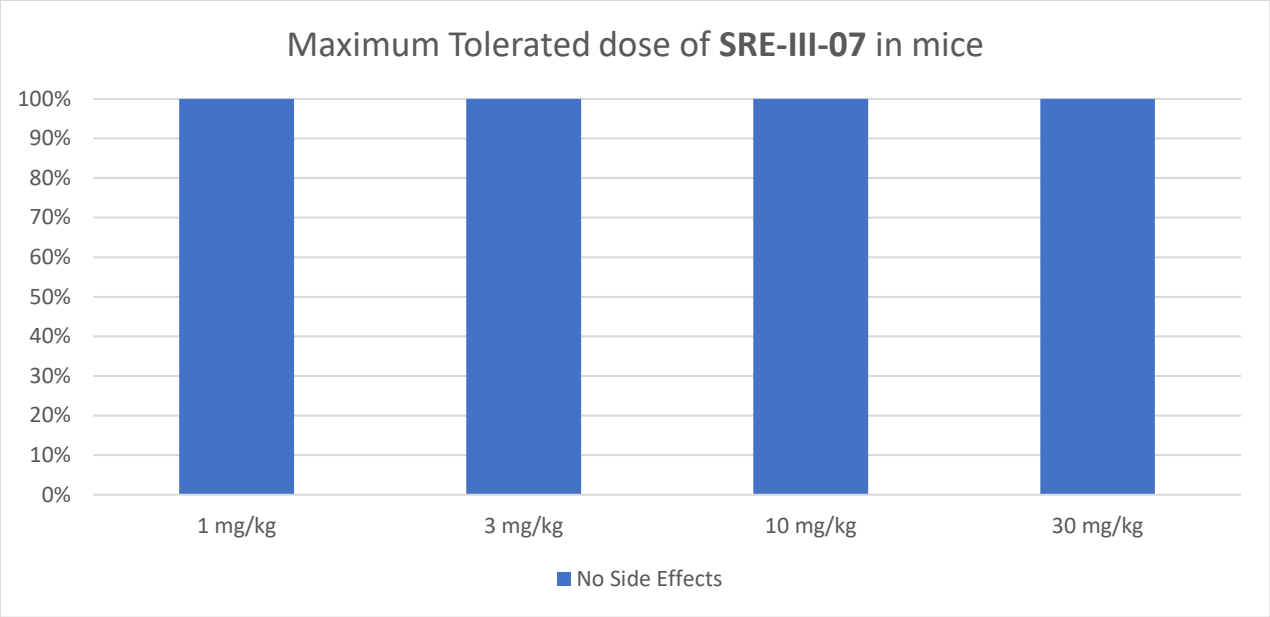


Figure 44. Maximum tolerated dose of SRE-III-07 in mice (Unpublished data)

2.3.19. Biological Activity: Metabolism, Cytotoxicity and Rotarod Studies with Mechelle Meyer and Anika Tylek, Dr. Arnold's group

To evaluate the potential for undesirable central nervous system (CNS) side effects mediated by α1 receptors, a study on locomotor coordination was carried out for each analog. Mice were subjected to the rotating rod test for a maximum of 3 minutes following oral administration via gavage at a 40 mg/kg dose (**Figure 45**). Additionally, the mice were monitored for the loss of the righting reflex, an indicator of undesired CNS effects. All of the mice treated with the compounds did not display sedation, ataxia, or loss of the righting reflex as compared to the control group treated with diazepam.

Most compounds demonstrated sensorimotor steadiness at all three time points, indicating an absence of sedative or ataxic effects. These findings suggested that the sedative/ataxic effects observed in certain amides may be attributed to their efficacy at the α1-GABAAR subtype.

The bulkier oxadiazoles SRE-II-42 and SRE-III-07, did not show any side effects as well as the amide SRE-II-11. **Work must continue to run the same cyclopropyl analogs at 100 mgs/kg.**

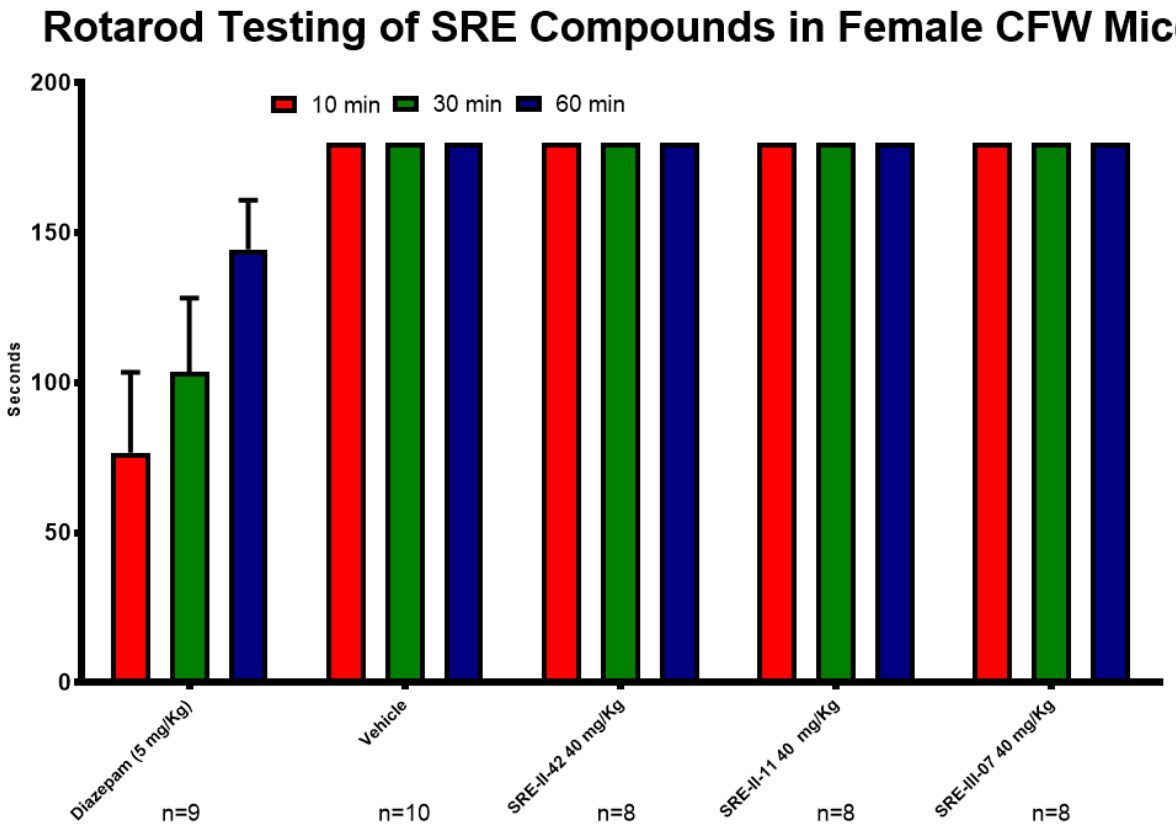


Figure 45. Effect of analogs of GL-I-54 on sensorimotor coordination. Mice were placed on the rotarod at three separate time points of 10, 30, and 60 minutes after each oral gavage drug administration at 40 mg/kg. Their performance on the rotarod for 3 minutes was

recorded and analyzed. After a second fall, it would be considered a fail, and that time point would be recorded. (Unpublished data)

2.3.20. Receptor binding studies

To assess potential off-target receptor binding, all newly developed ligands underwent evaluation at the National Institute of Mental Health (NIMH) Psychoactive Drug Screening Program (PDSP). A comprehensive screening, encompassing 47 receptors, ion channels, and transporters, was conducted to identify any interactions beyond the $GABA_A$ receptor. Dr. Bryan Roth from UNC spearheaded this initiative. Ligands exhibiting substantial inhibition (exceeding 50%) in primary binding underwent further scrutiny in secondary binding assays to determine their Ki (nM) values.

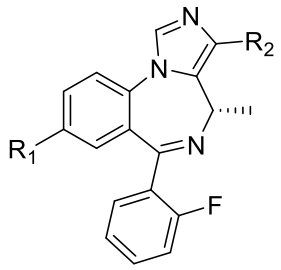
While most ligands demonstrated binding affinity at $GABA_ARs$, it's crucial to note that this data doesn't reflect their affinity for different Bz alpha/beta/gamma2-subtypes. Notably, there was no observed binding of the test compounds with calcium channels, indicating no physiological impact on cardiac and smooth muscle cells or NMDA receptors[157,158]

Screening the compounds for hERG binding in the initial stages of drug discovery is crucial. Unintended hERG binding can lead to blockage of hERG K+ channels in the heart, causing various side effects such as cardiac arrhythmias and sudden death. [159]Therefore, evaluating compounds for hERG binding is essential to delineate any off-target profiles.

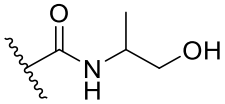
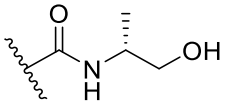
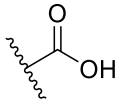
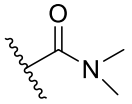
All α2,3 and 5 imidazodiazepines underwent testing for hERG binding, and fortunately, the test compounds did not exhibit undesired binding to voltage-sensitive K+ channel hERG. However, some imidazodiazepine intermediates with a C-8 cyclopropyl group were found to bind hERG

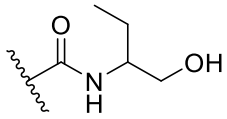
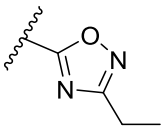
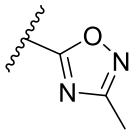
based on primary binding data. But their binding was less than 50% on the primary screen, indication no significant binding occurred to hERG. Other tested compounds did not exhibit any binding affinity towards voltage-sensitive K+ hERG channels (**Table 8**).

Table 8. Binding affinities at hERG, only the C-8 cyclopropyl compounds among the entire compound library have slight affinity to hERG (PDSP). Unpublished data.



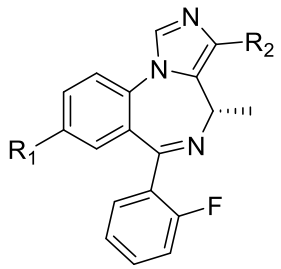
Core structure of α2,3 and 5 imidazodiazepines

PDSP Code	Cook Code	R_1	R_2	Binding affinity at hERG % inhibition (primary)
61387	SRE-I-95	Br		-2.08
61389	SRE-II-38	Br		8.14
61390	SRE-II-61	△		3.17
61391	SRE-II-11	△		4.67

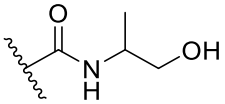
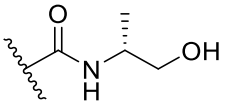
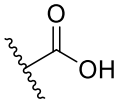
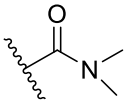
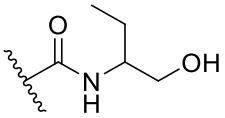
61397	SRE-II-36	Br		8.54
61398	SRE-II-42	△		46.61
61399	SRE-II-44	△		42.84

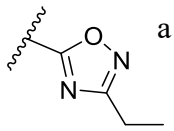
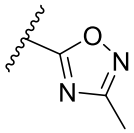
The compounds were studied at PDSP to investigate their interaction with the peripheral benzodiazepine receptor (PBR) as well. Various biological processes are linked to PBR, including the transport of anions for mitochondrial transmembrane potential, heme biosynthesis, regulation of neurological damage, proliferation, cell death (apoptosis), and steroidogenesis regulation. In the primary binding assay, the tested compounds were evaluated for the percentage of inhibition, and several compounds exhibited inhibition exceeding 50%. Subsequently, these compounds underwent a secondary screening to determine their Ki (nM) values for PBR receptors. The structures of the compounds and their binding affinities for PBR are outlined in **Table 9**.

Table 9. Binding affinities at peripheral benzodiazepine receptor (PBR) for the novel compounds (PDSP). Unpublished data.



Core structure of α2,3 and 5 imidazodiazepines

PDSP Code	Cook Code	R_1	R_2	Binding affinity at PBR % inhibition (primary)	Binding affinity at PBR Ki(nM) (Secondary)
61387	SRE-I-95	Br		2.86	
61389	SRE-II-38	Br		28.73	
61390	SRE-II-61	△		36.82	
61391	SRE-II-11	△		12.87	
61397	SRE-II-36	Br		-15.21	

61398	SRE-II-42	△	 a	100.04	575.70
61399	SRE-II-44	△	 a	92.45	706.81

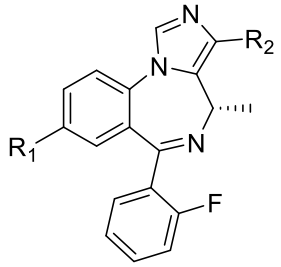
[a] . The two 1,2,4-oxadiazoles exhibited only very weak affinity at PBR receptor

Among all the tested compounds, just 2 oxadiazoles analogs were tested in the secondary screening at PBR receptor, but were found to be only weakly active.

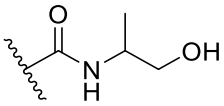
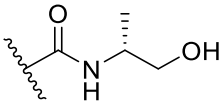
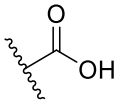
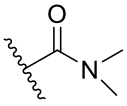
In addition to the robust binding affinity observed with the previously mentioned receptors, certain imidazodiazepines also demonstrated inhibitory effects on kappa opioid receptors (KOR). Opioid receptors constitute a family of inhibitory G-coupled protein receptors, with opioids serving as ligands. The family includes kappa opioid receptors (KOR), mu and delta opioid receptors (MOR and DOR), and nociception opioid receptors (NOP). It has been noted that the two oxadiazole imidazodiazepines here can elicit might same analgesic and anti-inflammatory properties through mediation by the kappa opioid receptor (KOR).

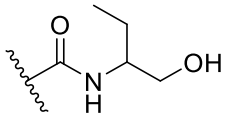
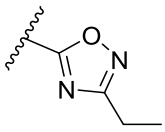
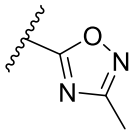
The affinities of the test compounds for KOR, DOR, and MOR were determined through radio ligand binding assays at a screening concentration of 10,000 nM in collaboration with the National Institute of Mental Health Psychoactive Drug Screening Program (PDSP), as mentioned earlier. Concentration-dependent experiments were conducted to establish Ki values for compounds that exhibited over 50% radio-ligand displacement in the primary binding assay. A number of these alpha-5 selective imidazodiazepines displayed affinities for KOR, and they are summarized in **Table 10** to indicate the percentage of KOR inhibition and Ki values for both chiral and achiral imidazodiazepines.

Table 10. KOR binding affinity from the primary binding assay. Unpublished data. (PDSP)



Core structure of α2,3 and 5 imidazodiazepines

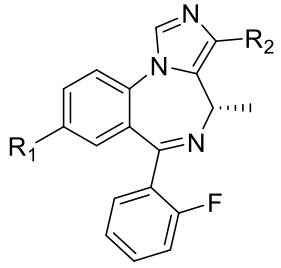
PDSP Code	Cook Code	R_1	R_2	Binding affinity at KOR % inhibition (primary)	Binding affinity at KOR Ki(nM) (Secondary)
61387	SRE-I-95	Br		49.94	
61389	SRE-II-38	Br		80.38	1264.15
61390	SRE-II-61	△		79.63	1020.70
61391	SRE-II-11	△		55.72	2122.27

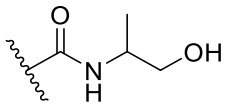
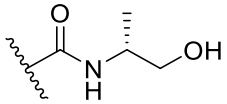
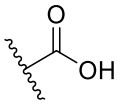
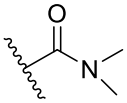
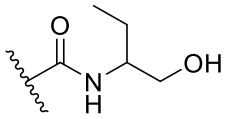
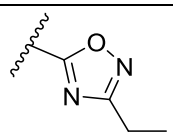
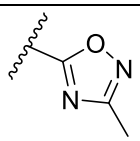
61397	SRE-II-36	Br		10.35	Not active
61398	SRE-II-42	△		90.15	195.52 [a]
61399	SRE-II-44	△		93.64	203.10 [a]

[a] . The two 1,2,4-oxadiazoles were shown to have some affinity at KOR.

Among all the imidazodiazapines, SRE-II-44 showed the second highest affinity for KOR (Ki=203.10 nM) (**Table 10**). The next highest binding affinity to KOR belonged to the other oxadiazole SRE-II-42, which was 90.15 (Ki=195.52) (**Table 10**). Except SRE-I-95 and SRE-II-36 which exhibited, slightly less binding sites to KOR, the rest of the imidazodiazapines demonstrated very weak binding affinity to KOR. The next assays for all the above compounds at BZR binding affinity by using rat brain Bzr homogenates. This is a mixture of all BZR which includes α1 at a level of 50-60%. Most of the compounds showed binding affinity to this BZR receptor with SRE-II-42 as the most potent at BZR. The data are presented in **Table 11**.

Table 11. BZR binding affinity from the primary binding assay. Unpublished data. (PDSP)



Core structure of α2,3 and 5 imidazodiazepines					
PDSP Code	**Cook Code**	**R_1**	**R_2**	**Binding affinity at BZR % inhibition (primary)**	**Binding affinity at BZR Ki(nM) (Secondary)**
61387	SRE-I-95	Br		85.41	417.64
61389	SRE-II-38	Br		91.68	25.91
61390	SRE-II-61	△		81.47	345.06
61391	SRE-II-11	△		81.35	378.98
61397	SRE-II-36	Br		15.58	
61398	SRE-II-42	△		56.45	1279.38 [a]
61399	SRE-II-44	△		65.05	1224.33 [a]

a . The key oxadiazoles SRE-II-42 and SRE-II-44 elicited poor affinity at BZR, but are must remember only 5% of the BZR is composed of α5 subtypes while approximatly 85% are α1, α2 and α3 subtypes.

2.3.21. Conclusion

Based on the in vivo profiles on both enantiomers the lead ligands of GL-II-73 and GL-I-54, not only they were active in anxiolytic and antidepressant studies in mice, but their racemic mixture of them (GL-RM) also indicated the potential anxiolytic effects of chronic treatment. GL-RM indicated a reduction in spine density induced by UCMS in both basal and apical segments. A series of analogs designed closely related to the structure of GL-I-54 andGL-II-73. They were synthesized incorporating various substitutions with functional groups such as amides, 1,2,4-oxadiazoles, and cyclopropyl groups. In vitro studies were conducted to assess the cytotoxicity, receptor binding affinity, and efficacy at different $GABA_AR$ subtypes for the analogs. Compounds that exhibited promising results in the in vitro assays were chosen for further investigation in in vivo animal models to identify potential central nervous system (CNS) side effects and to assess desired physiological effects, including anxiolytic, antidepressant, and pro-cognitive effects.

To date, several compounds have shown clinical potential for different diseases, though as of December 2023. Among these, the ethyl oxadiazole SRE-II-42 demonstrated pro-cognitive activity in the Y-maze task without causing side effects in the maximum tolerated dose (MTD) assay. SRE-II-11, a dimethyl amide, showed efficacy in reversing the percent alteration rate at an effective dose. Further testing of these compounds is essential to advance towards clinical trials, with a focus on assessing their potential as antidepressants and, ideally, anxiolytics, given the comorbidity of anxiety with depression.

2.4. Methods

2.4.1. Elevated plus maze assay with Dr Felipe V. Gomes, Adriana Jesus Souza, and coworkers

Animals

This experiment utilized male and female C57BL/6 mice aged 6-8 weeks. These mice were obtained from the colony maintained by the Central Animal House of the University of São Paulo, Ribeirão Preto campus. They were categorized into different groups and housed in a temperature-controlled room (24 ± 1 °C) with a 12-hour light cycle (lights on at 6:30 AM) and had access to food and water ad libitum. All procedures for these experiments were approved by the Ribeirão Preto Medical School Ethics Committee.

Drugs

GL-II-73, GL-I-54 and SH-053-2'F-R-CH3 were synthesized within our laboratory under the supervision of Dr. James Cook at the University of Wisconsin Milwaukee, WI, USA. MK-801 (Sigma, USA) was diluted with sterile saline. All drugs were administered intraperitoneally (i.p.) in a final volume of 10 mL/kg.

Elevated plus-maze (EPM)

In a sound-attenuated room the Elevated Plus Maze (EPM) was placed, which was equipped with a 60 lux incandescent light located 1.3 m away from the maze. For a duration of 5 minutes, animals were allowed to explore the EPM without any limitation, starting from the central platform with their head oriented towards one of the enclosed arms. Any Maze software (Stoelting, USA) was employed to capture data, including the percentage of entries into open arms and the time spent in

these arms (indicative of anti-anxiety response), as well as the number of entries into enclosed arms (indicative of locomotor activity).

2.4.2. Forced swim test (FST) with Dr Felipe V. Gomes, Adriana Jesus Souza, and coworkers

For the Forced Swim Test (FST), a glass cylinder with a height of 25 cm and a diameter of 17 cm was utilized, containing water at a depth of 10 cm and maintained at a temperature of 23–25 °C. Animals were placed in the tank and compelled to swim for a duration of 6 minutes. The last 4 minutes of immobility during the test were recorded using a videotape. Immobility was defined as floating with minor movements necessary to keep the head above water. Between each mouse, the water was replaced.

2.4.3. Electrophysiology with Ashley Bernardo, Dr Tom Prevot, Dr Etienne Sibille and coworkers

Electrophysiology experiments were conducted using HEK-293T cells. The human $GABA_A$ receptor subtypes (α1β3γ2, α2β3γ2, α3β3γ2, α4β3γ2, or α5β3γ2) were transfected into the HEK-293T cell line. A holding potential of -70mV was maintained. GL-II-73 or GL-I-54 were applied at concentrations of 0.033μM, 0.1μM, 0.33μM, 1μM, 3.33μM, 10μM, and 33.33μM to cells, each with varying concentrations, as specified above, in the presence of 5μM gamma-aminobutyric acid (GABA).

2.4.4. Y-maze assay with Ashley Bernardo, Dr Tom Prevot, Dr Etienne Sibille and coworkers

The Y maze, adapted from the T maze paradigm by Faucher et al.[159], was employed to evaluate spontaneous alternation, which is as indication of memory retention. This maze comprises three arms, each separated by 120 degrees, measuring 26 cm in length, 8 cm in width, and 13 cm in height. Two of these arms, designated as "goal arms," have sliding doors near the center of the maze, while the third arm, referred to as the "start box," features a sliding door close to its distal end. At the onset of each trial, a mouse is placed in the start box.

An initial habituation phase spans two consecutive days, during which mice freely explore the maze for 10 minutes. The subsequent training phase, initiated on the third day, consists of seven consecutive trials with a 30-second inter-trial interval (ITI). In each trial, the mouse spends 30 seconds in the start box, after which the sliding door opens, allowing the mouse to choose either of the goal arms. Once the choice is made, the door to the selected goal arm closes, and both the choice and latency to decide are recorded. The mouse remains in the chosen arm for 30 seconds before being returned to the start box for the next trial, beginning with a 30-second initial confinement. This sequence repeats over the seven trials, with the maze lightly wiped down with 70% ethanol between trials to eliminate olfactory cues.

The testing phase, conducted 24 hours later, replicates the training phase with a longer ITI of 90 seconds. On the eighth trial, the same procedure is repeated, but with a reduced inter-trial interval of 10 seconds to assess the animal's motivation to alternate. Animals failing to alternate on this trial are excluded from analysis due to potential bias from reduced motivation rather than cognitive performance.

The mean alternation rate is calculated as a percentage using the formula: Mean alternation % = [(Number of alternations/number of trials) x 100].

2.4.5. Liver microsomal assay with Ashley Bernardo, Dr Tom Prevot, Dr Etienne Sibille and coworkers

The disappearance rate of compounds in microsomal or hepatocyte incubations over time can be evaluated through a metabolic stability assay of the test compounds. The intrinsic clearance of a test compound can then be determined based on these assay results. Given that the liver plays a crucial role in drug metabolism, C57BL/6 mouse liver microsomes were employed for the metabolic stability assay. GLII-73 and its enantiomer, GL-I-54, were administered to liver microsomes at a concentration of 2μM and a matrix concentration of 0.5mg/mL following the established protocol. [160] Subsequently, an NADPH solution was introduced to the assay plate, and the test compounds were added. The plate was quenched, and microsomes/S9 were rapidly thawed from a -20°C freezer and introduced to the assay plate to initiate the reaction. The reaction time was recorded, and duplicate aliquots were transferred to a quench plate and mixed at T0. This process was repeated at various time points, including 30, 60, and 120 minutes. The sealed sample plate was placed in a refrigerated LC/MS/MS autosampler for assessment. Calculations for intrinsic hepatic clearance utilized 45mg microsomes/g liver and 87.5g liver/kg body weight for mice.

2.4.6. PhenoTyper™ (PT) Test with Ashley Bernardo, Dr Tom Prevot, Dr Etienne Sibille and coworkers

Animals

Two sets of C57BL/6 mice, both male and female, aged 8 weeks, were procured from Jackson Laboratories (Stock# 000664; Bar Harbor, MA, USA). Each cohort comprised 48 mice (N=12 per group, with four groups and a 50% female distribution). In each cohort, half of the mice underwent unpredictable chronic mild stress (UCMS), while the other half were subjected to the evaluation of the acute or chronic effects of GL-RM treatment (a combination of GL-I-54 and GL-II-73). All mice were individually housed and maintained on a 12-hour light/dark cycle (7:00 ON, 19:00 OFF), with unrestricted access to food and water unless specified by testing requirements. To minimize stress and anxiety during experiments and behavioral tests, the mice were handled for 5 minutes on three consecutive days. The mice were assigned blind numbers for all studies and were grouped to achieve a 50% sex ratio. All animal procedures were conducted in compliance with the Ontario Animals for Research Act (RSO 1990, Chapter A.22), adhering to the guidelines of the Canadian Council on Animal Care (CCAC) and approved by the Animal Care Committee at the Canadian Mental Health Institute (CAMH).

Drug preparation and administration

A racemic combination (50:50) of GL-II-73 and GL-I-54, denoted as GL-RM, was synthesized specifically for the two Unpredictable Chronic Mild Stress (UCMS) studies. In the case of acute administration, GL-RM was dissolved in a vehicle solution comprising 85% distilled H_2O, 14% propylene glycol (Sigma Aldrich), and 1% Tween 80 (Sigma Aldrich). This solution was injected 30 minutes before conducting behavioral testing, with the acute administration route being intraperitoneal (i.p.) and the dosage set at 10mg/kg. Mice received either saline or acutely administered GL-RM (10mg/kg) before 20:00hr for the acute drug treatment in the PhenoTyper test.

For chronic administration, GL-RM was given via the per oral (PO) route, with an administration volume of 266mL/kg, equivalent to a 30mg/kg dose. The preparation involved dissolving GL-RM in tap water overnight at rt, and this solution was freshly prepared every other day. The animals had access to GL-RM through their drinking water.

Stress paradigms

Chronic Restraint Stress (CRS)

For the chronic restraint stress procedure, a 50mL Falcon™ Tube was employed. This specific tube design features a hole at the conical tip and another in the lid, facilitating both breathing and providing physical space. Mice were positioned within this tube and left undisturbed for one hour upon returning the tube to their home cage. This process was repeated twice a day for one week, with a minimum one-hour interval between the two sessions.

In the case of the Unpredictable Chronic Mild Stress (UCMS), a range of mild stressors was introduced 1-2 times daily according to the UCMS paradigm. This regimen occurred randomly over a span of 6 weeks (considering 8 weeks with the inclusion of 2 weeks of behavioral testing). Each day, one stressor was applied after the testing session. Animals subjected to UCMS were housed in a separate room to minimize environmental disturbances.

PhenoTyper™ (PT) Test

The animals were brought to the testing room 30 minutes before the behavioral testing to allow them to adjust to the room and lighting conditions. Prior to placing any animal in the apparatus, the equipment was cleaned with 70% ethanol and thoroughly dried. The PhenoTyper™ (PT) test was conducted following the protocol outlined in Prevot et al. [161], utilizing a PhenoTyper box for the experiment. This box includes a home cage setup with a water bottle, food hopper, and shelter.

An infrared camera mounted on the ceiling enables video tracking using Ethovision, and there is a white light that can be activated as needed for experimental purposes. Notably, shining a white light above the food zone during the night hours (11 pm-12 am) serves as a stressful stimulus for the mouse. The primary focus of this study was to characterize the mouse's activity before, during, and after exposure to this stressful stimulus.

The investigation focused on analyzing the time spent in the food and shelter zones to quantify anxiety-like behavior, and residual avoidance could be determined based on the time spent in each zone. The calculation of a positive Residual Avoidance (RA) value involved using specific equations based on the time spent in the food or shelter zone. For the Food Zone, the formula was [1 - (Σ Time (12 am–5 am) – Time (11 pm–12 am))/Average control group (Σ Time (12 am–5 am) - Time (11 pm–12 am))] * 100, where "Time" represents the time spent in the food zone. For the Shelter Zone, the formula was [(Σ Time (12 am–5 am) – Time (11 pm–12 am))/Average control group (Σ Time (12 am–5 am) - Time (11 pm–12 am)) - 1] * 100, where "Time" denotes the time spent in the shelter zone. The PhenoTyper™ demonstrated its capability to identify a predictable avoidance behavioral pattern in chronically stressed mice following an aversive light stimulus, as detectable in the Phenotyper test.

2.4.7. Golgi Staining Analysis of mice brain with Ashley Bernardo, Dr Tom Prevot, Dr Etienne Sibille and coworkers

Cervical dislocation was employed as the method for euthanizing mice following the completion of the final behavioral test, which occurred 24 hours after the test. Brains were gathered from three groups: the non-Unpredictable Chronic Mild Stress (UCMS) group treated with the vehicle ("Control"), the UCMS group treated with the vehicle, and the UCMS group treated with GL-RM. The brains were immersed in Golgi-Cox staining solution (NeuroDigiTech LLC) post-extraction,

and NeuroDigiTech conducted a comprehensive analysis of the fully stained brains. Following Golgi-Cox staining, the brains were sectioned on a cryostat with a thickness of 100µm and mounted on glass slides. The basal and apical dendrites of pyramidal cells in the prefrontal cortex (PFC) and the CA1 region of the hippocampus were identified. For quantification of the dendrites, NeuroLucida v10 software (Microbrightfield, VT) was utilized on a Dell PC computer. The analysis involved assessing dendritic length, spine number, and spine density of the neurons, following the methods outlined in Wu et al.[162]

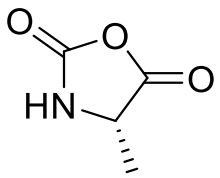
2.4.8. Radioligand binding assays on rat brain homogenates with the National Institute of Mental Health's Psychoactive Drug Screening Program (NIMH PDSP) at UNC with Dr Bryan Roth

The detailed procedures for primary and secondary radio-ligand binding assays are extensively outlined in the Assay Protocol Book of the National Institute of Mental Health's Psychoactive Drug Screening Program (NIMH PDSP). A final volume of 125 µL per well, prepared in the appropriate binding buffer, was utilized for conducting both primary and secondary radio-ligand binding assays. The concentration of the radioactive ligand closely approximated the dissociation constant (Kd) values ([3H]-U69593 0.83 nM, [3H]-DAMGO 1.20 nM, and [3H]-DADLE 2.69 nM). The binding of a ligand to a receptor, ion channel, or transporter was assessed in the absence and presence of 10 µM of the relevant reference compound. Nonspecific binding was also determined in the absence and presence of 10 µM of the appropriate reference compound. The plates were incubated in the dark for 90 minutes at rt, and the reactions were halted by vacuum filtration onto 0.3% polyethyleneimine (PEI)-soaked 96-well filter mats using a 96-well Filtermate harvester, followed by three washes with cold PBS buffer. Radioactivity was then quantified in a Microbeta counter. The data (N=6) were analyzed using nonlinear regression.

2.5. Experimental

All reactions were performed in oven-dried round-bottom flasks and cooled under an argon atmosphere. Chemicals and solvents were obtained from commercial suppliers and purified using the PURESOLV Solvent Purification System and KNF LABOPORT vacuum pumps. TLC plates from Dynamic Adsorbents Inc. were used to analyze and monitor the reactions. The reactions were monitored under a UV254 fluorescence indicator. Some compounds were purified using column chromatography on silica gel (230-400 mesh, Dynamic Adsorbents) with a glass column. Melting points were determined using a Stuart SMP3 apparatus from Barloworld Scientific US Ltd. 1H and 13C NMR spectra were obtained on a Bruker Spectrospin 500 MHz instrument in CDCl3 or DMSO-d6. Chemical shifts were reported in δ (ppm) relative to TMS as an internal standard. NMR multiplicities were represented as singlet (s), broad singlet (br s), doublet (d), triplet (t), quartet (q), and multiplet (m). Compound purity (> 95%) was determined by HPLC-MS on a Shimadzu LCMS-2020, and HRMS was performed on a Shimadzu LCMS-IT-TOF at the Milwaukee Institute for Drug Discovery in the Shimatzu Laboratory for Advanced and Applied Analytical Chemistry.

2.5.1. (S)-4-Methyloxazolidine-2,5-dione (15)



15

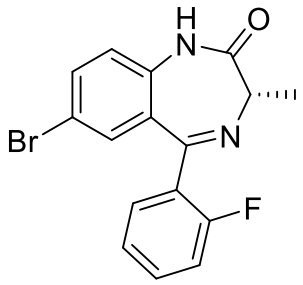
To form a homogeneous mixture, Boc-L-Alanine, **2** (60g, 317.106 mmol), triphosgene (37.63g, 126.81 mmol), and anhydrous ethyl acetate (1600mL) were combined. Triethylamine (81.0mL, 351.71 mmol) was then added dropwise over 60 min while maintaining the temperature between 25 and 30°C and observing the evolution of CO_2(g) and HCl(g). Afterward, the reaction mixture

was stirred at rt for 1 h and then heated to reflux for 2 h at 65-70°C until gas evolution ceased, indicating completion of the reaction.

The mixture, which resulted, appeared as a white slurry, and was cooled to rt. The white solid, consisting of TEA-HCl and residual L-Alanine, was separated by filtration, which resulted in a pale-yellow-colored solution. The solid was washed with two portions of ethyl acetate (2 x 50 mL), and the filtrates were combined. The solvent was then removed under reduced pressure, to yield a semisolid mass.

The semisolid mixture was dissolved in dichloromethane (300 mL), and hexane (350mL) was added dropwise over 1 hour with vigorous stirring to precipitate the product. The slurry, which resulted, was placed in a freezer at -20°C for 12 hours to maximize product precipitation. The solid was filtered and washed with hexanes (250 mL x 2) and then dried under vacuum at rt. This process afforded the product as an off-white colored solid **15** (20.1 g, 60.0%). **^{1}H NMR** (500 MHz, DMSO) δ 8.98 (s, 1H), 4.47 (q, J = 6.7 Hz, 1H), 1.28 (d, J = 58.3, 6.8 Hz, 3H). **^{13}C NMR** (126 MHz, DMSO) δ 172.85 (s), 152.15 (s), 53.27 (s), 17.18 (s). **HRMS** (ESI/IT-TOF): m/z [M + H]+ calcd for C4H6NO3: 116.0348; found: 116.0350. The spectral data for **15** were identical to the literature.[163]

2.5.2. (S)-7-Bromo-5-(2-fluorophenyl)-3-methyl-1,3-dihydro-2H-benzo[e][1,4]diazepin-2-one (4)



4

The procedure began with the dissolution of 2-amino-5-bromo-2'-fluorobenzophenone **1** (12.4 g, 42.15 mmol) in anhydrous toluene (160 mL) by adding the starting material and stirring at rt for 30 min. Next, the solid N-carboxy-L-alanine anhydride (5.8.0 g, 50.39 mmol) was introduced into the mixture, and the temperature was allowed to raise to 50-55°C. The reaction proceeded for 1 h until completion, as indicated by the formation of the intermediate TFA salt and less than 5% of 2-amino-5-bromo-2'-fluorobenzophenone remained (as determined by TLC analysis on silica gel using an EtOAc/hexanes 1:1 solvent system, Rf = 0.8).

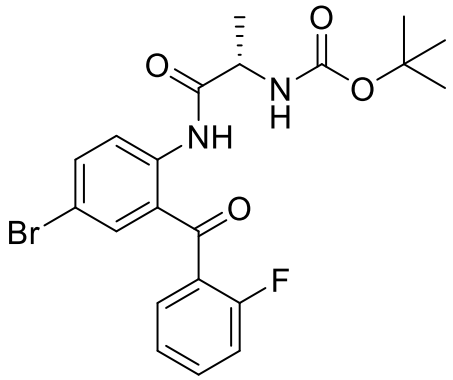
Following the reaction, anhydrous triethylamine (11.818 mL, 84.818 mmol) was added dropwise over 20 min, which maintained the temperature at 50-55°C. The reaction mixture was then held at 50-55°C for an additional 2 hours. The completion of the reaction was confirmed by the disappearance of the intermediate TFA salt (Rf = 0.1 on TLC using silica gel and EtOAc/hexanes, 1:1 as the solvent system).

Subsequently, the reaction mixture was cooled to rt and concentrated under reduced pressure. The residue, which resulted, was dissolved in a mixture of ethyl acetate (EtOAc) (100 mL) and water (50 mL), which led to the formation of a biphasic mixture. After allowing the layers to separate

for 15 min, they were carefully separated. The organic layer was washed with a 5% aq sodium bicarbonate ($NaHCO_3$) solution (150 mL) and then with a 10% aq sodium chloride (NaCl) solution (150 mL). The organic layer was then dried using sodium sulfate (Na_2SO_4, 5 g).

The ethyl acetate solvent was removed under reduced pressure, and the residue, which resulted, was dissolved in a mixture of 10% EtOAc/hexane (25 mL x 2). The solution was then converted to a slurry with 10% EtOAc/hexane (180 mL) at 60-65°C for 30 min. After cooling the mixture to rt and allowing it to stand for 2 hours, the solid product was filtered and washed with 10% EtOAc/hexane (50 mL x 2) and then with hexane (50 mL x 2). The resulting solid was vacuum-dried at 35-40°C, yielding the off-white-colored solid product **4** (11.0 g, 74.0% yield). **^{1}H NMR** (500 MHz, $CDCl_3$) δ 8.89 (s, 1H), 7.66 – 7.57 (m, 2H), 7.51 – 7.43 (m, 1H), 7.37 (d, *J* = 2.1 Hz, 1H), 7.25 (dd, *J* = 7.5, 0.9 Hz, 1H), 7.11 – 7.08 (m, 1H), 7.07 (dd, *J* = 5.3, 3.2 Hz, 1H), 3.80 (q, *J* = 6.5 Hz, 1H), 1.78 (d, *J* = 6.5 Hz, 3H). **^{13}C NMR** (126 MHz, $CDCl_3$) δ 171.89 (s), 164.45 (s), 161.43 (s), 159.43 (s), 136.24 (s), 134.71 (s), 132.30 – 131.90 (m), 131.50 (d, *J* = 2.3 Hz), 130.18 (s), 127.08 (d, *J* = 12.3 Hz), 124.45 (d, *J* = 3.6 Hz), 122.73 (s), 116.60 (s), 116.36 (s), 116.19 (s), 58.80 (s), 16.92 (s). **HRMS** (ESI/IT-TOF) m/z: $[M + H]^+$ Calcd for $C_{16}H_{13}BrFN_2O$ 347.0190; found 347.0187. The spectral data for **4** were identical to the literature.[163]

2.5.3. Tert-butyl (S)-(1-((4-bromo-2-(2-fluorobenzoyl) phenyl) amino)-1-oxopropan-2-yl) carbamate (3)

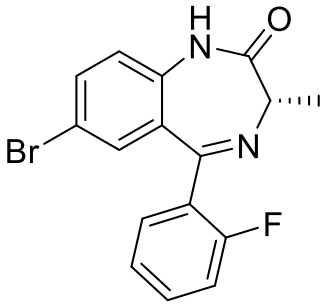


3

The procedure involved the addition of (2-amino-5-bromophenyl) (2 fluorophenyl) benzophenone **1** (50 g, 169.99 mmol) and Boc-L-alanine **2** (46.95 g, 248.15 mmol) to dry dichloromethane (DCM) (500 mL) in a 2 L round bottom flask at 0°C. The mixture was continuously stirred until complete dissolution. Separately, dicyclohexylcarbodiimide (DCC; 49.1 g, 237.96 mmol) was dissolved in dry DCM (50 mL) to form a homogeneous solution. This DCC solution was then added dropwise to the previous solution over a period of 30 min while maintaining a constant temperature of 0°C. The solution, which resulted in was continuously stirred for 22 h at rt. During the reaction, a byproduct, dicyclohexyl urea, was formed. The urea was filtered off and washed with DCM until the solid became completely colorless. The organic layers were combined and concentrated under reduced pressure. The crude solid, which resulted appeared as yellow colored gum. To purify the product, column chromatography was performed using silica gel and a DCM/hexane solvent system in a 1:1 ratio. This process yielded additional amide product **3** (69.27 g, 87.5%yield). **^{1}H NMR** (500 MHz, $CDCl_3$) δ 11.69 (s, 1H), 8.72 (d, *J* = 9.0 Hz, 1H), 7.70 (dd, *J* = 9.0, 2.3 Hz, 1H), 7.63 – 7.57 (m, 2H), 7.47 (dd, *J* = 11.2, 4.3 Hz, 1H), 7.32 (td, *J* = 7.6, 0.8 Hz,

1H), 7.22 (t, *J* = 9.1 Hz, 1H), 5.11 (s, 1H), 4.38 (s, 1H), 1.53 (d, *J* = 7.2 Hz, 3H), 1.46 (s, 9H). **^{13}C NMR** (126 MHz, $CDCl_3$) δ 195.48 (s), 172.41 (s), 160.56 (s), 158.55 (s), 139.67 (s), 137.97 (s), 135.97 (s), 133.62 (d, *J* = 8.4 Hz), 130.30 (s), 126.82 (s), 124.46 (s), 122.63 (s), 116.56 (d, *J* = 21.4 Hz), 116.47 – 116.29 (m), 114.96 (s), 80.44 (s), 51.85 (s), 28.27 (s), 18.60 (s). **HRMS** (ESI/IT-TOF) m/z: $[M + H]^+$ Calcd for $C_{21}H_{23}BrFN_2O_4$ 465.0820; found 465.0841. The spectral data for **3** were identical to the literature.[163]

2.5.4. (S)-7-Bromo-5-(2-fluorophenyl)-3-methyl-1,3-dihydro-2H-benzo[e][1,4]diazepin-2-one (4)

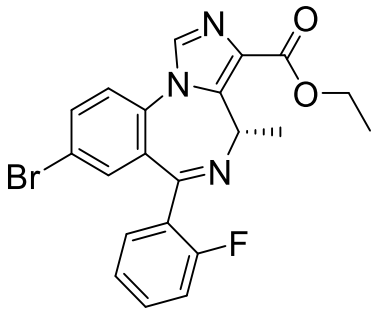


4

A total of 60 g (128.94 mmol) of amide **3** was added to 400 mL of dry dichloromethane (DCM), and the solution, which resulted was cooled to 0°C. Hydrogen chloride (dry)4M in dioxane was slowly added over a period of 2 hours to saturate the solution. The mixture was stirred at rt for 8 h. Once the reaction was complete, a saturated aq solution of sodium bicarbonate (2 x 1500 mL) and water (2 x 100 mL) were added while maintaining a pH of 8.5. The organic layers were combined and concentrated under reduced pressure, which resulted in an oily mixture.

Next, the reaction mixture was dissolved in 400 mL of methanol and stirred at rt overnight. Completion of the reaction was confirmed by analysis by TLC using a silica gel plate with an ethyl acetate/hexanes mixture in a 7:3 ratio. The methanol was removed under reduced pressure, leaving behind a concentrated oily mixture. Crystallization was performed by ethyl acetate: hexane- 1:10 and then the final product was filtered and washed with hexane to afford off white-colored precipitate **4** (36.70 g, 82%). **^{1}H NMR** (500 MHz, $CDCl_3$) δ 8.89 (s, 1H), 7.66 – 7.57 (m, 2H), 7.51 – 7.43 (m, 1H), 7.37 (d, *J* = 2.1 Hz, 1H), 7.25 (dd, *J* = 7.5, 0.9 Hz, 1H), 7.11 – 7.08 (m, 1H), 7.07 (dd, *J* = 5.3, 3.2 Hz, 1H), 3.80 (q, *J* = 6.5 Hz, 1H), 1.78 (d, *J* = 6.5 Hz, 3H). **^{13}C NMR** (126 MHz, $CDCl_3$) δ 171.89 (s), 164.45 (s), 161.43 (s), 159.43 (s), 136.24 (s), 134.71 (s), 132.30 – 131.90 (m), 131.50 (d, *J* = 2.3 Hz), 130.18 (s), 127.08 (d, *J* = 12.3 Hz), 124.45 (d, *J* = 3.6 Hz), 122.73 (s), 116.60 (s), 116.36 (s), 116.19 (s), 58.80 (s), 16.92 (s). **HRMS** (ESI/IT-TOF) m/z: $[M + H]^+$ Calcd for $C_{16}H_{13}BrFN_2O$ 347.0190; found 347.0187. The spectral data for **4** were identical to the literature.[163]

2.5.5. Ethyl (S)-8-bromo-6-(2-fluorophenyl)-4-methyl-4H-benzo[f]imidazo[1,5-a][1,4]diazepine-3-carboxylate (5)



5

(S)-7-Bromo-5-(2'fluorophenyl)-3-methyl-1,3-dihydro-2H-benzo[e][1,4]diazepin-2-one **4** (47.3 g, 136.23 mmol) was initially combined with anhydrous tetrahydrofuran (THF, 500 mL) and the

mixture, which resulted was then subjected to cooling to -20°C using a dry ice / IPA bath. Simultaneously, a separate solution containing potassium t-butoxide (19.88 g, 177.16 mmol) in THF (125 mL) was prepared and incrementally added to the prior reaction mixture over a 30-min period dropwise, all while maintaining a temperature between -20 to -15°C. Following this, the reaction mixture was allowed to stir for 1 h at -20°C.

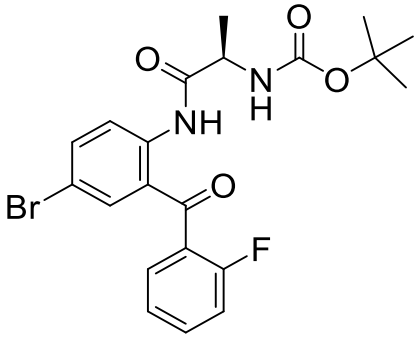
Subsequently, Diethyl chlorophosphate (25.61 mL, 177.46 mmol) was introduced dropwise into the mixture over 15 min, with the temperature was held at -20 to -15°C. The reaction mixture was then stirred for an additional 2 h at -20°C. To confirm the completion of the reaction, analysis by TLC (utilizing silica gel and 100% EtOAc as the solvent) was performed.

Once the reaction was confirmed to be complete, ethyl isocyanoacetate (17.94 mL, 234.34 mmol) was added dropwise to the reaction mixture over a 15-min period. Simultaneously, a solution of potassium t-butoxide (19.88 g, 177.16 mmol) in THF (125 mL) was added over 30 min while maintaining a temperature between -20 to -15°C. The mixture was then allowed to warm to rt and stirred for 12 h until the reaction was confirmed to be complete, as verified by analysis by TLC using silica gel and 100% EtOAc as the eluent.

Following the completion of the reaction, a 5% aq sodium bicarbonate solution (1 L) was added, followed by the introduction of ethyl acetate (1 L) to dilute the mixture, which resulted in a biphasic mixture. This biphasic mixture was allowed to sit for 30 min, at which point the layers were separated. The aq layer was subsequently extracted with ethyl acetate (750 mL). The combined organic layers underwent washing, initially with a 10% aq sodium bicarbonate solution (750 mL) and later with a 20% aq sodium chloride solution (1 L).

Following these steps, the organic layer was dried over sodium sulfate (Na_2SO_4, 100 g) and then concentrated under reduced pressure to remove the solvents. The solid residue, which resulted, was subjected to solvent exchange with t-butyl methyl ether (100 mL x 2) and then mixed with t-butyl methyl ether (400 mL) at a temperature range of 50 – 55°C for 30 min. Subsequently, the mixture was cooled to rt and allowed to stand for 12 h. The solid was then filtered, washed with t-butyl methyl ether (50 mL x 4), and dried under vacuum at a temperature of 35 – 40°C, to yield a white colored powder **5** (39.1 g, 65%). **^{1}H NMR** (500 MHz, $CDCl_3$) δ 7.92 (s, 1H), 7.79 – 7.70 (m, 1H), 7.61 (t, *J* = 7.1 Hz, 1H), 7.49 (d, *J* = 3.3 Hz, 1H), 7.48 – 7.42 (m, 2H), 7.26 (dd, *J* = 7.5, 1.0 Hz, 1H), 7.10 – 7.01 (m, 1H), 6.71 (q, *J* = 7.3 Hz, 1H), 4.46 – 4.36 (m, 2H), 1.43 (t, *J* = 7.1 Hz, 3H), 1.30 (d, *J* = 7.3 Hz, 3H). **^{13}C NMR** (75 MHz, $CDCl_3$) δ 162.88 (s), 162.65 (s), 160.06 (d, *J* = 250.7 Hz), 141.55 (s), 134.89 (s), 134.83 (s), 133.61 (s), 132.95 (s), 132.04 (d, *J* = 8.2 Hz), 131.16 (s), 131.04 (s), 129.52(s), 128.33 (d, *J* = 12.4 Hz), 124.55 (d, *J* = 3.5 Hz), 123.71 (s), 120.88 (s), 116.16 (d, *J* = 21.5 Hz), 60.75 (s), 50.05 (s), 14.85 (s), 14.41 (s); **HRMS** (ESI/IT-TOF) m/z: $[M + H]^+$ Calcd for $C_{21}H_{18}BrFN_3O_2$ 442.0561; found 442.0568. The spectral data for **5** were identical to the literature.[163]

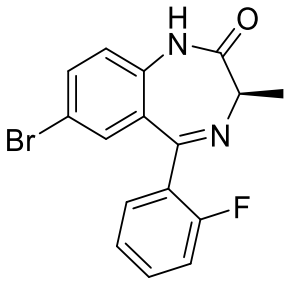
2.5.6. Tert-butyl-(R)-(1-((4-bromo-2-(2-fluorobenzoyl)phenyl)amino)-1-oxopropan-2-yl) carbamate (10)



10

A solution of (2-amino-5-bromophenyl)(2-fluorophenyl)methanone **1** (50 g, 170.0 mmol) and Boc-D-alanine **9** (46.95 g, 248.1 mmol) in dry DCM (170 mL) was prepared and stirred at 0°C. Dicyclohexylcarbodiimide (DCC; 49.19 g, 237.96 mmol) dissolved in dry DCM (85 mL) was added dropwise over a 15 min period at 0°C. The mixture was stirred for 12 h at rt. The dicyclohexyl urea byproduct was removed by filtration and washed with dichloromethane until the solid was clear. The organic layers, which resulted were then combined and concentrated under reduced pressure. To the crude solid, 10% EtOAc: hexane was added to afford a precipitate. Then the crystals **10** were filtrated and washed with hexane. (73 g, 93%): **^{1}H NMR** (500 MHz, $CDCl_3$) δ 11.69 (s, 1H), 8.72 (d, *J* = 9.0 Hz, 1H), 7.70 (dd, *J* = 9.0, 2.3 Hz, 1H), 7.63 – 7.57 (m, 2H), 7.50 – 7.44 (m, 1H), 7.32 (td, *J* = 7.6, 0.9 Hz, 1H), 7.22 (t, *J* = 9.1 Hz, 1H), 5.10 (s, 1H), 4.38 (s, 1H), 1.53 (d, *J* = 7.2 Hz, 3H), 1.47 (s, 9H). **^{13}C NMR** (126 MHz, $CDCl_3$) δ 195.47 (s), 172.42 (s), 159.56 (d, *J* = 253.2 Hz), 155.28 (s), 139.68 (s), 137.98 (s), 135.97 (d, *J* = 1.9 Hz), 133.62 (d, *J* = 8.4 Hz), 130.30 (d, *J* = 2.4 Hz), 126.77 (d, *J* = 14.5 Hz), 124.51 (s), 124.46 (s), 122.62 (s), 116.55 (d, *J* = 21.4 Hz), 114.95 (s), 80.26 (s), 51.86 (s), 28.27 (s), 18.64 (s). **HRMS** (ESI/IT-TOF) m/z: $[M + H]^+$ Calcd for $C_{21}H_{23}BrFN_2O_4$ 465.0820; found 465.0845. The spectral data for **10** were identical to the literature.[163]

2.5.7. (*R*)-7-Bromo-5-(2'fluorophenyl)-3-methyl-1,3-dihydro-2*H*-benzo[*e*][1,4]diazepin-2-one (11)

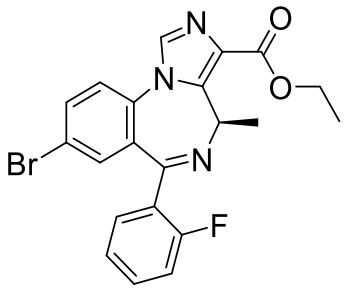


11

Amide **10** (67.9 g, 143.1 mmol) was dissolved in dry dichloromethane (350 mL) and cooled to 0 °C. Anhydrous hydrochloric acid gas was slowly added until the solution was saturated, taking approximately 2 h. The solution was then stirred overnight at rt. The reaction mixture was subsequently washed with a saturated aq solution of sodium bicarbonate (2 x 150 mL) and water (2 x 100 mL) to remove any excess acid and by-products. A mild exotherm was observed during the addition of a saturated aq solution of sodium bicarbonate as a workup. The organic layer was concentrated under reduced pressure and the oil, which resulted was dissolved in a mixture of methanol and water (3:2, 500 mL). The pH of the solution was then adjusted to 8.5 using a 1 M aq solution of sodium hydroxide. The reaction mixture was allowed to stir overnight rt. The solution was then concentrated under reduced pressure, cooled to 0 degrees Celsius and water (30 mL) was added. The organic layer was purified using DCM extraction and then washed with brine. The solvent was dried and removed using sodium sulfate as a drying agent, and this was followed by evaporation under reduced pressure to concentrate the solution. The precipitation was done in presence of 100 mL of MeOH overnight. The benzodiazepine **11** was recrystallized by adding seed crystals to a mixture of EtOAc and hexanes (1:9). The crystals **11**, which resulted were washed with a solution of EtOAc and hexanes (1:9), and the filtrate was combined and concentrated, no further purification was needed. **^{1}H NMR** (500 MHz, $CDCl_3$) δ 9.04 (s, 1H), 7.60 (dd, *J* = 8.8, 2.2 Hz, 2H), 7.49 – 7.45 (m, 1H), 7.36 (d, *J* = 2.1 Hz, 1H), 7.26 (td, *J* = 7.6, 1.0 Hz, 1H), 7.09 (s, 1H), 7.08 – 7.05 (m, 1H), 3.79 (q, *J* = 6.5 Hz, 1H), 1.78 (d, *J* = 6.5 Hz, 3H).); **^{13}C NMR** (75 MHz, $CDCl_3$) δ 172.30 (s), 164.48 (s), 160.43 (d, *J* = 251.9 Hz), 136.47 (s), 134.70 (s), 132.14 (d, *J* = 8.6 Hz), 132.06 (d, *J* = 2.0 Hz), 131.54 (d, *J* = 2.4 Hz), 130.11 (s), 127.12 (d, *J* = 12.4 Hz), 124.41 (d, *J* = 3.6 Hz), 122.89 (s), 116.48 (s), 116.28 (d, *J* = 21.6 Hz), 58.84 (s), 16.94 (s); **HRMS**

(ESI/IT-TOF) m/z: $[M + H]^+$ Calcd for $C_{16}H_{13}BrFN_2O$ 347.0190; found 347.0181. The spectral data for **11** were identical to the literature.[163]

2.5.8. Ethyl (*R*)-8-bromo-6-(2-fluorophenyl)-4-methyl-4*H*-benzo[*f*]imidazo[1,5-*a*][1,4] diazepine-3-carboxylate (12)



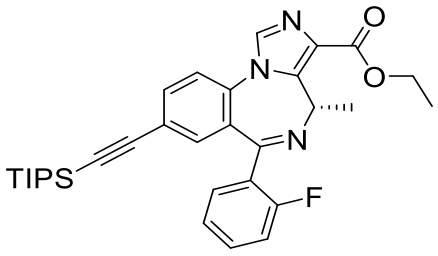
12

The 1,4-benzodiazepine **11** (20 g, 57.6 mmol) was dissolved in dry THF (300 mL) and allowed to cool to a temperature of –20 °C. Next, t-BuOK (7.76 g, 69.2 mmol) was added in one portion and the solution was allowed to warm up to rt, where it was kept for 30 min. Then, the reaction mixture was cooled to a temperature of -20 °C and diethyl chlorophosphate (14.16 g, 80.66 mmol) was added. The temperature was allowed to warm up to rt and kept at that temperature for 1 h. The reaction was kept at -20° C and ethyl isocyanoacetate (9.12 g, 80.66 mmol) was added, and this was followed by a second portion of t-BuOK (7.76 g, 69.2 mmol). The reaction mixture was then allowed to warm to rt and stirred overnight. To quench the reaction, a cold saturated aq solution of $NaHCO_3$ (200 mL) was added and the mixture was extracted with ethyl acetate. The organic layers were combined and washed with brine (2 × 50 mL), and then dried Na_2SO_4. The solvent was removed under reduced pressure, which resulted in a brown solid. The majority of the bromide **12** could be obtained by cooling from 60 ˚C and precipitated in methyl t-butyl ether or ethyl acetate, and the remaining portion was purified using flash column chromatography (using silica gel and a

mixture of ethyl acetate and hexane in a 3:2 ratio). This gave pure IMDZ **12** as an off-white-colored solid (19.12 g, 75% yield).

^{1}H NMR (500 MHz, $CDCl_3$) δ 7.92 (s, 1H), 7.80 – 7.70 (m, 1H), 7.60 (t, *J* = 7.0 Hz, 1H), 7.49 (s, 1H), 7.47 (d, *J* = 3.7 Hz, 1H), 7.45 – 7.42 (m, 1H), 7.26 (dd, *J* = 7.5, 1.0 Hz, 1H), 7.10 – 7.01 (m, 1H), 6.71 (q, *J* = 7.2 Hz, 1H), 4.46 – 4.36 (m, 2H), 1.42 (t, *J* = 7.1 Hz, 3H), 1.29 (d, *J* = 7.3 Hz, 3H); **^{13}C NMR** (126 MHz, $CDCl_3$) δ 162.91, 162.64, 161.07, 159.08, 141.57, 134.83, 134.73, 133.66, 133.03, 132.13, 132.06, 131.16, 129.58, 124.54, 123.63, 120.94, 116.32, 116.15, 60.80, 50.11, 14.87, 14.43. **HRMS** (ESI/IT-TOF) m/z: $[M + H]^+$ Calcd for $C_{21}H_{18}BrFN_3O_2$ 442.0561; found 442.0563. The spectral data for **12** were identical to the literature.[163]

2.5.9. Ethyl(S)-6-(2'fluorophenyl)-4-methyl-8-((triisopropylsilyl)ethynyl)-4H benzo [f] imidazo [1,5-a][1,4]diazepine-3-carboxylate (6)



6

A mixture was created by combining palladium acetate (0.180 g, 0.801 mmol) and tri-o-tolylphosphine (0.489 g 1.606 mmol) with 100 mL of acetonitrile. The mixture was then stirred at rt for 30 min.

Subsequently, the following substances were sequentially added to the mixture: ethyl (R)-8-bromo-6-(2’fluorophenyl)-4-methyl-4H-benzo[f]imidazo[1,5-a][1,4]diazepine-3-carboxylate **5** (7.1 g, 16.052 mmol), triethylamine (4.48 mL, 32.04 mmol), (triisopropylsilyl)acetylene (4.3 mL, 19.16 mmol), and an additional 200 mL of acetonitrile. The mixture was then heated to 75°C and held on reflux for 4 h until the reaction was complete, which was confirmed by analyzing it using TLC (Thin-Layer Chromatography) with a silica gel plate and a solvent mixture of 40% EtOAc and hexane.

Afterward, the reaction mixture was allowed to cool to rt, and 3 g of silica gel was added. The mixture was stirred for 30 min (open to the air), and the spent catalyst on the silica gel was filtered off and then it was washed with 50 mL of dichloromethane (50mL×2). The solvents were then removed under reduced pressure.

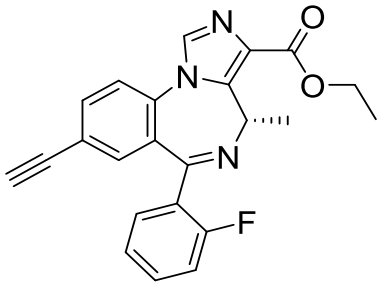
The residue, which resulted was dissolved in 150 mL of dichloromethane and 150 mL of a 5% aq sodium bicarbonate solution. This led to the formation of a two-phase mixture. After allowing it to stand for 15 min, the aq layer was separated from the organic layer by adding 150 mL of dichloromethane. The organic layer was subsequently washed with 150 mL of a 5% aq sodium bicarbonate solution and then with 150 mL of a 10% aq sodium chloride solution.

The organic layer was dried using sodium sulfate, concentrated under reduced pressure, and then purified through flash chromatography using silica gel and an EtOAc/hexane mixture in a 1:1 ratio. The pure fractions were combined and concentrated under reduced pressure.

The substance, which resulted was an oily product, which was dried at 40°C for 2 h under reduced pressure. This process yielded the final product as a clear, golden-colored oil **6** (7.15 g, 82%).^{1}**H**

NMR (500 MHz, $CDCl_3$) δ 7.94 (s, 1H), 7.67 (d, *J* = 8.3 Hz, 1H), 7.61 (t, *J* = 7.2 Hz, 1H), 7.53 (d, *J* = 8.3 Hz, 1H), 7.45 (ddd, *J* = 8.6, 4.3, 2.1 Hz, 1H), 7.34 (d, *J* = 4.0 Hz, 1H), 7.26 (td, *J* = 7.6, 0.9 Hz, 1H), 7.20 – 7.03 (m, 1H), 6.70 (q, *J* = 7.2 Hz, 1H), 4.42 (tdd, *J* = 10.8, 7.2, 3.8 Hz, 2H), 1.43 (t, *J* = 7.1 Hz, 2H), 1.28 (t, *J* = 7.2 Hz, 3H), 1.11 (d, *J* = 3.7 Hz, 18H). **^{13}C NMR** (126 MHz, $CDCl_3$) δ 171.14 (s), 163.38 (s), 162.95 (s), 143.48 (s), 141.69 (s), 135.31 (s), 134.81 (s), 133.38 (s), 132.89 (d, *J* = 12.8 Hz), 132.11 – 131.67 (m), 131.18 (s), 129.59 (s), 125.47 (d, *J* = 12.7 Hz), 124.43 (s), 122.03 (s), 116.23 (s), 116.06 (s), 104.55 (s), 60.77 (s), 60.40 (s), 50.10 (s), 18.60 (s), 14.85 (s), 14.44 (s), 14.21 (s), 11.22 (s). **HRMS** (ESI/IT-TOF) m/z: $[M + H]^+$ Calcd for $C_{32}H_{38}FN_3O_2Si$ 544.1769; found 544.1766. The spectral data for **6** were identical to the literature.[134]

2.5.10. Ethyl (S)-8-ethynyl-6-(2'fluorophenyl)-4-methyl-4H-benzo[f]imidazo[1,5-a] [1,4] diazepine-3-carboxylate (7)



7

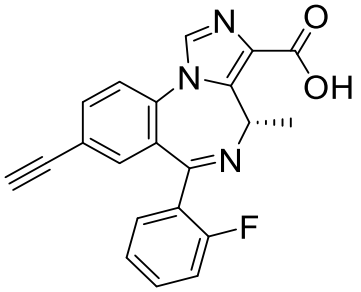
A mixture was created by combining Ethyl (S)-6-(2'fluorophenyl)-4-methyl-8-((triisopropylsilyl)ethynyl)-4H benzo[f]imidazo[1,5-a][1,4]diazepine-3-carboxylate **6** (9.9g, 18.68 mmol) with 1 mL water in 90 mL of tetrahydrofuran. This mixture was then chilled to -20 °C

using a dry ice/isopropanol bath. Next, tetrabutylammonium fluoride hydrate, a 1M solution in tetrahydrofuran (8.11 mL, 28.0 mmol), was gradually added over a 15-min period, while maintaining the temperature between -20 and -15°C. The mixture was then brought to rt and stirred for an additional hour until the reaction was deemed complete, as confirmed by analysis by thin-layer chromatography (using silica gel with 100% ethyl acetate as the eluent, with Rf values of 0.6 for starting material and 0.4 for product).

Subsequently, 100 mL of ethyl acetate and 100 mL of a 10% aq sodium chloride solution were added to the mixture to dilute it. This resulted in the formation of a two-phase mixture, which was allowed to sit for 15 min until the layers separated. The aq layer was extracted with 100 mL of ethyl acetate, and the organic layer was dried over sodium sulfate. The organic layer was then concentrated under reduced pressure to remove the solvents. The residue, which remained was mixed with 50 mL of methanol for 30 min while maintaining a temperature of 50–55°C. Water was added to the slurry, and the mixture was stirred for an additional 30 min in the same temperature range. The mixture was then cooled to 20–25°C and allowed to stand for 2 h. The solid, which resulted was filtered and washed with methanol/water (1:1, 50 mL × 4) and further washed with hexanes (50 mL × 3). Finally, the white crystalline solid product was dried at 40°C under vacuum to obtain the final ethynyl analog **7** (5.99g, 85%). **^{1}H NMR** (500 MHz, $CDCl_3$) δ 7.94 (s, 1H), 7.71 (d, *J* = 7.9 Hz, 1H), 7.60 (t, *J* = 7.1 Hz, 1H), 7.57 (t, *J* = 6.9 Hz, 1H), 7.50 – 7.40 (m, 2H), 7.26 (td, *J* = 7.6, 1.1 Hz, 1H), 7.05 (t, *J* = 9.7 Hz, 1H), 6.71 (q, *J* = 7.3 Hz, 1H), 4.49 – 4.36 (m, 2H), 3.15 (s, 1H), 1.43 (t, *J* = 7.1 Hz, 3H), 1.29 (d, *J* = 7.1 Hz, 3H). **^{13}C NMR** (126 MHz, $CDCl_3$). δ 163.95 (s), 162.69 (s), 160.12 (d, *J* = 252.3 Hz), 141.32 (s), 135.61 (s), 134.97 (s), 134.52 (s), 134.21 (s), 132.44 (d, *J* = 8.2 Hz), 131.35 (d, *J* = 2.1 Hz), 129.49 (s), 129.16 (s), 127.98 (s), 124.58 (d, *J* = 3.5 Hz), 122.39 (s), 121.85 (s), 116.27 (d, *J* = 21.4 Hz), 81.28 (s), 79.92 (s),

60.92 (s), 49.85 (s), 14.92 (s), 14.41 (s); **HRMS** (ESI/IT-TOF) m/z: $[M + H]^+$ Calcd for $C_{23}H_{19}FN_3O_2$ 388.1456; found 338.1448. The spectral data for **7** were identical to the literature.[134]

2.5.11. (S)-8-Ethynyl-6-(2'fluorophenyl)-4-methyl-4H-benzo[f]imidazo[1,5-a][1,4]diazepine-3-carboxylic acid (13)



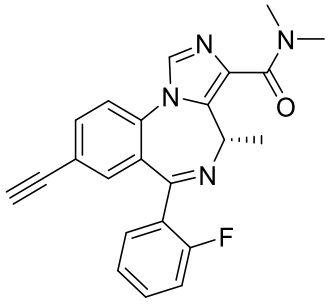
13

A uniform blend consisting of ethyl (S)-8-ethynyl-6-(2-fluorophenyl)-4-methyl-4H-benzo[f]imidazo[1,5-a][1,4]diazepine-3-carboxylic acid **7** (1.92g, 5.34 mmol) and 40 mL of tetrahydrofuran was prepared. To this mixture a solution of lithium hydroxide (0.48 g, 20.04 mmol) and 25 mL of water was slowly added while maintaining the temperature between 25 and 30°C. The reaction mixture was then heated to 50 to 55°C and allowed to proceed for 4 h. The completion of the reaction was confirmed by thin-layer chromatography (using silica gel and 100% ethyl acetate as the eluent). The reaction temperature was kept between 50 and 55°C, and the reaction duration did not exceed 4 h to prevent racemization of the product.

After cooling the mixture to rt, 20 mL of water was added to dilute it. Subsequently, 1.69 mL of glacial acetic acid were added dropwise to the reaction mixture over a period of 15 min, while maintaining the temperature between 20 and 25°C. The tetrahydrofuran was then removed under reduced pressure. To the resulting semi-solid slurry, 20 mL of methanol were added. The mixture

was stirred at 40 to 45°C for 30 min and then left at rt to allow for maximum precipitation. The solid product was filtered and washed with 10 mL of water four times. Finally, the solid product was dried under vacuum at 35 to 40°C to obtain the acid as an off-white powder **13** (1.33 g, 75%). **^{1}H NMR** (500 MHz, DMSO) δ 8.41 (s, 1H), 7.94 (d, *J* = 8.2 Hz, 1H), 7.81 (d, *J* = 7.9 Hz, 1H), 7.62 – 7.53 (m, 2H), 7.33 (t, *J* = 7.5 Hz, 1H), 7.23 (t, *J* = 9.2 Hz, 2H), 6.55 (d, *J* = 6.8 Hz, 1H), 4.36 (s, 1H), 1.15 (d, *J* = 6.8 Hz, 3H). **^{13}C NMR** (126 MHz, DMSO-d^6): δ 164.63 (s), 162.92 (s), 159.85 (d), 141.08 (s), 136.73 (s), 135.57 (s), 134.68 (d), 133.19 (s), 133.14 (s), 132.64 (d), 131.89 (s), 129.36 (d), 128.85 (d), 125.14 (d), 123.98 (s), 121.15 (s), 116.39 (d), 83.42 (s), 81.97 (s), 49.82 (s), 15.02 (s); **HRMS** (ESI/IT-TOF) m/z: $[M + H]^+$ Calcd for $C_{21}H_{15}FN_3O_2$ 360.1143; found 360.1142. The spectral data for **13** were identical to the literature.[134]

2.5.12. (S)-8-Ethynyl-6-(2'fluorophenyl)-N,N,4-trimethyl-4H-benzo[f]imidazo[1,5-a] [1,4] diazepine-3-carboxamide (GL-I-54, 14)

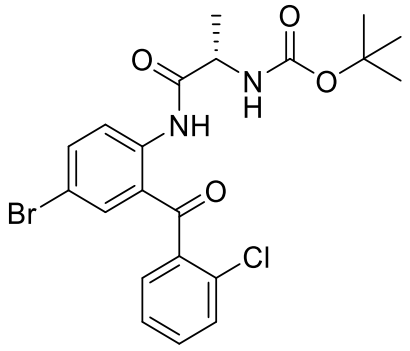


GL-I-54
14

A mixture of SH-053-2'F-S-CH_3-acid **13** (1.3 g, 3.64 mmol), thionyl chloride (0.407 mL, 36.10 mmol), and dry DCM (40 mL) was placed in a round-bottom flask, pre-dried in an oven, under argon. The suspension, which resulted was allowed to heat to reflux at 60˚C for 1 h under argon.

Confirmation of the absence of the starting material was achieved through analysis by TLC on silica gel. The organic solvent and excess thionyl chloride were then removed under reduced pressure using a rotavapor. This process was repeated five times with dry DCM (30 mL). The yellow residue, which remained was dissolved in dry DCM (40 mL) and cooled to 0 ˚C for 10 min under argon. Subsequently, the nucleophilic dimethylamine (0.025 mL, 5.6 mmol) and triethylamine (0.78 mL, 5.6 mmol) were added individually to the reaction mixture at 0 ˚C. The mixture was then allowed to warm to rt and stirred for 1-2 hours. Upon completion of the reaction, as confirmed by analysis by TLC on silica gel, the solvent was removed under reduced pressure. The residue was treated with ice-cold water (30 mL) and extracted with DCM (3 x 20 mL). The combined organic layer was washed with brine (30 mL) and dried with Na_2SO_4. After removing the solvent under reduced pressure, the residue underwent purification by column chromatography to obtain the dimethyl amide **14** as a light yellow powder (1.4 g, 72%): mp 142-144 °C; $\mathbf{[\alpha]_D^{25}}$ = -16.0 (*c* 0.75, $CHCl_3$); **^{1}H NMR** (300 MHz, $CDCl_3$): δ 7.94 (s, 1H), 7.73 (d, *J* = 8.1 Hz, 1H), 7.63 (t, *J* = 7.4 Hz, 1H), 7.52 (d, *J* = 8.2 Hz, 1H), 7.48 – 7.41 (m, 2H), 7.26 (t, *J* = 7.5 Hz, 1H), 7.04 (t, *J* = 9.3 Hz, 1H), 4.33 (q, *J* = 6.0 Hz, 1H), 3.16 (s, 1H), 3.14 (s, 3H), 3.01 (s, 3H), 1.94 (d, *J* = 6.5 Hz, 3H); **^{13}C NMR** (75 MHz, $CDCl_3$): δ 166.14 (s), 162.60 (s), 160.25 (d, J_{C-F} = 252.3 Hz), 135.31 (s), 134.73 (d, J_{C-F} = 7.2 Hz), 133.83 (s), 133.73 (s), 132.79 (d, J_{C-F} = 12.7 Hz), 132.05 (d, J_{C-F} = 9.4 Hz), 131.78 (s), 131.28 (s), 129.25 (s), 127.69 (d, J_{C-F} = 10.8 Hz), 124.51 (d, J_{C-F} = 3.4 Hz), 122.83 (s), 121.50 (s), 116.17 (d, J_{C-F} = 21.7 Hz), 81.57 (s), 79.46 (s), 52.21 (s), 39.09 (s), 35.03 (s), 18.50 (s); **HRMS** (ESI/IT-TOF) m/z: $[M + H]^+$ Calcd for $C_{23}H_{20}FN_4O$ 387.1616; found 387.1624. The spectral data for **14** were identical to the literature.[134]

2.5.13. Tert-butyl (S)-(1-((4-bromo-2-(2'chlorobenzoyl)phenyl)amino)-1-oxopropan-2-yl)carbamate (17)

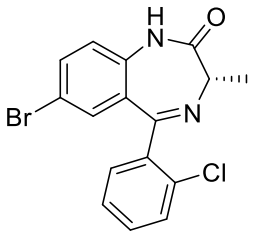


17

This procedure involved the addition of (2-amino-5-bromophenyl) (2' fluorophenyl) benzophenone **16** (100 g, 321.98 mmol) and Boc-L-alanine **2** (88.94 g, 470.08 mmol) to dry dichloromethane (DCM) (800 mL) in a 3 L round bottom flask at 0°C. The mixture was continuously stirred until complete dissolution. Separately, dicyclohexylcarbodiimide (DCC; 93.01 g, 450.78 mmol) was dissolved in dry DCM (90 mL) to form a homogeneous solution. This DCC solution was then added dropwise to the previous solution over a period of 30 min while maintaining a constant temperature of 0°C. The resulting solution was continuously stirred for 22 hours at rt. During the reaction, a byproduct, dicyclohexyl urea, was formed. The urea was filtered off and washed with DCM until the solid became completely colorless. The organic layers were combined and concentrated under reduced pressure. The resulting crude solid appeared as yellow gum. To purify the product, column chromatography was performed using silica gel and a DCM/hexane solvent system in a 1:1 ratio. This process yielded additional amide product **17** (69.27 g, 87.5%yield). **^{1}H NMR** (500 MHz, $CDCl_3$) δ 11.68 (s, 1H), 8.71 (d, J = 9.0 Hz, 1H), 7.69

(dd, J = 9.0, 2.3 Hz, 1H), 7.64 – 7.53 (m, 2H), 7.51 – 7.42 (m, 1H), 7.35 – 7.27 (m, 1H), 7.21 (t, J = 9.1 Hz, 1H), 5.13 (s, 1H), 4.37 (s, 1H), 1.52 (d, J = 7.2 Hz, 3H), 1.45 (s, 9H); **^{13}C NMR** (75 MHz, $CDCl_3$) δ 195.47 (s), 172.42 (s), 159.56 (d, J = 253.2 Hz), 155.28 161 (s), 139.68 (s), 137.97 (s), 135.97 (d, J = 1.9 Hz), 133.62 (d, J = 8.4 Hz), 130.31 (d, J = 2.4 Hz), 126.77 (d, J = 14.5 Hz), 124.51 (s), 124.46 (s), 122.63 (s), 116.55 (d, J = 21.4 Hz), 114.95 (s), 80.26 (s), 51.86 (s), 28.26 (s), 18.58 (s) **HRMS** (ESI/IT-TOF) m/z: [M + H]+ Calcd for $C_{18}H_{13}ClN_2O$ is 481.770 and found 481.750. The spectral data for **17** were identical to the literature.[164]

2.5.14. (S)-7-Bromo-5-(2'chlorophenyl)-3-methyl-1,3-dihydro-2H-benzo[e][1,4]diazepin-2-one (18)

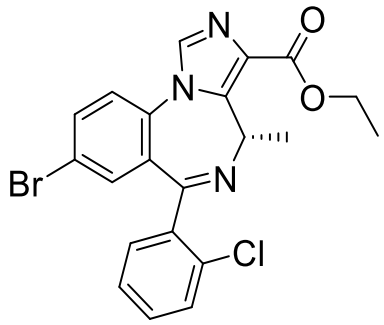


18

Benzodiazapine **17** (186.1 g, 392.14 mmol) was introduced into dry DCM (1 L), and the solution was cooled to 0 °C. Subsequently, anhydrous HCl (g) was added gradually over a span of 2 h at a to saturate the solution. The mixture was allowed to stir for 8 hours at rt. Upon completion of the reaction, a saturated aq solution of $NaHCO_3$ (2 x 500 mL) and water (2 x 300 mL) was added, to maintain a pH of 8.5. The combined organic layers were concentrated under reduced pressure, and an oily mixture was resulted. This reaction mixture was dissolved in dry methanol (400 mL) and stirred at rt overnight. Confirmation of the completion of the reaction was achieved by analysis by TLC (silica gel, EtOAc/hexanes, 7:3). The methanol was then removed under reduced pressure,

leaving a concentrated oily mixture. This mixture was dissolved in DCM and washed with water (2 x 400 mL). After combining the organic layers and washing with brine (2 x 400 mL), the solution was dried over Na_2SO_4. The organic layer was subsequently concentrated under reduced pressure, a yellow colored oily mixture was yielded. The mixture was dissolved in EtOAc and the flask was cooled to 0°C and hexane was added dropwise (1-9: EtOAc-hexane), which resulted the precipitation of benzodiazepine **18** without any further purification. (238.1 g, 80%). **^{1}H NMR** (500 MHz, $CDCl_3$) δ 9.79 (s, 1H), 7.58 (dd, J = 8.6, 2.2 Hz, 1H), 7.55 – 7.49 (m, 1H), 7.42 – 7.35 (m, 3H), 7.22 (d, J = 2.2 Hz, 1H), 7.11 (d, J = 8.6 Hz, 1H), 3.83 (q, J = 6.5 Hz, 1H), 1.79 (d, J = 6.5 Hz, 3H). **^{13}C NMR** (126 MHz, $CDCl_3$) δ 172.28 (s), 167.29 (s), 138.21 (s), 136.91 (s), 134.74 (s), 133.32 (s), 131.88 (s), 131.13 (s), 130.91 (s), 130.19 (s), 129.85 (s), 127.01 (s), 122.80 (s), 116.47 (s), 58.77 (s), 16.88 (s). **HRMS** (ESI/IT-TOF) m/z: [M + H]+ Calcd for $C_{16}H_{12}BrClN_2O$ is 362.9879 and found 362.9894. The spectral data for **18** were identical to the literature.[164]

2.5.15. Ethyl (S)-8-bromo-6-(2'chlorophenyl)-4-methyl-4H-benzo[f]imidazo[1,5-a] [1,4] diazepine-3-carboxylate (19)



19

(S)-7-Bromo-5-(2'chlorophenyl)-3-methyl-1,3-dihydro-2H-benzo[e][1,4]diazepin-2-one **18** (20.0 g, 54.99 mmol) was introduced into anhydrous tetrahydrofuran (175 mL) and the mixture was then cooled to -20 °C using a dry ice/IPA bath. Separately, a solution of potassium t-butoxide (8.02 g,

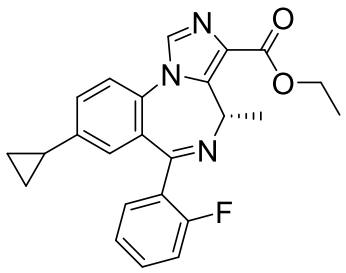
71.47 mmol) in tetrahydrofuran (50 mL) was prepared and added dropwise to the initial reaction mixture over 30 min at temperatures ranging from -20 to -15 °C. The reaction mixture was stirred for 1 h at -20 °C. Subsequently, diethyl chlorophosphate (10.33 mL, 71.58 mmol) was added dropwise to the mixture over 15 min while maintaining a temperature of -20 to -15 °C. The reaction mixture was allowed to stir for an additional 2 h at -20 °C. Confirmation of reaction completion was achieved through analysis by TLC (silica gel, 100% EtOAc).

Afterward, ethyl isocyanoacetate (7.24 mL, 66.24 mmol) was added dropwise to the reaction mixture over 15 min, followed by a solution of potassium t-butoxide (8.02 g, 71.47 mmol) in tetrahydrofuran (50 mL) over 30 min, while maintaining a temperature of -20 to -15 °C. The mixture was allowed to warm to rt and stirred for 12 h until the reaction was confirmed complete analysis by TLC (silica gel, 100% EtOAc).

A solution of 5% aq sodium bicarbonate (200 mL) and ethyl acetate (200 mL) was added to dilute the mixture, which resulted in a biphasic mixture. After standing for 30 min, the layers were separated, and the aq layer was extracted with ethyl acetate (1500 mL). The combined organic layers were then washed successively with a 10% aq $NaHCO_3$ solution (150 mL) and a 20% aq NaCl solution (200 mL). The organic layer was dried over Na_2SO_4 (200 g) and the solvent concentrated under reduced pressure. The solid residue, which resulted was subjected to solvent exchange with t-butyl methyl ether (50 mL x 2) and then slurred with t-butyl methyl ether (300 mL) at 50 – 55 °C for 30 min. After cooling to rt and standing for 12 h, the solid was filtered, washed with t-butyl methyl ether (50 mL x 4), and dried under vacuum at a temperature of 35 – 40 °C, to yield a white powder **19** (21.4 g, 65%); Rf = 0.4 (100% EtOAc); **^{1}H NMR** (500 MHz, $CDCl_3$) δ 7.91 (s, 1H), 7.72 (d, J = 7.7 Hz, 1H), 7.48 (d, J = 8.6 Hz, 1H), 7.39 (dd, J = 10.2, 7.8 Hz, 3H), 6.69 (q, J = 6.0 Hz, 1H), 4.42 (q, J = 13.3, 6.4 Hz, 2H), 1.42 (t, J = 1.5 Hz, 3H), 1.34 (d,

J = 5.8 Hz, 3H). **^{13}C NMR** (126 166 MHz, $CDCl_3$) δ 162.90 (s), 141.51 (s), 139.34 (s), 134.81 (s), 134.72 (s), 134.17 (s), 132.84 (s), 132.35 (s), 130.95 (s), 130.85 (s), 130.69 (s), 130.17 (s), 129.84 (s), 129.69 (s), 127.18 (s), 123.52 (s), 120.96 (s), 60.85 (s), 50.15 (s), 14.99 (s), 14.42 (s). **HRMS** (ESI/IT-TOF) m/z: [M + H]+ Calcd for $C_{21}H_{17}BrClN_3O_2$ is 458.0265 and found 458.0249. The spectral data for **18** were identical to the literature.[164]

2.5.16. Ethyl (S)-8-cyclopropyl-6-(2'fluorophenyl)-4-methyl-4H-benzo[f]imidazo[1,5-a][1,4]diazepine-3-carboxylate (20)



20

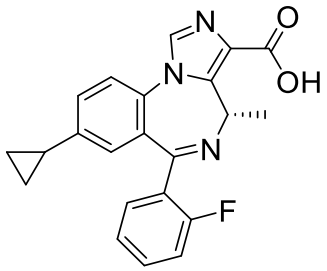
Palladium acetate (Pd $(OAc)_2$) (0.072 g, 0.32 mmol) and tri-(O-tolyl) phosphine (0.19 g, 0.62 mmol) were dissolved in toluene (10 mL) and stirred for 10 min under an argon atmosphere to generate the $Pd(OAc)_2$-p-O-$(tol)_3$-phosphine catalyst in-situ. Subsequently, the imidazodiazepine, ethyl (S)-8-bromo-6-(2'fluorophenyl)-4-methyl-4H-benzo[f]imidazo[1,5- a][1,4]diazepine-3-carboxylate **5** (2 g, 4.57 mmol), cyclopropyl boronic acid (0.43 g, 5 mmol), tri-basic potassium phosphate (3.83 g, 18.06 mmol), water (0.36 mL, 20 mmol), and additional toluene (15 mL) were sequentially added to the preceding reaction mixture under argon.

The reaction mixture, which resulted was stirred at 100°C for 12 h, and the consumption of the starting material was confirmed by LCMS 2020 (single quadrupole mass analyzer). Although the

rf value on TLC (silica gel; neutral alumina; 60% ethyl acetate-hexane) for both the starting material and product was almost identical, the reaction completion needed confirmation on the LCMS 2020. After cooling, the reaction mixture was exposed to air once all the starting material was consumed to convert the palladium salt to PdO. The mixture was passed through a pad of celite beads to eliminate any palladium salts. The filtrate was diluted with water (20 mL) and ethyl acetate (30 mL). The biphasic mixture, which resulted was allowed to stand to separat. The organic layer was collected, and the aq layer was extracted (2x10 mL). The combined organic layer was washed with 10% aq NaCl (3x10 mL) and dried (Na_2SO_4). The solvents were then removed under reduced pressure.

The orange-colored residue, which resulted was subjected to purification by flash chromatography (silica gel, 70% EtOAc-hexane). The desired fractions were pooled, and the solvents were removed under reduced pressure. The solid residue was dried under vacuum for 2 h to yield pure **20** as an off-white-colored powder. (1.27 g, 70%) **^{1}H NMR** (500 MHz, $CDCl_3$) δ 7.93 (s, 1H), 7.63 (td, J = 7.5, 1.7 Hz, 1H), 7.48 (d, J = 8.3 Hz, 1H), 7.46 – 7.41 (m, 1H), 7.29 (dd, J = 7.9, 2.4 Hz, 1H), 7.24 (t, J = 7.5 Hz, 1H), 7.03 (dd, J = 15.1, 5.3 Hz, 1H), 6.08 (d, J = 3.0 Hz, 1H), 4.42 (q, 2H), 4.11 (d, J = 10.8 Hz, 2H), 1.89 – 1.83 (m, 1H), 1.56 (d, 3 H), 1.43 (t, J = 7.1 Hz, 3H), 1.02 (dd, J = 8.4, 1.2 Hz, 2H), 0.85 – 0.57 (m, 2H). **^{13}C NMR** (126 MHz, $CDCl_3$) δ 166.40 (s), 163.04 (s), 160.26 (d, J = 251.5 Hz), 144.08 (s), 138.45 (s), 134.29 (s), 132.02 (s), 131.85 (s), 131.33 (d, J = 2.4 Hz), 129.04 (s), 128.89 (s), 128.76 (s), 128.17 (d, J = 12.0 Hz), 127.87 (s), 124.34 (d, J = 3.5 Hz), 122.35 (s), 116.07 (d, J = 21.7 Hz), 60.67 (s), 44.96 (s), 24.6(s), 15.10 (s), 14.48 (s), 8.86 (s). m/z: 403.17 (100.0%), 404.17 (27.1%), 405.18 (3.3%). **HRMS** (ESI/IT-TOF) m/z: [M + H]+ Calcd for $C_{24}H_{22}FN_3O_2$ is 403.1765 and found 403.5276.

2.5.17. (S)-8-Cyclopropyl-6-(2'fluorophenyl)-4-methyl-4H-benzo[f]imidazo[1,5-a] [1,4] diazepine-3-carboxylic acid (21)



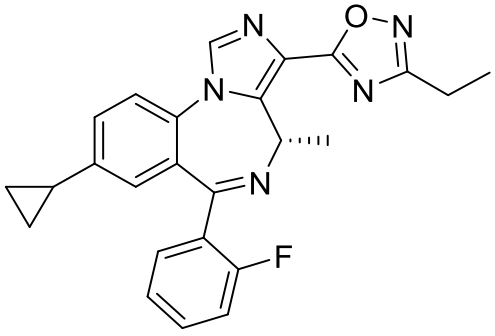
21

A solution, which consisted of ethyl (S)-8-cyclopropyl-6-(2'fluorophenyl)-4-methyl-4H-benzo[f]imidazo[1,5-a][1,4]diazepine-3-carboxylate **20** (1.8g, 4.46 mmol) and 40 mL of tetrahydrofuran was prepared. To this mixture, a solution of lithium hydroxide (0.41 g, 17.36 mmol) in 25 mL of water was slowly added while maintaining the temperature between 25 and 30°C. The reaction mixture was then allowed to heat, to 50 to 55°C and then allowed to proceed for 4 h. The completion of the reaction was confirmed by thin-layer chromatography (using silica gel and 100% ethyl acetate as the eluent). **The reaction temperature was kept between 50 and 55°C, and the reaction duration did not exceed 4 hours to prevent racemization of the product**.

After cooling the mixture to rt, 20 mL of water was added to dilute it. Subsequently, 1.69 mL of glacial acetic acid were added dropwise to the reaction mixture over a period of 15 min while maintaining the temperature between 20 and 25°C. The tetrahydrofuran was then removed under reduced pressure. To the resulting semi-solid slurry, 20 mL of methanol were added. The mixture was allowed to stir at 40 to 45°C for 30 min and then left at rt to allow for maximum precipitation. The solid acid was filtered and washed with 10 mL of water four times. Finally, the solid product was dried under vacuum at 35 to 40°C to obtain the acid as an off-white-colored powder **21** (1.17

g, 70%). %). **^{1}H NMR** (500 MHz, DMSO) δ 8.39 (s, 1H), 7.94 (d, *J* = 8.2 Hz, 1H), 7.81 (d, *J* = 7.9 Hz, 1H), 7.62 – 7.53 (m, 2H), 7.33 (t, *J* = 7.5 Hz, 1H), 7.23 (t, *J* = 9.2 Hz, 2H), 6.71 (d, *J* = 6.8 Hz, 1H), 4.31 (s, 1H), 1.88 – 1.82 (m, 1H), 1.58 (d, 3 H), 1.02 (dd, J = 8.4, 1.2 Hz, 2H), 0.85 – 0.57 (m, 2H). **^{13}C NMR** (126 MHz, $CDCl_3$) δ 168.40 (s), 163.04 (s), 160.26 (d, J = 251.5 Hz), 144.08 (s), 138.45 (s), 134.29 (s), 132.02 (s), 131.85 (s), 131.33 (d, J = 2.4 Hz), 129.04 (s), 128.89 (s), 128.76 (s), 128.17 (d, J = 12.0 Hz), 127.87 (s), 124.34 (d, J = 3.5 Hz), 122.35 (s), 116.07 (d, J = 21.7 Hz), 44.96 (s), 24.6(s), 15.10 (s), 14.48 (s), 8.61 (s). m/z: 375.14 (100.0%), 376.14 (25.2%), 377.15 (2.8%). **HRMS** (ESI/IT-TOF) m/z: [M + H]+ Calcd for $C_{22}H_{18}N_3O_2F$ is 376.1455 and found 375.1383.

2.5.18. (S)-5-(8-Cyclopropyl-6-(2-fluorophenyl)-4-methyl-4H-benzo[f]imidazo[1,5-a] [1,4] diazepin-3-yl)-3-ethyl-1,2,4-oxadiazole (22)

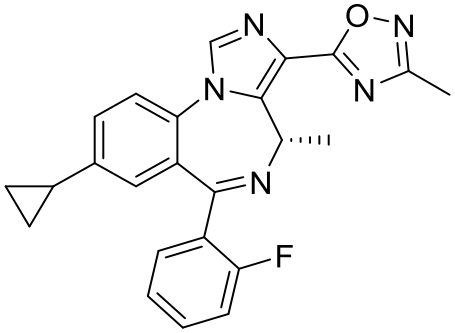


22

The ethyl oxime, N-hydroxypropionoimidamine (1.67 g, 18.95 mmol), was dissolved in dry THF (20 mL) under an argon atmosphere and treated with sodium hydride (60% dispersion in mineral oil, 0.12 g, 5.00 mmol) for one h with molecular sieves, 3°A, in a round-bottom flask. In a separate flask at rt under argon, the 8-cyclopropyl ethyl ester **20** (1.5 g, 3.71 mmol) was dissolved in dry THF (20 mL) and then added to the flask containing the oxime. The reaction mixture, which

resulted was stirred at rt for 2 h until the starting material was completely consumed, as indicated by analysis by TLC (silica gel, EtOAc: hexane = 50:50). The reaction mixture was quenched with a 100% aq $NaHCO_3$ solution (20 mL). Water (50 mL) was added, and the product was extracted with EtOAc (3 x 100 mL). The combined organic layers were washed with a 10% aq NaCl solution (2 x 30 mL) and dried with Na_2SO_4. The solvent was then removed under reduced pressure. The solid, which resulted was purified by flash column chromatography (silica gel, EtOAc: hexane = 50:50) to yield the pure oxadiazole **22** (white colored powder, 1.27 g, 80%); **^{1}H NMR** (500 MHz, $CDCl_3$) δ 8.06 (s, 1H), 7.64 (t, *J* = 7.0 Hz, 1H), 7.54 (d, *J* = 8.3 Hz, 1H), 7.47 – 7.43 (m, 1H), 7.25 (d, *J* = 7.5 Hz, 1H), 7.06 (d, *J* = 9.4 Hz, 1H), 7.02 (s, 1H), 6.72 (q, *J* = 7.1 Hz, 1H), 4.40 (d, *J* = 6.5 Hz, 1H), 2.81 (qd, *J* = 7.6 Hz, 2H), 1.91 – 1.85 (m, 1H), 1.37 (t, *J* = 7.6 Hz, 3H), 1.01 (d, *J* = 8.4 Hz, 2H), 0.67 (d, *J* = 5.0 Hz, 1H), 0.62 (d, *J* = 5.0 Hz, 1H). **^{13}C NMR** (126 MHz, $CDCl_3$) δ 171.83 (s), 170.90 (s), 164.52 (s), 161.14 (s), 159.14 (s), 144.17 (s), 139.10 (s), 136.23 (s), 135.55 (s), 131.86 (s), 131.25 (s), 129.17 – 128.38 (m), 128.15 (s), 127.31 (s), 124.59 (s), 124.37 (s), 121.92 (s), 116.15 (s), 115.98 (s), 50.14 (s), 19.76 (s), 15.09 (s), 14.80 (s), 11.55 (s), 9.96 (d, *J* = 4.3 Hz). m/z: 427.18 (100.0%), 428.18 (28.9%), 429.19 (3.8%). **HRMS** (ESI/IT-TOF) m/z: [M + H]+ Calcd for $C_{25}H_{22}N_5OF$ is 428.18795 and found 428.18811.

2.5.19. (S)-5-(8-Cyclopropyl-6-(2-fluorophenyl)-4-methyl-4H-benzo[f]imidazo[1,5-a] [1,4] diazepin-3-yl)-3-methyl-1,2,4-oxadiazole (23)

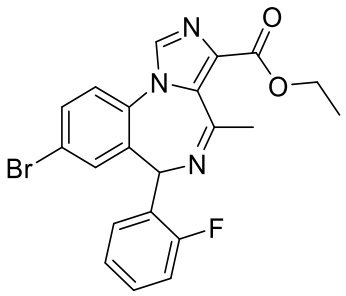


23

The methyl oxime (0.58 g, 7.82 mmol) was dissolved in dry THF (20 mL) under an argon atmosphere and treated with sodium hydride (60% dispersion in mineral oil, 0.052 g, 2.16 mmol) for one hour with molecular sieves, 3°A, in a round-bottom flask. In a separate flask at rt under argon, the 8-cyclopropyl ethyl ester **20** (0.8 g, 1.98 mmol) was dissolved in dry THF (20 mL) and then added to the flask containing the oxime. The reaction mixture, which resulted was stirred at rt for 2 h until the starting material was completely consumed, as indicated by analysis by TLC (silica gel, EtOAc: hexane = 50:50). The reaction mixture was quenched with a 100% aq$NaHCO_3$ solution (20 mL). Water (50 mL) was added, and the product was extracted with EtOAc (3 x 100 mL). The combined organic layers were washed with a 10% aq NaCl solution (2 x 30 mL) and dried over Na_2SO_4. The solvent was then removed under reduced pressure. The solid, which resulted was purified by flash column chromatography (silica gel, EtOAc: hexane = 50:50) to yield the pure oxadiazole **23** (white-colored powder, 1.27 g, 80%); **^{1}H NMR** (500 MHz, $CDCl_3$) δ 8.03 (s, 1H), 7.59 (t, *J* = 7.0 Hz, 1H), 7.52 (d, *J* = 8.3 Hz, 1H), 7.47 – 7.39 (m, 1H), 7.26 – 7.23 (m, 1H), 7.07 – 6.99 (m, 2H), 6.70 (q, *J* = 7.1 Hz, 1H), 2.44 (s, 3H), 1.33 (d, *J* = 7.2 Hz, 2H), 1.04 – 0.98 (m, 2H), 0.64 (dd, *J* = 21.6, 5.0 Hz, 1H). **^{13}C NMR** (126 MHz, $CDCl_3$) δ 170.96 (s), 167.35

(s), 164.47 (s), 161.14 (s), 159.15 (s), 144.19 (s), 139.18 (s), 136.27 (s), 131.81 (s), 131.66 – 131.54 (m), 131.36 (d, J = 22.0 Hz), 129.14 (s), 129.05 (d, J = 20.5 Hz), 128.69 (s), 128.11 (s), 124.38 (d, J = 9.0 Hz), 121.91 (s), 116.13 (s), 115.96 (s), 50.10 (s), 15.09 (s), 14.76 (s), 11.66 (s), 9.97 (d, J = 4.1 Hz). m/z: 413.17 (100.0%), 414.17 (26.2%), 415.17 (4.0%), 414.16 (1.8%). **HRMS** (ESI/IT-TOF) m/z: [M + H] Calcd for $C_{24}H_{20}N_5OF$ 414.17233; found 413.16519.

2.5.20. Ethyl 8-bromo-6-(2'fluorophenyl)-4-methyl-6H-benzo[f]imidazo[1,5-a] [1,4] diazepine-3-carboxylate (26)

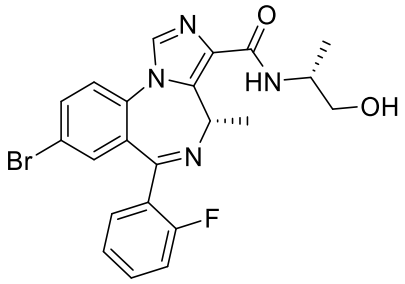


26

The ester **5** (0.5g, 6.78 mmol) was dissolved in anhydrous THF (10 mL) and a solution of potassium t-butoxide (0.837 g, 7.45 mmol) in THF (100 mL) was added dropwise at rt. The mixture, which resulted was stirred for an h at which point the reaction was deemed to be completed on analysis by TLC (silica gel, 100% EtOAc). The reaction was then quenched with water (10 mL) and DCM (20 mL) was added. The organic layer was collected and the aq layer was extracted with DCM (2x10 mL). The combined organic layers were washed with brine (2x20 mL) and dried (Na_2SO_4). The residue was purified by flash chromatography (silica gel, 60% EtOAc-hexane) to afford **26** as an off-white-colored powder (2.43 g, 81%). **^{1}H NMR** (500 MHz, $CDCl_3$) δ 7.79 (s, 1H), 7.52 – 7.49 (m, 1H), 7.38 (t, J = 7.0 Hz, 1H), 7.29 (s, 1H), 7.16 (d, J = 3.7 Hz, 1H), 7.14 – 7.11 (m, 1H), 7.09 (dd, J = 7.5, 1.0 Hz, 1H), 7.07 – 7.01 (m, 1H), 6.71 (q, J = 7.2 Hz, 1H),

4.49 (s, 1H), 1.42 (t, J = 7.1 Hz, 3H), 1.29 (d, J = 7.3 Hz, 3H); **^{13}C NMR** (126 MHz, $CDCl_3$) δ 162.91, 162.64, 161.07, 159.08, 141.57, 134.83, 134.73, 133.66, 133.03, 132.13, 132.06, 131.16, 129.58, 124.54, 123.63, 120.94, 116.32, 116.15, 60.80, 54.11, 14.87, 14.43. **HRMS** (ESI/IT-TOF) m/z: $[M + H]^+$ Calcd for $C_{21}H_{18}BrFN_3O_2$ 442.0561; found 442.0563.

2.5.21. (S)-8-Bromo-6-(2'fluorophenyl)-N-((R)-1-hydroxypropan-2-yl)-4-methyl-4H-benzo [f] imidazo[1,5-a] [1,4]diazepine-3-carboxamide (27)

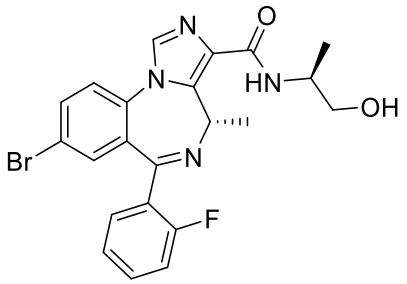


27

In a sealed tube, imidazodiazepine ester **5** (3.9 g, 8.81 mmol) and (R)-2-aminopropan-1-ol (5.06 g, 67.36 mmol) were combined, and the mixture, which resulted was heated at 90 °C (in a preheated oil bath) for 24 hours. Analysis by TLC indicated the disappearance of the starting material and the emergence of a new component (R_f 0.4, silica gel, EtOAc/hexane/methanol, 2:1:0.5, and a few drops of 14% aq NH_4OH). At this point the reaction mixture was cooled to rt, and 10 mL of cold water was added to the reaction mixture and most of the product will be precipitated without any further purification needed. To rest of the crude oil was followed by dilution with EtOAC (35 mL) and water (20 mL). The biphasic layers, which resulted were separated, and the aq layer was subjected to extraction with EtOAc (4 × 20 mL). The combined organic layer was washed with brine (20 mL) and dried with Na_2SO_4. The solvent was then removed under reduced pressure, and the residue underwent purification through crystallization

(15% MeOH in EtOAc). The solid, which was obtained, was dried under vacuum at 40 °C, yielding carboxamide **27** as a light-yellow colored solid (4.07 g, 98%).MP 255-256 °C; **^{1}H NMR** (500 MHz, CDCl3) δ 8.32 (d, J = 4.4 Hz, 1H), 8.12 (d, J = 8.0 Hz, 1H), 7.78 (td, J = 7.8, 1.7 Hz, 2H), 7.73 (dd, J = 8.6, 2.1 Hz, 1H), 7.54 (d, J = 2.1 Hz, 1H), 7.48 – 7.37 (m, 1H), 7.32 (ddd, J = 7.5, 4.8, 0.9 Hz, 1H), 7.24 (d, J = 8.2 Hz, 1H), 4.52 (q, 1H), 4.15 – 4.02 (m, 2H), 3.80 – 3.68 (m, 1H), 3.68 – 3.58 (m, 2H),1.67 (s, 1H), 1.57 (dd, J = 13.6, 6.7 Hz, 1H), 0.98 (d, J = 24.1 Hz, 3H); 13C NMR (126 MHz, CDCl3): δC 168.8 (s),163.3 (s), 156.3 (s), 148.5 (s), 137.0 (s), 135.8 (s), 135.3 (s), 134.9 (s), 134.6 (s), 133.2 (s), 131.2 (s), 128.5 (s), 124.8 (s), 124.2 (s), 124.0 (s), 120.4 (s), 65.4 (s), 53.4 (s), 44.7 (s), 24.3 (s), 10.7 (s); m/z: 470.08 (100.0%), 472.07 (97.3%), 471.08 (24.1%), 473.08 (23.6%), 472.08 (3.5%), 474.08 (3.1%), 471.07 (1.5%), 473.07 (1.4%). **HRMS** (ESI/IT-TOF) m/z: $[M + H]^+$ Calcd for $C_{22}H_{20}BrFN_4O_2$ 470.0822; found 470.1294.

2.5.22. (S)-8-Bromo-6-(2'fluorophenyl)-N-((S)-1-hydroxypropan-2-yl)-4-methyl-4H-benzo [f] imidazo[1,5-a][1,4]diazepine-3-carboxamide (28)

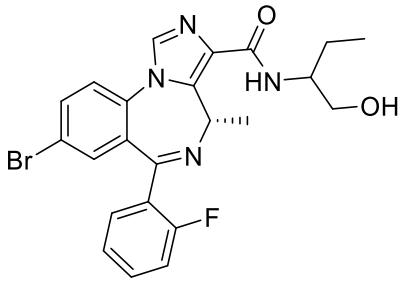


28

In a sealed tube, imidazodiazepine ester **5** (1.93 g, 4.35 mmol) and (R)-2-aminopropan-1-ol (2.3 g, 30.6 mmol) were combined, and the mixture, which resulted was heated at 90 °C (in a preheated oil bath) for 24 h. Analysis by TLC indicated the disappearance of the starting material and the emergence of a new component (R_f 0.4, silica gel, EtOAc/hexane/methanol, 2:1:0.5, and a few

drops of 14% aqueous NH_4OH). At this point, the reaction mixture was cooled to rt, and 8 mL of cold water was added to the reaction mixture. At this point most of the product will be precipitated without any further purification required. The rest of the crude was treated by dilution with EtOAC (20 mL) and water (10 mL). The biphasic layers, which resulted were separated, and the aq layer was subjected to extraction with EtOAc (4 x 10 mL). The combined organic layer was washed with brine (10 mL) and dried with Na_2SO_4. The solvent was then removed under reduced pressure, and the residue underwent purification through precipitation (15% MeOH in EtOAc). The solid. Which was obtained, was dried under vacuum at 40 °C, to yield carboxamide **28** as a light-yellow colored solid (4.07 g, 98%).MP 255-256 °C; **^{1}H NMR** (500 MHz, CDCl3) δ 8.33 (d, J = 4.4 Hz, 1H), 8.12 (d, J = 8.0 Hz, 1H), 7.78 (td, J = 7.8, 1.7 Hz, 2H), 7.63 (dd, J = 8.6, 2.1 Hz, 1H), 7.54 (d, J = 2.1 Hz, 1H), 7.48 – 7.37 (m, 1H), 7.32 (ddd, J = 7.5, 4.8, 0.9 Hz, 1H), 7.24 (d, J = 8.2 Hz, 1H), 4.52 (q, 1H), 4.25 – 4.12 (m, 2H), 3.80 – 3.68 (m, 1H), 3.68 – 3.58 (m, 2H),1.67 (s, 1H), 1.57 (dd, J = 13.6, 6.7 Hz, 1H), 0.98 (d, J = 24.1 Hz, 3H); 13C NMR (126 MHz, CDCl3): δ C 168.8 (s),163.3 (s), 156.3 (s), 148.5 (s), 137.0 (s), 135.8 (s), 135.3 (s), 134.9 (s), 134.6 (s), 133.2 (s), 131.2 (s), 128.5 (s), 124.8 (s), 124.2 (s), 124.0 (s), 120.4 (s), 65.4 (s), 53.4 (s), 44.7 (s), 24.3 (s), 10.7 (s); m/z: 470.08 (100.0%), 472.07 (97.3%), 471.08 (24.1%), 473.08 (23.6%), 472.08 (3.5%), 474.08 (3.1%), 471.07 (1.5%), 473.07 (1.4%). **HRMS** (ESI/IT-TOF) m/z: $[M + H]^+$ Calcd for $C_{22}H_{20}BrFN_4O_2$ 470.0822; found 470.1237.

2.5.23. (4S)-8-Bromo-6-(2'fluorophenyl)-N-(1-hydroxybutan-2-yl)-4-methyl-4H-benzo [f] imidazo [1,5-a][1,4]diazepine-3-carboxamide (33)

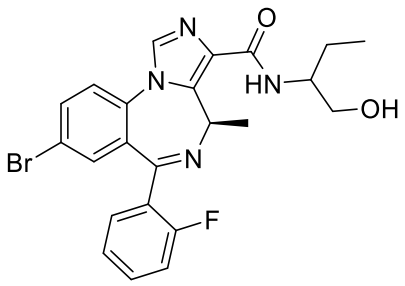


33

In a sealed tube imidazodiazepine ester **5** (1.93 g, 2.26 mmol) and rac-2-amino-1-butanol (2.3 g, 25.80 mmol) were combined, and the mixture, which resilted was heated at 90 °C (in a preheated oil bath) for 24 h. Analysis by TLC indicated the disappearance of the starting material and the emergence of a new component (R_f 0.4, silica gel, EtOAc/hexane/methanol, 2:1:0.5, and a few drops of 14% aq NH_4OH). At this point, the reaction mixture was cooled to rt, and 8 mL of cold water was added to the reaction mixture. Most of the product will be precipitated without any further purification required. The rest of the crude was treated by dilution with EtOAC (20 mL) and water (10 mL). The biphasic layers, which resulted were separated, and the aqueous layer was subjected to extraction with EtOAc (4 x 10 mL). The combined organic layer was washed with brine (10 mL) and dried with Na_2SO_4. The solvent was then removed under reduced pressure, and the residue underwent purification through precipitation (15% MeOH in EtOAc). The solid, which was obtained was dried under vacuum at 40 °C, to yield carboxamide **28** as a light-yellow colored solid (1.06 g, 97%). **^{1}H NMR** (500 MHz, CDCl3) δ 8.32 (d, 1H), 8.12 (d, 1H), 7.78 (td, 2H), 7.73 (dd, 1H), 7.54 (d, 1H), 7.48 – 7.37 (m, 1H), 7.32 (ddd, 1H), 7.24 (d, , 1H), 6.21 (t, 1H), 4.15 – 4.02 (q, 1H), 4.02 – 252 3.91 (m, 1H), 3.80 – 3.68 (m, 1H), 3.68 – 3.58 (m, 1H),1.67 (s, 1H), 1.57 (dd, J = 13.6, 6.7 Hz, 1H), 0.98 (d, J = 24.1 Hz, 3H); **^{13}C NMR** (126 MHz, CDCl3): δC 166.8 (s),163.3 (s), 156.3 (s), 148.5 (s), 137.0 (s), 135.8 (s), 135.3 (s), 134.9 (s), 134.6 (s), 133.2 (s), 131.2 (s), 128.5 (s), 124.8 (s), 124.2 (s), 124.0 (s), 120.4 (s), 65.4 (s), 53.4 (s), 44.7 (s), 24.3 (s), 10.7 (s).

m/z: 484.09 (100.0%), 486.09 (97.7%), 485.09 (26.4%), 487.09 (25.8%), 486.10 (3.5%), 488.10 (3.0%). **HRMS** (ESI/IT-TOF) m/z: [M + H] Calcd for $C_{23}H_{22}N_4O_2FBr$ 485.09858; found 485.09829.

2.5.24. (4R)-8-Bromo-6-(2'fluorophenyl)-N-(1-hydroxybutan-2-yl)-4-methyl-4H-benzo [f] imidazo[1,5-a][1,4]diazepine-3-carboxamide (34)

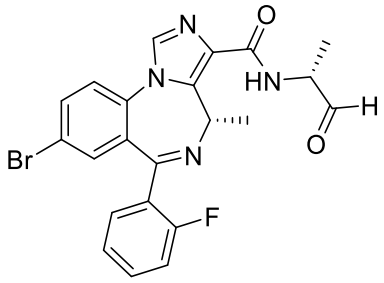


34

In a sealed tube imidazodiazepine ester **12** (2 g, 4.52 mmol) and rac-2-amino-1-butanol (4.6 g, 51.60 mmol) were combined, and the mixture, which resulted was heated at 90 °C (in a preheated oil bath) for 24 h. Analysis by TLC indicated the disappearance of the starting material and the emergence of a new component (R_f 0.4, silica gel, EtOAc/hexane/methanol, 2:1:0.5, and a few drops of 14% aq NH_4OH). At this point the reaction mixture was cooled to rt. 8 mL of cold water was added to the reaction mixture. Most of the product will be precipitated without any further purification required. The rest of the crude was treated by dilution with EtOAC (40 mL) and water (20 mL). The biphasic layers, which resulted were separated, and the aq layer was subjected to extraction with EtOAc (4 x 20 mL). The combined organic layer was washed with brine (20 mL) and dried with Na_2SO_4. The solvent was then removed under reduced pressure, and the residue underwent purification through precipitation (15% MeOH in EtOAc). The solid, which was obtained was dried under vacuum at 40 °C, to yield carboxamide **28** as a light-yellow colored solid

(1.06 g, 97%). 1H NMR (500 MHz, CDCl3) δ 8.25 (d, 1H), 8.09 (d, 1H), 7.78 (td, 2H), 7.73 (dd, 1H), 7.54 (d, 1H), 7.48 – 7.37 (m, 1H), 7.31 (ddd, 1H), 7.24 (d, , 1H), 6.21 (t, 1H), 4.15 – 4.02 (q, 1H), 4.02 – 252 3.91 (m, 1H), 3.80 – 3.68 (m, 1H), 3.68 – 3.58 (m, 1H),1.67 (s, 1H), 1.57 (dd, J = 13.6, 6.7 Hz, 1H), 0.98 (d, J = 24.1 Hz, 3H); 13C NMR (126 MHz, $CDCl_3$): δC 166.8 (s),163.3 (s), 156.3 (s), 148.5 (s), 137.0 (s), 135.8 (s), 135.3 (s), 134.9 (s), 134.6 (s), 133.2 (s), 131.2 (s), 128.5 (s), 124.8 (s), 124.2 (s), 124.0 (s), 120.4 (s), 64.9 (s), 53.4 (s), 44.7 (s), 24.3 (s), 10.5 (s). m/z: 484.09 (100.0%), 486.09 (97.7%), 485.09 (26.4%), 487.09 (25.8%), 486.10 (3.5%), 488.10 (3.0%). **HRMS** (ESI/IT-TOF) m/z: [M + H] Calcd for $C_{23}H_{22}N_4O_2FBr$ 485.09858; found 484.091024.

2.5.25. (S)-8-Bromo-6-(2'fluorophenyl)-4-methyl-N-((R)-1-oxopropan-2-yl)-4H-benzo[f] imidazo [1,5-a][1,4]diazepine-3-carboxamide (29)

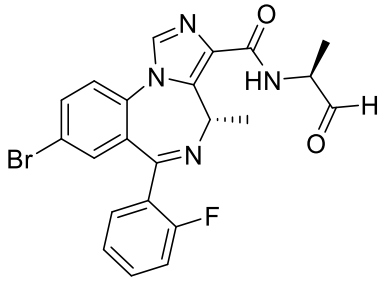


29

To a solution of carboxamide **27** (0.7 g, 1.48 mmol) in CH_2Cl_2 (70 mL), the Dess-Martin periodinane (0.75 g, 1.76 mmol) was added in one portion and the mixture was stirred at rt for 4 h. The reaction mixture was analyzed by TLC (silica gel, EtOAc/hexane/MeOH 2:1:0.5). After the completion of the reaction by TLC, the mixture was diluted with CH_2Cl_2 (100 mL) and quenched by addition of a sat aq $NaHCO_3$ solution (20 mL) and a sat solution of aq $Na_2S_2O_3$ (20 mL). The

mixture was stirred for 20 min and the layers were separated. The aq layer was extracted with CH_2Cl_2 (30 mL x 2) and the combined organic layer was washed with brine (30 mL) and dried (Na_2SO_4). The solvent was removed under reduced pressure and the residue was purified by flash chromatography (silica gel, 100% EtOAc) to provide amide **29** as a light-yellow-colored powder (0.54 g, 78%). **^{1}H NMR** (500 MHz, $CDCl_3$) δ 9.64 (d, *J* = 17.4 Hz, 1H), 7.85 (s, 1H), 7.71 (d, *J* = 7.8 Hz, 1H), 7.63 (d, *J* = 6.0 Hz, 2H), 7.47 – 7.39 (m, 3H), 7.24 (d, *J* = 7.5 Hz, 1H), 7.03 (t, *J* = 9.2 Hz, 1H), 6.83 (d, *J* = 7.3 Hz, 1H), 4.61 – 4.50 (m, 1H), 1.44 (d, *J* = 7.3 Hz, 3H), 1.28 (d, *J* = 7.7 Hz, 3H). **^{13}C NMR** (126 MHz, $CDCl_3$) δ 199.74 (s), 174.00 (s), 171.16 (s), 162.98 – 162.20 (m), 162.20 – 161.98 (m), 134.75 (s), 133.96 – 132.75 (m), 132.75 – 132.61 (m), 131.28 (d, *J* = 8.4 Hz), 124.55 (s), 123.58 (s), 116.21 (s), 116.04 (s), 60.40 (s), 49.85 (s), 25.85 (s), 14.52 (s). m/z: 468.06 (100.0%), 470.06 (98.0%), 469.06 (25.3%), 471.06 (23.5%), 472.06 (3.4%), 470.07 (2.8%), 471.05 (1.4%). **HRMS** (ESI/IT-TOF) m/z: [M + H] Calcd for $C_{22}H_{18}N_4O_2FBr$ 469.06689; found 469.06699.

2.5.26. (S)-8-Bromo-6-(2'fluorophenyl)-4-methyl-N-((S)-1-oxopropan-2-yl)-4H-benzo [f] imidazo [1,5-a][1,4]diazepine-3-carboxamide (30)

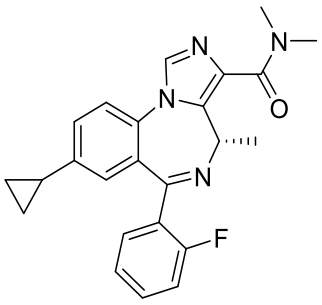


30

To a solution of carboxamide **28** (0.5 g, 1.06 mmol) in CH_2Cl_2 (50 mL), the Dess-Martin periodinane (0.53 g, 1.27 mmol) was added in one portion and the mixture was stirred at rt for 4h.

The reaction mixture was analyzed by TLC (silica gel, EtOAc/hexane/MeOH 2:1:0.5). After the completion of the reaction by TLC, the mixture was diluted with CH_2Cl_2 (100 mL) and quenched by addition of a sat aq $NaHCO_3$ solution (20 mL) and a sat solution of aq $Na_2S_2O_3$ (20 mL). The mixture was stirred for 20 min and the layers were separated. The aq layer was extracted with CH_2Cl_2 (30 mL x 2) and the combined organic layer was washed with brine (30 mL) and dried (Na_2SO_4). The solvent was removed under reduced pressure and the residue was purified by flash chromatography (silica gel, 100% EtOAc) to provide amide **29** as a light-yellow-colored powder (0.37 g, 75%). **^{1}H NMR** (500 MHz, $CDCl_3$) δ 9.64 (d, *J* = 17.4 Hz, 1H), 7.85 (s, 1H), 7.71 (d, *J* = 7.8 Hz, 1H), 7.63 (d, *J* = 6.0 Hz, 2H), 7.47 – 7.39 (m, 3H), 7.24 (d, *J* = 7.5 Hz, 1H), 7.03 (t, *J* = 9.2 Hz, 1H), 6.83 (d, *J* = 7.3 Hz, 1H), 4.61 – 4.50 (m, 1H), 1.44 (d, *J* = 7.3 Hz, 3H), 1.28 (d, *J* = 7.7 Hz, 3H). **^{13}C NMR** (126 MHz, $CDCl_3$) δ 199.74 (s), 174.00 (s), 171.16 (s), 162.98 – 162.20 (m), 162.20 – 161.98 (m), 134.75 (s), 133.96 – 132.75 (m), 132.75 – 132.61 (m), 131.28 (d, *J* = 8.4 Hz), 124.55 (s), 123.58 (s), 116.21 (s), 116.04 (s), 60.40 (s), 49.85 (s), 25.85 (s), 14.52 (s). m/z: 468.06 (100.0%), 470.06 (98.0%), 469.06 (25.3%), 471.06 (23.5%), 472.06 (3.4%), 470.07 (2.8%), 471.05 (1.4%). **HRMS** (ESI/IT-TOF) m/z: [M + H] Calcd for $C_{22}H_{18}N_4O_2FBr$ 469.06689; found 469.0671.

2.5.27. (S)-8-Cyclopropyl-6-(2'fluorophenyl)-N,N,4-trimethyl-4H-benzo[f]imidazo[1,5-a] [1,4] diazepine-3-carboxamide (24)

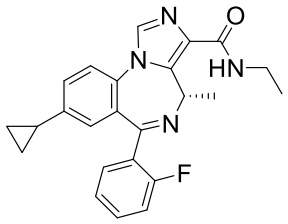


24

A mixture of cyclopropyl, acid **21** (1.09 g, 2.90 mmol), thionyl chloride (2.1 mL, 28.94 mmol), and dry DCM (40 mL) was placed in a round-bottom flask, pre-dried in an oven, under argon. The suspension, which resulted was allowed to reflux at 60˚C for 1 h under argon. Confirmation of the absence of the starting material was achieved through analysis by TLC on silica gel. The organic solvent and excess thionyl chloride were then removed under reduced pressure using a rotovapor. This process was repeated five times with dry DCM (30 mL) to get all HCl and $SOCl_2$ out. The remaining yellow residue was dissolved in dry DCM (40 mL) and cooled to 0 ˚C for 10 min under argon. Subsequently, the nucleophilic dimethylamine (0.025 mL, 5.6 mmol) and triethylamine (0.78 mL, 5.6 mmol) were added individually to the reaction mixture at 0 ˚C. The mixture was then allowed to warm to rt and stirred for 1-2 hours. Upon completion of the reaction, as confirmed by analysis by TLC on silica gel, the solvent was removed under reduced pressure. The residue was treated with ice-cold water (30 mL) and extracted with DCM (3 x 20 mL). The combined organic layer was washed with brine (30 mL) and dried with Na_2SO_4. After removing the solvent under reduced pressure, the residue was purified by column chromatography to obtain the dimethyl amide **24** as a light-yellow-colored powder. (0.81 g, 70%); **$[\alpha]_D^{25}$= -93.5**, **^{1}H NMR** (500 MHz,

$CDCl_3$) δ 7.89 (s, 1H), 7.61 (t, *J* = 7.0 Hz, 1H), 7.42 (d, *J* = 7.3 Hz, 2H), 7.25 (d, *J* = 7.3 Hz, 2H), 7.07 – 6.98 (m, 2H), 4.31 (d, *J* = 6.2 Hz, 1H), 3.12 (s, 3H), 3.00 (s, 3H), 1.92 (d, *J* = 6.0 Hz, 1H), 1.27 (s, 2H), 1.00 (d, *J* = 7.8 Hz, 2H). **^{13}C NMR** (126 MHz, $CDCl_3$) δ 166.42 (s), 163.45 (s), 161.25 (s), 159.26 (s), 143.58 (s), 134.75 (s), 133.72 (s), 132.30 (s), 131.51 (d, *J* = 40.7 Hz), 128.86 (s), 127.41 (s), 124.34 (s), 122.51 (s), 116.10 (s), 115.99 (d, *J* = 21.8 Hz), 49.43 (s), 39.11 (s), 18.56 (s), 9.71 (s). m/z: 402.19 (100.0%), 403.19 (26.3%), 404.19 (3.8%), 403.18 (1.5%). **HRMS** (ESI/IT-TOF) m/z: [M + H] Calcd for $C_{24}H_{23}N_4OF$ 403.19287; found 402.18559.

2.5.28. (S)-8-Cyclopropyl-N-ethyl-6-(2'fluorophenyl)-4-methyl-4H-benzo[f]imidazo[1,5-a] [1,4] diazepine-3-carboxamide (25)



25

A mixture of cyclopropyl, acid **21** (0.78 g, 2.07 mmol), thionyl chloride (1.5 mL, 20.67 mmol), and dry DCM (30 mL) was placed in a round bottom flask, that had been pre-dried in an oven, under argon. The suspension, which resulted was allowed to reflux at 60˚C for 1 hour under argon. Confirmation of the absence of the starting material was achieved through analysis by TLC on silica gel. The organic solvent and excess thionyl chloride were then removed under reduced pressure using a rotavapor. This process was repeated five times with dry DCM (20 mL). The yellow residue, which remained was dissolved in dry DCM (30 mL) and cooled to 0 ˚C for 10 minutes under argon. Subsequently, the nucleophilic ethylamine (0.74 mL, 13.29 mmol) and

triethylamine (0.78 mL, 5.6 mmol) were added individually to the reaction mixture at 0 ˚C. The mixture was then allowed to warm to rt and allowed to stir for 1-2 h. Upon completion of the reaction, as confirmed by analysis by TLC on silica gel, the solvent was removed under reduced pressure. The residue was treated with ice-cold water (30 mL) and extracted with DCM (3 x 20 mL). The combined organic layer was washed with brine (30 mL) and dried with Na_2SO_4. After removing the solvent under reduced pressure, the residue was purified by column chromatography to obtain the ethyl amide **25** as a light-yellow-colored powder. (0.58 g, 70%); mp 189-190 °C; **^{1}H NMR** (300 MHz, $CDCl_3$) δ 7.81 (s, 1H), 7.59 (t, *J* = 6.6 Hz, 1H), 7.41 (t, *J* = 10.0 Hz, 2H), 7.31 – 7.14 (m, 3H), 7.09 – 6.91 (m, 2H), 6.86 (d, *J* = 7.0 Hz, 1H), 3.62 – 3.24 (m, 2H), 1.94 – 1.71 (m, 1H), 1.22 (dd, *J* = 15.1, 7.6 Hz, 6H), 0.98 (d, *J* = 7.9 Hz, 2H), 0.70 – 0.46 (m, 2H); **^{13}C NMR** (75 MHz, $CDCl_3$) δ 163.84 (s), 162.71 (s), 160.15 (d, *J* = 249.0 Hz), 143.60 (s), 138.71 (s), 133.31 (s), 132.27 (s), 131.57 (s), 131.40 (s), 129.35 (s), 129.32 (s), 128.49 (s), 128.29 (s), 127.87 (s), 124.28 (s), 121.79 (s), 115.89 (d, *J* = 21.8 Hz), 49.82 (s), 33.65 (s), 15.03 (s), 14.82 (s), 9.82 (s); **HRMS** (ESI/IT-TOF) m/z: [M + H] Calcd for $C_{24}H_{24}FN_4O$ 403.1929; found 403.1927.

Chapter 3: Design and Synthesis of Achiral α2/3 Ligands for Anxiety, Epilepsy, and Pain: Large Scale Synthesis of Hz-166 and Analogs

3.1. Introduction

The gamma-aminobutyric acid type A receptors ($GABA_ARs$), which are pentameric ligand-gated ionotropic channels, serve as the primary inhibitory neurotransmitter receptors in the central nervous system (CNS).[165]These receptors play a crucial role in various brain functions, depending on the modulatory effects of ligands targeting $GABA_AR$.[166167–169] Classical benzodiazepines (BZDs) function as positive allosteric modulators of $GABA_AR$ by binding to the α+γ- interface of the receptor. [26,167–169] While these BZDs are utilized in treating CNS disorders such as anxiety, convulsions, and insomnia, their use is associated with side effects like sedation, ataxia, amnesia, and addiction. [169–171] These adverse reactions pose challenges for the long-term prescription of these drugs. Despite their drawbacks, these BZDs are still employed in treating various CNS disorders due to the absence of suitable alternatives with subtype selectivity and efficacy. For instance, selective serotonin reuptake inhibitors (SSRIs) are linked to sexual dysfunction, and barbiturates are prone to easy overdose and can lead to death.[26,168–173]

The creation of innovative $GABA_A$ receptor ligands specific to the α2β2/3γ2 and α3β2/3γ2 subtypes is crucial for achieving enhanced agonistic efficacy, as indicated by findings documented in various journals. These newly developed subtype-selective ligands demonstrate anxiolytic, antinociceptive, and anticonvulsant activities, with minimal or no efficacy observed at α1-subtypes when the appropriate profile is attained. [167,170,174–181] The use of $GABA_A$ α2 or α3 partial agonists holds promise for treating anxiety, epilepsy, and non-sedative neuropathic pain without inducing sedation, ataxia, amnesia, or dependence.

The primary compound under investigation, 5-(8-ethynyl-6-(pyridin-2-yl)-4H-benzo[f]imidazo[1,5-a][1,4]diazepin-3-yl)oxazole, referred to as KRM-II-81 (**Figure 1**), belongs to a novel series of orally bioavailable imidazodiazepines derived from the initial lead, HZ-166. This imidazodiazepine ester, featuring an ethynyl group at the C(8) position, exhibited diminished efficacy and/or binding affinity at the α1-subtype.[3,26]The replacement of the ester functionality of HZ-166 with a bioisosteric compound, MP-III-080, significantly enhanced pharmacokinetic properties in human, mouse, rat, and dog liver microsomes, as compared to the parent compound, HZ-166. Both KRM-II-81 and the structurally analogous, MP-III-080, function as positive allosteric modulators (PAM) of α2/3-containing $GABA_A$ receptors. These compounds have demonstrated analgesic effects in various rodent pain models, including acid-induced pain behaviors[11,182,183] and inflammatory pain.[184–187] KRM-II-81 has exhibited efficacy against pharmacoresistant epilepsies, traumatic brain injury, and neuropathic pain. Additionally, it produces anxiolytic- and antidepressant-like effects in rodent models. Noteworthy pharmacological features of this imidazodiazepine include low sedation, the absence of tolerance development, and the capability to prevent the development of seizure sensitization. [184,186,188]

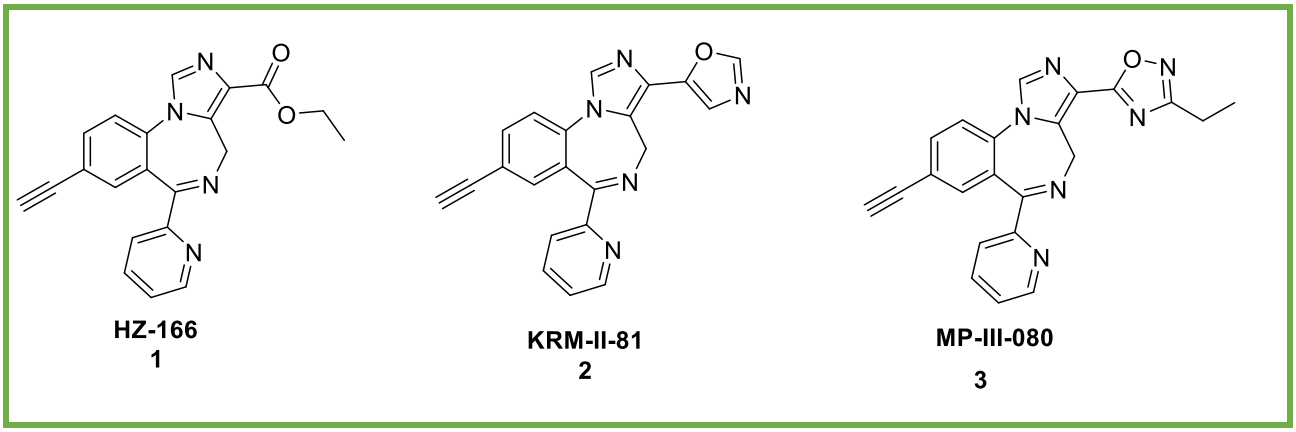


Figure 1. Structures of HZ-166, KRM-II-81, and MP-III-080

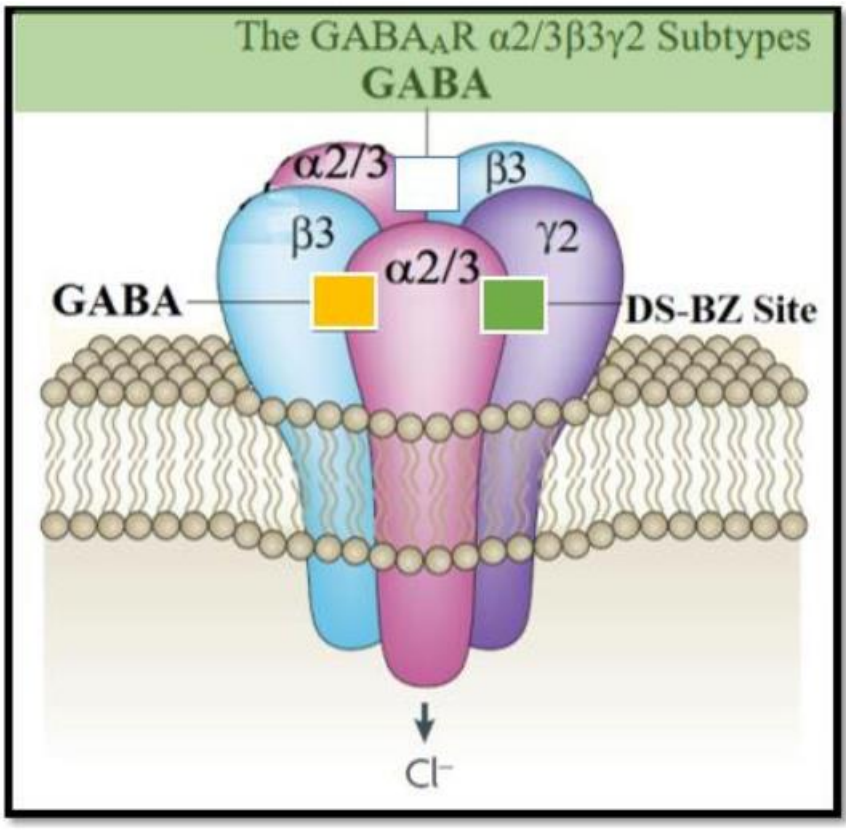


Figure 2. The GABA$_A$R α2/3β3γ2 subtypes are pentameric ligand-gated chloride channels. IBDZs (HZ-166 and KRM-II-81) mediate their effects at the DS-Bz site (α2/3+γ2- interface) as positive allosteric modulators (PAMs). Image modified from Jacob et al., Nature Reviews Neuroscience, 2008.[8]

An important characteristic of α2/3-potentiating GABAkines, specifically imidazodiazepines, is their profile of relatively low sedation and ataxia when compared to classical GABAkines like diazepam. A comparison between diazepam and KRM-II-81, based on a 'therapeutic index,' revealed that KRM-II-81 exhibited a larger separation or protective index than diazepam across various assays, as reported by Witkin et al. in 2018.[189] KRM-II-81 demonstrated antinociceptive effects at doses lower than those causing reductions in rates of food-maintained behavior or muscle relaxation, as assessed in rodent pain models.[182] Notably, KRM-II-81 selectively activates α2 and

α3-containing $GABA_A$ receptors, while diazepam interacts non-selectively with α1, α2, α3, and α5-containing $GABA_A$ receptors (**Figure 3**). [9]

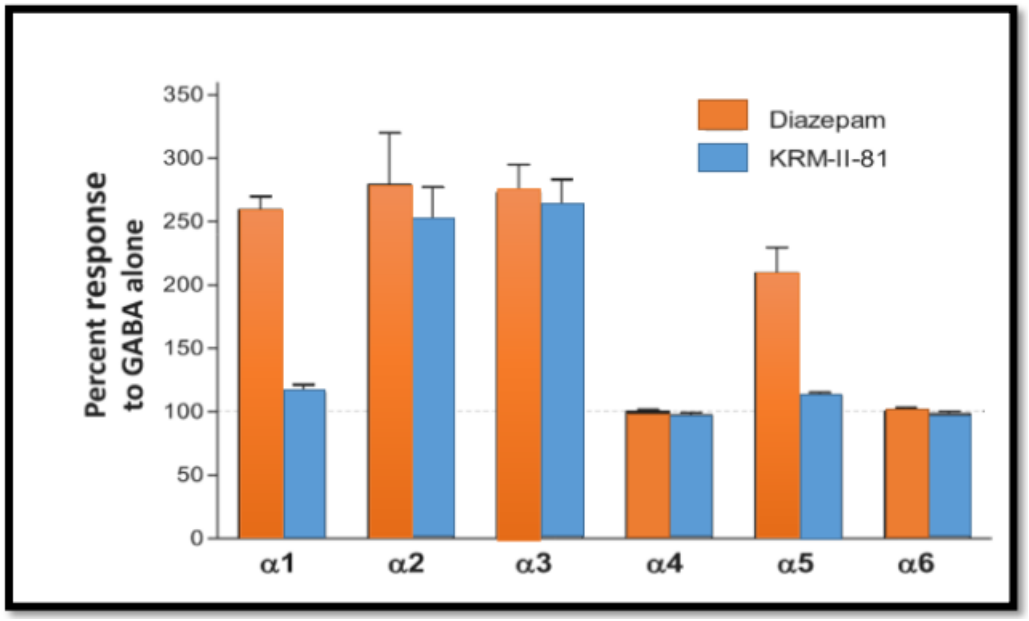


Figure 3: Average enhancement of the current evoked to GABA EC3 by 0.1 μM (α1, α2, α3, α5) or 1 μM (α4, α6) of either diazepam or KRM-II-81. This figure was redrawn from Cerne et al. 2021.[9]

In the docking studies conducted on the $GABA_A$ α1 receptor with KRM-II-81 and alprazolam, crucial features were identified that elucidated the reduced sedative profile of KRM-II-81. When overlaying the docking conformation of alprazolam bound to the CryoEM structure (6HUO) with the best pose of KRM-II-81, it was observed that both compounds exhibited similar bound conformations for the pendant ring. However, the diazepine ring and triazole/imidazole rings interacted differently with the protein, as reported by Witkin et al. in 2020.[190] A halogen bond was noted between the chlorine atom at the C-8 position of alprazolam and the carbonyl oxygen of the α1His102 amino acid backbone. Notably, KRM-II-81 did not interact with this α1His102, as its docking conformation lacked a chlorine atom at C-8, instead featuring an ethynyl moiety. The

docking scores for alprazolam and KRM-II-81 were -10.8 kcal/mol and -9.4 kcal/mol, respectively, indicating that alprazolam bound more tightly to the α1β3γ2L $GABA_A$ receptor, as compared to KRM-II-81 (**Figure 4**).

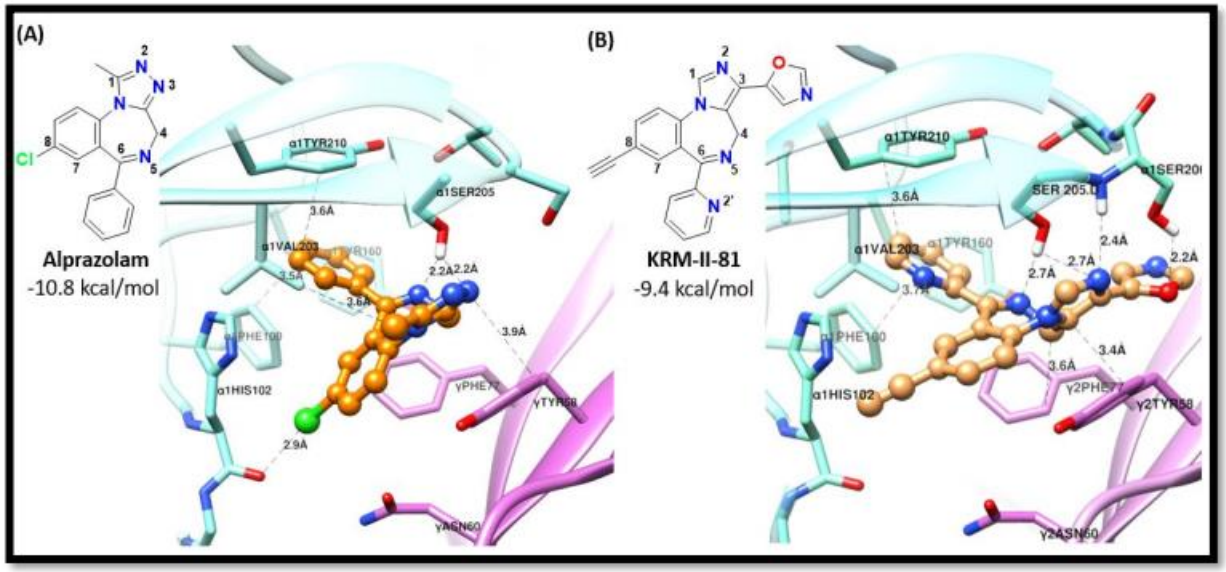


Figure 4. Alprazolam vs KRM-II-81 at the α+γ- interface of the GABAA receptor. (A) Alprazolam (orange) in the complex with the α1β3γ2L GABAA receptor 6HUO. (B) KRMII-81 docked (sandy brown) in the complex with the α1β3γ2L GABAA receptor 6HUO. α1 (aquamarine); γ2 (orchid) subunit. Dashed lines indicate π-π, hydrogen bond and halogen bond interactions. Data are modified from (Witkin et al., 2020, Golani, Mian et al 2021)[4,10]

KRM-II-81 demonstrated a reduction in pain behaviors across various acute pain provocation models in rodents, including acid-induced changes in writhing (Lewter et al., 2017)[182], intracranial self-stimulation behaviors (Moerke et al., 2019)[191], and nest-building (**Table 1**). Moreover, it proved effective in alleviating neonatal inflammatory bladder pain (**Table 1**). In contrast, diazepam failed to mitigate nociceptive behaviors in formalin-treated rats, even at a dose of 10 mg/kg, p.o. Similar results were observed in chronic pain models. KRM-II-81 exhibited significant efficacy in

two models of mechanical hyperalgesia induced by L5/6 nerve ligation (Witkin et al., 2019)[187]and demonstrated effectiveness against both mechanical and thermal hyperalgesia. In the case of neuropathic pain induced by paclitaxel chemotherapy in mice, both mechanical and thermal hyperalgesia pain models showed that MP-III-080, a structurally similar analog of KRM-II-81 (**Figure 1**), displayed comparable efficacy in pain reduction to the active KRM-II-81 (Biggerstaff et al., 2020).[188] The importance of this work is KRM-II-81nor MP-III-080 by day 37 did not develop tolerance to the antinociceptive efficacy while the billion dollar drug, gabapentin, clearly developed tolerance after 37 days.

Table 1: Effect of KRM-II-81 and it's analogs in different pain models [a]					
Compound	Models	Species	Activity	Comparator	References
KRM-II-81	Acetic acid induced writhing	Mice	Yes	Morphine	Lewter et al. (2017)
KRM-II-81	Lactic acid induced writhing	Mice	Yes	Morphine	Lewter et al. (2017)
KRM-II-81	Nesting	Mice	Yes	Morphine	Lewter et al. (2017)
KRM-II-81	Intracranial self-stimulation behaviors	Rats	Yes	Ketorolac and diazepam	Moerke et al (2019)
KRM-II-81	Tactile hyperalgesia (formalin induced)	Rats	Yes	Tramadol and diazepam	Witkin, et al. (2019)

KRM-II-81	Tactile hyperalgesia (L5/6 nerve ligation induced)	Rats	Yes	Gabapentin	Witkin, et al. (2019)
KRM-II-81	Thermal hyperalgesia (chemotherapy induced)	Mice	Yes	Gabapentin	Biggerstaff et al. (2020)
KRM-II-81	Tactile hyperalgesia (chemotherapy induced)	Mice	Yes	Gabapentin	Biggerstaff et al. (2020)
KRM-II-81B	Acetic acid induced writhing	Mice	Yes	Morphine	Lewter et al. (2017)
KRM-II-81B	Lactic acid induced writhing	Mice	Yes	Morphine	Lewter et al. (2017)
KRM-II-81B	Nesting	Mice	Yes	Morphine	Lewter et al. (2017)
MP-III-024	Mechanical hyperalgesia	Mice	Yes		Fischer et al. (2017)
MP-III-080	Thermal hyperalgesia (chemotherapy induced)	Mice	Yes	Gabapentin	Biggerstaff et al. (2020)
MP-III-080	Tactile hyperalgesia (chemotherapy induced)	Mice	Yes	Gabapentin	Biggerstaff et al. (2020)

a. Antinociceptive activity of KRM-II-81, MP-III-080 and some small ligands in pain models. Furthermore, these studies revealed that Gabapentin developed tolerance, whereas KRM-II-81 and MP-III-080 did not. There was ample pre-clinical data emphasizing the potential therapeutic activity of KRM-II-81 in neurological pharmacology, particularly in epilepsy (**Table 2**). KRM-II-81 demonstrated the ability to suppress hyper-excitation in a network of rat cortical neurons in

vitro, without affecting spontaneous neuronal activity (Witkin et al., 2018a)[189]. Additionally, KRM-II-81 exhibited efficacy against acute seizures, supported by a wide range of preclinical data. In rodent models, KRM-II-81 and its structural analogs, including MP-III-080, induced anxiolytic effects, as evidenced by behaviors such as marble-burying in mice (Poe et al., 2016; Knutson et al., 2020)[135,167] and the Vogel conflict test in rats (Poe et al., 2016; Witkin et al., 2017)[167,177] Notably, KRM-II-81 reduced marble-burying activity similarly to the clinical antianxiety drug chlordiazepoxide in a marble-burying assay. Furthermore, potential antidepressant-like effects of KRM-II-81 and MP-III-080 were observed in mice, with KRM-II-81 demonstrating antidepressant-like effects in the forced-swim test, although it did not produce such effects in the tail-suspension test. Unlike diazepam, which is a sedative, diazepam did not exhibit any activity in the forced-swim test.

Table 2: Effects of KRM-II-81 and it's analogs in different models of epilepsy

Compound	Models	Species	Activity	Efficacy	References
KRM-II-81	Dissociated cortical neurons	Rat	Yes, suppression of hyper excitation of cortical neurons	Witkin et al., 2018a	
KRM-II-81	Clonic seizure Convulsant, cocaine (COC)	Rat	Yes, Blockade of convulsion	KRM-II-81 efficacious, DZP not	Knutson et al., 2020
KRM-II-81	Clonic seizure-(4-aminopyridine or 4-AP)	Rat	Yes, Blockade of convulsion	KRM-II-81 efficacious, DZP not	Knutson et al., 2020

KRM-II-81	Clonic seizure Strychnine	Rat	Yes, Blockade of convulsion	KRM-II-81 efficacious, DZP not	Knutson et al., 2020
KRM-II-81	Pentylenetetrazol – clonic seizures	Rat	Yes, Blockade of convulsion	KRM-II-81= Diazepam	Knutson et al., 2020; Witkin et al., 2018
KRM-II-81	Electrical seizure provocation models 6Hz stimulation – 44mA	Mouse	Yes	Knutson et al., 2020; Witkin et al., 2018	
KRM-II-81	Electroconvulsive Shock (Electrical seizure provocation model)	Mouse	Yes	Knutson et al., 2020; Witkin et al., 2018	
KRM-II-81	Corneal kindling- (Seizure sensitization)	Mouse	Yes	KRM-II-81> Topiramate	Knutson et al., 2020; Witkin et al., 2018
KRM-II-81	Amygdala kindling ADT (Seizure sensitization)	Rat	Yes	KRM-II-81> Diazepam	Knutson et al., 2020; Witkin et al., 2018
KRM-II-81	Amygdala kindling ADD (Seizure sensitization)	Rat	Yes	KRM-II-81= Diazepam	Knutson et al., 2020; Witkin et al., 2018
KRM-II-81	Amygdala kindling Seizure Severity (Seizure sensitization)	Rat	Yes	KRM-II-81= Diazepam	Knutson et al., 2020; Witkin et al., 2018
KRM-II-81	Mesial temporal lobe epilepsy (Pharmacoresistant epilepsy model)	Mouse	Yes	KRM-II-81> Lamotrigine, Valproate	Witkin et al., 2020
KRM-II-81	Lamotrigine - insensitive kindling (Pharmacoresistant epilepsy model)	Rat	Yes	KRM-II-81> Lamotrigine, Topiramate	Witkin et al., 2020

KRM-II-81	Kainate-induced chronic epilepsy (Pharmacoresistant epilepsy model)	Rat	Yes	KRM-II-81> Lamotrigine, Levetiracetam	Witkin et al., 2020
KRM-II-81	Picrotoxin stimulation (Human epileptic tissue)	Human	Yes	Witkin et al., 2018	
ADT – After-discharge threshold, ADD- After-discharge duration The ligand is in column 1, the model is in column, the organism is in column 3, in column 4the word 'yes' means active, the comparative activity of the ligand is in column 5. These are studies of anticonvulsant activity vs known anticonvulsants.					

The selection of salt for a drug is a crucial aspect during the preformulation phase of drug development, as highlighted by Gardener et al. (2004) and Lipinski et al. (2002). [192,193] Forming a salt version of an ionizable molecule is instrumental in addressing suboptimal physicochemical and/or bio-pharmaceutical properties associated with such molecules, as emphasized by Serajuddin et al. (2007)[194] . Optimal salt selection early in the drug development process can significantly enhance the developability of a compound, and this is facilitated by a well-defined salt screening strategy. Such a strategy involves the assessment of various factors, including crystallinity, hygroscopicity, solubility, stability, purity, polymorphism/hydrate formation, and powder flowability. Additionally, practical considerations such as cost and reaction yield are taken into account (Hawley et al., 2010; Paulekuhn et al., 2013). [195,196] The creation of a salt is widely recognized for its ability to improve the physicochemical and biopharmaceutical properties of compounds, as exemplified by Mukesh et al. (2021)[197] , and it has been demonstrated to enhance compound bioavailability, as shown by Kumar et al. (2018)[198].
To enhance solubility, absorption, and distribution, as well as to facilitate efficient bulk synthesis, a hydrochloride salt was strategically introduced at the 2'-N position of the pyridine ring of KRM-II-81, as outlined by Mian et al. (2022). [199] The synthesis involved treating the free base with

anhydrous hydrochloric acid, resulting in the formation of KRM-II-81. HCl, which was then precipitated and filtered. Confirmation of the monohydrochloride salt was achieved through analysis of X-ray crystallography, 1H NMR, and 13C NMR spectroscopy. Physical characterization and solubility assessments of KRM-II-81. HCl were conducted. Additionally, a comparative pharmacokinetics study was carried out by orally dosing KRM-II-81. HCl and its free base in an anticonvulsant activity study. Both compounds exhibited similar efficacy in vivo against pentylenetetrazole-induced seizures. Oral administration of KRM-II-81. HCl mirrored that of the free base (KRM-II-81), showing comparable brain-to-plasma ratios. High concentrations of both compounds, approximately 1 μM in plasma and 0.5 μM in the brain at Cmax, were observed in rats. Oral dosing in mice significantly prolonged the latency to clonic and tonic convulsions and reduced pentylenetetrazole-induced lethality. The anticonvulsant effects for clonus persisted for at least 8 hours, and the activity of KRM-II-81 and its salt were very similar.

To assess ADME toxicity, a substantial quantity of KRM-II-81 is necessary, prompting the development of an enhanced synthetic pathway by Knutson et al. in 2020[135]. The precursor, HZ-166, was initially synthesized by Li et al. in 2018[11]. Knutson et al. made modifications and improvements at various stages of the synthesis process. The refined method offers several advantages over the previous one, with a crucial enhancement being the replacement of chromatographic purification steps with recrystallization purification in the five synthetic steps for preparing HZ-166. Additionally, the updated method resulted in reduced fewer of side products, shorter processing times, and improved yield. Knutson, Mian, and Sharmin have outlined a method for the large-scale production of both HZ-166 and KRM-II-81 through this newly developed approach.

In the current phase of drug development, the focus has been on designing and investigating new ester bioisosteres to enhance metabolic stability and pharmacological effectiveness[200–202] . While maintaining the key attributes of the lead compound **1** and aiming to prevent ester functionality hydrolysis, several bioisosteres were designed, synthesized, and evaluated by replacing the C(3) ester functional group [203–205]. AS previously mentioned, among these ligands, MP-III-080 and the 1,3-oxazole KRM-II-81 emerged as the most potent analogs, demonstrating improved pharmacokinetic properties in human, mouse, rat, and dog liver microsomes, as compared to the parent compound Hz-166.

Recent research has unveiled that oxazole **2**, administered intraperitoneally at 10 mg/kg in a rat Vogel conflict assay, displayed anxiolytic effects. Furthermore, in a mouse marble burying assay, ligand **3** exhibited significantly reduced marble burying activity at 10 mg/kg, indicative of potent anxiolytic-like effects. Both ligands **2** and **3** demonstrated anxiolytic activity at 30 mg/kg. Importantly, all three α2/3 subtype selective Positive Allosteric Modulators (PAMs) showed minimal or no agonist efficacy at α1-containing $GABA_ARs$, with no sedation or dependence reported.[176,177,182]

Additionally, in a mouse model of acetic acid- and lactic acid-induced pain, ligand **2** displayed potent antinociceptive activity. These findings collectively suggest the need to synthesize and investigate additional bioisosteres of ligand **2** in the pursuit of more potent drug candidates for treating seizures, pain, and anxiety, while avoiding amnesia, sedation, ataxia, or the potential for addiction/dependence.

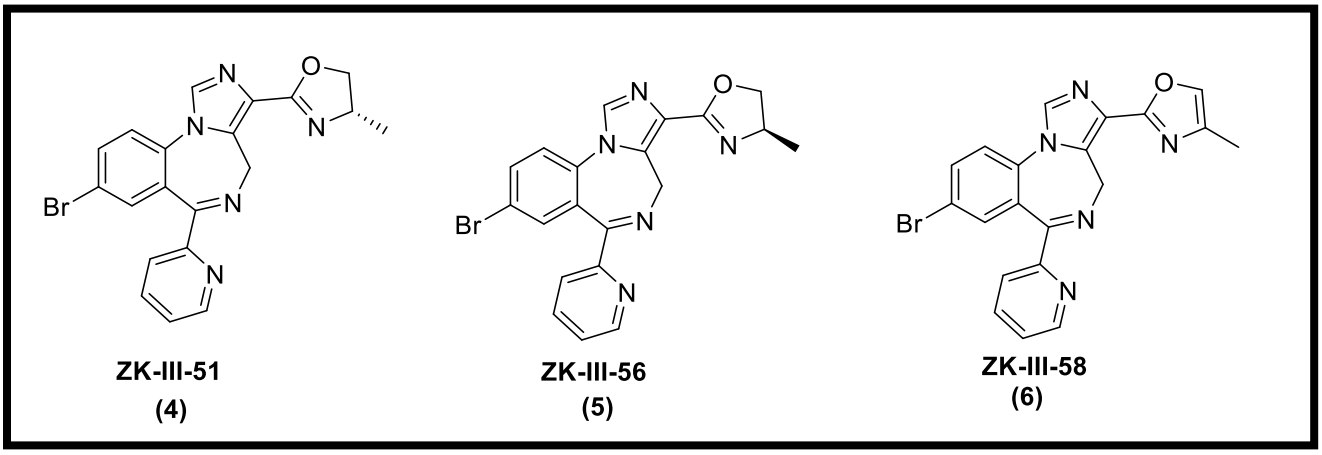
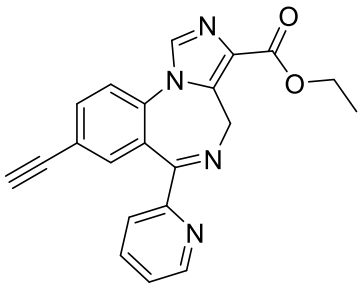
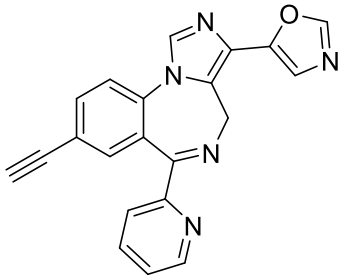
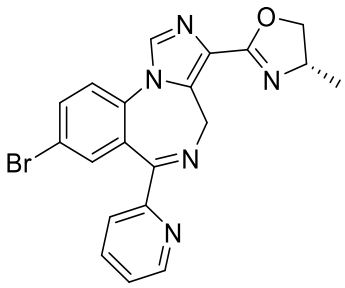
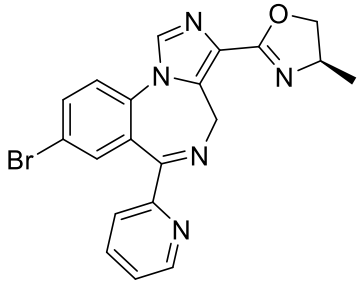


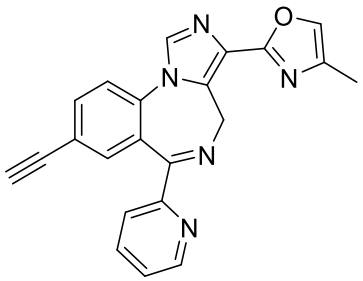
Figure 5. Structures of ZK-III-51, ZK-III-56 and ZK-III-58 made by MdZubair Ahmed Khan.

Newly devised bioisosteres of HZ-166 or direct analogs of KRM-II-81 were synthesized by Md Zubai Ahed Khan, through a comparative study involving molecular docking of KRM-II-81 **Figure 4B** using AutoDock Vina 1.5.6[206] . The molecular docking analyses utilized the recently published CryoEM structure of the human full-length α1β3γ2L $GABA_A$ receptor ion complex with alprazolam (PDB bound: 6HUO) by Masiulis S. et al..[207] The docking scores (binding affinity) of the designed ligands ZK-III-51, ZK-III-56, and ZK-III-58 were determined and presented in **Table 3**. Upon examination, it was observed that the binding poses of most of the ligands in this study closely resembled those of Hz-166 (specific data not shown) and KRM-II-81.

The binding affinities, as indicated by the docking scores, for all these ligands were found to be within a difference of +/- 1 kcal/mol from the lead compound Hz-166 (-9 kcal/mol) and KRM-II-81 (-9.4 kcal/mol). This observation suggests that the new bioisosteres are likely to bind to the receptor complex with a comparable affinity to both the lead compound ester Hz-166 and KRM-II-81.

Table 3. Docking score (computed binding affinity) of bioisosteric ligands

Compound	Structure	Binding affinity (kcal/mol) In the computed model
Hz-166 **(1)**		**-9**
KRM-II-81 **(2)**		**-9.4**
ZK-III-51 **(4)**		**-10**
ZK-III-56 **(5)**		**-9.8**

ZK-III-58 **(6)**		**-7.4**

Benzodiazepines that are substituted with halogens, such as diazepam and alprazolam, engage in a halogen bond interaction with the carbonyl oxygen of the α1His102 amino acid backbone, as evident in the CryoEM structure (**Figure 4A** and **6**). When analyzing the docking of ZK-III-51, ZK-III-56 and ZK-III-58 bioisosteres, a similar halogen bond interaction with the carbonyl oxygen of the α1His102 amino acid backbone is observed. However, it's noteworthy that most docking software, including AutoDock Vina[208], does not incorporate halogen bonding into their scoring functions. Consequently, these programs face challenges in accurately predicting the correct docking score for complexes involving such interactions.

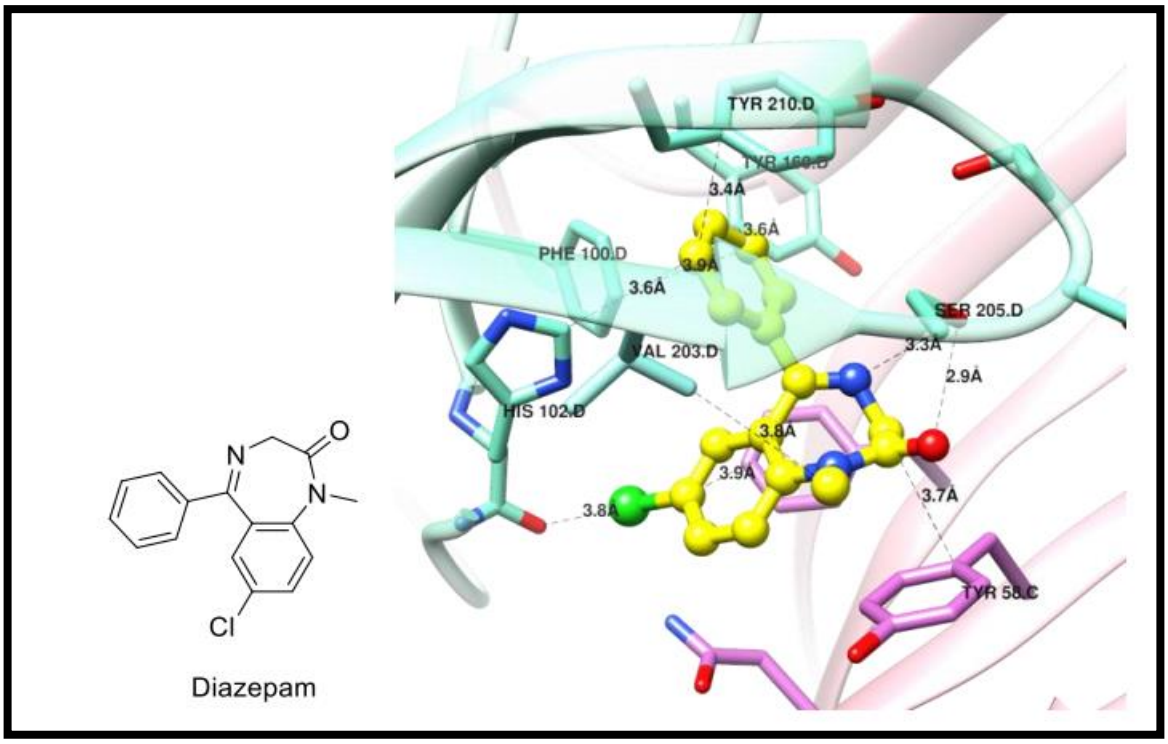
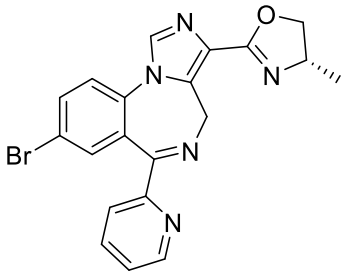
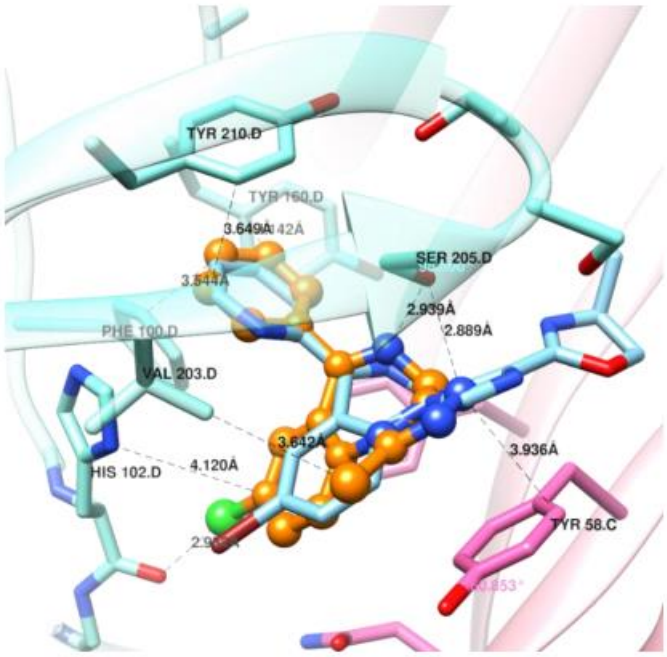


Figure 6. Enlarged cryoEM structure of the human full-length α1β3γ2L $GABA_A$ receptor ion complex with Diazepam (yellow) using AutoDock Vina

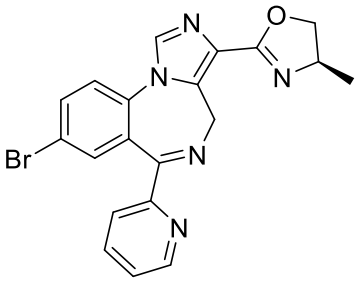
A



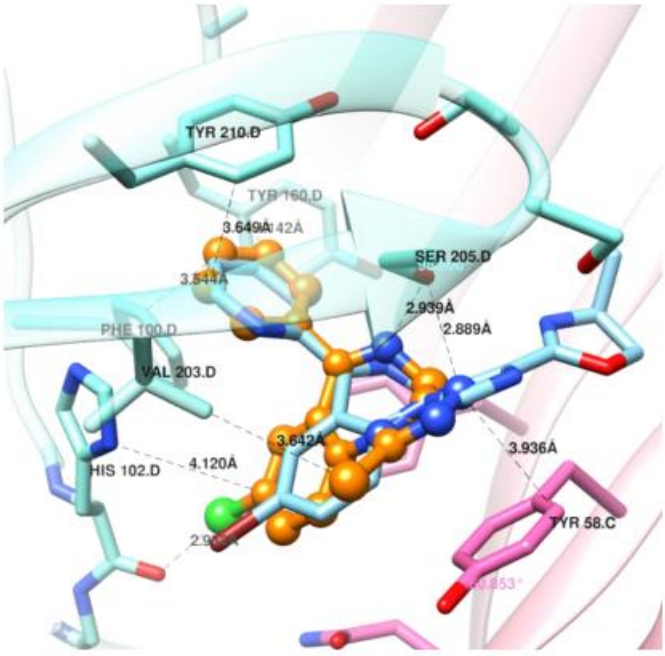
ZK-III-51
(4)



B



ZK-III-56
(5)



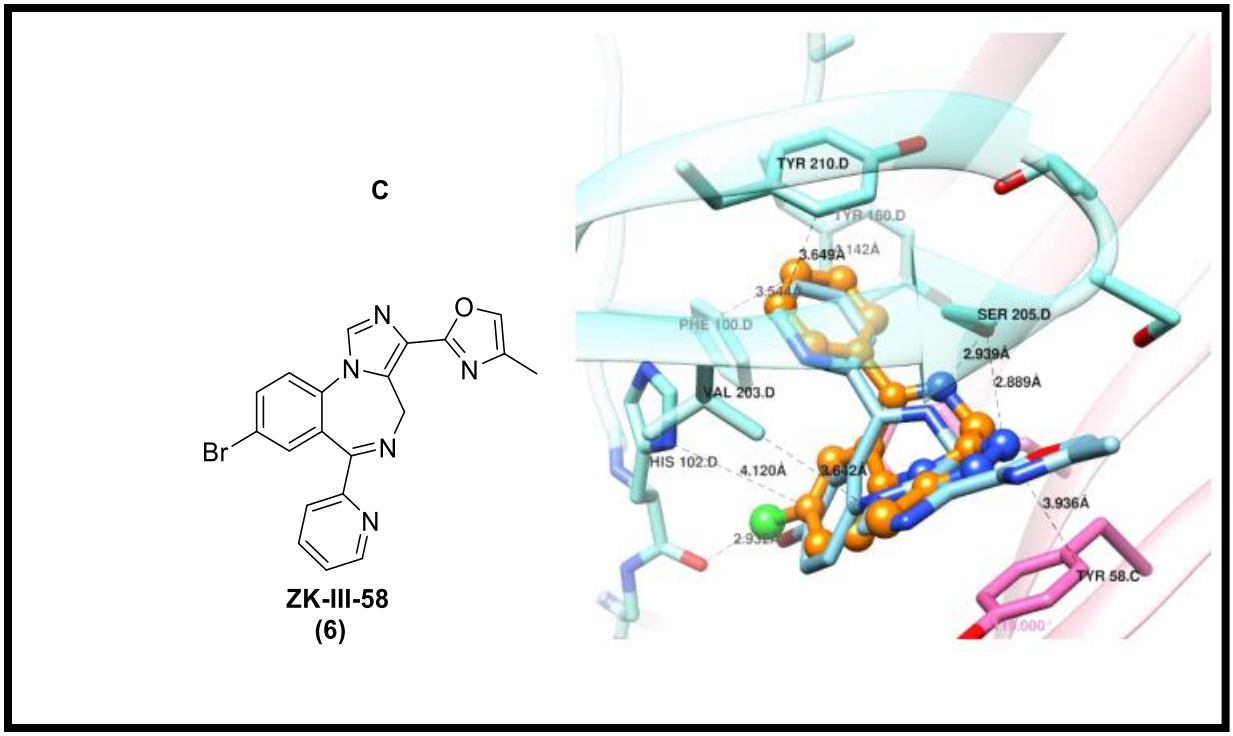


Figure 7. Overlay of the docked conformations of [A. Alprazolam (gold) and 4 (cadet blue) and B. Alprazolam(gold) and 5 (cadet blue)], in the complex with the α1β3γ2L $GABA_A$ receptor 6HUO at the α+β- interface BZ binding site [α1 (represented as chain D, color: aquamriane) and γ2 (represented as chain C, color: orchid)], dashed lines indicate hydrogen bonds.

Consequently, drawing on the ligands previously developed and collaborated with Dr. Lalit Golani, it is anticipated that ligands featuring bromine at position 8 would exhibit a higher binding affinity to the α1β3γ2L $GABA_A$ receptor complex compared to other ligands, including ZK-IV-04, ZK-IV-05, and ZK-IV-07, which were also designed and synthesized by Md Zubair Ahmed Khan (**Figure 8**). This enhanced binding is expected to result in heightened motor side effects, and ligands **7**, **8**, and **9** may potentially induce sedation. The distance of the halogen bond between the bromine atom and the Histidine carbonyl group is 2.93 A° , hence this ligand might be a super agonist.

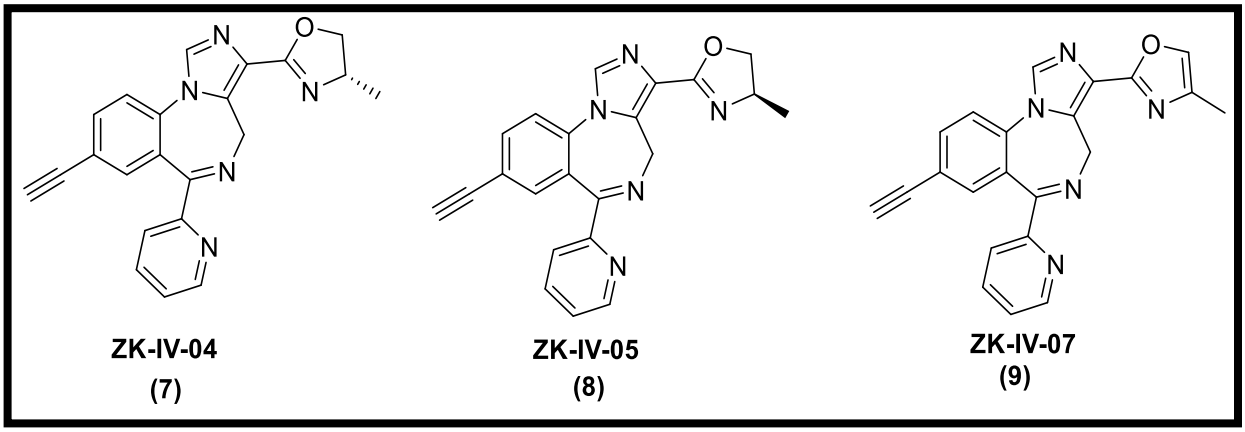


Figure 8. Structures of ZK-IV-04, ZK-IV-05 and ZK-IV-07 made by Md Zubair Ahmed Khan.

Unfortunately, the AutoDock Vina docking process could not accommodate the energy-minimized structures of ZK-IV-04, ZK-IV-05, and ZK-IV-07 due to their inability to fit into the complete α1β3γ2L $GABA_A$ receptor ion complex in humans. This suggests that these ligands are unlikely to exhibit sedative effects associated with the α1 subtype of $GABA_A$Rs. Conversely, it is plausible that they may not bind to BzR, underscoring the significance of their biological implications an probably a lack of activity.

Overall, the ZK series of imidazodiazapines showed potency and for further studies, they needed to be resynthesized.

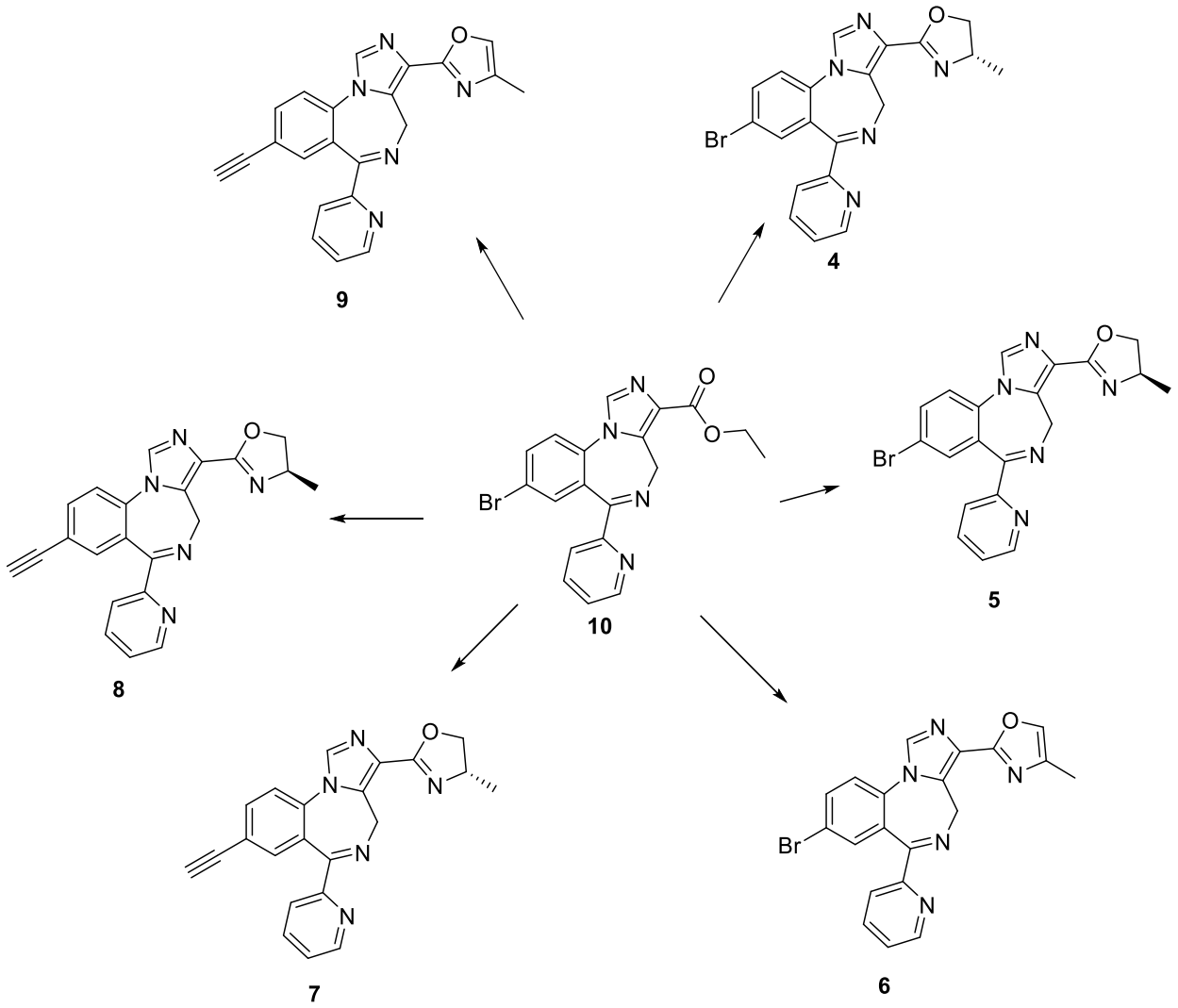


Figure 9. Structures of potential ZK series compounds, which were resynthesized in the present work.

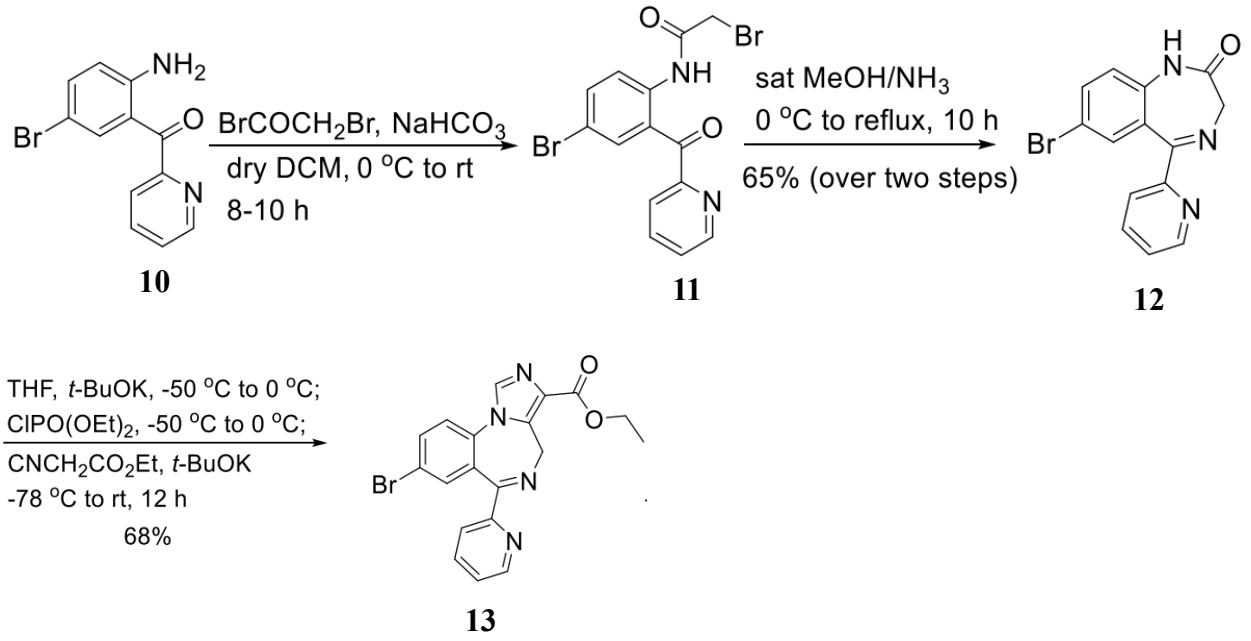
3.2. Chemistry

3.2.1. Synthesis of α2/3-GABA$_A$R Subtype-selective Imidazodiazepines

Due to the therapeutic promise highlighted for KRM-II-81, an enhanced and scalable synthesis was developed. [189,198,209] The initial synthesis of KRM-II-81 followed the procedure outlined by Li et al. 2018 **Scheme 1.** [209] Subsequently, the method was refined, resulting in the synthesis of

the key intermediate to synthesize KRM-II-81 using an improved procedure characterized by reduced reaction time, fewer side products, enhanced crystallization-purification techniques, and improved overall yield.

Scheme 1. Synthesis of the key intermidate by Li et al. 2018[11]

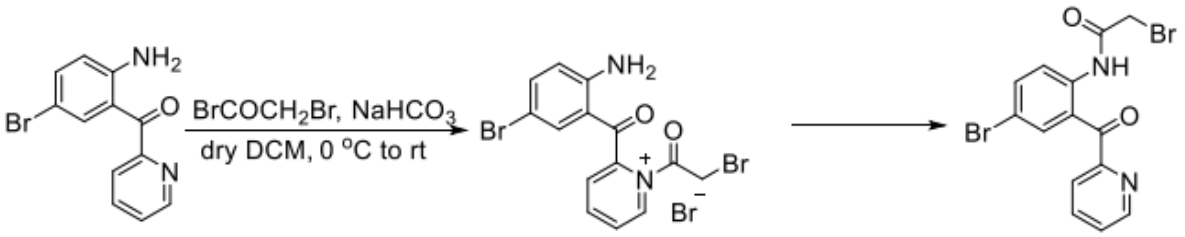


The amine, 2-amino-5-bromo-benzyl-2'-pyridyl ketone **10** was converted into the protected N-acetamide **11** using bromoacetyl bromide in the presence of sodium bicarbonate in anhydrous dichloromethane. To facilitate this process, the reaction mixture was cooled to 0°C before introducing bromoacetyl bromide. The addition of bromoacetyl bromide at this low temperature resulted in the formation of a thick red solid, complicating the stirring of the reaction mixture due to its increased viscosity.

The thick red mass in the reaction mixture was assumed to be the potential formation of a 2'-pyridinum salt of the bromoacetamide, as suggested by an analysis of a plausible reaction

mechanism **Scheme 2**. This viscosity-related agitation problem was effectively addressed in a novel procedure developed by Knutson et al. in 2020[135] **Scheme 4**. In this improved method, the less expensive chloroacetyl chloride replaced bromoacetyl bromide and was added at a temperature range of 25-30°C over a 60-minute period. The reaction was deemed complete (verified by TLC) right after the addition of chloroacetyl chloride. Higher temperatures expedited the reaction rate. The acetamide product **10**, which resulted, was directly utilized for the subsequent step without purification, as per Li et al. in 2019[134]. However, Knutson et al. in 2020[135] opted for purification through ethanol recrystallization of this halo-acetamide to obtain a pure product. Notably, the substitution of chloroacetyl chloride for bromoacetyl bromide did not adversely affect the reaction, yielding a remarkable 99% yield. For reaction scales exceeding 150 g, the use of an overhead stirrer was deemed essential over a magnetic stir bar during this step of large scale synthesis.

Scheme 2. Possible Route to Bromoacetamide via the Pyridium Salt

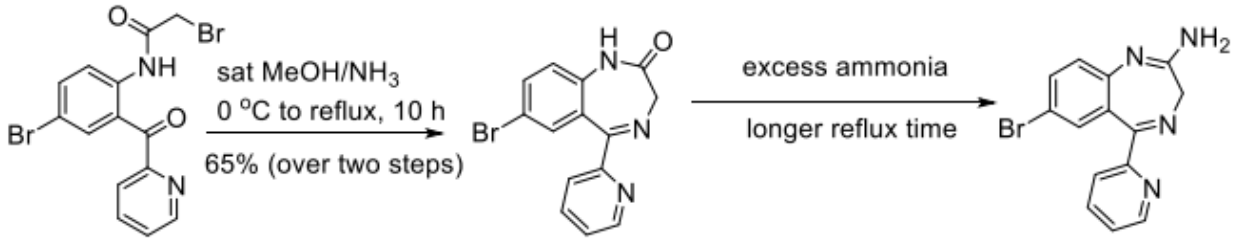


.

The next step of the reaction involved the synthesis of the benzodiazepine, namely 7-bromo-5-(pyridin-2-yl)-1,3-dihydro-2H-benzo[e][1,4]diazepin-2-one **12**. The 2-bromo-N-(4-bromo-2-picolinoylphenyl) acetamide **11** was treated with a saturated ammonia/methanol solution, which resulted in the formation of the benzodiazepine intermediate, as reported by Li et al. in 2019[134].

However, it is noteworthy that the use of the saturated ammonia/methanol system in large-scale quantities was associated with the generation of a β-amino imidate intermediate impurity. This imidate impurity was subsequently isolated and characterized by Knutson et al. in 2020[135].

Scheme 3. Route for the formation of the imidate impurity

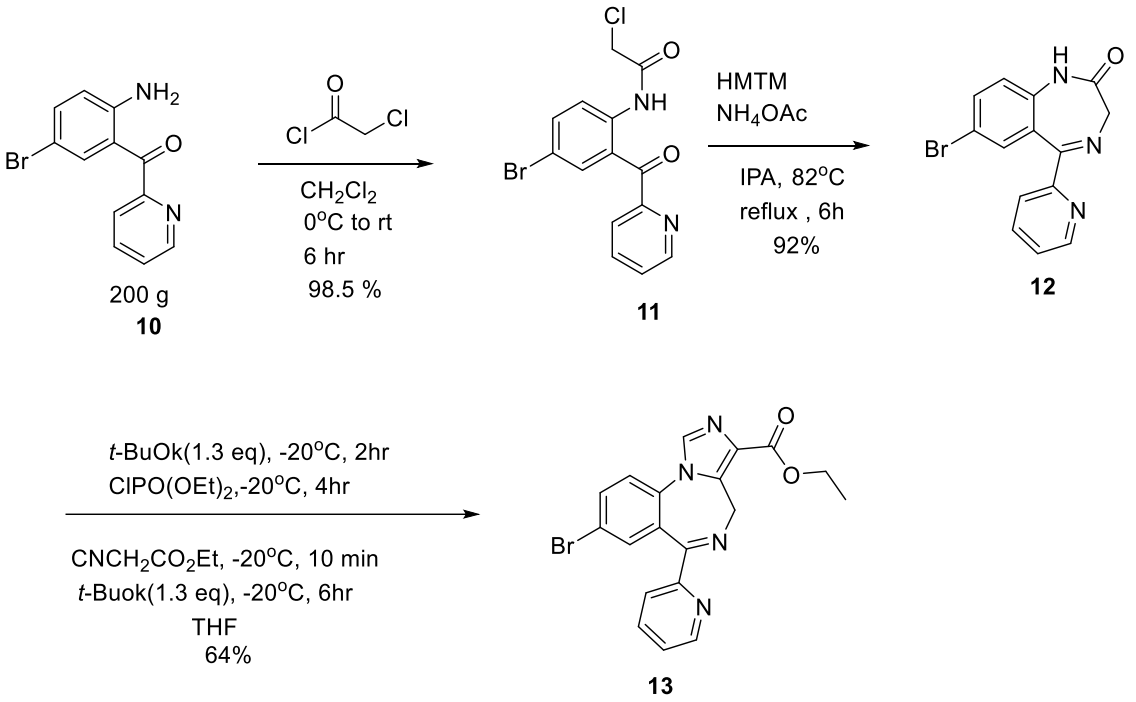


10 **11** **14**

After the findings by Knutson et al., Mian and Sharmin adopted a hexamethylenetetramine (HMTM)-based cyclization, specifically the Delepine-related reaction, in their newly developed method, successfully avoiding the occurrence of any imidate impurity, as reported in Knutson et al. 2020[135]. The third step of the reaction involved the installation of the imidazole top, with several improvements incorporated into this synthetic route. The benzodiazepine intermediate **12** was dissolved in anhydrous THF and treated with 1.5 equivalents of solid potassium t-butoxide. The reaction mixture was cooled to -50°C, then warmed to 0°C, and allow to stir for 30 minutes, following the previous procedure. In contrast, in the new synthetic procedure introduction a solution of 1.3 equivalents of potassium t-butoxide (in THF) at -20°C, with stirring at -20°C to -15°C for 30-40 minutes achieved complete deprotonation of the benzodiazepine N-H function.

Subsequently, diethyl chlorophosphate (1.5 eq) was added to the reaction mixture at -20°C, allowing it to warm up to 0°C and stirring for 2 hours in the old procedure. However, in the new approach, 1.3 equivalents of diethyl chlorophosphate were added dropwise over 15 minutes to the reaction mixture at -20°C, and the mixture was allowed to stir for 2 hours. Confirmed by TLC indicated the consumption of the starting material. Following this, 1.5 equivalents of ethyl isocyanoacetate were added at -78°C **in the previous route**, and it was allowed to reach room temperature, and stirred for 12 hours to yield imidazodiazepine **13**. In the updated route, 1.3 equivalents of ethyl isocyanoacetate were added at -20°C, and it was followed by the addition of 1.3 equivalents of potassium t-butoxide. The mixture was allowed to reach room temperature and stirred for 6 hours, resulting in the formation of imidazodiazepine **13**. Unlike the previous method, which involved column chromatography for purification, the new approach adopted the purification of the crude product by washing it with t-butyl methyl ether, yielding a pure imidazodiazepine product **13**.

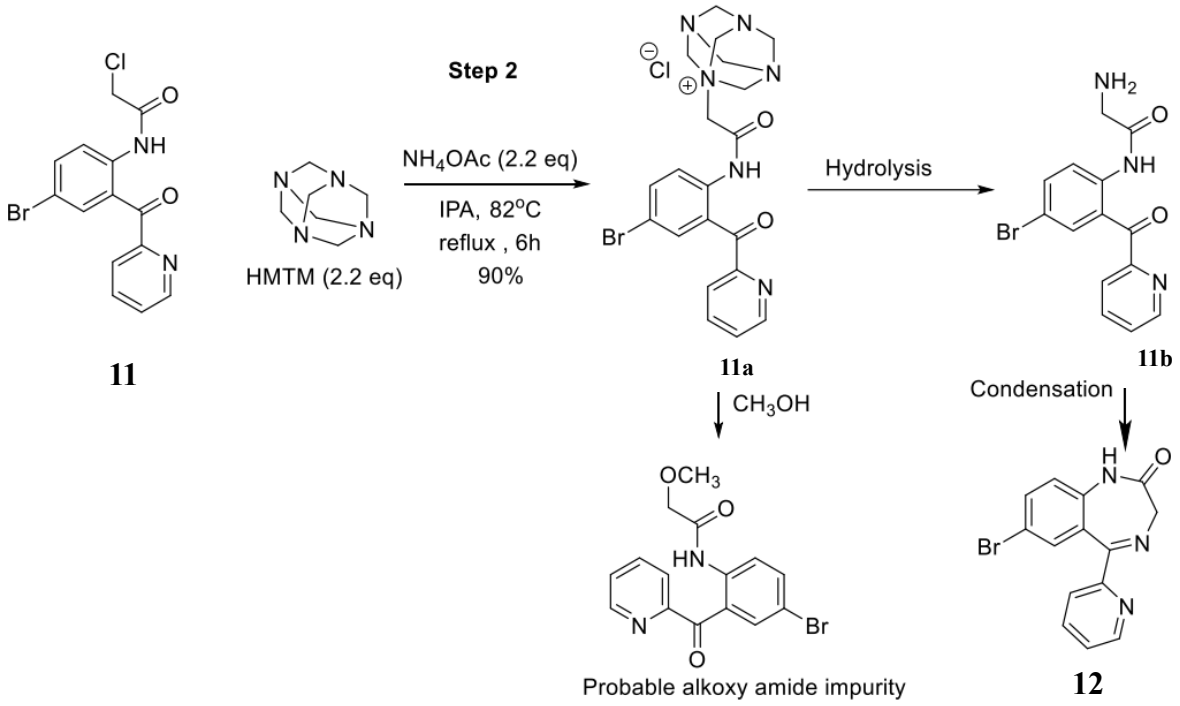
Scheme 4. Synthetic route of the key imidazodiazapine.



A Sonogashira coupling, free of copper, was employed for the imidazodiazepine, leading to the generation of silyl-protected Hz-166, **1**. In the prior method, a less stable trimethyl silyl group was utilized, prompting the adoption of a tri-isopropyl silyl group in the updated approach. The use of tri-isopropyl silyl offered two advantages: it significantly increased the Rf value of the product, facilitating the purification process by separating it distinctly from the bromo starting material. Chromatographic purification was conducted at this step in both methods to remove palladium salts.

Following this, the fluoride-mediated deprotection of the silyl protecting group yielded Hz-166, **1**. In the earlier method, Hz-166 underwent purification through a chromatographic technique, while the new method involved an IPA-water (50:50) wash for compound percipitation.

Scheme 5. Formation of Benzodiazepine by the Delepine- related Reaction[12–14]



Although the new approach demonstrated satisfactory performance, the yields achieved were slightly lower, approximately 60-65%, as compared to those reported in the literature.[14] Further investigation indicated the presence of a minor impurity, identified as a β-alkoxy amide, in the reaction mixture at a level of 5-10%. This impurity was believed to originate from a potential SN2 addition of a primary alcohol (like methanol or ethanol) used as a solvent, displacing the tetramine salt.

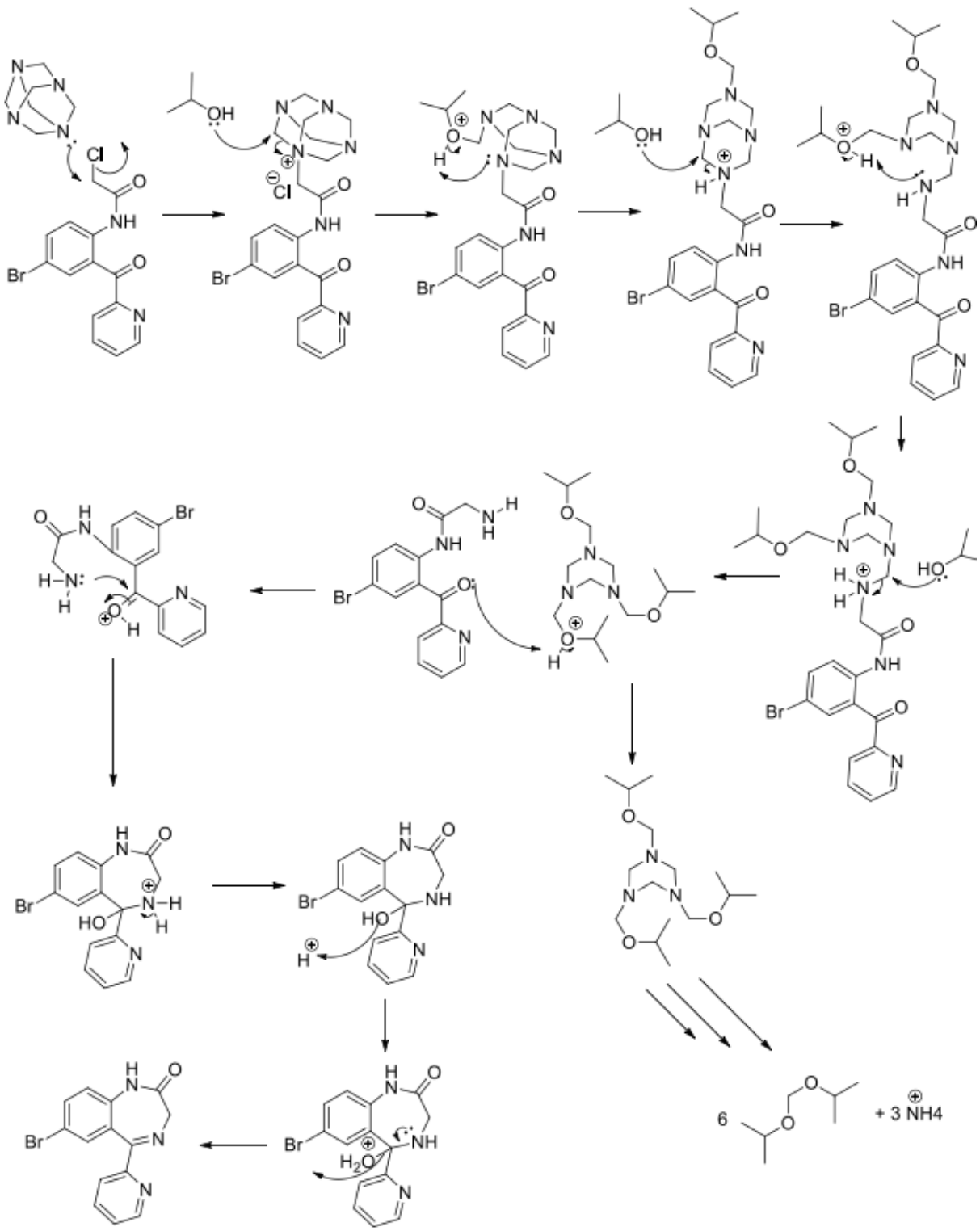
To address the issue of the undesired side reaction leading to the formation of the β-alkoxy amide impurity, a modification was introduced by substituting the primary alcohol solvent (methanol or ethanol) with a secondary alcohol, specifically 2-propanol (IPA). This modification effectively eliminated the side reaction and suppressed formation of the impurity. The switch from methanol

to IPA as the solvent significantly improved the yield, increasing it from the previous range of 60-65% to a higher range of 70-75%. This change in solvent proved to be a valuable modification, bringing about a notable enhancement in the overall efficiency of the synthetic process.

In recent developments led by Sharmin, there has been a specific focus on optimizing the isolation process to further boost the yield. Acknowledging the significance of maximizing the yield of the desired product, our group has directed efforts towards refining techniques employed during the isolation step. Through the implementation of advanced purification methods and meticulous control of parameters in the isolation process, it has become possible to achieve even higher yields than before. This increased attention to the isolation process has played a crucial role in maximizing the overall yield of the synthesis.

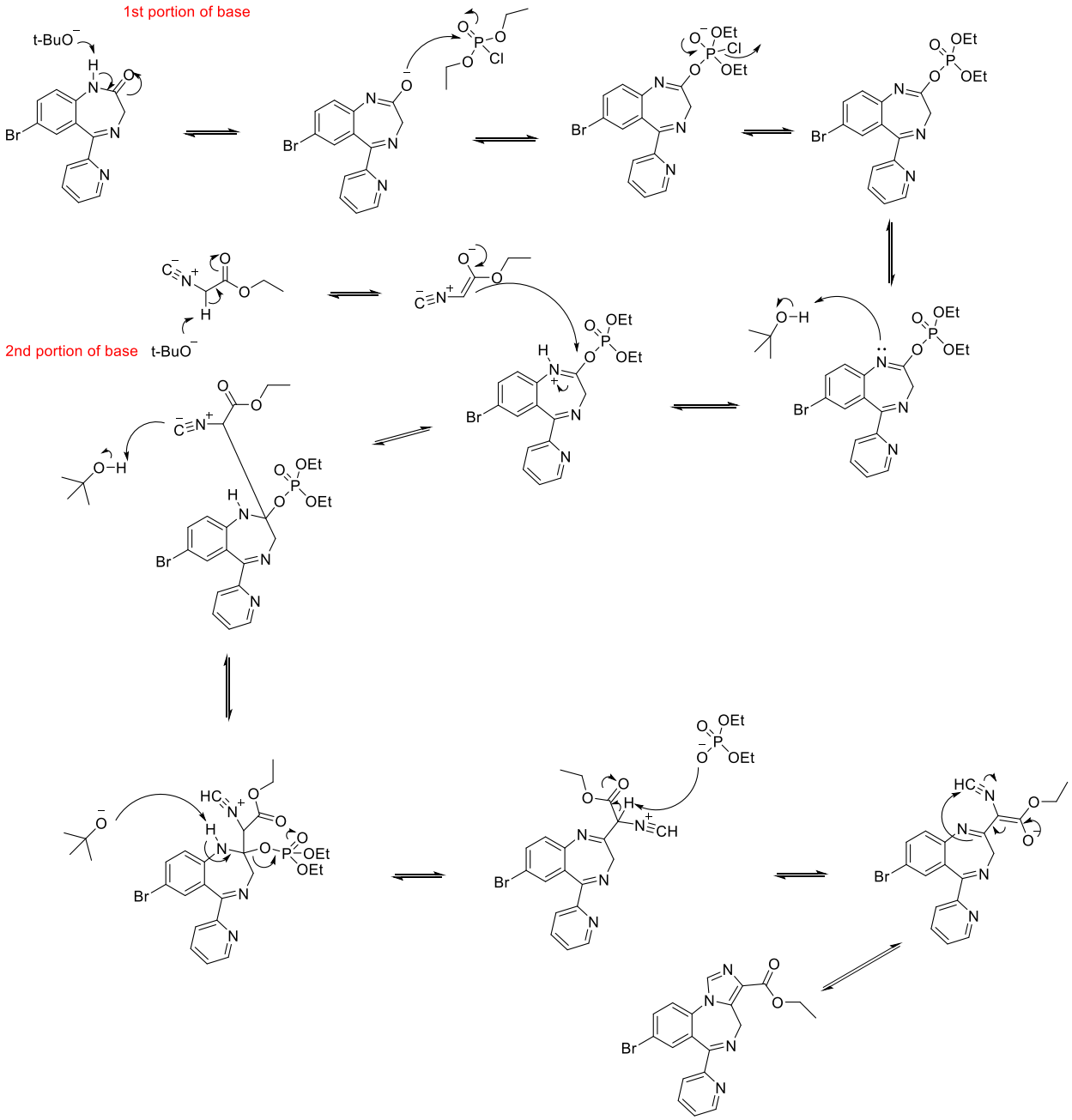
In the previously developed method by Knutson et al. in 2020, [135] the isolation of the benzodiazepine product followed a specific procedure. After completing the reaction, the reaction mixture was cooled to -5 °C using IPA as the cooling agent. Subsequently, the solids were filtered and washed with IPA and water. The filtrate , which was obtained, was washed and kept separate from the initial filtrate. Notably, analysis of the filtrate using HNMR revealed a substantial amount of the desired product. To further utilize this unisolated product, the filtrate was concentrated to approximately 1/6th of its original volume. The resulting concentrated mixture was then heated to 80 °C, and an equal volume of water (compared to the concentrated filtrate) was added dropwise at that temperature. The desired precipitate **13** was collected and dried in a vacuum oven.

Scheme 6. Possible mechanism of the Delepine reaction

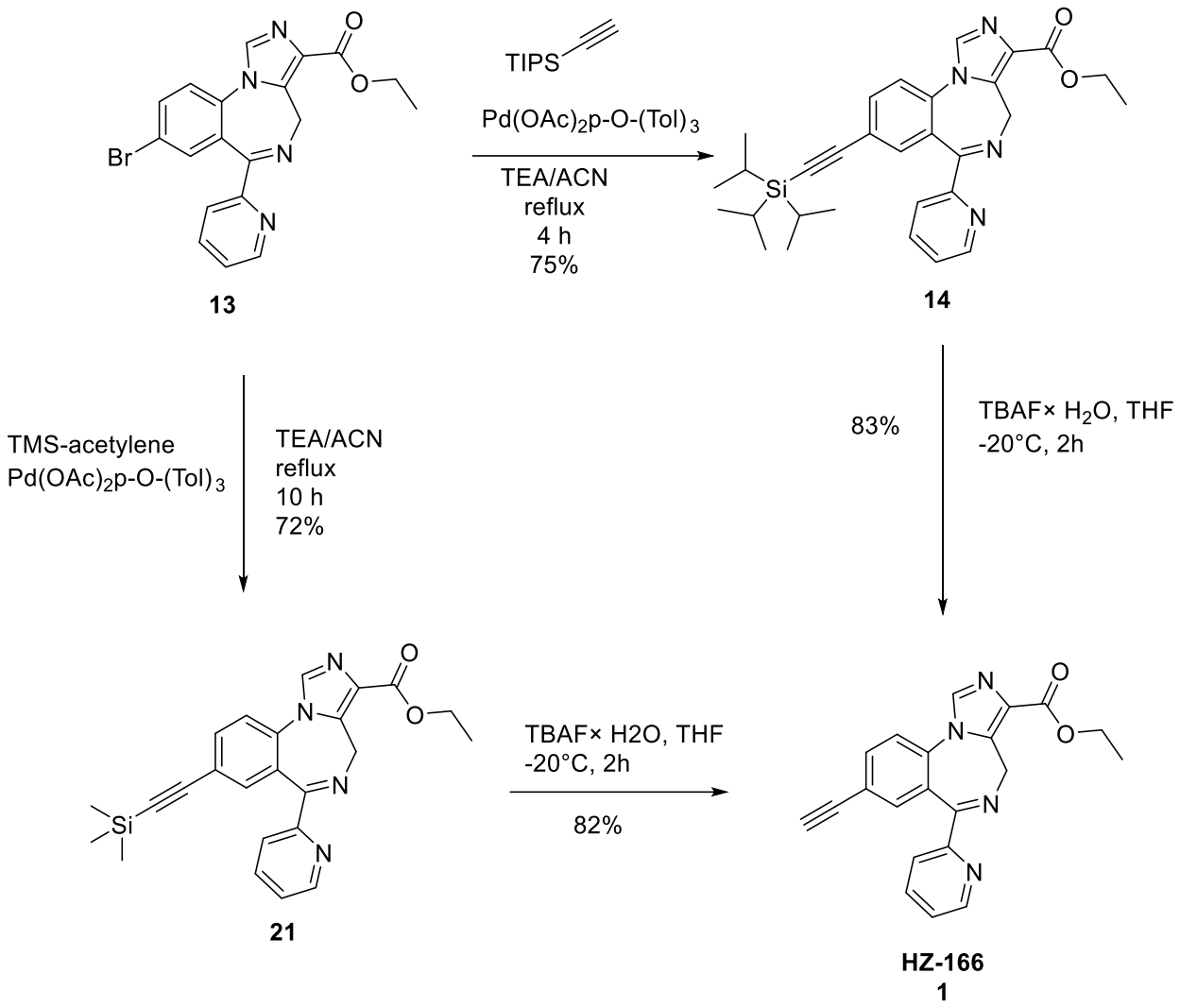


The mechanism of the imidazole formation is illustrated in **Scheme 7**, which offers a visual representation of the potential sequential steps in the formation of the imidazodiazepine. This mechanism serves as a valuable tool for comprehending the reaction pathway, highlighting the key intermediates, and identifying potential keys crucial to the transformation. It provides a detailed insight into the molecular-level intricacies of the imidazole top reaction, aiding in the understanding of the chemical transformations occurring throughout the synthesis of imidazodiazepine.

Scheme 7: Probable mechanism of installation of imidazole top on benzodiazepine



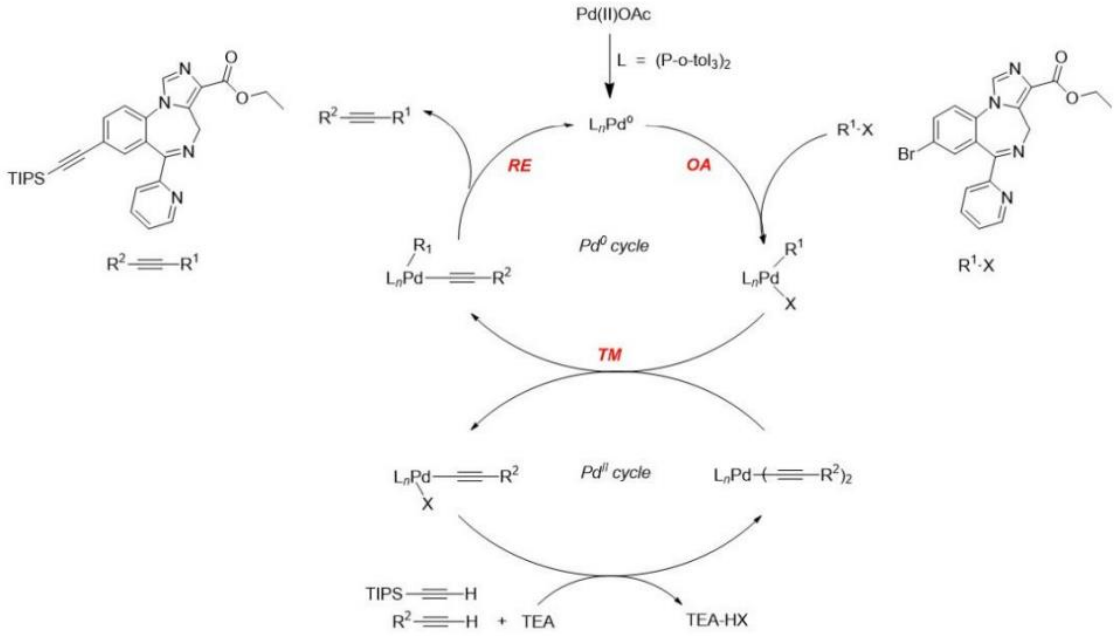
Scheme 8. Synthesis of Hz-166



In the previous approach, a trimethyl silyl group was used to protect the ethynyl intermediate, but it was found to be less stable. In the updated method, a triisopropyl silyl group was employed instead. This modification conferred two advantages. Firstly, the product obtained with the tri-isopropyl silyl group exhibited a significantly higher R_f value in comparison to the starting bromo compound. This facilitated the purification process, enabling easier separation of the product from impurities during chromatography.

Furthermore, chromatographic purification was conducted in both the previous and new methods at this stage. This was undertaken to eliminate palladium salts, commonly used as catalysts in Sonogashira coupling reaction. By stirring the reaction in the air for 30 minutes and then by subjecting the compounds to chromatographic purification, the palladium salts could be effectively removed, ensuring the purity of the final product.

Scheme 9: Possible mechanism for copper free Sonogashira coupling.



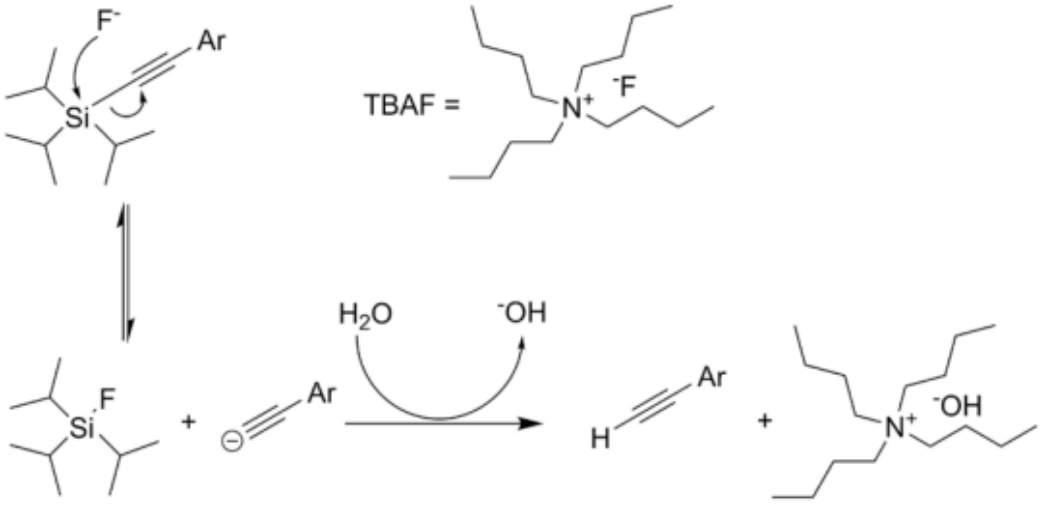
In the next step of the development process, the critical intermediate Hz-166 was derived by deprotecting the TIPS (tri-isopropylsilyl) ethynyl group by using fluoride anion. This deprotection step played an important role in the final formation of Hz-166.

First, the reaction temperature was fine-tuned to ensure the efficient and selective deprotection of the TIPS-acetylene function. By precisely controlling the reaction temperature, the desired deprotection reaction could be achieved in a high yield and minimal side reactions. Additionally,

the prior method, which involved purification by column chromatography, was replaced with precipitation. Precipitation was used as a purification technique for isolating Hz-166. This modification not only streamlined the process but also enhanced the overall efficiency of the synthesis. The solids were then washed with an IPA-water mixture in a 50:50 ratio. This wash solution effectively eliminated impurities and undesired byproducts, which resulted in a purified compound.

The IPA-water wash purification method, which was used, lead to an efficiently purified target, and then to an improved yield and purity of the final product. This alternative purification approach offered advantages over the previous chromatographic purification method, which simplified the overall process and improved the efficiency of the synthesis, as mentioned. The proposed mechanism for the cleavage of the TIPS (tri-isopropylsilyl) group is delineated in **Scheme 10**, providing a step-by-step illustration of the cleavage reaction.

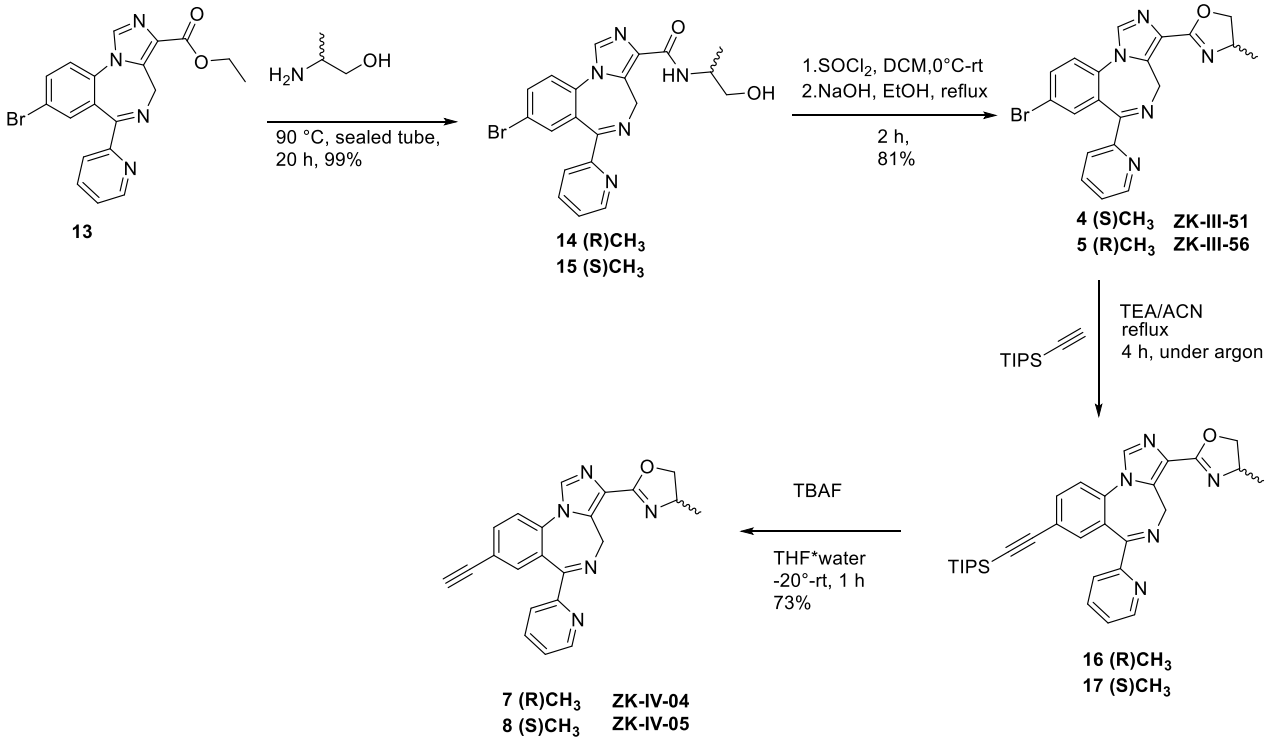
Scheme 10: Possible mechanism for fluoride mediated deprotection of the TIPS group



3.2.2. Synthesis of the ZK oxazolines analogs

In order to make a series of ZK compounds, ester **13** was heated to 90 °C in the presence of various substituted ethanolamines (individually) within a sealed tube. As a result, the α-hydroxy amides **14** and **15** were produced, which were subsequently purified through a combination of a cold-water wash and crystallization, achieving yields ranging from 95% 99%. For the cyclization, the first the α-hydroxy amides **14** and **15** were reacted (individually) with thionyl chloride in dichloromethane to produce α-halo amides. Then, the α-halo amides were heated with sodium hydroxide in ethanol to afford the cyclized five-membered oxazolines **4** and **5**.[147]

Scheme 11. Synthetic route to make oxazolines ZK series.

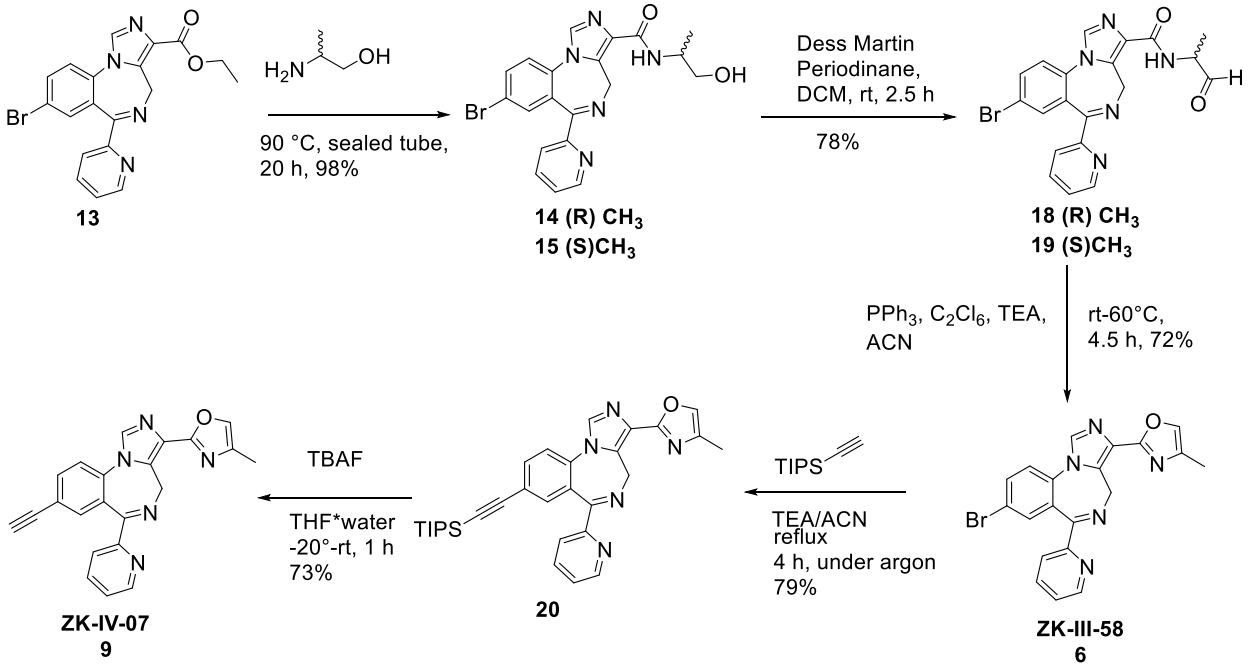


3.2.3. Synthesis of the ZK oxazole analogs

In order to make the next oxazole bioisoesters, the ester **13** was heated to 90 °C with substituted ethanolamines (separately) in a reflux apparatus for a duration of 20 h, which resulted in the formation of α-hydroxy amides **14** and **15**. The products, which were obtained, were purified through a combination of a cold water wash and crystallization, to furnish yields between 95% and 99%.Then, the α-hydroxy amide **14** and **15** were oxidized by treatment with the Dess-Martin periodinane reagent to provide the corresponding α-acylaminoaldehydes **18** and **19**, (individually), which were purified by crystallization in 78% yield. The oxazole (ZK-III-58) **6** was synthesized from the αacylaminoaldehyde **18** or **19**, by employing a cyclodehydration reaction (Robinson–Gabriel synthesis, Scheme 7) in 72% yield.

To obtain oxazole **9** (ZK-IV-07), the imidazodiazepine **6** was subjected to the copper-free Sonogashira coupling to provide the triisopropylsilyl (TIPS) protected ethynyl **20**. Subsequently, the deprotection of the TIPS group was performed by using fluoride anion, which resulted in the formation of the 8-ethynyl imidazodiazepines, the target compound **ZK-IV-07** (**9**), with a yield of 73%.

Scheme 12. Synthetic route to make oxazoles in the ZK series.

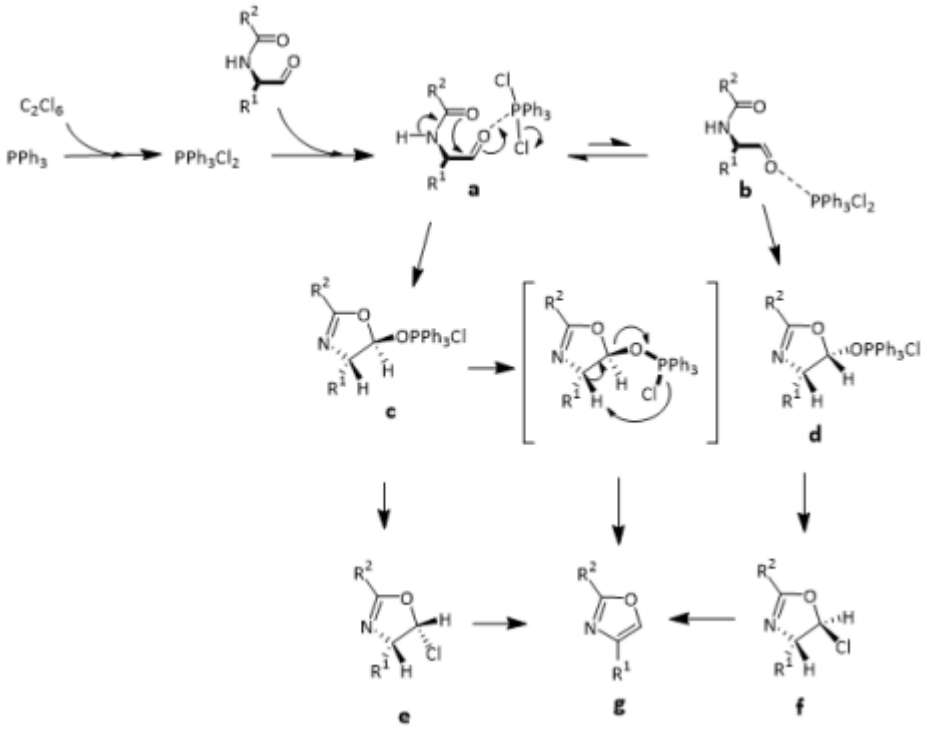


The mechanism for the formation of this oxazole follows several steps (**Scheme 13**). Initially, the reaction involves the interaction of triphenylphosphine dichloride or triphenyl phosphonium dichloride with hexachloroethane, which resulted in the formation of the triphenylphosphine dichloride salt. The activation of the aldehyde by the phosphine reagent sets in motion an intramolecular 5-exo-trig cyclization. Stereoinduction by R1 may promote conformation **a**,

resulting in **c**, which can directly advance to the oxazole through syn elimination, facilitated by a cyclic six-membered transition state.

Alternatively, this intermediate may undergo oxyphosphorane decomposition with inversion, giving rise to the transient minor chloro-oxazoline adduct **e**. In the presence of a base, **e** readily transforms into oxazole **g** through anti elimination (E2). The cyclization from an alternate conformation **b** yields intermediate **d**, lacking the option of syn elimination via the cyclic transition state. Decomposition with inversion of **d** to the halide produces the major, long-lived adduct, **f**. This intermediate then progresses through syn elimination of HCl to ultimately yield the final oxazole **g**.

Scheme 13. Proposed mechanism for the oxazole forming reaction for ZK-III-58.



3.3 Biology of KRM-II-81 analogs

3.3.1. Rotarod studies of novel compounds in female CFW mice via oral administration at various doses.

The rotarod studies of the ZK ligands were carried out in female Charles River Swiss Webster mice at the University of Wisconsin-Milwaukee, performed by Nick Zahn and Michelle Meyer in Dr. Arnold's laboratory. The primary aim of this experiment was to test the compounds for potential undesired motor side effects, which is believed to be α1-mediated and cannot be tolerated in the proposed antiepileptic drugs. Prior to the rotarod test, mice were trained on a rotating rod until they could maintain balance for three consecutive 3-minute sessions. Diazepam (1) served as the control. In the first study, the test ligands were orally administered to the mice at various doses of 40 mg/kg via gavage, after which the mice were placed on the rotating rod for a maximum of 3 minutes. A 2% hydroxypropyl methylcellulose solution served as the vehicle in this experiment. In addition to monitoring for sedation, the mice were also observed for ataxia, loss of rightening response, and tremors as indicators of undesired central nervous system effects. Both oxazolines ZK-III-51 (**4**) and ZK-III-56 (**5**) did not show sedation at 40 mg/kg dose in contrast to the control diazepam (5mg/kg) as shown in **Figure 10**. The oxazole ZK-III-58 (**6**) slightly showed sedation at the same dose due to its efficacy especially at the α1-$GABA_AR$ subtype or perhaps the α5 subtype. **Remember in the modeling, ZK-III-58 bound to the α1β3γ2 ion channel with a binding constant of -7.4, indicating tight binding at α1 and sedation.**

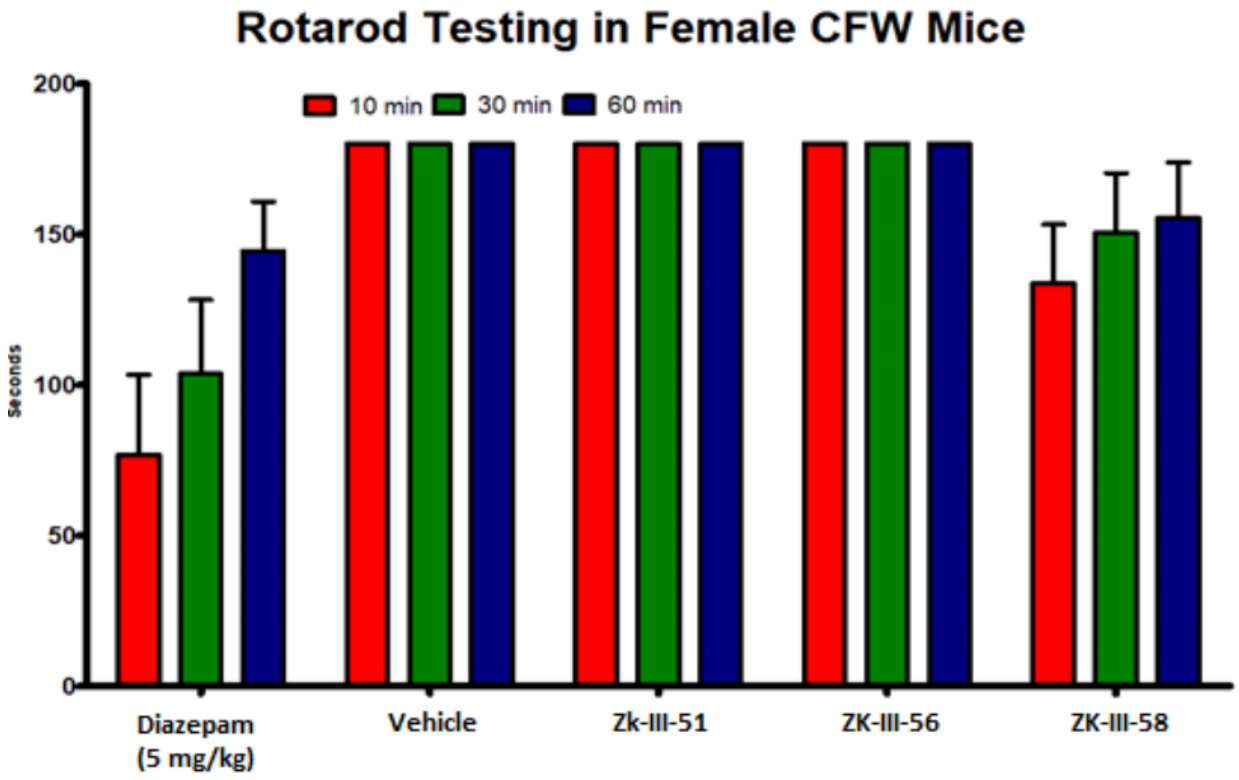


Figure 10. Effect of ligands ZK-III-51 (4), ZK-III-56 (5) and ZK-III-58 (7) on sensorimotor coordination. Mice were placed on the rotarod at three separate time points of 10, 30, and 60 minutes after each oral gavage drug administration at 40 mg/kg. Their performance on the rotarod for 3 minutes was recorded and analyzed. After a second fall, it would be considered a failure, and that time point would be recorded. ZK-III-58 (7) shows sedation.

Since some of the ZK series showed no sedation or ataxia, nor loss of righting reflex, as compared to the control diazepam, they were tested in the same study but this time at a higher dose. The oxazoline ZK-III-51(**4**) did not show any sedation or any other undesired CNS effects at 120 mg/kg (**Figure 11**). Although ZK-III-56 (**5**) did not show any sedation in a previous study at 40 mg/kg, it did this time at the higher dose of 120 mg/kg (see **Figure 11**). The oxazole ZK-III-58 (**6**) was tested with the same dose of 40 mg/kg, but this time it did not show any undesired CNS effects. This may

be an antifact for by this time the mice might have learned the rotarod too well. Certainlly at a higher dose (via modeling) you would expect sedation from ZK-III-58.

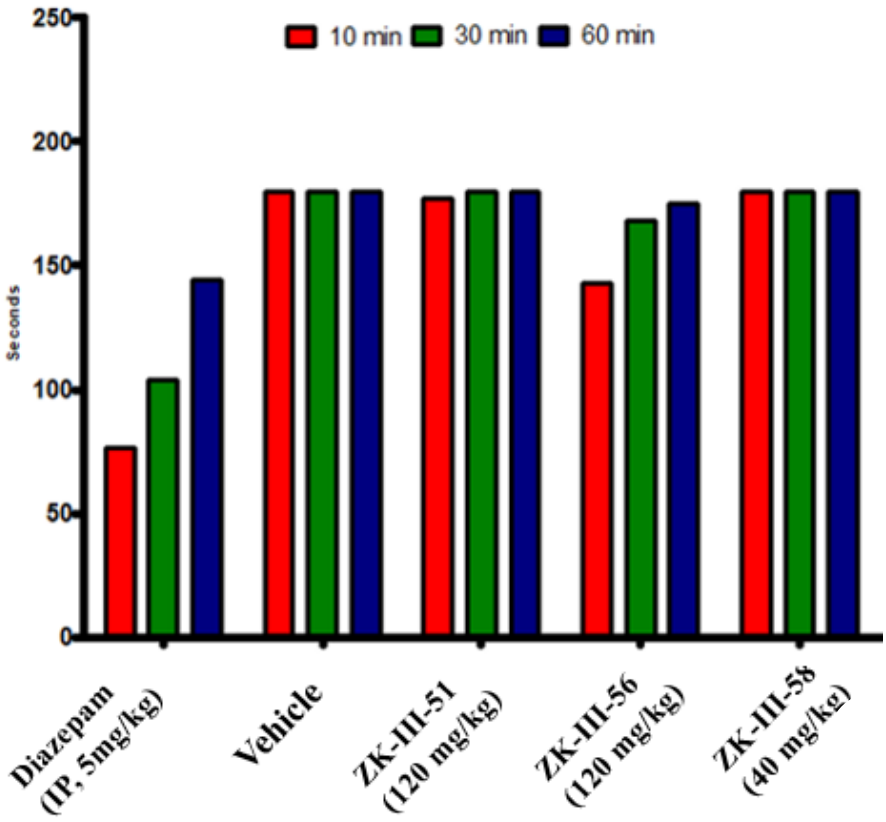


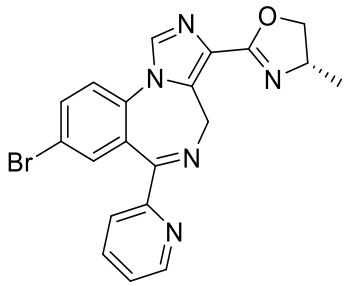
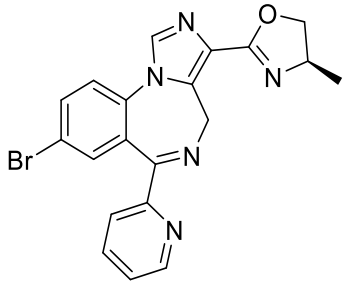
Figure 11. Rotarod studies ZK-III-51 (4), ZK-III-56 (5) and ZK-III-58 (6) at 120, 120, and 40 mg/kg dose respectively. Diazepam is the control. Confidential and unpublished data.

3.3.2. Cytotoxicity studies of novel analogs (by Michelle Meyer and Anika Tylek in Dr. Arnold's laboratory, UWM).

The necessary resynthesized ligands in my work in the ZK series were evaluated for cytotoxicity in HEK 293 cell lines (human embryonic kidney cells). The 3-dibutylamino-1-(4- hexyl-phenyl)-propan-1-one was used as a positive control at 150 μM; all cells were killed at this concentration

with this reagent. For all the oxazoles and oxazoline analogs of KRM-II-81 (**2**) discussed herein, the IC_{50} was >300 μM for cytotoxicity in HEK 293 cells (**Table 4**). It is obvious from the data in **Table 4**, that the ligands tested so far and discussed herein: the methyl substituted non-aromatic (oxazolines) ZK-III-51 (**4**) and ZK-III-56 (**5**), are both were are non-toxic in this HEK 293 cell line.

Table 4. Cytotoxicity studies of ligands in HEK 293 cell lines. (Unpublished data)

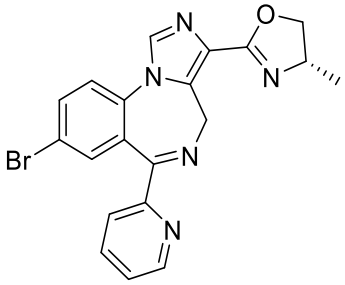
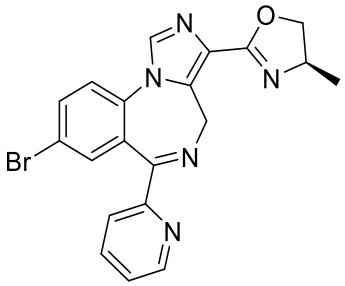
Compound number	**Compound code**	**Structure**	**Toxicity in HEK293 (IC_{50})**
4	**ZK-III-51**		**>400**
5	**ZK-III-56**		**>400**

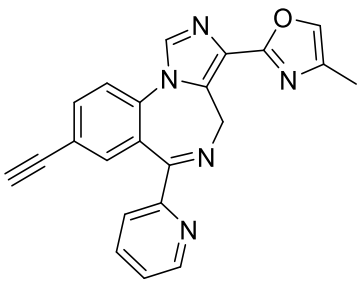
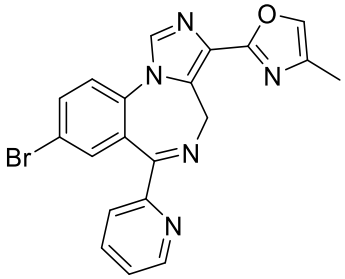
3.3.3. Summary of the primary and secondary binding affinity of novel ligands in the Psychoactive Drug Screening Program (PDSP) of NIMH run by Dr. Bryan Roth (UNC) in the 46 receptor and HERG assays and over seen by Dr. Jamie Driscoll (Po) at NIMH.

The novel ligands and potential intermediates synthesized were screened in primary and secondary binding screenings in the 46-receptor panel, including the HERG channel, PBR (translocator protein, TPSO), and ion channels. The National Institute of Mental Health Psychoactive Drug Screening Program (NIMH PDSP) conducted these screenings, and all PDSP data used in this study were generously provided by NIMH (PDSP), Dr. Bryan Roth, and Estela Lopez. Receptors that were cloned and expressed were executed in HEK-293 cells during the screening process. The screening protocol followed the published guidelines (details available in Roth, B.L., 2018, ASSAY PROTOCOL BOOK - Version III [WWW Document]. National Institute of Mental Health Psychoactive Drug Screening Program (NIMH PDSP), URL: University of North Carolina at Chapel Hill [unc.edu]). Generally, investigational compounds were screened at a single concentration of 10 μM in quadruplicate in 96-well plates in the primary screen. Compounds demonstrating at least 50% inhibition at this concentration in the primary screen were identified for further investigation in secondary radioligand binding assays. The aim of the secondary radioligand binding was to identify the equilibrium binding affinity at specific targets. In the presence or absence of 10 μM of the relevant reference compound, the affinities for total binding ([ref compound 3H]-flunitrazepam) and nonspecific binding (reference compound: DZP) were determined. The comprehensive summary of both primary and secondary binding outcomes is presented in Table 5. Further details regarding the PDSP binding results of all analogs and potential intermediates can be found in the Appendix herein. The inhibition of binding in primary and secondary receptor binding assays is shown in **Table 5**. Those receptors for which displacement

was >50% at 10 micromolar are shown out of the 47 receptors screened. All the KRM-II-81 analogs studied were free of HERG affinity (>100 mM). All of the ligands bound to the benzodiazepine binding site (BZP) of $GABA_AR$s with potencies that ranged in K_i values from 25 to 808 nM. The selectivity of the compounds for the benzodiazepine site on the $GABA_AR$ over the other binding sites ranged from 51 to 80 or greater.

Table 5. Receptor binding profile of KRM-II-81 analogs. (Unpublished data)

Compound	Structure	Receptor	Primary (mean% inhibition)	Secondary (K_i in nM)	Fold selectivity
ZK-III-51 **(4)**		BZP	87.5	669.27	---
		5-HT1A	51.9	3806.2	5.7
		KOR	67 .2	1393.5	2.1
ZK-III-56 **(5)**		BZR	87.7	581.03	---
		KOR	68.3	1751.5	3.0
ZK-IV-07		BZP	87.8	351.48	---

(9)		H2	54.8	>10000	>28.5
		5-HT2C	71.1	5381.5	15.3
		PBR	62.6	721.11	2.0
ZK-III-58 **(6)**		BZP	86.3	394.64	---
		KOR	83.1	2134.0	5.4
		V2	60.2	>10,000	>25.3

Any binding in the secondary screen >500 nM is considered weak affinity.

Except for ZK-IV-07, the compounds exhibited some affinity for the kappa opioid receptor (KOR), which was the receptor most shared in common with BZP binding. The relationship of KOR binding to BZP receptor binding is shown in **Figure 12**. Compounds displayed potency groupings with 3 compounds < 1000 nM K_i and the other compounds > 1000 nM K_i at KORs. In all cases, the ethynyl compound was less potent than its direct bromine analog at KORs. Notably, KRM-II-81 (**2**) and ZK-IV-07 (**9**), both ethynyl-substituted compounds, had Ki values > 10,000 nM. Enantiomeric comparisons revealed that the S isomer was less potent than the R isomer at KOR (ZK-III-51 (**4**) vs ZK-III-56 (**5**)).

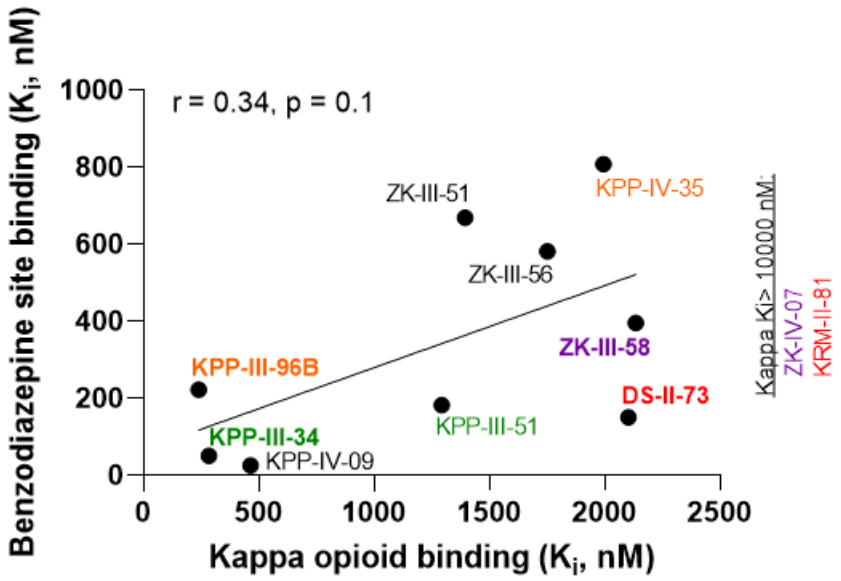


Figure 12. Relationship of potencies of compounds to bind benzodiazepine receptors vs. kappa opioid receptors. Direct structural analogs are shown in matching colors; non-structurally related analogs are in black. Bold = Bromine analog; non-Bold = Ethynyl analog. Only the 9 compounds shown on the regression line were used for computing the linear regression. (Unpublished data)

3.3.4. Effects of ZK series in the pentylenetetrazol (PTZ) seizure model by Dr. Witkin, and Dr. Ping (Indiana University School of Medicine).

The KRM-II-81(**2**) analogs were screened in the pentylenetetrazol seizure model by Dr. Jeffrey Witkin and coworkers (Indiana University School of Medicine, IN). Clonic and tonic seizures were induced in the mice (total number = 6) by subcutaneous injection of PTZ (75 mg/kg). The pentylenetetrazole (PTZ) was dissolved in 0.9% saline. This is a PTZ dose that causes convulsions in >90% of the mice. When given orally at 10 mg/kg, 2 h prior to PTZ, some compounds significantly attenuated clonic and/or tonic seizures induced by PTZ (**Figure 13**). Analysis of effects of all compounds revealed a significant effect of compound on clonus ($F_{7,53}$ = 19.4, P <

0.0001) and on tonus ($F_{7,43}$ = 8.0, P < 0.0001). In the clonic seizure (**Figure 13, left**), ZK-IV-07 (**9**) exhibited a great latency to clonic seizure. On the other hand in the tonic seizure (**Figure 13, right**), most of the ZK series ligands showed significant activity against tonic seizures, specifically ZK-IV-07 (**9**) and ZK-III-56 (**5**). In addition, the compounds that significantly attenuated tonic seizures also significantly prevented PTZ-induced lethality (**Table 6**). Another compound, ZK-III-58 (**6**), was also active against lethality although it did not significantly increase seizure thresholds.

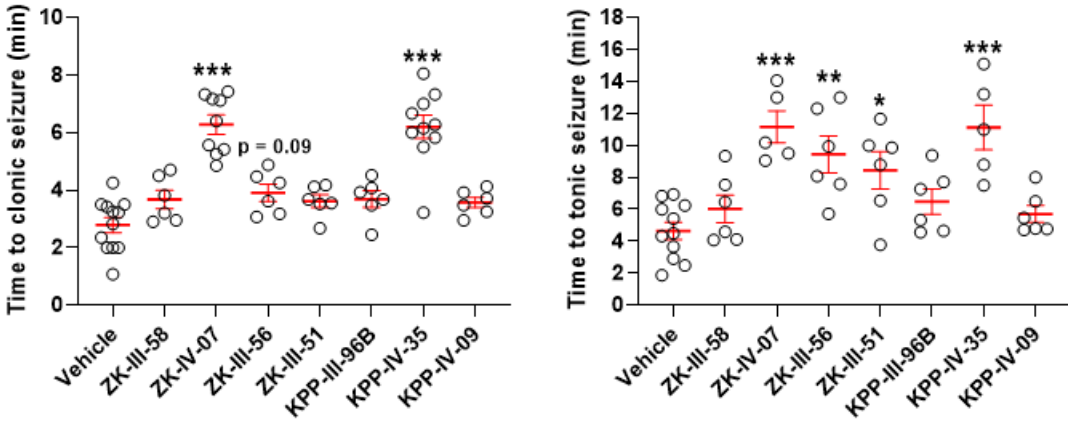
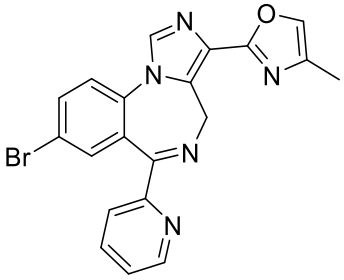
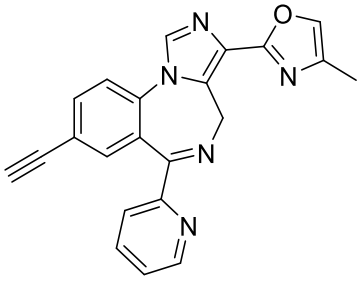


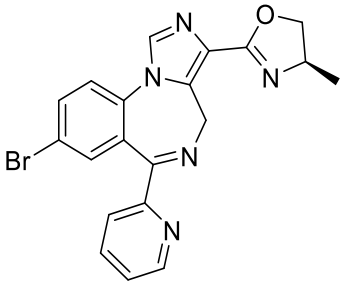
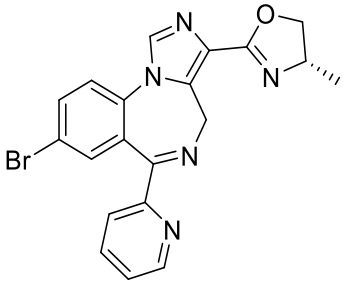
Figure 13. Effects of compounds (p.o., 2 h prior) on clonic (left) and tonic (right) seizures induced by PTZ (75 mg/kg, s.c.). The latency to exhibit convulsions are shown for each animal tested. Means and S.E.M. of those data are shown for each compound as a horizontal red line and error bars. * P < 0.05; ** P < 0.01; *** P < 0.001 compared to vehicle values by Dunnett's test. (Unpublished data)

3.3.5. Protection against lethality by oral administration of KRM-II-81 analogs against PTZ (s.c) (75 mg/kg) induced seizures in mice (data source: Dr. Jeffrey Witkin and coworker, Indiana University School of Medicine).

In the PTZ induced seizure model, all mice were protected against lethality (total 6 and 9) by oral administration of ZK-III-58 (**6**), ZK-IV-07 (**9**), ZK-III-56 (**5**) and ZK-III-51 (**4**) at the lower dose of 10 mg/kg (**Table 6**). From the PTZ model and lethality observations in mice, it is clear that all ligands were found to have oral antiepileptic activity in mice.

Table 6. Protection against lethality induced by 75 mg/kg PTZ (s.c.) after oral administration (60 min prior) of test compounds in male, C57BL/6N mice.

Compound	Structure	Lethality
Vehicle		**8/13**
ZK-III-58 **(6)**		**0/6 ***
ZK-IV-07 **(9)**		**0/9 ****

ZK-III-56 **(5)**		**0/6 ***
ZK-III-51 **(4)**		**0/6 ***

0/6 died in this assay.

3.3.6. In-vivo pharmacokinetic (PK) study of KRM-II-81 analogs

The in-vivo pharmacokinetic study of the test ligands was conducted by Dr. Savic and coworkers (Serbia) following the published procedure.[210,211] The neurophamacokinetic studies of the novel investigational compounds was carried out in male Sprague Dawley adult rats (280-330 g) to obtain the pharmacokinetic profiles of the compounds in plasma and brain. Each test compound was administered orally at the dose of 2.0 mg/kg (concentration of 0.4 mg/mL in 0.25% methyl cellulose solution). This assay was done by the cassette method. T1/2 indicated the stability of the compounds in plasma. The time-dependent systemic distribution of these ligands is shown in **Figure 14-17**. The pharmakokinetics was also improved, as hypothesized, while designing the compounds by replacing the ester functional group of the earlier lead compound HZ-166 (**1**) with the metabolically more stable oxazoles and oxazolines analogs discussed above.

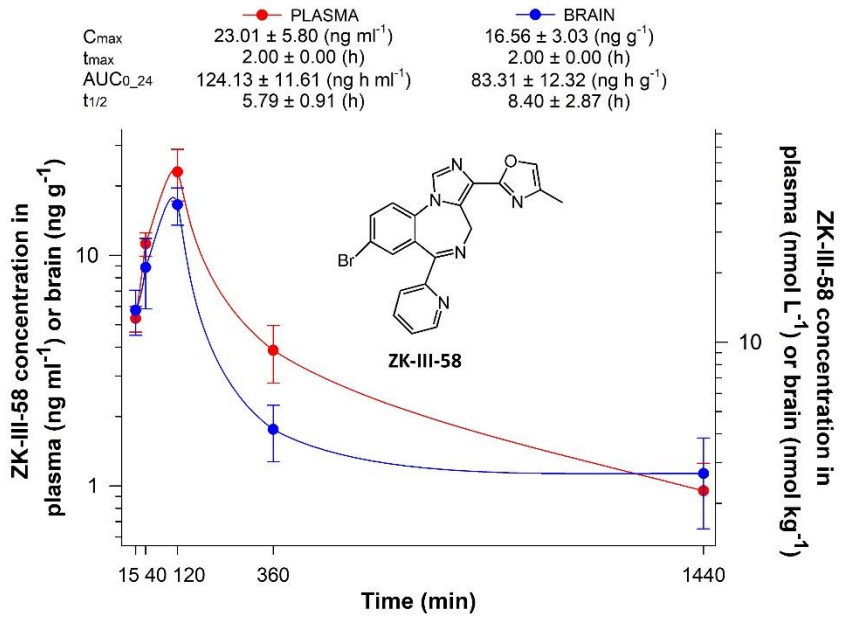


Figure 14. Pharmacokinetics of ZK-III-58 in plasma and brain after oral administration of 2.0 mg/kg in rats. Each point represents the mean ± standard error of the mean in three rats. AUC: area under the curve from 0 -24 h; C_{max}: maximal concentration achieved; T_{max}: time of maximum concentration; $t_{1/2}$ - terminal elimination half-life. (Unpublished data)

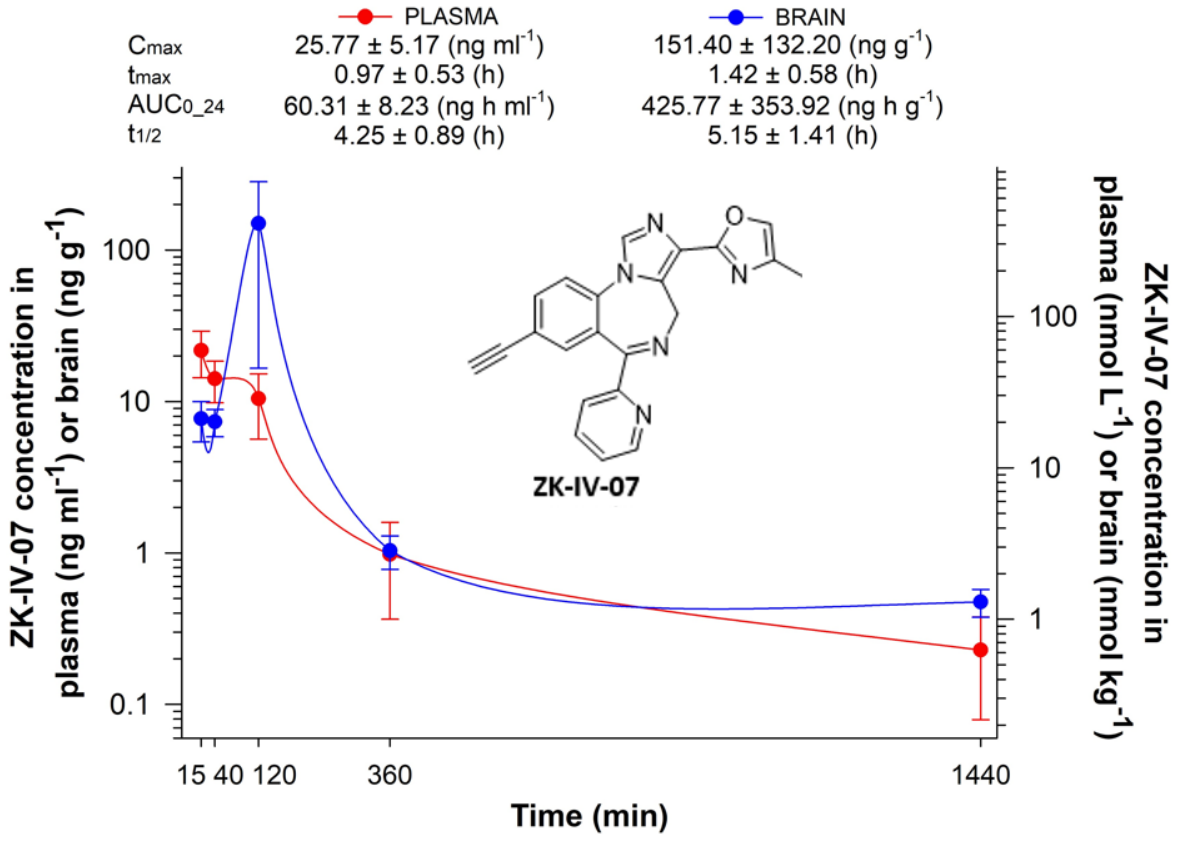


Figure 15. Pharmacokinetics of ZK-IV-07 in plasma and brain after oral administration of 2.0 mg/kg in rats. Each point represents the mean ± standard error of the mean in three rats. AUC: area under the curve from 0 -24 h; C_{max}: maximal concentration achieved; T_{max}: time of maximum concentration; $t_{1/2}$ - terminal elimination half-life. (Unpublished data)

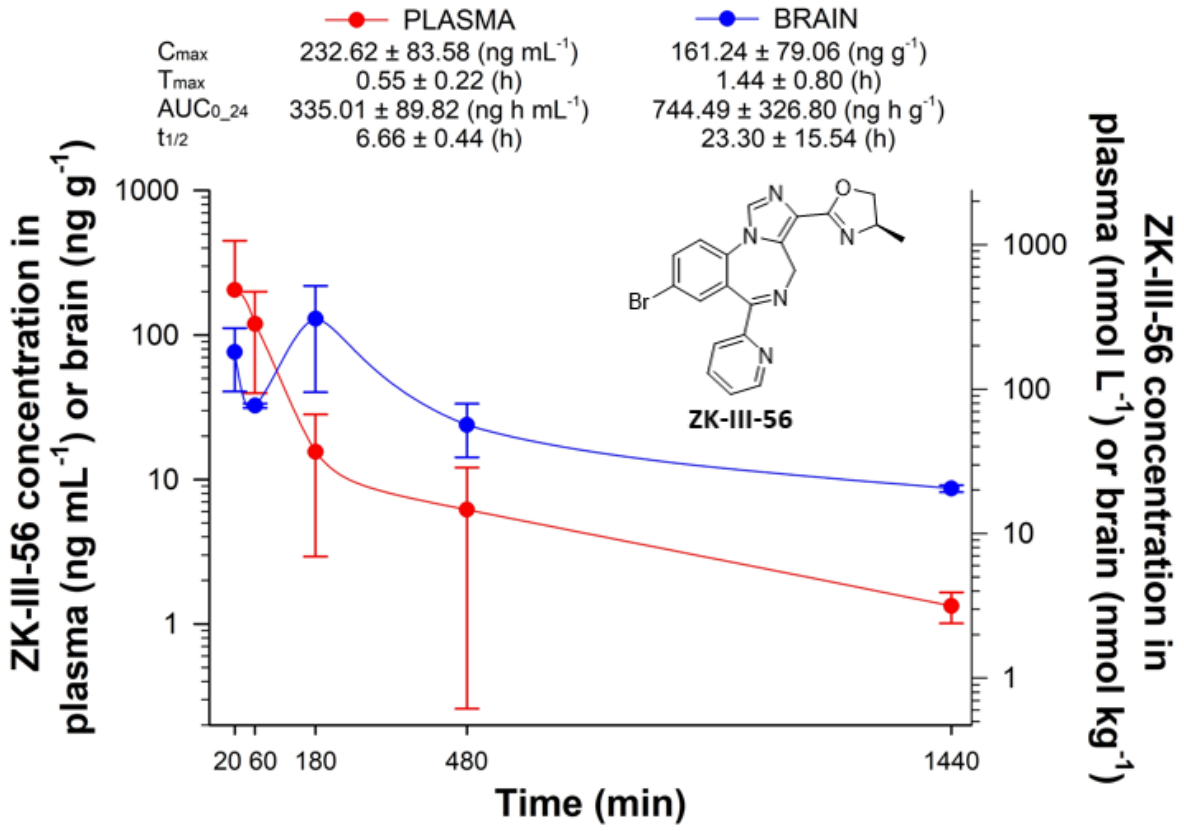


Figure 16. Pharmacokinetics of ZK-III-56 in plasma and brain after oral administration of 2.0 mg/kg in rats. Each point represents the mean ± standard error of the mean in three rats. AUC: area under the curve from 0 -24 h; C_{max}: maximal concentration achieved; T_{max}: time of maximum concentration; $t_{1/2}$ - terminal elimination half-life. (Unpublished data)

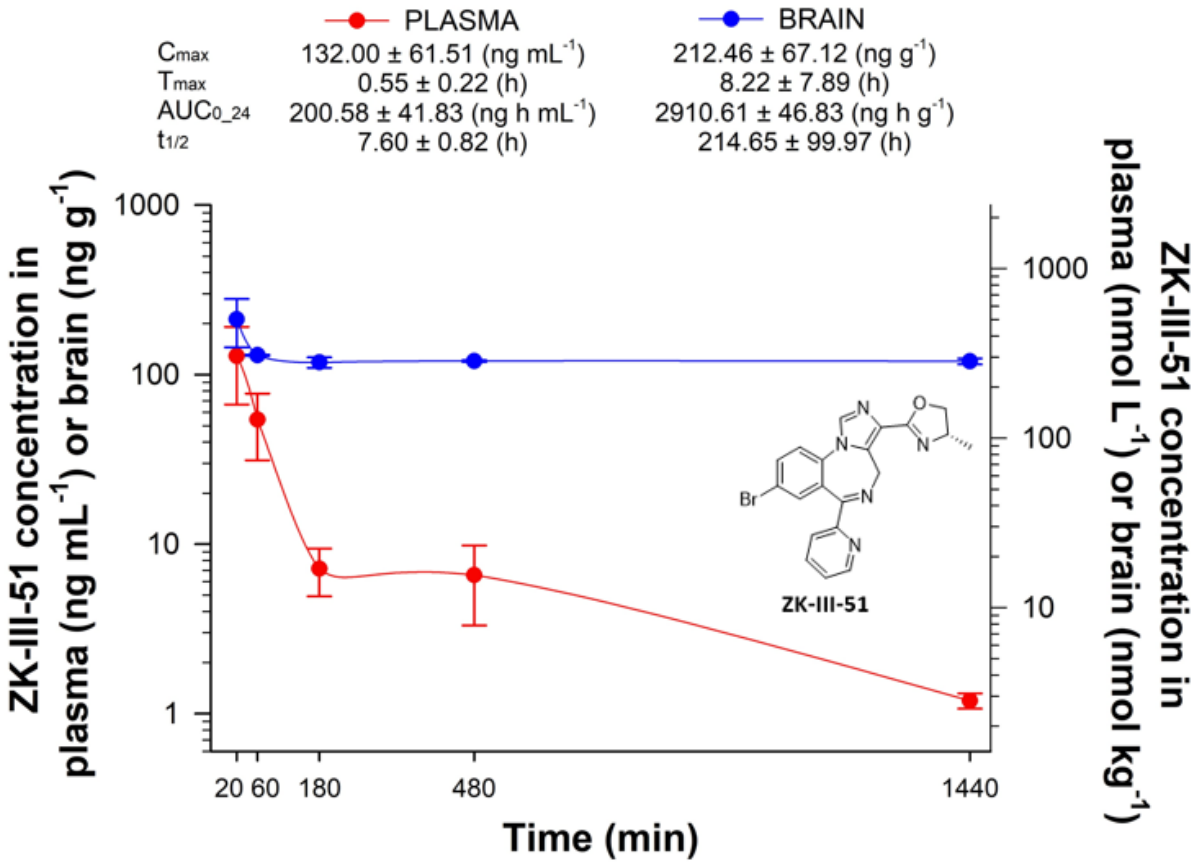


Figure 17. Pharmacokinetics of ZK-III-51 in plasma and brain after oral administration of 2.0 mg/kg in rats. Each point represents the mean ± standard error of the mean in three rats. AUC: area under the curve from 0 -24 h; C_{max}: maximal concentration achieved; T_{max}: time of maximum concentration; $t_{1/2}$ - terminal elimination half-life. (Unpublished data)

A first assessment of the exposures of these compounds to plasma and brain after oral dosing was made using rats given 2 mg/kg. Plasma and brain concentrations over 24 h post dosing along with relevant pharmacokinetic parameters are shown in **Figures 14-17**. Large variation in exposures were observed with these compounds as also shown in **Table 7**. The ligand ZK-III-51 (**4**) showed unusually prolonged brain concentrations. The maximal concentrations of compound delivered to plasma or brain after 2 mg/kg was typically less than the K_i for binding of the compound at

$GABA_AR$s (**Table 7**). Evaluation of the relationship of plasma to brain levels using area under the curve (AUC) data shows a partitioning of compounds into groups (**Figure 18**). Three compounds had plasma AUC values $\leq$ 124 ng h ml^{-1}, whereas the other four compounds studied achieved great plasma exposures. Three compounds had brain AUC levels $\leq$ 426 ng h g^{-1}, whereas the other four compounds achieved greater brain exposures. Thus, four compounds achieved brain/plasma AUC ratios > 1 as illustrated in **Table 7** and **Figure 18**.

Table 7. Plasma and brain concentrations of compounds at C_{max} and brain/plasma ratios. (Unpublished data)

Compound	C_{max} (Plasma)	C_{max} (Brain)	C_{max} (Brain/Plasma)	AUC 24 h (Brain/Plasma)
ZK-III-58	54.8	39.4	0.72	0.67
ZK-IV-07	70.5	414.4#	5.9	7.0
ZK-III-56	550.9	381.8	0.69	2.2
ZK-III-51	312.6	503.1	1.6	14.5
KPP-III-96B	157.6	50.5	0.32	1.5
KPP-IV-35	818.3#	306.0	0.37	5.5
KPP-IV-09	553.4#	195.2#	0.35	0.51

Concentrations are in nM.

 # Concentration > K_i for benzodiazepine binding site

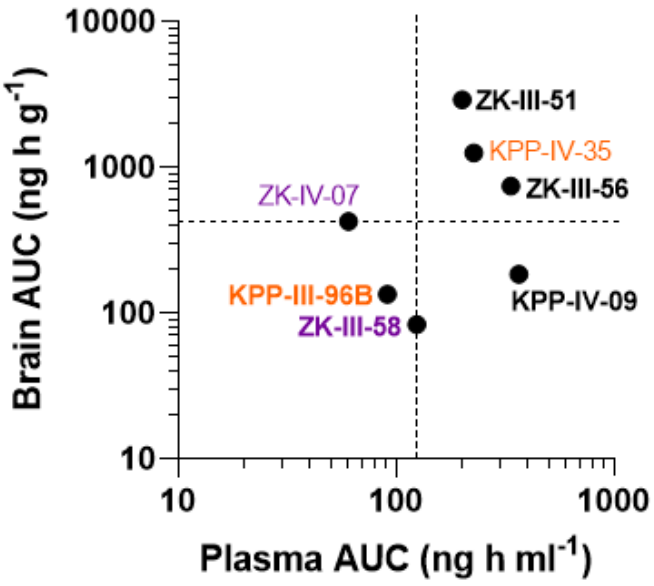


Figure 18. Relationship of plasma and brain concentrations of compounds. Dotted lines show boundaries of compounds with relatively low vs. high plasma and brain levels. Direct structural analogs are shown in matching colors; non-structurally related analogs are in black. Bold = Bromine analog; non-Bold = ethynyl analog. (Unpublished data)

The relationship between the overall brain exposure produced by the compounds (AUC) and the increase in tonic seizure latency is plotted in **Figure 20**. An asymptotic function is observed with increases in tonic seizure latencies associated with brain AUC levels up to about 400 ng h g^{-1}. Shown in **Figure 20** is all parameters that were evaluated; two indicated a positive association with tonic seizure reduction (trend for LogS).

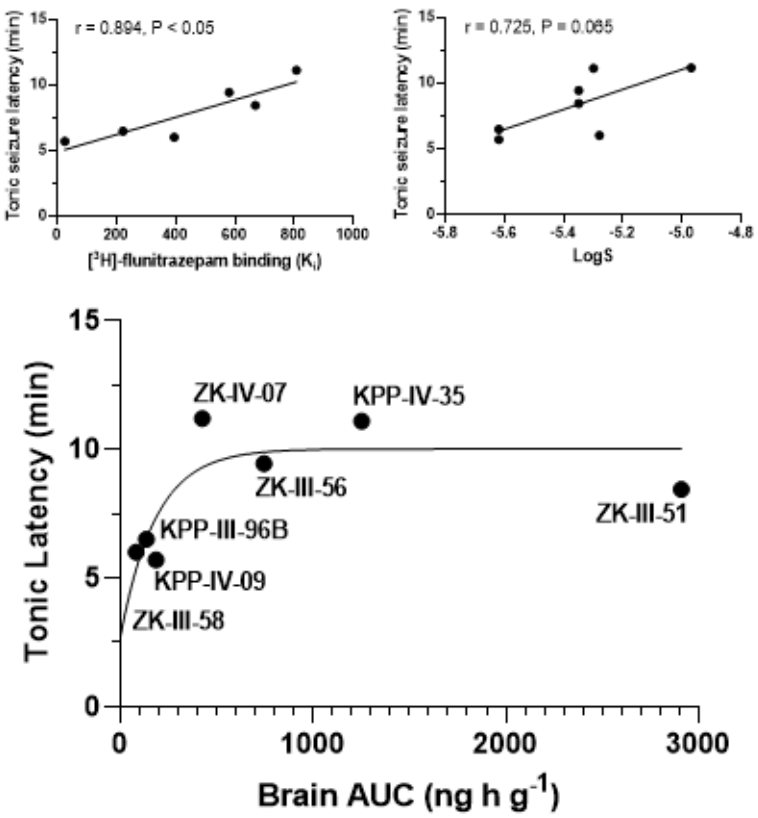


Figure 19. Relationships of compound parameters to antiseizure efficacy. Top panels: linear regression analysis of the two parameters that were associated with tonic seizure latency. Bottom panel: tonic seizure latency as a function of the brain concentration of compounds as assessed over 24 h (AUC).

3.4. Discussion and Conclusion

The novel analogs of KRM-II-81 (**2**) (denoted the ZK-series) were resynthesiyzed on a gram scale to obtain biological information. These promising analogs were evaluated in various in-vitro and in-vivo animal models, administered orally or intraperitoneally in mice, targeting neurological conditions such as epilepsy, anxiety, and pain. Notably, the α2/α3 subtype-selective lead imidazodiazepine, KRM-II-81 (**2**), displayed promising activity in preclinical studies across

diverse seizure models, including therapy-resistant (Lamotrigine) seizures and Dravet syndrome, and is advancing toward clinical trials without adverse effects of sedation, ataxia, tolerance, or addiction.

Certainly, the importance of identifying potential backup compounds if the lead (KRM-II-81, **2**) faces challenges in clinical trials, must be executed; novel compounds (oxazoles and oxazolines) were designed, introducing subtle modifications to the structure of KRM-II-81 (**2**). These ligands were studied for convulsions, toxicity, motor effects, and various behavioral impacts. Additionaly, they were screened against a 47-receptor panel (PDSP, NIMH), cytotoxicity on HEK-293 cell lines, and rotarod studies in mice at different doses (40, 80, or 120 mg/kg). Importantly they had no heart Herg activity.

In PDSP assays, the majority of compounds in the primary screen exhibited effective and selective binding (>85%) to the targeted rat benzodiazepine receptor site, notably with no binding to the HERG receptor, as intended. None of the novel ZK ligands displayed cytotoxicity in HEK-293 cell lines. Particularly, the ethynyl oxazole ZK-IV-07 (**9**) demonstrated significant anticonvulsant activity in the PTZ seizure model when administered orally, proving non-toxic in the lethality test conducted in mice. Further evaluation revealed that the ethyl-substituted oxazolines ZK-III-51 (**4**) and ZK-III-56 (**5**) exhibited potent anticonvulsant activity in the PTZ-induced seizure model. Notably, these oxazolines (**4** and **5**) were found to be non-sedating, devoid of ataxia, tremor, and loss of rightening response even at a dose of 120 mg/kg. They are potentially novel back upi compounds to KRM-II-81.

In summary, ZK-IV-07 (**9**) has the potencial to be the backup lead compound in Milwaukee, demonstrating full efficacy across various seizure models, including pharmacoresistant epilepsy, and carrying an excellent safety profile, as expected. The synthesis of this compound has been

optimized and developed for cost-effectiveness on a gram scale, as discussed earlier. Notably, the purification of the final product or any intermediates does not require column chromatography except in one step. Further testing of these compounds is essential to advance them towards clinical trials, with a focus on assessing their potential for treatment of pharmaco-resistant epilepsy, and in a Dravet syndrome model for children, as well as drug abuse.

3.5. Methods

3.5.1. Rotarod studies carried out by Nick Zahn and Michelle Meyer (Dr. Arnold's laboratory, MIDD).

Nick Zahn and Michelle Meyer, from Dr. Alexander Arnold's labratory at MIDD, UWM, conducted the rotarod studies following a documented protocol.[11,147] Female Swiss Webster mice were initially trained to sustain their balance on a rotating rod (Omnitech Electronics Inc., Nova Scotia, Canada) at a consistent speed of 15 rounds per minute. Training continued until the mice could perform for 3 minutes in three consecutive trials without falling. The vehicle for oral dosing consisted of 2% hydroxypropyl methylcellulose and 2.5% polyethylene glycol.

Different groups of mice received either the vehicle or test compounds (40, 80, or 120 mg/kg) orally (via gavage) in a 200 µL volume before the initiation of the test. Diazepam (ip) served as a control at 5 mg/kg in a solution containing 10% DMSO, 40% propylene glycol, and 50% PBS [42]. Subsequent to the oral administration of test compounds, mice were tested in a rotarod study at three different time points (10, 30, or 60 minutes). They were observed for indicators such as falling, ataxia, tremors, and loss of the rightening response. If mice fell off the rod twice before the 3-minute mark, it was considered a 'fail,' and the time was recorded. It was deemed normal for mice given the vehicle (i.p.) to fall once, so one fall was not considered significant.[11]

3.5.2. Cytotoxicity studies by Michelle Meyer and coworkers in Dr. Arnold's lab, University of Wisconsin-Milwaukee and MIDD.

Cytotoxicity investigations were conducted in Dr. Arnold's lab at the University of Wisconsin-Milwaukee. The methodology employed in this experiment adhered to a published procedure, utilizing cultured human embryonic kidney HEK293T cells.[167] In this particular study, dimethyl sulfoxide (DMSO) served as the negative control, while 3-dibutylamino-1-(4-hexyl-phenyl)-propan-1-one (150 μM in DMSO) functioned as the positive control. Cell death was assessed by standard methods after an 18-hour incubation period.

3.5.3. Analysis of ligands in the pentylenetetrazol seizure model (PTZ) by Dr. Jeffery Witkin and Dr. Xingjie at Indiana University, School of Medicine.

For the pentylenetetrazol (PTZ) seizure model, male C57BL/6N mice from Charles River LAbs(Indianapolis, Indiana) were used. The PTZ solution was prepared by dissolving it in a 0.9% NaCl solution, and the test compounds were suspended in 1% carboxymethylcellulose. The oral administration of test compounds (10 mL/kg) by gavage was followed by placing the mice back into their home cages. Subsequently, these mice received PTZ subcutaneously (75 mg/kg) after a 60-minute interval. The elapsed time for clonic or tonic seizures to occur was measured using a stopwatch. Within the 60-minute timeframe post-PTZ administration, the number of mice that succumbed (if any) was recorded, and the latency to clonus and tonus was analyzed separately through one-way ANOVA and Dunnett's T-test. A priori probabilities of 0.05 were established for statistical significance. The assessment of lethality involved the use of Fisher's Exact Probability test at a 0.05 significance level. [135]

3.5.4. Methods of molecular docking with the help of Dr. Lalit Golani (UWM).

The molecular binding (docking) studies of the compounds were performed, and ligand-protein interactions were analyzed using AutoDock Vina 1.5.6 [26]. The PDB file of the CryoEM structure of the human full-length α1β3γ2L $GABA_A$ receptor in the complex with alprazolam (6HUO) was downloaded from the Protein Data Bank. The file was further improved for docking by fixing missing bonds or atoms, adding polar hydrogens, and assigning charges by AM1-BCC, and removing water molecules. The proteins were validated by first removing the bound ligand (alprazolam) and this was followed by docking it in the same binding site. The compounds were drawn, and energy minimized in Chimera.1 A grid size of 17 Å x 17 Å x 17 Å and centered at coordinates 152.80 (x), 163.02 (y), and 161.14 (z) were used. Illustrations of the 3D models were generated using Chimera and Python.1-2. The dockings were performed with The standard search parameters and the poses with the best scores were used in these dockings.[4,147]

3.5.5. Neuropharmacokinetic in vivo evaluation of ligands in plasma and brain (Source: Dr. Savic and coworkers, University of Belgrade, Serbia)

The neuropharmacokinetic investigation of ligands in both the brain and plasma was carried out on adult male Sprague Dawley rats, weighing between 280-330 g on the day of the experiment. These rats were bred in the vivarium of the Faculty of Pharmacy in Belgrade, Serbia, and were group-housed (five animals per cage) under standard laboratory conditions, maintaining a temperature of 21±2 °C, relative humidity at 40–45%, and an illumination level of 120 lx. The rats had ad libitum access to tap water and chow pellets. They were subjected to a 12:12 h light/dark cycle, with lights on at 06:00 h, and the pharmacokinetic testing occurred during the light phase of the diurnal cycle. The utilization of animals in this in-vivo neuropharmacokinetic evaluation

was optimized to minimize their numbers. The experiment was carried out within the project approved by the Ethical Council for the Protection of Experimental Animals of the Ministry of Agriculture, Forestry and Water Management of the Republic of Serbia. A cassette dosing experiment was conducted to determine the 240 pharmacokinetic parameters characterizing both the amount and rate of transport of the chosen ligands (such as ZK-III-51 (**4**), ZK-III-56 (**5**), ZK-III-58 (**6**) and ZK-IV-07 (**9**)) administered via oral gavage. Furthermore, the aim of this experiment was to obtain the respective pharmacokinetic profiles in both systemic circulation and the brain. The rats were categorized into varying cohorts and groups, depending on the number of ligands under examination. Each group consisted of three animals and was associated with predetermined time intervals (20 min, 60 min, 180 min, 480 min, and 1440 min (24 h)). The administered doses for a specific ligand were 2.0 mg/kg, with each ligand having a concentration of 0.4 mg/mL in a 0.25% methyl cellulose solution, administered orally.

At the appropriate time intervals, the animals underwent anesthesia through intraperitoneal administration of ketamine hydrochloride (90 mg/kg, Ketamidor, Richter Pharma AG, Wels, Austria). Subsequently, blood samples were obtained through cardiac puncture using heparinized syringes, and brain samples were harvested. After centrifugation for 10 minutes at 1000 x g (MiniSpin® plus centrifuge, Eppendorf, Germany), plasma samples were collected. Brain tissue samples were weighed and homogenized in 1 mL of methanol using an ultrasonic probe (70% amplitude, 2 x 20 s). Supernatants were separated after centrifugation for 20 minutes at 3400 × g (MiniSpin® plus centrifuge, Eppendorf, Germany).

The obtained plasma and supernatants underwent further processing through solid-phase extraction utilizing Oasis HLB cartridges (Waters Corporation, Milford, Massachusetts). The concentration of ligands was determined using ultraperformance liquid chromatography–tandem

mass spectrometry (UPLC–MS/MS) with an ACELLA UHPLC chromatograph (Thermo Fisher Scientific Inc., Madison, WI, USA) coupled to a triple quadrupole mass spectrometer TSQ Quantum Access MAX (Thermo Fisher Scientific Inc., Madison, WI, USA) with a heated electrospray ionization (HESI) interface.

Calibration curves covering the range of 0.0005 – 2.5 μmol/L were prepared, with the peak area ratios of the analyte and the internal standard used for their construction. Non-compartmental pharmacokinetics were analyzed using the Phoenix WinNonlin Software package (Certara L.P.). Graphs were generated using the commercially available statistical software Sigma Plot 12 (Systat Software Inc., USA).[210,211]

3.6. Experimental

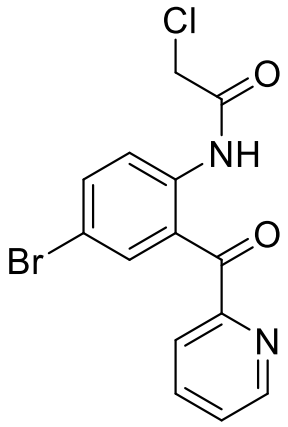
3.6.1. General experimental conditions

All reactions were conducted in round-bottom flasks or screw-cap test tubes that had been dried in an oven. Dry solvents were utilized for all chemical reactions, and unless otherwise specified, chemicals underwent purification through standard techniques or were procured from chemical vendors with the desired purity. The progression of reactions was tracked using TLC from Dynamic Adsorbents, Inc. (silica gel, neutral alumina, or basic alumina) under ultraviolet (UV) light. For the purification of certain intermediates or products, flash column chromatography techniques were employed on silica gel (230-400 mesh, Dynamic Adsorbents) or neutral alumina.

A Stuart melting point SMP3 apparatus (Barloworld Scientific US Ltd.) was employed to determine the melting point of specific compounds. The enantiomeric excess (% ee) was ascertained using a CHIRALPAK® IB-N3 HPLC Column from Daicel Corporation. To establish the % purity of the compounds, a C18 1.8 mM column (Shimadzu Nexol company) was used.

Optical rotations were measured on a JASCO Model DIP-370 digital polarimeter using a standard. The 1H and 13C NMR spectra were acquired on Bruker Spectrospin 500 MHz or 300 MHz instruments in $CDCl_3$, DMSO, or DMSO-d6. The chemical shifts are reported in δ (ppm), and multiplicities are indicated as singlet (s), broad signal (br), doublet (d), triplet (t), quartet (q), dd (doublet of doublets), dt (doublet of triplets), td (triplet of doublets), and multiplet (m). HRMS was determined using LCMS-IT-TOF techniques at the Milwaukee Institute for Drug Discovery (MIDD) in the Shimadzu Laboratory for Advanced and Applied Analytical Chemistry.

3.6.2. N-(4-Bromo-2-picolinoylphenyl)-2-chloroacetamide (11)

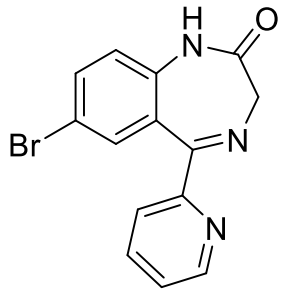


11

Chloroacetyl chloride (88 mL, 1106 mmol) was added dropwise to a stirred solution of (2- amino-5-bromophenyl) (pyridine-2yl)methanone **10** (200 g, 721.7 mmol), sodium bicarbonate (121.2 g, 1442.68 mmol), and anhydrous DCM (2000 mL) over a period of 60 min while keeping the temperature between 25−30 °C. The bright red solution, which resulted, during the addition of chloroacetyl chloride turned to a light-yellow colored solution indicating the consumption of starting material. The completion of the reaction was confirmed by silica gel TLC (EtOAc: hexane = 20:80 with 1% triethylamine). The reaction mixture was quenched slowly by adding water (1500

mL) over a 30 min period as carbon dioxide gas was evolved. The biphasic mixture, which resulted, was allowed to stand for 25 min and the layers were separated. The organic layer was separated and the aq layer was extracted with DCM (2x500 mL) and the combined organic layers were washed with 5% aq sodium bicarbonate solution (1x 1000 mL), 10% aq sodium chloride solution (2x 1000 mL) and dried over Na_2SO_4. The solvents were removed under reduced pressure and the residue was stirred with ethanol (1000 mL) at 50−55 °C for 30 min. The mixture was cooled to rt and kept at that temperature for 3 h. The solid was filtered, washed with ethanol (150 mL × 3) and dried under vacuum at 40 °C to afford the N-(4-bromo-2- picolinoylphenyl)-2-chloroacetamide (**11**) as an off-white-colored powder (252.9 g, 99%). **^{1}H NMR** (500 MHz, $CDCl_3$) δ 11.66 (s, 1H), 8.76 (ddd, 1H), 8.58 (d, J = 9.0 Hz, 1H), 8.05 (dd, J = 9.5, 5.1 Hz, 208 2H), 7.96 (ddd, J = 7.7, 1.6, 0.8 Hz, 1H), 7.71 (dd, J = 9.0, 2.3 Hz, 1H), 7.58 – 7.53 (m, 1H), 4.21 (s, 2H). **^{13}C NMR** (126 MHz, $CDCl_3$) δ 195.26 (s), 165.33 (s), 154.74 (s), 148.81 (s), 138.78 (s), 137.42 (s), 137.17 (s), 136.86 (s), 126.69 (s), 124.98 (s), 124.61 (s), 122.98 (s), 115.80 (s), 43.15 (s). **HRMS** (ESI/ITTOF): m/z [M + H]+ calcd for $C_{14}H_{11}BrClN_2O_2$: 352.9693; found: 352.9691. The spectral data for **11** were identical to the literature.[135]

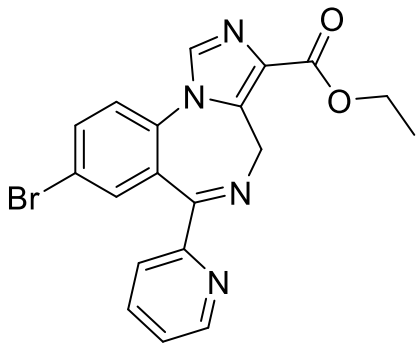
3.6.3. 7-Bromo-5-(pyridin-2-yl)-1,3-dihydro-2H-benzo[e][1,4]diazepin-2-one (12)



12

A 12 L 3-neck round bottom flask was charged with N-(4-bromo-2-picolinoylphenyl)-2-chloroacetamide **11** (601 g, 1699.6 mmol), isopropanol (6000 mL) hexamethylenetetramine (HMTM, 524 g, 3737.7 mmol), ammonium acetate (288.3 g, 3740.2 mmol), and was heated to reflux (78 °C) with continuous stirring with an overhead stirrer. The reaction mixture was held at reflux for 5 h at which point it was deemed complete by analysis by TLC (silica gel, EtOAc: hexane = 50:50 with 1 % triethylamine). The reaction mixture was then cooled to 0−5 °C using an ice bath. The solid, which resulted, was filtered, and washed with cold isopropanol (500 mL × 2) and then water (1000 mL × 4). The solid was dried under vacuum at 50 °C for 6 h to afford the 7-bromo-5-(pyridin-2-yl)-1,3-dihydro-2H-benzo[e][1,4]diazepin-2-one (**12**) as an off-white-colored solid (405.95 g, 82%). The isopropanol filtrate was concentrated, and cold water (500mL) was added while stirring over a period of 30 min. The solid residue, which resulted, was filtered, washed with IPA-water (50:50, 300 mL) and water (3x300mL). The solid was then dried under vacuum at 50°C for 4 h to obtain additional product **12** (38.2 g, 7.1%). **^{1}H NMR** (500 MHz, CDCl3) δ 209 9.81 (s, 1H), 8.66 (ddd, J = 4.8, 1.6, 0.9 Hz, 1H), 8.01 (dt, 1H), 7.84 (td, J = 7.7, 1.8 Hz, 1H), 7.57 (dd, J = 8.6, 2.3 Hz, 1H), 7.49 (d, J = 2.2 Hz, 1H), 7.40 (ddd, J = 7.6, 4.8, 1.1 Hz, 1H), 7.02 (d, J = 8.7 Hz, 1H), 4.38 (s, 2H). ^{13}C NMR (126 MHz, CDCl3) δ 171.21 (s), 168.43 (s), 156.13 (s), 148.94 (s), 137.83 (s), 136.93 (s), 134.69 (s), 134.09 (s), 127.78 (s), 124.82 (s), 124.12 (s), 122.93 (s), 116.17 (s), 56.82 (s). HRMS (ESI/IT-TOF): m/z [M + H]+ calcd for $C_{14}H_{11}BrN_3O$: 316.0080; found: 316.0076. The spectral data for **12** were identical to the literature.[135]

3.6.4. Ethyl 8-bromo-6- (pyridin-2-yl)-4H-benzo[f]imidazo[1,5-a][1,4]diazepine-carboxylate (13)

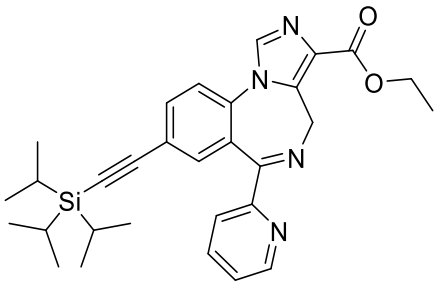


13

The vacuum dried cyclized benzodiazepine **12** (100 g, 316.3 mmol) was dissolved in very dry THF (1000 mL), and the solution, which resulted, was cooled to – 20 °C. To the stirring solution, potassium tert-butoxide (53.22 g, 474.28 mmol) was added in one portion. The reaction mixture was allowed to stir until it reached 0 °C and then stirred for an additional 0.5 h at 0 °C. The mixture was then cooled to -20 °C after which, diethyl chlorophosphate (59.42 mL, 411.15 mmol) was added and the mixture was allowed to stir until it reached 0 °C. At this point, the mixture which resulted, was allowed to stir for 0.5 h, and then the solution was cooled to -78 °C, and ethyl isocyanoacetate (41.64 mL,380.87 mmol) was added. This was followed by the addition of a second portion of potassium tert-butoxide (53.22 g, 474.28 mmol) at 0 °C. This mixture, which resulted, was allowed to stir overnight, during which time, it was allowed to warm to rt. The competition of the reaction mixture was confirmed by analysis by TLC (silica gel, 1.5 mL EtOAc, 1 mL hexane, 2 drops methanol, and 1 drop of 10% aq NH_4OH), after which the reaction solution was quenched by addition of a cold saturated aq solution of $NaHCO_3$ (1000 mL) and extracted with EtOAc (1500 mL). The organic layers were combined and washed with brine (2 × 500 mL),

and then dried over Na_2SO_4. The solvent was removed under reduced pressure to 1/4th the original volume and then tert-butylmethyl ether (1000 mL) was added. Addition of the ether resulted in precipitation, after which the tert-butylmethyl ether (TBME) was removed by decanting. TBME was added again to the precipitate, and this was stirred for 5 min (this process was repeated 3-5 times). The solid material obtained after final decantation was dried under reduced pressure to afford a light brown to yellow colored solid. The solid material was characterized by analysis by NMR without further purification (not required), and the mother liquor was purified by flash column chromatography (silica gel, EtOAc/hexane, 4:1) to afford more imidazodiazepine ester (**13**) as an off-white colored solid (83.2 g, 64%): **^{1}H NMR** (500 MHz, $CDCl_3$) δ 8.56 (d, J = 3.1 Hz, 1H), 8.07 (d, J = 7.7 Hz, 1H), 7.91 (s, 1H), 7.87 – 7.72 (m, 2H), 7.58 (s, 1H), 7.47 (d, J = 8.6 Hz, 1H), 7.40 – 7.33 (m, 1H), 6.10 (d, J = 10.3 Hz, 1H), 4.41 (d, J = 5.8 Hz, 2H), 4.14 (d, J = 10.7 Hz, 1H), 1.42 (t, J = 7.1 Hz, 3H); **^{13}C NMR** (126 MHz, $CDCl_3$) δ 167.08 (s), 162.91 (s), 156.15 (s), 148.70 (s), 138.44 (s), 136.97 (s), 135.29 (s), 135.01 (s), 134.56 (s), 134.44 (s), 129.33 (s), 128.51 (s), 124.92 (s), 124.32 (s), 124.00 (s), 120.58 (s), 60.81 (s), 45.02 (s), 14.44 (s). The proton and carbon NMR data for this compound were identical in all respects with that reported in the literature.[135]

3.6.5. Ethyl 6-(pyridin-2-yl)-8-((triisopropylsilyl)ethynyl) 4H benzo[f]imidazo[1,5a][1,4] diazepine-3-carboxylate (14)



14

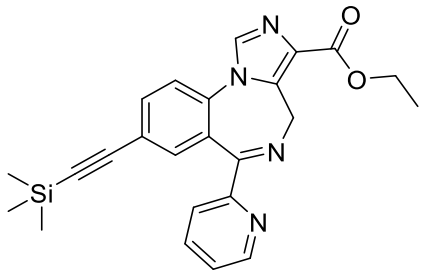
Palladium acetate (2.2 g, 9.79 mmol) and tri-o-tolylphosphine (5.96 g, 19.58 mmol) were mixed in a 2-L roundbottom flask, and acetonitrile (700 mL) was added. The mixture was stirred for 30 min at rt. Ethyl 8-bromo-6-(pyridin-2-yl)-4H-benzo[f]imidazo[1,5-a][1,4]diazepine-3-carboxylate **13** (40.3 g, 97.99 mmol) was then added to the reaction mixture, and this was followed by addition of triethylamine (41 mL, 294.9 mmol) and (triisopropylsilyl)acetylene (28.57 mL, 127.4 mmol). The reaction mixture was heated to reflux (75 °C) and stirred for 6 hours. The completion of the reaction was confirmed analysis by TLC on silica gel, using an ethyl acetate and hexane solvent mixture (50:50) with 1% triethylamine added to the mobile phase.

The reaction mixture was cooled to rt and opened to the air, then silica gel (100 g) was introduced, and the mixture was stirred for 20 min. Subsequently, the reaction mixture was filtered through a pad of celite, and the residue was washed with dichloromethane (3× 100 mL).

The solvents were then evaporated under reduced pressure, and the residue was dissolved in dichloromethane (700 mL). Then 5% aq sodium bicarbonate solution (150 mL) was added, which resulted, in a biphasic mixture. Then the mixture was allowed to stand for 15 minutes; the organic and aq layers were separated. The organic layer was collected, and the aq layer underwent further extraction with dichloromethane (2 × 100 mL). The combined organic layers were washed with 10% aq sodium chloride solution (2× 100 mL) and dried over sodium sulfate (Na_2SO_4). Next, the solvents were removed under reduced pressure and the residue was purified by flash chromatography using silica gel and a solvent mixture of 50% ethyl acetate and hexanes with 3% triethylamine added. The desired fractions were collected, and the solvents were evaporated under reduced pressure. The resulting semi-solid was then dried under reduced pressure at 40 °C for 2 h, which yielded the protected imidazodiazapine **14** as a clear, light brown semi-solid (37g, 75%). R_f

= 0.7 (EtOAc-hexanes, 1:1 and 1% of TEA) **^{1}H NMR** (500 MHz, $CDCl_3$) δ 8.58 (ddd, J = 4.6, 1.5, 0.8 Hz, 1H), 8.08 (d, J = 7.9 Hz, 1H), 7.90 (s, 1H), 7.82 (td, J = 7.6, 1.1 Hz, 1H), 7.72 (dd, J = 8.4, 1.5 Hz, 1H), 7.53 – 7.51 (m, 2H), 7.37 (dd, J = 7.5, 4.8 Hz, 1H), 6.11 (d, J = 11.2 Hz, 1H), 4.44 (q, 2H), 4.14 (d, J = 11.2 Hz, 1H), 1.44 (t, J = 7.1 Hz, 3H), 1.12 (d, J = 3.6 Hz, 21H). **^{13}C NMR** (126 MHz, $CDCl_3$) δ 167.78 (s), 162.96 (s), 156.48 (s), 148.72 (s), 138.51 (s), 136.82 (s), 135.71 (s), 135.33 (s), 134.93 (s), 134.47 (s), 129.28 (s), 126.99 (s), 124.77 (s), 124.02 (s), 122.67 (s), 122.65 (s), 104.87 (s), 93.86 (s), 60.78 (s), 45.05 (s), 18.61 (s), 14.45 (s), 11.23 (s). The spectral data for **14** were identical to the literature.[135]

3.6.6. Ethyl-6-(pyridin-2-yl)-8-((trimethylsilyl)ethynyl)-4H-benzo[f] imidazo[1,5a]-[1,4]dia zepine-3-carboxylate (21)

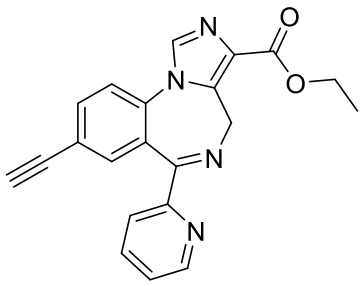


21

In a 3-neck round-bottom flask equipped with a reflux condenser, the imidazodiazepine ethyl ester **13** (50 g, 121.55 mmol) was dissolved in triethylamine (TEA) (52 mL, 364.7 mmol) and dry acetonitrile (CH_3CN) (500 mL). The solution underwent degassing three times under vacuum and argon. Subsequently, trimethylsilylacetylene (18 g, 182.4 mmol) and bis(triphenyl phosphine)-palladium (II) acetate (5.1 g, 6.68 mmol) were introduced into the solution under argon, and the mixture underwent degassing four times. The reaction mixture was heated to reflux under argon

and stirred overnight. The development of the reaction was monitored by analysis by TLC (silica gel, ethyl acetate/hexanes, 7:3, and 1% TEA) and LC-MS 2020, and after 15 h, the reaction reached completion. The mixture was then cooled to rt and filtered through a pad of celite. After washing with ethyl acetate and drying over Na_2SO_4, the filtrate was concentrated under reduced pressure. The resulting black residue was loaded onto a silica plug and subjected to purification by flash chromatography, which yielded **21** as an off-white colored solid (37 g, 72%). R_f = 0.5 (EtOAc-hexanes, 1:1 and 1% of TEA); **^{1}H NMR** (300 MHz, $CDCl_3$): δ = 8.58 (d, J = 4.1 Hz, 1H), 8.06 (d, J = 7.8 Hz, 1H), 7.91 (s, 1H), 7.78 (t, J = 7.7 Hz, 1H), 7.71 (d, J = 8.3 Hz, 1H), 7.51 (d, J = 9.2 Hz, 2H), 7.34 (t, J = 5.9 Hz, 1H), 6.08 (d, J = 9.2 Hz, 1H), 4.47 – 4.31 (m, 2H), 4.10 (d, J = 6.9 Hz, 1H), 1.41 (t, J = 7.0 Hz, 3H), 0.21(s, 9H); **^{13}C NMR** (75 MHz, $CDCl_3$): δ = 167.8, 162.7, 156.8, 148.8, 138.5, 136.8, 135.7, 135.2, 135.1, 134.5, 129.3, 214 127.0, 124.7, 124.0, 122.7, 122.2, 102.8, 97.0, 60.7, 45.0, 14.4, 0.2; **HRMS** (ESI/IT-TOF): m/z [M + H]+ calcd for $C_{24}H_{25}N_4O_2Si$: 429.1742; found: 429.1747. The spectral data for **21** were identical to the literature.[135]

3.6.7. Ethyl 8-ethynyl-6-(pyridin-2-yl)-4H-benzo[f]imidazo[1,5-a][1,4]diazepine-3-carboxylate (1, Hz-166)



HZ-166
1

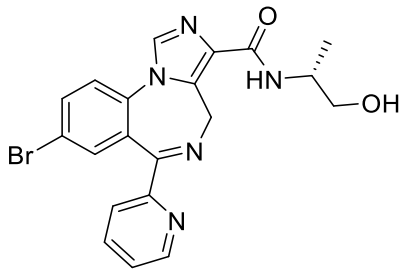
The ethyl-6-(pyridin-2-yl)-8-((trimethylsilyl)ethynyl)-4H-benzo[f] imidazo[1,5a]-[1,4]dia zepine-3-carboxylate **21** (7.2 g, 16.80 mmol), was dissolved in tetrahydrofuran (THF) (50 mL), and 0.7

mL of water was introduced into the mixture. The reaction mixture was cooled to 0 °C using an ice bath, and tetrabutylammonium fluoride hydrate, 1 M in THF (20.16 mL, 20.16 mmol), was added dropwise over 10 min, while the temperature was maintained at 0 °C. Upon the addition of the TBAF solution, the reaction mixture was allowed to warm to rt and stirred for 2 h. The completion of the reaction was verified by analysis by TLC (silica gel, ethyl acetate: hexane = 80:20 with 1% triethylamine).

Subsequently, dichloromethane (1500 mL) was added, and this was followed by 10% aq sodium chloride solution (1500 mL). The mixture underwent stirring for 20 min. After standing for 15 min, the biphasic mixture was separated into organic and aq layers. The organic layer was collected, and the aq layer underwent further extraction with dichloromethane (2x 1000 mL). The combined organic layers were washed with 10% aq sodium chloride solution (1500 mL) and dried with sodium sulfate (Na_2SO_4). The solvents were removed under reduced pressure, and the residue was stirred with isopropanol (IPA, 500 mL) at 60−65 °C for 30 min. Upon cooling to rt, cold water (500 mL) was added to the mixture, which was stirred for an additional 30 min and left for 2 h. The solid, which formed was filtered and washed with cold IPA: water (50:50, 3x100 mL). The solid, which resulted, was dried under vacuum at 40 °C for 4 h, which yielded Hz-166 (**1**) as a white-colored crystalline solid (4.96, 83%). R_f = 0.3 (EtOAc-hexanes, 1:1 and 1% of TEA). **^{1}H NMR** (500 MHz, $CDCl_3$) δ 8.52 (d, J = 4.2 Hz, 1H), 8.02 (d, J = 7.9 Hz, 1H), 7.89 (s, 1H), 7.76 (td, J = 7.8, 1.7 Hz, 1H), 7.70 (dd, J = 8.3, 1.7 Hz, 1H), 7.54 – 7.50 (m, 2H), 7.31 (ddd, 1H), 6.06 (d, J = 10.4 Hz, 1H), 4.39 (q, J = 16.9 Hz, 2H), 4.12 (d, J = 10.5 Hz, 1H), 3.16 (s, 1H), 1.38 (t, J = 7.1 Hz, 3H). **^{13}C NMR** (126 MHz, $CDCl_3$) δ 167.7 (s), 162.94 (s), 156.45 (s), 148.77 (s), 138.48 (s), 136.87 (s), 136.23 (s), 135.46 (s), 135.26 (s), 134.49 (s), 129.36 (s), 127.10 (s), 124.79 (s), 124.40 (d, J = 99.3 Hz), 124.00 (s), 122.84 (s), 121.19 (s), 81.69 (s), 79.49 (s), 60.81 (s), 45.05 (s),

14.44 (s). HRMS (ESI/IT-TOF): m/z [M + H]+ calcd for $C_{21}H_{17}N_4O_2$: 357.1346; found: 357.1344. The spectral data for **1** were identical to the literature.[135]

3.6.8. (R)-8-Bromo-N-(1-hydroxypropan-2-yl)-6-(pyridin-2-yl)-4H-benzo[f]imidazo[1,5-a][1,4]diazepine-3-carboxamide (14)

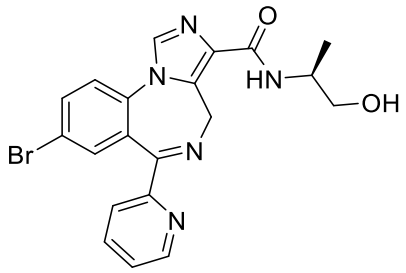


14

In a sealed tube, imidazodiazepine ester **13** (2 g, 4.86 mmol) and (R)-2-aminopropan-1-ol (6 mL, 64 mmol) were added, and the mixture, which resulted, was heated at 90 °C (preheated oil bath) for 18 h. Analysis by TLC indicated the disappearance of starting material and the appearance of a new component (R_f 0.3, silica gel, EtOAc/hexane/methanol, 2:1:0.5 and a few drops of 14% aq NH_4OH). At this point, the reaction mixture was cooled to rt. Cold water (8 mL) was added to the reaction mixture and most of the product precipitated without any further purification required. The rest of the crude was treated with dilution with EtOAC (20 mL) and water (15 mL). The biphasic layers were separated and the aq layer was extracted with EtOAc (4 × 20 mL). The combined organic layer was washed with brine (10 mL) and dried (Na_2SO_4). The solvent was removed under reduced pressure and the residue was purified by precipitation (15 % MeOH in EtOAc). The solid, which resulted, was dried under vacuum at 40 °C to afford carboxamide **14** as light-yellow colored solid **14** (2.11, 99%). **MP** 259-260 °C; **$[\alpha]_D^{25}$** = -7.2 (c 1.0, $CHCl_3$). **^{1}H NMR** (300 MHz, $CDCl_3$): δH 8.55 (d, J 4.7 Hz, 1H), 8.14 (d, J 7.9 Hz, 1H), 7.90 – 7.81 (m, 1H), 7.77

(dd, J 8.6, 2.7 Hz, 2H), 7.59 (d, J 2.3 Hz, 1H), 7.50 – 7.39 (m, 1H), 7.39 – 7.32 (m, 1H), 7.24 (d, J 7.2 Hz, 1H), 6.24 (d, J 10.8 Hz, 1H), 4.22 (qd, J 6.7, 3.2 Hz, 1H), 4.12 (s, 1H), 3.75 (d, J 9.3 Hz, 1H), 3.64 (dd, J 11.0, 6.4 Hz, 1H), 1.98 (s, 1H), 1.28 (d, J 6.8 Hz, 3H). **^{13}C NMR** (75 MHz, $CDCl_3$): δ 166.8 (s), 163.4 (s), 156.3 (s), 148.5 (s), 136.9 (s), 135.9 (s), 135.4 (s), 134.9 (s), 134.6 (s), 133.2 (s), 131.2 (s), 128.6 (s), 124.8 (s), 124.2 (s), 124.0 (s), 120.4 (s), 67.6 (s), 48.0 (s), 44.8 (s), 17.1(s). **HRMS** (ESI/IT-TOF) m/z: [M + H]+ Calculated for $C_{20}H_{18}BrN_5O_2$: 440.0722; found 440.0694. The spectral data for **14** were identical to the literature.[212]

3.6.9. (S)-8-Bromo-N-(1-hydroxypropan-2-yl)-6-(pyridin-2-yl)-4H-benzo[f]imidazo[1,5-a][1,4]diazepine-3-carboxamide (15)

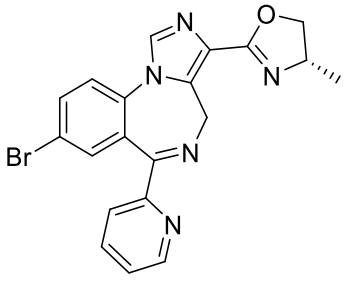


15

In a sealed tube, imidazodiazepine ester **13** (3 g, 7.29 mmol) and (S)-2-aminopropan-1-ol (6 mL, 64 mmol) were added, and the mixture, which resulted, was heated at 90 °C (preheated oil bath) for 18 h. Analysis by TLC indicated the disappearance of starting material and the appearance of a new component (R_f 0.3, silica gel, EtOAc/hexane/methanol, 2:1:0.5 and a few drops of 14% aq NH_4OH). At this point the reaction mixture was cooled to rt. Cold water (12 mL) was added to the reaction mixture and most of the product precipitated without any further purification required. The rest of the crude was treated by dilution with EtOAC (25 mL) and water (20 mL). The biphasic layers were separated and the aq layer was extracted with EtOAc (4 × 20 mL). The combined

organic layer was washed with brine (15 mL) and dried (Na_2SO_4). The solvent was removed under reduced pressure and the residue was purified by precipitation (15 % MeOH in EtOAc). The solid was dried under vacuum at 40 °C to afford carboxamide **15** as light-yellow colored solid (3.14 g, 98%). **MP**: 261-262 °C (20% MeOH in EtOAc). **1H NMR** (300 MHz, $CDCl_3$): δH 8.56 (d, J 4.4 Hz, 1H), 8.15 (d, J 7.9 Hz, 1H), 7.83 (dd, J 7.7, 1.8 Hz, 1H), 7.77 (dd, J 8.5, 2.3 Hz, 2H), 7.59 (d, J 2.2 Hz, 1H), 7.43 (d, J 8.6 Hz, 1H), 7.39 – 7.32 (m, 1H), 7.23 (d, J 7.2 Hz, 1H), 6.26 (d, J 12.6 Hz, 1H), 4.22 (qd, J 6.9, 3.4 Hz, 1H), 4.13 (d, J 13.2 Hz, 1H), 3.75 (d, J 10.9 Hz, 1H), 3.64 (dd, J 11.1, 6.5 Hz, 1H), 1.87 (s, 1H), 1.28 (d, J 6.6 Hz, 3H). **^{13}C NMR** (75 MHz, $CDCl_3$): δ 166.8 (s), 163.5 (s), 156.3 (s), 148.5 (s), 136.9 (s), 136.0 (s), 135.4 (s), 134.9 (s), 134.6 (s), 133.2 (s), 131.2 (s), 128.6 (s), 124.8 (s), 124.2 (s), 124.0 (s), 120.5 (s), 67.7 (s), 48.1 (s), 44.8 (s), 17.1 (s). **HRMS** (ESI/IT-TOF) m/z: [M + H]+ Calcd for $C_{20}H_{18}BrN_5O_2$ 440.0722; found 440.0699. The spectral data for **15** were identical to the literature.[212]

3.6.10. 2-(8-Bromo-6-(pyridin-2-yl)-4H-benzo[f]imidazo[1,5-a][1,4]diazepin-3-yl)-4-methyl-4,5-dihydrooxazole (4, ZK-III-51)



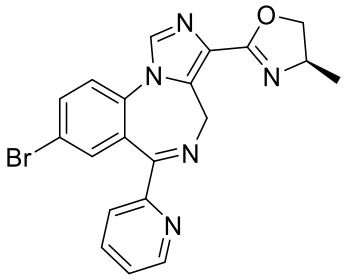
4

ZK-III-51

The solution of (R)-carboxamide **15** (1.8 g, 4.08 mmol) in CH_2Cl_2 (40 mL) was cooled with stirring to 0 °C (ice bath) and thionyl chloride (1.78 mL, 23.93 mmol) was added to the solution dropwise. The reaction mixture was allowed to warm to rt and then allowed to stir for 16 h. After completion

of the reaction by analysis by TLC (silica gel), the reaction mixture was cooled to 0 °C and a saturated aq solution of $NaHCO_3$ (70 mL) was added slowly. At this point the solution, which resulted, was stirred for 30 min at 0 °C. The organic layer was separated, and the aq layer was extracted with CH_2Cl_2 (3 × 50 mL). The combined organic layer was dried (Na_2SO_4). The solvent was removed under reduced pressure, and an off-white-colored solid residue, so formed, was used directly for the next step. The crude material was dissolved in 200 proof ethanol (30 mL) and NaOH (0.313 g, 7.8 mmol) was added to it. The solution, which was obtained, was heated to reflux for 2 h. The reaction mixture was cooled to rt, and the ethanol was removed under reduced pressure to afford a solid residue. The solid residue, which resulted, was dissolved in CH_2Cl_2 (100 mL) and washed with a saturated aq solution of $NaHCO_3$ (50 mL). The organic layer was separated and the aq layer was extracted with CH_2Cl_2 (3 × 50 mL). The combined organic layer was dried (Na_2SO_4), and this was followed by removal of the organic solvents under reduced pressure. Finally, the crude solid was purified by crystallization (5% MeOH in EtOAc) to afford ethyl (S)-oxazoline as a white colored solid **4**. **MP**: 199-200 °C (crystallized from 5% MeOH in EtOAc). **$[\alpha]_D^{25}$** = -40 (c 1.0, CHCl3). **^{1}H NMR** (300 MHz, $CDCl_3$) δH 8.58 (d, J 4.9 Hz, 1H), 8.08 (d, J 7.9 Hz, 1H), 7.91 (d, J 1.0 Hz, 1H), 7.83 (d, J 7.6 Hz, 1H), 7.78 (ddd, J 8.5, 2.3, 1.0 Hz, 1H), 7.57 (dd, J 2.2, 1.0 Hz, 1H), 7.51 – 7.44 (m, 1H), 7.41 – 7.33 (m, 1H), 6.05 (d, J 12.6 Hz, 1H), 4.53 (s, 1H), 4.40 (h, J 6.9 Hz, 1H), 4.18 (d, J 12.7 Hz, 1H), 3.97 (t, J 7.7 Hz, 1H), 1.38 (d, J 6.5 Hz, 3H). **^{13}C NMR** (75 MHz, CDCl3): δ 167.1 (s), 159.0 (s), 156.4 (s), 148.8 (s), 136.9 (s), 135.3 (s), 135.2 (s), 135.0 (s), 134.9 (s), 134.6 (s), 128.5 (s), 127.4 (s), 124.8 (s), 124.2 (s), 124.0 (s), 120.3 (s), 73.9 (s), 61.9 (s), 45.1 (s), 21.5 (s). **HRMS** (ESI/IT-TOF) m/z: [M + H]+ Calculated for $C_{20}H_{16}BrN_5O$ 422.0616; found 422.0608. The spectral data for **4** were identical to the literature.[212]

3.6.11. (R)-2-(8-Bromo-6-(pyridin-2-yl)-4H-benzo[f]imidazo[1,5-a][1,4]diazepin-3-yl)-4-methyl-4,5-dihydrooxazole (5, ZK-III-56)



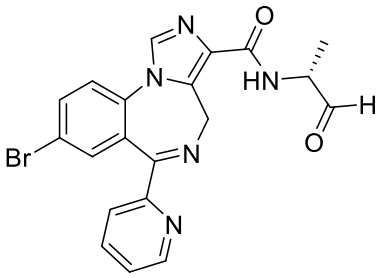
5

ZK-III-56

The solution of (S)-carboxamide **14** (3 g, 6.8 mmol) with stirring in CH_2Cl_2 (120 mL) was cooled to 0 °C (ice bath) and thionyl chloride (2.96 mL, 40.8 mmol) was added to the solution dropwise. The reaction mixture was allowed to warm to rt and then allowed to stir for 16 h. After completion of the reaction by analysis by TLC (silica gel), the reaction mixture was cooled to 0 °C and a saturated aq solution of $NaHCO_3$ (100 mL) was added slowly. At this point the solution, which resulted, was stirred for 30 min at 0 °C. The organic layer was separated, and the aq layer was extracted with CH_2Cl_2 (3 × 100 mL). The combined organic layer was dried (Na_2SO_4). The solvent was removed under reduced pressure, and an off-white-colored solid residue, so formed, was used directly for the next step. The crude material was dissolved in 200 proof ethanol (80 mL) and NaOH (1.05 g, 26.2 mmol) was added to it. The solution, which was obtained, was heated to reflux for 2 h. The reaction mixture was cooled to rt, and the ethanol was removed under reduced pressure to afford a solid residue. The solid residue, which resulted, was dissolved in CH_2Cl_2 (150 mL) and washed with a saturated aq solution of $NaHCO_3$ (150 mL). The organic layer was separated and the aq layer was extracted with CH_2Cl_2 (3 × 150 mL). The combined organic layer was dried (Na_2SO_4), and this was followed by removal of the organic solvents under reduced pressure.

Finally, the crude solid was purified by crystallization (5% MeOH in EtOAc) to afford ethyl (S)-oxazoline as a white colored solid **5**. **MP**: 201-202 °C (crystallized from 5% MeOH in EtOAc). **[α]D 25**= +44 (c 1.0, $CHCl_3$). **^{1}H NMR** (500 MHz, CDCl3): δH 8.58 (d, J 4.0 Hz, 1H), 8.07 (d, J 7.9 Hz, 1H), 7.91 (s, 1H), 7.81 (td, J 7.8, 1.8 Hz, 1H), 7.77 (dd, J 8.6, 2.2 Hz, 1H), 7.56 (d, J 2.3 Hz, 1H), 7.47 (d, J 8.6 Hz, 1H), 7.37 (ddd, J 7.6, 4.8, 1.2 Hz, 1H), 6.05 (d, J 11.1 Hz, 1H), 4.53 (dd, J 7.2, 2.1 Hz, 1H), 4.45 – 4.35 (m, 1H), 4.17 (d, J 12.7 Hz, 1H), 4.00 – 3.91 (m, 1H), 1.37 (d, J 6.6 Hz, 3H). **^{13}C NMR** (126 MHz, $CDCl_3$): δC 167.1 (s), 159.0 (s), 156.4 (s), 148.8 (s), 136.9 (s), 135.3 (s), 135.2 (s), 135.0 (s), 134.9 (s), 134.7 (s), 128.5 (s), 127.4 (s), 124.8 (s), 124.3 (s), 124.0 (s), 120.3 (s), 73.9 (s), 61.9 (s), 45.1 (s), 21.5 (s). **HRMS** (ESI/IT-TOF) m/z: [M + H]+ Calcd for $C_{20}H_{16}BrN_5O$ 422.0616; found 422.0594. The spectral data for **5** were identical to the literature.[212]

3.6.12. (R)-8-Bromo-N-(1-oxopropan-2-yl)-6-(pyridin-2-yl)-4H-benzo[f]imidazo[1,5-a][1,4]diazepine-3-carboxamide (18)

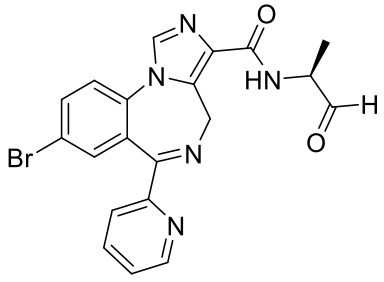


18

The Dess-Martin periodinane (1.27 g, 2.99 mmol) was added in one portion to the stirring solution of (R) carboxamide **14** (1.01g, 2.3 mmol) in CH_2Cl_2 (30 mL) at rt and the mixture, which resulted, was stirred at rt for 4 h. The progress of the reaction was monitored by analysis by TLC (silica gel, EtOAc/hexane/MeOH 2:1:0.5; less polar product spot turns yellow with 2, 4 DNP spray reagent).

When the reaction was completed, the mixture was diluted with CH_2Cl_2 (50 mL) and quenched by addition of a saturated aq $NaHCO_3$ solution (25 mL), and this was followed by a saturated aq solution of $Na_2S_2O_3$ (25 mL). The mixture, which resulted, was stirred for 20 min and the biphasic layers were separated. The aq layer was extracted with CH_2Cl_2 (2 x 30 mL) and the combined organic layer was washed with brine (20 mL) and dried (Na_2SO_4). The solvent was removed under reduced pressure and the residue was purified by crystallization (15 % MeOH in EtOAc). The solid was dried under vacuum at 40 °C to afford carboxamide **18** as a light yellow colored solid (0.78 g, 78%). **MP**: 246-249 °C, **$[\alpha]_D^{25}$** = +32.7 (c 1.02, $CHCl_3$) **^{1}H NMR** (500 MHz, $CDCl_3$): δH 9.67 (s, 1H), 8.57 (ddd, J 4.8, 1.8, 0.9 Hz, 1H), 8.15 (dt, J 7.9, 1.1 Hz, 1H), 7.87 – 7.80 159 (m, 2H), 7.78 (dd, J 8.6, 2.2 Hz, 1H), 7.61 (t, J 4.5 Hz, 2H), 7.45 (d, J 8.5 Hz, 1H), 7.37 (ddd, J 7.6, 4.8, 1.2 Hz, 1H), 6.25 (d, J 12.5 Hz, 1H), 4.63 (m, 1H), 4.14 (d, J 12.7 Hz, 1H)), 1.46 (d, J 7.4 Hz, 3H). **^{13}C NMR** (75 MHz, $CDCl_3$): δC 199.5 (s), 166.8 (s), 162.7 (s), 156.3 (s), 148.6 (s), 136.9 (s), 136.1 (s), 135.4 (s), 134.9 (s), 134.6 (s), 133.3 (s), 130.7 (s), 128.6 (s), 124.8 (s), 124.2 (s), 124.0 (s), 120.5 (s), 54.0 (s), 44.8 (s), 14.6 (s). **HRMS** (ESI/IT-TOF) m/z: [M + H]+ Calcd for $C_{20}H_{16}BrN_5O_2$ 438.0566; found 438.0549. The spectral data for **18** were identical to the literature.[212]

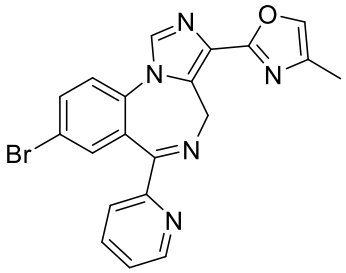
3.6.13. (S)-8-Bromo-N-(1-oxopropan-2-yl)-6-(pyridin-2-yl)-4H-benzo[f]imidazo[1,5-a][1,4]diazepine-3-carboxamide (19)



19

The Dess-Martin periodinane (1.86 g, 4.38 mmol) was added in one portion to the stirring solution of (R) carboxamide **14** (1.41 g, 3.2 mmol) in CH_2Cl_2 (30 mL) at rt and the mixture, which resulted, was stirred at rt for 4 h. The progress of the reaction was monitored by analysis by TLC (silica gel, EtOAc/hexane/MeOH 2:1:0.5; less polar product spot turns to yellow with 2, 4 DNP spray reagent). When the reaction was completed, the mixture was diluted with CH_2Cl_2 (50 mL) and quenched by addition of a saturated aq $NaHCO_3$ solution (30 mL), and this was followed by a saturated aq solution of $Na_2S_2O_3$ (30 mL). The mixture, which resulted, was stirred for 20 min and the biphasic layers were separated. The aq layer was extracted with CH_2Cl_2 (2 x 30 mL) and the combined organic layer was washed with brine (20 mL) and dried (Na_2SO_4). The solvent was removed under reduced pressure and the residue was purified by crystallization (15 % MeOH in EtOAc). The solid was dried under vacuum at 40 °C to afford carboxamide **19** as a light yellow colored solid. **MP**: 246-249 °C, **$[\alpha]_D^{25}$** = +32.7 (c 1.02, $CHCl_3$) **^{1}H NMR** (500 MHz, $CDCl_3$): δH 9.67 (s, 1H), 8.57 (ddd, J 4.8, 1.8, 0.9 Hz, 1H), 8.15 (dt, J 7.9, 1.1 Hz, 1H), 7.87 – 7.80 159 (m, 2H), 7.78 (dd, J 8.6, 2.2 Hz, 1H), 7.61 (t, J 4.5 Hz, 2H), 7.45 (d, J 8.5 Hz, 1H), 7.37 (ddd, J 7.6, 4.8, 1.2 Hz, 1H), 6.25 (d, J 12.5 Hz, 1H), 4.63 (m, 1H), 4.14 (d, J 12.7 Hz, 1H)), 1.46 (d, J 7.4 Hz, 3H). **^{13}C NMR** (75 MHz, $CDCl_3$): δC 199.5 (s), 166.8 (s), 162.7 (s), 156.3 (s), 148.6 (s), 136.9 (s), 136.1 (s), 135.4 (s), 134.9 (s), 134.6 (s), 133.3 (s), 130.7 (s), 128.6 (s), 124.8 (s), 124.2 (s), 124.0 (s), 120.5 (s), 54.0 (s), 44.8 (s), 14.6 (s). **HRMS** (ESI/IT-TOF) m/z: [M + H]+ Calcd for $C_{20}H_{16}BrN_5O_2$ 438.0566; found 438.0549. The spectral data for **19** were identical to the literature.[212]

3.6.14. 2-(8-Bromo-6-(pyridin-2-yl)-4H-benzo[f]imidazo[1,5-a][1,4]diazepin-3-yl)-4-methyloxazole (6, ZK-III-58)

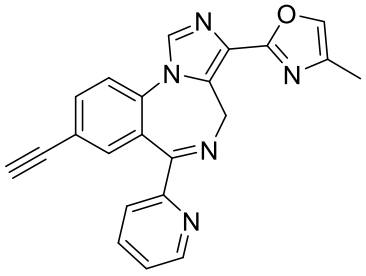


ZK-III-58
6

The general procedure for the synthesis of ZK-III-58 (**6**) was published by Pandey et. al. in 2020.[147] The hexachloroethane (1.99 g, 8.40 mmol) was dissolved in anhydrous acetonitrile (30 mL) and stirred until complete dissolution of the hexachloroethane in the solvent. Then the carboxamide **18** or **19** (1.23 g, 2.80 mmol) was added (individually) to the above solution, with stirring, in one portion. The mixture, which resulted, was cooled to 0 °C (ice bath), and triethylamine (2.35 mL, 60.88 mmol) was added dropwise. At this point, triphenylphosphine (2.20 g, 8.42 mmol) was added into the reaction mixture in three portions over 30 min. After the third addition, the ice bath was removed after 10 min of stirring at 0 °C, and the reaction mixture was allowed to warm to rt and it was stirred for an additional 2 h. It was observed that the light-yellow colored solution gradually changed into a dark brown color. The reaction progress was monitored by analysis by TLC (silica gel, EtOAc/hexane/ methanol 2:1:0.5 and a few drops of 14% aq NH_4OH). After the completion of the reaction, water (20 mL) was added and the aq layer was extracted with ethyl acetate (2 × 30 mL). The combined organic layer was washed with brine (30 mL) and dried (Na_2SO_4). The solvents were reduced to 1/3rd of the original volume and the oxazole was purified by precipitation (15 % MeOH in EtOAc) to afford a light yellow colored solid. The solid was dried

under vacuum at 40 °C to provide a light yellow colored solid of ZK-III-58 (**6**) (0.84 g, 72%). **MP**: 238-240 °C. **^{1}H NMR** (500 MHz, $CDCl_3$) δ 8.58 (d, J = 4.5 Hz, 1H), 8.09 (d, J = 7.9 Hz, 1H), 7.95 (s, 1H), 7.80 (ddd, J = 10.8, 8.2, 1.7 Hz, 2H), 7.58 (d, J = 2.0 Hz, 1H), 7.50 (d, J = 8.6 Hz, 1H), 7.43 (s, 1H), 7.37 (dd, J = 7.0, 5.2 Hz, 1H), 6.17 (d, J = 11.4 Hz, 1H), 4.28 (d, J = 11.7 Hz, 1H), 2.26 (s, 3H). **^{13}C NMR** (126 MHz, $CDCl_3$) δ 167.1 (s), 156.8 (s), 156.4 (s), 148.7 (s), 137.4 (s), 136.9 (s), 135.4 (s), 134.9 (d, J = 16.5 Hz), 133.5 (s), 132.8 (s), 128.5 (s), 127.7 (s), 124.8 (s), 124.2 (s), 124.0 (s), 120.3 (s), 53.4 (s), 45.0 (s), 11.7 (s). **HRMS** (ESI/IT-TOF) m/z: [M + H]+ Calcd for $C_{20}H_{14}BrN_5O$ 420.0454; found 420.0492. The spectral data for **6** were identical to the literature.[212]

3.6.15. 2-(8-ethynyl-6-(pyridin-2-yl)-4H-benzo[f]imidazo[1,5-a][1,4]diazepin-3-yl)-4-methyloxazole (9, ZK-IV-07)



ZK-IV-07
9

A mixture of paladium (II) acetate (16 mg, 0.07 mmol), tri-o-tolylphosphine (42 mg, 0.13 mmol) and anhydrous acetonitrile (10 mL) was allowed to stir at rt for 15 min. The bromide **6** (300 mg, 0.7 mmol), triisopropylsilylacetylene (208 mg, 1.1 mmol), triethylamine (298 mg, 2.9 mmol), and acetonitrile (10 mL) were added to the mixture in sequence. The reaction mixture was them heated to reflux (75 ◦C) and held for 4 h, at which point the reaction was deemed complete on analysis by TLC (silica gel, EtOAc/hexane/methanol 2:1:0.5 and a few drops of triethylamine). Upon

completion of the reaction, the mixture was cooled to rt and silica gel (152 mg) was added. After stirring for 15 min, the spent catalyst on silica gel was removed by adding CH_2Cl_2 (25mL) and filtered through a pad of celite. The filtrate was washed with brine (25 mL) and dried (Na_2SO_4). The solvent was removed under reduced pressure and the residue was passed through a short pad of silica gel (silica gel, EtOAc/ hexanes 3:1 with 3% triethylamine) to afford a light yellow colored solid (320.2 mg, 86%), which was used for the next step without further purification. To the mixture of this solid (310 mg, 0.59 mmol), THF (20 mL) and water (0.1 mL), tetrabutylammonium fluoride hydrate, 1M in THF (0.71 mL) was added dropwise at 0°C and the mixture was allowed to stir at rt for 1 h. Analysis by TLC (Silica gel, EtOAc/hexane/MeOH 2:1:0.5 and a few drops of 14% aq. NH_4OH) indicated the disappearance of starting material. The reaction mixture was then quenched with water and diluted with EtOAc (30 mL). The organic layer was separated and washed with brine (20mL) and dried (Na_2SO_4). The solvents were removed under reduced pressure and the residue was purified using flash column chromatography (silica gel, EtOAc/hexane 2:1 and 3% triethylamine) to yield a light yellow colored solid, **9** (172.57 mg, 77%). m.p. 235-240 °C. **^{1}H NMR** (500 MHz, $CDCl_3$) δH 8.59 (d, J = 3.5 Hz, 1H), 8.08 (d, J = 7.7 Hz, 1H), 7.98 (s, 1H), 7.84 – 7.74 (m, 2H), 7.59 (d, J = 8.2 Hz, 1H), 7.56 (s, 1H), 7.44 (s, 1H), 7.41 – 7.33 (m, 1H), 6.17 (s, 1H), 4.28 (s, 1H), 3.17 (s, 1H), 2.27 (s, 3H). **^{13}C NMR** (126 MHz, $CDCl_3$) δC 167.7 (s), 156.7 (s), 148.8 (s), 137.4 (s), 136.8 (s), 136.3 (s), 135.8 (s), 135.3 (s), 134.9 (s), 133.5 (s), 132.8 (s), 127.7 – 127.6 (m), 127.1 (s), 124.7 (s), 124.0 (s), 122.8 (s), 120.9 (s), 81.8 (s), 79.3 (s), 45.0 (s), 11.7 (s). **HRMS** (ESI/IT-TOF) m/z: $[M + H]^+$ calcd for $C_{22}H_{15}N_5O_5$ 365.1349; found 365.1437. The spectral data for **9** were identical to the literature.[212]

Chapter 4: Design and Synthesis of α5 Subtype Selective GABA(A)ergic Ligands for Treatment of Different Types of Cancer

4.1. Introduction

The central nervous system (CNS) comprises the brain and spinal cord, controling essential functions such as cognition, speech, and physical strength. The brain tumor occurs when normal brain cells undergo alterations, leading to uncontrolled growth and the formation of a tumor mass. Tumors can be either benign or cancerous. Cancerous cells with malignant tumors have the potential to grow and spread to other body parts, while benign tumors grow but do not spread.

One specific type of brain tumor is **Medulloblastoma**, which is known as pediatric brain cancer and originated in the cells of the cerebellum located at the base of skull called the posterior fossa. [213,214] The cerebellum regulates body movement and coordination. [215] Medulloblastomas are typically fast-growing tumors that spread through the cerebrospinal fluid, often metastasizing to different locations on the surface of the brain and spinal cord. This metastasis, extending down to the cauda equina at the end of the spinal cord, is referred to as "drop metastasis". [215]

Each year, approximately 250 to 500 children are diagnosed with medulloblastoma. This type of brain tumor accounts for 18% to 20% of all childhood brain tumor cases, making it the most prevalent cancerous brain tumor among children. Medulloblastomas are predominantly observed in children under the age of 16, with over 70% of diagnosed cases occurring in those younger than 10 years. The likelihood of developing medulloblastoma decreases after the age of 9.[214]

While medulloblastoma can also be identified in adults, it is less common, as compared to its occurrence in children. In the United States, approximately 33% of medulloblastoma cases are found in adults aged 20 to 44.[213–215]

The survival rate is indicated by the percentage of children who survive after the detection of the tumor. The survival rate for children with medulloblastoma is affected by various factors including the risk level associated with the disease and the age of the child at the time of diagnosis. Children under the age of 3 may experience a lower survival rate, possibly due to the typically more aggressive nature of the disease in this age group.[216]

In general, the survival rate for patients with medulloblastoma whose tumors have not metastasized is approximately 70% to 80%. However, when the tumor has spread to the spinal cord, the survival rate is lower, around 60%.

It is crucial to consider that survival rate statistics for children with medulloblastoma are approximations, derived from yearly data reflecting the occurrence of this tumor type in the United States. Moreover, this data is updated every 5 years. Ongoing research is being conducted by medical professionals to comprehend the origins of most childhood tumors, including medulloblastoma. Factors associated with an elevated risk of medulloblastoma include:

- **Gender**: Medulloblastoma is less prevalent in girls compared to boys.
- **Age**: The occurrence of medulloblastoma is most frequent in the initial 8 years of life, with approximately 50% of cases arising in children under 6 years old.
- **Genetics**: Specific genetic conditions, such as Nevoid Basal Cell Carcinoma Syndrome (NBCCS), Turcot syndrome (a subtype of Familial Adenomatous Polyposis (FAP) or Lynch syndrome), and BRCA1 gene mutations, are correlated with an increased risk of developing medulloblastoma.

Various standard-of-care approaches, including surgical resection followed by radiotherapy and chemotherapy, result in neurocognitive side effects. [216–218] Genomic studies have identified four

distinct subgroups of medulloblastoma: wingless (WNT), sonic hedgehog (SHH), group 3, and group 4. [219–221] Among these, WNT and SHH exhibit abnormal expression of genes related to the Wnt and Shh pathways, demonstrating consistency with genomic alterations. However, group 3 and group 4 do not display any subgroup-specific genomic alterations (**Figure 1**). [222–224] The group 3 subtype is particularly lethal, with a 20% survival rate under standard care treatment. Despite reports suggesting that the Group 3 subtype is MYC-driven, only a subset of group 3 tumors expresses MYC. [225–227] TP53 wild-type group 3 medulloblastoma carries a very poor prognosis. **Moreover, the medulloblastoma subtype, subgroup 3, [220,221,224] also demonstrates high expression of the GABRA5 gene**.

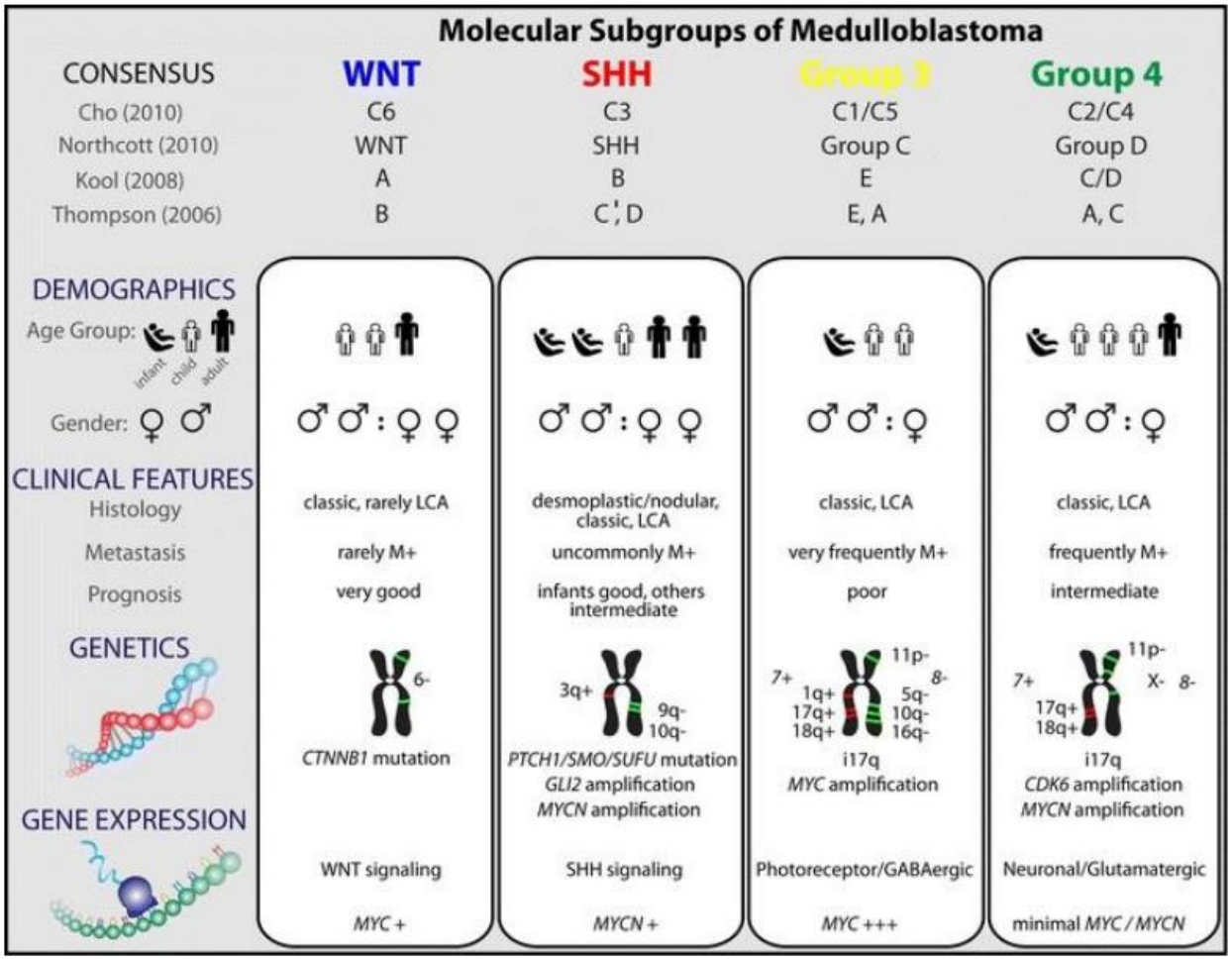


Figure 1. Comparison of the various subgroups of medulloblastoma including their affiliations with previously published papers on medulloblastoma molecular subgrouping.

In another cancer the incidence of **melanoma** is on the rise, and advanced or metastatic disease is associated with a poor prognosis.[228] Around 50% of melanomas carry somatic B-raf (BRAF) mutations, predominantly V600E (80%) or V600K (14%),[229–231] making them susceptible to treatment with BRAF inhibitors or combinations of BRAF/MEK inhibitors. [232] The initial clinically active BRAF inhibitor, vemurafenib, demonstrated high systemic objective response rates. [232–235] Subsequent developments introduced next-generation combination therapies like dabrafenib and trametinib, leading to further improvements in progression-free survival. Despite these advancements, resistance to these therapies often develops due to various genetic or adaptive mechanisms, or in some cases, intrinsic resistance.

More recently, a combination of immune checkpoint inhibitors targeting programmed cell death-1 (PD-1) and cytotoxic T-lymphocyte-associated protein 4 (CTLA-4), such as nivolumab and ipilimumab, have shown an overall response rate of approximately 60% and durable responses in certain patients, even those with melanoma brain metastases. Notably, these immune checkpoint inhibitors operate independently of the BRAF mutational status. Nevertheless, a significant portion of metastatic melanoma patients fail to achieve durable responses to immune checkpoint inhibitors. [234–237]Despite the considerable progress made, there is a pressing need for novel therapeutic strategies to address BRAF/MEK inhibitor or immune checkpoint inhibitor-resistant disease.[237–240]

Moreover, there are distinctive clinical hurdles, such as the occurrence of melanoma brain metastases, which pose substantial morbidity and mortality risks. The brain, due to the blood-brain barrier, may be considered a therapeutic sanctuary site.[241,242] The development of treatments with the capability to penetrate the blood-brain barrier would confer a crucial advantage in addressing these challenges.[243–245]

Gene expression analysis conducted by The Cancer Genome Atlas (TCGA) on melanoma patient tumors revealed a notable elevation in the expression of GABR genes, which encode subunits of the Type A γ-aminobutyric acid (GABA) neurotransmitter receptor ($GABA_AR$). A more extensive examination by Dr. Sengupta et al. [246]delved into GABR expression in metastatic melanoma tumors and characterized melanoma cells for intrinsic $GABA_AR$ activity. The study observed varying GABR gene expression in melanoma patients, particularly in the molecular subgroups defined by TCGA, such as the MITF-low and Keratin groups. Additionally, functional $GABA_ARs$ were identified in melanoma cells through whole-cell patch-clamp electrophysiology experiments.[246]

Furthermore, Dr. Sengupta et al. [246] demonstrated that enhanced $GABA_AR$-mediated membrane permeability to anions, achieved with $GABA_AR$ subtype-selective benzodiazepines, led to depolarized mitochondria in melanoma cells and compromised melanoma cell viability in vitro. In a syngeneic melanoma mouse model, the benzodiazepine with anticancer properties alone contributed to a reduction in tumor growth, and its combination with radiation and/or the programmed death ligand immune checkpoint inhibitor (α-PD-L1) significantly enhanced efficacy. The benzodiazepine target, when combined with radiation, promoted both ipsilateral and abscopal antitumor activity, accompanied by increased tumor infiltration with antigen-specific polyfunctional CD8 T-cells. This study highlights a potential innovative anti-tumor strategy that

involves combining radiation and/or immune checkpoint inhibitors with the modulation of $GABA_ARs$ in melanoma, utilizing a subtype-preferring anticancer benzodiazepine.

Lung cancer stands as the foremost cause of cancer-related fatalities in the United States, resulting in approximately 350 deaths each day. [247] The predominant lung cancer type, non-small cell lung cancer (NSCLC), constitutes 80-85% of cases, with an overall 5-year survival rate of 64%, declining to 37% when tumor cells infiltrate the lymphatic system.[247] Most NSCLC cases manifest as metastatic disease at clinical presentation, often proving incurable. Brain metastasis is particularly challenging, comprising 30% of NSCLC metastatic occurrences, although post-mortem analysis suggests a notably higher incidence.

Standard-of-care for lung cancer brain metastasis involves surgical resection for large solitary lesions and stereotactic brain radiosurgery (SRS) for cases with fewer than ten lesions. Whole brain radiation therapy (WBRT) is utilized otherwise. [248] However, both SRS and WBRT are associated with toxicity, including radiation necrosis and neurocognitive effects. [249] Managing these potential toxicities and overcoming ensuing radiation resistance present significant challenges. Despite cranial radiotherapy being part of a multimodal treatment approach for NSCLC brain metastasis, the median survival remains at approximately 7-10 months.

To enhance the effectiveness of radiation, the plant alkaloid docetaxel (Taxotere) is commonly used as a chemotherapeutic in combination with radiotherapy for advanced-stage NSCLC. [250] However, docetaxel is linked to significant comorbidities, such as compromised immunity and peripheral neuropathy. Moreover, it is not employed for treating brain metastasis due to its limited ability to penetrate the brain.

Considerable attention has recently been directed toward exploiting autophagy, the process of self-degradation, as a strategic approach against cancer. There is ongoing exploration of agents that either inhibit or induce autophagy to disrupt cancer cell viability. [251] Inhibitors of autophagy, such as the immunosuppressive anti-parasitic drugs chloroquine and hydroxychloroquine, interfere with the assembly of double-layered autophagosomes. Notably, engineered cell-penetrant peptides have emerged as more selective autophagy inhibitors by targeting autophagy-specific protein-protein interactions. On the other hand, inducers of autophagy encompass the anti-diabetic metformin and mTor inhibitors (everolimus, temsirolimus, and rapamycin).[251–253]

Supporting an approach that involves inducing autophagy for anticancer effects, recent reports suggest that enhanced expression of key autophagy-associated proteins contributes to prolonged patient survival. The plant-derived compound methyl jasmonate has demonstrated therapeutic effects in human non-small cell lung cancer (NSCLC) cell cultures by inducing autophagy. [254]Additionally, radiation has been reported to enhance the expression of autophagy-associated proteins.[255–257]

While the investigation of stress-induced autophagy is under intensive study, the utilization of stress response, particularly autophagy, as an anticancer approach remains relatively unexplored. For instance, induction of autophagy is often triggered in response to mitochondrial stress. [258,259] Mediating the stress response are membrane-associated proteins signaling to alter cellular metabolic states. Among these, ligand-gated ion channels, representing a significant pharmacological target for neurological disorders, are poorly explored as therapeutic vulnerabilities in cancer. Notably, Type-A GABA receptors among ion channels are a primary target, functioning as major inhibitory neurotransmitter receptors. Enhanced expression of GABA(A) receptor subunits in various cancers, along with the functional responsiveness of cancer

cells' GABA(A) receptors to GABA, prompted investigations into the receptor as a therapeutic vulnerability for cancer cells. [260,261] This exploration led to the identification of brain-penetrant molecules activating GABA(A) receptors, which not only impaired cancer cell viability but also exhibited efficacy in controlling tumors in mouse models of these cancers. [262,263]

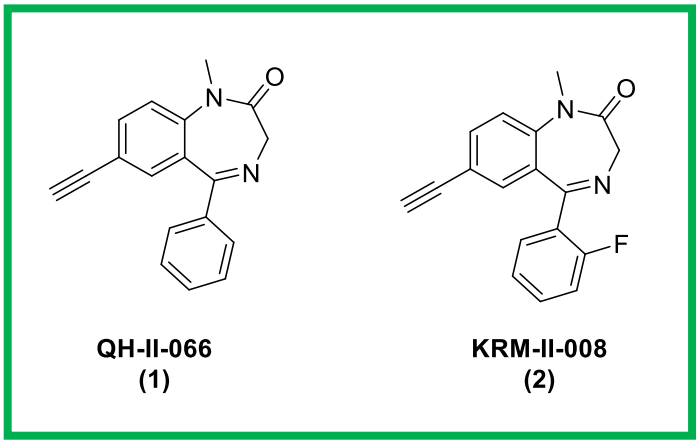


Figure 2. Structures of the lead compounds, QH-II-066 and KRM-II-008

QH-II-066 (**1**) and KRM-II-008 (**2**) function as positive allosteric modulators for α5GABA$_A$R and demonstrated exceptional potency in the cell viability assay. Their effectiveness was attributed to the reduction in the expression of HOXA5, a homeobox transcription factor that regulates p53 expression. Dr. Soma Sengupta conducted a study involving 763 primary medulloblastoma patient tumors to understand the role of α5-GABA$_A$R in the viability of group 3 cells.

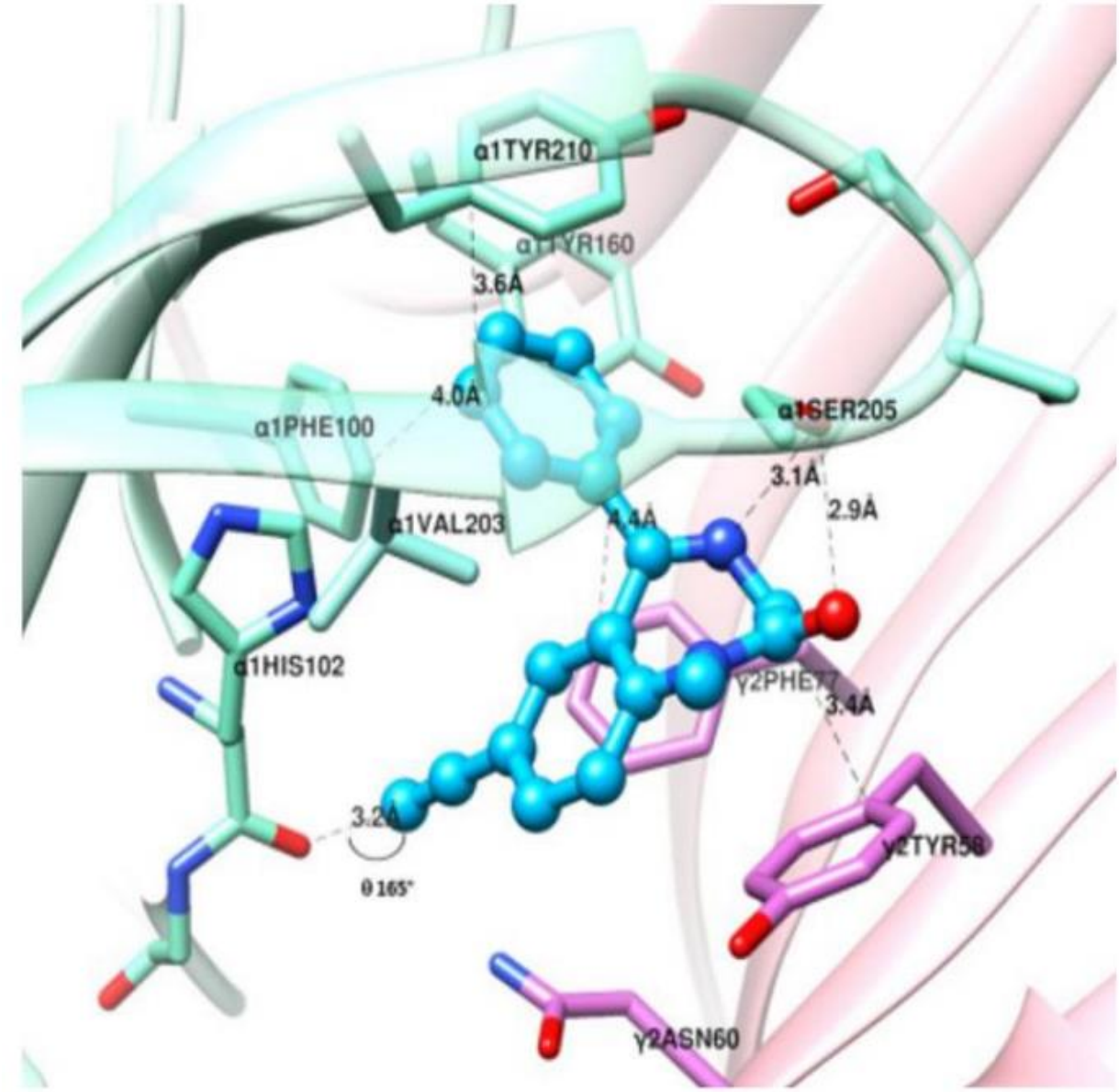


Figure 3. QH-II-066 at α+ γ - Interface of $GABA_A$ Receptor in the α1β3γ2 em cryostructure (Nature 2019)

The cryo-ER structures of QH-II-066 (**1**) indicated the three crucial interactions that contribute to its positive allosteric modulator (PAM) function: i) a bifurcated hydrogen bond with α1Ser205 at distances of 3.1 Å and 2.9 Å with the N atom in the seven-member ring and the oxygen atom,

respectively; ii) a hydrogen bond with the backbone of α1His102, which was less significant than the halogen bond formed by diazepam with α1His102 via halogen bonding with the backbone carbonyl; iii) pi-pi stacking with α1Tyr210 and α1Phe100. In the cryo-ER structures, the distance between the chlorine atom and the carbonyl oxygen of α1His102 was 3.8 Å for QH-II-066 (**1**) (6HUO), compared to 3.2 Å in the DZP-bound cryo-ER structure (6HUP). The σ-hole angle remained consistent at 165 degrees in both cryo-ER structures. The shorter and bifurcated hydrogen bond interactions of QH-II-066 (**1**) with α1Ser205 are in line with its sedative effect via α1β3γ2, although it is much less than that of diazepam (US patent, Cook et al. 2006).

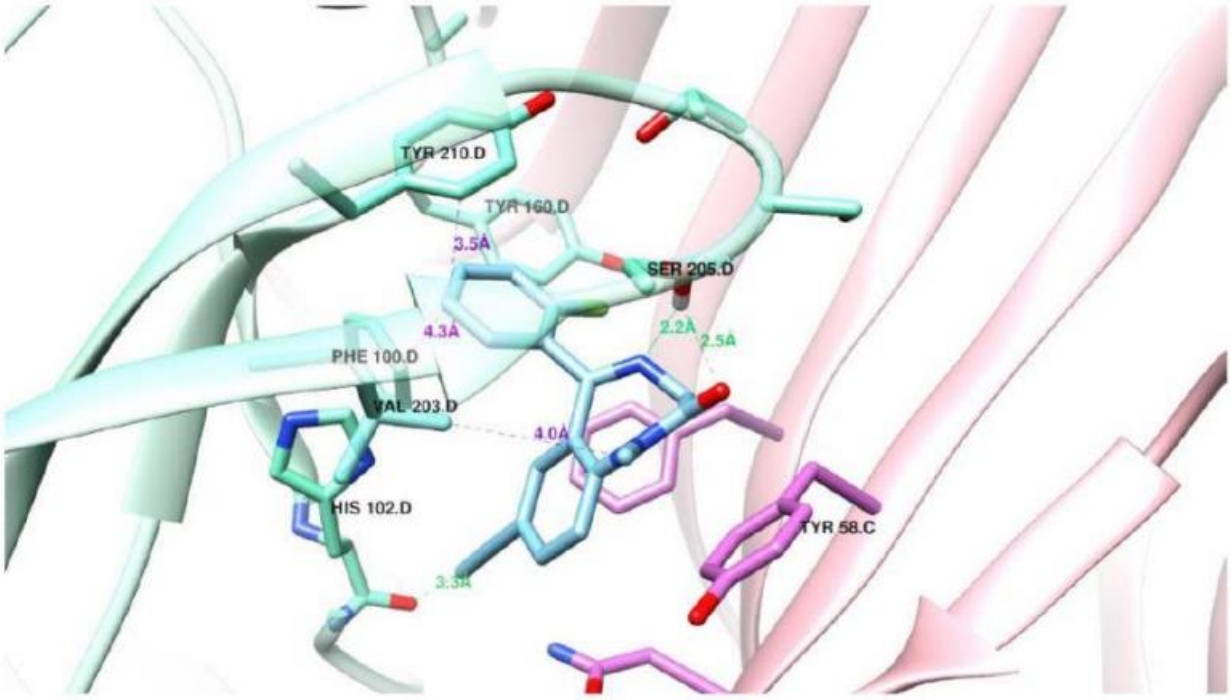


Figure 4. KRM-II-008 (19) at the α + γ - Interface of GABA$_A$ Receptor

The most critical hydrogen bonding bifurcation is: - with α1Ser205, the N atom in the seven-member ring was 2.2A, and the oxygen atom was 2.5A. And -the pi-pi stacking with α1Tyr210 and α1Phe100. The bifurcated hydrogen bond formed by QH-II-066 with α1Ser205 is longer than

that configured with bound KRM-II-008. As the hydrogen bond of KRM-II-008 is shorter than QH-II-066, so it exhibits more potent affinity for α1 than QH-II-066 as well as α5 subtypes.

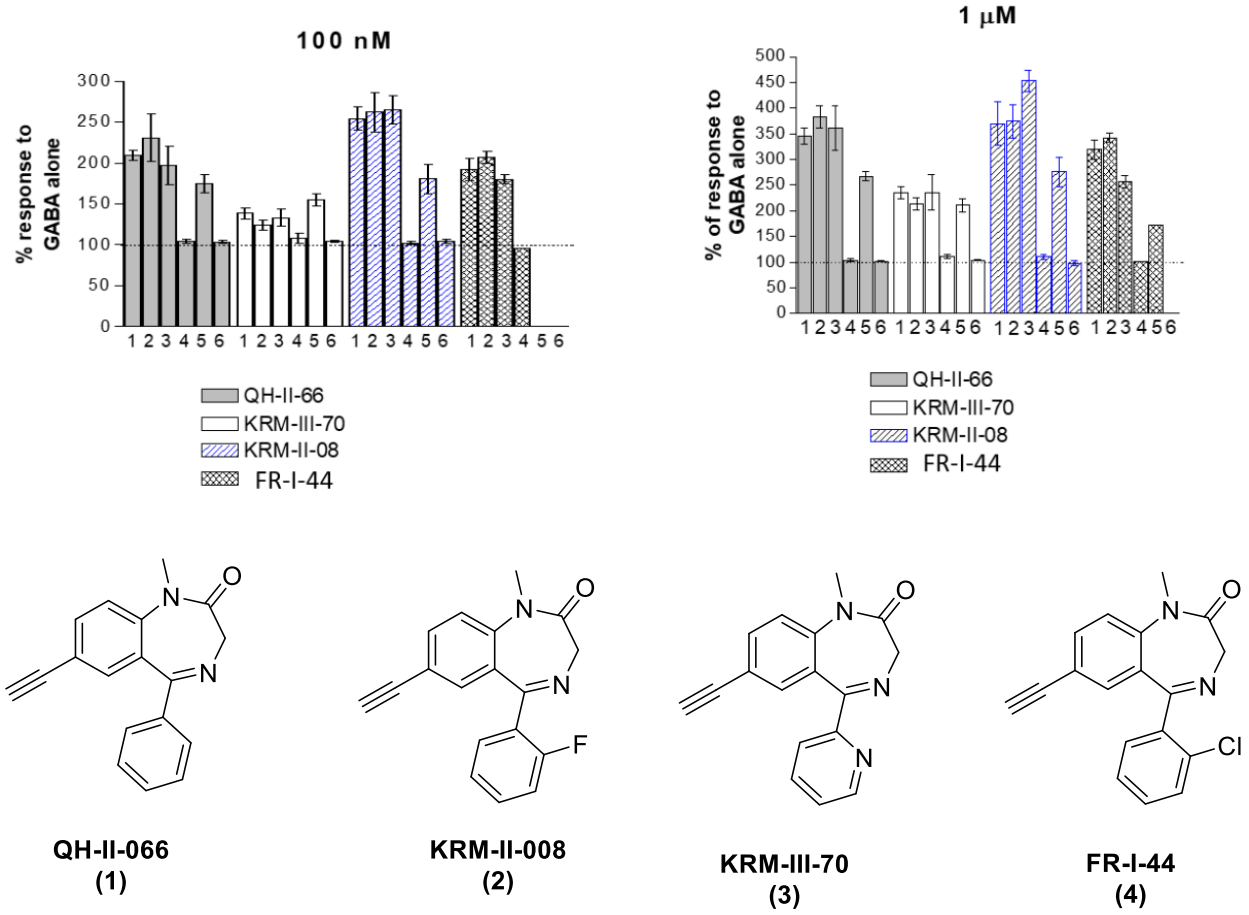


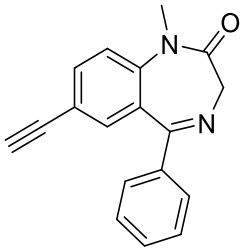
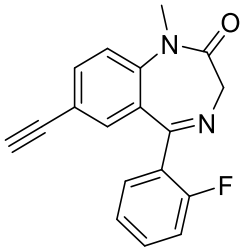
Figure 5. The efficacy of ligands expressed in HEK, α1-6,β3γ2 GABA ion channels with EC3 GABA.

4.2. Cytotoxicity

Ligands were incubated with HEK293T cells and HEPG2 cells, respectively, over 48 hours followed by detection of cell viability using a Cell-Titer Glo (Promega). The normalized data was performed by using DMSO as a negative control and 3-dibutylamino-1-(4-hexyl-phenyl)-propan-1- one (150 mM in DMSO final concentration used as a positive control).

Results were indicated by three independent experiments carried out in quadruplet. The LD50 values in HEK293 and HEPG2 cell lines of each compound were presented in the last two columns, respectively. According to the LD50 value, most of the compounds are non-toxic to normal cells. (**Table 1**) In HEPG2 cell lines the LD50 values for most of the compounds were greater than 200 μM, which indicate these compounds are safe and not cytotoxic to normal cells.

Table1. Cytotoxicity data of the lead ligands in HEK293T and HEPG2 cells.

	Code	Structure	HEK293 LD50	HEPG2 LD50
1	**QH-II-066**		**174.6 ± 13**	**242.7 ± 10**
2	**KRM-II-008**		**257.5 ± 12.9**	**277.4 ± 15.5**

In both cases, the LD50 value of the same compound is higher in the liver HEPG2 cell lines than the kidney HEK293 cell lines due to the presence of more metabolic enzymes in liver than in kidney.

4.3. IC_{50} value of lead compounds with their nor-analogs

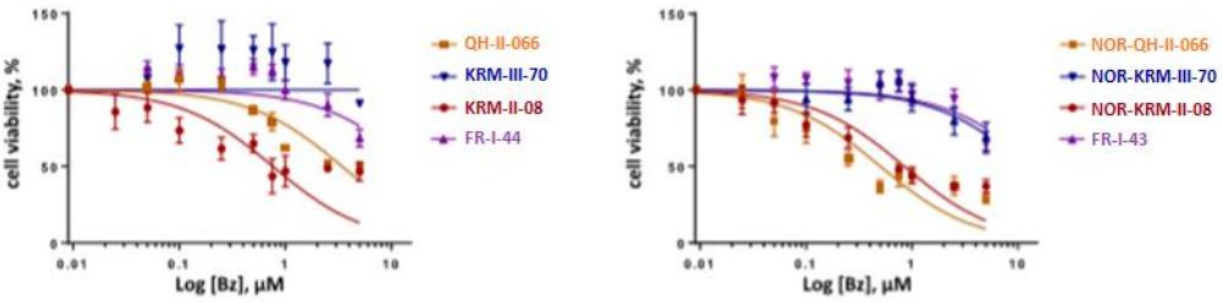
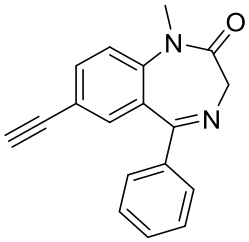
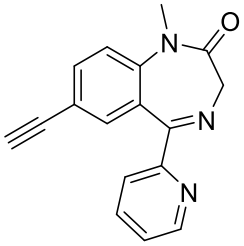
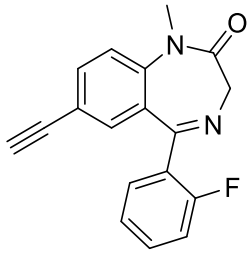
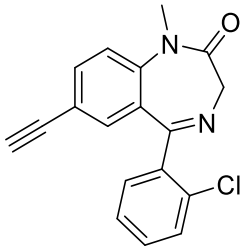
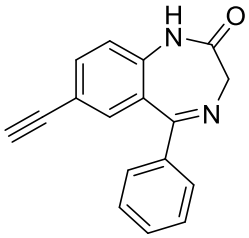
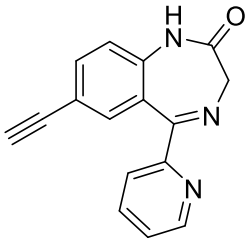
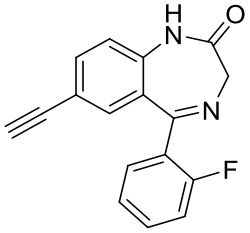
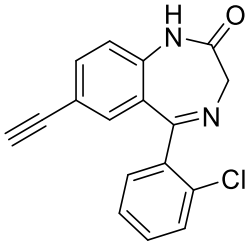


Figure 6. The potency of the ligands

Table 2. The IC50 value of the ligands in D283 cell line.		
Code	**Structure**	**IC_{50} (µM)**
QH-II-066	 **(1)**	**3.4 ± 0.3**
KRM-III-70	 **(3)**	**-**

KRM-II-008	 **(2)**	**0.8 ± 0.1**
FR-I-44	 **(4)**	**16.3 ± 3.4**
NOR-QH-II-066	 **(5)**	**0.51 ± 0.06**
NOR-KRM-III-70	 **(6)**	**12.16 ± 1.85**

NOR-KRM-II-08	 **(7)**	**0.85 ± 0.09**
FR-I-43	 **(8)**	**14.97 ± 2.54**

To find the potency of different kinds of α5 preferring ligands were screened in D283 cell lines. All the ligands showed very good potency except KRM-III-70, it might bind to an alternative target such as the peripheral benzodiazepine channel TSPO. According to the IC_{50} value, QH-II-066, NOR QH-II-066, KRM-II-008 and NOR KRM-II-008 exhibit the greatest potency.

4.4. Gene expression of Medulloblastoma

As noted previously, an examination of GABR and MYC expression in various subtypes of medulloblastoma involved the analysis of 763 resected tumor cells. Online resources indicated the following findings: 1) Elevated expression of specific GABR genes was observed across all medulloblastoma subgroups. 2) GABAR expression varied among subgroups, with certain subgroups exhibiting higher GABAR expression, as compared to others.[225] 3) Positive correlations between GABAR and MYC were reported in Group 3 and WNT tumors. Within all medulloblastoma subgroups, the GABRB3 gene demonstrated consistently high expression, albeit

with variations between groups. Similarly, GABRG2 expression varied among subgroups, with Group 3 and 4 displaying the highest levels. Notably, the expression levels of GABR genes differed in the SHHγ subtype, distinguishing it from SHHα, SHHβ, and SHHδ. Across all SHH subgroups, high expression of GABRA2 and GABRG1 was documented, [263] **while Group 3 medulloblastoma patients exhibited elevated expression of the GABRA5 gene**.

To find distinctions in both GABRA5 and MYC within the Group 3 and WNT subgroups, supervised heatmaps and boxplots were employed. No statistically significant correlation between MYC and GABRA5 was identified in Group 3 ($p = 0.202$). However, in the Group 3α subtype ($p = 0.006$), a positive correlation between MYC and GABRA5 was observed, coinciding with the loss of MYC expression[24]. Conversely, in the Group 3γ subtype ($p = 0.634$), no significant correlation between MYC and GABRA5 was evident, despite high MYC expression. Notably, WNT tumors exhibited elevated MYC expression, albeit with poorer expression of GABRA5 compared to Group 3.

Selecting a cell line that faithfully reproduces the molecular profile of Group 3 patient tumors is crucial for investigating the potential role of benzodiazepines in impairing Group 3 cell viability. The differentiation of Group 3 subtypes and other medulloblastoma subgroups is contingent on the GABRA5 gene's expression levels. Typically, Group 3 tumors exhibit high MYC expression and low N-MYC expression. Various patient-derived cell lines, including Daoy, D283, and D425, were subjected to qRT-PCR to assess N/C-MYC and GABRA5 expression. The Daoy cell line, derived from the SHH subgroup, the D283 cell line associated with Group 3 medulloblastoma (TP53-wildtype), [24]and the D425 cell line representing Group 3 medulloblastoma (TP53-mutated) were analyzed.

The qRT-PCR results indicated uniformly low expression of N-MYC in Daoy, D283, and D425 cell lines. Notably, Daoy showed no expression of MYC, while D283 and D425 exhibited higher MYC expression. Strong correlative expression of GABRA5, GABRB3, and GABRG2 was identified in Group 3 tumors. The D283 cell line demonstrated elevated expression of the GABRA5 gene, as compared to other GABRA genes. Remarkably, the consistency in GABRA5 expression between the D283 cell line and Group 3 tumors was evident. The D283 cell line is commonly utilized for Group 3β or 3γ, as Group 3α typically displays higher GABRA1 expression than GABRA5.

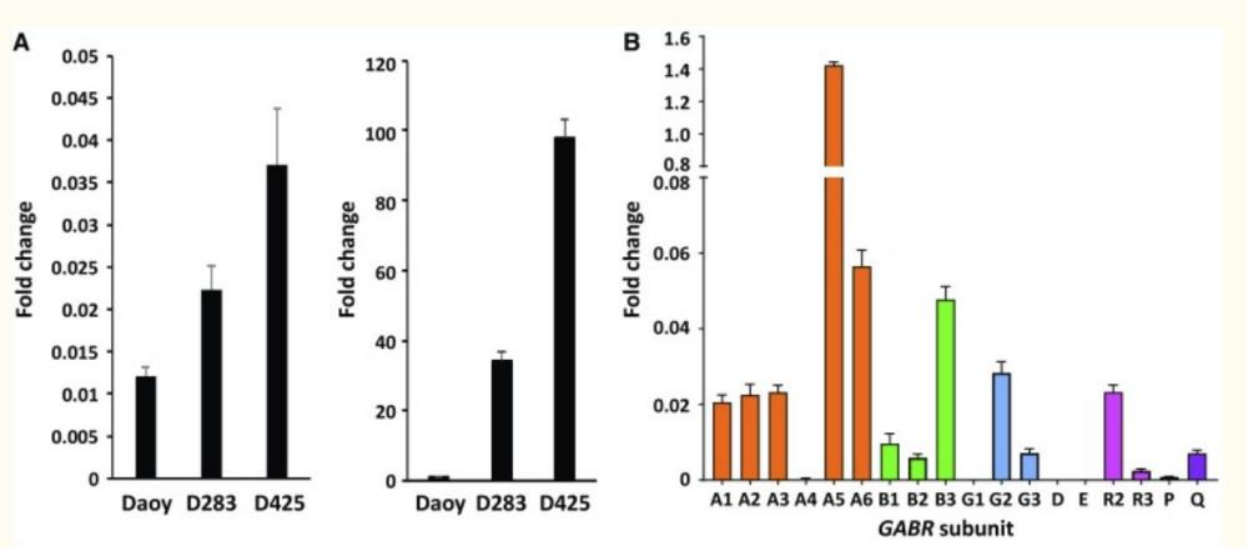


Figure 7. GABR expression MYC and in medulloblastoma and evidence for a functional α5-GABAA receptor in patient cell lines Daoy, D283, and D425 a. qRT-PCR of N-MYC (left) and MYC (right). b. in D283 qRT-PCR of GABR expression.

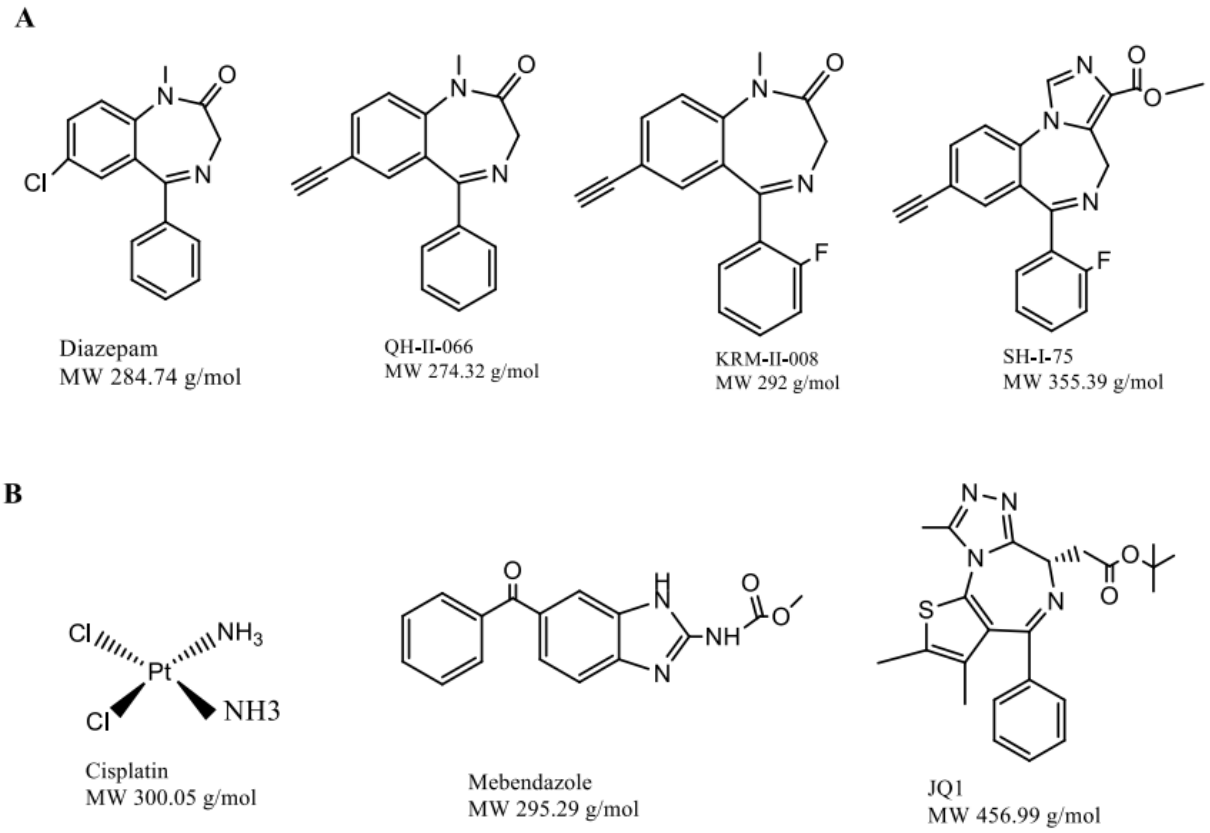


Figure 8. The structures of compounds for comparison in treatment of medulloblastoma (A) Structurally α5 subtype selective benzodiazepine(B) The structures of the standard-of case treatment compounds. JQ1 shares a similar structural similarity as the ligand SH-I-75.

In various tumor models, the intratumor microdose effectiveness of multiple benzodiazepines (**Figure 8**), which enhance GABA action at 5-$GABA_A$ receptors, was compared to different clinically relevant treatments such as cisplatin, mebendazole, and the bromodomain inhibitor JQ1. Nude mice flank xenografts were generated using medulloblastoma tumor cell lines,[18] specifically D425 and D283, known for having higher expression of 5-$GABA_A$ receptors. These xenografts were observed to be more susceptible ($p < 0.01$) to benzodiazepine derivatives compared to DAOY flank xenografts, a cell line expressing non-5-GABAA receptor medulloblastoma. This insight was gained through microdevice technology. [264]

Positive allosteric modulators of 5-$GABA_A$ receptors, such as KRM-II-008, exhibited increased activity against D425 tumors. Additionally, substances like SH-I-75 and QH-II-066 displayed sensitivity to tumor cells, inducing cell death. Within 24 hours, KRM-II-008 demonstrated a 38% apoptosis rate, while SH-I-75 and QH-II-066 exhibited rates of 21% and 13%, respectively, in exposed tumor cells (**Figure 9**). Notably, in this tumor model, KRM-II-008 proved more effective than standard-of-care treatments. In the D283 tumor cell line, both KRM-II-008 (AI = 32%) and QH-II-066 (AI = 30%) showed a high apoptosis rate. Conversely, in the non-5-GABAA receptor-expressing tumor cell line DAOY (**Figure 9**), cisplatin, JQ1, and mebendazole demonstrated a more significant effect.

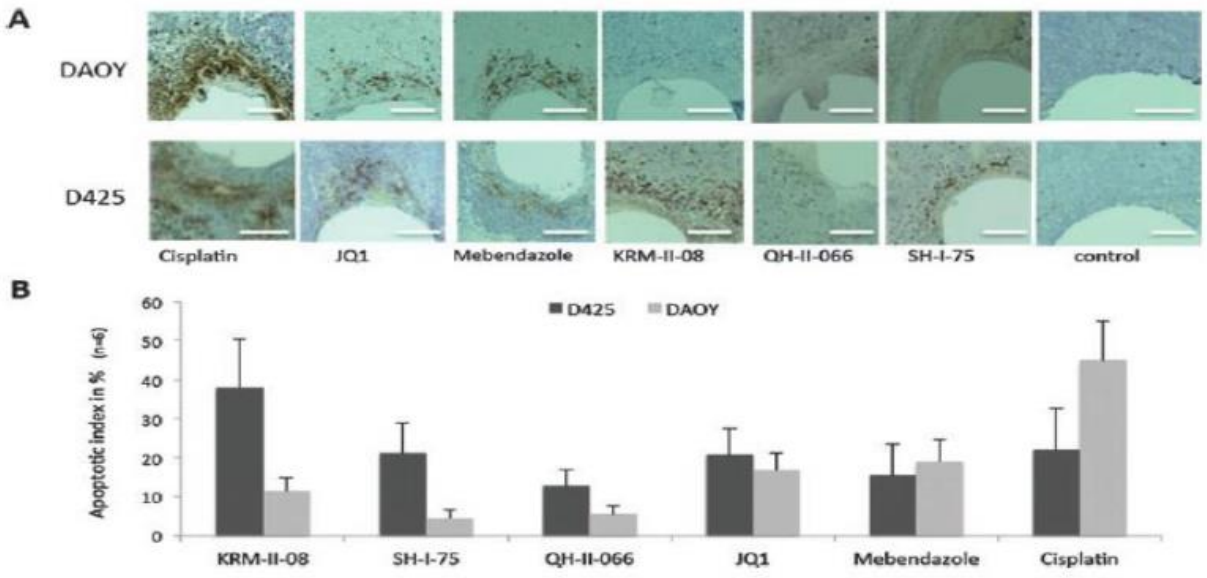


Figure 9. Representative images of D425 and DAOY tumor sections removed 24 hours after exposure to a microdose of each drug from the device, showing distinct regions of apoptosis assessed by cleaved-caspase-3 expression (brown) after 24 hours. Scale bars, 250 µm. (B) Apoptotic index (%apoptotic cells/all cells in drug-affected tissue region) for human D425 and DAOY tumors exposed to KRM-II-08, SH-I-75, QH-II-066, JQ1, mebendazole and

cisplatin (all 35% drug in PEG1450). Averages are taken from 6 spatially distinct reservoirs from at least 3 tumors please give ($p < 0.01$).

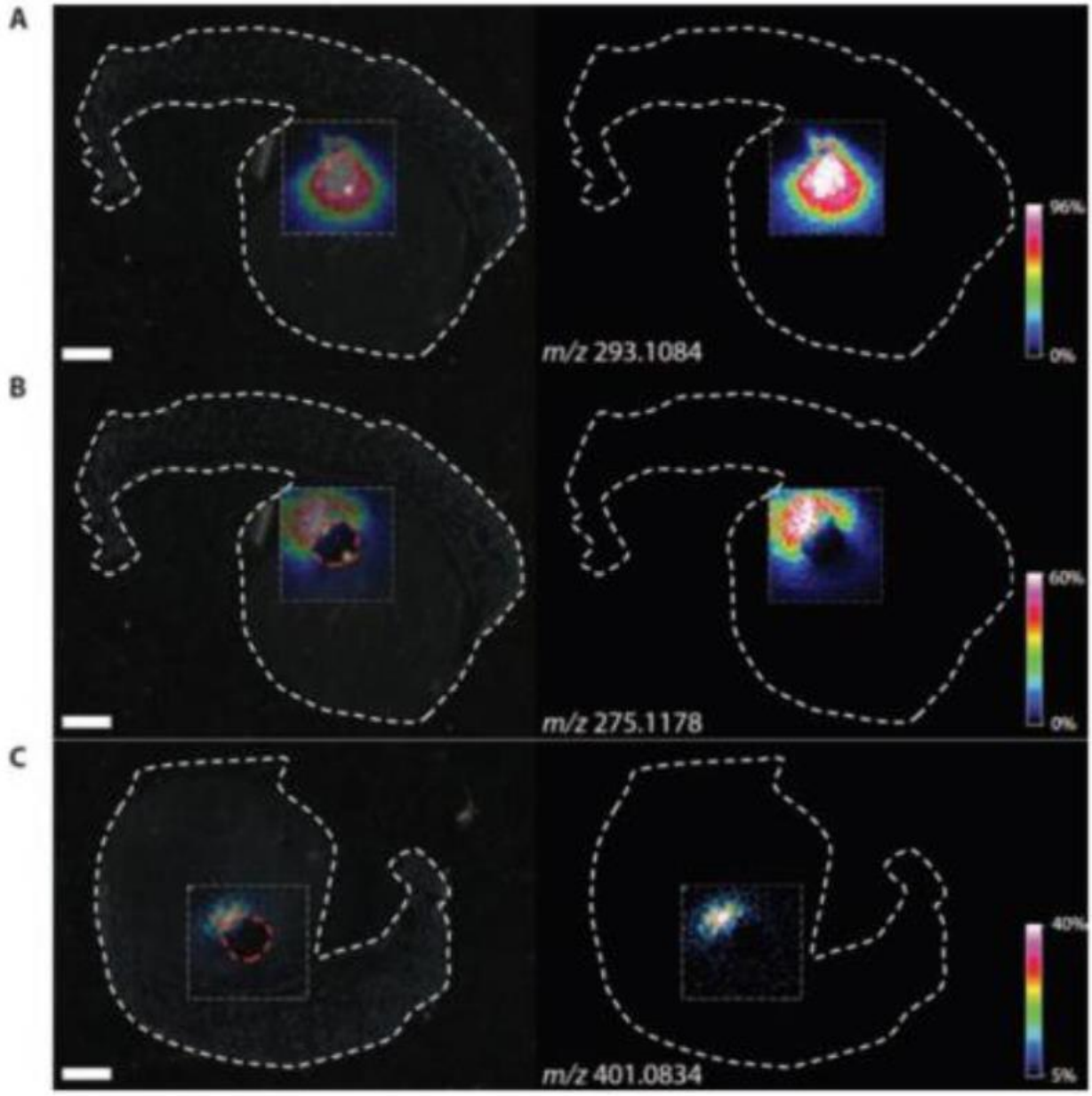


Figure 10. The molecular imaging of compound distribution in MALDI FTICR mass spectrometry. The distribution of three drugs in sections of a mouse flank tumor with an implanted device via Matrix-assisted laser desorption/ionization Fourier-transform ion

cyclotron resonance (MALDI FTICR) mass spectrometric imaging (MSI): (A) KRM-II-008 (m/z 293.1084); (B) QH-II-066 (m/z 275.1178); and (C) a fragment of JQ1 (m/z 401.0834).

MALDI mass spectrometry imaging analyses (1213) were employed to ascertain the spatial distribution of compounds released through the microdevice on cross-sectioned frozen flank tissue from mice. The distribution patterns of KRM-II-008 (**Figure 10 A**), QH-II-066 (**Figure 10B**), and JQ1 (**Figure 10C**) were visualized using MALDI mass spectroscopy. High mass accuracy measurements, achieved through an FTICR analyzer with precision better than 1 ppm, confirmed the release of each compound from the microdevice. Notably, in the case of JQ1, ions from the fragmented parent molecule were detected, attributed to in-source fragmentation induced by the high laser intensity (i.e., 35%).

All the compounds were observed to permeate the tumor tissue, with maximum diffusion distances of 560 μm for JQ1 and over 1150 μm for both KRM-II-08 and QH-II-066 (**Figure 10**). These distances were determined based on correlation with eosin (H/E) and hematoxylin-stained serial sections. This analysis establishes a correlation between the area of drug exposure and the induction of apoptosis.

4.5. Chemistry

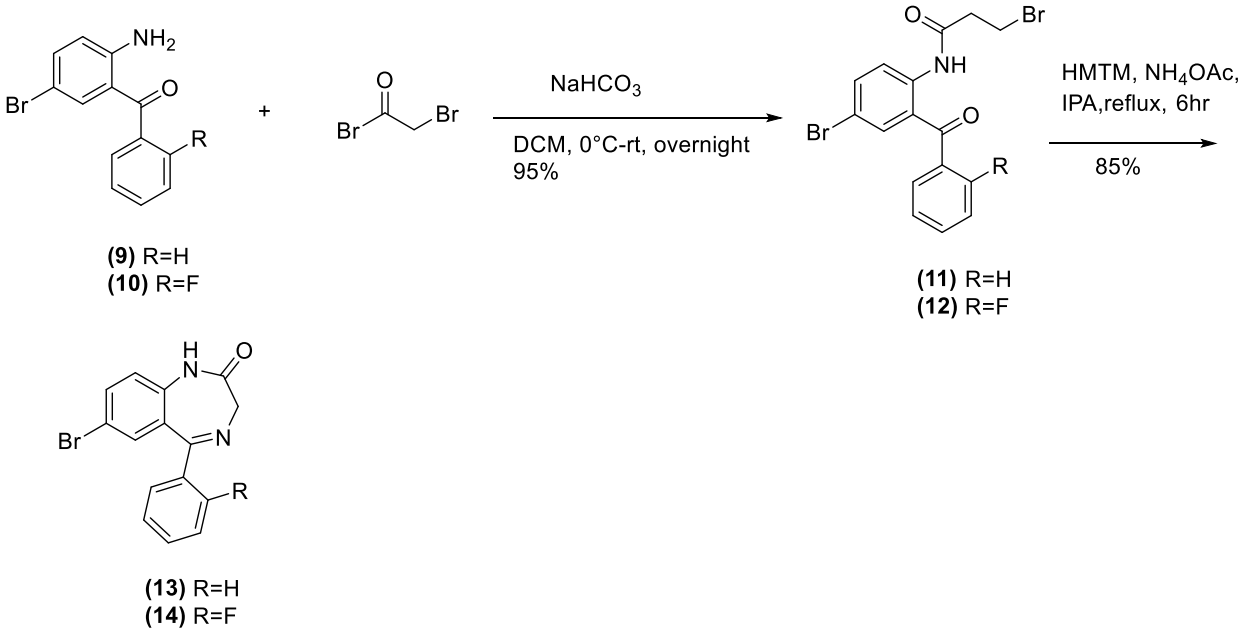
4.5.1. Synthesis of the QH-II-066 and KRM-II-008

In order to make the key intermediate for the lead compounds **1** and **2**, The amine **9/10** was converted into the protected acetamide **11** or **12** (respectively) using bromoacetyl bromide in the presence of sodium bicarbonate in anhydrous dichloromethane. To facilitate this process, the reaction mixture was cooled to 0°C before introducing bromoacetyl bromide. The addition of

bromoacetyl bromide at this low temperature resulted in the formation of a thick red solid, complicating the stirring of the reaction mixture due to its increased viscosity.

The reaction was deemed complete (verified by TLC) after the addition of bromoacetyl bromide. The next step was the cyclization, which was done by replacing ammonia with hexamethylenetetramine (HMTM) developed by Dan Knutson in the presence of ammonium acetate. The reaction was done in isopropyl alcohol by heating to reflux for 6 hours. The reaction is known as the Delapine-related reaction. This approach solved the imidate byproduct issue faced in the previous route mentioned in an earlier chapter. There was only one product formed. The benzodiazepine was purified by crystallization with 30:70 ethyl acetate: hexanes. The yield of pure benzodiazepine was 85%. (**scheme 1**)

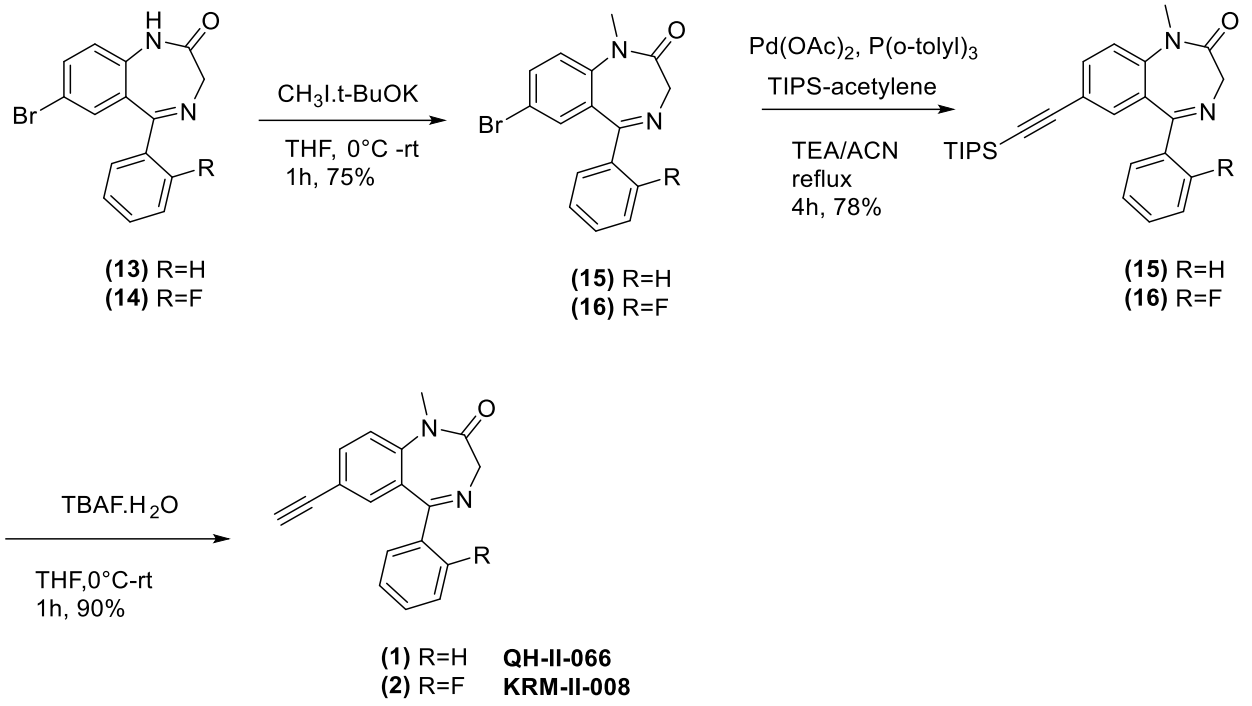
Scheme1. Synthesis of the key intermediate for the lead compounds 1 and 2



In the following step the N-methylation was performed. The reasons of applying N-methylation in this step are1) The Heck-type coupling provides a lot of impurities if there is an N-H group present.

If the N-H group is protected, the Heck-type coupling process proceeds well, which makes the purification very easy. 2) If this step is done after the installation of the acetylene function the base can abstract the ethynyl proton which can generate one more impurity. In previous routes sodium hydride was used which caused problems by producing more than two unnecessary byproducts. This problem was solved by using potassium tert-butoxide, a more hindered base than sodium hydride and one in which it was easier to control. This approach provided 75% yield of the desired N-methyl amide **15** or **16**. The next step involved the Heck-type coupling in the presence of ortho tolyl phosphine as the ligand which solved the problem of forming triphenylphosphine oxide byproduct due to the presence of air. Ortho tolyl phosphine does not become oxidized by oxygen from the air, so degassing was not required at this stage. This was discovered by Greg Fu and the ortho tolyl ligand has a bigger bite angle. [135]The TIPS acetylene function was used to form a greater R_f difference between the starting bromide and the desired ethynyl analog. The TIPS group was also easier to remove on chromatography, which reduced byproducts. The percent yield of this stage was 78%. - In the final step the TIPS group was removed by using tetrabutyl ammonium fluoride (TBAF) in THF at -20 °C to room temperature. This step takes about 1 hour with stirring. QH-II-066 (**1**) or KRM-II-008 (**2**) (individually) were both crystallized from isopropanol in 90% yield. (**Scheme 2**)

Scheme2. Synthetic route to make the lead compounds QH-II-066 (1) and KRM-II-008 (2)



(13) R=H
(14) R=F

(15) R=H
(16) R=F

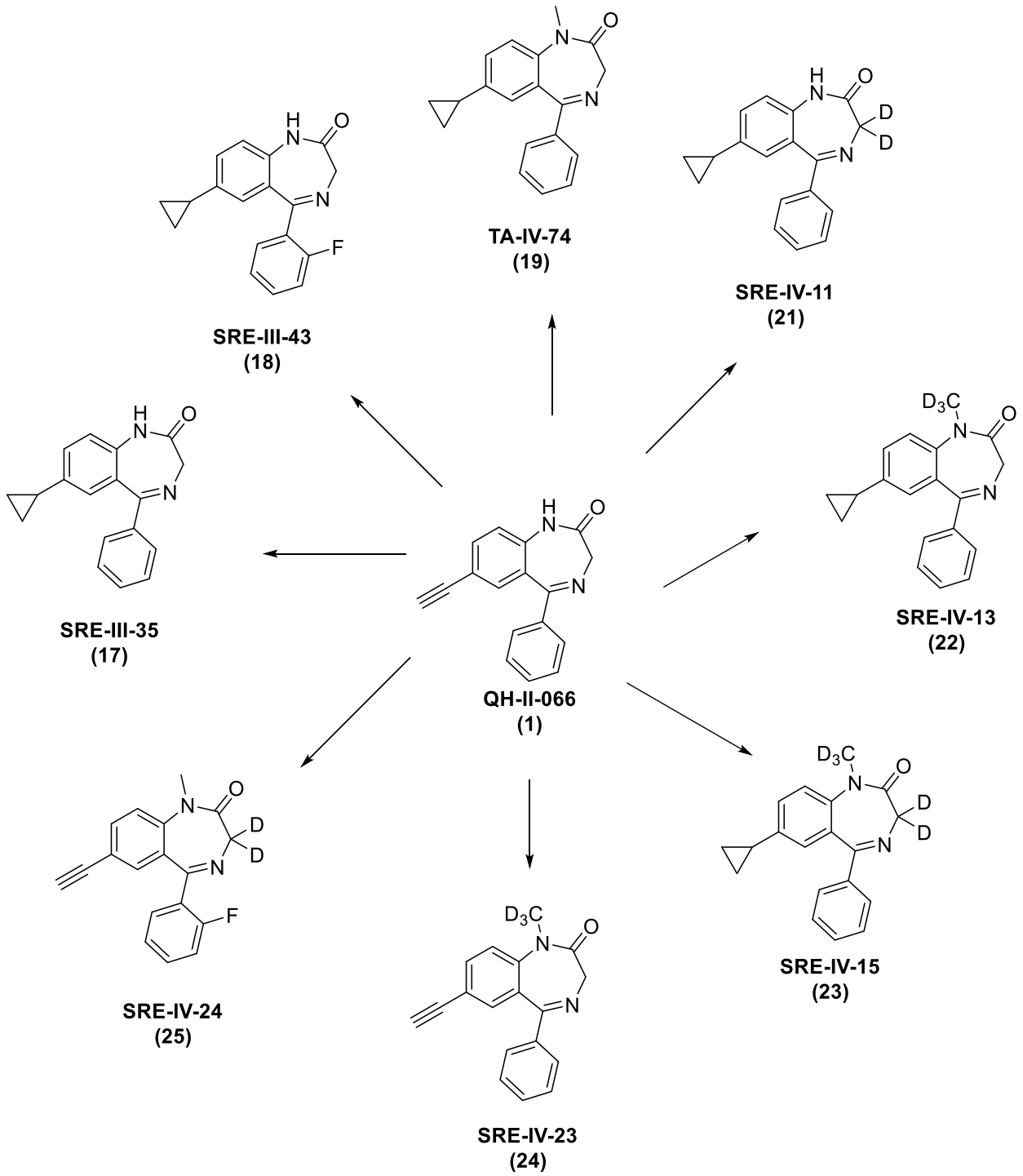
(15) R=H
(16) R=F

(1) R=H **QH-II-066**
(2) R=F **KRM-II-008**

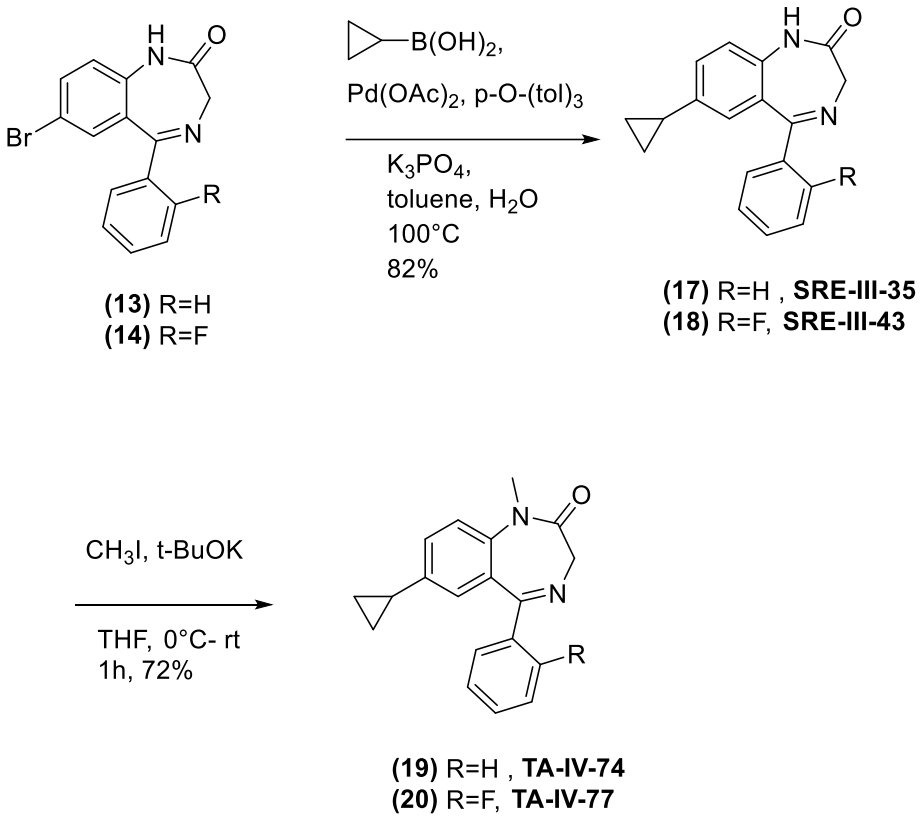
4.5.2. Synthetic route to make 7-cyclopropyl analogs.

The cyclopropyl ligands **(17/18)** were designed and synthesized by Rezvanian and Ahmed at UW-Milwaukee, from cyclopropyl boronic acid *via* a Suzuki-coupling reaction with the aryl bromide (**13/14**). The coupling reaction was carried out in the presence of potassium phosphate, palladium (II) acetate and tri-o-tolyl phosphine in toluene at 100 ^{o}C for 12 hours. This process was executed in good yield (82%), as shown in **Scheme 3**.

Scheme 3. Structure of analogs of QH-II-066



Scheme 4. Synthesis of cyclopropyl analogs to replace a 7-ethynyl group.

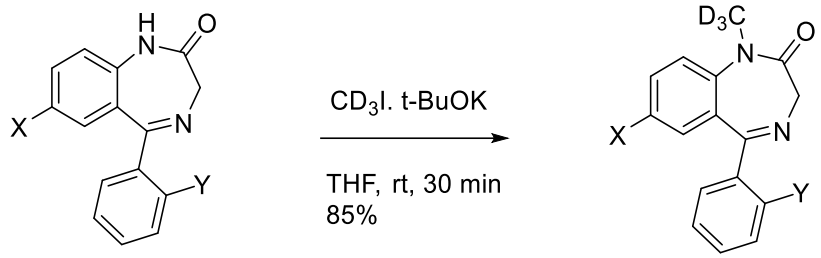


4.5.3. Synthetic route to make deuterated analogs.

In order to improve the metabolic stability of the synthesized ligands, the deuterated analogs of them were also made (**Scheme 5** and **6**)

Two N-CD3 ligands were designated and synthesized by Ahmed and Rezvanian, D3-QH-II-066 (**24**) and SRE-IV-13 (**22**) (respectively). The D3-QH-II-066 (**24**) can be synthesized from Nor QH-II-066 by treating the amide with deuterated methyl iodide in the presence of potassium tert-butoxide in THF at 0 ^{o}C to rt. SRE-IV-13 (**22**) can be synthesized from SRE-III-35 (**17**) via a similar route (**Scheme 5**). The final products can be purified by column chromatography with ethyl acetate-hexanes (20:80).

Scheme 5. Synthetic route to make D3-analogs.

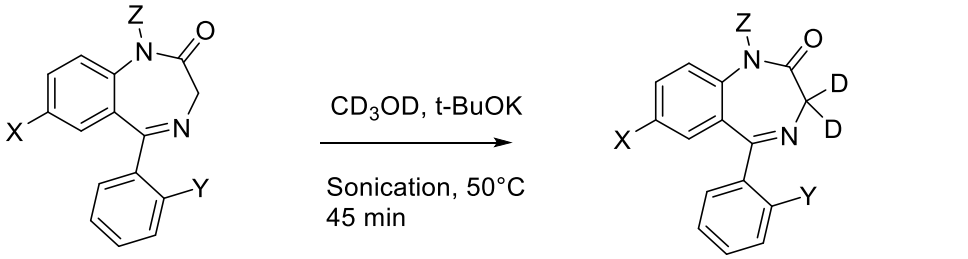


X=ethynyl, Y=H, (5)
X= cyclopropyl, Y=H (17)

X=ethynyl, Y=H, (24)
X= cyclopropyl, Y=H, (22)

To synthesize D2 or D5 analogs, the ligands **2** or **17** or **22** was dissolved in D4-methanol. Then potassium tert-butoxide was employed. The mixture was sonicated at 50 ^{o}C for 45 min. Then the D4-methanol was removed under reduced pressure, and to verify the deuterium exchange, the HNMR was taken. Then the reaction mixture was cooled to rt. To neutralize the reaction mixture, a mixture of D_2O and DCL was added dropwise, after each addition the pH must be checked by pH paper. In order to prevent the possible exchange of NH to ND, in the next step, the mixture was dissolved in methanol and stirred for 30 min at 40 ^{o}C.

Scheme 6. Synthetic route to make the D3 and D5 analogs.



X=ethynyl, Y=F, Z=CH_3 (2)
X= cyclopropyl, Y=H, Z=H, (17)
X= cyclopropyl, Y=H, Z=CD_3, (22)

X=ethynyl, Y=F, Z=CH_3 (25)
X= cyclopropyl, Y=H, Z=H, (21)
X= cyclopropyl, Y=H, Z=CD_3, (23)
(>97% D)

4.6. Result and Discussion

4.6.1. Lung adenocarcinomas express GABA(A) receptor subunits by Drs. Bhattacharya, Krummel, Sengupta and coworkers

As previously mentioned, $GABA_A$ receptors assemble as pentamers, with potential combinations from the translation products of nineteen GABR genes. An examination of primary lung cancer patient tumors from The Cancer Genome Atlas Program (TCGA) reveals expression patterns of GABR genes across non-small cell lung cancer (NSCLC) subtypes, specifically squamous cell carcinoma and adenocarcinoma.[2]

In squamous cell carcinoma, tumors exhibit a unique set of GABR genes, including GABRE and GABRA3, not observed in normal tissue (**Figure 11A**). Conversely, adenocarcinomas display a distinct expression signature in a subset of patients, while overall GABR gene expression is more widespread (**Figure 11B**). **Western blots of human lung adenocarcinoma primary tumor cell lines (H1792, A549, H1703, H460) and patient-derived brain metastatic lung adenocarcinoma cell lines (UW-lung-2 and UW-lung-16) indicate the expression of GABRA5 in all cases, consistent with RT-PCR analysis (Figure 11C).** RT-PCR analysis also reveals variable levels of GABRA3 mRNA expression in all NSCLC cell lines (**Figure 11D**). Furthermore, immunohistochemistry (IHC) conducted on sections from both human lung adenocarcinoma primary and corresponding secondary (brain metastatic) tissue demonstrates the expression of GABRA5 and GABRA3 (**Figure 11E).**[2]

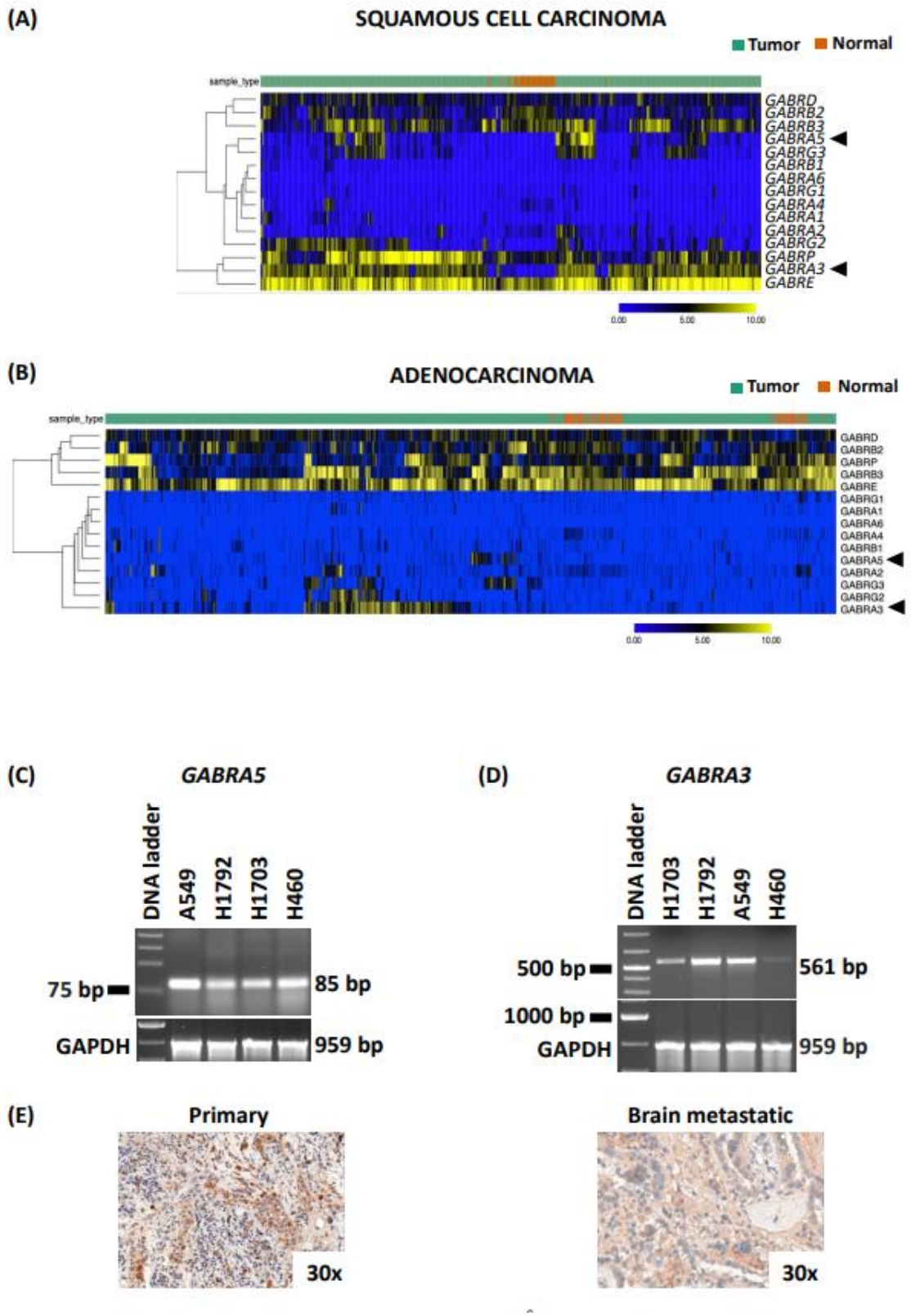


Figure 11. GABA(A) receptor subunit gene expression in lung cancers.[2]

4.6.2. Activation of GABA(A) receptors is depolarizing and triggers cancer cell death by Drs. Bhattacharya, Krummel, Sengupta and coworkers. The ley mechanism of action.

Although the increased gene expression and elevated protein levels of GABA(A) receptor subunits suggest the presence of a functional receptor, it is not confirmatory. To demonstrate intrinsic, functional GABA(A) receptors, patch clamp electrophysiology on single primary patient-derived adenocarcinoma cells was used. A current signal was observed in response to GABA (**Figure 12**). Treatment with benzodiazepine sensitized GABA(A) receptors, leading to a potentiation effect of GABA. An enhanced response to GABA plus the benzodiazepine analog AM-101 (**1**) (1 and 4 μM, respectively) over GABA (1 μM) alone was observed in H1792 cells (**Figure 12**). This functional analysis revealed that H1792 cells possess: (1) intrinsic functional GABA(A) receptors; and (2) receptors that form a canonical assembly with an α-γ interface, as evidenced by the ability of benzodiazepine to bind and elicit a positive response.[2]

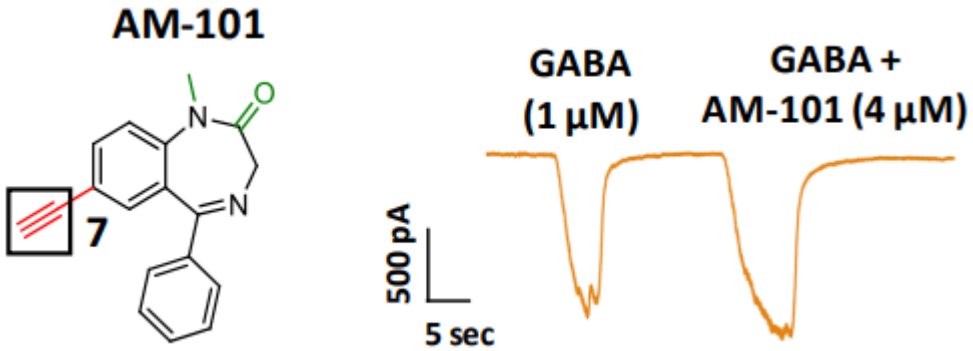


Figure 12. AM-101 or QH-II-066 (1) (left and single cell patch clamp electrophysiology trace of patient-derived adenocarcinoma lung cell line H1793 (right)

The benzodiazepine analog employed in our studies, AM-101, is an experimental drug. We have previously reported its anti-tumor effects in various cancer settings, including medulloblastoma and melanoma. In a prior study, it was reported that GABA(A) receptor activation by QH-II-066 leads to the efflux of chloride anions across the extracellular membrane, which contributed to the depolarization of the mitochondrial transmembrane. Similarly, we investigated whether AM-101 induces a shift in the electric charge distribution of a lung adenocarcinoma cell type. Using the cationic fluorescent dye Tetramethyl rhodamine, ethyl ester (TMRE) and monitoring its binding by Fluorescence-Activated Cell Sorting (FACS), we observed a rapid depolarization of H1792 cell mitochondria within 15 minutes of AM-101 treatment (Figure 13), equivalent to the depolarization induced by the mitochondrial uncoupler FCCP.[2] It is well known that in group III tumors, there is a Bz/GABA(A) efflux of chloride anions leading to intense depolarization, mitochondrial dysfunction and apoptosis. In normal adult GABA ion channels, there is a chloride anion influx.

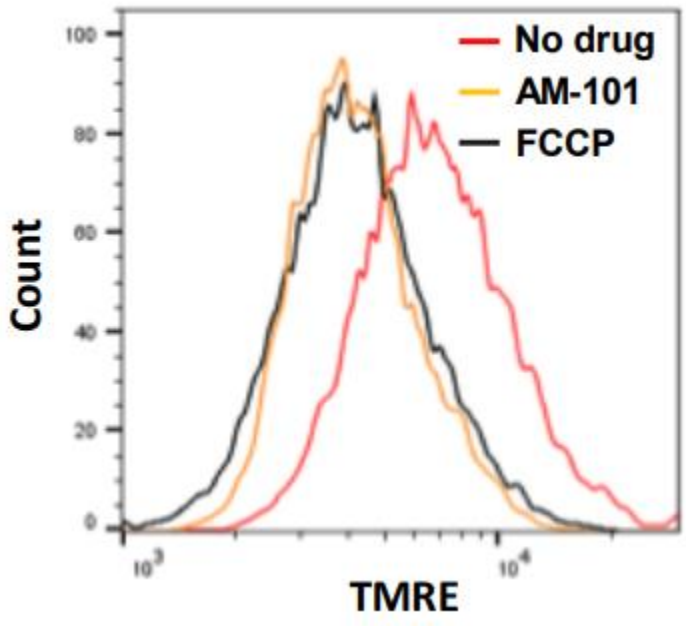


Figure 13. Lung adenocarcinoma (H1792) cells incubated with QH-II-066 are depolarized, as assessed by the TMRE assay and Fluorescence Activated Cell Sorting (FACS) analysis. Shown is the degree of depolarization relative to treatment with DMSO alone treatment and FCCP, which provide negative and positive controls in this experiment, respectively.[2]

Membrane depolarization triggers cell death through the activation of the intrinsic (mitochondrial) apoptotic pathway, a phenomenon in cell lines of pediatric brain cancer medulloblastoma and melanoma. Possible similarly of QH-II-066 impairs the viability of lung adenocarcinoma cells, including KRAS- and TP53-mutated cells, as well as patient-derived cells of other NSCLC subtypes, such as squamous cell and large cell, with IC50 values ranging from 2 to 4 μM (**Table 3** and **Figure 14A**) were tested. Cell proliferation impairment occurred after a 72-hour incubation with QH-II-066, correlating with key events in autophagy. Importantly, a single 7-ethynyl group in the 1,4-benzodiazepine ring system of QH-II-066 conferred this cytotoxic response (**Figure 12** and **14C**), as diazepam (Valium) exhibited no cytotoxicity to lung adenocarcinoma cells, even at exceedingly higher concentrations (**Figures 14C** and **14D**) nor any other group III cancers.[2]

Table 3. Viability of lung adenocarcinoma cells

Line	Type	IC_{50} (μM)	KRAS	p53
H1792	Adenocarcinoma	2.5	M	M
A549	Adenocarcinoma	2.3	M	WT
UW lung-16	Adenocarcinoma (brain metastatic)	2.48	M	M
H460	Large cell	2.9	M	WT
H1703	Squamous cell	3.6	WT	M
H520	Squamous cell	2.8	WT	WT

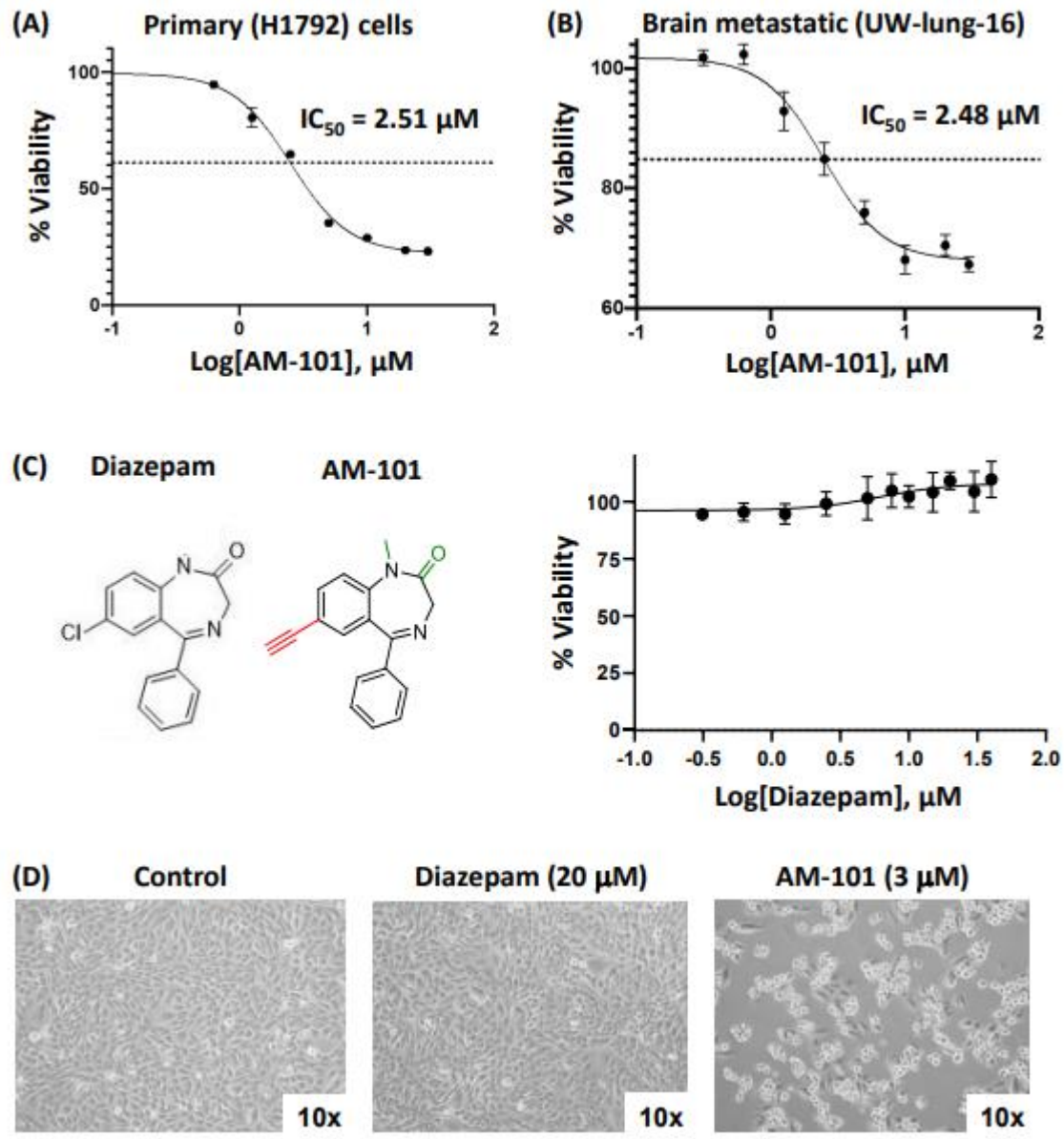


Figure 14. Effect of AM-101 and diazepam on survival of non-small cell lung cancer cells

4.6.3. GABA(A) receptor activation potentiates radiation by Drs. Bhattacharya,Krummel, Sengupta and coworkers2

Given that AM-101 exhibits cytotoxicity in lung cancer cells, albeit in the low micromolar range (2 - 3 µM), The potency of AM-101 was investigated and compared its efficacy to the anti-microtubular agent docetaxel (Taxotere), a commonly used chemotherapeutic for clinical radiation

sensitization in advanced-stage NSCLC. Initially, an ex vivo micro-scale 'chip' composed of human-derived alveolar lung was used, endothelial lung, and GFP-tagged H1792 cells to create an assay that partially replicates the lung tumor microenvironment (Figure 15A). The 'chips' co-cultured with H1792 cells displayed staining for phalloidin (an epithelial cell marker) and PECAM1 (an endothelial cell marker) (Figures 16A and 16B). Over time, H1792-GFP cells grew and spread through the epithelial compartment of the 'chip' (Figures 16C and 16D). Docetaxel concentration-dependent cell death was observed in H1792-GFP cells, as indicated by a reduction in the number of GFP-positive cells (Figures 16E and 16F). The analysis revealed that AM-101 is equally efficacious as docetaxel in terms of its impact on H1792 cell killing, and it is more effective at a significantly lower concentration (Figure 15B).

Then the ability of AM-101 to act as a radiation sensitizer for lung adenocarcinoma cells was explored. AM-101 was found to rapidly permeate the blood-brain barrier within 30 minutes without side effects, including neuropathic pain, in rodents and monkeys. Using a clonogenic assay with lung adenocarcinoma H1792 cells, it was observed a significant effect of AM-101 alone on clonogenicity. However, AM-101 combined with radiation exhibited a greater inhibitory effect on H1792 cell colony formation than either radiation or AM-101 alone (**Figures 15C**).

This heightened potency of AM-101 in combination with radiation prompted one to conduct mouse efficacy studies, generating heterotopic xenograft bilateral tumors in NOD SCID Gamma (NSG) mice using H1792 cells (**Figure 15D**). The treatment protocol involved administering a single intraperitoneal (i.p.) dose of AM-101 (2.5 mg/kg) or docetaxel (8 mg/kg) for seven consecutive days once the tumor was palpable. For mice in the radiation treatment groups, a single dose of radiation (5 Gy) was administered on the left flank only on the first day of AM-101 or docetaxel i.p. injection. Tumor weight at the experimental endpoint and tumor growth delay over time were

analyzed by measuring tumor volume. The visual inspection of resected tumors highlighted that radiation alone did not consistently affect final tumor size, while AM-101 or docetaxel alone did not significantly control tumors, as compared to the vehicle. However, combined treatment of AM-101 or docetaxel with radiation resulted in a lowered mean weight of xenograft tumors at the experimental endpoint and consistently smaller tumor sizes (**Figures 15E and 17A**). There was no significant difference between the median days to endpoint of the control-vehicle group mice versus those receiving radiation, while there was a significant difference for mice in the combined (AM-101 plus radiation) group (**Figure 17B**).[2] Docetaxel also demonstrated a statistically similar effect when combined with radiation (**Figure 17A**). Thus, both therapeutic agents appear to sensitize to radiation equally well, aligning with the clinical use of docetaxel as a radiation sensitizer. Analyzing tumor growth delay over time revealed that AM-101 plus radiation delayed mouse tumor growth compared to vehicle control, drug alone, or radiation alone (**Figure 15F**). This effect persisted even with a single radiation dose and seven days of AM-101 administration early in the tumor formation. The curves of the radiation versus combined treatment groups displayed similar slopes up to around 68 days, after which they diverged, indicating a prolonged impact of the combined treatment on tumor growth. This was evident in the increase in median days to endpoint for mice receiving the combination treatment, AM-101 plus radiation (**Figure 17B**).[2]

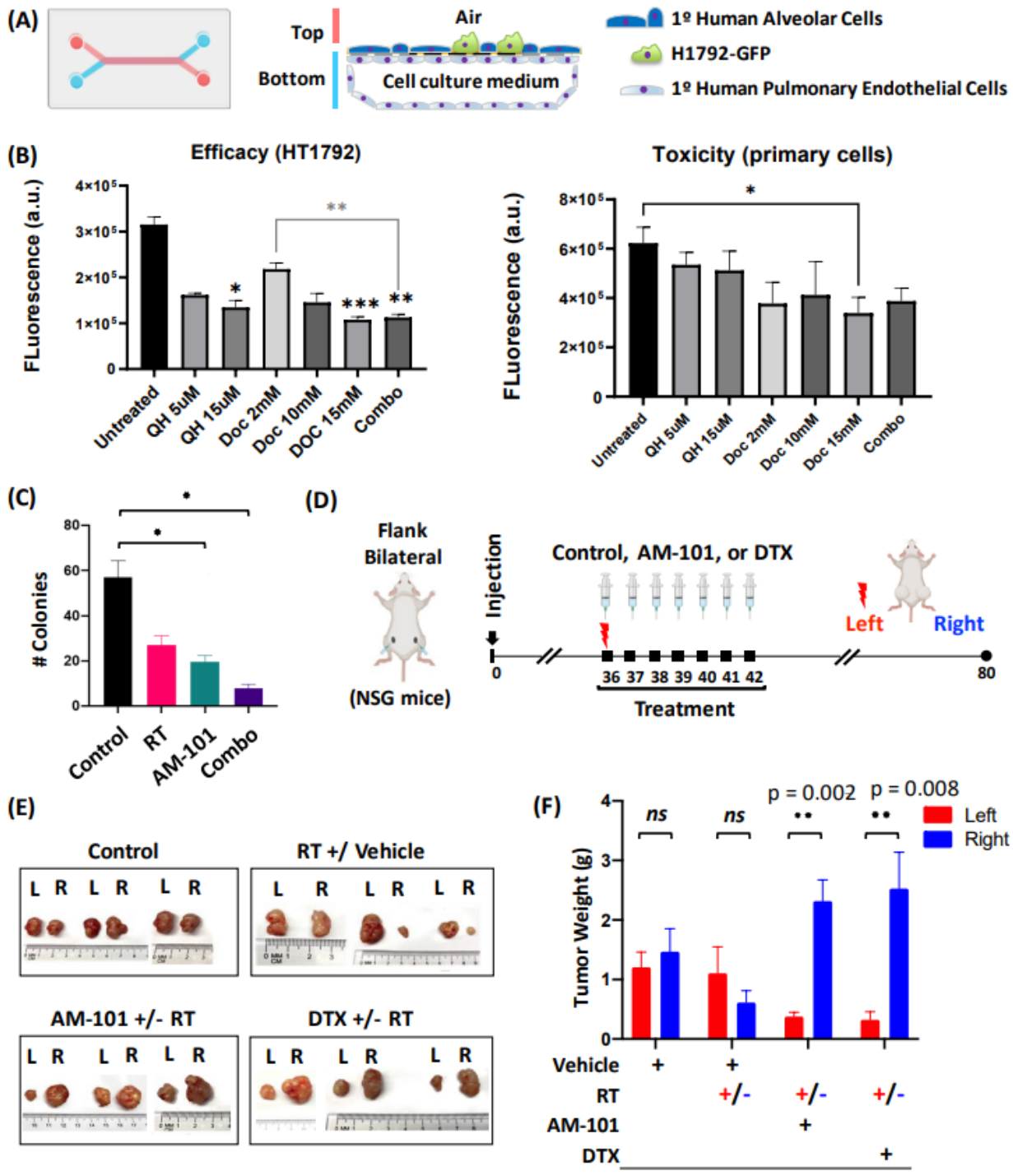


Figure 15. GABA(A) receptor activation potentiates radiation.[2]

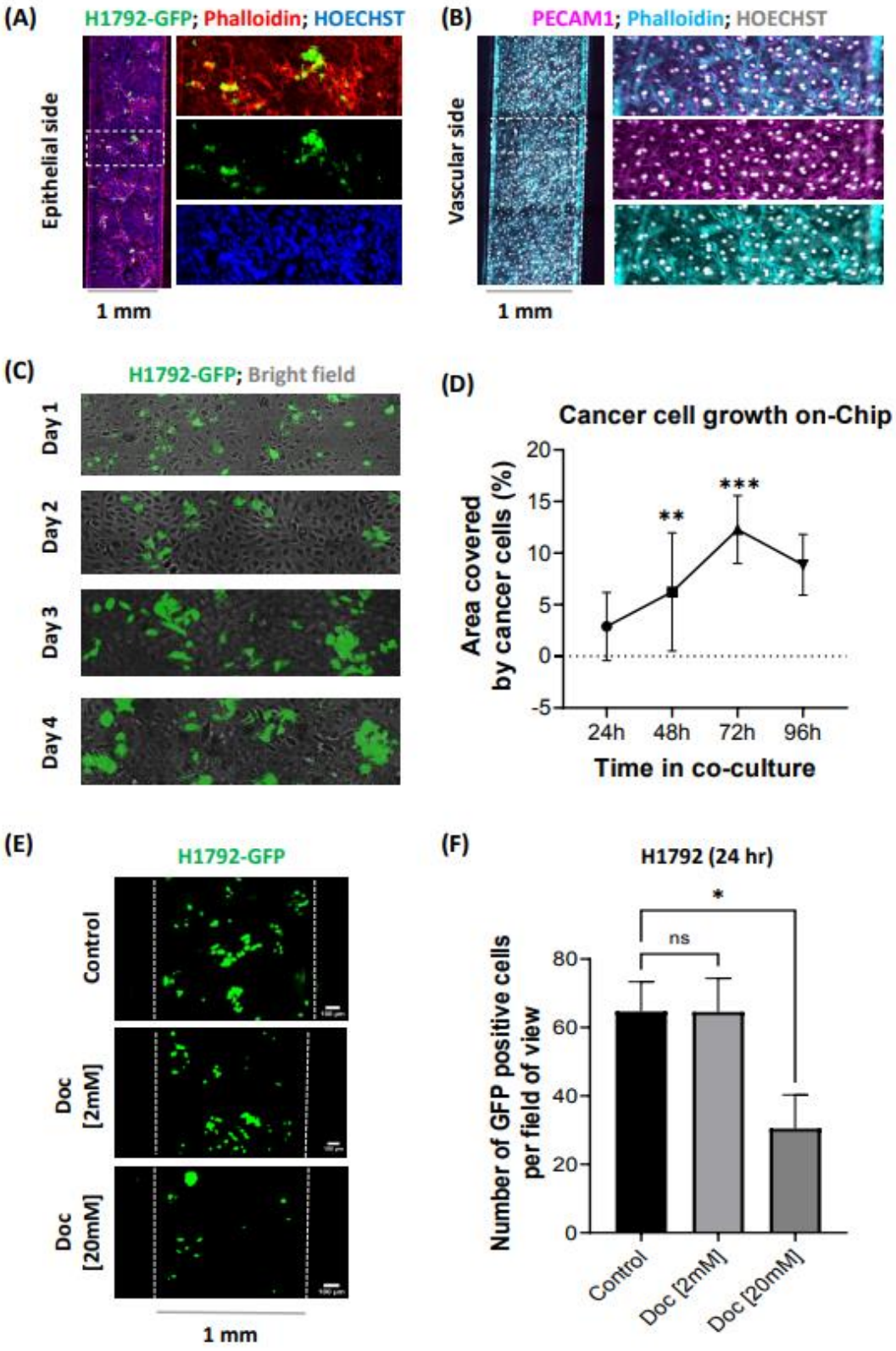


Figure 16. Human-relevant ex vivo 'lung-on-chip' data. [2]

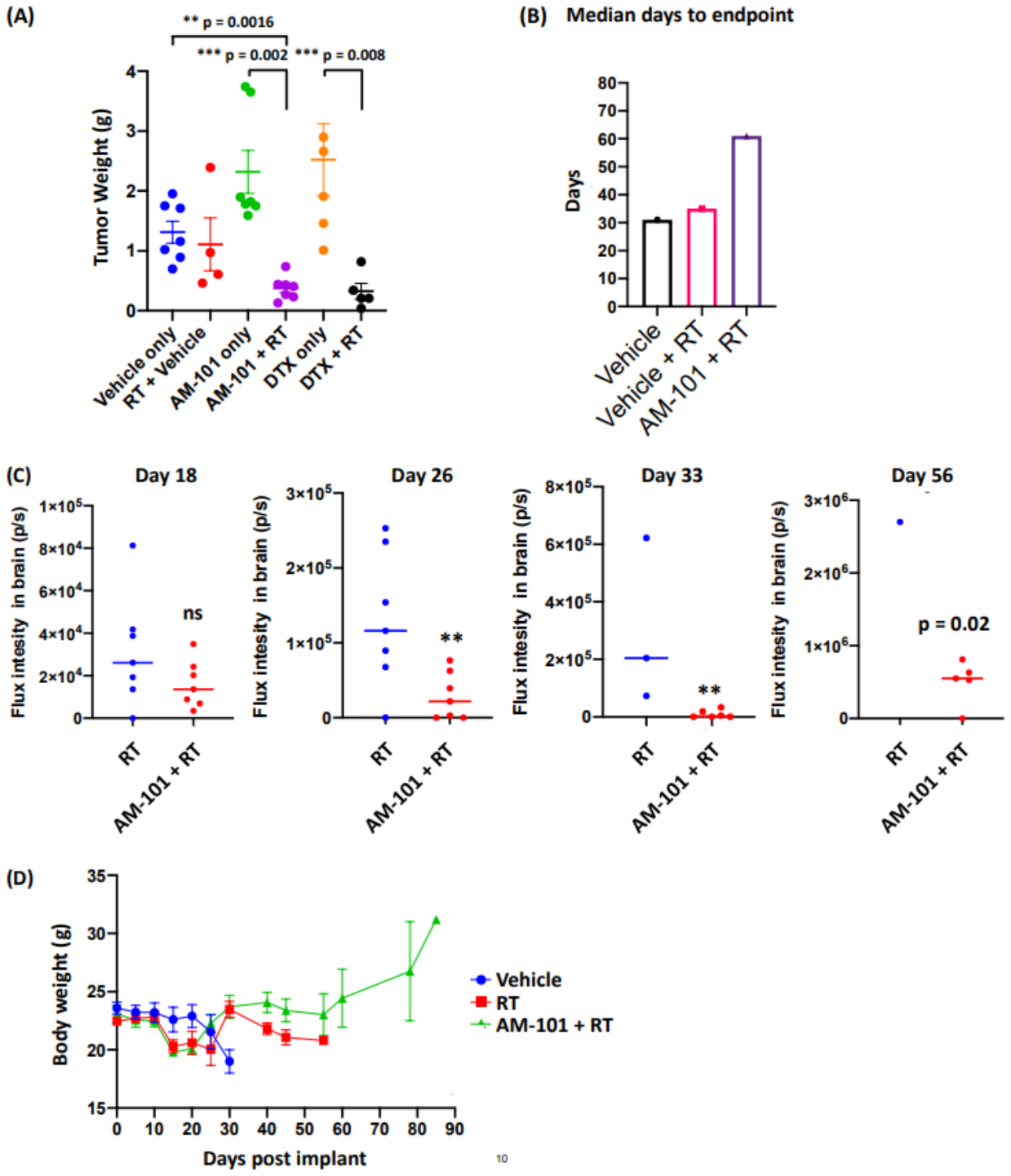


Figure 17. Mouse xenograft experiments[2]

4.6.4. Increased survival of mice bearing a lung brain metastatic tumor by Drs. Bhattacharya, Krummel, Sengupta and coworkers

The assessment of AM-101 and docetaxel in the context of heterotopic tumors revealed that both are equally effective in enhancing the potency of radiation. There is a substantial need for brain-penetrant and non-toxic radiation-sensitizing agents to enhance the standard-of-care for treating lung brain metastasis. **Docetaxel, due to its lack of brain-penetrance, is not utilized for treating lung brain metastasis and is associated with notable co-morbidities, including neuropathic pain**.

As previously discussed, GABA(A) receptors are present in both patient adenocarcinoma primary and brain metastatic lesions. The effectiveness of AM-101 in enhancing radiation in a brain setting was investigated. Initially, the effect of AM-101 on the clonogenicity of a patient-derived brain metastatic line, UW-lung-16 was tested. AM-101 alone not only impairs the viability of these cells but also significantly inhibits their clonogenicity (**Figure 18A**). When combined with radiation, the effect is approximately two-fold better than AM-101 alone.

Subsequently, the luciferase-tagged UW-lung-16 cells from the parental cell line was generated and this line, was employed for in vivo experiments. Intracranial xenograft tumors were generated by stereotaxic injection in athymic nude mice, and tumor growth was monitored using bioluminescent imaging (BLI), as well as by observing symptoms of mice and overall survival (**Figure 18B**). The experimental protocol involved a seven-day consecutive intraperitoneal injection of AM-101 (5 mg/kg/day) and a five-day consecutive whole-brain radiation exposure (2.5 Gy/day), overlapping with the first five days of AM-101 administration (**Figure 18B**). In control mice treated with the vehicle (a co-solvent formulation), tumors developed within 18 days post-implantation, as visualized by BLI (**Figure 18C**). By day 26, tumors caused severe neurologic

symptoms, including impaired mobility and a hunched physical appearance. Kaplan-Meir survival analysis revealed that whole-brain radiation alone did not provide a survival benefit (**Figure 18D**), as observed in BLI (**Figure 18C**). In contrast, mice treated with AM-101 plus radiation exhibited a significant survival benefit, with 70% of mice surviving beyond those treated with radiation alone (**Figure 18D**). The median days to the endpoint of mice treated with AM-101 plus radiation were notably higher than those treated with vehicle and radiation alone, reaching 61 days versus 35 days, respectively (**Figure 17C**). One mouse did not show evidence of intracranial tumor recurrence by BLI at 105 days post-injection, nor at the end of the study when the brain was resected to identify macroscopic evidence of tumor. Importantly, there was no significant change in the body weight of mice treated with AM-101 plus radiation throughout the experiment, indicating no added toxicity (**Figure 17D**). **It's noteworthy that about half of all mice in each treatment group had cancerous cells in the spinal region (Figure 18C). Interestingly, mice receiving radiation localized to the brain plus AM-101 exhibited a loss of tumor cells in both the brain and spine**. Further studies are needed to comprehend the effect of AM-101 with radiation on possible spinal or leptomeningeal metastasis. Since our heterotopic xenograft mouse experiments demonstrated that AM-101 alone does not provide significant tumor control in immunocompromised NSG mice, we did not include an AM-101 alone treated group in the intracranial brain metastatic mouse xenograft experiments.[2]

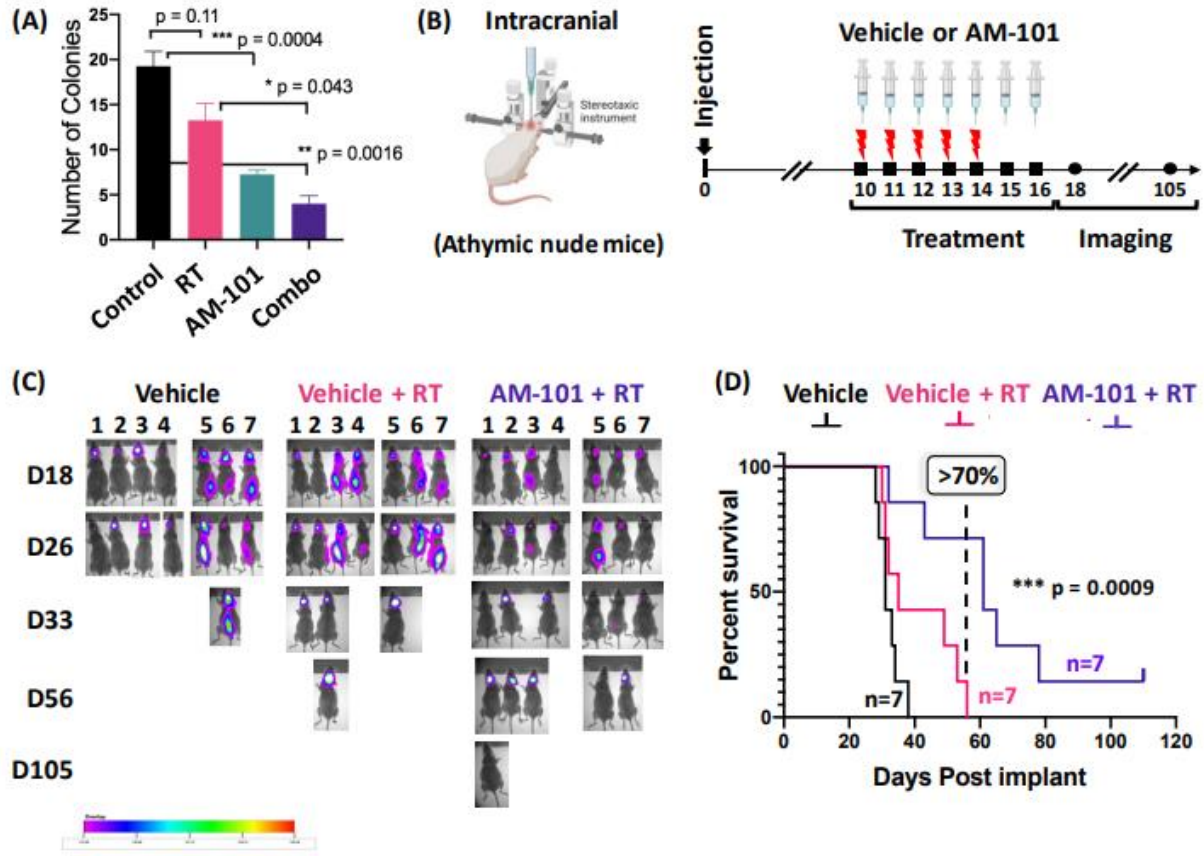
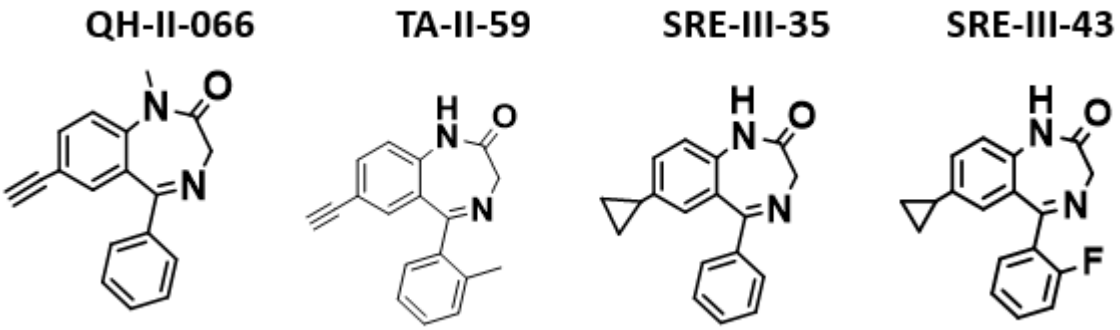


Figure 18. GABA(A) receptor activation increases survival of mice bearing lung brain metastatic tumors.[2]

4.6.5. Depolarization of cancer cells by different benzodiazepines, by Drs. Toukam, Krummel and coworkers

An efflux of chloride anions induced by binding of the anti-cancer benzodiazepine analogs depolarizes the cancer cells. Shown are graphical representations of the binding of the cationic fluorescent dye TMRE (Tetramethylrhodamine, ethyl ester) to Lewis Lung Carcinoma cells monitored by Fluorescence-Activated Cell Sorting (FACS). Each of four graphs is of a different benzodiazepine analog: QH-II-066; and newly synthesized variants: TA-II-59, SRE-III-35, and SRE-III-43. Binding of the benzodiazepines causes a shift in electric charge distribution

(depolarization) and thus reduced TMRE binding, as graphically reflected by a leftward shift. This occurs within 15 minutes of incubation with the benzodiazepine analogs. FCCP (2-[2-[4-(trifluoromethoxy)phenylhydrazinylidene]-propanedinitrile) is a potent mitochondrial oxidative phosphorylation uncoupler and serves as a positive control in this experiment.



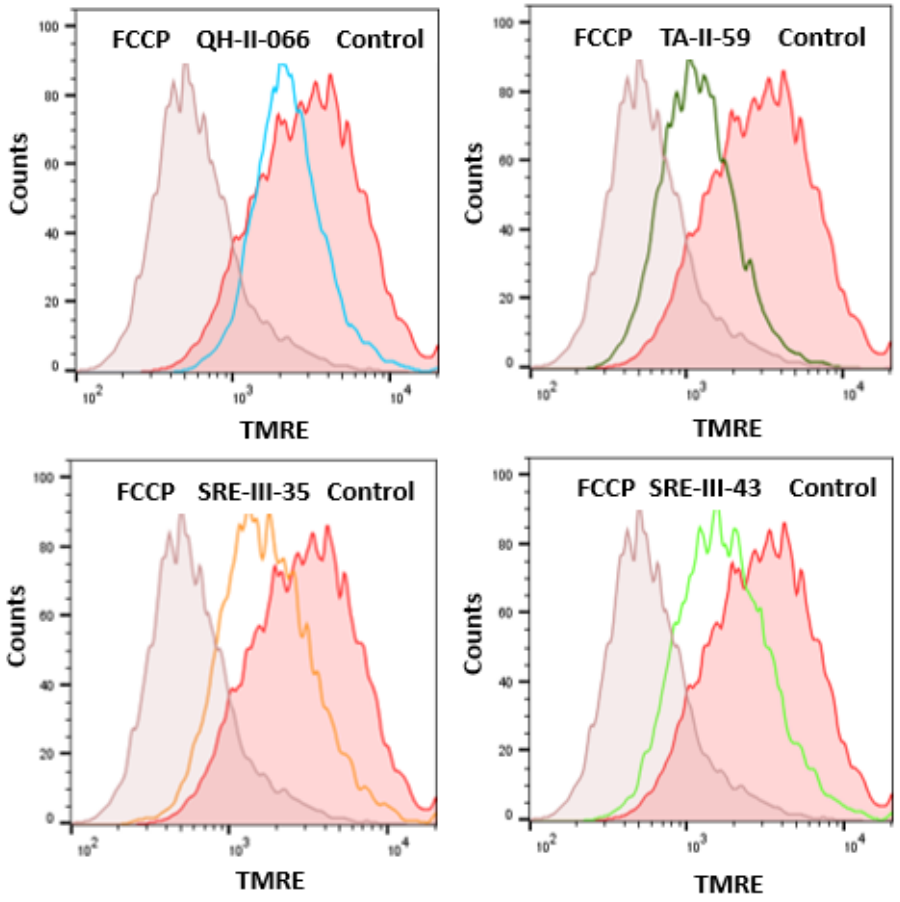


Figure 19. Benzodiazepines depolarize cancer cells. (Unpublished data)

4.6.6. Cytotoxicity of different benzodiazepine analogs by Drs. Toukam, Krummel and coworkers

Cytotoxicity (IC_{50} values) of different benzodiazepine analogs for different cancer cell lines (melanoma, A375; lung cancer, H1792; glioma, LN18; Lewis Lung Carcinoma (LLC) were Tested in vivo.

Table 4. IC_{50} (μM)

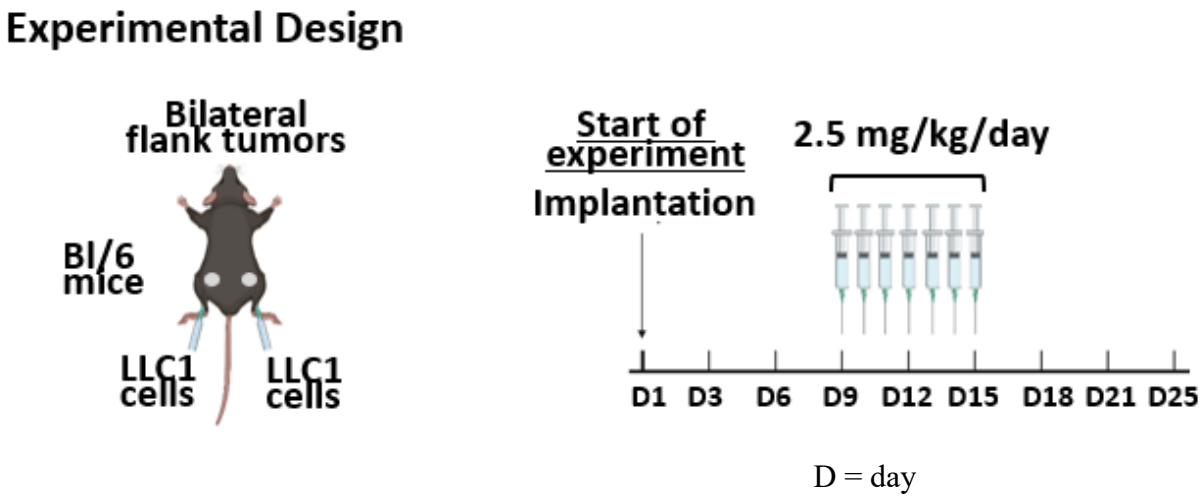
Compound	A375	H1792	H1703	A549	LN18	LLC	UW Lung 2	UW Lung 16
QH-II-066*	2.6	4.5	2.6	2.56	3.1	4.4	4.2	5.9
Nor-QH-066	1.1	2.47		0.69	2.5			
TA-IV-74*	2.57	3.78			2.55	4.2		1.4
SRE-III-35*	0.6	0.98			0.82	0.8		
SRE-III-43	2.2	2.61			1.22	2.7		
SRE-III-53	NA	NA						
SRE-III-54	NA	NA						

NA= Not active **(Unpublished data)**

Among of the all benzodiazepine analogs which were tested in cancer cytotoxicity assays, QH-II-066 (**1**), TA-IV-74 (**19**) and SRE-III-35 (**17**) demonstrated the greatest activity, although several others were close behind.

4.6.7. In vivo effectiveness of benzodiazepine analogs on Lewis Lung Carcinoma (LLC) tumors by Drs. Toukam, Krummel and coworkers

The newly synthesized benzodiazepine analogs in mice were tested. The C57Bl6 (Black 6) immune-competent mice with bilateral flank Lewis Lung Carcinoma (LLC) tumors were used to test the in vivo effectiveness of the benzodiazepine analogs. Mice were implanted with $5x10^5$ LLC cells in both left and right flanks. When flank tumors were palpable mice received, by intraperitoneal injection, either vehicle control or one of four benzodiazepine analogs (**Figure 20**) for seven consecutive days. There were N = 3 mice per group and each mouse received a benzodiazepine analog at 2.5 mg/Kg body weight per day for seven days. Tumor size was monitored over time and plotted relative to vehicle (control) mice.



Comparing LLC tumor response to the target agents

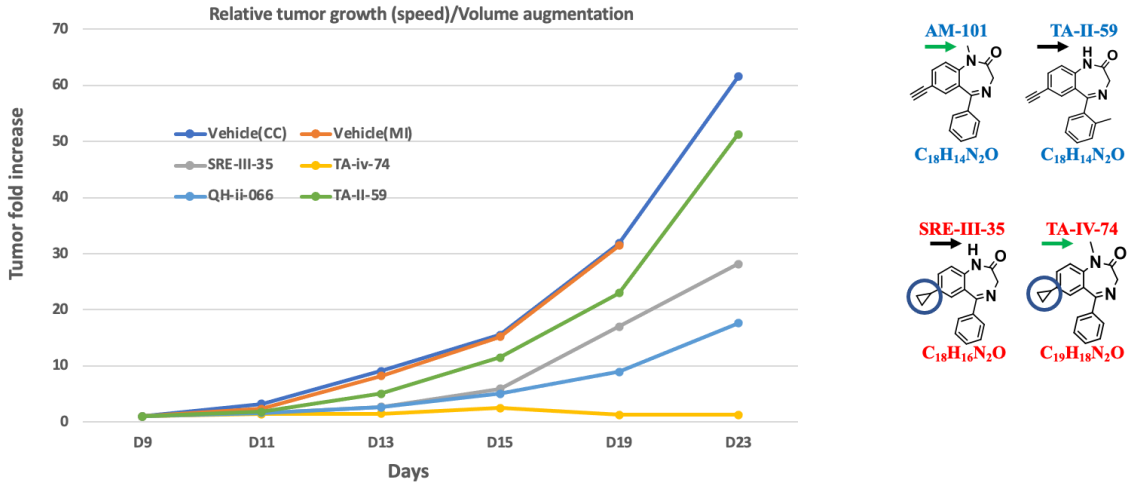
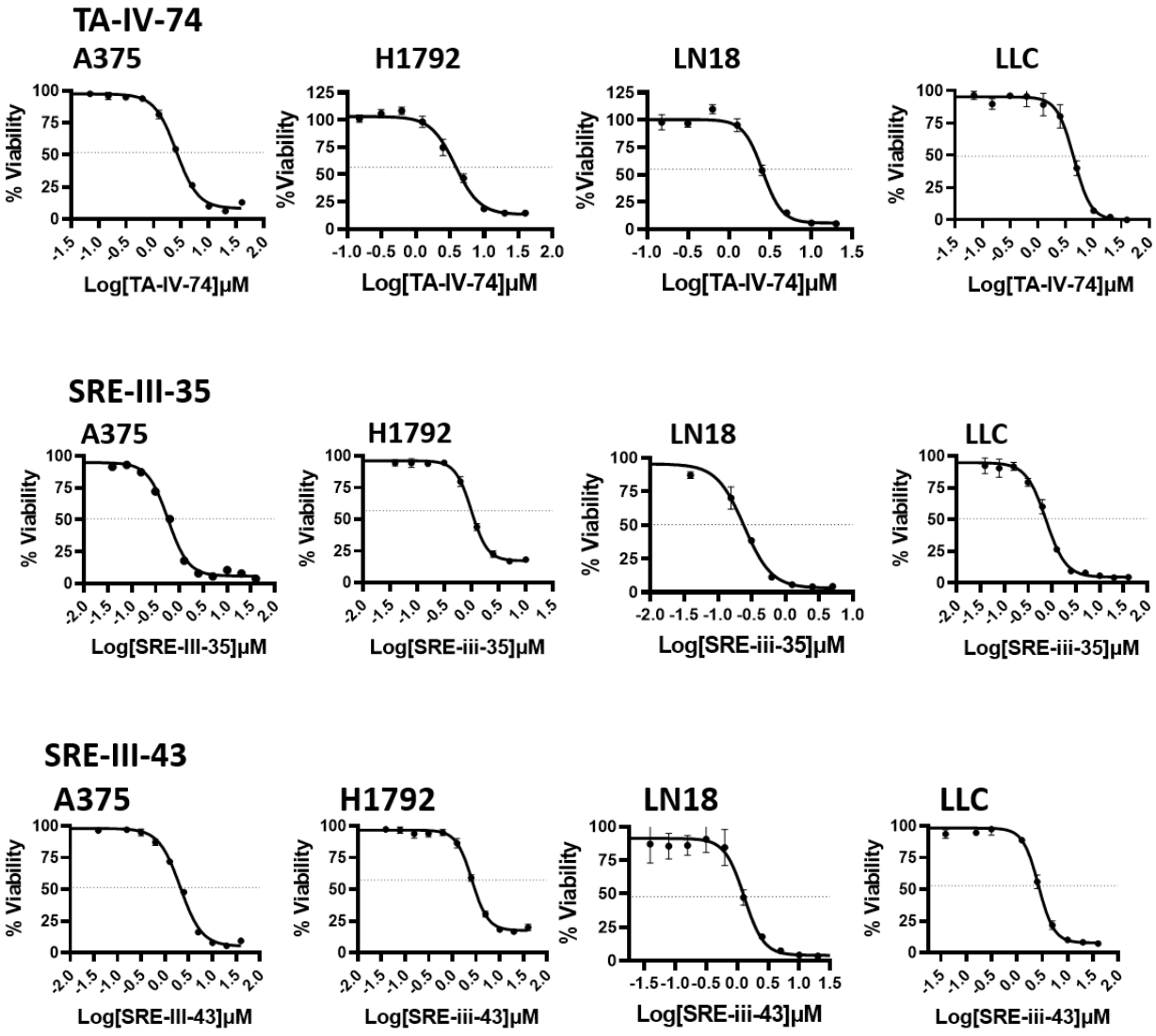


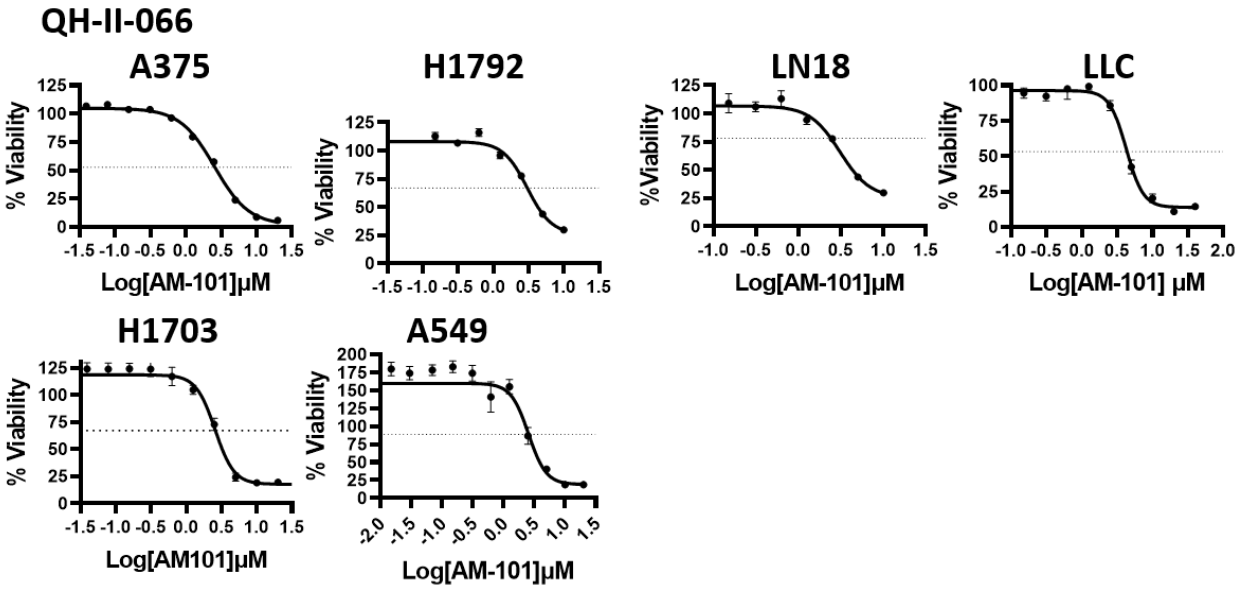
Figure 20. In vivo test for different benzodiazepine analogs in LLC tumor growth. (Unpublished data)

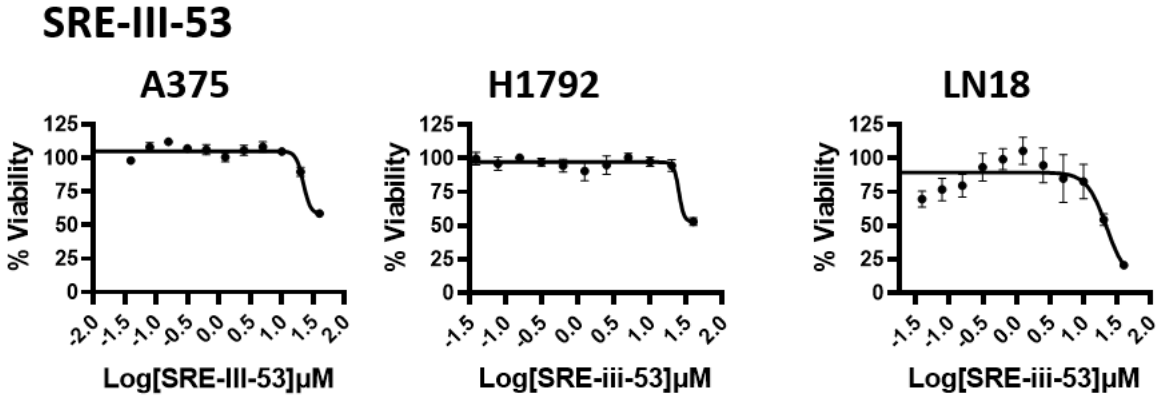
Among all tested analogs, the TA-IV-74 was the most effective compound. The next 2 effective ligands were QH-II-066 as well as SRE-III-35 which showed very good to outstanding activity.

4.6.8. MTS cytotoxicity assay by Drs. Toukam, Krummel and coworkers

The **MTS assay** is used to assess **cell proliferation**, **cell** viability and **cytotoxicity**. The **MTS assay** protocol is based on the reduction of the **MTS** tetrazolium compound by viable mammalian **cells.**[265]


TA-IV-74
A375
H1792
LN18
LLC
% Viability
Log[TA-IV-74]μM
SRE-III-35
A375
H1792
LN18
LLC
% Viability
Log[SRE-III-35]μM
Log[SRE-iii-35]μM
SRE-III-43
A375
H1792
LN18
LLC
% Viability
Log[SRE-III-43]μM
Log[SRE-iii-43]μM


QH-II-066
A375
H1792
LN18
LLC
H1703
A549
% Viability
Log[AM-101]μM
Log[AM101]μM
Log[AM-101] μM


SRE-III-53
A375
H1792
LN18
% Viability
Log[SRE-III-53]μM
Log[SRE-iii-53]μM

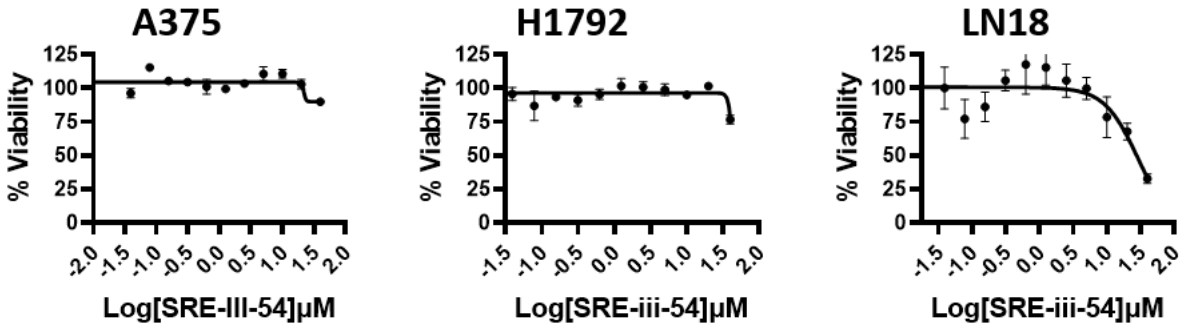

SRE-III-54
A375
H1792
LN18
% Viability
Log[SRE-III-54]μM
Log[SRE-iii-54]μM

Figure 21. MTS cell proliferation/cytotoxicity assays. A375 = Human melanoma, H1792 = Human Lung cancer, LN18 = Human glioblastoma, and LLC = mouse lung carcinoma cell lines. (Unpublished data)

As illustrated in **Table 3**, among all benzodiazepine analogs that were tested in cancer cytotoxicity assay, QH-II-066 (**1**), TA-IV-74 (**19**) and SRE-III-35 (**17**) showed very good to outstanding activity.

4.6.9. Receptor binding studies

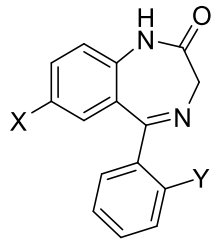
To assess potential off-target receptor binding, all newly developed ligands underwent evaluation at the National Institute of Mental Health (NIMH) Psychoactive Drug Screening Program (PDSP). A comprehensive screening, encompassing 47 receptors, ion channels, and transporters, was conducted to identify any interactions beyond the $GABA_A$ receptor. Dr. Bryan Roth from UNC spearheaded this initiative. Ligands exhibiting substantial inhibition (exceeding 50%) in primary binding underwent further scrutiny in secondary binding assays to determine their Ki (nM) values.

While most ligands demonstrated binding affinity at $GABA_A$Rs, it's crucial to note that this data doesn't reflect their affinity for different Bz alpha/beta/gamma2-subtypes. Notably, there was no observed binding of the test compounds with calcium channels, indicating no physiological impact on cardiac and smooth muscle cells or NMDA receptors[157,158]

Screening the compounds for hERG binding in the initial stages of drug discovery is critical. Unintended hERG binding can lead to blockage of hERG K+ channels in the heart, causing various side effects such as cardiac arrhythmias and sudden death. [159]Therefore, evaluating compounds for hERG binding is essential to delineate any off-target profiles.

All benzodiazepine analogs underwent testing for hERG binding, and fortunately, the test compounds did not exhibit undesired binding to voltage-sensitive K+ channel hERG (**Table 5**).

Table 5. Binding affinities at hERG (PDSP). Unpublished data.



Core structure of QH-II-066 analogs

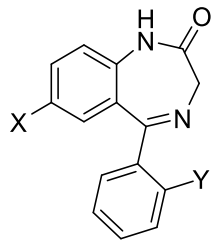
PDSP Code	Cook Code	X	Y	Binding affinity at hERG % inhibition (primary)
71288	SRE-III-35	△	H	-1.2
71289	SRE-III-43	△	F	7.33
71290	SRE-III-53	Br	H	12.47
71291	SRE-III-54	Br	F	14.87

These compounds do not interact with hERG channels.

The compounds were studied at PDSP to investigate their interaction with the peripheral benzodiazepine receptor (PBR) as well. Various biological processes are linked to PBR, including the transport of anions for mitochondrial transmembrane potential, heme biosynthesis, regulation of neurological damage, proliferation, cell death (apoptosis), and steroidogenesis regulation. In the primary binding assay, the compounds were tested evaluated for the percentage

of inhibition, and several compounds exhibited inhibition exceeding 50%. Subsequently, these compounds underwent a secondary screening to determine their Ki (nM) values for PBR receptors. The structures of the compounds and their binding affinities for PBR are outlined in **Table 6**.

Table 6. Binding affinities at PBR (PDSP). Unpublished data.



Core structure of QH-II-066 analogs

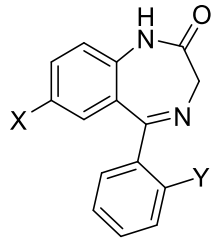
PDSP Code	Cook Code	X	Y	Binding affinity at PBR % inhibition (Primary)	Binding affinity at PBR Ki(nM) (Secondary)
71288	SRE-III-35	△	H	11.20	
71289	SRE-III-43	△	F	18.37	
71290	SRE-III-53	Br	H	9.70	
71291	SRE-III-54	Br	F	53.77	1859.94

These compounds were not active at PBR.

Among all the tested compounds, only 1 analog (SRE-III-54) was tested in the secondary screening at PBR receptor and it was not active at PBR.

In addition to the robust binding affinity observed with the previously mentioned receptors, certain benzodiazepines also demonstrated inhibitory effects on kappa opioid receptors (KOR). Opioid receptors constitute a family of inhibitory G-coupled protein receptors, with opioids serving as ligands. The family includes kappa opioid receptors (KOR), mu and delta opioid receptors (MOR and DOR), and nociception opioid receptors (NOP). The affinities of the tested compounds for KOR, DOR, and MOR were determined through radio ligand binding assays at a screening concentration of 10,000 nM in collaboration with the National Institute of Mental Health's Psychoactive Drug Screening Program (PDSP), as mentioned earlier. Concentration-dependent experiments were conducted to establish Ki values for compounds that exhibited over 50% radio-ligand displacement in the primary binding assay. Summarized **in Table 7** is the percentage of KOR inhibition and Ki values exhibited by some benzodiazepine analogs of QH-II-066.

Table 7. Binding affinities at KOR (PDSP). Unpublished data.



Core structure of QH-II-066 analogs

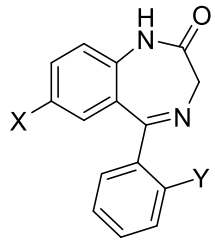
PDSP Code	Cook Code	X	Y	Binding affinity at KOR % inhibition	Binding affinity at KOR Ki(nM)

				(Primary)	(Secondary)
71288	SRE-III-35	△	H	53.15	3784.43
71289	SRE-III-43	△	F	44.02	
71290	SRE-III-53	Br	H	53.81	3620.76
71291	SRE-III-54	Br	F	66.02	2246.98

Among all tested benzodaziapine analogs, SRE-III-35 showed the weakest affinity for KOR (Ki=3784.43 nM) (**Table 7**). The rest of the analogs also did not bind to KOR with any significant affinity.

The next assay for the above compounds was conducted to determine BZR binding affinity by using rat brain BZR homogenates. Most of the compounds showed good binding affinity in this receptor. The data are presented in **Table 8**.

Table 8. Binding affinities at BZR (PDSP). (Rat brain homogenates are sysnaptosomal membranes containing all 6 benzodiazepine / GABA(A) subtypes) Unpublished data.



Core structure of QH-II-066 analogs

PDSP Code	Cook Code	X	Y	Binding affinity at BZR % inhibition (Primary)	Binding affinity at BZR Ki(nM) (Secondary)
71288	SRE-III-35	△	H	78.75	278.55
71289	SRE-III-43	△	F	100.26	222.23
71290	SRE-III-53	Br	H	101.65	67.16
71291	SRE-III-54	Br	F	105.66	72.29

SRE-III-53 and SRE-III-54 exhibited the most potent activity but since α5 subtypes comprise only 5% of the homogenate, SRE-III-35 and SRE-III-43 could be α5 selective. The data is a homogenate of receptors.

4.7. Conclusion

In targeting Group 3 medulloblastomas tumor cells, α5 selective $GABA_A$ receptors ligands exhibited very promising results, among them KRM-II-008 and QH-II-066 showed better efficacy to induce the apoptosis of tumor cells than standard-of care treatment Cisplatin. The involvement of the GABA(A) pathway was found in several other tumor types, including neuroblastoma [266,267]and pancreatic cancer.[268] The IC_{50} values vary in different cell lines. AM-101(QH-II-066) is a novel agent with promising anti-tumor activity against various types of group III cancers, including primary and metastatic brain tumors. The GABA(A)R drug selectively targets α5

subtypes of GABA(A) as an aminobutyric acid receptors. Not only is AM-101 being developed as an individual but also an 'add-on' to potentiate the treatment of primary and metastatic brain cancers with radiation and/or check point inhibitors. It penetrates the BBB in 25 minutes.as well as the lung. Basically, $GABA_A$ receptors in these cancer cells expell Cl^- out of the cells, analogous to embryonic GABA(A) receptors, but AM-101 enhances this Cl^- ion efflux seriously degrading mitochondrial function.

Additionally, AM-101 is nontoxic in normal cells in rodents and monkeys. This lead agent is cytotoxic in cancer cells and can potentiate radiation and DNA-damaging chemo synergistically. AM-101 enhances the infiltration of anti-tumor immune cells and it can treat primary site and metastatic lesions of different solid tumors.AM-101 has been deuterated to block metabolism and provide a material with a potential composition of matter designation. To date, the new cyclopropyl analogs have shown very potent activity. Further testing of these compounds is essential to advance toward clinical trials.

4.8. Methods

4.8.1. Radioligand binding assays on rat brain homogenates with the National Institute of Mental Health's Psychoactive Drug Screening Program (NIMH PDSP) at UNC with Dr Bryan Roth

The detailed procedures for primary and secondary radio-ligand binding assays are extensively outlined in the Assay Protocol Book of the National Institute of Mental Health's Psychoactive Drug Screening Program (NIMH PDSP). A final volume of 125 µL per well, prepared in the appropriate binding buffer, was utilized for conducting both primary and secondary radio-ligand binding assays. The concentration of the radioactive ligand closely approximated the dissociation constant (Kd) values ([3H]-U69593 0.83 nM, [3H]-DAMGO 1.20 nM, and [3H]-DADLE 2.69

nM); [H^3] flumazenil and [H^3] flurazepam. The binding of a ligand to a receptor, ion channel, or transporter was assessed in the absence and presence of 10 μM of the relevant reference compound. Nonspecific binding was also determined in the absence and presence of 10 μM of the appropriate reference compound. The plates were incubated in the dark for 90 minutes at rt, and the reactions were halted by vacuum filtration onto 0.3% polyethyleneimine (PEI)-soaked 96-well filter mats using a 96-well Filtermate harvester, followed by three washes with cold PBS buffer. Radioactivity was then quantified in a Microbeta counter. The data (N=6) were analyzed using nonlinear regression.

4.8.2. Mitochondrial depolarization by Drs. Bhattacharya, Krummel, Sengupta and coworkers[2]

QH-II-066 was diluted to 4 μM in RPMI-1640 culture media. Carbonyl cyanide 4-(trifluoromethoxy) phenylhydrazone (FCCP) was diluted to 20 μM in the culture medium. Tetramethylrhodamine ethyl ester perchlorate (TMRE) was diluted to 400 nM in the culture medium. H1792 cells were grown in culture to 75 – 90% confluency. Cells (5x105 cells/mL) were harvested and resuspended in media. Cell suspension (200 μL) was dispensed and AM-101 or FCCP (200 μL) added to final concentrations of 2 μM and 10 μM, respectively. The solution was briefly vortexed and incubated for 10 minutes. TMRE (40 μL of 400 nM stock) was added (final concentration 10 nM), vortexed, incubated for 2 minutes and sample reading was acquired using a BD LSR Fortessa. Data was analyzed using Flowjo v10 software.

4.8.3. Lung cancer-chips by Drs. Bhattacharya, Krummel, Sengupta and coworkers[2]

Human Alveolar Epithelial Cells (HPAECs) were cultured on a Matrigel/collagen coated T25 flask for 4-7 days in serum-free Small Airway Epithelial Cell Growth Medium (SAGM) and were used without further passaging. Human Lung-Microvascular Endothelial Cells (HMVEC-L) were grown on a collagen I coated flask (T75) in microvascular cell culture medium and used between passage 4-5. Lung-chips are composed of transparent material made of a tetrafluoroethylenepropylene (FEPM) elastomer containing two parallel microchannels separated by a thin collagen vitrigel membrane, previously described, and characterized. [269] In contrast to previous organ-onChip models of the lung, [270–272]we used a Polydimethylsiloxane (PDMS)-free design. The chips were a kind gift of Naoki Matsuoka. Before the experiment, both microchannels were chemically functionalized using 3-aminopropyl-trimethoxysilane (APTMES) to covalently bind extracellular matrix (ECM) proteins before seeding human cells, as previously described. [273]The apical or epithelial channel (1 × 1 mm) was coated with a mix of human placenta collagen IV (200 μg/mL), human placenta laminin (10 μg/mL), and human plasma fibronectin (30 μg/mL), all resuspended in Hanks' Balanced Salt Solution (HBSS). The bottom or vascular channel (200 μm × 1 mm) was coated with human placenta collagen type IV (200 μg/mL) and human plasma fibronectin (30 μg/mL). Chips were incubated overnight at 37°C to complete the surface coating. The next day, HPAECs were seeded in the epithelial channel at a density of ~ 0.8 × 106 cells/mL in SAGM and chips were incubated at 37°C. Three h after cell seeding, both epithelial and vascular channels were rinsed 2X with 100 μL SAGM to remove unattached cells. The medium was then replaced with SAGM supplemented with keratinocyte growth factor (10 ng/mL), isobutylmethylxanthine (100 μM), 8-bromo-cyclicAMP (100 μM), and dexamethasone (200 μM). The medium in the epithelial channel (SAGM + KIAD) was replaced once a day for 6 days. Three days after epithelial cell seeding, the vascular compartment was seeded with HMVEC-L at a

density of ~ 8×106 cells/mL in microvascular cell culture medium (EGM-2 MV); chips were then incubated at 37°C. One hour after endothelial cell seeding, the vascular channel was rinsed 2X with cell culture medium to remove free cells. The vascular medium was then refreshed once a day with EGM-2 MV for 3 days. One day after endothelial cell seeding, H1792- GFP cancer cells were seeded on the epithelial compartment at a density of ~ 3.5×105 cells/mL, as previously described. [271] The epithelial channel was rinsed with fresh cell culture medium 3-5 hrs after seeding of cancer cells and an air-liquid interface (ALI) was established the next day, via pipetting 50 µL of air in the epithelial channel. Chips were then connected to flow using a syringe pump and perfused with a modified endothelial cell culture medium (ALI medium) made with Medium 199 supplemented with 2% HyClone FetalClone II Serum; 10 ng/mL Epidermal Growth Factor, 10 ng/mL Keratinocyte Growth Factor, 0.25 ng/mL Vascular Endothelial Growth, 1 µg/mL Hydrocortisone, 1 U/mL Heparin, 50 µM 8-Bromoadenosine 3′,5′-cyclic monophosphate, GlutaMAX, 20 nM Dexamethasone, and Penicillin-Streptomycin.

4.8.4. Viability assays by Drs. Bhattacharya, Krummel, Sengupta and coworkers[2]

For the clonogenic assay, a fixed number of cells were seeded (120 cells per well, H1792; 150 cells per well, UW-lung-16), grown overnight in humidified conditions at 37°C, and treated with QH-II-066 or DSMO for 1 hr before irradiation. Each treatment group had four replicates. Once colonies averaged 40 or more cells (14-18 days in control wells), media was removed, and cells washed with sterile PBS. Cells were fixed for 20 min with methanol-acetone (3:1 by volume) and stained with 1% (w/v) crystal violet in methanol for 20 minutes. Stained colonies were gently washed with distilled water, dried, and imaged. Colonies of 40 or more cells were counted. Cells in radiation groups were irradiated one day after seeding with a single fraction X-ray source (Xstrahl Ltd.) at room-temperature. XenX irradiator has a collimator that delivers a uniform dose

and a PA beam (posterior-anterior) focused on top of wells. In the Control group, the media was replaced by fresh media after 72 hr. Colonies were allowed to grow in each of the experimental groups for 14 days (H1792 cells) and 18 days (UW-lung-16 cells) following irradiation. Media was refreshed after every 4 days, and QH-II-066 treatment was done for 72 hours. Media was removed and colonies washed with PBS and fixed staining. The clonogenic survival curve for each condition was fitted to a linear quadratic model according to a least squares fit, weighted to minimize the relative distances squared, and was compared using the extra sum of-squares F test. Each point represents the mean surviving fraction calculated from four replicates and error bars represent the standard error (SE). Data is represented as mean ± SE of colonies using bar graphs and was analyzed using GraphPad Prism 8. P-values were calculated using one-way ANOVA. Cell proliferation viability studies employed the Cell Titer 96® Aqueous One Solution Assay. [274]The IC50 values were determined using the [Inhibitor] versus normalized response nonlinear regression function and the log of inhibitor concentration in GraphPad Prism 8. For cell survival assays with Pen3-ortho stapled-peptide and AM-101, H1792 cells were plated with phenol-red free RPMI-1640 media (2500 cells per well in 100 μL media) and grown overnight. The next day media was removed, fresh 100 μL phenol-red free RPMI media added, and the following treatment groups setup: (1) Pen3-ortho group (15 μM); (2) Pen3-ortho (25 μM); (3) QH-II-066 (AM-101) group (3 μM); (4) combination group at AM-101 (3 μM) and Pen3-ortho (15 μM); (5) combination group at AM-101 (3 μM) and Pen3-ortho (25 μM); (6) DMSO control with no drug added; (7) control with no cells added, i.e. media alone. Cells were then incubated at 37°C, 5% CO2 for 48 hrs. Following, this 20 μL of diluted MTS reagent was added, and cells incubated at 37°C for 1 h, and absorbance (490 nm) measured using a microplate reader. The mean of the absorbance of media only samples was subtracted from control and test group samples. The percentage of

inhibition in each group was calculated by the formula (C-T)/C x 100%; where: ‘C’, is the mean absorbance reading for Control group; ‘T, is the mean absorbance reading for each treated group. The percentage of survival was calculated (GraphPad Prism 8.0.1) by subtracting percentage of inhibition of each group from 100% and expressed as mean ± SEM. Student’s t test (paired) for two groups were used for statistical comparison. A $p < 0.05$ is considered significant.

4.9. Experimental

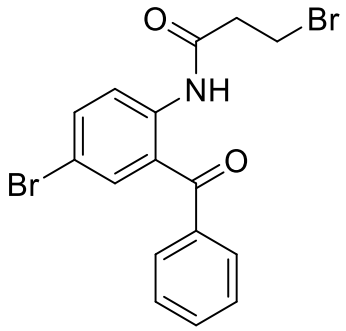
4.9.1. General experimental conditions

All reactions were conducted in round-bottom flasks or screw-cap test tubes that had been dried in an oven. Dry solvents were utilized for all chemical reactions, and unless otherwise specified, chemicals underwent purification through standard techniques or were procured from chemical vendors with the desired purity. The progression of reactions was tracked using TLC from Dynamic Adsorbents, Inc. (silica gel, neutral alumina, or basic alumina) under ultraviolet (UV) light. For the purification of certain intermediates or products, flash column chromatography techniques were employed on silica gel (230-400 mesh, Dynamic Adsorbents) or neutral alumina.

A Stuart melting point SMP3 apparatus (Barloworld Scientific US Ltd.) was employed to determine the melting point of specific compounds. The enantiomeric excess (% ee) was ascertained using a CHIRALPAK® IB-N3 HPLC Column from Daicel Corporation. To establish the % purity of the compounds, a C18 1.8 mM column (Shimadzu Nexol company) was used. Optical rotations were measured on a JASCO Model DIP-370 digital polarimeter against a standard. The 1H and 13C NMR spectra were acquired on a Bruker Spectrospin 500 MHz or 300 MHz instruments in $CDCl_3$, DMSO, or DMSO-d6. The chemical shifts are reported in δ (ppm), and multiplicities are indicated as singlet (s), broad signal (br), doublet (d), triplet (t), quartet (q),

dd (doublet of doublets), dt (doublet of triplets), td (triplet of doublets), and multiplet (m). HRMS was determined using LCMS-IT-TOF techniques at the Milwaukee Institute for Drug Discovery (MIDD) in the Shimadzu Laboratory for Advanced and Applied Analytical Chemistry.

4.9.2. N-(2-Benzoyl-4-bromophenyl)-3-bromopropanamide (11)

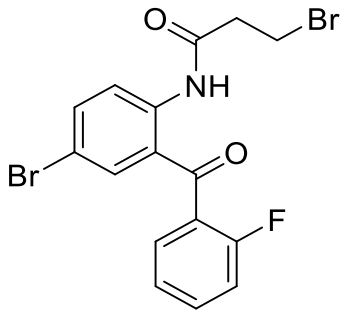


(11)

To a mixture of (2-amino-5-bromophenyl) (phenyl) methanone (**9**, 6 g, 21.72 mmol), sodium bicarbonate (3.65 g, 434.58 mmol), and DCM (60 mL), bromoacetyl bromide (2.46 mL, 28.24 mmol) was added dropwise over a 60-min period. The temperature was kept between -10°C – 0°C with continuous stirring. The white colored reaction mixture, which resulted, was then allowed to stir for longer than 3 h at rt. The completion of the reaction was verified by analysis by TLC (silica gel) and 50% ethyl acetate / hexanes. The reaction mixture was then slowly diluted over 30 min with water (30 mL) as carbon dioxide bubbles evolved. The biphasic mixture, which resulted, was allowed to stand for 15 min and the layers were separated. The aq layer was extracted with dichloromethane (30 mL) and the combined organic layers were washed with 5% aq sodium bicarbonate solution (30 mL) and then 10% aq sodium chloride solution (30 mL). The organic layer was dried (Na_2SO_4). The solvents were removed under reduced pressure and the residue was slurred with ethanol (300 mL) at 50 – 55°C for 30 min. Upon cooling to rt and after holding the

temperature for 1 h, the solid, which formed, was filtered and washed with ethanol (60 mL x 3). The solid was dried under vacuum at 40°C to afford the product *N*-(2-benzoyl-4-bromophenyl)-2-bromoacetamide **11** as an off-white colored solid (82.6 g, 95.5%). **^{1}H NMR** (500 MHz, $CDCl_3$): δ11.60 (s,1H) 7.66-7.64 (m, 2H, 2 x ArH), 7.60-7.57 (m, 2H, 2 x ArH), 7.52-7.49 (m, 2H, 2xArH), 7.38 (dd, 1H, J=8.5, 2.0Hz,H-4), 6.67(d, 1H, J=8.5Hz, H-3), 4.21 (s, 2H). **^{13}C NMR** (500 MHz, $CDCl_3$): 198.2,165.21, 149.4, 139.5, 134.4, 133.4, 131.7, 129.3, 128.5, 120.3, 119.2, 118.8, 42.3. The spectral data for this material were identical to the published values.[275]

4.9.3. 3-Bromo-N-(4-bromo-2-(2-fluorobenzoyl)phenyl)propenamide (12)

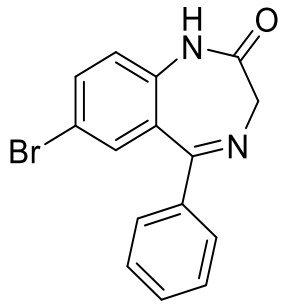


(12)

To a mixture of (2-amino-5-bromophenyl) (2' fluorophenyl) methanone **10** (5 g, 16.99 mmol), sodium bicarbonate (2.85 g, 33.99 mmol), and dichloromethane (50 mL), bromoacetyl bromide (1.76 mL, 20.39 mmol) was added dropwise over a 60 min period. The temperature was kept between -10°C – 0°C with continuous stirring. The white colored reaction mixture, which resulted, was then allowed to stir for longer than 3 h at rt. The completion of the reaction was verified by analysis by TLC (silica gel) with 50% ethyl acetate / hexanes eluent. The reaction mixture was then slowly diluted over 30 min with water (30 mL) since carbon dioxide bubbles evolved. The biphasic mixture, which resulted, was allowed to stand for 15 min and the layers were separated. The aq layer was extracted with dichloromethane (30 mL) and the combined organic layers were

washed with 5% aq sodium bicarbonate solution (30 mL) and then 10% aq sodium chloride solution (30 mL). The organic layer was dried (Na_2SO_4). The solvents were removed under reduced pressure and the residue was slurried with ethanol (30 mL) at 50 – 55ºC for 30 min. Upon cooling to rt and after holding the temperature for 1 h, the solid, which formed, was filtered, and washed with ethanol (10 mL x 3). The solid was dried under vacuum at 40ºC to afford the 2-bromo-*N*-[4-bromo-2-(2-fluorobenzoyl)phenyl]-acetamide **12** as an off-white solid (6.73 g, 96%). **^{1}H NMR** (500 MHz, $CDCl_3$): δ11.60 (s,1H) 7.66-7.64 (m, 2H, 2 x ArH), 7.60-7.57 (m, 2H, 2 x ArH), 7.52-7.49 (m, 2H, 2xArH), 7.38 (dd, 1H, J=8.5, 2.0Hz,H-4), 6.67(d, 1H, J=8.5Hz, H-3), 4.21 (s, 2H). **^{13}C NMR** (500 MHz, $CDCl_3$): 198.2,165.21, 149.4, 139.5, 134.4, 133.4, 131.7, 129.3, 128.5, 120.3, 119.2, 118.8, 42.3. The spectral data for this material were identical to the published values.[275]

4.9.4. 7-Bromo-5-phenyl-1,3-dihydro-2H-benzo[e][1,4]diazepin-2-one (13)

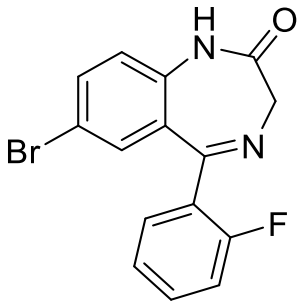


(13)

A mixture of *N*-(2-benzoyl-4-bromophenyl)-2-bromoacetamide **(11)** (7 g, 17.63 mmol), hexamethylenetetramine (HMTM, 5.43 g, 38.79 mmol), ammonium acetate (29.9 g, 387.9 mmol), and isopropanol (70 mL) was heated to reflux (82ºC). The reaction mixture was held at reflux for 6 h, at which point the reaction progress was deemed complete on analysis by TLC (silica gel and 1:1, ethyl acetate/hexanes). The reaction mixture was then cooled to 0 – 5ºC using an ice bath. The

solid, which resulted, was filtered, and washed with cold isopropanol (20 mL x 2) and then water (20mL x 4). The solid was dried under vacuum at 40°C to afford 32 g of the benzodiazepine **13** as an off-white colored solid. The IPA was removed from the mother liquor under reduced pressure. The solid, which resulted, was then extracted with ethyl acetate. The ethyl acetate was removed under reduced pressure and the residue was purified by column chromatography using 1:4 ethyl acetate/hexanes to afford 7-bromo-5-phenyl-1,3-dihydro-2*H*-1,4-benzodiazepin-2-one (**13**). (3.89 g, 70%)**^{1}H NMR** (500 MHz, $CDCl_3$): δ9.89 (s,1H), 7.82(d, 1H) 7.66-7.64 (m, 2H, 2 x ArH), 7.60-7.57 (m, 2H, 2 x ArH), 7.52-7.49 (m, 2H, 2xArH), 7.38 (dd, 1H, J=8.5, 2.0Hz,H-4), 4.32 (s, 2H). **^{13}C NMR** (500 MHz, $CDCl_3$): 170.2,165.21, 149.4, 139.5, 134.4, 133.4, 131.7, 129.3, 128.5, 120.3, 119.2, 118.8, 56.2. The spectral data for this material were identical to the published values.[275]

4.9.5. 7-Bromo-5-(2-fluorophenyl)-1,3-dihydro-2H-benzo[e][1,4]diazepin-2-one (14)

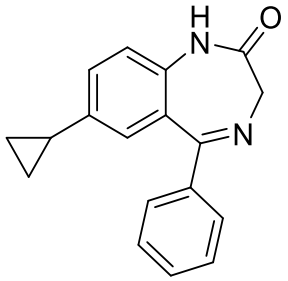


(14)

A mixture of 2-bromo-*N*-[4-bromo-2-(2'fluorobenzoyl)phenyl]-acetamide (**12**), (50 g, 120.48 mmol), hexamethylenetetramine (HMTM, 35.47 g, 252.99 mmol), ammonium acetate (19.5 g, 252.99 mmol), and isopropanol (500 mL) was heated to reflux (82°C). The reaction mixture was held at reflux for 6 h, at which point the reaction progress was deemed complete on analysis by

TLC (silica gel and 1:1, ethyl acetate/hexanes). The reaction mixture was then cooled to 0 – 5°C using an ice bath. The solid, which resulted, was filtered, and washed with cold isopropanol (100 mL x 2) and then water (100mL x 4). The solid was dried under vacuum at 40°C to afford 32 g of the benzodiazepine 6 as an off-white solid. The IPA was removed from the mother liquor under reduced pressure. The solid was then extracted with ethyl acetate. The ethyl acetate was removed under reduced pressure and the residue was purified by column chromatograpy using 1:4 etheyl acetate/hexanes to afford 7-bromo-5-(2-fluorophenyl)-1,3-dihydrobenzo[e]-1,4-diazepin-2-one. (**14**) (28.1 g, 70%) **^{1}H NMR** (500 MHz, $CDCl_3$): δ9.89 (s,1H), 7.82(d, 1H) 7.66-7.64 (m, 2H, 2 x ArH), 7.60-7.57 (m, 2H, 2 x ArH), 7.52-7.49 (m, 2H, 2xArH), 7.38 (dd, 1H, J=8.5, 2.0Hz,H-4), 4.32 (s, 2H). **^{13}C NMR** (500 MHz, $CDCl_3$): 170.2,165.21, 149.4, 139.5, 134.4, 133.4, 131.7, 129.3, 128.5, 120.3, 119.2, 118.8, 56.2. The spectral data for this material were identical to the published values.[275]

4.9.6. 7-Cyclopropyl-5-phenyl-1,3-dihydro-2H-benzo[e][1,4]diazepin-2-one (17)

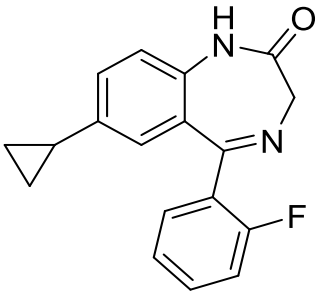


(17)

To a solution of palladium (II) acetate (0.099g, 0.44 mmol) and tri-o-tolyl phosphine (0.27 g, 0.88 mmol) in toluene, the 7-bromo-5-phenyl-1,3-dihydro-2H-benzo[e][1,4]diazepin-2-one **13** (2.0 g, 6.3 mmol) was added. Then in sequence, cyclopropyl boronic acid (2.45 g, 28.52 mmol), and bis(triphenylphosphine) (5.38g, 25.37 mmol) and water (0.5 mL) were added under argon. A reflux

condenser was attached, and the reaction mixture was heated to reflux. The mixture was stirred and allowed to heat to 100 °C. After 12 h the reaction was completed on analysis by mass spectroscopy, and it was then cooled to rt and silica gel (3 g) was added. After stirring for 30 min open to the air, the spent catalyst on silica gel was removed by filtration through a pad of celite then and washed with EtOAc. Then the filtrate was concentrated under reduced pressure. The residue, which resulted, was purified by a wash column (silica gel, EtOAc) to afford the desired product as a white solid **17** (1.29g, 74 %)**^{1}H NMR** (500 MHz, $CDCl_3$) δ 9.67 (s, 1H), 7.65 (d, *J* = 7.5 Hz, 1H), 7.55 (dd, *J* = 14.8, 7.3 Hz, 2H), 7.47 (t, *J* = 7.5 Hz, 2H), 7.25 (d, *J* = 7.6 Hz, 1H), 7.21 (d, *J* = 8.0 Hz, 1H), 7.02 (d, *J* = 1.7 Hz, 1H), 4.29 (s, 2H), 1.89 – 1.82 (m, 1H), 0.98 – 0.94 (m, 2H), 0.64 – 0.57 (m, 2H). **^{13}C NMR** (126 MHz, $CDCl_3$) δ170.3, 166.00, 139.66, 138.35, 137.24, 132.71, 131.34, 130.98, 130.68, 129.95, 129.57, 129.22, 121.85, 121.69, 47.10, 14.83, 9.32, 9.18. **HRMS** (ESI/IT-TOF) m/z: $[M + H]^+$ calcd for $C_{18}H_{16}N_2O$ 277.1330; found 277.1335

4.9.7. 7-Cyclopropyl-5-(2'fluorophenyl)-1,3-dihydro-2H-benzo[e][1,4]diazepin-2-one (18)

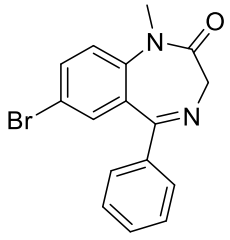


(18)

To a solution of palladium (II) acetate (0.07g, 0.31 mmol) and tri-o-tolyl phosphine (0.19g, 0.63 mmol) in toluene, the 7-bromo-5-(2'fluorophenyl)-1,3-dihydro-2H-benzo[e][1,4]diazepin-2-one **14** (1.5 g, 4.5 mmol) was added . Then in sequence, cyclopropyl boronic acid (1.74 g, 20.25 mmol),

and bis(triphenylphosphine) (3.81g, 18 mmol) and water (0.36 mL) were added under argon. A reflux condenser was attached, and the reaction mixture was heated to reflux. The mixture was stirred and allowed to heat to 100 °C. After 12 h the reaction was completed on analysis by mass spectroscopy, and it was then cooled to rt and silica gel (2.5 g) was added. After stirring for 30 min open to the air, the spent catalyst on silica gel was removed by filtration through a pad of celite and washed with EtOAc. Then the filtrate was concentrated under reduced pressure. The residue, which resulted, was purified by a wash column (silica gel, EtOAc) to afford the desired product as a white colred solid **18** (0.99 g, 75 %). **^{1}H NMR** (500 MHz, $CDCl_3$) δ 9.66 (s, 1H), 7.62 (t, *J* = 7.2 Hz, 1H), 7.57 (t, *J* = 7.4 Hz, 1H), 7.31 (d, *J* = 8.2 Hz, 1H), 7.29 (s, 1H), 7.26 (d, *J* = 7.1 Hz, 1H), 7.24 (s, 1H), 6.95 (s, 1H), 4.36 (s, 2H), 1.86 – 1.80 (m, 1H), 0.94 (dt, *J* = 6.3, 3.1 Hz, 2H), 0.59 (dt, *J* = 10.0, 4.9 Hz, 2H). **^{13}C NMR** (126 MHz, $CDCl_3$) δ 170.2, 165.27, 161.59, 159.57, 140.13, 139.0, 134.6, 132.61, 132.14, 124.40, 123.95, 121.72, 116.46, 116.40, 116.23, 14.80, 9.25, 9.05. **HRMS** (ESI/IT-TOF) m/z: $[M + H]^+$ calcd for $C_{18}H_{15}N_2OF$ 295.1225; found 295.1241

4.9.8. 7-Bromo-1-methyl-5-phenyl-1,3-dihydro-2H-benzo[e][1,4]diazepin-2-one (16)

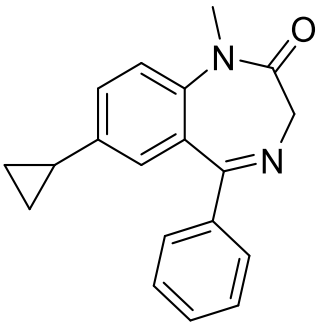


(16)

The 7-bromo-5-phenyl-1,3-dihydro-2H-1,4-benzodiazepin-2-one **13**, (3.80 g, 12.06 mmol) was dissolved in THF, (50 mL) and the solution was cooled to 0°C using an ice bath. Then potassium tert butoxide (1.62 g, 14.47 mmol), which was dissolved in 50 mL of THF, was added dropwise by using an addition funnel. Then methyl iodide (0.82 mL, 13.27 mmol) was added dropwise to

the reaction mixture over a 5 min period, while maintaining the temperature at 0 ◦C. Upon completion of the addition, the reaction mixture was allowed to warm to rt and stirred for 60 min, at which point the reaction was deemed complete on analysis by TLC (silica gel). The reaction mixture was then diluted with ethyl acetate (70 mL) and a solution of 10% aq sodium chloride (70 mL) was added. The biphasic mixture, which resulted, was allowed to stand for 15 min and the layers were separated. The aq layer was then extracted with ethyl acetate (50 mL) and the combined organic layers were washed with 10% aq sodium chloride solution (50 mL). The organic layer was dried (Na_2SO_4). The solvent was removed under reduced pressure. The brown solid, which was obtained, was purified by crystallization using 15:85(ethyl acetate/hexanes), to give 7-bromo-1-methyl-5-phenyl-1,3-dihydro-2H-1,4- benzodiazepin-2-one **16** (2.96 g, 75%) as a brownish white solid. **^{1}H NMR** (500 MHz, $CDCl_3$): 7.82(d, 1H) 7.66-7.64 (m, 2H, 2 x ArH), 7.60-7.57 (m, 2H, 2 x ArH), 7.52-7.49 (m, 2H, 2xArH), 7.38 (dd, 1H, J=8.5, 2.0Hz,H-4), 4.6 (D, 1H), 3.6(D,1H), 3.3(S,3H). **^{13}C NMR** (500 MHz, $CDCl_3$): 171.2, 168.21, 149.4, 139.5, 134.4, 133.4, 131.7, 129.3, 128.5, 120.3, 119.2, 118.8, 82.3, 79.2, 56.2, 34.2. The spectral data for this material were identical to the published values.[275]

4.9.9. 7-Cyclopropyl-1-methyl-5-phenyl-1,3-dihydro-2H-benzo[e][1,4]diazepin-2-one (19, TA-IV-74)

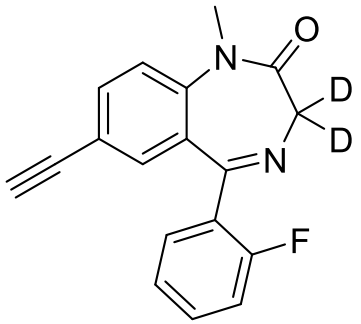


TA-IV-74
(19)

To a solution of palladium (II) acetate (0.047g, 0.21 mmol) and tri-o-tolyl phosphine (0.129g, 0.42 mmol) in toluene, the 7-bromo-5-(2-fluorophenyl)-1,3-dihydro-2H-benzo[e][1,4]diazepin-2-one **26** (1.0 g, 3.037 mmol) was added . Then in sequence, cyclopropyl boronic acid (1.17 g, 13.66 mmol), and bis(triphenylphosphine) (2.57g, 12.15 mmol) and water (0.24 mL) were added under argon. A reflux condenser was attached, and the reaction mixture was heated to reflux. The mixture was stirred and heated to 100 °C. After 12 h the reaction was completed on analysis by mass spectroscopy, and it was then cooled to rt and silica gel (2 g) was added. After stirring for 30 min open to the air, the spent catalyst on silica gel was removed by filtration through a pad of celite and that solid was washed with EtOAc. Then the combined filtrates were concentrated under reduced pressure. The residue, which resulted, was purified by a wash column (silica gel, EtOAc) to afford the desired product as a white solid (0.99 g, 75 %). **^{1}H NMR** (500 MHz, $CDCl_3$) δ 7.66 – 7.62 (m, 2H), 7.50 – 7.45 (m, 1H), 7.43 – 7.39 (m, 2H), 7.25 – 7.23 (m, 2H), 7.01 (d, *J* = 1.8 Hz, 1H), 4.80 (d, *J* = 10.6 Hz, 1H), 3.80 (d, *J* = 10.6 Hz, 1H), 3.39 (s, 3H), 1.88 (ddd, *J* = 8.4, 6.7, 4.2 Hz, 1H), 1.00 – 0.95 (m, 2H), 0.66 – 0.62 (m, 2H). **^{13}C NMR** (126 MHz, $CDCl_3$) δ 170.31, 170.15, 141.69, 139.86, 138.87, 130.36, 129.57, 128.54, 128.53, 128.22, 127.47, 120.97, 57.04, 34.77,

14.85, 9.48, 9.33. **HRMS** (ESI/IT-TOF) m/z: $[M + H]^+$ calcd for $C_{19}H_{18}N_2O$ 291.1503; found 291.1491. The spectral data for this material were identical to the published values.[275]

4.9.10. 7-Ethynyl-5-(2'fluorophenyl)-1-methyl-1,3-dihydro-2H-benzo[e][1,4]diazepin-2-one-3,3-d2 (25)

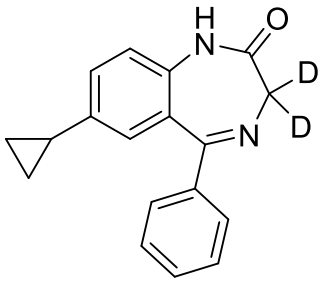


(25)

The 7-ethynyl-5-(2'fluorophenyl)-1-methyl-1,3-dihydro-2H-benzo[e][1,4]diazepin-2-one (**2**), (0.4 g, 1.36 mmol) was dissolved in d4 -methanol (3 mL). Then potassium tert-butoxide (0.16 g, 1.5 mmol) was added to the solution. The mixture was sonicated for 45 min starting from rt to 50°C. After the reaction was completed (checked by NMR), the reaction mixture was cooled to rt. To neutralize the reaction mixture a 3 mL solution of the mixture of D_2O-DCl was added dropwise with cooling. After each addition the pH was checked with pH paper to reach pH=7. The biphasic mixture, which resulted, was allowed to stand for 15 min and the layers were separated. Then the mixture was extracted with (5mL) of ethyl acetate. The aq layer was removed and this process was repeated three times. The organic layer was removed and dried over Na_2SO_4. It was dried further by first with blowing argon over it and then placing it under high vacuum. Then the solid was dissolved with methanol and kept on stirring at 50°C for 30 min. Then the solvent was removed under reduced pressure to afford D2-KRM-II-008, with 97% deuteration at the C-3 position (**25**)

(0.39 g, 97%) as a white solid. **^{1}H NMR** (500 MHz, $CDCl_3$): 7.82(d, 1H) 7.66-7.64 (m, 2H, 2 x ArH), 7.60-7.57 (m, 2H, 2 x ArH), 7.52-7.49 (m, 2H, 2xArH), 7.38 (dd, 1H, J=8.5, 2.0Hz,H-4), 4.6 (D, 1H), 3.6(D,1H), 3.3(S,3H), 3.1(s,1H). **^{13}C NMR** (500 MHz, $CDCl_3$): 171.2, 168.21, 149.4, 139.5, 134.4, 133.4, 131.7, 129.3, 128.5, 120.3, 119.2, 118.8, 82.3, 79.2, 56.2, 34.2. **HRMS** (ESI/IT-TOF) m/z: $[M + H]^+$ calcd for $C_{18}H_{11}D_2N_2OF$ 295.1216; found 29295.1210.

4.9.11. 7-Cyclopropyl-5-phenyl-1,3-dihydro-2H-benzo[e][1,4]diazepin-2-one-3,3-d2 (21)

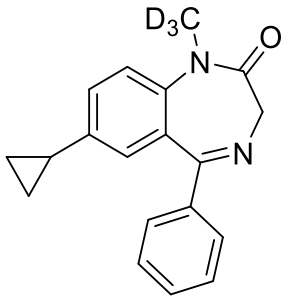


(21)

The 7-cyclopropyl-5-phenyl-1,3-dihydro-2H-benzo[e][1,4]diazepin-2-one (**17**) (0.5 g, 1.80 mmol) was dissolved in d4 -methanol (3 mL). Then potassium tert-butoxide (0.22 g, 1.96 mmol) was added to the solution. The mixture was sonicated for 45 min starting from rt to 50°C. After the reaction was completed (checked by NMR), the reaction mixture was cooled to rt. To neutralize the reaction mixture a 3 mL solution of the mixture of D_2O-DCl was added dropwise with cooling. After each addition the pH was checked by pH paper to reach pH=7. The biphasic mixture, which resulted, was allowed to stand for 15 min and the layers were separated. Then the mixture was extracted with (5mL) ethyl acetate. The aq layer was removed and repeated this process 3 times. The organic layer was removed and dried over Na_2SO_4. It was dried initially by blowing argon over it and then placing it under high vacuum. Then the solid was dissolved in methanol and was kept on stirring at 50°C for 30 min. Then the solvent was removed under reduced pressure to afford

D2-KRM-II-008, with 97% deuteration at the C-3 position (**21**) (0.48 g, 97%) as a light-pink-colored solid. **^{1}H NMR** (500 MHz, $CDCl_3$) δ 9.67 (s, 1H), 7.65 (d, *J* = 7.5 Hz, 1H), 7.55 (dd, *J* = 14.8, 7.3 Hz, 2H), 7.47 (t, *J* = 7.5 Hz, 2H), 7.25 (d, *J* = 7.6 Hz, 1H), 7.21 (d, *J* = 8.0 Hz, 1H), 7.02 (d, *J* = 1.7 Hz, 1H), 4.29 (s, 2H), 1.89 – 1.82 (m, 1H), 0.98 – 0.94 (m, 2H), 0.64 – 0.57 (m, 2H). **^{13}C NMR** (126 MHz, $CDCl_3$) δ170.3, 166.00, 139.66, 138.35, 137.24, 132.71, 131.34, 130.98, 130.68, 129.95, 129.57, 129.22, 121.85, 121.69, 47.10, 14.83, 9.32, 9.18. **HRMS** (ESI/IT-TOF) m/z: $[M + H]^+$ calcd for $C_{18}H_{14}D_2N_2O$ 279.1470; found 279.1460.

4.9.12. 7-Cyclopropyl-1-(methyl-d3)-5-phenyl-1,3-dihydro-2H-benzo[e][1,4]diazepin-2-one (22)

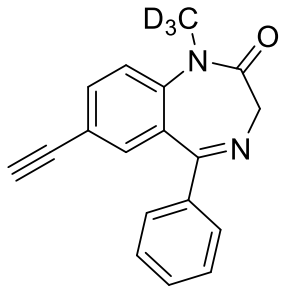


(22)

The nor 7-cyclopropyl-5-phenyl-1,3-dihydro-2H-benzo[e][1,4]diazepin-2-one (**17**), (0.13 g, 0.47 mmol) was dissolved in THF (10 mL) and the solution was cooled to 0°C using an ice bath. Then potassium tert-butoxide (0.058 g, 0.51 mmol), which was dissolved in 5 mL of THF, was added dropwise by using an addition funnel. Then trideuterio methyl iodide (0.035 mL, 0.56 mmoL) was added dropwise to the reaction mixture over a 5 min period, while maintaining the temperature at 0°C. Upon completion of the addition, the reaction mixture was allowed to warm to rt and stirred for 60 min, at which point the reaction was deemed complete on analysis by TLC (silica gel). The reaction mixture was then diluted with ethyl acetate (10 mL) and a solution of 10% aq sodium

chloride solution (10 mL) was added. The biphasic mixture, which resulted, was allowed to stand for 15 min and the layers were separated. The aq layer was then extracted with ethyl acetate (20 mL) and the combined organic layers were washed with 10% aq sodium chloride solution (20 mL). The organic layer was dried (Na_2SO_4). The solvent was removed under reduced pressure. The brown solid, which was obtained, was purified by crystallization using 15:85(ethyl acetate/hexanes), to give 7-ethynyl-1-(methyl-d3)-5-phenyl-1,3-dihydro-2H-benzo[e] [1,4] diazepin-2-one (**22**) (3.7 g, 86%) as a white solid. **^{1}H NMR** (500 MHz, $CDCl_3$) δ 7.65 (d, *J* = 7.5 Hz, 1H), 7.55 (dd, *J* = 14.8, 7.3 Hz, 2H), 7.47 (t, *J* = 7.5 Hz, 2H), 7.25 (d, *J* = 7.6 Hz, 1H), 7.21 (d, *J* = 8.0 Hz, 1H), 7.02 (d, *J* = 1.7 Hz, 1H), 4.29 (s, 2H), 1.89 – 1.82 (m, 1H), 0.98 – 0.94 (m, 2H), 0.64 – 0.57 (m, 2H). **^{13}C NMR** (126 MHz, $CDCl_3$) δ170.3, 166.00, 139.66, 138.35, 137.24, 132.71, 131.34, 130.98, 130.68, 129.95, 129.57, 129.22, 121.85, 121.69, 47.10, 14.83, 9.32, 9.18. **HRMS** (ESI/IT-TOF) m/z: $[M + H]^+$ calcd for $C_{19}H_{14}D_3N_2O$ 294.1690; found 294.1457.

4.9.13. 7-Ethynyl-1-(methyl-d3)-5-phenyl-1,3-dihydro-2H-benzo[e][1,4]diazepin-2-one (24)

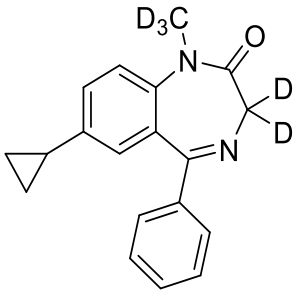


(24)

The 5-phenyl-7-((ethynyl)-1,3-dihydro-2H-1,4-benzodiazepin-2-one (7), (1.0 g, 3.83 mmol) was dissolved in THF (10 mL) and the solution was cooled to 0°C using an ice bath. Then potassium tert-butoxide (0.47 g, 4.23 mmol), which was dissolved in 5 mL of THF, was added dropwise by using an addition funnel. Then trideuterio methyl iodide (0.31 mL, 4.98 mmoL) was added

dropwise to the reaction mixture over a 5 min period, while maintaining the temperature at 0°C. Upon completion of the addition, the reaction mixture was allowed to warm to rt and stirred for 60 min, at which point the reaction was deemed complete on analysis by TLC (silica gel). The reaction mixture was then diluted with ethyl acetate (10 mL) and a solution of 10% aq sodium chloride solution (10 mL) was added. The biphasic mixture, which resulted, was allowed to stand for 15 min and the layers were separated. The aq layer was then extracted with ethyl acetate (10 mL) and the combined organic layers were washed with 10% aq sodium chloride solution (10 mL). The organic layer was dried (Na_2SO_4). The solvent was removed under reduced pressure. The brown solid, which was obtained, was purified by crystallization using 15:85(ethyl acetate/hexanes), to give 7-ethynyl-1-(methyl-d3)-5-phenyl-1,3-dihydro-2H-benzo[e][1,4]diazepin-2-one (24) (0.925 g, 86%) as a white solid. **^{1}H NMR** (500 MHz, $CDCl_3$): 7.82(d, 1H) 7.66-7.64 (m, 2H, 2 x ArH), 7.60-7.57 (m, 2H, 2 x ArH), 7.52-7.49 (m, 2H, 2xArH), 7.38 (dd, 1H, J=8.5, 2.0Hz,H-4), 4.6 (D, 1H), 3.6(D,1H), 3.1(s,1H). **^{13}C NMR** (500 MHz, $CDCl_3$): 171.2, 168.21, 149.4, 139.5, 134.4, 133.4, 131.7, 129.3, 128.5, 120.3, 119.2, 118.8, 82.3, 79.2, 56.2, 34.2. Rf = 0.5 (silica gel, ethyl acetate/hexanes 1:2) **HRMS** (ESI/IT-TOF): m/z [M +H] + calcd for $C_{18}H_{11}D_3N_2O$: 277.3350; found 277.3329.

4.9.13. 7-Cyclopropyl-1-(methyl-d3)-5-phenyl-1,3-dihydro-2H-benzo[e] [1,4] diazepin-2-one-3,3-d2



(23)

The 7-cyclopropyl-5-phenyl-1,3-dihydro-2H-benzo[e][1,4]diazepin-2-one-3,3-d2 **(21)** (0.2 g, 0.71 mmol) was dissolved in THF (10 mL) and the solution was cooled to 0°C using an ice bath. Then potassium tert-butoxide (0.066 g, 0.58 mmol), which was dissolved in 5 mL of THF, was added dropwise by using an addition funnel. Then trideuterio methyl iodide (0.04 mL, 0.63 mmol) was added dropwise to the reaction mixture over a 5 min period, while maintaining the temperature at 0°C. Upon completion of the addition, the reaction mixture was allowed to warm to rt and stirred for 60 min, at which point the reaction was deemed complete on analysis by TLC (silica gel). The reaction mixture was then diluted with ethyl acetate (10 mL) and a solution of 10% aq sodium chloride solution (10 mL) was added. The biphasic mixture, which resulted, was allowed to stand for 15 min and the layers were separated. The aq layer was then extracted with ethyl acetate (20 mL) and the combined organic layers were washed with 10% aq sodium chloride solution (20 mL). The organic layer was dried (Na_2SO_4). The solvent was removed under reduced pressure. The brown solid, which was obtained, was purified by crystallization using 15:85(ethyl acetate/hexanes), to give 7-Cyclopropyl-1-(methyl-d3)-5-phenyl-1,3-dihydro-2H-benzo[e] [1,4] diazepin-2-one-3,3-d2 (23)(0.18 g, 86%) as a yellow- colored solid. **^{1}H NMR** (500 MHz, $CDCl_3$)

δ 7.65 (d, *J* = 7.5 Hz, 1H), 7.55 (dd, *J* = 14.8, 7.3 Hz, 2H), 7.47 (t, *J* = 7.5 Hz, 2H), 7.25 (d, *J* = 7.6 Hz, 1H), 7.21 (d, *J* = 8.0 Hz, 1H), 7.02 (d, *J* = 1.7 Hz, 1H), 4.29 (s, 2H), 1.89 – 1.82 (m, 1H), 0.98 – 0.94 (m, 2H), 0.64 – 0.57 (m, 2H). **^{13}C NMR** (126 MHz, $CDCl_3$) δ170.3, 166.00, 139.66, 138.35, 137.24, 132.71, 131.34, 130.98, 130.68, 129.95, 129.57, 129.22, 121.85, 121.69, 47.10, 14.83, 9.32, 9.18. **HRMS** (ESI/IT-TOF) m/z: $[M + H]^+$ calcd for $C_{19}H_{13}D_5N_2O$ 296.1807; found 296.1805.

REFERENCES

1. Bernardo, A. *et al.* Symptomatic and neurotrophic effects of GABAA receptor positive allosteric modulation in a mouse model of chronic stress. *Neuropsychopharmacology* **47**, 1608–1619 (2022).

2. Bhattacharya, D. *et al.* GABA(A) receptor activation drives GABARAP-Nix mediated autophagy to radiation-sensitize primary and brain-metastatic lung adenocarcinoma tumors. *bioRxiv* 2023.11.29.569295 (2023) doi:10.1101/2023.11.29.569295.

3. Clayton, T. *et al.* A Review of the Updated Pharmacophore for the Alpha 5 GABA(A) Benzodiazepine Receptor Model. *Int J Med Chem* **2015**, 430248 (2015).

4. Golani, L. K. *et al.* Rationalizing the binding and α subtype selectivity of synthesized imidazodiazepines and benzodiazepines at GABAA receptors by using molecular docking studies. *Bioorg Med Chem Lett* **62**, 128637 (2022).

5. Laverty, D. *et al.* Cryo-EM structure of the human α1β3γ2 GABAA receptor in a lipid bilayer. *Nature* **565**, 516–520 (2019).

6. McCoy, A. M. *et al.* GL-II-73, a Positive Allosteric Modulator of α5GABAA Receptors, Reverses Dopamine System Dysfunction Associated with Pilocarpine-Induced Temporal Lobe Epilepsy. *Int J Mol Sci* **24**, 11588 (2023).

7. Souza, A. J. *et al.* Distinct sex-dependent behavioral responses induced by two positive allosteric modulators of alpha 5 subunit-containing GABAA receptors. *Behavioural brain research* **428**, 113832 (2022).

8. Jacob, T. C., Moss, S. J. & Jurd, R. GABA(A) receptor trafficking and its role in the dynamic modulation of neuronal inhibition. *Nat Rev Neurosci* **9**, 331–43 (2008).

9. Cerne, R. *et al.* Chapter 11 - The orally bioavailable imidazodiazepine, KRM-II-81, is a novel potentiator of α2/3-containing GABAA receptors with analgesic efficacy. in *The Neurobiology, Physiology, and Psychology of Pain* (eds. Rajendram, R., Patel, V. B., Preedy, V. R. & Martin, C. R.) 117–127 (Academic Press, 2022). doi:https://doi.org/10.1016/B978-0-12-820589-1.00011-7.

10. Witkin, J. M. *et al.* The Positive Allosteric Modulator of α2/3-Containing GABAA Receptors, KRM-II-81, Is Active in Pharmaco-Resistant Models of Epilepsy and Reduces Hyperexcitability after Traumatic Brain Injury. *J Pharmacol Exp Ther* **372**, 83–94 (2020).

11. Li, G., Golani, L. K., Jahan, R., Rashid, F. & Cook, J. M. Improved Synthesis of Anxiolytic, Anticonvulsant and Antinociceptive α2/α3-GABA(A)ergic Receptor Subtype Selective Ligands as Promising Agents to Treat Anxiety, Epilepsy, as well as Neuropathic Pain. *Synthesis (Stuttg)* **50**, 4124–4132 (2018).

12. Li, J. J. Delépine amine synthesis. in *Name Reactions* 198–199 (Springer International Publishing, 2014). doi:10.1007/978-3-319-03979-4_83.

13. Blaević, N. & Kajfez, F. D. I. A new ring closure synthesis of 1,4-benzodiazepines. II. *J Heterocycl Chem* **8**, 845–846 (1971).

14. Cepanec, I., Litvić, M. & Pogorelić, I. Efficient Synthesis of 3-Hydroxy-1,4-benzodiazepines Oxazepam and Lorazepam by New Acetoxylation Reaction of 3-Position of 1,4-Benzodiazepine Ring. *Org Process Res Dev* **10**, 1192–1198 (2006).

15. Watanabe, M., Maemura, K., Kanbara, K., Tamayama, T. & Hayasaki, H. GABA and GABA receptors in the central nervous system and other organs. *Int Rev Cytol* **213**, 1–47 (2002).

16. Sieghart, W. Structure and pharmacology of gamma-aminobutyric acidA receptor subtypes. *Pharmacol Rev* **47**, 181 (1995).

17. Alexander, S. P. H., Mathie, A. & Peters, J. A. Guide to Receptors and Channels (GRAC), 3rd edition. *Br J Pharmacol* **153 Suppl 2**, S1-209 (2008).

18. Twyman, R. E., Rogers, C. J. & Macdonald, R. L. Differential regulation of gamma-aminobutyric acid receptor channels by diazepam and phenobarbital. *Ann Neurol* **25**, 213–20 (1989).

19. Hyland, N. P. & Cryan, J. F. A Gut Feeling about GABA: Focus on GABA(B) Receptors. *Front Pharmacol* **1**, 124 (2010).

20. Guidotti, A. *et al.* GABAergic dysfunction in schizophrenia: new treatment strategies on the horizon. *Psychopharmacology (Berl)* **180**, 191–205 (2005).

21. Sieghart, W. & Ernst, M. Heterogeneity of GABAA Receptors: Revived Interest in the Development of Subtype-selective Drugs. *Current Medicinal Chemistry-Central Nervous System Agents* **5**, 217–242 (2005).

22. Bowser, D. N. *et al.* Altered kinetics and benzodiazepine sensitivity of a $GABA_A$ receptor subunit mutation [γ_2 (R43Q)] found in human epilepsy. *Proceedings of the National Academy of Sciences* **99**, 15170–15175 (2002).

23. Munro, G., Hansen, R. R. & Mirza, N. R. GABAA receptor modulation: Potential to deliver novel pain medicines? *Eur J Pharmacol* **716**, 17–23 (2013).

24. Barnard, E. A. *et al.* International Union of Pharmacology. XV. Subtypes of gamma-aminobutyric acidA receptors: classification on the basis of subunit structure and receptor function. *Pharmacol Rev* **50**, 291–313 (1998).

25. Burt, D. R. & Kamatchi, G. L. GABAA receptor subtypes: from pharmacology to molecular biology. *FASEB J* **5**, 2916–23 (1991).

26. Clayton, T. *et al.* An updated unified pharmacophore model of the benzodiazepine binding site on gamma-aminobutyric acid(a) receptors: correlation with comparative models. *Curr Med Chem* **14**, 2755–75 (2007).

27. Bast, T., Pezze, M. & McGarrity, S. Cognitive deficits caused by prefrontal cortical and hippocampal neural disinhibition. *Br J Pharmacol* **174**, 3211–3225 (2017).

28. Benes, F. M. *et al.* Regulation of the GABA cell phenotype in hippocampus of schizophrenics and bipolars. *Proc Natl Acad Sci U S A* **104**, 10164–9 (2007).

29. Zhang, Z. J. & Reynolds, G. P. A selective decrease in the relative density of parvalbumin-immunoreactive neurons in the hippocampus in schizophrenia. *Schizophr Res* **55**, 1–10 (2002).

30. Fee, C., Banasr, M. & Sibille, E. Somatostatin-Positive Gamma-Aminobutyric Acid Interneuron Deficits in Depression: Cortical Microcircuit and Therapeutic Perspectives. *Biol Psychiatry* **82**, 549–559 (2017).

31. Petty, F. & Schlesser, M. A. Plasma GABA in affective illness. A preliminary investigation. *J Affect Disord* **3**, 339–43 (1981).

32. Griffin, C. E., Kaye, A. M., Bueno, F. R. & Kaye, A. D. Benzodiazepine pharmacology and central nervous system-mediated effects. *Ochsner journal* **13**, 214–23 (2013).

33. Perez, S. M. & Lodge, D. J. New approaches to the management of schizophrenia: focus on aberrant hippocampal drive of dopamine pathways. *Drug Des Devel Ther* **8**, 887–96 (2014).

34. Lieberman, J. A. *et al.* Effectiveness of antipsychotic drugs in patients with chronic schizophrenia. *N Engl J Med* **353**, 1209–23 (2005).

35. Abi-Dargham, A. Do we still believe in the dopamine hypothesis? New data bring new evidence. *Int J Neuropsychopharmacol* **7 Suppl 1**, S1-5 (2004).

36. Laruelle, M. & Abi-Dargham, A. Dopamine as the wind of the psychotic fire: new evidence from brain imaging studies. *J Psychopharmacol* **13**, 358–71 (1999).

37. Heckers, S. & Konradi, C. Hippocampal pathology in schizophrenia. *Curr Top Behav Neurosci* **4**, 529–53 (2010).

38. Nelson, M. D., Saykin, A. J., Flashman, L. A. & Riordan, H. J. Hippocampal volume reduction in schizophrenia as assessed by magnetic resonance imaging: a meta-analytic study. *Arch Gen Psychiatry* **55**, 433–40 (1998).

39. Lodge, D. J. & Grace, A. A. Aberrant hippocampal activity underlies the dopamine dysregulation in an animal model of schizophrenia. *J Neurosci* **27**, 11424–30 (2007).

40. Perez Stephanie M. Convergent Inputs from the Hippocampus and Thalamus to the Nucleus Accumbens Regulate Dopamine Neuron Activity. (2018).

41. Perez, S. M., Carreno, F. R., Frazer, A. & Lodge, D. J. Vagal nerve stimulation reverses aberrant dopamine system function in the methylazoxymethanol acetate rodent model of schizophrenia. *J Neurosci* **34**, 9261–7 (2014).

42. Perez, S. M. & Lodge, D. J. Hippocampal interneuron transplants reverse aberrant dopamine system function and behavior in a rodent model of schizophrenia. *Mol Psychiatry* **18**, 1193–8 (2013).

43. Perez, S. M., Shah, A., Asher, A. & Lodge, D. J. Hippocampal deep brain stimulation reverses physiological and behavioural deficits in a rodent model of schizophrenia. *Int J Neuropsychopharmacol* **16**, 1331–9 (2013).

44. Donegan, J. J. & Lodge, D. J. Cell-based therapies for the treatment of schizophrenia. *Brain Res* **1655**, 262–269 (2017).

45. Kilpatrick, D. G. *et al.* National estimates of exposure to traumatic events and PTSD prevalence using DSM-IV and DSM-5 criteria. *J Trauma Stress* **26**, 537–47 (2013).

46. Kilpatrick, D. G. *et al.* Violence and risk of PTSD, major depression, substance abuse/dependence, and comorbidity: results from the National Survey of Adolescents. *J Consult Clin Psychol* **71**, 692–700 (2003).

47. Battle, D. E. Diagnostic and Statistical Manual of Mental Disorders (DSM). *Codas* **25**, 191–2 (2013).

48. Braakman, M. H., Kortmann, F. A. M. & van den Brink, W. Validity of 'post-traumatic stress disorder with secondary psychotic features': a review of the evidence. *Acta Psychiatr Scand* **119**, 15–24 (2009).

49. Lieberman, J. A. *et al.* Effectiveness of antipsychotic drugs in patients with chronic schizophrenia. *N Engl J Med* **353**, 1209–23 (2005).

50. GBD 2017 Disease and Injury Incidence and Prevalence Collaborators. Global, regional, and national incidence, prevalence, and years lived with disability for 354 diseases and injuries for 195 countries and territories, 1990-2017: a systematic analysis for the Global Burden of Disease Study 2017. *Lancet* **392**, 1789–1858 (2018).

51. Malhi, G. S. & Mann, J. J. Depression. *Lancet* **392**, 2299–2312 (2018).

52. Gartlehner, G. *et al.* Pharmacological and non-pharmacological treatments for major depressive disorder: review of systematic reviews. *BMJ Open* **7**, e014912 (2017).

53. Gartlehner, G. *et al.* Pharmacological and non-pharmacological treatments for major depressive disorder: review of systematic reviews. *BMJ Open* **7**, e014912 (2017).

54. Fogaça, M. V & Duman, R. S. Cortical GABAergic Dysfunction in Stress and Depression: New Insights for Therapeutic Interventions. *Front Cell Neurosci* **13**, 87 (2019).

55. Hirschfeld, R. M. History and evolution of the monoamine hypothesis of depression. *J Clin Psychiatry* **61 Suppl 6**, 4–6 (2000).

56. Chávez-Castillo, M. *et al.* Depression as a Neuroendocrine Disorder: Emerging Neuropsychopharmacological Approaches beyond Monoamines. *Adv Pharmacol Sci* **2019**, 7943481 (2019).

57. Duman, C. H. & Duman, R. S. Spine synapse remodeling in the pathophysiology and treatment of depression. *Neurosci Lett* **601**, 20–9 (2015).

58. Conradi, H. J., Ormel, J. & de Jonge, P. Presence of individual (residual) symptoms during depressive episodes and periods of remission: a 3-year prospective study. *Psychol Med* **41**, 1165–74 (2011).

59. Fossati, P., Ergis, A. M. & Allilaire, J. F. [Executive functioning in unipolar depression: a review]. *Encephale* **28**, 97–107 (2002).

60. Bortolato, B. *et al.* Cognitive remission: a novel objective for the treatment of major depression? *BMC Med* **14**, 9 (2016).

61. Lee, R. S. C., Hermens, D. F., Porter, M. A. & Redoblado-Hodge, M. A. A meta-analysis of cognitive deficits in first-episode Major Depressive Disorder. *J Affect Disord* **140**, 113–124 (2012).

62. Majer, M. *et al.* Impaired divided attention predicts delayed response and risk to relapse in subjects with depressive disorders. *Psychol Med* **34**, 1453–63 (2004).

63. Kang, H. J. *et al.* Decreased expression of synapse-related genes and loss of synapses in major depressive disorder. *Nat Med* **18**, 1413–7 (2012).

64. Holmes, S. E. *et al.* Lower synaptic density is associated with depression severity and network alterations. *Nat Commun* **10**, 1529 (2019).

65. Kang, H. J. *et al.* Decreased expression of synapse-related genes and loss of synapses in major depressive disorder. *Nat Med* **18**, 1413–7 (2012).

66. Feyissa, A. M., Chandran, A., Stockmeier, C. A. & Karolewicz, B. Reduced levels of NR2A and NR2B subunits of NMDA receptor and PSD-95 in the prefrontal cortex in major depression. *Prog Neuropsychopharmacol Biol Psychiatry* **33**, 70–5 (2009).

67. Christoffel, D. J., Golden, S. A. & Russo, S. J. Structural and synaptic plasticity in stress-related disorders. *Rev Neurosci* **22**, 535–49 (2011).

68. Izquierdo, A., Wellman, C. L. & Holmes, A. Brief Uncontrollable Stress Causes Dendritic Retraction in Infralimbic Cortex and Resistance to Fear Extinction in Mice. *The Journal of Neuroscience* **26**, 5733–5738 (2006).

69. Liston, C. *et al.* Stress-induced alterations in prefrontal cortical dendritic morphology predict selective impairments in perceptual attentional set-shifting. *J Neurosci* **26**, 7870–4 (2006).

70. Shansky, R. M. & Morrison, J. H. Stress-induced dendritic remodeling in the medial prefrontal cortex: effects of circuit, hormones and rest. *Brain Res* **1293**, 108–13 (2009).

71. Qiao, H. *et al.* Dendritic Spines in Depression: What We Learned from Animal Models. *Neural Plast* **2016**, 8056370 (2016).

72. Newton, D. F., Fee, C., Nikolova, Y. S. & Sibille, E. Chapter 28 - Altered GABAergic Function, Cortical Microcircuitry, and Information Processing in Depression. in *Neurobiology of Depression* (eds. Quevedo, J., Carvalho, A. F. & Zarate, C. A.) 315–329 (Academic Press, 2019). doi:https://doi.org/10.1016/B978-0-12-813333-0.00028-7.

73. Berrettini, W. H. *et al.* Reduced plasma and CSF gamma-aminobutyric acid in affective illness: effect of lithium carbonate. *Biol Psychiatry* **18**, 185–94 (1983).

74. Petty, F., Kramer, G. L., Dunnam, D. & Rush, A. J. Plasma GABA in mood disorders. *Psychopharmacol Bull* **26**, 157–61 (1990).

75. Petty, F., Kramer, G. L., Fulton, M., Davis, L. & Rush, A. J. Stability of plasma GABA at four-year follow-up in patients with primary unipolar depression. *Biol Psychiatry* **37**, 806–10 (1995).

76. Petty, F., Kramer, G. L., Gullion, C. M. & Rush, A. J. Low plasma gamma-aminobutyric acid levels in male patients with depression. *Biol Psychiatry* **32**, 354–63 (1992).

77. Petty, F. & Sherman, A. D. Plasma GABA levels in psychiatric illness. *J Affect Disord* **6**, 131–8 (1984).

78. Bhagwagar, Z. *et al.* Low GABA concentrations in occipital cortex and anterior cingulate cortex in medication-free, recovered depressed patients. *Int J Neuropsychopharmacol* **11**, 255–60 (2008).

79. Goddard, A. W. *et al.* Reductions in occipital cortex GABA levels in panic disorder detected with 1h-magnetic resonance spectroscopy. *Arch Gen Psychiatry* **58**, 556–61 (2001).

80. Price, R. B. *et al.* Amino acid neurotransmitters assessed by proton magnetic resonance spectroscopy: relationship to treatment resistance in major depressive disorder. *Biol Psychiatry* **65**, 792–800 (2009).

81. Sanacora, G. *et al.* Subtype-specific alterations of gamma-aminobutyric acid and glutamate in patients with major depression. *Arch Gen Psychiatry* **61**, 705–13 (2004).

82. Sanacora, G., Mason, G. F., Rothman, D. L. & Krystal, J. H. Increased occipital cortex GABA concentrations in depressed patients after therapy with selective serotonin reuptake inhibitors. *Am J Psychiatry* **159**, 663–5 (2002).

83. Sanacora, G. *et al.* Subtype-specific alterations of gamma-aminobutyric acid and glutamate in patients with major depression. *Arch Gen Psychiatry* **61**, 705–13 (2004).

84. Sanacora, G. *et al.* Reduced cortical gamma-aminobutyric acid levels in depressed patients determined by proton magnetic resonance spectroscopy. *Arch Gen Psychiatry* **56**, 1043–7 (1999).

85. Hasler, G. *et al.* Reduced prefrontal glutamate/glutamine and gamma-aminobutyric acid levels in major depression determined using proton magnetic resonance spectroscopy. *Arch Gen Psychiatry* **64**, 193–200 (2007).

86. Gabbay, V. *et al.* Anterior cingulate cortex γ-aminobutyric acid in depressed adolescents: relationship to anhedonia. *Arch Gen Psychiatry* **69**, 139–49 (2012).

87. Plante, D. T., Jensen, J. E., Schoerning, L. & Winkelman, J. W. Reduced γ-aminobutyric acid in occipital and anterior cingulate cortices in primary insomnia: a link to major depressive disorder? *Neuropsychopharmacology* **37**, 1548–57 (2012).

88. Engin, E., Liu, J. & Rudolph, U. α2-containing GABA(A) receptors: a target for the development of novel treatment strategies for CNS disorders. *Pharmacol Ther* **136**, 142–52 (2012).

89. Collinson, N. *et al.* Enhanced Learning and Memory and Altered GABAergic Synaptic Transmission in Mice Lacking the α5 Subunit of the GABA_AReceptor. *The Journal of Neuroscience* **22**, 5572 (2002).

90. Korpi, E. R., Mattila, M. J., Wisden, W. & Lüddens, H. GABA(A)-receptor subtypes: clinical efficacy and selectivity of benzodiazepine site ligands. *Ann Med* **29**, 275–82 (1997).

91. Olsen, R. W. & Sieghart, W. GABA A receptors: subtypes provide diversity of function and pharmacology. *Neuropharmacology* **56**, 141–8 (2009).

92. Fritschy, J. M. & Mohler, H. GABAA-receptor heterogeneity in the adult rat brain: differential regional and cellular distribution of seven major subunits. *J Comp Neurol* **359**, 154–94 (1995).

93. Sur, C., Fresu, L., Howell, O., McKernan, R. M. & Atack, J. R. Autoradiographic localization of alpha5 subunit-containing GABAA receptors in rat brain. *Brain Res* **822**, 265–70 (1999).

94. Hauser, J. *et al.* Hippocampal alpha5 subunit-containing GABAA receptors modulate the expression of prepulse inhibition. *Mol Psychiatry* **10**, 201–7 (2005).

95. Donegan, J. J. *et al.* Stem cell-derived interneuron transplants functionally integrate within the existing circuitry. *Mol Psychiatry* **22**, 1369 (2017).

96. Crestani, F. *et al.* Trace fear conditioning involves hippocampal alpha5 GABA(A) receptors. *Proc Natl Acad Sci U S A* **99**, 8980–5 (2002).

97. Lodge, D. J. & Grace, A. A. Hippocampal dysfunction and disruption of dopamine system regulation in an animal model of schizophrenia. *Neurotox Res* **14**, 97–104 (2008).

98. Gill, K. M., Lodge, D. J., Cook, J. M., Aras, S. & Grace, A. A. A Novel α5GABAAR-Positive Allosteric Modulator Reverses Hyperactivation of the Dopamine System in the MAM Model of Schizophrenia. *Neuropsychopharmacology* **36**, 1903–1911 (2011).

99. Gill, K. M., Cook, J. M., Poe, M. M. & Grace, A. A. Prior antipsychotic drug treatment prevents response to novel antipsychotic agent in the methylazoxymethanol acetate model of schizophrenia. *Schizophr Bull* **40**, 341–50 (2014).

100. Benes, F. M. A new paradigm for understanding gamma-aminobutyric acid cell pathology in schizophrenia? *Biol Psychiatry* **72**, 712–3 (2012).

101. Fischer, B. D. *et al.* Anxiolytic-like effects of 8-acetylene imidazobenzodiazepines in a rhesus monkey conflict procedure. *Neuropharmacology* **59**, 612–8 (2010).

102. Gill, K. M., Cook, J. M., Poe, M. M. & Grace, A. A. Prior antipsychotic drug treatment prevents response to novel antipsychotic agent in the methylazoxymethanol acetate model of schizophrenia. *Schizophr Bull* **40**, 341–50 (2014).

103. Delgado-Lezama, R. *et al.* The role of spinal cord extrasynaptic α5 GABAA receptors in chronic pain. *Physiol Rep* **9**, e14984 (2021).

104. Fischer, B. D. *et al.* Anxiolytic-like effects of 8-acetylene imidazobenzodiazepines in a rhesus monkey conflict procedure. *Neuropharmacology* **59**, 612–618 (2010).

105. Richetto, J. *et al.* Behavioral effects of the benzodiazepine-positive allosteric modulator SH-053-2'F-S-CH_3 in an immune-mediated neurodevelopmental disruption model. *Int J Neuropsychopharmacol* **18**, (2015).

106. Hörtnagl, H. *et al.* Patterns of mRNA and protein expression for 12 GABAA receptor subunits in the mouse brain. *Neuroscience* **236**, 345–372 (2013).

107. Howell, O. W., Atack, J. R., Dewar, D., McKernan, R. M. & Sur, C. Density and pharmacology of α5 subunit-containing GABAA receptors are preserved in hippocampus of Alzheimer's disease patients. *Neuroscience* **98**, 669–675 (2000).

108. Rissman, R. A. *et al.* Biochemical analysis of GABA(A) receptor subunits alpha 1, alpha 5, beta 1, beta 2 in the hippocampus of patients with Alzheimer's disease neuropathology. *Neuroscience* **120**, 695–704 (2003).

109. Rissman, R. A., Bennett, D. A. & Armstrong, D. M. Subregional analysis of GABA(A) receptor subunit mRNAs in the hippocampus of older persons with and without cognitive impairment. *J Chem Neuroanat* **28**, 17–25 (2004).

110. Brady, M. L. & Jacob, T. C. Synaptic localization of α5 GABA (A) receptors via gephyrin interaction regulates dendritic outgrowth and spine maturation. *Dev Neurobiol* **75**, (2015).

111. Prevot, T. D. *et al.* Novel Benzodiazepine-Like Ligands with Various Anxiolytic, Antidepressant, or Pro-Cognitive Profiles. *Mol Neuropsychiatry* **5**, 84–97 (2019).

112. Koh, M. T., Rosenzweig-Lipson, S. & Gallagher, M. Selective GABAA α5 positive allosteric modulators improve cognitive function in aged rats with memory impairment. *Neuropharmacology* **64**, 145–152 (2013).

113. Prevot, T. D. *et al.* Reversal of Age-Related Neuronal Atrophy by α5-GABAA Receptor Positive Allosteric Modulation. *Cereb Cortex* **31**, 1395–1408 (2021).

114. Curto, Y., Garcia-Mompo, C., Bueno-Fernandez, C. & Nacher, J. Chronic benzodiazepine treatment decreases spine density in cortical pyramidal neurons. *Neurosci Lett* **613**, 41–6 (2016).

115. Gerhard, D. M. *et al.* GABA interneurons are the cellular trigger for ketamine's rapid antidepressant actions. *Journal of Clinical Investigation* **130**, 1336–1349 (2020).

116. Ghosal, S. *et al.* Ketamine rapidly reverses stress-induced impairments in GABAergic transmission in the prefrontal cortex in male rodents. *Neurobiol Dis* **134**, 104669 (2020).

117. Hörtnagl, H. *et al.* Patterns of mRNA and protein expression for 12 GABAA receptor subunits in the mouse brain. *Neuroscience* **236**, 345–372 (2013).

118. Butler, T. *et al.* Neuroimaging of frontal-limbic dysfunction in schizophrenia and epilepsy-related psychosis: toward a convergent neurobiology. *Epilepsy Behav* **23**, 113–22 (2012).

119. Irwin, L. G. & Fortune, D. G. Risk factors for psychosis secondary to temporal lobe epilepsy: a systematic review. *J Neuropsychiatry Clin Neurosci* **26**, 5–23 (2014).

120. Maguire, M., Singh, J. & Marson, A. Epilepsy and psychosis: a practical approach. *Pract Neurol* **18**, 106–114 (2018).

121. Sachdev, P. S. Alternating and Postictal Psychoses: Review and a Unifying Hypothesis. *Schizophr Bull* **33**, 1029–1037 (2007).

122. Curia, G., Longo, D., Biagini, G., Jones, R. S. G. & Avoli, M. The pilocarpine model of temporal lobe epilepsy. *J Neurosci Methods* **172**, 143–157 (2008).

123. Cavalheiro, E. A. The pilocarpine model of epilepsy. *The Italian Journal of Neurological Sciences* **16**, 33–37 (1995).

124. Cifelli, P. & Grace, A. A. Pilocarpine-induced temporal lobe epilepsy in the rat is associated with increased dopamine neuron activity. *International Journal of Neuropsychopharmacology* **15**, 957–964 (2012).

125. Laruelle, M. & Abi-Dargham, A. Dopamine as the wind of the psychotic fire: new evidence from brain imaging studies. *J Psychopharmacol* **13**, 358–71 (1999).

126. Abi-Dargham, A. Do we still believe in the dopamine hypothesis? New data bring new evidence. *Int J Neuropsychopharmacol* **7 Suppl 1**, S1-5 (2004).

127. Howes, O. D. *et al.* Elevated Striatal Dopamine Function Linked to Prodromal Signs of Schizophrenia. *Arch Gen Psychiatry* **66**, 13–20 (2009).

128. Elam, H. B., Perez, S. M., Donegan, J. J. & Lodge, D. J. Orexin receptor antagonists reverse aberrant dopamine neuron activity and related behaviors in a rodent model of stress-induced psychosis. *Transl Psychiatry* **11**, 114 (2021).

129. Perez, S. M., Elam, H. B. & Lodge, D. J. Increased Presynaptic Dopamine Synthesis Capacity Is Associated With Aberrant Dopamine Neuron Activity in the Methylazoxymethanol Acetate Rodent Model Used to Study Schizophrenia-Related Pathologies. *Schizophr Bull Open* **3**, sgac067 (2022).

130. Grace, A. A. & Gomes, F. V. The Circuitry of Dopamine System Regulation and its Disruption in Schizophrenia: Insights Into Treatment and Prevention. *Schizophr Bull* **45**, 148–157 (2019).

131. Lodge, D. J. & Grace, A. A. Aberrant Hippocampal Activity Underlies the Dopamine Dysregulation in an Animal Model of Schizophrenia. *The Journal of Neuroscience* **27**, 11424–11430 (2007).

132. McCoy, A. M. *et al.* Extrasynaptic localization is essential for α5GABA_A receptor modulation of dopamine system function. *bioRxiv* 2023.07.12.548744 (2023) doi:10.1101/2023.07.12.548744.

133. Davenport, C. M. *et al.* Relocation of an Extrasynaptic GABAA Receptor to Inhibitory Synapses Freezes Excitatory Synaptic Strength and Preserves Memory. *Neuron* **109**, 123-134.e4 (2021).

134. Guanguan Li. DESIGN AND SYNTHESIS OF ACHIRAL AND CHIRAL IMIDAZODIAZEPINE (IMDZ) GABA(A)R SUBTYPE SELECTIVE LIGANDS FOR THE TREATMENT OF CNS DISORDERS, AS WELL AS ASTHMA. (University of Wisconsin-Milwaukee, 2019).

135. Knutson, D. E. *et al.* Improved scale-up synthesis and purification of clinical asthma candidate MIDD0301. *Org Process Res Dev* **24**, 1467–1476 (2020).

136. Fier, P. S. & Whittaker, A. M. An Atom-Economical Method To Prepare Enantiopure Benzodiazepines with N-Carboxyanhydrides. *Org Lett* **19**, 1454–1457 (2017).

137. Bailey, J. L. 679. The synthesis of simple peptides from anhydro-N-carboxyamino-acids. *Journal of the Chemical Society (Resumed)* 3461–3466 (1950) doi:10.1039/JR9500003461.

138. Brenner, M. & Photaki, I. Zur Herstellung der Chlorid-hydrochloride der α-Aminosäuren. *Helv Chim Acta* **39**, 1525–1528 (1956).

139. Daly, W. H. & Poché, D. The preparation of N-carboxyanhydrides of α-amino acids using bis(trichloromethyl)carbonate. *Tetrahedron Lett* **29**, 5859–5862 (1988).

140. Yang, J., Teng, Y., Ara, S., Rallapalli, S. & Cook, J. M. An Improved Process for the Synthesis of 4H-Imidazo[1,5-a][1,4]benzodiazepines. *Synthesis (Stuttg)* **2009**, 1036–1040 (2009).

141. Cassar, L. Synthesis of aryl- and vinyl-substituted acetylene derivatives by the use of nickel and palladium complexes. *J Organomet Chem* **93**, 253–257 (1975).

142. Dieck, H. A. & Heck, F. R. Palladium catalyzed synthesis of aryl, heterocyclic and vinylic acetylene derivatives. *J Organomet Chem* **93**, 259–263 (1975).

143. Pirker, S., Schwarzer, C., Wieselthaler, A., Sieghart, W. & Sperk, G. GABAA receptors: immunocytochemical distribution of 13 subunits in the adult rat brain. *Neuroscience* **101**, 815–850 (2000).

144. Batinić, B. *et al.* Positive modulation of α5 GABA_A receptors in preadolescence prevents reduced locomotor response to amphetamine in adult female but

not male rats prenatally exposed to lipopolysaccharide. *Int J Dev Neurosci* **61**, 31–39 (2017).

145. Piantadosi, S. C. *et al.* Sex-Dependent Anti-Stress Effect of an α5 Subunit Containing GABAA Receptor Positive Allosteric Modulator. *Front Pharmacol* **7**, 446 (2016).

146. Rashid Roni, M. S. *et al.* Comparative pharmacodynamic and pharmacokinetic study of MIDD0301 and its (S) enantiomer. *Drug Dev Res* **83**, 979–992 (2022).

147. Pandey, K. P. *et al.* Design, synthesis and characterization of novel gamma-aminobutyric acid type A receptor ligands. *ARKIVOC* **2020**, 242–256 (2020).

148. MacQueen, G. M. & Memedovich, K. A. Cognitive dysfunction in major depression and bipolar disorder: Assessment and treatment options. *Psychiatry Clin Neurosci* **71**, 18–27 (2017).

149. Malhi, G. S. & Mann, J. J. Depression. *Lancet* **392**, 2299–2312 (2018).

150. Gartlehner, G. *et al.* Pharmacological and non-pharmacological treatments for major depressive disorder: review of systematic reviews. *BMJ Open* **7**, e014912 (2017).

151. Hirschfeld, R. M. History and evolution of the monoamine hypothesis of depression. *J Clin Psychiatry* **61 Suppl 6**, 4–6 (2000).

152. Xia, C.-Y. *et al.* Targeting the dysfunction of glutamate receptors for the development of novel antidepressants. *Pharmacol Ther* **226**, 107875 (2021).

153. Davis, M. T., DellaGiogia, N., Maruff, P., Pietrzak, R. H. & Esterlis, I. Acute cognitive effects of single-dose intravenous ketamine in major depressive and posttraumatic stress disorder. *Transl Psychiatry* **11**, 205 (2021).

154. Gill, H. *et al.* The Effects of Ketamine on Cognition in Treatment-Resistant Depression: A Systematic Review and Priority Avenues for Future Research. *Neurosci Biobehav Rev* **120**, 78–85 (2021).

155. Nollet, M., Guisquet, A. Le & Belzung, C. Models of Depression: Unpredictable Chronic Mild Stress in Mice. *Curr Protoc Pharmacol* **61**, (2013).

156. Hauser, J. *et al.* Hippocampal alpha5 subunit-containing GABAA receptors modulate the expression of prepulse inhibition. *Mol Psychiatry* **10**, 201–7 (2005).

157. Catterall, W. A. Voltage-gated calcium channels. *Cold Spring Harb Perspect Biol* **3**, a003947 (2011).

158. Carvajal, F. J., Mattison, H. A. & Cerpa, W. Role of NMDA Receptor-Mediated Glutamatergic Signaling in Chronic and Acute Neuropathologies. *Neural Plast* **2016**, 2701526 (2016).

159. Fernandez, D., Ghanta, A., Kauffman, G. W. & Sanguinetti, M. C. Physicochemical features of the HERG channel drug binding site. *J Biol Chem* **279**, 10120–7 (2004).

160. Di, L. *et al.* Optimization of a higher throughput microsomal stability screening assay for profiling drug discovery candidates. *J Biomol Screen* **8**, 453–62 (2003).

161. Prevot, T. D. *et al.* Novel Benzodiazepine-Like Ligands with Various Anxiolytic, Antidepressant, or Pro-Cognitive Profiles. *Mol Neuropsychiatry* **5**, 84–97 (2019).

162. Wu, C.-C. *et al.* Selective vulnerability of dentate granule cells prior to amyloid deposition in PDAPP mice: digital morphometric analyses. *Proc Natl Acad Sci U S A* **101**, 7141–6 (2004).

163. Huang, S. Synthesis of Optically Active Subtype Selective Benzodiazepine Receptor Ligands. (University of Wisconsin-Milwaukee, 2007).

164. Farjana Rashid. DESIGN AND SYNTHESIS OF ACHIRAL AND CHIRAL BENZODIAZEPINES AND IMIDAZODIAZEPINES TO MODULATE THE ACTIVITY OF GABAA RECEPTORS FOR THE TREATMENT OF CANCER, CNS DISORDERS AND PAIN. (University of Wisconsin-Milwaukee, 2021).

165. Richter, L. *et al.* Diazepam-bound GABAA receptor models identify new benzodiazepine binding-site ligands. *Nat Chem Biol* **8**, 455–464 (2012).

166. Rudolph, U. & Möhler, H. GABA-based therapeutic approaches: GABAA receptor subtype functions. *Curr Opin Pharmacol* **6**, 18–23 (2006).

167. Poe, M. M. *et al.* Synthesis and Characterization of a Novel γ-Aminobutyric Acid Type A (GABAA) Receptor Ligand That Combines Outstanding Metabolic Stability, Pharmacokinetics, and Anxiolytic Efficacy. *J Med Chem* **59**, 10800–10806 (2016).

168. Sieghart, W. & Ernst, M. Heterogeneity of GABAA Receptors: Revived Interest in the Development of Subtype-selective Drugs. *Current Medicinal Chemistry-Central Nervous System Agents* **5**, 217–242 (2005).

169. Li, G., Golani, L. K., Jahan, R., Rashid, F. & Cook, J. M. Improved Synthesis of Anxiolytic, Anticonvulsant and Antinociceptive α2/α3-GABA(A)ergic Receptor Subtype Selective Ligands as Promising Agents to Treat Anxiety, Epilepsy, as well as Neuropathic Pain. *Synthesis (Stuttg)* **50**, 4124–4132 (2018).

170. Löw, K. *et al.* Molecular and neuronal substrate for the selective attenuation of anxiety. *Science* **290**, 131–4 (2000).

171. Rudolph, U. *et al.* Benzodiazepine actions mediated by specific γ-aminobutyric acidA receptor subtypes. *Nature* **401**, 796–800 (1999).

172. Mendelson, W. B., Martin, J. V, Perils, M. & Wagner, R. Sleep and benzodiazepine receptor sub-types. *J Neural Transm* **70**, 329–336 (1987).

173. Insel, T. R. *et al.* A benzodiazepine receptor-mediated model of anxiety. Studies in nonhuman primates and clinical implications. *Arch Gen Psychiatry* **41**, 741–50 (1984).

174. Cook, J. M. ; H. Q. ; H. X. ; L. X. ; Y. J. ; H. D. ; L. S. ; M. J. F. Anxiolytic agents with reduced sedative and ataxic effects. (2006).

175. Cook, J. M. ; Z. H. ; H. S. ; S. P. V. V. S. ; Z. C. Stereospecific anxiolytic and anticonvulsant agents with reduced muscle-relaxant, sedative-hypnotic and ataxic effects. (2009).

176. Fischer, B. D. *et al.* Anxiolytic-like effects of 8-acetylene imidazobenzodiazepines in a rhesus monkey conflict procedure. *Neuropharmacology* **59**, 612–8 (2010).

177. Witkin, J. M. *et al.* Further evaluation of the potential anxiolytic activity of imidazo[1,5-a][1,4]diazepin agents selective for α2/3-containing GABAA receptors. *Pharmacol Biochem Behav* **157**, 35–40 (2017).

178. Atack, J. R. *et al.* MRK-409 (MK-0343), a GABAA receptor subtype-selective partial agonist, is a non-sedating anxiolytic in preclinical species but causes sedation in humans. *J Psychopharmacol* **25**, 314–28 (2011).

179. Mirza, N. R. *et al.* NS11394 [3'-[5-(1-hydroxy-1-methyl-ethyl)-benzoimidazol-1-yl]-biphenyl-2-carbonitrile], a unique subtype-selective GABAA receptor positive allosteric modulator: in vitro actions, pharmacokinetic properties and in vivo anxiolytic efficacy. *J Pharmacol Exp Ther* **327**, 954–968 (2008).

180. Munro, G. *et al.* Comparison of the novel subtype-selective GABAA receptor-positive allosteric modulator NS11394 [3'-[5-(1-hydroxy-1-methyl-ethyl)-benzoimidazol-1-yl]-biphenyl-2-carbonitrile] with diazepam, zolpidem, bretazenil, and gaboxadol in rat models of inflammatory and neuropathic pain. *J Pharmacol Exp Ther* **327**, 969–81 (2008).

181. Fischer, W. H. & Schubert, D. Characterization of a novel platelet-derived growth factor-associated protein. *J Neurochem* **66**, 2213–6 (1996).

182. Lewter, L. A. *et al.* Antinociceptive Effects of a Novel α2/α3-Subtype Selective GABAA Receptor Positive Allosteric Modulator. *ACS Chem Neurosci* **8 6**, 1305–1312 (2017).

183. pmc_9787737.

184. Kannampalli, P. *et al.* Neonatal bladder inflammation induces long-term visceral pain and altered responses of spinal neurons in adult rats. *Neuroscience* **346**, 349–364 (2017).

185. Cerne, R. *et al.* GABAkines - Advances in the discovery, development, and commercialization of positive allosteric modulators of GABAA receptors. *Pharmacol Ther* **234**, 108035 (2022).

186. Fischer, B. D. *et al.* Pharmacological and antihyperalgesic properties of the novel α2/3 preferring GABAA receptor ligand MP-III-024. *Brain Res Bull* **131**, 62–69 (2017).

187. Witkin, J. M. *et al.* The α2,3-selective potentiator of GABAA receptors, KRM-II-81, reduces nociceptive-associated behaviors induced by formalin and spinal nerve ligation in rats. *Pharmacol Biochem Behav* **180**, 22–31 (2019).

188. Biggerstaff, A. *et al.* The α2,3-selective potentiators of GABAA receptors, KRM-II-81 and MP-III-80, produce anxiolytic-like effects and block chemotherapy-induced hyperalgesia in mice without tolerance development. *Pharmacol Biochem Behav* **196**, 172996 (2020).

189. Witkin, J. M. *et al.* Bioisosteres of ethyl 8-ethynyl-6-(pyridin-2-yl)-4H-benzo[f]imidazo [1,5-a][1,4]diazepine-3-carboxylate (HZ-166) as novel alpha 2,3 selective potentiators of GABAA receptors: Improved bioavailability enhances anticonvulsant efficacy. *Neuropharmacology* **137**, 332–343 (2018).

190. Witkin, J. M. *et al.* The imidazodiazepine, KRM-II-81: An example of a newly emerging generation of GABAkines for neurological and psychiatric disorders. *Pharmacol Biochem Behav* **213**, 173321 (2022).

191. Moerke, M. J., Li, G., Golani, L. K., Cook, J. & Negus, S. S. Effects of the α2/α3-subtype-selective GABAA receptor positive allosteric modulator KRM-II-81 on pain-depressed behavior in rats: comparison with ketorolac and diazepam. *Behavioural pharmacology* **30**, 452–461 (2019).

192. Gardner, C. R., Walsh, C. T. & Almarsson, O. Drugs as materials: valuing physical form in drug discovery. *Nat Rev Drug Discov* **3**, 926–34 (2004).

193. Lipinski, C. A. & Lipinski, C. A. Poor aqueous solubility-an industry wide problem in drug discovery. in (2002).

194. Serajuddin, A. T. M. Salt formation to improve drug solubility. *Adv Drug Deliv Rev* **59**, 603–16 (2007).

195. Hawley, M. & Morozowich, W. Modifying the diffusion layer of soluble salts of poorly soluble basic drugs to improve dissolution performance. *Mol Pharm* **7**, 1441–9 (2010).

196. Paulekuhn, G. S., Dressman, J. B. & Saal, C. Salt screening and characterization for poorly soluble, weak basic compounds: case study albendazole. *Pharmazie* **68**, 555–64 (2013).

197. Mukesh, S. *et al.* Amorphous Salts Solid Dispersions of Celecoxib: Enhanced Biopharmaceutical Performance and Physical Stability. *Mol Pharm* **18**, 2334–2348 (2021).

198. Kumar, V., Bharate, S. B., Vishwakarma, R. A. & Bharate, S. S. Selection of a Water-Soluble Salt Form of a Preclinical Candidate, IIIM-290: Multiwell-Plate Salt Screening and Characterization. *ACS Omega* **3**, 8365–8377 (2018).

199. Mian, M. Y. *et al.* Hydrochloride Salt of the GABAkine KRM-II-81. *ACS Omega* **7**, 27550–27559 (2022).

200. Boström, J., Hogner, A., Llinàs, A., Wellner, E. & Plowright, A. T. Oxadiazoles in medicinal chemistry. *J Med Chem* **55**, 1817–30 (2012).

201. Burger, A. Isosterism and bioisosterism in drug design. *Prog Drug Res* **37**, 287–371 (1991).

202. Gugliotti, M. Irving langmuir: o milagre da ciência. *Quim Nova* **24**, 568–572 (2001).

203. Cook, J. H. , S. ; E. R. ; N. O. A. ; W. Z. J. Selective agents for pain suppression. (2014).

204. Cook, J. M. Z. , H. ; H. S. ; S. P. V. V. S. ; Z. C. Stereospecific anxiolytic and anticonvulsant agents with reduced muscle-relaxant, sedative-hypnotic and ataxic effects. (2009).

205. Cook, J. P. , M. M. J. ; M. K. R. ; L. G. GABAergic ligands and their uses. (2016).

206. Trott, O. & Olson, A. J. AutoDock Vina: improving the speed and accuracy of docking with a new scoring function, efficient optimization, and multithreading. *J Comput Chem* **31**, 455–61 (2010).

207. Masiulis, S. *et al.* GABAA receptor signalling mechanisms revealed by structural pharmacology. *Nature* **565**, 454–459 (2019).

208. Koebel, M. R., Schmadeke, G., Posner, R. G. & Sirimulla, S. AutoDock VinaXB: implementation of XBSF, new empirical halogen bond scoring function, into AutoDock Vina. *J Cheminform* **8**, 27 (2016).

209. Witkin, J. M. *et al.* The α2,3-selective potentiator of GABAA receptors, KRM-II-81, reduces nociceptive-associated behaviors induced by formalin and spinal nerve ligation in rats. *Pharmacol Biochem Behav* **180**, 22–31 (2019).

210. Watanabe, T., Schulz, D., Morisseau, C. & Hammock, B. D. High-throughput pharmacokinetic method: cassette dosing in mice associated with minuscule serial bleedings and LC/MS/MS analysis. *Anal Chim Acta* **559**, 37–44 (2006).

211. Nagilla, R., Nord, M., McAtee, J. J. & Jolivette, L. J. Cassette dosing for pharmacokinetic screening in drug discovery: comparison of clearance, volume of distribution, half-life,

mean residence time, and oral bioavailability obtained by cassette and discrete dosing in rats. *J Pharm Sci* **100**, 3862–74 (2011).

212. Md Zubair Ahmed Khan. DESIGN, SYNTHESIS & BIOLOGICAL STUDY OF SOME NOVEL GAMMA-AMINOBUTYRIC ACID TYPE (GABAA) RECEPTOR LIGANDS. (2021).

213. Cho, Y.-J. *et al.* Integrative genomic analysis of medulloblastoma identifies a molecular subgroup that drives poor clinical outcome. *J Clin Oncol* **29**, 1424–30 (2011).

214. Taylor, M. D. *et al.* Molecular subgroups of medulloblastoma: the current consensus. *Acta Neuropathol* **123**, 465–72 (2012).

215. Roussel, M. F. & Hatten, M. E. Cerebellum development and medulloblastoma. *Curr Top Dev Biol* **94**, 235–82 (2011).

216. Sturm, D., Pfister, S. M. & Jones, D. T. W. Pediatric Gliomas: Current Concepts on Diagnosis, Biology, and Clinical Management. *J Clin Oncol* **35**, 2370–2377 (2017).

217. Marini, B. L. *et al.* Blood-brain barrier-adapted precision medicine therapy for pediatric brain tumors. *Transl Res* **188**, 27.e1-27.e14 (2017).

218. Wang, Z., Sun, H. & Yakisich, J. S. Overcoming the blood-brain barrier for chemotherapy: limitations, challenges and rising problems. *Anticancer Agents Med Chem* **14**, 1085–93 (2014).

219. Schwalbe, E. C. *et al.* Novel molecular subgroups for clinical classification and outcome prediction in childhood medulloblastoma: a cohort study. *Lancet Oncol* **18**, 958–971 (2017).

220. Cho, Y.-J. *et al.* Integrative genomic analysis of medulloblastoma identifies a molecular subgroup that drives poor clinical outcome. *J Clin Oncol* **29**, 1424–30 (2011).

221. Northcott, P. A. *et al.* Medulloblastoma comprises four distinct molecular variants. *J Clin Oncol* **29**, 1408–14 (2011).

222. Kool, M. *et al.* Molecular subgroups of medulloblastoma: an international meta-analysis of transcriptome, genetic aberrations, and clinical data of WNT, SHH, Group 3, and Group 4 medulloblastomas. *Acta Neuropathol* **123**, 473–84 (2012).

223. Northcott, P. A. *et al.* Subgroup-specific structural variation across 1,000 medulloblastoma genomes. *Nature* **488**, 49–56 (2012).

224. Pugh, T. J. *et al.* Medulloblastoma exome sequencing uncovers subtype-specific somatic mutations. *Nature* **488**, 106–10 (2012).

225. Cavalli, F. M. G. *et al.* Intertumoral Heterogeneity within Medulloblastoma Subgroups. *Cancer Cell* **31**, 737-754.e6 (2017).

226. Gessi, M., von Bueren, A. O., Rutkowski, S. & Pietsch, T. p53 expression predicts dismal outcome for medulloblastoma patients with metastatic disease. *J Neurooncol* **106**, 135–41 (2012).

227. Northcott, P. A. *et al.* The whole-genome landscape of medulloblastoma subtypes. *Nature* **547**, 311–317 (2017).

228. Shonka, N., Venur, V. A. & Ahluwalia, M. S. Targeted Treatment of Brain Metastases. *Curr Neurol Neurosci Rep* **17**, 37 (2017).

229. Millington, G. W. M. Mutations of the BRAF gene in human cancer, by Davies et al. (Nature 2002; 417: 949–54). *Clin Exp Dermatol* **38**, 222–223 (2013).

230. 28467829.

231. 22817889.

232. McArthur, G. A. *et al.* Vemurafenib in metastatic melanoma patients with brain metastases: an open-label, single-arm, phase 2, multicentre study. *Ann Oncol* **28**, 634–641 (2017).

233. Falchook, G. S. *et al.* Dabrafenib in patients with melanoma, untreated brain metastases, and other solid tumours: a phase 1 dose-escalation trial. *Lancet* **379**, 1893–901 (2012).

234. Falchook, G. S. *et al.* Dabrafenib in patients with melanoma, untreated brain metastases, and other solid tumours: a phase 1 dose-escalation trial. *Lancet* **379**, 1893–901 (2012).

235. Long, G. V *et al.* Dabrafenib in patients with Val600Glu or Val600Lys BRAF-mutant melanoma metastatic to the brain (BREAK-MB): a multicentre, open-label, phase 2 trial. *Lancet Oncol* **13**, 1087–95 (2012).

236. Subbiah, V. *et al.* Dabrafenib plus trametinib in patients with BRAFV600E-mutated biliary tract cancer (ROAR): a phase 2, open-label, single-arm, multicentre basket trial. *Lancet Oncol* **21**, 1234–1243 (2020).

237. Hauschild, A. *et al.* Dabrafenib in BRAF-mutated metastatic melanoma: a multicentre, open-label, phase 3 randomised controlled trial. *Lancet* **380**, 358–65 (2012).

238. Long, G. V *et al.* Overall Survival and Durable Responses in Patients With BRAF V600–Mutant Metastatic Melanoma Receiving Dabrafenib Combined With Trametinib. *Journal of Clinical Oncology* **34**, 871–878 (2016).

239. Turajlic, S. *et al.* Whole-genome sequencing reveals complex mechanisms of intrinsic resistance to BRAF inhibition. *Ann Oncol* **25**, 959–67 (2014).

240. Sosman, J. A. *et al.* Survival in BRAF V600-mutant advanced melanoma treated with vemurafenib. *N Engl J Med* **366**, 707–14 (2012).

241. Tirosh, I. *et al.* Dissecting the multicellular ecosystem of metastatic melanoma by single-cell RNA-seq. *Science* **352**, 189–96 (2016).

242. Luke, J. J., Flaherty, K. T., Ribas, A. & Long, G. V. Targeted agents and immunotherapies: optimizing outcomes in melanoma. *Nat Rev Clin Oncol* **14**, 463–482 (2017).

243. Tawbi, H. A., Boutros, C., Kok, D., Robert, C. & McArthur, G. New Era in the Management of Melanoma Brain Metastases. *Am Soc Clin Oncol Educ Book* **38**, 741–750 (2018).

244. Tawbi, H. A. *et al.* Combined Nivolumab and Ipilimumab in Melanoma Metastatic to the Brain. *N Engl J Med* **379**, 722–730 (2018).

245. Postow, M. A., Sidlow, R. & Hellmann, M. D. Immune-Related Adverse Events Associated with Immune Checkpoint Blockade. *N Engl J Med* **378**, 158–168 (2018).

246. Pomeranz Krummel, D. A. *et al.* Melanoma Cell Intrinsic GABAA Receptor Enhancement Potentiates Radiation and Immune Checkpoint Inhibitor Response by Promoting Direct

and T Cell-Mediated Antitumor Activity. *Int J Radiat Oncol Biol Phys* **109**, 1040–1053 (2021).

247. Siegel, R. L., Miller, K. D., Fuchs, H. E. & Jemal, A. Cancer statistics, 2022. *CA Cancer J Clin* **72**, 7–33 (2022).

248. Fuchs, J. *et al.* Resection of isolated brain metastases in non-small cell lung cancer (NSCLC) patients - evaluation of outcome and prognostic factors: A retrospective multicenter study. *PLoS One* **16**, e0253601 (2021).

249. Sørensen, J. B., Hansen, H. H., Hansen, M. & Dombernowsky, P. Brain metastases in adenocarcinoma of the lung: frequency, risk groups, and prognosis. *Journal of Clinical Oncology* **6**, 1474–1480 (1988).

250. Fossella, F. V. Docetaxel in second-line treatment of non-small-cell lung cancer. *Clin Lung Cancer* **3 Suppl 2**, S23-8 (2002).

251. Amaravadi, R. K. *et al.* Principles and current strategies for targeting autophagy for cancer treatment. *Clin Cancer Res* **17**, 654–66 (2011).

252. Wang, X., Du, Z., Li, L., Shi, M. & Yu, Y. Beclin 1 and p62 expression in non-small cell lung cancer: relation with malignant behaviors and clinical outcome. *Int J Clin Exp Pathol* **8**, 10644–52 (2015).

253. Debnath, J., Gammoh, N. & Ryan, K. M. Autophagy and autophagy-related pathways in cancer. *Nat Rev Mol Cell Biol* **24**, 560–575 (2023).

254. Zhang, M., Su, L., Xiao, Z., Liu, X. & Liu, X. Methyl jasmonate induces apoptosis and pro-apoptotic autophagy via the ROS pathway in human non-small cell lung cancer. *Am J Cancer Res* **6**, 187–99 (2016).

255. Cao, C. *et al.* Inhibition of mammalian target of rapamycin or apoptotic pathway induces autophagy and radiosensitizes PTEN null prostate cancer cells. *Cancer Res* **66 20**, 10040–7 (2006).

256. Chaurasia, M., Bhatt, A. N., Das, A., Dwarakanath, B. S. & Sharma, K. Radiation-induced autophagy: mechanisms and consequences. *Free Radic Res* **50**, 273–90 (2016).

257. Gao, P., Hao, F., Dong, X. & Qiu, Y. The role of autophagy and Beclin-1 in radiotherapy-induced apoptosis in thyroid carcinoma cells. *Int J Clin Exp Pathol* **12**, 885–892 (2019).

258. Kroemer, G., Mariño, G. & Levine, B. Autophagy and the integrated stress response. *Mol Cell* **40**, 280–93 (2010).

259. Senft, D. & Ronai, Z. A. UPR, autophagy, and mitochondria crosstalk underlies the ER stress response. *Trends Biochem Sci* **40**, 141–8 (2015).

260. Rao, R. *et al.* Ligand-Gated Ion Channels as Targets for Treatment and Management of Cancers. *Front Physiol* **13**, 839437 (2022).

261. Bhattacharya, D. *et al.* Therapeutically leveraging GABAA receptors in cancer. *Exp Biol Med (Maywood)* **246**, 2128–2135 (2021).

262. Pomeranz Krummel, D. A. *et al.* Melanoma Cell Intrinsic GABAA Receptor Enhancement Potentiates Radiation and Immune Checkpoint Inhibitor Response by Promoting Direct

and T Cell-Mediated Antitumor Activity. *International Journal of Radiation Oncology*Biology*Physics* **109**, 1040–1053 (2021).

263. Kallay, L. *et al.* Modulating native GABAA receptors in medulloblastoma with positive allosteric benzodiazepine-derivatives induces cell death. *J Neurooncol* **142**, 411–422 (2019).

264. Jonas, O. *et al.* An implantable microdevice to perform high-throughput in vivo drug sensitivity testing in tumors. *Sci Transl Med* **7**, 284ra57 (2015).

265. Arora, P., Gudelsky, G. & Desai, P. B. Gender-based differences in brain and plasma pharmacokinetics of letrozole in sprague-dawley rats: Application of physiologically-based pharmacokinetic modeling to gain quantitative insights. *PLoS One* **16**, e0248579 (2021).

266. Roberts, S. S. *et al.* GABAergic system gene expression predicts clinical outcome in patients with neuroblastoma. *J Clin Oncol* **22**, 4127–4134 (2004).

267. Hiyama, E. *et al.* Correlating telomerase activity levels with human neuroblastoma outcomes. *Nat Med* **1**, 249–55 (1995).

268. Al-Wadei, H. A. N., Al-Wadei, M. H., Ullah, M. F. & Schuller, H. M. Celecoxib and GABA cooperatively prevent the progression of pancreatic cancer in vitro and in xenograft models of stress-free and stress-exposed mice. *PLoS One* **7**, e43376 (2012).

269. Sano, E. *et al.* Tetrafluoroethylene-Propylene Elastomer for Fabrication of Microfluidic Organs-on-Chips Resistant to Drug Absorption. *Micromachines (Basel)* **10**, (2019).

270. Huh, D. *et al.* Reconstituting organ-level lung functions on a chip. *Science* **328**, 1662–8 (2010).

271. Hassell, B. A. *et al.* Human Organ Chip Models Recapitulate Orthotopic Lung Cancer Growth, Therapeutic Responses, and Tumor Dormancy In Vitro. *Cell Rep* **21**, 508–516 (2017).

272. Thacker, V. V *et al.* A lung-on-chip model of early Mycobacterium tuberculosis infection reveals an essential role for alveolar epithelial cells in controlling bacterial growth. *Elife* **9**, (2020).

273. Jain, A. *et al.* Primary Human Lung Alveolus-on-a-chip Model of Intravascular Thrombosis for Assessment of Therapeutics. *Clin Pharmacol Ther* **103**, 332–340 (2018).

274. Bhattacharya, D. *et al.* Therapeutically leveraging GABAA receptors in cancer. *Exp Biol Med (Maywood)* **246**, 2128–2135 (2021).

275. Taukir Ahmed. THE ACTIVITY OF QH II 66 AND IT'S ANALOGS IN MEDULLOBLASTOMA, MELANOMA AND NON-SMALL CELL LUNG CANCER CELL LINES. (2022).

276. Md Yeunus Mian. DESIGN AND SYNTHESIS OF CHIRAL AND ACHIRAL BENZODIAZEPINES AND IMIDAZODIAZEPINES AS α–SUBTYPE SELECTIVE GABAAR POSITIVE MODULATORS TO TREAT SCHISTOSOMIASIS, EPILEPSY, ASTHMA AND SOME MENTAL DISORDERS. (2022).

APPENDIX

PDSP

PDSP code	Compound code	M.W.	Chemical formula
61387	SRE-I-95(2)	457.30	C21H18BrN4O2
61388	SRE-I-95(3)	457.30	C21H18BrFN4O2
61389	SRE-II-38	469.31	C22H18BrFN4O2
61390	SRE-II-61	375.40	C22H18FN3O2
61391	SRE-II-11	402.46	C24H23FN4O
61397	SRE-II-36	485.35	C23H22BrFN4O2
61398	SRE-II-42	466.31	C22H17BrFN5O

61399	SRE-II-59	452.28	C21H15BrFN5O
61400	SRE-II-46	485.35	C23H22BrFN4O2
61836	SRE-II-42(2)	427.4	C25H22FN5O
61837	SRE-II-44	413.4	C24H20FN5O
71288	SRE-III-35	276.33	C18H16N2O
71289	SRE-III-43	294.32	C18H15FN2O
71290	SRE-III-53	315.16	C15H11BrN2O
71291	SRE-III-54	333.16	C15H10BrFN2O

Compound #	Receptor	Inhibition 1	Inhibition 2	Inhibition 3	Inhibition 4	Mean %	Secondary	Date
61387	Alpha2Beta2	-5.93	-18.51	-2.92	-3.48	-7.71		Feb 01, 2022
61387	Alpha2Beta4	0.69	3.32	6.58	-1.62	2.24		Feb 01, 2022
61387	Alpha3Beta2	-15.51	2.87	-21.26	-3.78	-9.42		Feb 01, 2022
61387	Alpha3Beta4	-7.87	-15.47	-4.96	-9.51	-9.45		Feb 01, 2022
61387	Alpha4Beta2	5.99	-1.43	-0.54	-0.20	0.96		Feb 01, 2022
61387	Alpha4Beta2 (Rat Brain)	0.68	1.28	-1.71	1.41	0.42		Feb 01, 2022
61387	Alpha4Beta4	-7.77	-5.49	-3.36	-5.25	-5.47		Feb 01, 2022
61387	Alpha7	-4.73	2.24	-15.22	10.88	-1.71		Feb 01, 2022
61387	5-HT1A	23.63	0.78	-17.81	-38.25	-7.91		Feb 23, 2022
61387	5-HT1B	-9.18	-67.09	-60.28	54.08	-20.62		Feb 21, 2022
61387	5-HT1D	3.65	-0.49	-8.78	-23.11	-7.18		Feb 21, 2022
61387	5-HT1E	-17.74	-9.74	-15.82	-2.20	-11.38		Feb 23, 2022
61387	5-HT2A	31.74	9.98	-9.29	-9.29	5.79		Feb 24, 2022
61387	5-HT2B	29.63	14.21	16.13	20.36	20.08		Feb 23, 2022
61387	5-HT2C	19.29	12.67	9.20	5.33	11.62		Feb 23, 2022
61387	5-HT3	6.37	12.83	-3.68	-12.10	0.86		May 17, 2022
61387	5-HT4	7.23	-1.04	-2.60	9.97	3.39		Feb 21, 2022
61387	5-HT5A	3.50	3.04	-4.12	-15.84	-3.36		Feb 11, 2022
61387	5-HT6	4.21	-6.34	-7.77	0.01	-2.47		Feb 24, 2022
61387	5-HT7A	-7.16	-7.16	7.94	-17.70	-6.02		Feb 11, 2022
61387	A1	56.65	-7.27	29.86	56.27	33.88		Feb 11, 2022
61387	A2A	5.48	38.48	10.31	2.63	14.23		Jun 15, 2022
61387	Alpha1A	12.09	13.31	-13.38	-31.46	-4.86		Feb 21, 2022
61387	Alpha1B	-16.70	-20.44	-8.71	17.83	-7.01		Feb 21, 2022
61387	Alpha1D	7.49	2.32	15.27	-2.39	5.67		Feb 24, 2022
61387	Alpha2A	15.44	0.85	-1.25	23.83	9.72		May 15, 2022
61387	Alpha2B	48.31	31.89	27.17	24.66	33.01		Mar 09, 2022
61387	Alpha2C	30.08	19.64	5.66	6.04	15.36		Mar 09, 2022
61387	Beta1	-42.20	-16.12	8.86	23.42	-6.51		Feb 25, 2022
61387	Beta2	-6.21	-2.37	-1.25	0.91	-2.23		Feb 21, 2022

61387	Beta3	23.45	22.86	-52.95	8.88	0.56		Feb 18, 2022
61387	AT2	44.60	34.56	20.07	11.18	27.60		Feb 25, 2022
61387	BZP Rat Brain Site	90.41	84.71	85.80	80.73	85.41	Secondary	Feb 24, 2022
61387	D1	11.27	-1.52	10.38	-3.29	4.21		Mar 27, 2022
61387	D2	41.43	11.70	-17.14	52.61	22.15		Feb 17, 2022
61387	D3	0.87	-59.23	2.71	-0.80	-14.11		Feb 17, 2022
61387	D4	15.59	-10.13	-14.17	-25.68	-8.60		Feb 22, 2022
61387	D5	-9.91	-23.13	-12.52	-1.80	-11.84		Feb 23, 2022
61387	DAT	1.23	-0.21	13.53	-5.74	2.20		Jul 12, 2022
61387	DOR	-31.21	-40.07	-9.76	-12.40	-23.36	Secondary	Feb 24, 2022
61387	GABAA	-9.53	-6.39	-41.73	-5.61	-15.82		Mar 03, 2022
61387	H1	-3.96	-30.38	-12.18	-13.16	-14.92		Feb 28, 2022
61387	H2	6.51	34.63	21.20	2.68	16.26		Feb 25, 2022
61387	H3	-2.44	-18.10	-11.27	-17.39	-12.30		Mar 02, 2022
61387	H4	7.45	-13.11	-14.37	-3.88	-5.98		Feb 18, 2022
61387	KOR	66.24	44.78	40.79	47.94	49.94		Feb 21, 2022
61387	M1	-3.10	4.60	-9.11	0.00	-2.54		Feb 22, 2022
61387	M2	-18.25	-12.47	9.11	17.21	-1.10		Feb 22, 2022
61387	M3	30.71	29.79	20.53	45.41	31.61		Feb 21, 2022
61387	M4	34.16	-2.02	-13.59	-1.03	4.38		Feb 22, 2022
61387	M5	2.29	-23.84	-11.27	-9.09	-10.48		Feb 22, 2022
61387	MOR	-3.05	-7.73	-7.41	-0.11	-4.58		Feb 24, 2022
61387	NET	31.82	24.07	-0.33	9.71	16.32		Feb 28, 2022
61387	PBR	15.98	-2.06	-14.14	11.66	2.86		Feb 17, 2022
61387	SERT	-9.35	-3.25	-1.17	-7.40	-5.29		Feb 24, 2022
61387	Sigma 1	-4.70	13.56	22.88	7.21	9.74		Feb 22, 2022
61387	Sigma 2	67.71	25.90	33.02	46.13	43.19		Feb 18, 2022
61387	AMPA	17.31	-15.97	-19.41	-9.21	-6.82		Feb 18, 2022
61387	Kainate (Rat Brain)	3.20	-2.80	4.14	18.03	5.64		Feb 25, 2022
61387	NMDA	72.88	72.05	81.06	83.95	77.49	Secondary	Feb 22, 2022

61387	NR2B	47.66	16.90	-53.06	-8.11	0.85		Feb 10, 2022
61387	HCA2	-2.95	-79.63	-7.16	6.06	-20.92		Aug 15, 2022
61387	Ca channel human	42.20	-11.58	-5.57	32.62	14.42		Feb 10, 2022
61387	HERG	-0.37	-9.37	-13.05	14.48	-2.08		Feb 21, 2022
61387	M1 D	4.92	13.29	6.70	18.50	10.85		Mar 02, 2022
61387	M2 D	33.45	35.70	6.82	16.30	23.07		Mar 02, 2022
61387	M3D	1.34	-3.56	-5.65	-6.37	-3.56		Mar 02, 2022
61387	M4 D	18.09	-7.13	-10.57	-13.43	-3.26		Mar 02, 2022
61387	M5 D	-0.06	10.19	7.52	7.22	6.22		Mar 02, 2022
61387	NTS1	21.82	15.81	-3.92	-2.72	7.75		Feb 10, 2022
61387	NOP	60.83	-1.29	33.37	13.56	26.62		Feb 18, 2022
61387	OT	25.73	19.72	13.58	14.70	18.43		Feb 10, 2022
61387	V1A	26.17	39.75	28.32	33.71	31.99		Feb 11, 2022
61387	V1B	1.69	1.43	15.01	-16.23	0.48		Feb 28, 2022
61387	V2	2.53	2.07	-4.58	-3.14	-0.78		Jun 21, 2022

61387	5-HT6	5.82	-3.47	15.01	19.14	9.13		Feb 18, 2022
61388	Alpha2Beta2	-9.05	-7.60	-4.48	8.32	-3.20		Feb 01, 2022
61388	Alpha2Beta4	-0.11	10.41	1.76	7.94	5.00		Feb 01, 2022
61388	Alpha3Beta2	-9.19	-3.45	-4.02	5.66	-2.75		Feb 01, 2022
61388	Alpha3Beta4	-13.46	-11.59	-5.63	-15.25	-11.48		Feb 01, 2022
61388	Alpha4Beta2	-1.16	-4.09	3.20	-7.29	-2.34		Feb 01, 2022
61388	Alpha4Beta2 (Rat Brain)	8.67	-0.38	4.83	-6.62	1.63		Feb 01, 2022
61388	Alpha4Beta4	-6.91	-12.02	2.70	-3.60	-4.96		Feb 01, 2022
61388	Alpha7	9.35	-6.82	-11.74	1.45	-1.94		Feb 01, 2022
61388	5-HT1A	12.85	-4.05	-6.32	-12.42	-2.49		Feb 23, 2022
61388	5-HT1B	-31.08	42.40	-31.08	33.31	3.39		Feb 21, 2022
61388	5-HT1D	2.23	-4.03	-15.19	-23.23	-10.06		Feb 21, 2022
61388	5-HT1E	-14.57	-14.75	19.59	-9.79	-4.88		Feb 23, 2022
61388	5-HT2A	39.15	13.15	-0.53	3.24	13.75		Feb 24, 2022
61388	5-HT2B	25.31	23.29	31.00	27.97	26.89		Feb 23, 2022

61388	5-HT2C	17.08	13.85	17.72	9.91	14.64		Feb 23, 2022
61388	5-HT3	6.25	2.84	-4.62	7.46	2.98		May 17, 2022
61388	5-HT4	10.41	-13.02	3.61	20.83	5.46		Feb 21, 2022
61388	5-HT5A	62.14	56.41	44.12	51.15	53.46	Secondary	Feb 11, 2022
61388	5-HT6	-0.29	-1.93	-17.29	-7.87	-6.85		Feb 24, 2022
61388	5-HT7A	-10.02	-92.81	-32.93	-4.95	-35.18		Feb 11, 2022
61388	A1	47.46	-13.40	13.78	43.64	22.87		Feb 11, 2022
61388	A2A	22.12	25.96	18.99	17.85	21.23		Jun 15, 2022
61388	Alpha1A	1.74	-4.56	-13.09	-16.51	-8.11		Feb 21, 2022
61388	Alpha1B	-13.44	-8.60	2.37	10.19	-2.37		Feb 21, 2022
61388	Alpha1D	5.57	15.91	25.61	16.90	16.00		Feb 24, 2022
61388	Alpha2A	20.24	14.74	-15.98	-19.75	-0.19		May 15, 2022
61388	Alpha2B	18.88	10.61	24.75	4.53	14.69		Mar 15, 2022
61388	Alpha2C	24.83	16.75	12.05	15.93	17.39		Mar 09, 2022
61388	Beta1	-13.94	-13.47	-14.61	-13.48	-13.88		Feb 25, 2022

61388	Beta2	-11.16	0.98	4.88	-13.57	-4.72		Feb 21, 2022
61388	Beta3	-7.34	4.86	-14.57	12.56	-1.12		Feb 18, 2022
61388	AT2	37.55	20.65	22.29	12.53	23.26		Feb 25, 2022
61388	BZP Rat Brain Site	93.77	89.94	87.52	92.13	90.84	Secondary	Feb 24, 2022
61388	D1	5.95	-1.90	4.81	-14.82	-1.49		Mar 27, 2022
61388	D2	27.59	33.19	30.54	43.78	33.78		Feb 17, 2022
61388	D3	-1.53	-21.38	6.04	-24.71	-10.40		Feb 17, 2022
61388	D4	25.60	25.15	-7.89	18.58	15.36		Feb 22, 2022
61388	D5	-8.32	-29.37	-2.48	-4.35	-11.13		Feb 23, 2022
61388	DAT	-50.35	-0.17	-24.54	-11.00	-21.52		Jul 12, 2022
61388	DOR	4.88	-9.59	-2.95	-3.29	-2.74		Feb 24, 2022
61388	GABAA	7.74	16.38	20.30	-11.10	8.33		Mar 03, 2022
61388	H1	3.86	-7.68	-4.94	-27.84	-9.15		Feb 28, 2022
61388	H2	12.93	10.83	18.27	14.19	14.06		Feb 25, 2022
61388	H3	8.95	-8.56	-11.84	-25.65	-9.28		Mar 02, 2022

61388	H4	0.87	-22.90	-10.17	21.29	-2.73		Feb 18, 2022
61388	KOR	84.70	79.88	82.54	78.71	81.46	Secondary	Feb 21, 2022
61388	M1	28.64	20.38	10.42	-5.73	13.43		Feb 22, 2022
61388	M2	-4.84	-6.41	-16.63	-20.57	-12.11		Feb 22, 2022
61388	M3	2.61	28.59	14.22	20.53	16.49		Feb 21, 2022
61388	M4	-0.70	8.88	2.11	8.05	4.59		Feb 22, 2022
61388	M5	-12.26	9.64	-18.02	-19.81	-10.11		Feb 22, 2022
61388	MOR	13.94	4.89	11.71	17.43	11.99		Feb 24, 2022
61388	NET	32.79	19.84	16.49	20.55	22.42		Feb 28, 2022
61388	PBR	54.01	-8.33	22.10	20.75	22.13		Feb 17, 2022
61388	SERT	-5.08	-19.01	-9.35	-8.50	-10.49		Feb 24, 2022
61388	Sigma 1	34.95	42.37	32.40	42.08	37.95		Feb 22, 2022
61388	Sigma 2	55.63	45.98	36.27	42.67	45.14		Feb 18, 2022
61388	AMPA	13.10	12.08	5.32	-3.22	6.82		Feb 18, 2022
61388	Kainate (Rat Brain)	-3.79	4.40	6.04	1.13	1.95		Feb 18, 2022

61388	NMDA	79.61	80.37	85.67	91.58	84.31	Secondary	Feb 22, 2022
61388	NR2B	5.41	4.06	-39.54	-13.18	-10.81		Feb 10, 2022
61388	HCA2	-51.03	26.50	5.35	35.11	3.98		Feb 24, 2022
61388	Ca channel human	47.37	-28.86	-43.36	-6.15	-7.75		Feb 10, 2022
61388	HERG	3.06	-5.99	-12.86	6.93	-2.22		Feb 21, 2022
61388	M1 D	11.37	5.19	14.52	-0.29	7.70		Mar 02, 2022
61388	M2 D	35.70	-3.55	13.14	17.65	15.74		Mar 02, 2022
61388	M3D	8.78	5.78	-6.04	-7.61	0.23		Mar 02, 2022
61388	M4 D	31.27	-10.71	4.19	9.78	8.63		Mar 02, 2022
61388	M5 D	7.97	-10.16	0.98	5.44	1.06		Mar 02, 2022
61388	NTS1	-9.33	15.71	-7.72	1.79	0.11		Feb 10, 2022
61388	NOP	7.26	18.51	-16.15	-18.85	-2.31		Feb 18, 2022
61388	OT	3.94	21.96	-6.53	14.98	8.59		Feb 10, 2022
61388	V1A	2.02	14.09	-13.72	5.25	1.91		Feb 11, 2022
61388	V1B	-0.30	2.53	-8.53	-6.54	-3.21		Feb 28, 2022

61388	V2	-0.35	3.42	-3.18	4.39	1.07		Jun 21, 2022
61388	5-HT6	17.76	-7.03	11.79	13.74	9.07		Feb 18, 2022
61389	Alpha2Beta2	6.54	-4.04	0.19	-6.38	-0.92		Feb 01, 2022
61389	Alpha2Beta4	1.56	-2.50	2.12	4.87	1.51		Feb 01, 2022
61389	Alpha3Beta2	-7.39	-7.22	-14.28	-12.15	-10.26		Feb 01, 2022
61389	Alpha3Beta4	-9.06	-13.68	-10.40	-16.14	-12.32		Feb 01, 2022
61389	Alpha4Beta2	-5.31	-7.76	-0.14	5.17	-2.01		Feb 01, 2022
61389	Alpha4Beta2 (Rat Brain)	-12.22	-2.52	-0.09	-4.06	-4.72		Feb 01, 2022
61389	Alpha4Beta4	0.96	-8.16	2.77	-3.84	-2.07		Feb 01, 2022
61389	Alpha7	-4.22	-15.69	1.73	-2.03	-5.05		Feb 01, 2022
61389	5-HT1A	-22.07	-3.76	-24.06	-8.30	-14.55		Feb 23, 2022
61389	5-HT1B	-7.40	-1.72	27.31	17.09	8.82		Feb 21, 2022
61389	5-HT1D	1.61	-7.85	-29.02	-35.39	-17.66		Feb 21, 2022
61389	5-HT1E	-21.00	-19.43	-16.49	-9.57	-16.62		Feb 23, 2022
61389	5-HT2A	36.79	-5.52	16.18	11.26	14.68		Feb 24, 2022
61389	5-HT2B	-1.86	0.62	-6.82	14.39	1.58		Feb 23, 2022
61389	5-HT2C	13.93	-42.46	-47.90	-23.22	-24.91	Secondary	Feb 23, 2022
61389	5-HT3	5.83	10.03	7.16	13.05	9.02		May 17, 2022
61389	5-HT4	-2.97	-3.70	-23.29	-11.32	-10.32		Feb 21, 2022
61389	5-HT5A	6.53	-1.02	-8.85	-3.79	-1.78		Feb 11, 2022
61389	5-HT6	78.86	57.76	67.39	62.78	66.70		Feb 24, 2022
61389	5-HT7A	-8.98	-25.64	-5.08	-18.74	-14.61		Feb 11, 2022
61389	A1	60.10	8.80	-17.22	25.65	19.33		Feb 11, 2022
61389	A2A	13.16	20.70	-4.62	58.82	22.02		Jun 15, 2022
61389	Alpha1A	3.98	-18.37	-33.87	-18.29	-16.64		Feb 21, 2022
61389	Alpha1B	-7.49	-8.34	-26.25	-36.79	-19.72		Feb 21, 2022
61389	Alpha1D	12.66	0.11	8.88	33.51	13.79		Feb 24, 2022
61389	Alpha2A	8.59	0.52	-20.40	-0.03	-2.83		May 15, 2022
61389	Alpha2B	26.38	15.56	13.79	5.59	15.33		Mar 15, 2022
61389	Alpha2C	15.99	21.29	4.21	-3.16	9.58		Mar 15, 2022

61389	Beta1	-16.23	-21.05	2.10	-11.52	-11.68		Feb 25, 2022
61389	Beta2	-5.65	2.09	-8.87	-7.82	-5.06		Feb 21, 2022
61389	Beta3	28.07	-11.37	1.18	9.48	6.84		Feb 18, 2022
61389	AT2	26.44	-0.41	-4.08	16.11	9.52		Feb 25, 2022
61389	BZP Rat Brain Site	88.46	90.33	95.33	92.60	91.68	Secondary	Feb 24, 2022
61389	D1	29.51	12.16	8.74	16.72	16.78		Mar 27, 2022
61389	D2	56.44	55.26	21.12	56.14	47.24		Feb 17, 2022
61389	D3	45.64	6.13	15.36	7.88	18.75		Feb 17, 2022
61389	D4	31.58	37.26	7.96	-10.73	16.52		Feb 22, 2022
61389	D5	-7.64	-18.76	-17.63	-58.58	-25.65		Feb 23, 2022
61389	DAT	-49.73	-39.84	-58.27	-11.66	-39.88	Secondary	Jul 12, 2022
61389	DOR	3.27	-16.57	-17.93	6.50	-6.18		Feb 24, 2022
61389	GABAA	2.24	10.10	-16.60	-11.10	-3.84		Mar 03, 2022
61389	H1	19.32	-6.70	-16.88	-2.98	-1.81		Feb 28, 2022
61389	H2	1.66	18.81	7.53	6.93	8.73		Feb 25, 2022
61389	H3	-0.02	-6.57	-13.40	-20.67	-10.17		Mar 02, 2022
61389	H4	-43.04	15.98	-16.47	7.31	-9.06		Feb 18, 2022
61389	KOR	83.20	84.37	80.54	73.39	80.38	Secondary	Feb 21, 2022
61389	M1	1.41	12.49	8.17	34.46	14.13		Feb 22, 2022
61389	M2	14.23	-4.45	-4.84	-23.12	-4.55		Feb 22, 2022
61389	M3	6.66	9.93	0.99	0.44	4.51		Feb 21, 2022
61389	M4	13.34	8.72	-0.54	3.76	6.32		Feb 22, 2022
61389	M5	68.73	60.19	55.16	57.21	60.32	Secondary	Feb 22, 2022
61389	MOR	6.79	1.56	25.36	45.68	19.85		Feb 24, 2022
61389	NET	50.94	37.02	34.55	32.79	38.83		Feb 28, 2022
61389	PBR	36.41	41.48	-11.01	48.04	28.73		Feb 17, 2022
61389	SERT	-13.51	-25.24	-1.78	-10.82	-12.84		Feb 24, 2022
61389	Sigma 1	1.67	6.87	7.92	14.69	7.79		Feb 22, 2022
61389	Sigma 2	54.03	44.12	48.35	54.75	50.31	Secondary	Feb 18, 2022
61389	AMPA	21.90	6.85	3.16	3.03	8.74		Feb 18, 2022

61389	Kainate (Rat Brain)	19.55	10.95	-0.10	-3.38	6.76		Feb 18, 2022
61389	NMDA	81.47	82.71	85.73	90.48	85.10	Secondary	Feb 22, 2022
61389	NR2B	4.73	-33.80	-2.37	6.42	-6.26		Feb 10, 2022
61389	HCA2	37.46	30.41	-9.53	29.63	21.99		Feb 24, 2022
61389	Ca channel human	60.38	-4.27	-18.45	9.25	11.73		Feb 10, 2022
61389	HERG	21.49	4.46	-4.25	10.85	8.14		Feb 21, 2022
61389	M1 D	26.59	12.60	32.35	25.91	24.36		Mar 02, 2022
61389	M2 D	43.82	25.32	16.30	0.96	21.60		Mar 02, 2022
61389	M3D	20.47	-5.58	-0.10	-1.67	3.28		Mar 02, 2022
61389	M4 D	38.43	12.93	8.06	9.20	17.16		Mar 02, 2022
61389	M5 D	13.61	2.62	5.29	14.20	8.93		Mar 02, 2022
61389	NTS1	-1.21	-2.02	-3.02	-11.13	-4.35		Feb 10, 2022
61389	NOP	48.23	16.71	3.66	-10.75	14.46		Feb 18, 2022
61389	OT	8.41	8.83	22.38	14.70	13.58		Feb 10, 2022
61389	V1A	9.14	-8.97	9.78	2.24	3.05		Feb 11, 2022
61389	V1B	5.99	-23.52	5.73	2.43	-2.34		Feb 28, 2022
61389	V2	-1.51	-3.74	-2.63	6.62	-0.32		Jun 21, 2022
61389	5-HT6	4.10	-5.19	7.78	12.02	4.68		Feb 18, 2022
61390	Alpha2Beta2	3.76	-3.48	-4.04	-0.36	-1.03		Feb 01, 2022
61390	Alpha2Beta4	1.84	6.90	1.40	3.64	3.45		Feb 01, 2022
61390	Alpha3Beta2	-1.48	-9.69	-1.81	-1.81	-3.70		Feb 01, 2022
61390	Alpha3Beta4	-9.21	-18.01	-6.23	-6.67	-10.03		Feb 01, 2022
61390	Alpha4Beta2	4.70	5.45	8.99	1.77	5.23		Feb 01, 2022
61390	Alpha4Beta2 (Rat Brain)	14.27	3.76	-2.99	-4.06	2.75		Feb 01, 2022
61390	Alpha4Beta4	-13.20	0.96	-7.77	-3.99	-6.00		Feb 01, 2022
61390	Alpha7	3.54	7.12	-20.29	-13.74	-5.84		Feb 01, 2022
61390	5-HT1A	-36.55	3.90	-15.12	-18.81	-16.65		Feb 23, 2022
61390	5-HT1B	1.70	-34.28	-15.37	7.47	-10.12		Feb 27, 2022
61390	5-HT1D	1.96	-19.11	-29.07	-37.88	-21.03		Feb 21, 2022
61390	5-HT1E	-13.00	-12.38	-6.31	-9.83	-10.38		Feb 23, 2022

61390	5-HT2A	47.10	-2.01	8.83	15.77	17.42		Feb 24, 2022
61390	5-HT2B	15.22	-17.28	-19.58	9.06	-3.15		Feb 23, 2022
61390	5-HT2C	18.03	6.04	-35.20	-7.05	-4.55		Feb 23, 2022
61390	5-HT3	-0.39	-14.28	2.66	-6.52	-4.63		May 17, 2022
61390	5-HT4	-12.72	3.17	5.76	18.02	3.56		Feb 21, 2022
61390	5-HT5A	14.72	9.86	10.60	4.04	9.81		Feb 11, 2022
61390	5-HT6	9.23	-11.25	-4.08	-5.00	-2.78		Feb 24, 2022
61390	5-HT7A	-17.05	-10.28	-14.71	-7.68	-12.43		Feb 11, 2022
61390	A1	60.48	17.22	23.35	38.28	34.83		Feb 11, 2022
61390	A2A	103.20	-168.07	-4.34	43.03	-6.55		Jun 15, 2022
61390	Alpha1A	-9.41	-14.02	-21.75	-36.58	-20.44		Feb 21, 2022
61390	Alpha1B	-16.28	-23.04	-14.76	-19.27	-18.34		Feb 21, 2022
61390	Alpha1D	2.37	-13.48	6.85	31.77	6.88		Feb 24, 2022
61390	Alpha2A	15.86	4.95	-0.87	3.83	5.94		May 15, 2022
61390	Alpha2B	3.90	-0.34	1.63	7.01	3.05		Mar 15, 2022
61390	Alpha2C	9.16	8.98	1.61	10.87	7.66		Mar 15, 2022
61390	Beta1	25.86	28.19	35.35	37.74	31.79		Feb 25, 2022
61390	Beta2	1.78	-1.50	-12.89	-8.99	-5.40		Feb 21, 2022
61390	Beta3	35.06	-37.31	-29.97	-21.08	-13.33		Feb 18, 2022
61390	AT2	3.55	12.63	11.37	23.64	12.80		Feb 25, 2022
61390	BZP Rat Brain Site	87.37	77.76	83.62	77.13	81.47	Secondary	Feb 24, 2022
61390	D1	19.00	8.36	7.98	17.73	13.27		Mar 27, 2022
61390	D2	43.49	28.18	-7.14	51.43	28.99		Feb 17, 2022
61390	D3	81.64	69.46	64.10	77.12	73.08	Secondary	Feb 17, 2022
61390	D4	29.49	26.20	-8.04	29.94	19.40		Feb 22, 2022
61390	D5	-14.00	-8.32	-49.10	-32.66	-26.02		Feb 23, 2022
61390	DAT	-56.02	-57.17	-35.15	-39.59	-46.98	Secondary	Jul 12, 2022
61390	DOR	11.78	-0.05	-9.76	0.37	0.59		Feb 24, 2022
61390	GABAA	27.37	-1.68	-6.39	2.24	5.39		Mar 03, 2022
61390	H1	2.69	-33.32	7.78	-25.88	-12.18		Feb 28, 2022

61390	H2	10.89	18.75	11.97	8.67	12.57		Feb 25, 2022
61390	H3	-6.71	-12.69	-13.12	-11.27	-10.95		Mar 02, 2022
61390	H4	7.17	12.06	-27.65	12.06	0.91		Feb 18, 2022
61390	KOR	88.19	82.54	75.22	72.56	79.63	Secondary	Feb 21, 2022
61390	M1	15.68	9.30	7.98	-9.30	5.92		Feb 22, 2022
61390	M2	-2.09	-22.33	-26.07	5.38	-11.28		Feb 22, 2022
61390	M3	32.00	21.96	12.24	6.94	18.29		Feb 21, 2022
61390	M4	13.34	4.09	16.65	15.99	12.52		Feb 22, 2022
61390	M5	-15.04	-16.70	-13.79	-16.50	-15.51		Feb 22, 2022
61390	MOR	3.86	15.13	40.76	48.69	27.11		Feb 24, 2022
61390	NET	46.53	52.17	21.16	43.36	40.81		Feb 28, 2022
61390	PBR	58.04	63.40	-26.97	52.82	36.82		Feb 17, 2022
61390	SERT	-33.18	-3.49	-9.35	-37.21	-20.81		Feb 24, 2022
61390	Sigma 1	11.22	-2.32	-9.23	19.41	4.77		Feb 22, 2022
61390	Sigma 2	27.19	19.60	30.44	33.48	27.68		Feb 18, 2022

61390	AMPA	23.68	11.95	6.47	-9.47	8.16		Feb 18, 2022
61390	Kainate (Rat Brain)	17.50	13.82	26.92	8.50	16.69		Feb 18, 2022
61390	NMDA	77.07	81.13	83.81	86.90	82.23	Secondary	Feb 22, 2022
61390	NR2B	35.49	-19.26	1.01	43.94	15.30		Feb 10, 2022
61390	HCA2	20.23	-12.66	49.21	28.06	21.21		Feb 24, 2022
61390	Ca channel human	53.91	-27.05	-10.87	2.33	4.58		Feb 10, 2022
61390	HERG	8.14	-4.05	5.96	2.62	3.17		Feb 21, 2022
61390	M1 D	11.09	25.63	9.72	14.93	15.34		Mar 02, 2022
61390	M2 D	47.88	44.28	16.30	11.79	30.06		Mar 02, 2022
61390	M3D	6.89	7.02	-7.28	-6.24	0.10		Mar 02, 2022

61390	M4 D	27.54	9.49	0.04	6.34	10.85		Mar 02, 2022
61390	M5 D	17.32	17.17	4.25	8.71	11.86		Mar 02, 2022
61390	NTS1	-3.52	4.09	-5.22	0.59	-1.02		Feb 10, 2022
61390	NOP	-22.89	-5.35	-3.48	-11.78	-10.88		Mar 23, 2022
61390	OT	12.32	20.14	15.81	17.77	16.51		Feb 10, 2022
61390	V1A	23.79	18.84	5.25	1.59	12.37		Feb 11, 2022
61390	V1B	-8.48	4.05	-9.47	-1.77	-3.92		Feb 28, 2022
61390	V2	15.96	12.76	13.50	30.37	18.15		Jun 21, 2022
61390	5-HT6	-5.19	8.00	13.97	9.38	6.54		Feb 18, 2022
61391	Alpha2Beta2	-6.26	4.98	-4.26	-1.81	-1.84		Feb 01, 2022
61391	Alpha2Beta4	-3.66	6.78	6.31	2.00	2.86		Feb 01, 2022
61391	Alpha3Beta2	-7.14	0.41	-3.53	3.86	-1.60		Feb 01, 2022
61391	Alpha3Beta4	-9.95	-5.63	-8.16	-15.69	-9.86		Feb 01, 2022
61391	Alpha4Beta2	6.81	7.63	2.18	6.60	5.81		Feb 01, 2022
61391	Alpha4Beta2 (Rat Brain)	4.91	4.87	-2.35	2.52	2.49		Feb 01, 2022
61391	Alpha4Beta4	-0.06	1.75	-3.92	-1.16	-0.85		Feb 01, 2022
61391	Alpha7	3.96	0.10	10.51	6.89	5.37		Feb 01, 2022
61391	5-HT1A	-28.18	-24.20	2.48	-11.71	-15.40		Feb 23, 2022
61391	5-HT1B	5.58	-18.59	-11.62	-27.51	-13.04		Feb 21, 2022
61391	5-HT1D	2.01	-10.82	-28.72	-40.18	-19.43		Feb 21, 2022
61391	5-HT1E	-11.98	-13.36	-0.99	-9.70	-9.01		Feb 23, 2022
61391	5-HT2A	31.13	24.06	21.90	11.87	22.24		Feb 24, 2022
61391	5-HT2B	31.74	14.02	27.24	26.69	24.92		Feb 23, 2022
61391	5-HT2C	-23.14	15.27	-10.36	8.80	-2.36		Feb 23, 2022
61391	5-HT3	6.65	10.36	11.46	-4.81	5.92		Jun 10, 2022
61391	5-HT4	-4.89	-2.82	-7.99	13.44	-0.57		Feb 21, 2022
61391	5-HT5A	11.03	-6.58	-5.52	5.87	1.20		Feb 11, 2022
61391	5-HT6	21.82	16.40	8.20	-2.85	10.89		Feb 24, 2022
61391	5-HT7A	-5.99	-11.85	-5.86	4.04	-4.92		Feb 11, 2022

61391	A1	40.57	8.80	-0.77	24.88	18.37		Feb 11, 2022
61391	A2A	9.46	-20.70	-10.31	-14.58	-9.03		Jun 15, 2022
61391	Alpha1A	6.17	-5.65	-8.23	-15.20	-5.73		Feb 21, 2022
61391	Alpha1B	71.49	22.82	5.97	10.48	27.69		Feb 21, 2022
61391	Alpha1D	14.81	29.62	29.85	32.12	26.60		Feb 24, 2022
61391	Alpha2A	45.41	19.08	27.60	35.90	32.00		May 15, 2022
61391	Alpha2B	34.37	-7.20	-5.15	-5.79	4.06		Mar 15, 2022
61391	Alpha2C	27.71	-3.64	-8.22	-1.03	3.71		Mar 15, 2022
61391	Beta1	45.42	25.19	51.94	23.13	36.42		Feb 25, 2022
61391	Beta2	-3.67	-5.77	5.62	0.42	-0.85		Feb 21, 2022
61391	Beta3	50.22	16.58	12.67	25.82	26.32		Feb 18, 2022
61391	AT2	4.42	14.37	-67.74	16.20	-8.19		Feb 25, 2022
61391	BZP Rat Brain Site	83.93	77.91	82.37	81.20	81.35	Secondary	Feb 24, 2022
61391	D1	12.54	8.99	9.12	9.50	10.04		Mar 27, 2022
61391	D2	4.34	44.67	19.35	55.56	30.98		Feb 17, 2022
61391	D3	-2.46	-6.89	8.80	-6.24	-1.70		Feb 17, 2022
61391	D4	29.34	5.72	8.71	12.00	13.94		Feb 22, 2022
61391	D5	-8.21	-13.94	-22.90	-1.74	-11.70		Feb 23, 2022
61391	DAT	-34.71	-25.01	-11.72	-39.09	-27.63	Secondary	Jul 12, 2022
61391	DOR	-8.06	-16.57	-21.76	7.61	-9.70		Feb 24, 2022
61391	GABAA	-25.24	18.73	14.81	-7.96	0.09		Mar 03, 2022
61391	H1	-6.31	-18.84	99.76	-4.35	17.57		Feb 28, 2022
61391	H2	21.62	10.53	34.58	8.79	18.88		Feb 25, 2022
61391	H3	-27.64	-17.53	-14.83	-15.11	-18.78		Mar 02, 2022
61391	H4	-33.95	7.87	-5.98	22.41	-2.41		Feb 18, 2022
61391	KOR	63.41	57.42	61.08	40.96	55.72	Secondary	Feb 21, 2022
61391	M1	14.74	4.23	-23.00	25.82	5.45		Feb 22, 2022
61391	M2	24.64	-27.64	-14.67	-20.37	-9.51		Feb 22, 2022
61391	M3	46.15	21.87	-12.46	6.57	15.53		Feb 21, 2022
61391	M4	21.11	29.53	9.54	23.25	20.86		Feb 22, 2022

61391	M5	8.38	-5.18	107.10	5.14	28.86		Feb 22, 2022
61391	MOR	7.62	2.55	6.27	47.12	15.89		Feb 24, 2022
61391	NET	64.41	47.24	48.47	39.04	49.79		Feb 28, 2022
61391	PBR	38.66	-12.21	11.25	13.78	12.87		Jul 01, 2022
61391	SERT	2.74	-9.60	-41.12	-23.77	-17.94		Feb 24, 2022
61391	Sigma 1	6.46	4.45	10.70	13.94	8.89		Feb 22, 2022
61391	Sigma 2	39.01	5.76	-12.25	13.09	11.40		Feb 18, 2022
61391	AMPA	5.71	-13.29	8.38	-24.89	-6.02		Feb 18, 2022
61391	Kainate (Rat Brain)	10.95	-5.83	-0.51	-31.63	-6.76		Feb 18, 2022
61391	NMDA	-24.34	-24.48	93.57	-4.33	10.11		Feb 22, 2022
61391	NR2B	-12.51	-10.48	-11.49	36.50	0.50		Feb 10, 2022
61391	HCA2	21.01	13.97	11.62	24.15	17.69		Feb 24, 2022
61391	Ca channel human	-8.15	-6.67	-11.58	-0.65	-6.76		Feb 10, 2022
61391	HERG	7.85	12.40	-1.63	0.06	4.67		Feb 21, 2022
61391	M1 D	-2.90	0.12	-12.78	19.60	1.01		Mar 02, 2022
61391	M2 D	-18.89	-8.07	-13.93	2.76	-9.53		Mar 02, 2022
61391	M3D	5.58	-4.80	-11.39	-13.75	-6.09		Mar 02, 2022
61391	M4 D	12.64	-4.26	-2.26	-6.27	-0.04		Mar 02, 2022
61391	M5 D	19.25	13.16	6.93	19.25	14.65		Mar 02, 2022
61391	NTS1	11.40	3.89	14.31	2.39	8.00		Feb 10, 2022
61391	NOP	2.31	-7.60	18.96	-24.25	-2.65		Feb 18, 2022
61391	OT	5.62	17.07	10.37	6.88	9.99		Feb 10, 2022
61391	V1A	-2.72	24.01	10.64	4.82	9.19		Feb 11, 2022
61391	V1B	6.51	-3.29	-3.65	-2.40	-0.71		Feb 28, 2022
61391	V2	5.19	-12.22	-16.04	-1.71	-6.20		Jun 28, 2022
61391	5-HT6	52.27	44.67	25.03	-3.92	29.51		Feb 18, 2022
61392	Alpha2Beta2	2.20	-1.36	-2.14	1.31	0.00		Feb 01, 2022
61392	Alpha2Beta4	23.68	25.11	13.24	16.23	19.57		Feb 01, 2022
61392	Alpha3Beta2	4.84	2.05	-6.65	1.97	0.55		Feb 01, 2022
61392	Alpha3Beta4	25.83	21.66	20.09	24.79	23.09		Feb 01, 2022

61397	Alpha2Beta2	-1.81	-4.48	-4.59	-1.48	-3.09		Feb 01, 2022
61397	Alpha2Beta4	-6.01	-5.25	-3.54	0.21	-3.65		Feb 01, 2022
61397	Alpha3Beta2	-7.14	-2.71	-9.77	-13.22	-8.21		Feb 01, 2022
61397	Alpha3Beta4	-14.95	-10.03	-5.93	-1.30	-8.05		Feb 01, 2022
61397	Alpha4Beta2	1.63	15.73	-4.49	-3.61	2.32		Feb 01, 2022
61397	Alpha4Beta2 (Rat Brain)	3.93	-0.17	-1.03	-2.14	0.15		Feb 01, 2022
61397	Alpha4Beta4	4.74	-2.26	-7.06	-4.62	-2.30		Feb 01, 2022
61397	Alpha7	-1.10	-10.95	-1.47	-10.07	-5.90		Feb 01, 2022
61397	5-HT1A	-15.83	-19.52	-22.50	9.16	-12.17		Feb 23, 2022
61397	5-HT1B	-8.91	-40.97	-11.45	-21.83	-20.79		Feb 27, 2022
61397	5-HT1D	-14.79	-13.62	-1.54	1.98	-6.99		Feb 21, 2022
61397	5-HT1E	8.45	3.80	2.29	-2.27	3.07		Feb 23, 2022
61397	5-HT2A	6.34	5.13	5.67	4.05	5.30		Feb 24, 2022
61397	5-HT2B	42.60	21.25	1.31	6.09	17.81		Feb 23, 2022

vestigator/web/assay/primary-binding/index?page=24&p...

61397	5-HT2C	45.70	16.08	3.37	5.86	17.75		Feb 23, 2022
61397	5-HT3	8.25	8.59	9.10	12.90	9.71		Jun 10, 2022
61397	5-HT4	17.36	-17.67	-18.26	16.47	-0.53		Feb 21, 2022
61397	5-HT5A	-20.87	-26.93	-20.37	-0.99	-17.29		Feb 11, 2022
61397	5-HT6	24.54	11.30	-0.30	4.36	9.98		Feb 24, 2022
61397	5-HT7A	-7.42	-22.26	-16.14	-14.97	-15.20		Feb 11, 2022
61397	A1	37.89	15.31	25.26	33.68	28.04		Feb 11, 2022
61397	A2A	-4.34	-8.75	3.63	-8.04	-4.38		Jun 15, 2022
61397	Alpha1A	-18.67	-10.68	-7.09	-5.70	-10.54		Feb 21, 2022
61397	Alpha1B	-10.59	-18.03	-17.69	-19.32	-16.41		Feb 21, 2022
61397	Alpha1D	-7.74	-13.13	-23.54	-25.89	-17.58		Feb 24, 2022
61397	Alpha2A	3.41	9.05	3.41	25.88	10.44		May 15, 2022
61397	Alpha2B	12.68	21.00	6.74	4.57	11.25		May 15, 2022
61397	Alpha2C	23.93	23.41	15.87	17.26	20.12		May 15, 2022
61397	Beta1	-18.76	-0.32	-31.64	45.06	-1.42		Feb 25, 2022

61397	Beta2	-2.06	-4.10	4.94	-4.04	-1.32		Feb 21, 2022
61397	Beta3	15.75	20.97	18.00	18.48	18.30		Feb 18, 2022
61397	AT2	31.31	6.57	-14.56	-36.69	-3.34		Feb 25, 2022
61397	BZP Rat Brain Site	25.74	13.55	14.02	9.02	15.58		Feb 24, 2022
61397	D1	13.30	1.90	1.39	12.16	7.19		Mar 27, 2022
61397	D2	22.38	-52.40	7.80	2.73	-4.87		Feb 17, 2022
61397	D3	32.30	16.92	31.62	31.48	28.08		Feb 17, 2022
61397	D4	-17.16	-23.58	-23.88	0.49	-16.03		Feb 22, 2022
61397	D5	2.83	-3.55	-4.01	2.54	-0.55		Feb 23, 2022
61397	DAT	5.14	39.37	19.85	46.44	27.70		Jul 12, 2022
61397	DOR	1.44	-9.70	-12.80	3.46	-4.40		Feb 24, 2022
61397	GABAA	-15.03	14.81	-1.68	-5.61	-1.88		Mar 03, 2022
61397	H1	-11.99	-18.64	-11.59	3.08	-9.79		Feb 28, 2022
61397	H2	20.83	2.86	30.01	15.49	17.30		Feb 25, 2022
61397	H3	4.79	-11.89	-11.52	-14.64	-8.32		Feb 23, 2022
61397	H4	11.54	-8.60	18.25	3.48	6.17		Feb 24, 2022
61397	KOR	10.02	2.20	31.81	-2.62	10.35		Feb 21, 2022
61397	M1	-12.30	-1.03	118.59	5.92	27.80		Feb 22, 2022
61397	M2	1.45	-21.55	-22.53	-20.17	-15.70		Feb 22, 2022
61397	M3	4.13	32.33	20.12	31.68	22.07		Feb 21, 2022

61397	M4	25.57	28.21	17.14	33.83	26.19		Feb 22, 2022
61397	M5	-7.37	-11.20	1.37	25.72	2.13		Feb 22, 2022
61397	MOR	17.38	4.93	5.24	6.59	8.54		Feb 24, 2022
61397	NET	48.16	19.48	1.46	6.88	19.00		Feb 28, 2022
61397	PBR	-1.85	-20.84	-14.85	-23.28	-15.21		Jul 01, 2022
61397	SERT	30.38	-25.93	-7.72	3.98	0.18		May 10, 2022
61397	Sigma 1	24.34	30.96	0.38	15.21	17.72		Feb 22, 2022
61397	Sigma 2	37.10	6.74	25.48	-1.57	16.94		Feb 18, 2022
61397	AMPA	-18.14	-1.05	14.63	2.90	-0.42		Feb 18, 2022
61397	Kainate (Rat Brain)	12.59	14.23	20.78	19.14	16.69		Feb 18, 2022
61397	NMDA	83.81	77.35	73.36	72.53	76.76	Secondary	Feb 22, 2022
61397	NR2B	-17.57	-18.93	-21.63	64.22	1.52		Feb 10, 2022
61397	HCA2	32.76	42.94	21.80	52.34	37.46		Feb 24, 2022
61397	Ca channel human	4.01	-7.25	-9.00	-3.62	-3.97		Feb 10, 2022
61397	HERG	17.14	12.11	2.72	2.19	8.54		Feb 21, 2022

61397	M1 D	4.64	-4.00	4.92	14.52	5.02		Mar 02, 2022
61397	M2 D	29.84	11.79	7.73	23.52	18.22		Mar 02, 2022
61397	M3D	2.71	-9.70	0.03	5.39	-0.39		Mar 02, 2022
61397	M4 D	11.93	6.91	-11.57	-2.97	1.08		Mar 02, 2022
61397	M5 D	6.03	0.84	15.54	2.32	6.18		Mar 02, 2022
61397	NTS1	-8.92	11.20	14.11	-4.72	2.92		Feb 10, 2022
61397	NOP	0.94	0.40	4.15	0.94	1.61		Mar 23, 2022
61397	OT	-4.57	15.12	5.06	14.98	7.65		Feb 10, 2022
61397	V1A	16.90	25.09	34.79	20.99	24.44		Feb 11, 2022
61397	V1B	24.50	1.87	-0.36	-4.72	5.32		Feb 28, 2022
61397	V2	9.27	5.49	-3.94	-2.08	2.19		Jul 12, 2022
61397	5-HT6	75.06	47.97	33.78	31.20	47.00		Feb 18, 2022
61398	Alpha2Beta2	-1.03	2.76	-18.62	-2.59	-4.87		Feb 01, 2022
61398	Alpha2Beta4	1.76	5.35	3.08	7.26	4.36		Feb 01, 2022
61398	Alpha3Beta2	-6.32	-10.67	-12.15	-16.75	-11.47		Feb 01, 2022

61398	Alpha3Beta4	1.01	-4.21	-8.61	-2.87	-3.67		Feb 01, 2022
61398	Alpha4Beta2	13.28	10.89	10.76	1.50	9.11		Feb 01, 2022
61398	Alpha4Beta2 (Rat Brain)	-1.54	-1.15	-7.01	-5.85	-3.89		Feb 01, 2022
61398	Alpha4Beta4	14.18	17.88	40.47	9.86	20.60		Feb 01, 2022
61398	Alpha7	-7.89	0.85	4.24	-7.84	-2.66		Feb 01, 2022
61398	5-HT1A	-28.46	-16.96	-17.39	-1.77	-16.15		Feb 23, 2022
61398	5-HT1B	18.71	-17.78	22.12	-40.65	-4.40		Feb 21, 2022
61398	5-HT1D	8.85	-5.13	3.90	9.39	4.25		Feb 21, 2022
61398	5-HT1E	-18.02	-5.66	-28.82	-12.99	-16.37		Feb 23, 2022
61398	5-HT2A	43.93	18.06	13.82	15.10	22.73		Feb 24, 2022
61398	5-HT2B	9.92	-10.86	-10.11	-17.23	-7.07		Feb 23, 2022
61398	5-HT2C	7.15	-9.77	-8.39	-4.44	-3.86		Feb 23, 2022
61398	5-HT3	5.42	19.92	21.77	5.21	13.08		Jun 10, 2022
61398	5-HT4	25.93	-3.93	9.67	20.39	13.02		Feb 21, 2022
61398	5-HT5A	1.27	-29.96	-45.74	3.90	-17.63		Feb 11, 2022
61398	5-HT6	37.38	10.57	8.71	10.98	16.91		Feb 24, 2022
61398	5-HT7A	5.47	-20.70	0.52	6.64	-2.02		Feb 11, 2022
61398	A1	76.94	83.83	68.90	63.54	73.30	Secondary	Feb 11, 2022
61398	A2A	52.84	32.79	39.19	49.43	43.56		Jun 15, 2022
61398	Alpha1A	20.71	0.39	6.93	8.83	9.22		Feb 21, 2022
61398	Alpha1B	-5.69	-4.79	-9.07	-1.97	-5.38		Feb 21, 2022
61398	Alpha1D	30.13	8.47	2.18	2.84	10.91		Feb 24, 2022
61398	Alpha2A	41.39	32.96	28.36	17.67	30.10		May 15, 2022
61398	Alpha2B	100.12	101.52	94.53	91.66	96.96	Secondary	May 15, 2022
61398	Alpha2C	21.67	28.68	-9.18	8.33	12.38		May 15, 2022
61398	Beta1	-20.50	-5.77	-4.34	-2.45	-8.27		Feb 25, 2022
61398	Beta2	0.29	-1.38	5.43	6.55	2.72		Feb 21, 2022
61398	Beta3	36.01	51.29	41.69	60.41	47.35		Feb 18, 2022
61398	AT2	89.85	44.23	40.75	37.02	52.96	Secondary	Feb 25, 2022

61398	BZP Rat Brain Site	69.32	46.28	49.79	60.42	56.45	Secondary	Feb 24, 2022
61398	D1	48.88	23.94	19.88	28.37	30.27		Mar 27, 2022
61398	D2	6.22	-43.84	-26.73	22.69	-10.42		Feb 17, 2022
61398	D3	51.60	31.20	35.81	44.52	40.78		Feb 17, 2022
61398	D4	-33.45	-13.87	-14.61	-4.75	-16.67		Feb 22, 2022
61398	D5	27.00	19.17	9.96	1.78	14.48		Feb 23, 2022
61398	DAT	22.38	0.67	8.65	-3.74	6.99		Jul 12, 2022
61398	DOR	51.44	25.82	18.01	24.43	29.93		Feb 24, 2022
61398	GABAA	-13.46	-0.11	7.74	9.31	0.87		Mar 03, 2022
61398	H1	20.69	7.19	-24.12	16.78	5.14		Feb 28, 2022
61398	H2	36.10	23.22	18.32	3.30	20.24		Feb 25, 2022
61398	H3	2.95	3.50	-2.91	1.12	1.17		Feb 23, 2022
61398	H4	15.23	3.48	15.90	4.15	9.69		Feb 24, 2022
61398	KOR	97.01	93.68	73.72	96.17	90.15	Secondary	Feb 21, 2022
61398	M1	-18.12	8.73	1.41	-2.91	-2.72		Feb 22, 2022
61398	M2	-2.68	-15.45	118.40	-19.78	20.12		Feb 22, 2022
61398	M3	16.01	29.47	47.25	20.25	28.25		Feb 21, 2022
61398	M4	2.93	4.25	2.93	5.74	3.96		Feb 22, 2022
61398	M5	-9.88	-6.97	7.06	14.14	1.09		Feb 22, 2022
61398	MOR	48.30	27.92	28.56	20.39	31.29		Feb 24, 2022
61398	NET	60.29	20.85	23.80	20.03	31.24		Feb 28, 2022
61398	PBR	115.22	104.05	96.23	84.66	100.04	Secondary	Jul 01, 2022
61398	SERT	-6.30	-8.50	-6.30	-26.46	-11.89		Feb 24, 2022
61398	Sigma 1	46.13	12.51	15.42	4.95	19.75		Feb 22, 2022
61398	Sigma 2	87.22	80.82	59.04	69.16	74.06	Secondary	Feb 18, 2022
61398	AMPA	-15.71	0.48	12.08	6.09	0.74		Feb 18, 2022
61398	Kainate (Rat Brain)	14.23	19.55	27.74	14.23	18.94		Feb 18, 2022
61398	NMDA	87.45	84.57	84.43	80.37	84.21	Secondary	Feb 22, 2022
61398	NR2B	22.31	38.53	24.33	77.74	40.73		Feb 10, 2022
61398	HCA2	48.42	61.74	7.70	48.42	41.57		Feb 24, 2022

61398	Ca channel human	55.01	41.87	40.64	8.15	36.42		Feb 10, 2022
61398	HERG	72.87	46.45	30.59	36.54	46.61		Feb 21, 2022
61398	M1 D	4.23	28.10	11.64	17.26	15.31		Mar 02, 2022
61398	M2 D	28.03	8.63	20.36	29.84	21.72		Mar 02, 2022
61398	M3D	9.31	4.54	2.25	13.29	7.35		Mar 02, 2022
61398	M4 D	7.92	2.33	-0.25	1.47	2.87		Mar 02, 2022
61398	M5 D	16.58	17.77	7.22	13.46	13.76		Mar 02, 2022
61398	NTS1	-26.15	-3.72	5.09	-9.53	-8.58		Feb 10, 2022
61398	NOP	16.71	5.91	24.37	-39.56	1.86		Feb 18, 2022
61398	OT	19.86	16.37	12.60	26.01	18.71		Feb 10, 2022
61398	V1A	7.19	3.53	-4.66	-11.99	-1.48		Feb 11, 2022
61398	V1B	10.59	1.53	1.67	26.63	10.11		Feb 28, 2022
61398	V2	-4.55	0.92	-6.13	-11.71	-5.37		Dec 05, 2022
61398	5-HT6	44.67	35.35	8.83	-12.67	19.05		Feb 18, 2022
61399	Alpha2Beta2	1.98	2.53	-7.93	-9.05	-3.12		Feb 01, 2022
61399	Alpha2Beta4	-0.11	26.75	7.26	-9.63	6.07		Feb 01, 2022
61399	Alpha3Beta2	-7.06	-7.55	-8.13	-5.09	-6.96		Feb 01, 2022
61399	Alpha3Beta4	-12.34	-6.08	-3.91	-3.77	-6.53		Feb 01, 2022
61399	Alpha4Beta2	8.71	-1.50	-4.29	-8.92	-1.50		Feb 01, 2022
61399	Alpha4Beta2 (Rat Brain)	-0.13	1.15	-3.38	2.48	0.03		Feb 01, 2022
61399	Alpha4Beta4	8.99	14.34	7.57	15.44	11.59		Feb 01, 2022
61399	Alpha7	-6.31	-0.22	6.51	14.13	3.53		Feb 01, 2022
61399	5-HT1A	3.47	6.92	-12.31	0.14	-0.45		Feb 23, 2022
61399	5-HT1B	24.23	29.26	-13.89	-17.94	5.42		Feb 21, 2022
61399	5-HT1D	-2.96	-12.30	8.62	2.48	-1.04		Feb 21, 2022
61399	5-HT1E	-23.54	-13.95	-13.16	-20.53	-17.80		Feb 23, 2022
61399	5-HT2A	69.60	66.64	57.74	74.72	67.18	Secondary	Feb 24, 2022
61399	5-HT2B	72.93	31.64	47.47	41.76	48.45		Feb 23, 2022
61399	5-HT2C	82.36	75.66	65.02	62.36	71.35	Secondary	Feb 23, 2022
61399	5-HT3	26.46	23.19	19.18	-0.19	17.16		Jun 16, 2022

61399	5-HT4	-1.34	24.75	16.69	18.32	14.61		Feb 21, 2022
61399	5-HT5A	-1.92	-24.53	-13.24	14.79	-6.23		Feb 11, 2022
61399	5-HT6	37.48	-2.78	-2.26	-5.06	6.85		Feb 24, 2022
61399	5-HT7A	-2.86	-21.61	-71.33	2.08	-23.43		Feb 11, 2022
61399	A1	73.49	53.97	48.61	71.20	61.82	Secondary	Feb 11, 2022
61399	A2A	58.39	48.72	22.97	52.70	45.70		Jun 15, 2022
61399	Alpha1A	16.40	-12.92	5.24	6.13	3.71		Feb 21, 2022
61399	Alpha1B	-16.11	-12.51	-0.79	6.87	-5.64		Feb 21, 2022
61399	Alpha1D	22.26	9.56	7.02	-10.89	6.99		Feb 24, 2022
61399	Alpha2A	42.25	35.71	36.75	26.96	35.42		May 15, 2022
61399	Alpha2B	44.90	33.44	32.81	39.45	37.65		May 15, 2022
61399	Alpha2C	16.97	12.33	4.73	16.97	12.75		May 15, 2022
61399	Beta1	-26.31	-4.83	-13.75	-7.29	-13.05		Feb 25, 2022
61399	Beta2	-11.47	-6.39	13.29	14.90	2.58		Feb 21, 2022
61399	Beta3	17.89	35.89	28.66	45.72	32.04		Feb 18, 2022

61399	AT2	59.65	11.67	19.12	-4.00	21.61		Feb 25, 2022
61399	BZP Rat Brain Site	64.17	64.40	61.12	70.49	65.05	Secondary	Feb 24, 2022
61399	D1	26.97	20.39	22.42	15.45	21.31		Mar 27, 2022
61399	D2	37.27	2.73	4.32	21.11	16.36		Feb 17, 2022
61399	D3	55.85	36.83	42.95	46.58	45.55		Feb 17, 2022
61399	D4	10.20	-22.99	10.65	-23.43	-6.39		Feb 22, 2022
61399	D5	56.85	23.58	22.88	26.47	32.45		Feb 23, 2022
61399	DAT	36.38	20.89	-2.60	-63.71	-2.26		Feb 24, 2022
61399	DOR	38.28	4.69	23.27	25.28	22.88		Feb 24, 2022
61399	GABAA	-9.53	-9.53	1.46	-6.39	-6.00		Mar 03, 2022
61399	H1	27.94	-6.90	-3.18	20.69	9.64		Feb 28, 2022
61399	H2	29.13	9.02	18.51	16.62	18.32		Feb 25, 2022
61399	H3	-4.01	-11.89	-4.74	-23.43	-11.02		Feb 23, 2022
61399	H4	-12.56	2.21	-28.09	-2.25	-10.17		Feb 18, 2022
61399	KOR	95.18	96.67	92.35	90.35	93.64	Secondary	Feb 21, 2022

vestigator/web/

61399	M1	-22.44	17.18	22.63	13.80	7.79		Feb 22, 2022
61399	M2	-25.28	-15.65	17.57	-20.96	-11.08		Feb 22, 2022
61399	M3	8.41	16.15	31.17	28.96	21.17		Feb 21, 2022
61399	M4	2.44	8.38	23.59	7.89	10.58		Feb 22, 2022
61399	M5	-8.09	-10.34	-9.62	18.70	-2.34		Feb 22, 2022
61399	MOR	20.15	19.68	9.05	12.30	15.30		Feb 24, 2022
61399	NET	41.81	21.59	14.14	15.06	23.15		Feb 28, 2022
61399	PBR	82.42	94.30	101.31	91.76	92.45	Secondary	Jul 01, 2022
61399	SERT	-12.65	-28.29	-3.49	-16.81	-15.31		Feb 24, 2022
61399	Sigma 1	30.46	16.27	16.11	-1.78	15.27		Feb 22, 2022
61399	Sigma 2	52.84	60.17	52.38	48.04	53.36	Secondary	Feb 18, 2022
61399	AMPA	-8.70	4.94	2.39	14.63	3.32		Feb 18, 2022
61399	Kainate (Rat Brain)	12.59	36.34	18.73	26.51	23.54		Feb 18, 2022
61399	NMDA	93.78	89.03	86.97	84.77	88.64	Secondary	Feb 22, 2022
61399	NR2B	7.77	3.38	14.87	24.67	12.67		Feb 10, 2022

61399	HCA2	56.26	56.26	15.53	59.39	46.86		Feb 24, 2022
61399	Ca channel human	29.32	19.87	20.84	25.18	23.80		Feb 10, 2022
61399	HERG	56.27	44.18	28.80	42.10	42.84		Feb 21, 2022
61399	M1 D	12.19	42.09	21.11	43.74	29.78		Mar 02, 2022
61399	M2 D	23.52	22.62	18.10	46.08	27.58		Mar 02, 2022
61399	M3D	7.15	-3.10	9.57	13.68	6.83		Mar 02, 2022
61399	M4 D	-1.97	-1.68	3.04	1.18	0.14		Mar 02, 2022
61399	M5 D	10.49	12.27	18.21	17.77	14.69		Mar 02, 2022
61399	NTS1	-9.93	-12.13	-3.12	-8.12	-8.33		Feb 10, 2022
61399	NOP	-13.00	14.91	6.81	-32.81	-6.02		Feb 18, 2022
61399	OT	27.26	15.26	28.80	14.00	21.33		Feb 10, 2022
61399	V1A	14.74	21.85	5.04	-19.97	5.42		Feb 11, 2022
61399	V1B	2.83	9.13	0.02	5.84	4.46		Feb 28, 2022
61399	V2	-3.81	-4.19	-0.51	4.06	-1.11		Dec 05, 2022
61399	5-HT6	21.73	10.55	33.63	-20.55	11.34		Feb 18, 2022

61400	Alpha2Beta2	-2.37	8.32	-1.48	-4.70	-0.06		Feb 01, 2022
61400	Alpha2Beta4	1.25	-1.23	5.27	-5.77	-0.12		Feb 01, 2022
61400	Alpha3Beta2	-0.16	-11.16	1.15	-12.89	-5.77		Feb 01, 2022
61400	Alpha3Beta4	-8.61	-7.05	-6.52	-10.77	-8.24		Feb 01, 2022
61400	Alpha4Beta2	8.65	5.17	2.25	7.49	5.89		Feb 01, 2022
61400	Alpha4Beta2 (Rat Brain)	6.11	-11.71	5.81	-10.25	-2.51		Feb 01, 2022
61400	Alpha4Beta4	7.50	13.79	8.36	2.62	8.07		Feb 01, 2022
61400	Alpha7	17.94	-21.64	-6.54	-8.54	-4.70		Feb 01, 2022
61400	5-HT1A	7.04	2.97	-8.86	-19.82	-4.67		Feb 23, 2022
61400	5-HT1B	-7.14	-31.19	-36.74	-21.94	-24.25		Feb 27, 2022
61400	5-HT1D	-23.73	-30.22	-30.57	4.15	-20.09		Feb 21, 2022
61400	5-HT1E	17.61	3.92	-3.95	-5.41	3.04		Feb 23, 2022
61400	5-HT2A	6.00	18.60	9.78	9.78	11.04		Feb 24, 2022
61400	5-HT2B	21.35	10.67	17.04	24.62	18.42		Feb 23, 2022
61400	5-HT2C	29.39	7.92	-6.16	33.85	16.25		Feb 23, 2022
61400	5-HT3	-2.43	5.31	9.14	-5.70	1.58		Jun 16, 2022
61400	5-HT4	5.09	-29.64	3.54	20.09	-0.23		Feb 21, 2022
61400	5-HT5A	8.30	-19.04	-27.33	4.50	-8.39		Feb 11, 2022
61400	5-HT6	11.81	3.95	-7.03	-9.10	-0.09		Feb 24, 2022
61400	5-HT7A	-13.54	-18.61	-49.72	-17.57	-24.86		Feb 11, 2022
61400	A1	22.97	40.96	15.31	32.15	27.85		Feb 11, 2022
61400	A2A	22.83	15.43	36.06	35.35	27.42		Jun 15, 2022
61400	Alpha1A	-30.20	-29.94	-21.07	-16.00	-24.30		Feb 21, 2022
61400	Alpha1B	-25.30	-17.18	-16.06	-2.31	-15.21		Feb 21, 2022
61400	Alpha1D	-9.26	-16.34	-31.64	-2.78	-15.01		Feb 24, 2022
61400	Alpha2A	25.65	13.52	7.88	16.86	15.98		May 15, 2022
61400	Alpha2B	26.10	40.22	30.71	33.37	32.60		May 15, 2022
61400	Alpha2C	20.85	23.35	16.62	25.72	21.64		May 15, 2022
61400	Beta1	31.32	-2.82	0.21	21.98	12.67		Feb 25, 2022
61400	Beta2	-16.67	-2.24	9.33	13.48	0.97		Feb 21, 2022

vestigator/web/

61400	Beta3	27.95	46.31	17.41	27.36	29.76		Feb 18, 2022
61400	AT2	4.58	-37.18	-7.23	-24.13	-15.99		Feb 25, 2022
61400	BZP Rat Brain Site	39.80	41.75	19.88	35.11	34.14		Feb 24, 2022
61400	D1	30.77	10.00	9.75	12.92	15.86		Mar 27, 2022
61400	D2	33.47	21.11	-4.55	4.32	13.59		Feb 17, 2022
61400	D3	45.62	38.41	33.95	38.83	39.20		Feb 17, 2022
61400	D4	50.12	34.72	10.05	29.49	31.10		Feb 22, 2022
61400	D5	18.01	-2.56	-23.03	-12.88	-5.12		Feb 23, 2022
61400	DAT	32.82	18.68	24.70	20.52	24.18		Feb 24, 2022
61400	DOR	0.21	-2.04	-5.75	-0.80	-2.10		Feb 24, 2022
61400	GABAA	-18.96	-7.96	17.16	-28.38	-9.54		Mar 03, 2022
61400	H1	11.89	-6.70	-18.84	36.35	5.68		Feb 28, 2022
61400	H2	9.27	12.72	-8.77	6.38	4.90		Feb 25, 2022
61400	H3	-6.02	-25.45	-17.94	-8.04	-14.36		Feb 23, 2022
61400	H4	11.13	-8.86	-59.02	-1.79	-14.64		Feb 18, 2022
61400	KOR	33.14	-2.29	9.69	-1.29	9.81		Feb 21, 2022
61400	M1	22.82	15.87	21.69	35.21	23.90		Feb 22, 2022
61400	M2	13.64	8.72	-1.30	9.31	7.59		Feb 22, 2022
61400	M3	-0.85	0.21	57.25	28.69	21.33		Feb 21, 2022
61400	M4	23.75	13.18	6.07	14.17	14.29		Feb 22, 2022
61400	M5	-10.08	-5.38	-12.86	23.73	-1.15		Feb 22, 2022
61400	MOR	9.05	6.83	6.67	5.40	6.99		Feb 24, 2022
61400	NET	30.60	9.92	16.81	-17.11	10.06		Feb 28, 2022
61400	PBR	15.20	-24.09	-81.86	-42.16	-33.23		Jul 01, 2022
61400	SERT	-9.23	-13.02	-21.45	-31.59	-18.82		Feb 24, 2022
61400	Sigma 1	71.41	64.64	59.33	61.76	64.29	Secondary	Feb 22, 2022
61400	Sigma 2	13.92	0.81	26.00	24.55	16.32		Feb 18, 2022
61400	AMPA	9.02	6.60	10.29	6.85	8.19		Feb 18, 2022
61400	Kainate (Rat Brain)	14.23	28.15	12.18	29.38	20.99		Feb 18, 2022
61400	NMDA	90.13	87.18	86.56	83.95	86.96	Secondary	Feb 22, 2022

61400	NR2B	36.50	43.94	-3.38	49.01	31.52		Feb 10, 2022
61400	HCA2	10.83	60.95	13.97	52.34	34.52		Feb 24, 2022
61400	Ca channel human	-2.20	11.58	-29.45	46.86	6.70		Feb 10, 2022
61400	HERG	-20.74	27.39	1.42	18.20	6.57		Feb 21, 2022
61400	M1 D	43.74	16.85	14.66	58.28	33.38		Mar 02, 2022
61400	M2 D	38.86	12.69	32.54	83.08	41.79		Mar 02, 2022
61400	M3D	11.92	4.54	9.83	20.47	11.69		Mar 02, 2022
61400	M4 D	7.49	4.91	9.35	-1.83	4.98		Mar 02, 2022
61400	M5 D	17.92	5.74	16.73	13.02	13.35		Mar 02, 2022
61400	NTS1	3.49	20.32	17.11	4.89	11.45		Feb 10, 2022
61400	NOP	37.42	29.32	28.87	27.07	30.67		Feb 18, 2022
61400	OT	14.56	20.84	20.14	12.18	16.93		Feb 10, 2022
61400	V1A	23.36	-0.57	8.70	6.76	9.56		Feb 11, 2022
61400	V1B	2.25	-0.22	-2.98	6.37	1.36		Feb 28, 2022
61400	V2	-10.84	2.62	-4.30	-6.02	-4.64		Dec 05, 2022

vestigator/web/

61836	5-HT1A	12.20	14.16	12.20	-12.52	6.51		May 06, 2022
61836	5-HT1B	21.57	18.78	7.30	6.59	13.56		May 06, 2022
61836	5-HT1D	36.24	34.02	36.07	25.85	33.05		May 06, 2022
61836	5-HT1E	-0.28	12.59	-3.79	3.75	3.07		Apr 07, 2022
61836	5-HT2A	28.44	21.78	27.92	42.62	30.19		May 06, 2022
61836	5-HT2B	30.35	16.75	27.21	21.70	24.00		May 06, 2022
61836	5-HT2C	14.26	-2.66	-6.83	9.49	3.57		May 10, 2022
61836	5-HT3	8.80	5.31	3.27	12.23	7.40		May 06, 2022
61836	5-HT4	-0.37	5.85	3.70	22.58	7.94		Aug 23, 2022
61836	5-HT5A	19.14	27.38	24.76	31.08	25.59		May 06, 2022
61836	5-HT6	69.39	52.54	40.79	47.97	52.67	Secondary	Jun 15, 2022
61836	5-HT7A	49.69	1.80	-1.03	20.39	17.71		May 10, 2022
61836	A1	47.74	-4.22	60.14	82.58	46.56		Jul 06, 2022
61836	A2A	35.53	35.58	45.10	48.25	41.12		Jun 28, 2022

61836	Alpha1A	22.07	45.35	54.04	55.09	44.14		Jun 17, 2022
61836	Alpha1B	-35.51	1.95	15.36	34.16	3.99		Jun 08, 2022
61836	Alpha1D	38.32	10.51	29.41	31.77	27.50		May 26, 2022
61836	Alpha2A	35.12	10.66	1.13	8.98	13.97		Jun 23, 2022
61836	Alpha2B	64.15	43.47	40.58	39.38	46.90		Jun 08, 2022
61836	Alpha2C	63.05	45.44	30.56	24.88	40.98		Jun 08, 2022
61836	Beta1	-14.23	-12.66	3.22	6.04	-4.41		Apr 07, 2022
61836	Beta2	2.79	10.86	21.47	4.53	9.91		Apr 07, 2022
61836	Beta3	19.26	9.92	10.57	23.29	15.76		Apr 07, 2022
61836	AT2	79.75	58.01	67.47	68.38	68.40	Secondary	May 13, 2022
61836	BZP Rat Brain Site	86.48	66.09	70.62	79.40	75.65	Secondary	Jun 16, 2022
61836	D1	69.25	55.12	52.41	46.63	55.85	Secondary	May 10, 2022
61836	D2	-10.01	11.94	7.84	9.53	4.83		Jun 17, 2022
61836	D3	40.96	4.62	21.63	14.41	20.41		Jun 17, 2022
61836	D4	31.49	34.85	8.54	9.05	20.98		Jun 17, 2022
61836	D5	43.32	29.30	37.03	29.21	34.72		May 10, 2022
61836	DAT	22.18	27.72	43.74	66.28	39.98		Apr 05, 2022
61836	DOR	52.66	32.37	32.66	33.31	37.75		Jun 08, 2022
61836	GABAA	15.75	10.07	-14.76	-72.18	-15.28		Jun 07, 2022
61836	H1	57.51	36.59	41.90	21.96	39.49		May 06, 2022
61836	H2	16.75	14.45	24.66	12.14	17.00		Apr 07, 2022
61836	H3	9.90	7.84	-24.89	-23.52	-7.67		Jun 22, 2022
61836	H4	32.67	-12.95	7.96	-6.77	5.23		Jun 15, 2022
61836	KOR	102.29	99.53	90.55	89.69	95.52	Secondary	May 11, 2022
61836	M1	24.85	5.29	2.06	0.79	8.25		Apr 05, 2022
61836	M2	-1.76	-5.06	7.30	15.50	4.00		Apr 05, 2022
61836	M3	-0.30	15.89	13.00	14.67	10.82		Apr 05, 2022
61836	M4	-9.88	2.25	8.61	0.29	0.32		Apr 05, 2022
61836	M5	47.72	51.95	29.66	33.05	40.60		Apr 05, 2022
61836	MOR	44.82	40.12	36.77	35.03	39.19		May 11, 2022

61836	NET	26.89	6.68	27.81	9.81	17.80		May 31, 2022
61836	PBR	112.99	107.88	105.35	97.92	106.04	Secondary	Jun 17, 2022
61836	SERT	-17.90	-13.21	2.22	-13.88	-10.69		May 10, 2022
61836	Sigma 1	6.44	14.64	30.25	13.08	16.10		May 31, 2022
61836	Sigma 2	86.63	87.69	61.90	68.22	76.11	Secondary	May 02, 2022
61836	AMPA	16.55	-10.34	25.52	89.66	30.35		May 09, 2023
61836	Kainate (Rat Brain)	-6.48	0.00	-31.05	-3.11	-13.55		May 13, 2022
61836	NMDA	35.14	25.90	32.90	40.71	33.66		Jul 01, 2022
61836	NR2B	38.63	4.47	29.19	-33.75	9.64		Aug 30, 2022
61836	HCA2	-5.48	-2.95	6.42	-1.47	-0.87		May 13, 2022
61836	Ca channel human	19.52	11.57	-2.42	24.09	13.19		Jul 05, 2022
61836	HERG	49.60	54.30	22.62	13.63	35.04		May 11, 2022
61836	M3D	14.54	-16.09	-9.12	-39.75	-12.61		Jan 20, 2023
61836	M4 D	33.63	23.34	-2.84	4.74	14.72		Sep 06, 2022

61836	Alpha2Beta2	2.13	-3.22	-2.78	2.02	-0.46		Mar 31, 2022
61836	Alpha2Beta4	1.51	4.58	3.35	8.80	4.56		Mar 31, 2022
61836	Alpha3Beta2	24.34	-9.59	2.31	-6.64	2.61		Mar 31, 2022
61836	Alpha3Beta4	6.36	9.01	8.73	17.13	10.31		Mar 31, 2022
61836	Alpha4Beta2	13.21	-2.79	4.78	-1.54	3.42		Apr 01, 2022
61836	Alpha4Beta2 (Rat Brain)	-1.24	9.74	-2.79	1.78	1.87		Apr 01, 2022
61836	Alpha4Beta4	19.55	16.34	19.47	18.16	18.38		Apr 01, 2022
61836	Alpha7	9.62	-21.88	-5.50	-24.69	-10.61		Apr 01, 2022
61836	NOP	21.80	3.63	8.90	5.58	9.98		May 11, 2022
61836	OT	18.19	4.57	32.97	9.11	16.21		Jun 28, 2022
61836	V1A	10.83	13.04	-21.86	18.08	5.02		Aug 16, 2022
61836	V1B	9.25	-4.90	8.89	0.80	3.51		Jun 28, 2022
61836	V2	11.74	-2.73	0.61	15.97	6.40		Jun 28, 2022
61837	5-HT1A	43.53	32.23	20.56	25.10	30.36		May 06, 2022
61837	5-HT1B	13.65	22.81	-2.35	6.71	10.21		May 06, 2022

61837	5-HT1D	45.20	17.69	26.68	19.79	27.34		May 06, 2022
61837	5-HT1E	15.61	-0.83	-2.46	-3.30	2.26		Apr 07, 2022
61837	5-HT2A	5.96	16.42	-22.86	9.82	2.34		May 06, 2022
61837	5-HT2B	28.45	21.10	25.15	24.76	24.87		May 06, 2022
61837	5-HT2C	44.30	32.08	28.80	15.56	30.19		May 10, 2022
61837	5-HT3	36.05	26.40	21.59	29.13	28.29		May 06, 2022
61837	5-HT4	19.77	6.34	11.85	34.63	18.15		Aug 23, 2022
61837	5-HT5A	12.08	14.70	27.45	27.45	20.42		May 06, 2022
61837	5-HT6	27.52	15.89	11.11	28.83	20.84		Jun 15, 2022
61837	5-HT7A	0.99	-22.64	13.04	-1.99	-2.65		May 10, 2022
61837	A1	76.68	-62.08	60.14	100.30	43.76		Jul 06, 2022
61837	A2A	24.21	26.66	28.12	34.77	28.44		Jun 28, 2022
61837	Alpha1A	-2.78	44.03	56.06	60.89	39.55		Jun 17, 2022
61837	Alpha1B	22.27	28.35	17.85	37.06	26.38		Jun 08, 2022
61837	Alpha1D	22.07	12.11	31.37	27.47	23.26		May 26, 2022
61837	Alpha2B	58.21	49.72	43.55	49.00	50.12	Secondary	Jun 08, 2022
61837	Alpha2C	25.74	29.69	27.72	31.18	28.58		Jun 08, 2022
61837	Beta1	-13.51	-7.06	-14.16	-10.93	-11.42		Apr 07, 2022
61837	Beta2	-1.18	10.37	0.00	17.68	8.96		Apr 07, 2022
61837	Beta3	11.05	9.44	-32.27	6.54	-1.31		Apr 07, 2022
61837	AT2	34.52	-4.39	17.35	33.30	20.20		May 13, 2022
61837	BZP Rat Brain Site	81.95	85.63	80.53	77.70	81.45	Secondary	Jun 16, 2022
61837	D1	21.00	20.86	18.36	34.56	23.70		May 10, 2022
61837	D2	74.43	-18.46	56.82	-17.97	23.71		Jun 17, 2022
61837	D3	55.56	38.80	40.29	56.55	47.80		Jun 17, 2022
61837	D4	42.80	43.72	37.20	35.46	39.80		Jun 17, 2022
61837	D5	42.37	46.81	29.93	43.28	40.60		May 10, 2022
61837	DAT	-17.05	8.34	41.93	49.34	20.64		Apr 05, 2022
61837	DOR	46.96	30.86	29.84	22.27	32.48		Jun 08, 2022

61837	GABAA	9.50	35.27	28.16	31.20	26.03		Jun 07, 2022
61837	H1	77.52	64.90	65.57	54.22	65.55	Secondary	May 06, 2022
61837	H2	-14.56	-18.81	-12.61	-15.32	-15.33		Apr 07, 2022
61837	H3	-15.55	-11.30	-20.64	16.21	-7.82		Jun 22, 2022
61837	H4	-23.25	-9.78	-5.19	10.34	-6.97		Jun 15, 2022
61837	KOR	103.50	102.80	102.29	105.31	103.48	Secondary	May 11, 2022
61837	M1	-0.34	24.18	17.13	7.99	12.24		Apr 05, 2022
61837	M2	-22.88	2.49	2.02	-5.72	-6.02		Apr 05, 2022
61837	M3	8.95	25.07	16.01	2.66	13.17		Apr 05, 2022
61837	M4	11.39	31.50	37.75	17.86	24.63		Apr 05, 2022
61837	M5	14.42	24.02	20.91	23.73	20.77		Apr 05, 2022
61837	MOR	30.26	32.33	27.67	25.58	28.96		May 11, 2022
61837	NET	34.85	40.98	25.98	18.16	29.99		May 31, 2022
61837	PBR	110.95	9.06	99.22	76.23	73.87	Secondary	Jun 17, 2022
61837	SERT	-5.16	12.27	-2.92	7.73	2.98		May 10, 2022
61837	Sigma 1	26.32	18.32	43.69	21.29	27.41		May 31, 2022
61837	Sigma 2	78.62	82.70	64.61	82.86	77.20	Secondary	May 02, 2022
61837	AMPA	4.14	-2.07	13.79	17.93	8.45		May 09, 2023
61837	Kainate (Rat Brain)	-14.89	0.00	-34.08	-11.86	-20.28		May 13, 2022
61837	NMDA	39.73	25.57	29.51	36.18	32.75		Jul 01, 2022
61837	NR2B	29.19	-22.51	-1.15	-7.67	-0.54		Aug 30, 2022
61837	HCA2	14.31	-5.63	-15.01	-6.82	-3.29		May 13, 2022
61837	Ca channel human	14.64	24.47	9.34	13.74	15.55		Sep 23, 2022
61837	HERG	47.97	43.61	15.56	13.10	30.06		May 11, 2022
61837	M3D	118.38	111.65	112.40	77.54	104.99		Jan 20, 2023
61837	M4 D	101.39	0.00	96.92	94.84	97.72		Sep 06, 2022
61837	Alpha2Beta2	2.24	7.04	-6.93	1.69	1.01		Mar 31, 2022
61837	Alpha2Beta4	4.28	1.56	-6.03	2.32	0.53		Mar 31, 2022
61837	Alpha3Beta2	7.56	13.00	-3.32	-1.57	3.92		Mar 31, 2022

61837	Alpha3Beta4	-0.32	-2.41	2.91	0.04	0.06		Mar 31, 2022
61837	Alpha4Beta2	0.72	4.94	3.92	4.23	3.45		Apr 01, 2022
61837	Alpha4Beta2 (Rat Brain)	-8.25	2.06	-5.85	-4.06	-4.03		Apr 01, 2022
61837	Alpha4Beta4	9.47	2.61	7.47	5.91	6.37		Apr 01, 2022
61837	Alpha7	-8.43	-29.23	-10.76	-6.75	-13.79		Apr 01, 2022
61837	NOP	-8.00	26.98	-13.08	-3.41	0.62		May 11, 2022
61837	OT	23.45	26.97	14.82	35.02	25.07		Jun 28, 2022
61837	V1A	19.93	19.56	30.86	5.42	18.94		Aug 16, 2022
61837	V1B	-0.17	8.85	-0.13	-1.62	1.73		Jun 28, 2022
61837	V2	9.14	13.38	27.98	19.72	17.56		Jun 28, 2022
71288	5-HT1A	19.22	45.83	-20.28	-23.55	5.31		Jan 13, 2023
71288	5-HT1B	21.21	17.60	1.68	-10.25	7.56		Jan 10, 2023
71288	5-HT1D	23.50	-4.70	-3.97	4.92	4.94		Jan 10, 2023
71288	5-HT1E	-6.68	-1.05	-18.11	-7.92	-8.44		Mar 03, 2023
71288	5-HT2A	16.60	14.07	-2.57	-1.72	6.60		Jan 10, 2023
71288	5-HT2B	28.49	20.25	22.99	26.97	24.68		Jan 13, 2023
71288	5-HT2C	-13.42	31.78	14.43	1.21	8.50		Jan 11, 2023
71288	5-HT3	-5.68	5.52	-25.76	-3.93	-7.46		Jan 11, 2023
71288	5-HT5A	28.82	29.39	29.49	7.13	23.71		Jan 13, 2023
71288	5-HT6	-2.12	-10.12	-7.69	-4.46	-6.10		Jan 13, 2023
71288	5-HT7A	9.61	28.35	-23.66	17.33	7.91		Jan 13, 2023
71288	A1	56.80	-17.75	15.38	26.04	20.12		Jan 25, 2023
71288	A2A	12.89	-2.80	-5.81	-3.23	0.26		Apr 19, 2023
71288	Alpha1A	4.31	2.59	3.41	7.67	4.50		Jan 23, 2023
71288	Alpha1B	7.88	0.13	-3.61	6.38	2.70		Jan 23, 2023
71288	Alpha1D	10.09	10.74	9.88	15.82	11.63		Jan 23, 2023
71288	Alpha2A	12.27	1.35	5.13	6.81	6.39		Jan 25, 2023
71288	Alpha2B	22.91	19.78	12.11	12.97	16.94		Jan 25, 2023
71288	Alpha2C	15.21	1.36	0.36	-1.64	3.82		Jan 25, 2023
71288	Beta1	-21.64	-6.94	19.96	-17.07	-6.42		Jan 25, 2023

71288	Beta2	24.45	32.02	12.62	5.18	18.57		Jan 25, 2023
71288	AT2	22.68	2.93	-26.37	18.99	4.56		Apr 10, 2023
71288	BZP Rat Brain Site	76.33	80.61	67.20	90.85	78.75	Secondary	Mar 06, 2023
71288	D1	68.68	-32.70	14.88	-5.11	11.44		Jan 25, 2023
71288	D2	8.90	41.54	3.84	16.31	17.65		Jan 13, 2023
71288	D3	11.42	44.49	-19.50	8.05	11.12		Jan 13, 2023
71288	D4	-5.57	50.53	-28.88	-9.01	1.77		Jan 13, 2023
71288	D5	12.78	12.34	-11.54	3.10	4.17		Jan 13, 2023
71288	DAT	8.75	-10.89	-19.61	-55.24	-19.25		Jan 13, 2023
71288	DOR	12.32	-5.53	5.98	0.81	3.40		Jan 25, 2023
71288	GABAA	-1.50	23.10	10.93	67.00	24.88		Jan 24, 2023
71288	H1	38.18	7.09	8.48	10.37	16.03		Jan 13, 2023
71288	H2	-4.04	-14.76	-12.45	-6.79	-9.51		Jan 13, 2023
71288	H3	-0.09	33.05	11.04	13.04	14.26		Jan 17, 2023
71288	H4	1.11	2.44	1.62	-2.19	0.75		Jan 17, 2023

71288	KOR	63.37	50.69	51.35	47.19	53.15	Secondary	Jan 25, 2023
71288	M1	-2.98	3.45	-47.27	-10.58	-14.35		Jan 13, 2023
71288	M2	1.75	0.99	8.14	-7.08	0.95		Jan 17, 2023
71288	M3	4.65	10.98	-95.78	5.23	-18.73		Jan 20, 2023
71288	M4	-9.25	-7.11	-32.52	-17.90	-16.70		Jan 20, 2023
71288	M5	-5.29	-1.74	-23.87	21.21	-2.42		Jan 20, 2023
71288	MOR	-5.45	-0.76	-15.37	-15.11	-9.17		Jan 25, 2023
71288	NET	19.47	-35.29	-71.73	35.82	-12.93		Jan 19, 2023
71288	PBR	17.50	-2.74	15.40	14.63	11.20		Jan 10, 2023
71288	SERT	5.03	-17.60	10.47	5.92	0.96		Jan 25, 2023
71288	Sigma 1	-15.09	-16.13	-9.94	-14.99	-14.04		Jan 10, 2023
71288	Sigma 2	-5.29	-22.06	-11.64	-19.89	-14.72		Jan 10, 2023
71288	Kainate (Rat Brain)	6.72	15.56	20.32	-56.87	-3.57		Mar 09, 2023
71288	NMDA	-11.08	-2.10	-29.03	-41.09	-20.83		Feb 17, 2023
71288	NR2B	-18.46	-14.89	-10.72	2.59	-10.37		Jan 23, 2023

71288	HCA2	-59.49	16.98	-25.80	51.20	-4.28		Feb 16, 2023
71288	Ca channel human	16.42	-66.88	10.51	80.27	10.08		Jan 31, 2023
71288	HERG	5.95	9.52	-20.04	-0.22	-1.20		Jan 13, 2023
71288	Alpha2Beta2	-5.67	-0.06	-7.08	5.79	-1.76		Mar 24, 2023
71288	Alpha2Beta4	7.53	15.15	-1.91	5.72	6.62		Mar 24, 2023
71288	Alpha3Beta2	9.90	-2.79	-0.60	-3.45	0.77		Mar 24, 2023
71288	Alpha3Beta4	-1.88	-2.78	0.08	5.48	0.23		Mar 24, 2023
71288	Alpha4Beta2	2.56	3.85	-11.81	-4.30	-2.43		Mar 24, 2023
71288	Alpha4Beta2 (Rat Brain)	7.63	7.70	2.11	5.05	5.62		Mar 24, 2023
71288	Alpha4Beta4	2.12	13.59	6.71	-6.14	4.07		Mar 24, 2023
71288	Alpha7	1.00	15.83	19.13	10.89	11.71		Mar 24, 2023
71288	NOP	6.59	-15.67	-3.61	-2.02	-3.68		Jan 23, 2023
71288	OT	22.52	-14.85	18.63	29.64	13.99		Jan 25, 2023
71288	V1A	-7.96	3.90	-2.60	-11.73	-4.60		Jan 10, 2023
71288	V1B	-11.29	16.50	-11.48	-2.34	-2.15		Jan 31, 2023

71288	V2	18.37	16.71	25.19	39.19	24.87		Jan 31, 2023
71289	5-HT1A	0.75	16.14	11.56	-19.67	2.20		Jan 13, 2023
71289	5-HT1B	14.07	10.45	4.40	8.37	9.32		Jan 10, 2023
71289	5-HT1D	-1.06	-0.70	-11.36	1.02	-3.03		Jan 10, 2023
71289	5-HT1E	26.59	10.73	5.86	-32.56	2.66		Jan 13, 2023
71289	5-HT2A	1.12	8.38	6.80	7.23	5.88		Jan 10, 2023
71289	5-HT2B	21.91	4.13	22.56	5.07	13.42		Jan 13, 2023
71289	5-HT2C	37.76	26.25	22.33	21.97	27.08		Jan 11, 2023
71289	5-HT3	-3.06	8.65	-7.83	-11.17	-3.35		Jan 11, 2023
71289	5-HT5A	26.16	15.03	21.40	16.36	19.74		Jan 13, 2023
71289	5-HT6	3.50	4.74	22.27	9.85	10.09		Jan 13, 2023
71289	5-HT7A	17.99	30.55	30.55	32.75	27.96		Jan 13, 2023
71289	A1	56.44	12.45	7.42	16.59	23.23		Jan 25, 2023
71289	A2A	2.06	-3.78	0.83	17.57	4.17		Apr 19, 2023
71289	Alpha1A	11.11	9.44	6.03	7.11	8.42		Jan 23, 2023

71289	Alpha1B	4.14	-0.65	4.85	-0.62	1.93		Jan 23, 2023
71289	Alpha1D	25.07	22.85	14.58	24.64	21.79		Jan 23, 2023
71289	Alpha2A	9.48	4.51	4.08	-0.64	4.36		Jan 25, 2023
71289	Alpha2B	22.10	20.48	15.97	22.02	20.14		Jan 25, 2023
71289	Alpha2C	3.23	-2.62	-3.24	-1.62	-1.06		Jan 25, 2023
71289	Beta1	11.64	1.64	9.22	16.81	9.83		Jan 25, 2023
71289	Beta2	34.29	38.69	10.58	13.93	24.37		Jan 25, 2023
71289	AT2	35.92	37.66	26.37	30.06	32.50		Apr 10, 2023
71289	BZP Rat Brain Site	102.77	92.53	96.81	108.92	100.26	Secondary	Mar 06, 2023
71289	D1	56.80	73.34	65.29	75.56	67.75	Secondary	Jan 25, 2023
71289	D2	27.53	-7.82	20.93	2.01	10.66		Jan 13, 2023
71289	D3	13.57	8.12	9.74	-11.60	4.96		Jan 13, 2023
71289	D4	15.08	-39.65	5.08	10.34	-2.29		Jan 13, 2023
71289	D5	20.32	11.97	8.64	-1.34	9.90		Jan 13, 2023
71289	DAT	-32.99	1.62	48.45	22.42	9.88		Jan 13, 2023

71289	DOR	9.39	3.00	7.25	4.58	6.06		Jan 25, 2023
71289	GABAA	28.65	33.94	45.84	50.60	39.76		Jan 24, 2023
71289	H1	39.67	36.49	26.26	18.31	30.18		Jan 13, 2023
71289	H2	6.36	-12.73	-3.10	4.16	-1.33		Jan 13, 2023
71289	H3	15.38	2.31	6.16	10.77	8.66		Jan 17, 2023
71289	H4	-3.73	2.24	-3.11	-14.11	-4.68		Jan 17, 2023
71289	KOR	49.51	42.21	41.85	42.52	44.02		Jan 25, 2023
71289	M1	8.28	11.20	6.08	-5.90	4.92		Jan 13, 2023
71289	M2	-6.77	4.49	2.51	-3.42	-0.80		Jan 17, 2023
71289	M3	4.27	35.32	41.65	19.61	25.21		Jan 20, 2023
71289	M4	-1.45	-23.23	-3.16	-7.97	-8.95		Jan 20, 2023
71289	M5	7.80	21.86	18.14	17.65	16.36		Jan 20, 2023
71289	MOR	17.57	5.22	-4.37	1.61	5.01		Jan 25, 2023
71289	NET	71.91	19.29	15.91	-12.53	23.65		Jan 19, 2023
71289	PBR	33.00	26.96	-0.42	13.93	18.37		Jan 10, 2023

71289	SERT	-12.13	0.57	16.08	13.06	4.40		Jan 25, 2023
71289	Sigma 1	-7.71	-9.94	-16.33	-16.38	-12.59		Jan 10, 2023
71289	Sigma 2	-4.93	-17.44	-8.01	-4.18	-8.64		Jan 10, 2023
71289	Kainate (Rat Brain)	16.58	35.96	22.70	28.82	26.02		Mar 09, 2023
71289	NMDA	-4.35	21.18	-18.09	-15.01	-4.07		Feb 17, 2023
71289	NR2B	15.42	8.28	6.65	5.98	9.08		Jan 23, 2023
71289	HCA2	37.44	50.79	-66.20	-0.64	5.35		Feb 16, 2023
71289	Ca channel human	107.95	95.78	32.45	84.64	80.21	Secondary	Jan 31, 2023
71289	HERG	23.54	-26.28	20.34	11.70	7.33		Jan 13, 2023
71289	Alpha2Beta2	-13.16	-3.33	-8.25	-10.58	-8.83		Mar 24, 2023
71289	Alpha2Beta4	9.47	-4.52	1.73	-12.94	-1.57		Mar 24, 2023
71289	Alpha3Beta2	9.03	-14.39	-15.26	-6.73	-6.84		Mar 24, 2023
71289	Alpha3Beta4	11.94	7.73	8.93	12.54	10.29		Mar 24, 2023
71289	Alpha4Beta2	11.88	8.12	-5.47	0.74	3.82		Mar 24, 2023
71289	Alpha4Beta2 (Rat Brain)	1.47	5.76	3.54	0.97	2.94		Mar 24, 2023
71289	Alpha4Beta4	1.66	13.59	2.81	1.66	4.93		Mar 24, 2023
71289	Alpha7	17.48	35.37	-1.59	25.96	19.31		Mar 24, 2023
71289	NOP	2.88	-29.71	7.52	-11.69	-7.75		Jan 23, 2023
71289	OT	41.20	-44.44	28.13	7.40	8.07		Jan 25, 2023
71289	V1A	0.94	3.63	-5.22	-0.76	-0.35		Jan 10, 2023
71289	V1B	-1.59	1.33	2.87	2.15	1.19		Jan 31, 2023
71289	V2	15.62	11.85	24.18	17.87	17.38		Jan 31, 2023
71290	5-HT1A	-8.09	-5.53	5.34	-4.66	-3.24		Jan 13, 2023
71290	5-HT1B	9.73	4.85	-2.11	15.70	7.04		Jan 10, 2023
71290	5-HT1D	-20.83	-16.30	-20.47	-14.48	-18.02		Jan 10, 2023
71290	5-HT1E	12.83	-17.43	-14.71	4.50	-3.70		Jan 13, 2023
71290	5-HT2A	6.17	1.12	18.28	-6.78	4.70		Jan 10, 2023
71290	5-HT2B	-4.26	-15.46	-1.94	12.87	-2.20		Jan 13, 2023
71290	5-HT2C	31.53	-15.53	-8.84	-7.33	-0.04		Jan 11, 2023
71290	5-HT3	-8.76	-7.42	-13.53	-8.86	-9.64		Jan 11, 2023

71290	5-HT5A	5.33	5.04	9.70	-15.60	1.12		Jan 13, 2023
71290	5-HT6	-15.23	-1.61	10.03	-40.08	-11.72		Jan 13, 2023
71290	5-HT7A	-3.83	8.95	21.52	-30.94	-1.08		Jan 13, 2023
71290	A1	62.28	20.23	45.26	30.82	39.65		Jan 25, 2023
71290	A2A	9.45	-0.71	5.63	10.31	6.17		Apr 19, 2023
71290	Alpha1A	7.84	9.52	-0.25	-0.25	4.22		Jan 23, 2023
71290	Alpha1B	8.32	2.44	2.71	-1.30	3.04		Jan 23, 2023
71290	Alpha1D	6.69	1.39	2.58	3.98	3.66		Jan 23, 2023
71290	Alpha2A	-4.98	-4.54	-4.92	-11.87	-6.58		Jan 25, 2023
71290	Alpha2B	8.61	1.72	8.35	4.46	5.79		Jan 25, 2023
71290	Alpha2C	-4.40	-12.69	-10.96	-14.72	-10.69		Jan 25, 2023
71290	Beta1	-8.42	-12.24	9.96	11.04	0.09		Jan 25, 2023
71290	Beta2	39.91	19.10	0.06	20.64	19.93		Jan 25, 2023
71290	AT2	39.39	30.28	9.88	2.28	20.46		Apr 10, 2023
71290	BZP Rat Brain Site	99.60	107.61	100.72	98.67	101.65	Secondary	Mar 06, 2023

71290	D1	60.29	71.01	52.30	79.67	65.82	Secondary	Jan 25, 2023
71290	D2	33.03	20.56	-4.23	32.15	20.38		Jan 13, 2023
71290	D3	17.87	7.36	4.67	-13.28	4.16		Jan 13, 2023
71290	D4	36.57	13.78	8.59	10.73	17.42		Jan 13, 2023
71290	D5	1.84	-2.37	9.16	-42.07	-8.36		Jan 13, 2023
71290	DAT	2.49	-20.92	4.38	-64.84	-19.72		Jan 13, 2023
71290	DOR	-3.52	-13.84	-8.07	-16.38	-10.45		Jan 25, 2023
71290	GABAA	0.35	-18.16	45.84	26.27	13.58		Jan 24, 2023
71290	H1	14.74	29.34	6.49	-4.53	11.51		Jan 13, 2023
71290	H2	2.95	-8.55	0.20	-4.75	-2.54		Jan 13, 2023
71290	H3	1.56	-9.93	-7.45	-1.47	-4.32		Jan 17, 2023
71290	H4	-13.29	0.08	-7.43	-15.35	-9.00		Jan 17, 2023
71290	KOR	70.21	47.40	42.67	54.95	53.81	Secondary	Jan 25, 2023
71290	M1	0.38	0.38	-10.29	-33.38	-10.73		Jan 13, 2023
71290	M2	0.84	-0.68	-12.55	-5.25	-4.41		Jan 17, 2023

71290	M3	14.62	3.31	2.74	31.68	13.09		Jan 20, 2023
71290	M4	-9.89	-9.68	0.79	7.41	-2.84		Jan 20, 2023
71290	M5	14.75	2.79	12.16	11.35	10.26		Jan 20, 2023
71290	MOR	11.21	5.06	8.35	-0.82	5.95		Jan 25, 2023
71290	NET	31.73	-15.91	-9.87	-36.89	-7.74		Jan 19, 2023
71290	PBR	51.30	12.15	0.98	-25.62	9.70		Jan 10, 2023
71290	SERT	14.47	13.97	36.84	94.56	39.96		Jan 25, 2023
71290	Sigma 1	-14.65	-14.70	-11.43	-16.73	-14.38		Jan 10, 2023
71290	Sigma 2	3.87	-5.68	-26.13	-10.77	-9.68		Jan 10, 2023
71290	Kainate (Rat Brain)	27.80	14.54	-49.73	21.68	3.57		Mar 09, 2023
71290	NMDA	25.39	28.47	19.78	-6.59	16.76		Feb 17, 2023
71290	NR2B	7.62	-7.39	-8.66	-8.78	-4.30		Jan 23, 2023
71290	HCA2	4.86	4.07	-45.79	18.99	-4.47		Feb 16, 2023
71290	Ca channel human	121.75	-3.80	108.55	11.62	59.53	Secondary	Jan 31, 2023
71290	HERG	34.43	15.89	-0.55	0.10	12.47		Jan 13, 2023

71290	Alpha2Beta2	-4.97	-0.76	-10.12	-3.33	-4.80		Mar 24, 2023
71290	Alpha2Beta4	19.14	-5.20	-1.00	3.78	4.18		Mar 24, 2023
71290	Alpha3Beta2	-10.89	-11.32	-1.26	-10.67	-8.54		Mar 24, 2023
71290	Alpha3Beta4	27.85	12.24	16.74	17.04	18.47		Mar 24, 2023
71290	Alpha4Beta2	4.63	0.74	1.26	5.40	3.01		Mar 24, 2023
71290	Alpha4Beta2 (Rat Brain)	16.00	9.56	3.26	15.00	10.96		Mar 24, 2023
71290	Alpha4Beta4	2.12	-4.30	-4.99	-13.02	-5.05		Mar 24, 2023
71290	Alpha7	-3.47	25.96	30.90	21.95	18.84		Mar 24, 2023
71290	NOP	13.75	1.95	9.77	8.31	8.45		Jan 23, 2023
71290	OT	49.95	-5.99	26.08	-37.85	8.05		Jan 25, 2023
71290	V1A	-0.52	-3.26	2.75	-3.22	-1.06		Jan 10, 2023
71290	V1B	-3.59	4.51	10.40	-8.87	0.61		Jan 31, 2023
71290	V2	11.48	11.12	16.05	6.55	11.30		Jan 31, 2023
71291	5-HT1A	31.37	19.48	-15.85	16.17	12.79		Jan 13, 2023
71291	5-HT1B	6.39	7.65	3.22	6.84	6.03		Jan 10, 2023

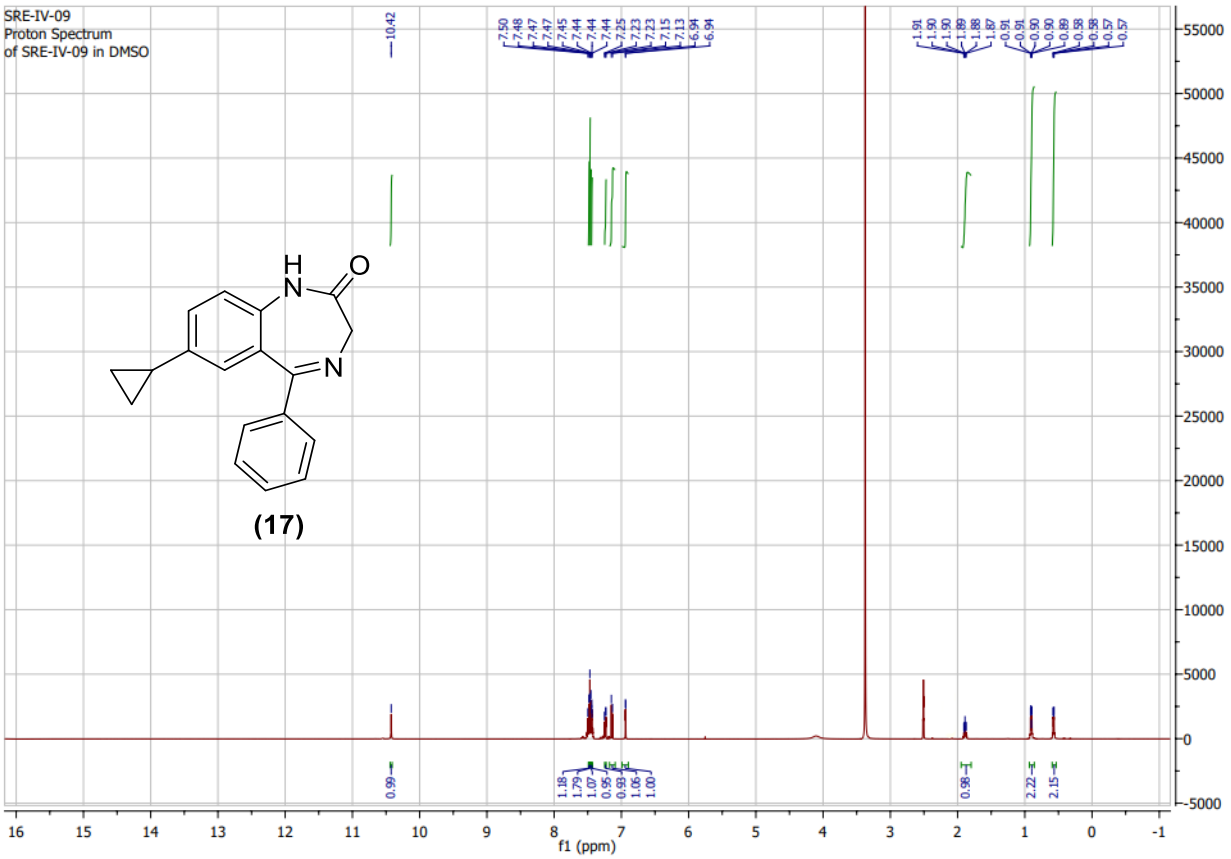
71291	5-HT1D	-18.33	-20.36	-21.30	-17.34	-19.33		Jan 10, 2023
71291	5-HT1E	20.21	0.10	5.50	-9.84	3.99		Jan 13, 2023
71291	5-HT2A	31.65	11.23	29.76	13.54	21.55		Jan 10, 2023
71291	5-HT2B	-8.81	-8.45	-2.81	-4.69	-6.19		Jan 13, 2023
71291	5-HT2C	14.99	17.85	32.93	20.16	21.48		Jan 11, 2023
71291	5-HT3	-11.79	-3.72	-6.60	-0.13	-5.56		Jan 11, 2023
71291	5-HT5A	-0.67	1.90	3.99	1.05	1.57		Jan 13, 2023
71291	5-HT6	-22.46	-4.28	14.73	8.28	-0.93		Jan 13, 2023
71291	5-HT7A	-5.37	-3.83	10.72	6.97	2.12		Jan 13, 2023
71291	A1	66.85	17.05	58.78	32.41	43.77		Jan 25, 2023
71291	A2A	5.08	-8.65	-6.80	7.72	-0.66		Apr 19, 2023
71291	Alpha1A	-5.16	-2.54	-3.01	2.46	-2.06		Jan 23, 2023
71291	Alpha1B	-5.20	0.20	-6.77	1.05	-2.68		Jan 23, 2023
71291	Alpha1D	6.04	4.63	5.71	5.71	5.52		Jan 23, 2023
71291	Alpha2A	5.26	-5.23	-3.37	-7.58	-2.73		Jan 25, 2023

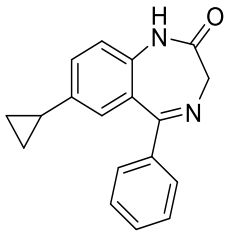
71291	Alpha1D	6.04	4.63	5.71	5.71	5.52		Jan 23, 2023
71291	Alpha2A	5.26	-5.23	-3.37	-7.58	-2.73		Jan 25, 2023
71291	Alpha2B	3.03	3.39	7.44	15.71	7.39		Jan 25, 2023
71291	Alpha2C	-0.78	-0.58	-14.25	-10.34	-6.49		Jan 25, 2023
71291	Beta1	13.18	10.77	13.99	-3.45	8.62		Jan 25, 2023
71291	Beta2	23.50	17.65	0.01	-8.24	8.23		Jan 25, 2023
71291	AT2	30.06	40.91	2.50	7.49	20.24		Apr 10, 2023
71291	BZP Rat Brain Site	114.13	107.43	101.28	99.79	105.66	Secondary	Mar 06, 2023
71291	D1	77.56	61.74	66.85	79.34	71.37	Secondary	Jan 25, 2023
71291	D2	70.37	53.79	45.94	64.57	58.67	Secondary	Jan 13, 2023
71291	D3	-13.44	3.14	13.34	32.14	8.80		Jan 13, 2023
71291	D4	57.41	60.92	45.79	47.28	52.85	Secondary	Jan 13, 2023
71291	D5	-2.52	22.09	1.25	27.93	12.19		Jan 13, 2023
71291	DAT	-41.72	26.92	3.37	33.76	5.58		Jan 13, 2023
71291	DOR	1.16	0.51	1.86	-3.87	-0.09		Jan 25, 2023

71291	GABAA	51.92	45.31	-49.63	77.05	31.16		Jan 24, 2023
71291	H1	8.78	9.77	6.39	36.09	15.26		Jan 13, 2023
71291	H2	3.94	-1.18	2.12	-24.39	-4.88		Jan 13, 2023
71291	H3	23.49	-3.94	-0.03	-7.73	2.95		Jan 17, 2023
71291	H4	-16.17	-7.22	-1.77	15.19	-2.49		Jan 17, 2023
71291	KOR	69.23	66.30	64.15	64.40	66.02	Secondary	Jan 25, 2023
71291	M1	6.38	2.58	32.98	-6.49	8.86		Jan 13, 2023
71291	M2	-2.97	-6.16	-9.97	-13.01	-8.03		Jan 17, 2023
71291	M3	19.03	33.79	12.32	20.18	21.33		Jan 20, 2023
71291	M4	-6.37	17.34	-25.69	-9.46	-6.05		Jan 20, 2023
71291	M5	1.01	-12.40	1.33	7.80	-0.57		Jan 20, 2023
71291	MOR	-15.32	-8.80	-2.60	-6.15	-8.22		Jan 25, 2023
71291	NET	76.00	58.76	37.96	5.42	44.54		Jan 19, 2023
71291	PBR	72.32	62.70	40.06	39.98	53.77	Secondary	Jan 10, 2023

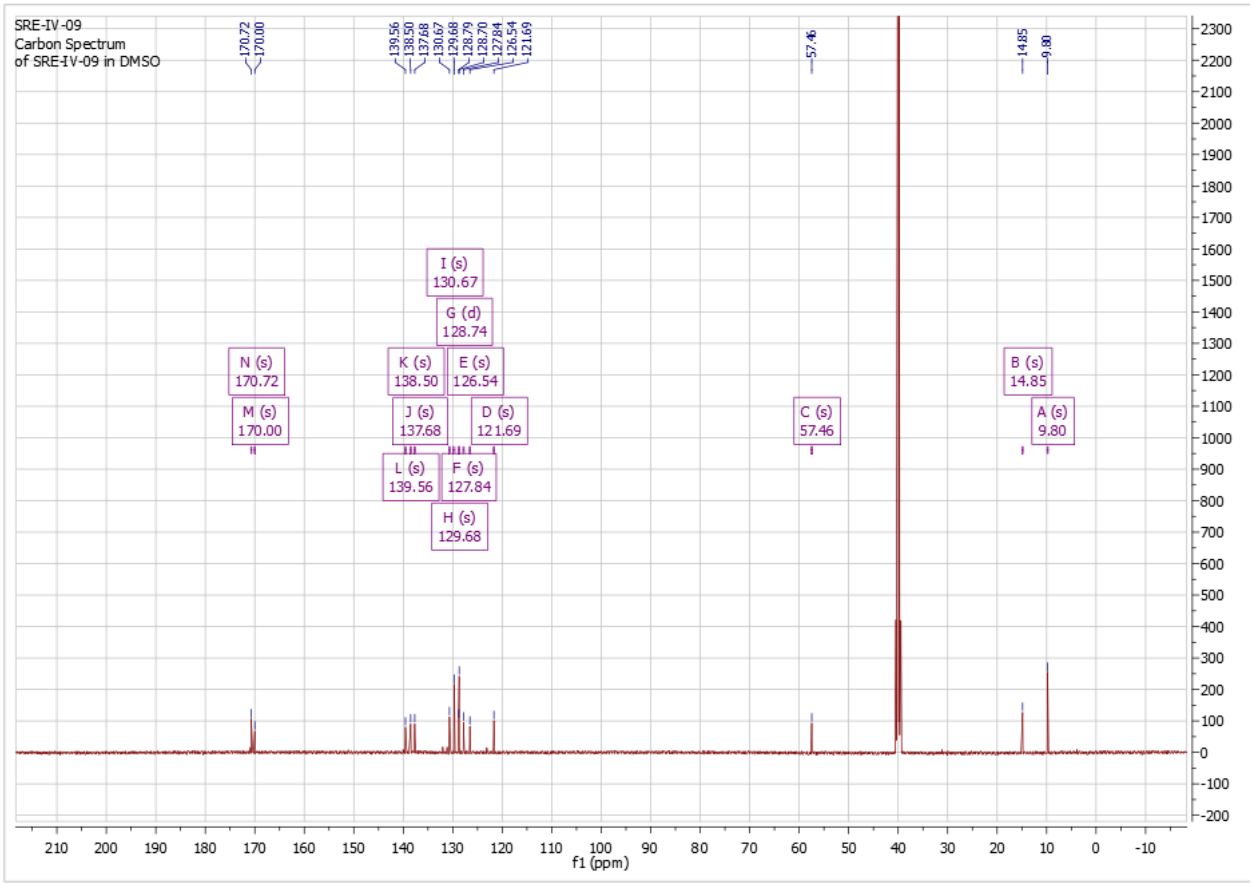
71291	SERT	26.28	21.99	18.76	27.58	23.65		Jan 25, 2023
71291	Sigma 1	7.21	13.01	2.85	9.79	8.22		Jan 10, 2023
71291	Sigma 2	60.23	48.51	43.10	42.19	48.51		Jan 10, 2023
71291	Kainate (Rat Brain)	25.42	7.74	-33.75	29.84	7.31		Mar 09, 2023
71291	NMDA	38.85	17.53	23.42	16.69	24.12		Feb 17, 2023
71291	NR2B	15.91	24.50	15.73	7.68	15.96		Jan 23, 2023
71291	HCA2	20.56	-3.39	-98.00	33.52	-11.83		Feb 16, 2023
71291	Ca channel human	-15.72	32.11	-69.71	53.70	0.10		Jan 31, 2023
71291	HERG	28.69	10.42	8.35	12.02	14.87		Jan 13, 2023
71291	Alpha2Beta2	-3.33	6.26	-6.84	2.28	-0.41		Mar 24, 2023
71291	Alpha2Beta4	1.28	10.38	3.67	-0.20	3.78		Mar 24, 2023
71291	Alpha3Beta2	-26.42	-5.63	7.93	-6.07	-7.55		Mar 24, 2023
71291	Alpha3Beta4	16.89	24.25	11.19	11.34	15.92		Mar 24, 2023
71291	Alpha4Beta2	-2.36	9.42	-1.07	-0.94	1.26		Mar 24, 2023
71291	Alpha4Beta2 (Rat Brain)	4.26	-2.76	-0.18	6.55	1.97		Mar 24, 2023

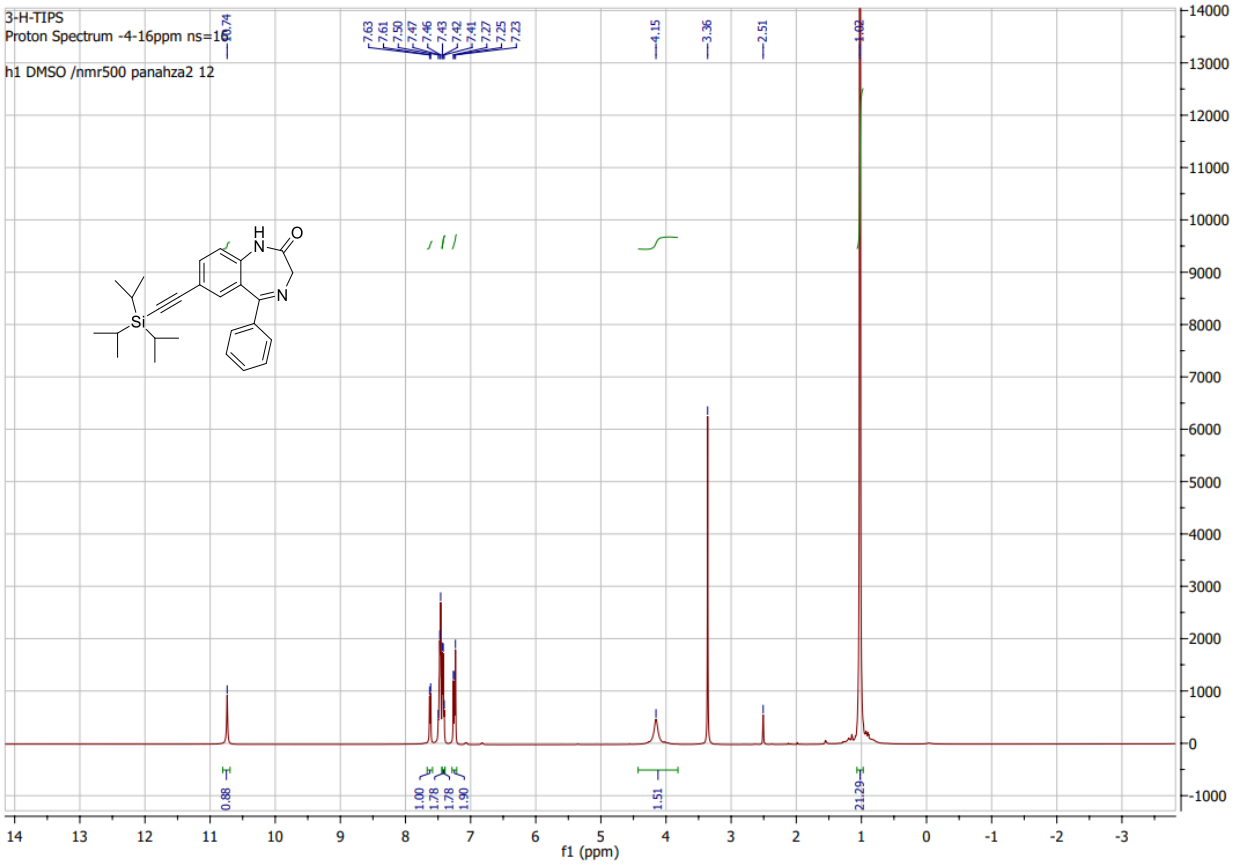
71291	Alpha4Beta4	-2.69	-5.91	-8.43	-6.36	-5.85		Mar 24, 2023
71291	Alpha7	27.13	46.91	47.62	52.80	43.62		Mar 24, 2023
71291	NOP	-9.44	2.35	-11.30	-1.62	-5.00		Jan 23, 2023
71291	OT	25.22	22.73	38.61	-18.52	17.01		Jan 25, 2023
71291	V1A	-10.50	4.29	-0.29	-0.87	-1.84		Jan 10, 2023
71291	V1B	-11.81	0.27	15.01	9.46	3.23		Jan 31, 2023
71291	V2	6.48	11.27	15.40	17.21	12.59		Jan 31, 2023

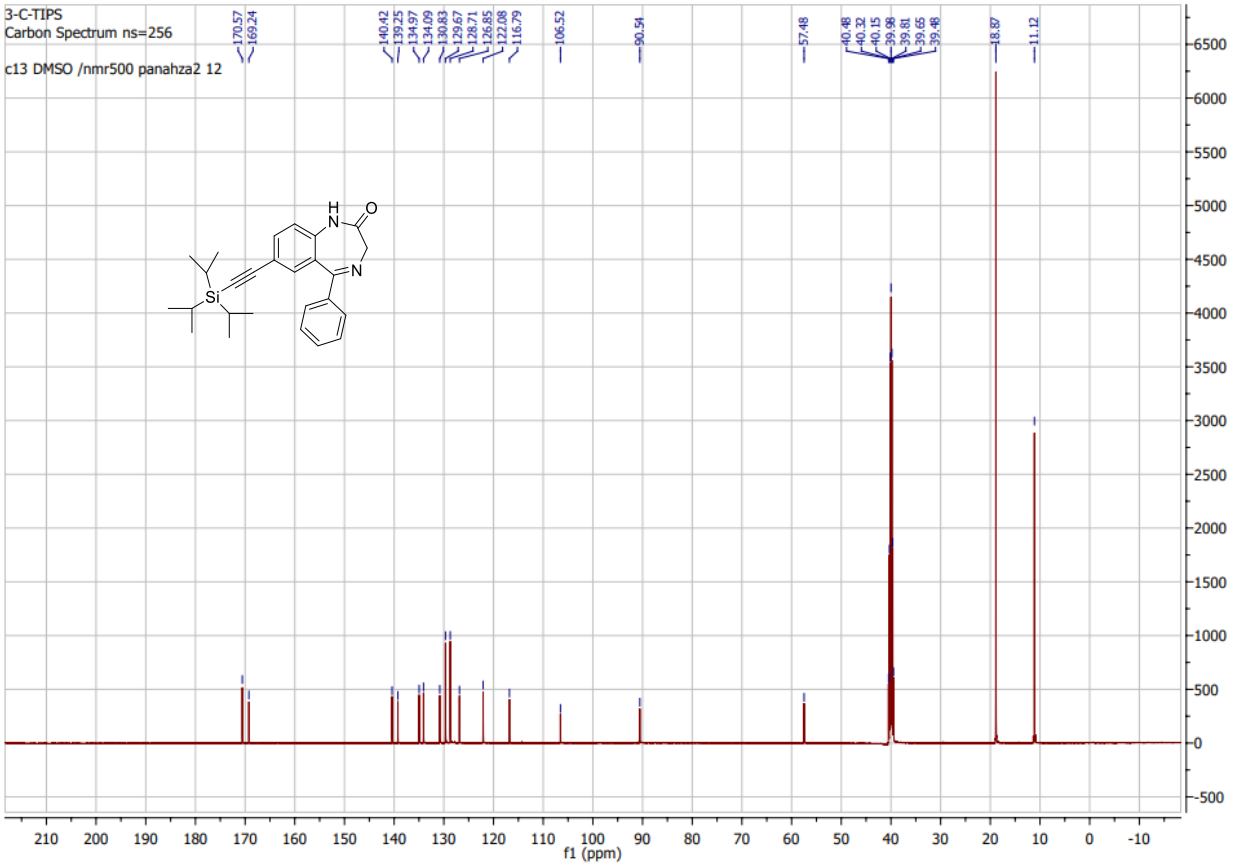

SRE-IV-09
Proton Spectrum
of SRE-IV-09 in DMSO
H
N
O
N
(17)
f1 (ppm)

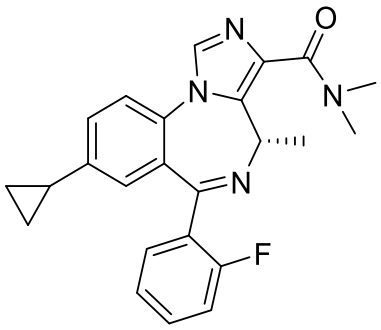


(17)

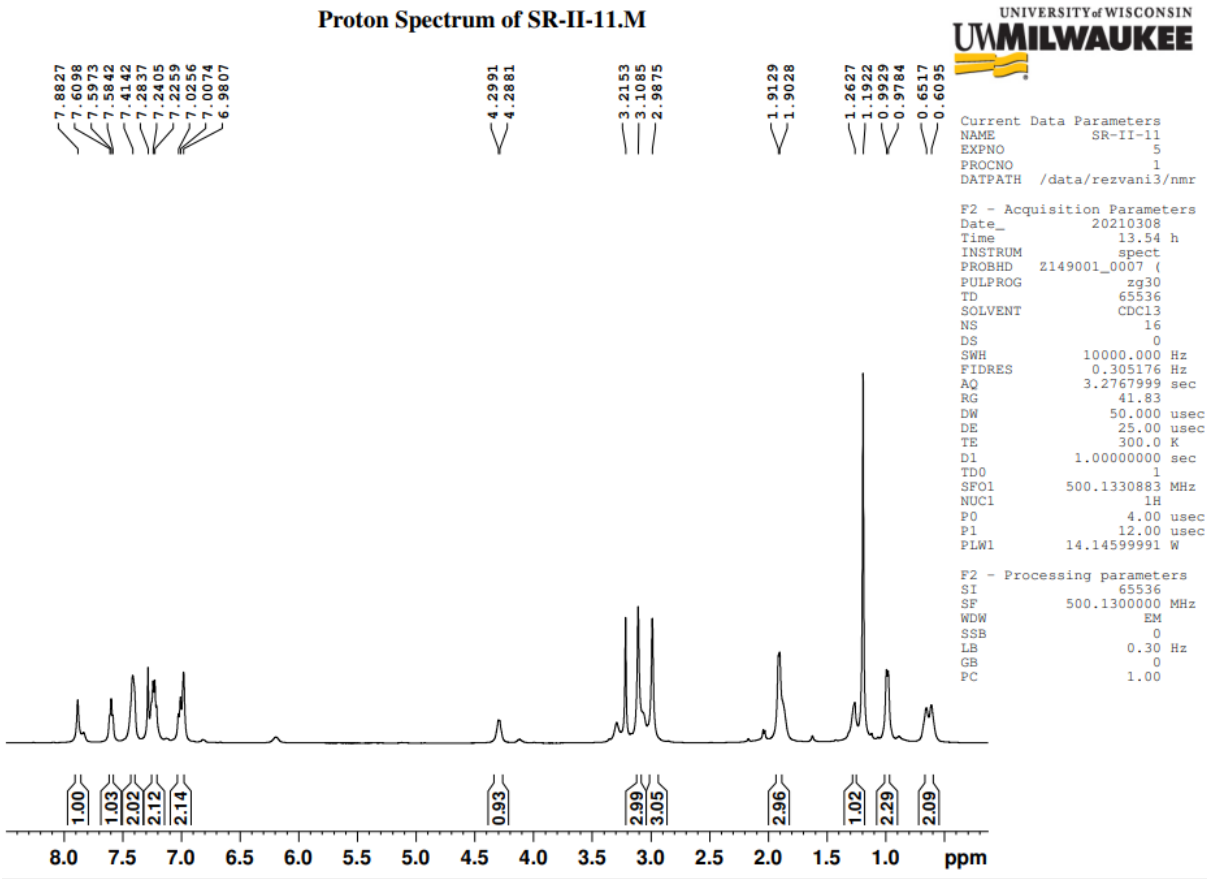

SRE-IV-09
Carbon Spectrum
of SRE-IV-09 in DMSO
170.72
170.00
139.56
138.50
137.68
130.67
129.68
128.79
128.70
127.84
126.54
121.69
57.46
14.85
9.80
I (s) 130.67
G (d) 128.74
N (s) 170.72
K (s) 138.50
E (s) 126.54
B (s) 14.85
M (s) 170.00
J (s) 137.68
D (s) 121.69
C (s) 57.46
A (s) 9.80
L (s) 139.56
F (s) 127.84
H (s) 129.68
f1 (ppm)

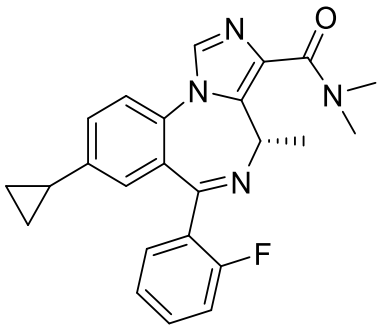

3-H-TIPS
Proton Spectrum -4-16ppm ns=16
h1 DMSO /nmr500 panahza2 12
10.74
7.63
7.61
7.50
7.47
7.46
7.43
7.42
7.41
7.27
7.25
7.23
4.15
3.36
2.51
1.02
H
N
O
N
Si
0.88
1.00
1.78
1.78
1.90
1.51
21.29
f1 (ppm)


3-C-TIPS
Carbon Spectrum ns=256
c13 DMSO /nmr500 panahza2 12
170.57
169.24
140.42
139.25
134.97
134.09
130.83
129.67
128.71
126.85
122.08
116.79
106.52
90.54
57.48
40.48
40.32
40.15
39.98
39.81
39.65
39.48
18.87
11.12
H
N
O
N
Si
f1 (ppm)



SRE-II-11
24

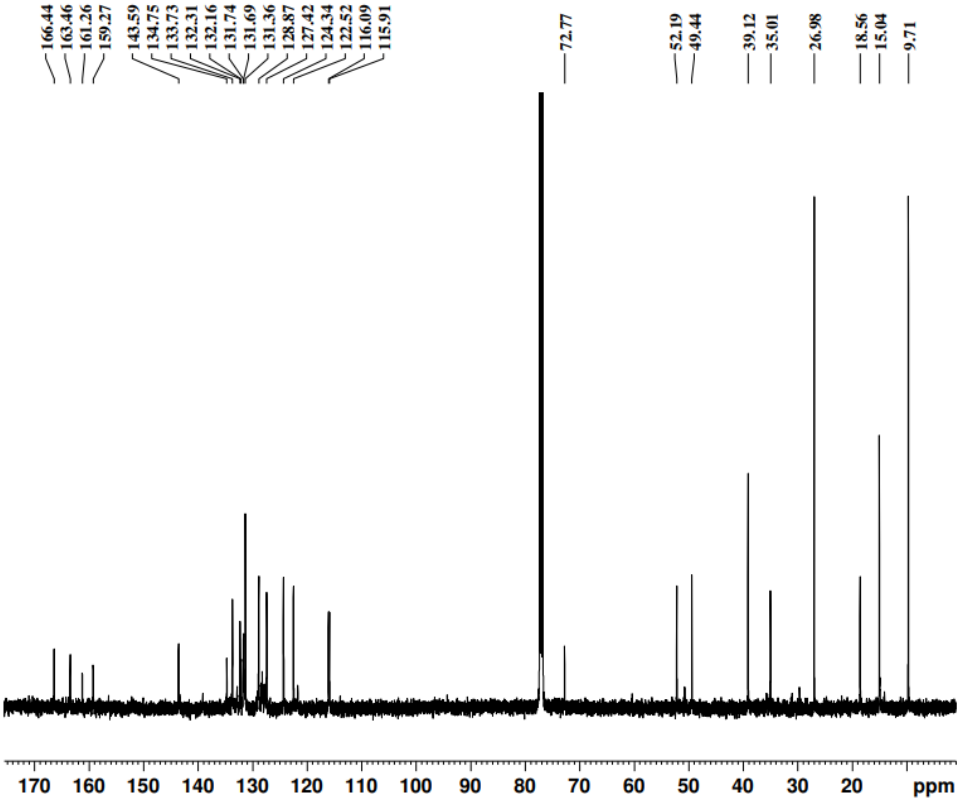

Proton Spectrum of SR-II-11.M
UNIVERSITY of WISCONSIN
UWMILWAUKEE
7.8827
7.6098
7.5973
7.5842
7.4142
7.2837
7.2405
7.2259
7.0256
7.0074
6.9807
4.2991
4.2881
3.2153
3.1085
2.9875
1.9129
1.9028
1.2627
1.1922
0.9929
0.9784
0.6517
0.6095
Current Data Parameters
NAME SR-II-11
EXPNO 5
PROCNO 1
DATPATH /data/rezvani3/nmr
F2 - Acquisition Parameters
Date_ 20210308
Time 13.54 h
INSTRUM spect
PROBHD Z149001_0007 (
PULPROG zg30
TD 65536
SOLVENT CDCl3
NS 16
DS 0
SWH 10000.000 Hz
FIDRES 0.305176 Hz
AQ 3.2767999 sec
RG 41.83
DW 50.000 usec
DE 25.00 usec
TE 300.0 K
D1 1.00000000 sec
TD0 1
SFO1 500.1330883 MHz
NUC1 1H
P0 4.00 usec
P1 12.00 usec
PLW1 14.14599991 W
F2 - Processing parameters
SI 65536
SF 500.1300000 MHz
WDW EM
SSB 0
LB 0.30 Hz
GB 0
PC 1.00
1.00
1.03
2.02
2.12
2.14
0.93
2.99
3.05
2.96
1.02
2.29
2.09
8.0
7.5
7.0
6.5
6.0
5.5
5.0
4.5
4.0
3.5
3.0
2.5
2.0
1.5
1.0
ppm



SRE-II-11
24

Carbon Spectrum of SR-II-11.M

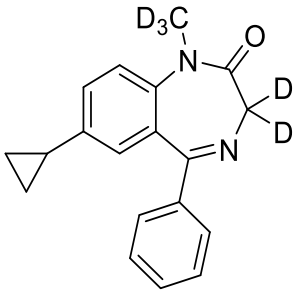
UWMILWAUKEE



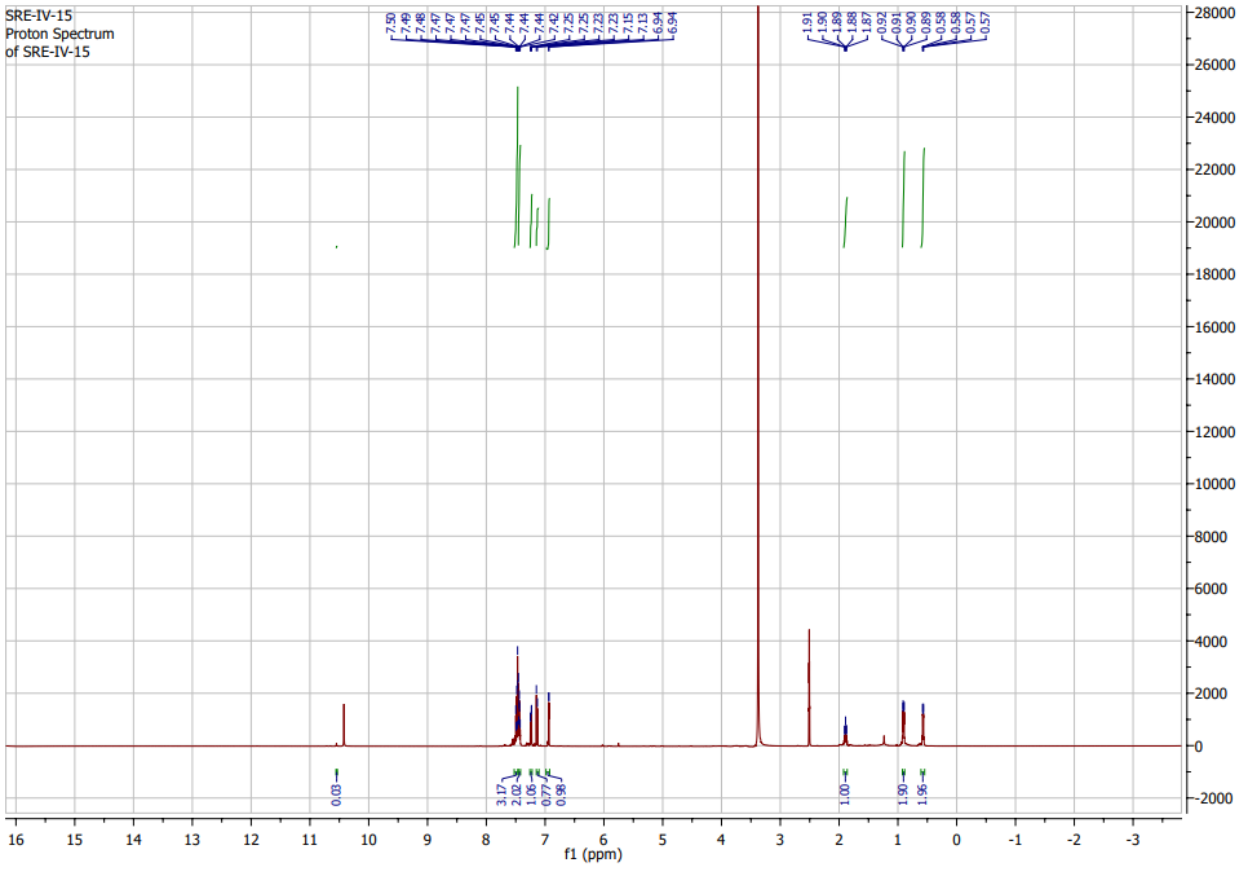

```
Current Data Parameters
NAME                  SR-II-11
EXPNO                        6
PROCNO                       1
DATPATH  /data/rezvani3/nmr

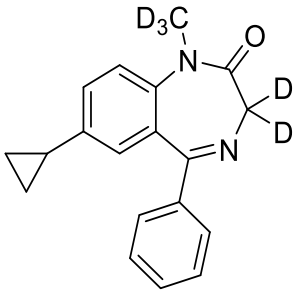
F2 - Acquisition Parameters
Date_              20210308
Time                 14.12 h
INSTRUM               spect
PROBHD    Z149001_0007 (
PULPROG              zgpg30
TD                    65536
SOLVENT               CDCl3
NS                      100
DS                        0
SWH               29761.904 Hz
FIDRES            0.908261 Hz
AQ                1.1010048 sec
RG                   190.86
DW                   16.800 usec
DE                   22.42 usec
TE                   300.0 K
D1             2.00000000 sec
D11            0.03000000 sec
TD0                       1
SFO1          125.7703643 MHz
NUC1                    13C
P0                    3.33 usec
P1                   10.00 usec
PLW1          64.21800232 W
SFO2          500.1320005 MHz
NUC2                    1H
CPDPRG[2          waltz16
PCPD2                80.00 usec
PLW2          14.14599991 W
PLW12          0.31829000 W
PLW13          0.16010000 W

F2 - Processing parameters
SI                    65536
SF            125.7577885 MHz
WDW                     EM
SSB                      0
LB                    1.00 Hz
GB                       0
PC                    1.40
```

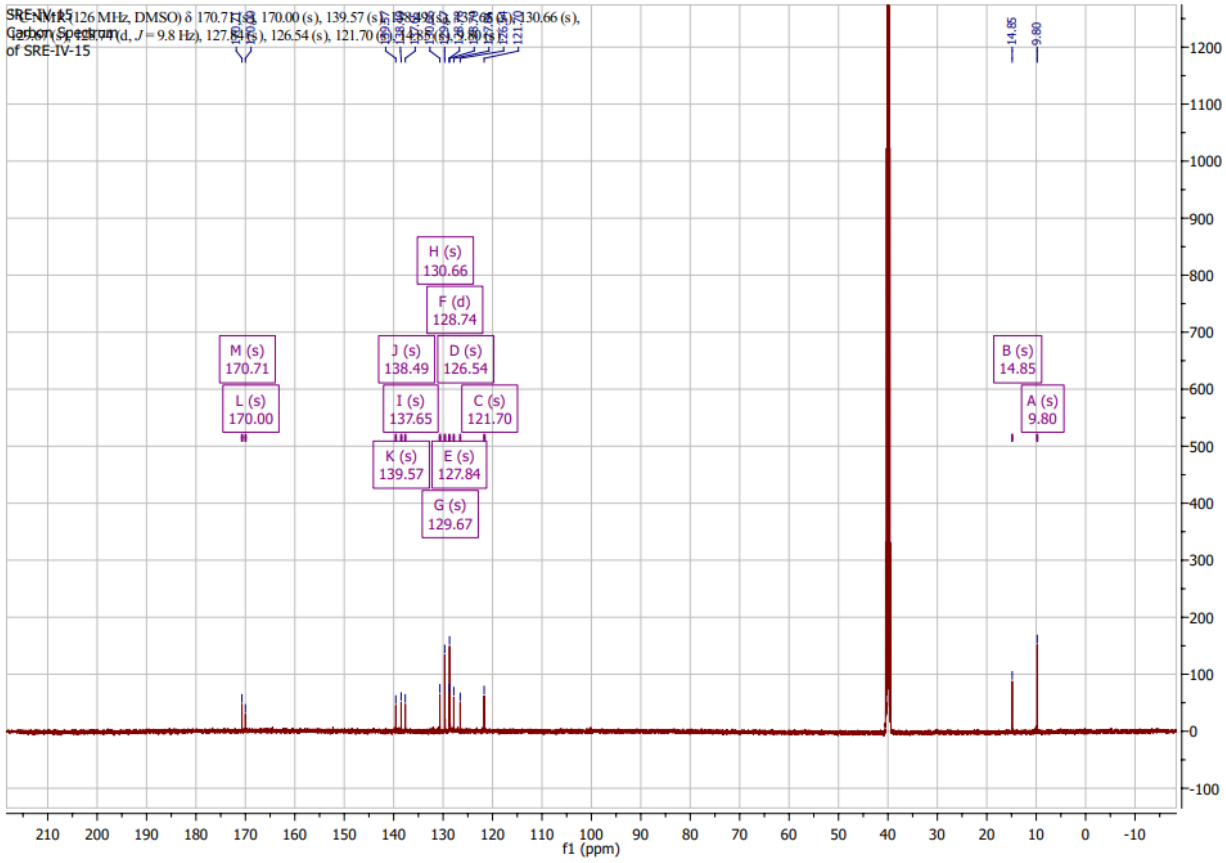


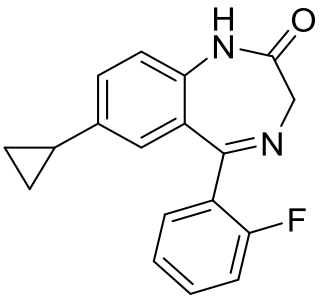
(23)



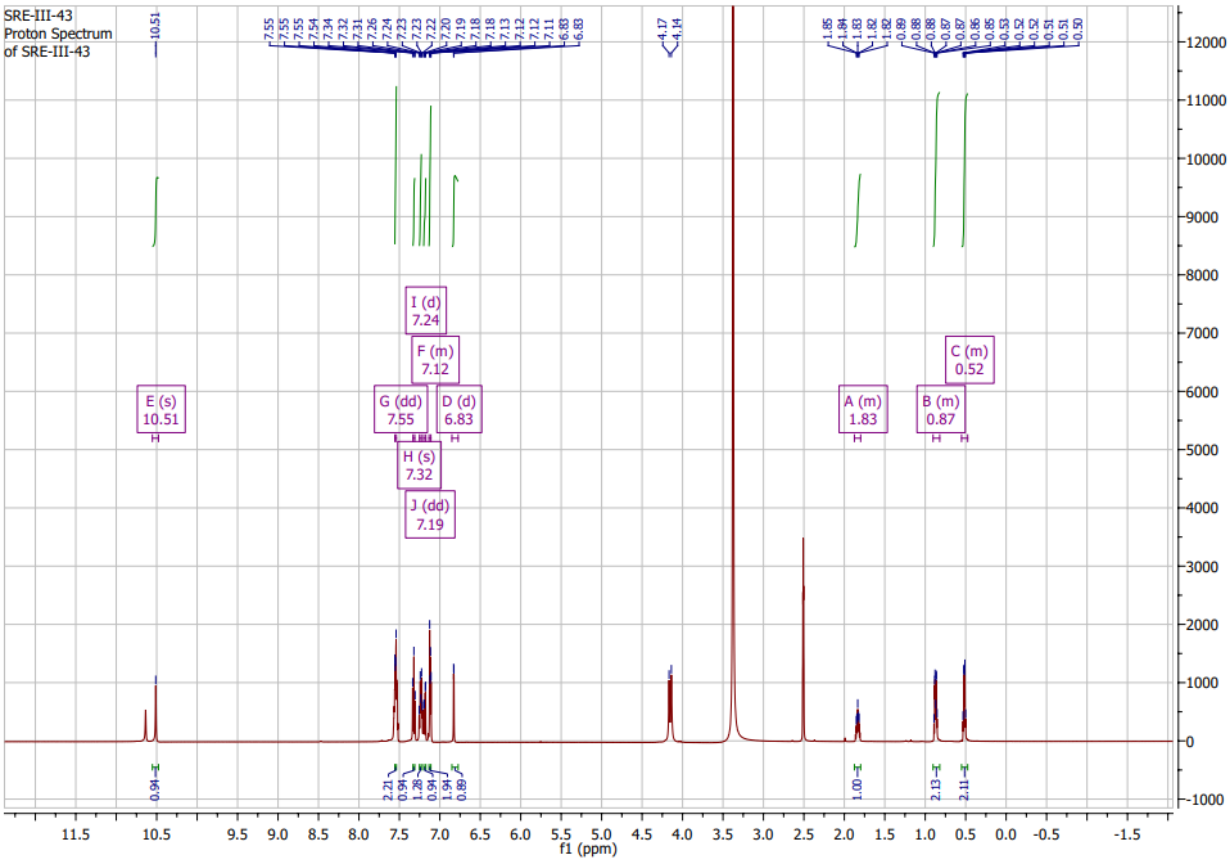

D3C
N
O
D
D
N

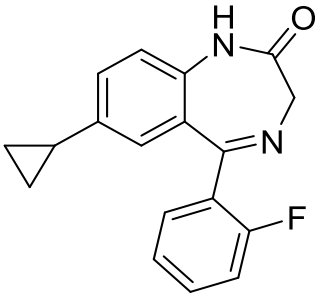
(23)


SRE-IV-15
Carbon Spectrum
of SRE-IV-15
H (s)
130.66
F (d)
128.74
M (s)
170.71
J (s)
138.49
D (s)
126.54
B (s)
14.85
L (s)
170.00
I (s)
137.65
C (s)
121.70
A (s)
9.80
K (s)
139.57
E (s)
127.84
G (s)
129.67
f1 (ppm)

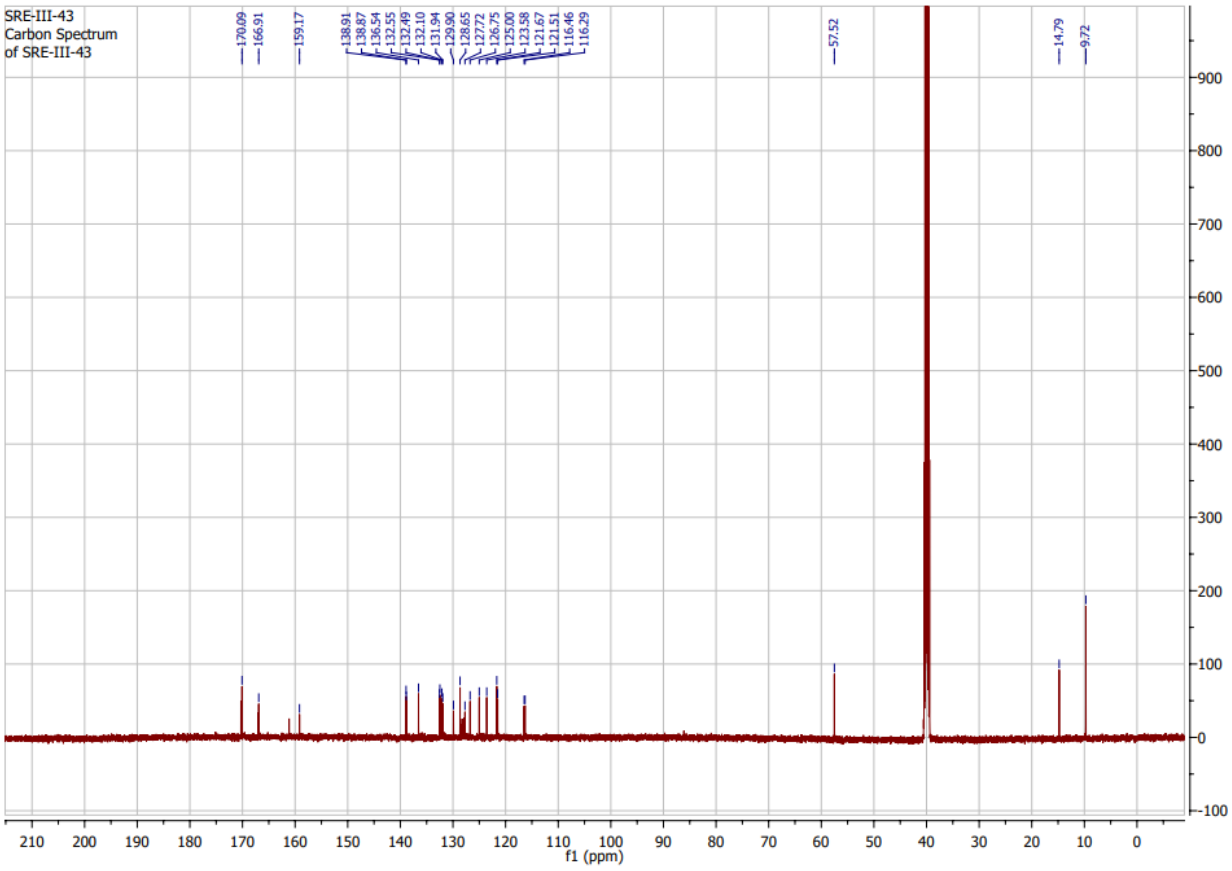

H
N
O
N
F

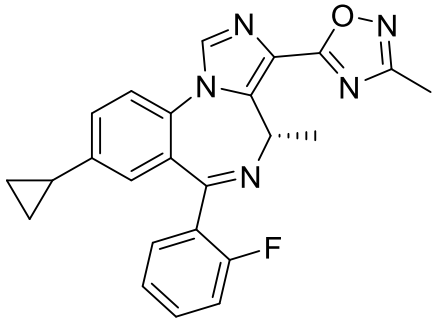
(18)


SRE-III-43
Proton Spectrum
of SRE-III-43
I (d)
7.24
F (m)
7.12
C (m)
0.52
E (s)
10.51
G (dd)
7.55
D (d)
6.83
A (m)
1.83
B (m)
0.87
H (s)
7.32
J (dd)
7.19
f1 (ppm)

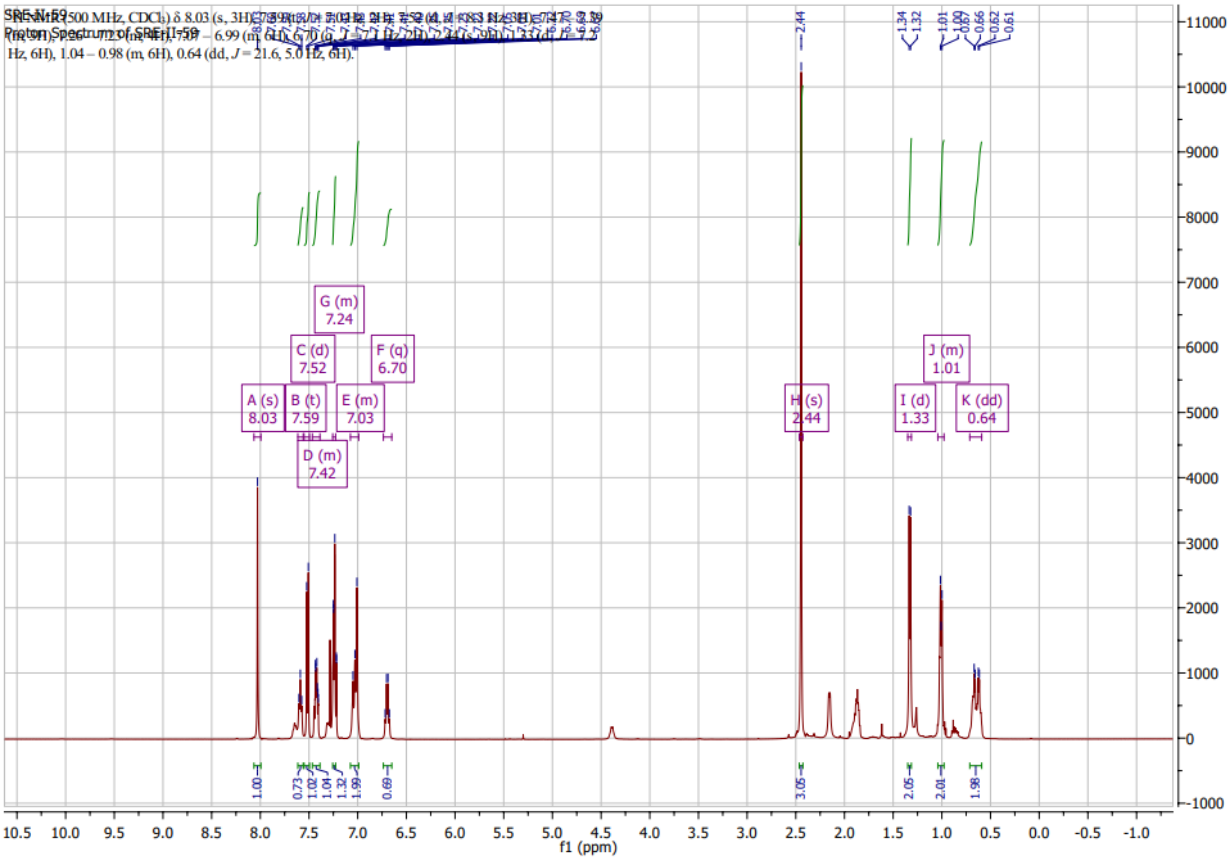

H
N
O
N
F

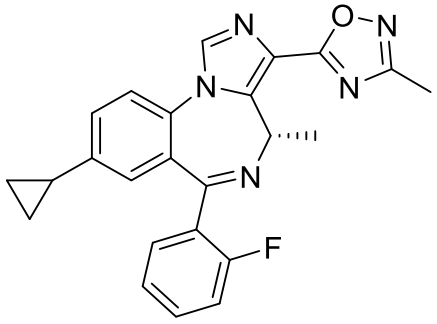
(18)


SRE-III-43
Carbon Spectrum
of SRE-III-43
170.09
166.91
159.17
138.91
138.87
136.54
132.55
132.49
132.10
131.94
129.90
128.65
127.72
126.75
125.00
123.58
121.67
121.51
116.46
116.29
57.52
14.79
9.72
f1 (ppm)

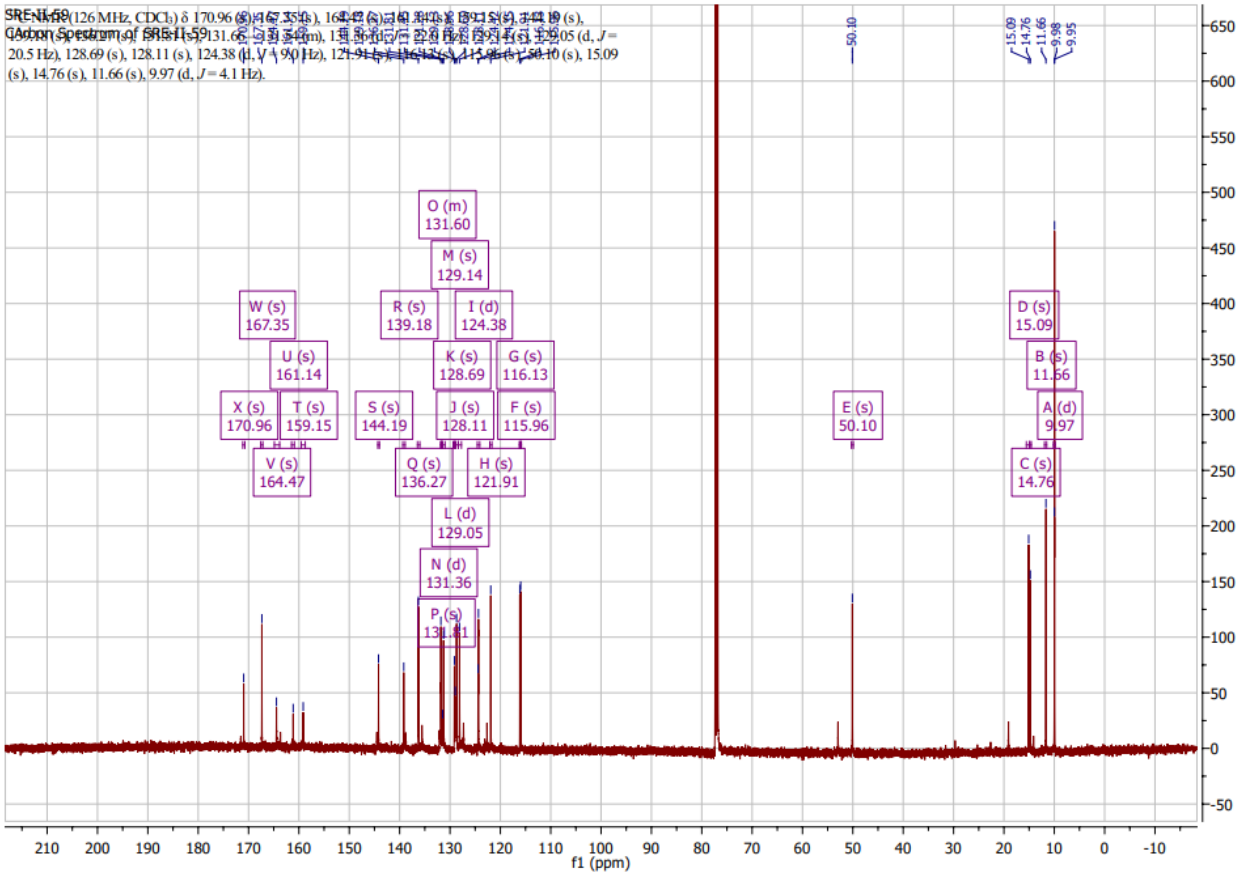

N
O
N
N
N
N
F

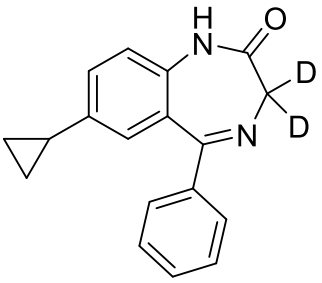
23
SRE-II-44


G (m)
7.24
C (d)
7.52
F (q)
6.70
A (s)
8.03
B (t)
7.59
E (m)
7.03
D (m)
7.42
H (s)
2.44
J (m)
1.01
I (d)
1.33
K (dd)
0.64
f1 (ppm)

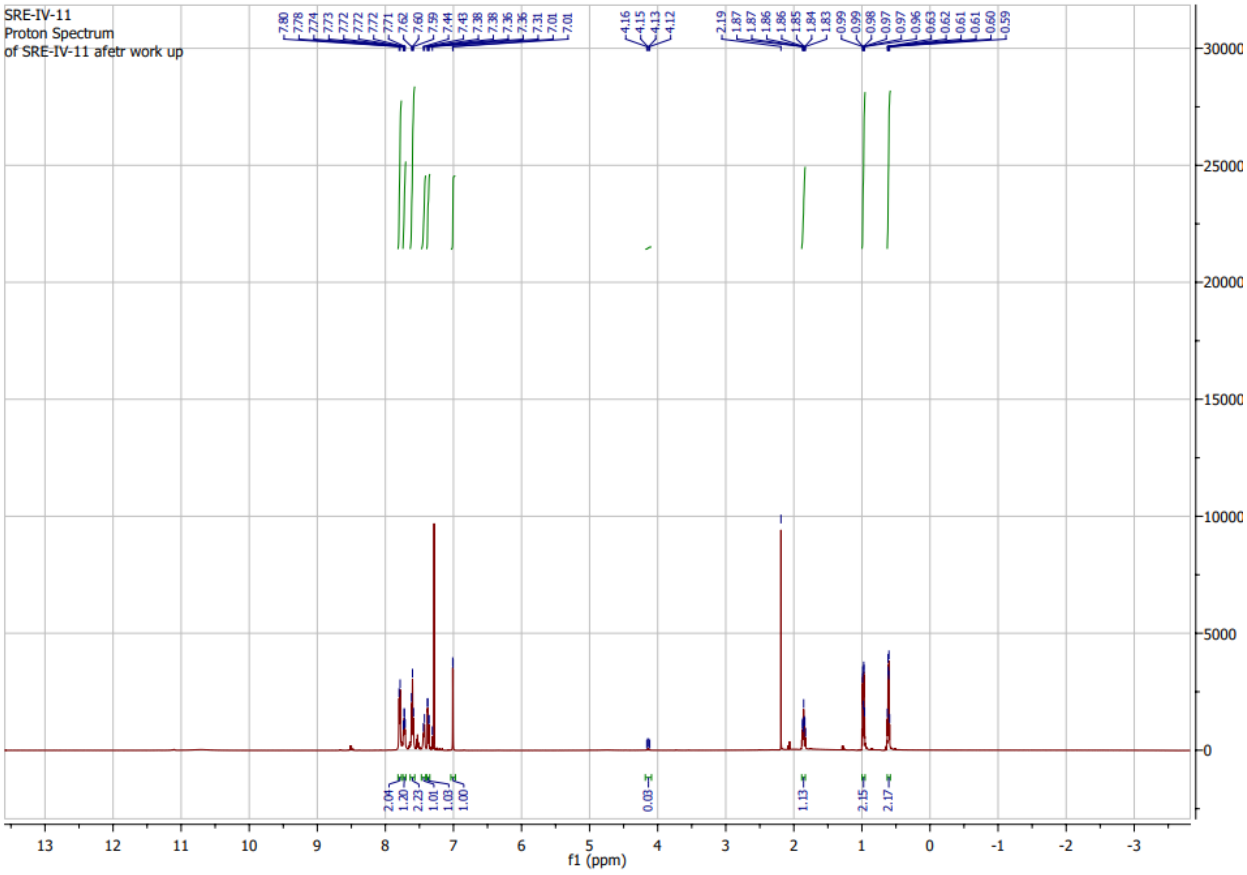

N
O
N
N
N
N
F

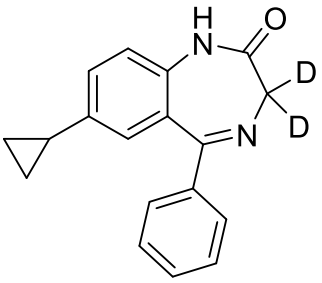
23
SRE-II-44


SRE-II-59
Carbon Spectrum of SRE-II-59
O (m)
131.60
M (s)
129.14
W (s)
167.35
R (s)
139.18
I (d)
124.38
D (s)
15.09
U (s)
161.14
K (s)
128.69
G (s)
116.13
B (s)
11.66
X (s)
170.96
T (s)
159.15
S (s)
144.19
J (s)
128.11
F (s)
115.96
E (s)
50.10
A (d)
9.97
V (s)
164.47
Q (s)
136.27
H (s)
121.91
C (s)
14.76
L (d)
129.05
N (d)
131.36
f1 (ppm)

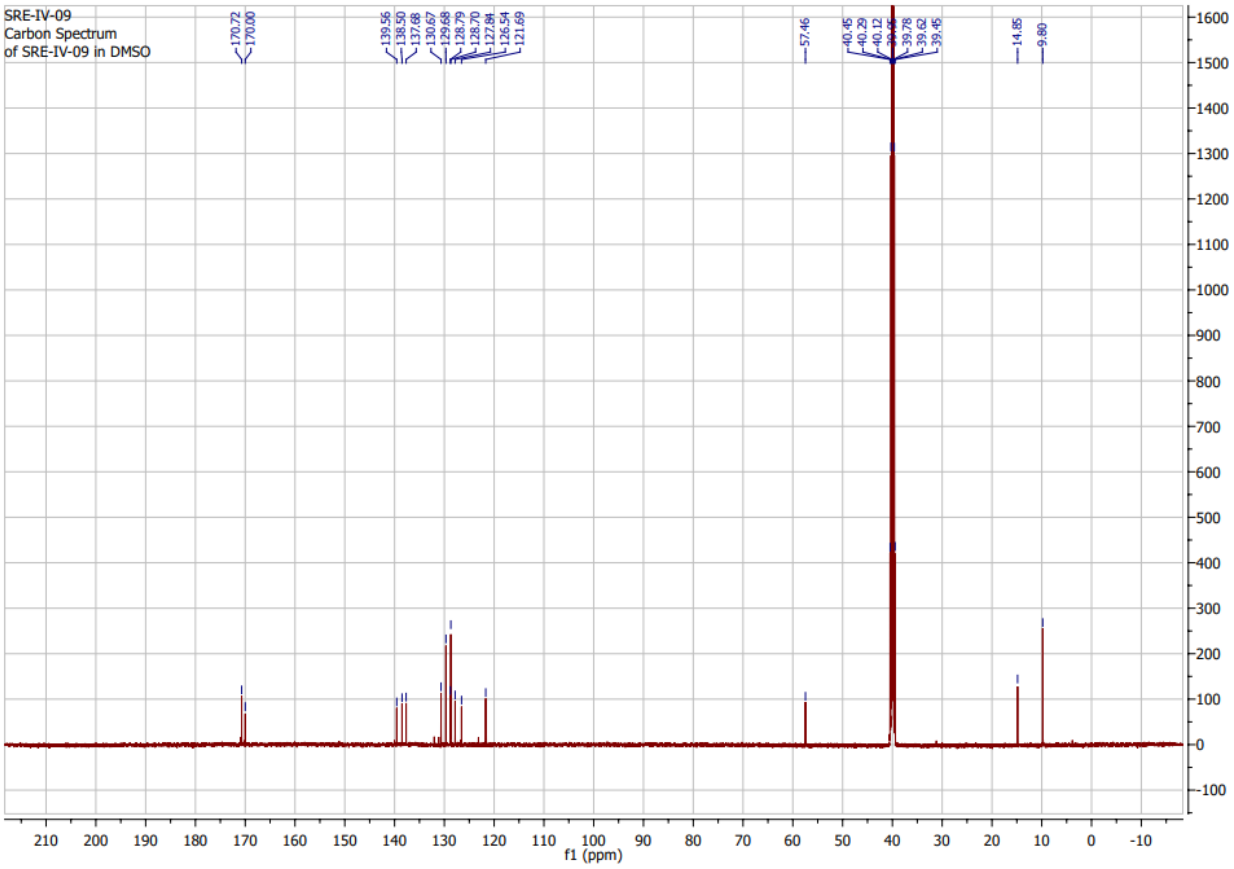

H
N
O
D
D
N

(21)


SRE-IV-11
Proton Spectrum
of SRE-IV-11 afetr work up
f1 (ppm)


H
N
O
D
D
N

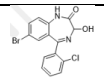
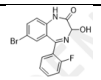
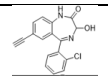
(21)


SRE-IV-09
Carbon Spectrum
of SRE-IV-09 in DMSO
170.72
170.00
139.56
138.50
137.68
130.67
129.68
128.79
128.70
127.84
126.54
121.69
57.46
40.45
40.29
40.12
39.78
39.62
39.45
14.85
9.80
f1 (ppm)

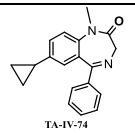
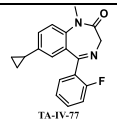
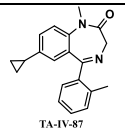
Molecular modeling method: Ligand-protein interactions were analyzed by molecular docking using AutoDock Vina 1.5.6.[1] The PDB file of the cryo-EM structure of the human full-length α1β3γ2L $GABA_A$ receptor in complexes alprazolam (6HUO)[2] were downloaded from the Protein Data Bank and was prepared for docking by fixing missing bonds or atoms, adding polar hydrogens, and assigning charges by AM1-BCC, and removing water molecules. The proteins were validated by first removing the bound ligand (alprazolam) followed by docking it in the same binding site. The compounds were drawn, and energy minimized in Chimera.[3] A grid size of 17 Å x 17 Å x 17 Å and centered at coordinates 152.80 (*x*), 163.02 (*y*), and 161.14 (*z*) of the 6HUO PDB structure was used. Illustrations of the 3D models were generated using Chimera and Python.[3-4] Dockings were performed with standard search parameters and poses with the best scores were selected for the analysis.

1. Trott O, Olson A J. AutoDock Vina: improving the speed and accuracy of docking with a new scoring function, efficient optimization, and multithreading. *J Comput Chem* 2010**;** *31* (2): 455. DOI: 10.1002/jcc.21334
2. Laverty D, Desai R. Uchanski T, Masiulis S, Stec WJ, Malinauskas T, Zivanov J, Pardon E, Steyaert J, Miller KW, Aricescu AR.. Cryo-EM structure of the human alpha1beta3gamma2 GABAA receptor in a lipid bilayer. *Nature* 2019**;** *565* (7740): 516. DOI: 10.1038/s41586-018-0833-4
3. Pettersen EF, Goddard TD, Huang CC, Couch GS, Greenblatt DM, Meng EC, Ferrin TE. UCSF Chimera--a visualization system for exploratory research and analysis. *J Comput Chem* 2004**;** *25* (13): 1605. DOI: 10.1002/jcc.20084
4. Sanner MF. Python: a programming language for software integration and development. *J Mol Graph Model* 1999**;** *17* (1): 57. PMID: 10660911

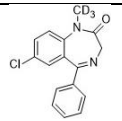
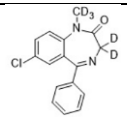
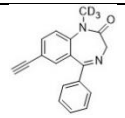
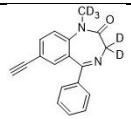
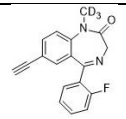
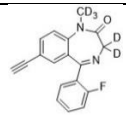
Cook Compounds IC_{50}s

	MYM-iv-95	MYM-I-59	MYM-i-43	TA-IV-08	QH-ii-066	Nor-QH-ii-066	TA-II-59	TA-II-73	MYM-V-17
A375					1.83		0.61	2.05	
H1792				NA	4.5		0.94	2.1	
LN18	NA	NA	NA	NA	2.8	0.69	0.82	0.92	5.17
LLC							0.97		
B16F10					10.7				
MB002									
U-87 MG-Luc2									
									

	TA-IV-74	TA-IV-77	TA-IV-87			
A375	2.57	5.32	10.48			
H1792	3.92	8.68	15.46			
LN18	2.55	7	11.23			

LLC	4.18					
B16F10						
MB002						
U-87 MG-Luc2						
	 TA-IV-74	 TA-IV-77	 TA-IV-87			

	D3 DIAZ TA (DiD3)	**D5 DIAZ TA (DiD5)**	**MYM-III-85 (QHD3)**	**TA-II-70-TA-III-72 (QHD5)**	**TA-I-16 (KRMD3)**	**TA-III-66-TA-IV-62 (KRMD5)**
A375	NA	NA	0.31	0.46	0.35	0.63
H1792	NA	NA	1.75 / 3.3	1.98	2.13	2.52
LN18	NA	NA	1.81 / 2.2	2.51	2.43	2.67
LLC						
B16F10			12.4			
MB002			2.2			
U-87 MG-Luc2			4			

Key:

A-375: Human melanoma (epithelial morphology)

H1792: Human Lung Adenocarcinoma (Epithelial morphology)

LN18: Human Glioblastoma (Epithelial morphology)

LLC: Lewis lung carcinoma, mouse

B16F10: Mouse melanoma (mixed Spindle & epithelial-like)

MB002: Human Medulloblastoma (non-WNT/non-SHH, group 3)

U-87 MG-Luc2: Human Glioblastoma (Epithelial morphology)

NA = Not Active

Synthesis and Analysis of the Anti-depressant Activity of GL-I-54, a Positive Allosteric $GABA_A$ Receptor Modulator

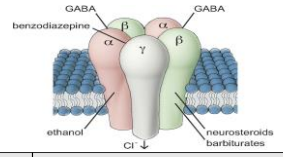
Sepideh Rezvanian[1], Farjana Rashid[1], Md Yeunus Mian[1], Pirthu Mondal[1], Dishary Sharmin[1], Kamal Pandey[1], Ashley Bernardo[2], Philippe Lee[3], Michael Marcotte[2], Etienne Sibille[2,3,4], Thomas D. Prevot[2,4], James M Cook[1]

[1]Department of Chemistry and Biochemistry, Milwaukee Institute for Drug Discovery, University of Wisconsin Milwaukee, Milwaukee, WI 53211
[2]Campbell Family Mental Health Research Institute of CAMH, Toronto, Canada
[3]Department of Pharmacology and Toxicology, University of Toronto, Toronto, Canada
[4]Department of Psychiatry, University of Toronto, Toronto, Canada

Abstract

Benzodiazepines (BZD) are a common class of psychoactive medications for the treatment of CNS disorders such as anxiety and depression. However, not all patients have a positive response to BZDs, as well as the presence of serious side effects including amnesia, sedation, addiction, ataxia, withdraw and dependence. GL-I-54, a chiral 4-(S)-CH_3 imidazodiazepine is being investigated for the treatment of Major Depressive Disorder (MDD). Human studies have shown that patients with MDD exhibit an impaired excitation/ inhibition balance, caused in part by altered GABAergic (inhibitory) functions. A series of novel new imidazodiazepine chiral ligands were designed, synthesized, and analyzed for selective $GABA_A$ receptor effects, that enhanced cognition in mice subjected to chronic mild stress. Recent results will be presented.

GABA/ BzR Chloride Ion Complex



Subtype	Associated Effect
α1	Sedation, anterograde amnesia, some anticonvulsant action, ataxia, addiction
α2	Anxiolytic, analgesic, anticonvulsant, may be hypnotic at high doses, may be some muscle relaxation at high doses
α3	Some anxiolytic action, some anticonvulsant action, some analgesia, may be some muscle relaxation at high doses
α4	Diazepam-insensitive site
α5	Cognition, temporal and spatial memory, depression and schizophrenia
α6	Diazepam-insensitive site

Synthesis of GL-I-54

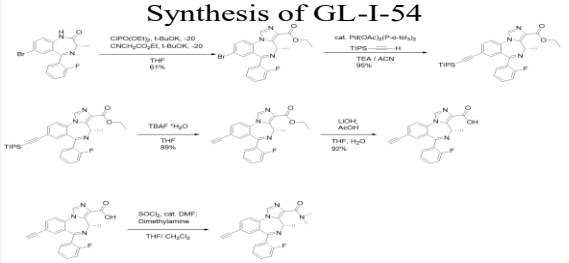


Table 1. In vitro cytotoxicity of Dimethyl amide enantiomers

Entry	Structure	HEK293LD50 (μM)[a]	HEPG2 LD50 (μM)[a]
GL-I-54		>400	>400
GL-II-73		>200	>400

[a] Compounds were incubated at different concentrations with the specific cells for 48 h, followed by detection of cell viability using a Cell-Titer Glo (Promega). The results were normalized using DMSO (negative control) and 3-dibutylamino-1-(4-hexyl-phenyl)-propan-1-one (150 mM in DMSO final concentration, positive control). No Cytotoxicity observed

Elevated Plus Maze Test of GL-I-54[a,b]

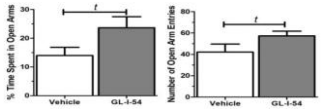


Figure 1. [a]GL-I-54 is anxiolytic in this assay. [b]All animal cohorts were obtained from Jackson Laboratories (Stock# 000664; Bar Harbor, MA, USA) consisting of 8-week old C57BL/6 mice with 50% female mice in each cohort

Y-Maze Test of GL-I-54

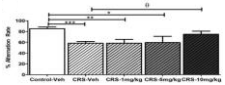
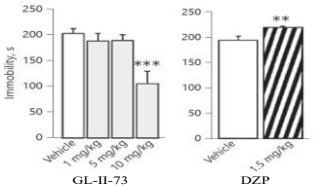


Figure 2. GL-I-54 was tested in the Y maze task, assessing working memory. To induce a working memory deficit mice were subjected to 7 day of chronic restraint stress. 30 min prior to testing, mice were injected with vehicle or 1, 5 or 10 mg/kg of GL-54. Animals Subjected to CRS and receiving vehicle showed a significant decrease in alternation rate, suggesting a working memory deficit. Animal subjected to CRS and receiving the highest dose of GL-I-54 showed significant increase in alternation rate, suggesting reversal of working memory deficits induced by CRS.

Forced Swim Test



Anxiolytic and antidepressant properties of GLII-73 compared to diazepam (DZP). Potential antidepressant properties of the ligands were assessed in male mice using the forced swim test. Significant decreased immobility characterized the potential antidepressant-like efficacy of the ligand

Results and Conclusion

GL-II-73, the enantiomer of GL-I-54, displayed antidepressant-predictive property in the Forced Swim Test. Results presented here indicate that GL-I-54 has potential as an anti-depressive agent devoid of adverse effects. Consequently, GL-I-54 represents a promising lead compound for further studies. Since anxiety is comorbid with depression, the anti-anxiety results are important. Moreover, cognitive problems are a major problem with depression and GL-I-54 is also precognitive.

References

- *Li, G. et al. Arkivoc,* ***2018****, iv, 158-182*
- *Prevot, T. et al. Mol Neuropsychiatry,* ***2019****;5:84–97*
- *Bernardo, A. et al. BioRxiv* ***2021****; 03.22.436517*
- *Prevot, T. et al. ACS Chem. Neurosci. 2019, 10, 2088−2090*

Acknowledgment

We wish to acknowledge the NIH for generous financial support (R01MH096463, R01NS076517, R01HL118561). We also thank the Milwaukee Institute for Drug Discovery and the Shimatzu Laboratory for Advanced Applied and Analytical Chemistry.

Positive Allosteric Modulation at GABAA Receptor Effects on Symptomatic and Neurotrophic in a Mouse Model of Chronic Stress

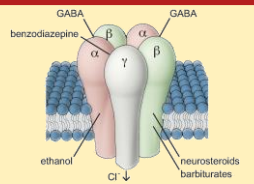
Sepideh Rezvanian[1], Pirthu Mondal[1],Dishary Sharmin[1], Kamal Pandey[1], Ashley Bernardo[2], Philippe Lee[3], Michael Marcotte[2], Etienne Sibille[2,3,4], Thomas D. Prevot[2,4], James M Cook[1]

[1]Department of Chemistry and Biochemistry, Milwaukee Institute for Drug Discovery, University of Wisconsin Milwaukee, Milwaukee, WI 53211
[2]Campbell Family Mental Health Research Institute of CAMH, Toronto, Canada
[3]Department of Pharmacology and Toxicology, University of Toronto, Toronto, Canada
[4]Department of Psychiatry, University of Toronto, Toronto, Canada

Abstract

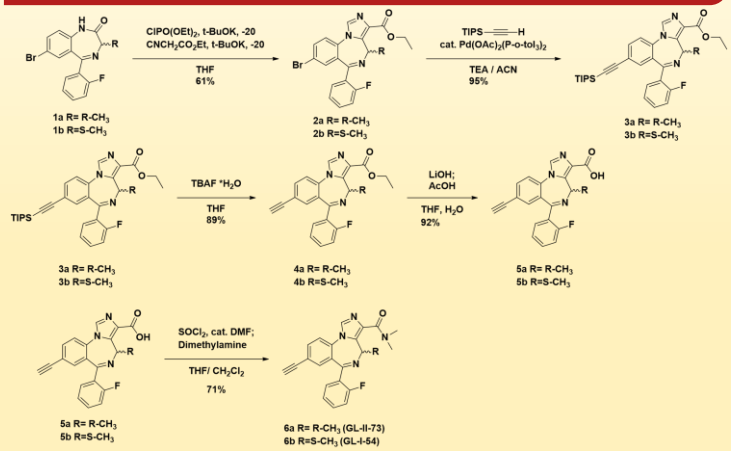
Chronic stress represents a major risk factor for developing Major Depressive Disorder (MDD). Chronic stress is also linked to increased anxiety and cognitive dysfunctions. While therapies focused on dopaminergic and serotoninergic functions for the treatment of MDD, expression levels and function of the main inhibitory neurotransmitter GABA are also reduced in MDD and in chronic stress states. Therefore, neuronal dysfunctions and deficits in GABAergic signaling, contribute to symptom severity but remain poorly targeted. Activity at α2-GABAA-Rs effects on anxiolytic properties, α5-GABAA-Rs on cognitive functions, and α1-GABAA-Rs on sedation. Thus far, refined and selective activity at the α2/3/5-subunit is hypothesized to exert beneficial effect, devoid of side effects. Here, GL-II-73 and GL-I-54 were shown to exert positive allosteric modulation at the α5, and α2/3/5- containing GABAA receptors respectively. They are effective both independently and in combination as a racemic mixture. In this study, results represent the value of selectively targeting GABAA receptors, excluding the α1-subunit, to overcome chronic stress-induced mood symptoms and cognitive deficits, as well as detriments in neuronal morphology.

GABA/ BzR Chloride Ion Complex

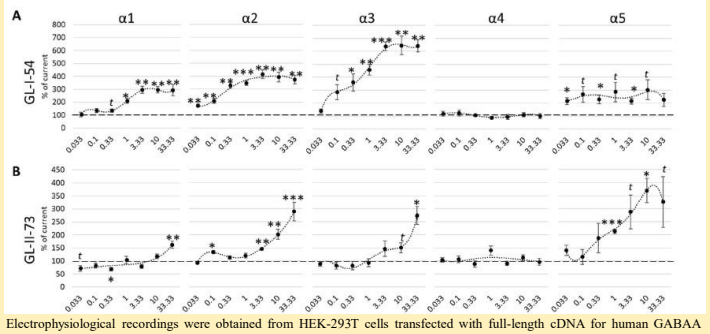


Subtype	Associated Effect
α1	Sedation, anterograde amnesia, some anticonvulsant action, ataxia, addiction
α2	Anxiolytic, analgesic, anticonvulsant, may be hypnotic at high doses, may be some muscle relaxation at high doses
α3	Some anxiolytic action, some anticonvulsant action, some analgesia, may be some muscle relaxation at high doses
α4	Diazepam-insensitive site
α5	Cognition, temporal and spatial memory, depression and schizophrenia
α6	Diazepam-insensitive site

Synthesis of Dimethyl amide Enantiomers

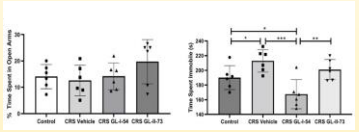


Electrophysiology

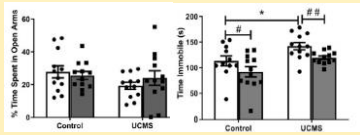


Electrophysiological recordings were obtained from HEK-293T cells transfected with full-length cDNA for human GABAA receptor subtypes α1β3γ2, α2β3γ2, α3β3γ2, α4β3γ2 or α5β3γ2, in presence of GL-I-54 (A) or GL-II-73 (B), and in the presence of GABA in the medium (5 μM).

Behavioral Tests



GL-I-54 and GL-II-73 were tested in the elevated plus maze and forced swim test at the dose of 5mg/kg, in mice previously exposed to chronic restraint stress (CRS). Drugs were administered IP, 30min prior to testing. Percent time spent in the open arms (A) showed no difference between groups. Time immobile (B) showed more time spent immobile in the CRS-Vehicle group, and less time immobile in animals receiving GL-I-54, compared to CRS-Vehicle. GL-II-73 did not show an effect.



The racemic mixture of two enantiomers were tested in the elevated plus maze and forced swim test in subjected mice to UCMS. In the elevated plus maze, time spent in the open arms were measured with no significant effect of UCMS, treatment or interaction. In the forced swim test mice subjected to UCMS showed increased immobility, while mice treated with GL-RM showed a reduction in immobility

Results and Conclusion

GL-II-73, the enantiomer of GL-I-54, displayed antidepressant-predictive property in the Forced Swim Test. Results presented here indicate that GL-I-54 has potential as an anti-depressive agent devoid of adverse effects. Consequently, GL-I-54 represents a promising lead compound for further studies. Since anxiety is comorbid with depression, the anti-anxiety results are important. Moreover, cognitive problems are a major problem with depression and GL-I-54 is also precognitive.

Refrences

- Li, G. et al. Arkivoc, **2018**, iv, 158-182
- Prevot, T. et al. Mol Neuropsychiatry,**2019**;5:84–97
- Bernardo, A. et al. BioRxiv**2021**; 03.22.436517
- Bernardo, A. et al. Neuropsychopharmacol. **2022; 47,** 1608–1619

Acknowledgements

We wish to acknowledge the NIH for generous financial support (R01MH096463, R01NS076517, R01HL118561). We also thank the Milwaukee Institute for Drug Discovery and the Shimatzu Laboratory for Advanced Applied and Analytical Chemistry..

Activating an ion channel promotes radiation-sensitizing immune-driven anti-tumor activity

D. Kamdem Toukam[1], D. Bhattacharya[1], V. Gawali[1], L. Kallay[1], T. Ahmed[2], A. Karve[3], P. Desai[2], J. Cook[2], T. D. Ionascu[4], S. Tridandapani[5], D. P. Krummel[1,6], S. Sengupta[1]

[1]Dept. Neuro.& Rehab. Medicine, Univ. Cincinnati College of Medicine; [2]Dept. Chemistry, Univ. Wisconsin-Milwaukee; [3]Coll. Pharmacy, Univ. Cincinnati; [4]Dept. Rad. Onc., Univ. Cincinnati College of Medicine; [5]Dept. Internal Medicine, The Ohio State Univ. College of Medicine; [6]Amlal Pharmaceuticals Inc.

University of CINCINNATI

BACKGROUND

Standard-of-care for melanoma brain metastases is moving to stereotactic radiosurgery (SRS) with immunotherapy. Although this combined approach shows improved patient survival, responses are not durable. SRS can also cause adverse reactions such as radiation necrosis, which can result in significant morbidity and even mortality. Lowering SRS dose without negatively impacting its effectiveness would therefore be beneficial clinically.

Our published data[1] suggests that when treating syngeneic mouse model B16F10 melanoma tumors, radiation dose can be reduced and its effectiveness improved, by activating intrinsic melanoma $GABA_A$ receptor ($GABA_AR$) activity using a novel agent, AM-101. This agent acts to enhance $GABA_AR$ mediated chloride transport in melanoma cells, which in turn triggers mitochondrial dysregulation associated with tumor regression in mice.[1,2] AM-101 also enhances infiltration into tumors of anti-tumor immune cells.

METHODS

Human and mouse melanoma cells (A-375 and B16F10, respectively) were used for electrophysiology, MTS assays, combination treatments with cytokine and RT. C57Bl/6 immunocompetent mice were used to assess benefits of AM-101 in induction of an anti-cancer immune response. Immune cell infiltration into the tumor was assessed by flow cytometry analysis of tumor derived lymphocytes and by immunostaining of tumor sections harvested from drug-treated and control mice.

RESULTS

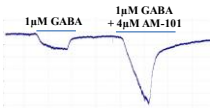


Figure 1. AM-101 potentiates Cl^- flux in B16F10 Cells. Electrophysiology recordings of GABA (1 μM) and GABA-A + AM-101 effects on B16F10 mouse melanoma cells.

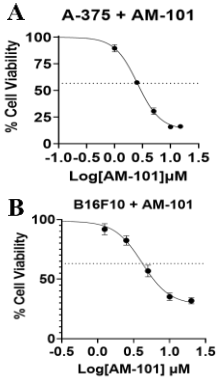


Figure 2. AM-101 cytotoxicity. AM-101 is cytotoxic to human A-375 (A) and mouse B16F10 (B) melanoma cells with $IC_{50} \approx 6$ μM and 2 μM, respectively.

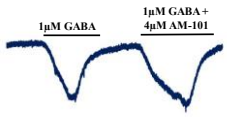


Figure 3. AM-101 potentiates Cl^- flux in splenic T cells. Electrophysiology recordings shows effect of GABA (1 μM) and GABA + AM-101 on splenic $CD8^+$ T cells.

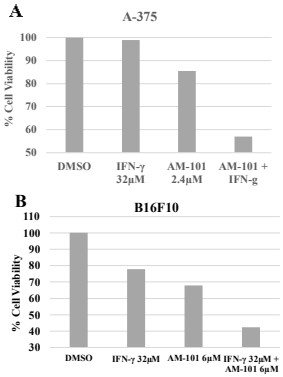


Figure 4. AM-101 synergizes with IFN-γ to kill cancer cells. Human A-375 (A) and mouse B16F10 (B) cells were treated with DMSO, AM-101, IFN-γ or a combination of both. Combination of both drugs further impairs cell viability.

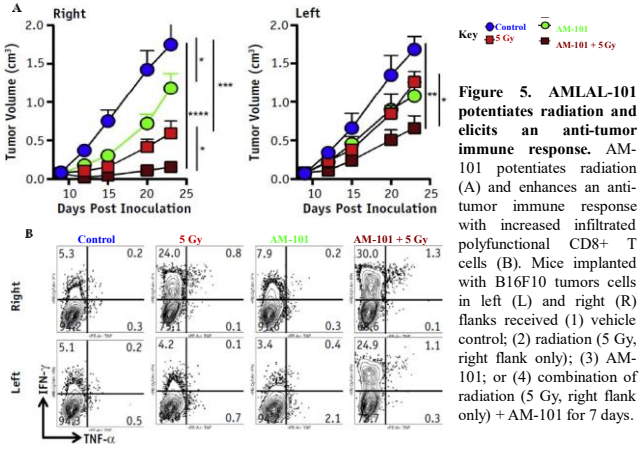


Figure 5. AMLAL-101 potentiates radiation and elicits an anti-tumor immune response. AM-101 potentiates radiation (A) and enhances an anti-tumor immune response with increased infiltrated polyfunctional CD8+ T cells (B). Mice implanted with B16F10 tumors cells in left (L) and right (R) flanks received (1) vehicle control; (2) radiation (5 Gy, right flank only); (3) AM-101; or (4) combination of radiation (5 Gy, right flank only) + AM-101 for 7 days.

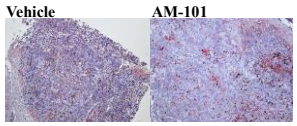


Figure 6. AM-101 increases CD8+ T cell infiltration into tumor: Mice implanted with B16F10 cells in flanks received i.p. injection of vehicle control or AM-101 (2.5mg/Kg daily for 7 days). Two weeks after the last injection, tumor were harvested and stained for CD86.

CONCLUSIONS

- AM-101 combined with radiation results in near complete regression of irradiated tumor and shrinking of tumor not in the radiation field due to an immune response, i.e., a potent abscopal effect.
- AM-101 induces increased infiltration of polyfunctional CD8+ T cells, and tumor-associated macrophages of potentially the tumor inhibitory M1-phenotype, possibly due to IFN-γ stimulation.
- We posit that activating $GABA_AR$ with AM-101 promotes both a 'direct' anti-tumor response and an 'indirect', immune-driven anti-tumor activity in metastatic melanoma tumors.
- AM-101 may address an urgent unmet need for a therapeutic that can potentiate radiation and mitigate its toxicity profile.

REFERENCE

1. Pomeranz Krummel et al. *International Journal of Radiation Oncology, Biology, Physics*. Vol. 109, 2021.
2. Bhattacharya et al. *Experimental Biology and Medicine*. Vol.246, 2021.

ACKNOWLEDGEMENTS

This work is supported by the Department of Neurology & Rehabilitation Medicine, University of Cincinnati.

438

Systemic and Brain Pharmacokinetics of a GABAA Receptor Agonist AMLAL -101, as an Investigational Therapeutic for the Treatment of Primary and Metastatic Brain Cancers

Aniruddha Karve [1], Taukir Ahmed [2], Janki Desai[1], Debanjan Bhattacharya [3], Kamdem Toukkam [3], Sidharth Gadgil[1], Merissa Pemberton[4], Laura Kallay [3], Gary Gudelsky [1], Larry Sallans [5], David R. Plas[4], James Cook [2], Daniel Pomeranz Krummel [3,6], Soma Sengupta [3], Pankaj B. Desai [1]

1. Division of Pharmaceutical Sciences, James L. Winkle College of Pharmacy, University of Cincinnati, Cincinnati, OH; 2. Dep artment of Chemistry, University of Wisconsin, Milwaukee, WI; 3. Department of Neurology & Rehabilitation Medicine, University of Cincinnati College of Medicine, Cincinnati, OH; 4. Department of Cancer Biology, University of Cincinnati College of Medic ine, Cincinnati, OH; 5. Rieveschl Laboratories for Mass Spectrometry, Department of Chemistry, University of Cincinnati, OH; 6. Amlal Pharmaceuticals Inc.

INTRODUCTION

- AMLAL-101 is a novel agent which preferentially targets α3, α5 subtypes of γ-amino butyric acid receptors and shows anti-tumor activity against disparate cancer types.
- AMLAL-101 is being advanced as an 'add-on' to potentiate treatment of primary and metastatic brain cancers.
- However, AMLAL-101 the blood-brain barrier (BBB) penetration of AMLAL-101 is unknown.
- The primary purpose of this study was to determine the plasma pharmacokinetics (PK) and quantitative estimate of the BBB permeability of AMLAL-101.

METHODS

- We performed intracranial microdialysis, employing jugular vein cannulated Sprague-Dawley rats (N=6) which facilitated simultaneous serial blood and brain extracellular fluid (ECF) sampling.
- AMLAL-101 was injected i.p. at 5 mg/kg and serial blood and brain ECF samples collected up to 10 h post-dosing.
- Plasma and ECF samples were analyzed by LC/MS-MS and plasma and ECF concentration vs time PK profiles determined. In vivo recovery analysis was performed using retrodialysis and rapid equilibrium dialysis employed to determine the extent of protein binding.
- The data were analyzed using Phoenix® WinNonLin® v 8.3 to determine the $AUC_{(0\text{-}inf)}$ ratio for protein unbound drug in plasma and brain ECF($K_{p,u,brain}$)

RESULTS

- AMLAL-101 plasma protein binding was 85% and in vivo recovery from ECF was 25%. The brain partitioning of unbound AMLAL-101 ($K_{p,u,brain}$); ranged between 1.02 to 1.44. The elimination half-life of AMLAL-101 was between 3-4 h for both brain ECF and plasma.

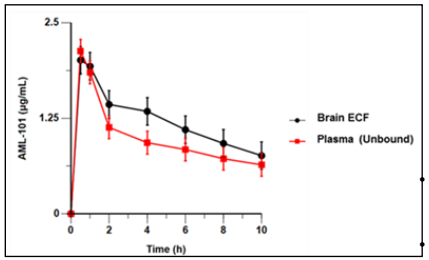


Fig.1: Concentration vs time profile of AMLAL-101 in plasma (unbound) and brain ECF in male SD rats.

PK Parameter	Plasma (Unbound)	Brain ECF (Corrected for in vivo recovery)
$AUC_{(0\text{-}inf)}$	32 h*µg/mL	33.4 h*µg/mL
Elimination half-life	3 h	4 h
Clearance	48.4 mL/h	45.32 mL/h
Tmax	0.5 h	0.5 h
Cmax	1.835 µg/mL	1.790 µg/mL
Volume of Distribution	0.8 L/kg	-

Table 1:Plasma and Brain ECF PK parameters of AML-101 in SD-rats after intraperitoneal dosing

- These results suggest that AMLAL-101 has the requisite BBB permeability required for brain cancer therapeutics.
- The current study provides critical information necessary to develop a dosing regimen for in vivo efficacy studies of AMLAL-101.
- Further studies are underway to assess the efficacy of AMLAL-101 against patient-derived CNS cancer cells and in vivo efficacy assessment in tumor-bearing mice.

CONCLUSION

- AMLAL-101 shows significant brain retention when compared to a chemically similar agent that does not show anti-cancer activity, which may contribute to efficacy of AMLAL-101 as an anti-tumor agent for treatment of brain cancers.

REFERENCES

1. Desai, J. M., Karve, A. S., Gudelsky G. A., Gawali, M. V., Seibel, W., Sallans L., DasGupta B., & Desai, P. B. (2022). Brain pharmacokinetics and metabolism of the AMP-activated protein kinase selective inhibitor SBI-0206965 an investigational agent for the treatment of glioblastoma Investigationalnew drugs, 40(5), 944–952.
2. Sengupta S., Weeraratne S. D., Sun, H., Phallen J., Rallapalli S. K., Teider, N., Kosaras B., Amani, V., Pierre-Francois, J., Tang, Y., Nguyen, B., Yu, F., Schubert, S., Balansay B., Mathios, D., Lechpammer M., Archer, T. C., Tran, P., Reimer, R. J., Cook, J. M., … Cho, Y. J. (2014). α5-GABAA receptors negatively regulate MYC-amplified medulloblastomagrowth. Acta neuropathologica 127(4), 593–603.

University of CINCINNATI JAMES L. WINKLE COLLEGE OF PHARMACY

University of CINCINNATI COLLEGE OF MEDICINE

GL-I-54, a α_5-GABA$_A$ Receptor Positive Allosteric Modulator Shows Disease Modifying Effects in Chronic Stress of Mouse Models

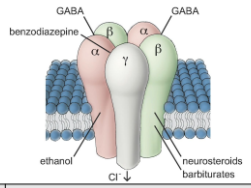
Sepideh Rezvanian[1], Farjana Rashid[1], Md Yeunus Mian[1], Prithu Mondal[1],Dishary Sharmin[1], Ashley Bernardo[2], Philippe Lee[3], Michael Marcotte[2], Etienne Sibille[2,3,4], Thomas D. Prevot[2,4], James M Cook[1]

[1]Department of Chemistry and Biochemistry, Milwaukee Institute for Drug Discovery, University of Wisconsin Milwaukee, Milwaukee, WI 53211
[2]Campbell Family Mental Health Research Institute of CAMH, Toronto, Canada
[3]Department of Pharmacology and Toxicology, University of Toronto, Toronto, Canada
[4]Department of Psychiatry, University of Toronto, Toronto, Canada

Abstract

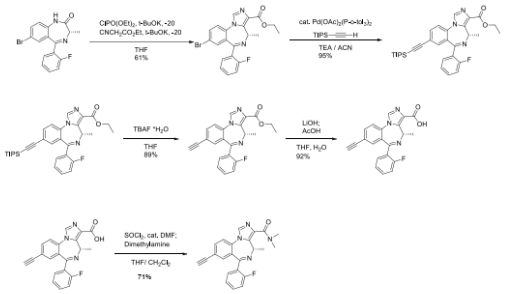
People experience mood and cognitive dysfunction if they are exposed to chronic stress, a major risk factor for developing depressive like behaviors. This is in part because of neuronal shrinking in brain region that are involved in several cognitive function. Cellular, molecular and behavioral changes that are observed in human depression can be recapitulated with mouse model of stress. In addition, the expression and function of γ-aminobutyric acid, main inhibitory neurotransmitter of GABA A receptor are reduced in context of chronic stress and depression. Drugs targeting this deficit are not able to produce desired effects due to non-selectivity at various GABA receptor subunits including the α1-subunit which causes side effects such as sedation and ataxia. GL-I-54, a α_5-GABA$_A$ subtype positive allosteric modulators was able to reduce stress induced disorder in chronic stress of mouse model devoid of adverse effects. The acute and chronic administration of GL-I-54 reduced anxiety-like phenotypes and reversed a working memory deficit in UCMS exposed mice in unpredictable chronic mild stress (UCMS) experiments. The drug selectively targeted GABAA receptors without interfering the α1-subunit, to overcome chronic stress-induced mood symptoms and cognitive deficits and the results were observed in old mice as well as young mice.

GABA/ BzR Chloride Ion Complex

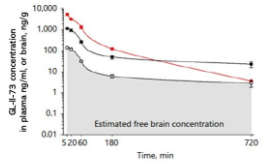


Subtype	Associated Effect
α1	Sedation, anterograde amnesia, some anticonvulsant action, ataxia, addiction
α2	Anxiolytic, analgesic, anticonvulsant, may be hypnotic at high doses, may be some muscle relaxation at high doses
α3	Some anxiolytic action, some anticonvulsant action, some analgesia, may be some muscle relaxation at high doses
α4	Diazepam-insensitive site
α5	Cognition, temporal and spatial memory, depression and schizophrenia
α6	Diazepam-insensitive site

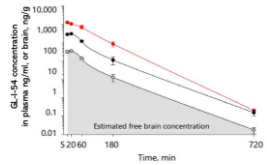
Synthesis of GL-I-54



Pharmacokinetic Properties of GL-II-73 and GL-I-54



	Plasma	Brain	
C_{max}	5,384.54 ± 838.04	1,195.94 ± 51.75	(ng/mL)
T_{max}	5.00 ± 0	10.00 ± 5.00	(min)
AUC_{0-720}	4,620.09 ± 323.21	1,311.86 ± 85.86	(ng*h/mL)
$AUC_{0-\infty}$	4,626.35 ± 322.80	1,397 ± 119.3	(ng*h/mL)
$T_{1/2}$	72.06 ± 1.44	146.58 ± 12.30	(min)
β	0.0096 ± 0.0002	0.0048 ± 0.0004	(1/min)
K_p	0.30 ± 0.04		
$K_{p,uu}$	0.18 ± 0.02		

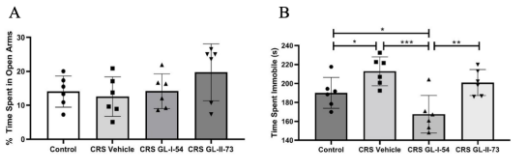


	Plasma	Brain	
C_{max}	1283.79 ± 4.18	320.13 ± 2.22	(ng/mL)
T_{max}	5.00 ± 0.00	15.00 ± 4.80	(min)
AUC_{0-720}	2445.94 ± 401.30	467.03 ± 36.06	(ng*h/mL)
$AUC_{0-\infty}$	2445.96 ± 401.30	467.05 ± 36.06	(ng*h/mL)
$T_{1/2}$	44.82 ± 0.45	49.20 ± 1.80	(min)
β	0.0155 ± 0.0002	0.0140 ± 0.0005	(1/min)
K_p	0.20 ± 0.20		
$K_{p,uu}$	0.10 ± 0.01		

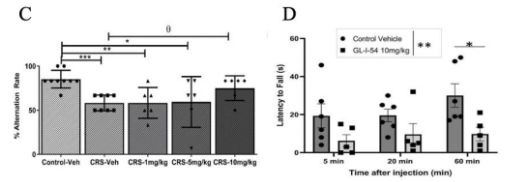
In vitro Cytotoxicity

	HEK293LD$_{50}$(μM)[a]	HEPG2 LD50 (μM)[a]
GL-I-54	>400	>400
GL-II-73	>200	>400

Behavioral Tests



GL-I-54 and GL-II-73 were tested in the elevated plus maze and forced swim test at the dose of 5mg/kg, in mice previously exposed to chronic restraint stress (CRS). Drugs were administered IP, 30min prior to testing. Percent time spent in the open arms (A) showed no difference between groups. Time immobile (B) showed more time spent immobile in the CRS-Vehicle group, and less time immobile in animals receiving GL-I-54, compared to CRS-Vehicle. GL-II-73 did not show an effect.



GL-I-54 was tested in the Y-maze task, assessing working memory (C). Animals subjected to CRS and receiving vehicle showed a significant decrease in alternation rate, suggesting a working memory deficit. Animal subjected to CRS and receiving the highest dose of GL-I-54 showed significant increase in alternation rate, suggesting reversal of working memory deficits induced by CRS. Finally, independent mice were tested in the rotarod (G, N=5 Control Vehicle and N=6 GL-I-54). Mice were trained to maintain themselves on a rotating rod (rotarod) for 3 trials. Then, they were injected with GL-I-54 at 10 mg/kg, and tested 5 min, 20 min and 60 min past injection time. Latency to fall from the rod was recorded and showed significant reductions in latency to fall in mice receiving GL-I-54.

Results and Conclusion

GL-II-73, the enantiomer of GL-I-54, displayed antidepressant-predictive property in the Forced Swim Test. Results presented here indicate that GL-I-54 has potential as an anti-depressive agent devoid of adverse effects. Consequently, GL-I-54 represents a promising lead compound for further studies. Since anxiety is comorbid with depression, the anti-anxiety results are important. Moreover, cognitive problems are a major problem with depression and GL-I-54 is also precognitive.

References

•*Li, G. et al. Arkivoc,* ***2018****, iv, 158-182*

•*Prevot, T. et al. Mol Neuropsychiatry,* ***2019****;5:84–97*

•*Bernardo, A. et al. BioRxiv,****2021****; 03.22.436517*

•*Prevot, T. et al. ACS Chem. Neurosci.* ***2019****, 10, 2088−2090.*

Acknowledgment

We wish to acknowledge the NIH for generous financial support (R01MH096463, R01NS076517, R01HL118561). We also thank the Milwaukee Institute for Drug Discovery and the Shimatzu Laboratory for Advanced Applied and Analytical Chemistry..

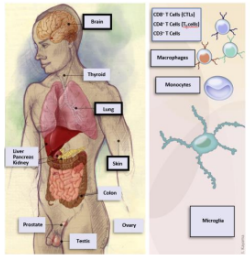
Synthesis and Activity of AM-101 in Medulloblastoma, Melanoma and Non-small Cell Lung Cancers.

Sepideh Rezvanian[1], Donatien Kamdem Toukam[2], Daniel Pomeranz Krummel[2], Soma Sengupta, James M. Cook,
[1]Department of Chemistry and Biochemistry, Milwaukee Institute for Drug Discovery, University of Wisconsin-Milwaukee, Milwaukee, WI
[2]Department of Neurology and Rehab Medicine, University of Cincinnati College of Medicine, Cincinnati, OH

Abstract

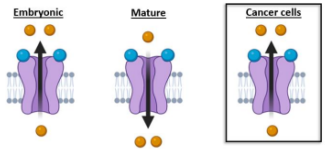
AM-101(QH-II-066) is a novel agent with promising anti-tumor activity against various types of group III cancers , including primary and metastatic brain tumors. The GABA(A)R drug selectively targets α5 subtypes of gaba-aminobutyric acid receptors. Not only is AM-101 being developed as an individual but also an 'add-on' to potentiate the treatment of primary and metastatic brain cancers with radiation and/or check point inhibitors. It penetrates the BBB in 25 minutes.as well as the lung. Basically, $GABA_A$ receptors in these cancer cells expell Cl^- ions out of the cells, analogous to embryonic GABA(A) receptors , but AM-101 enhances this Cl^- ion efflux seriously degrading mitochondrial function.
Additionally, AMLAL-101 is nontoxic in normal cells in rodents and monkeys. This lead agent is cytotoxic in cancer cells and can potentiate radiation and DNA-damaging chemo synergistically.
AM-101 enhances the infiltration of anti-tumor immune cells and it can treat primary site and metastatic lesions of different solid tumors.
This study shows AM-101 combined with radiation results in a significant reduction in the volume of cancer tumors, and the 'add on' works just as well with checkpoint inhibitors.

$GABA_A$ receptors are present in cancer & immune cells



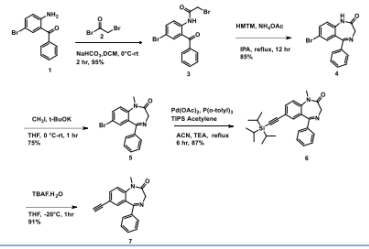
Tissue	Malignancy Type
Central nervous system	
Brain	Glioblastoma
	Medulloblastoma
	Neuroblastoma
Systemic	
Lung	NSCLC
Skin	Melanoma (Stage III/IV)
Liver	Hepatocellular carcinoma
Kidney	Renal cell carcinoma
Breast	Basal like
Pancreas	Ductal adenocarcinoma
Colon	Colorectal
Ovarian	Ovarian carcinoma
	Ovarian metastasis
Thyroid	Thyroid carcinomas
Prostate	Acinar adenocarcinoma
	Ductal adenocarcinoma

$GABA_A$ receptors in cancer move chloride anions out, not in

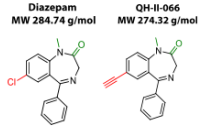


$GABA_A$ receptors in cancer cells move Cl^- out of the cells, like embryonic receptor

Synthesis of AM-101

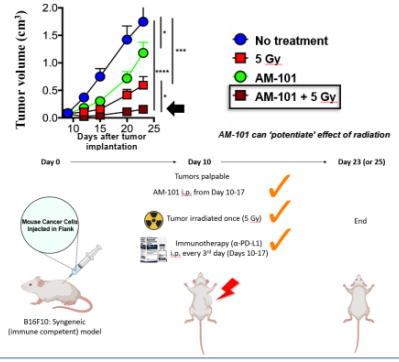


Significant difference in brain retention in rodents

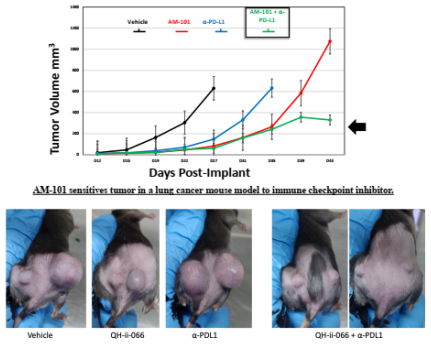


	Diazepam	AM-101
$t_{1/2}$, hrs (Plasma)	0.88	2.88
$t_{1/2}$, hrs (Brain ECF)	0.89	2.09

$GABA_A$ receptor 'activators' radiosensitize melanoma tumors



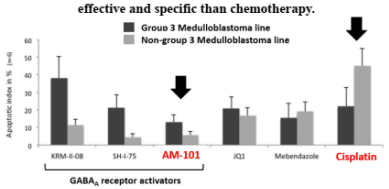
$GABA_A$ receptor 'activators' modulate the immune system



AM-101 sensitives tumor in a lung cancer mouse model to immune checkpoint inhibitor.

$GABA_A$ receptor 'activators' as effective as standard-of-care chemotherapy

Data from Intratumor drug sensitivity assay, 'activators' more effective and specific than chemotherapy.



Conclusions

- AM-101 combined with radiation results in near complete regression of irradiated tumor and shrinking of tumor not in the radiation field due to an immune response, i.e., a potent abscopal effect.
- when treating syngeneic mouse model B16F10 melanoma tumors, radiation dose can be reduced and its effectiveness improved, by activating intrinsic melanoma $GABA_A$ receptor ($GABA_AR$) activity using a novel agent, AM-101. This agent acts to enhance $GABA_AR$ mediated chloride transport in melanoma cells, which in turn triggers mitochondrial dysregulation associated with tumor regression in mice. AM-101 also enhances infiltration into tumors of anti-tumor immune cells.

Contact

Sepideh Rezvanian
University of Wisconsin Milwaukee
rezvani3@uwm.edu

References

- *Pomeranz Krummel et al. International Journal of Radiation Oncology, Biology, Physics. Vol. 109, 2021*
- *Huang, Zhang, Liu, McKernan, Cook. Medicinal Chem Res 1996; 6(3): 384–391..*
- *Bhattacharya et al. Experimental Biology and Medicine. Vol.246, 2021.*
- *Rao, et al. Ligand-gated ion channels as targets for treatment and management of cancers. Frontiers in Physiology, 2022.*

UNIVERSITY of WISCONSIN
UWMILWAUKEE

Synthesis of Chiral Imidazodiazepines as a-Subtype Selective GABA(A) R Modulators to Treat Schizophrenia and Depression

Sepideh Rezvanian, Guanguan Li, Farjana Rashid and James M. Cook

Department of Chemistry and Biochemistry, University of Wisconsin -Milwaukee, Milwaukee, WI

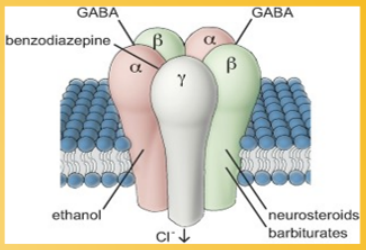


UNIVERSITY of WISCONSIN UWMILWAUKEE

Abstract

A series of new imidazodiazepine chiral ligands with various substituents were designed, synthesized and evaluated for their alpha 2,3, and 5 subtype selective GABA(A) receptor efficacy. The alp5 GABAergic ligand reversed PCP- induced prepulse inhibition (PPI) of acoustic startle. Based on the data up to date, it has been clearly illustrated that the R and S-4- substituted chiral IMZDs exhibited different subtype selectivity at Bz/GABA(A)ergic receptors. It has been shown that the ligands which contain a chiral(S) methyl group at the C (4) position of the IMDZ tend to be α2/3/5 subtype selective ligand, whereas the (R) isomers are a5 subtype selective ligands. GL-I-54, a chiral S-CH3 ligand is targeted for the treatment of schizophrenia and depression. The design and synthesis of alp 5 (R) and (S) isomeric ligands route will be presented.

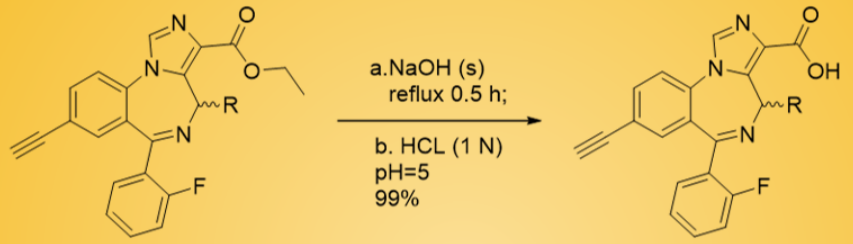
GABA/ BzR Chloride Ion Complex



Subtype	Associated Effect
α1	Sedation, anterograde amnesia, some anticonvulsant action, ataxia, addiction
α2	Anxiolytic, analgesic, anticonvulsant, may be hypnotic at high doses, may be some muscle relaxation at high doses
α3	Some anxiolytic action, some anticonvulsant action, some analgesia, may be some muscle relaxation at high doses
α4	Diazepam -insensitive site
α5	Cognition, temporal and spatial memory, depression and schizophrenia
α6	Diazepam -insensitive site

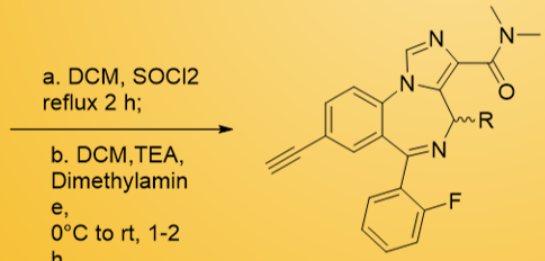
UNIVERSITY of WISCONSIN
UWMILWAUKEE

Synthesis of Dimethyl amide Enantiomers



1a R= R-CH3
1b R=S-CH3

2a R= R-CH3
2b R=S-CH3

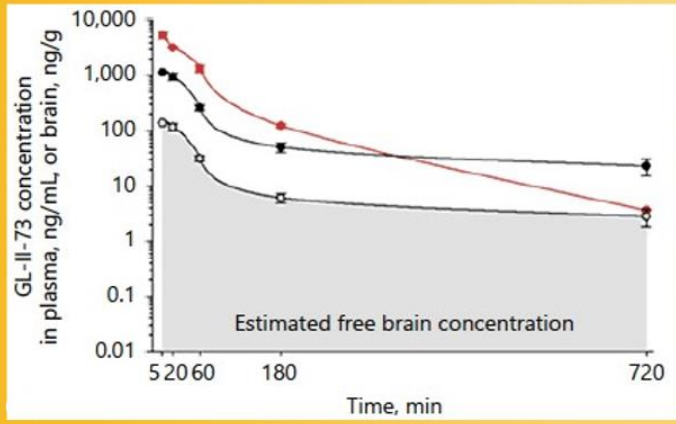


3a R= R-CH3 (GL-II-73)
3b R=S-CH3 (GL-I-54)

UNIVERSITY of WISCONSIN
UWMILWAUKEE

Biology of GL-II-73

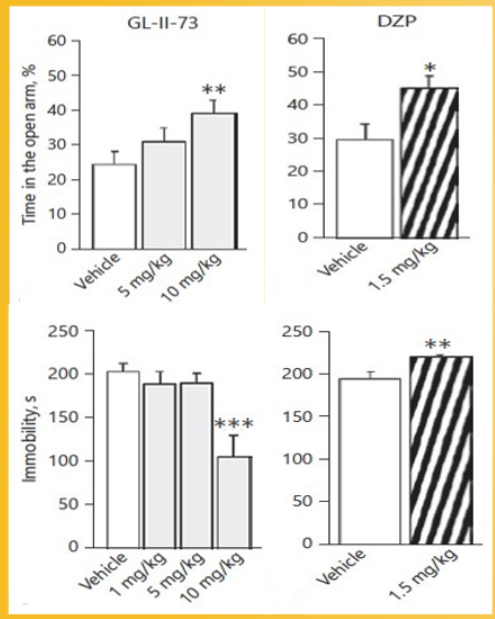
pharmacokinetic properties



	Plasma	Brain	
C_{max}	5,384.54 ± 838.04	1,195.94 ± 51.75	(ng/mL)
T_{max}	5.00 ± 0	10.00 ± 5.00	(min)
AUC_{0-720}	4,620.09 ± 323.21	1,311.86 ± 85.86	(ng*h/mL)
$AUC_{0-\infty}$	4,626.35 ± 322.80	1,397 ± 119.3	(ng*h/mL)
$T½$	72.06 ± 1.44	146.58 ± 12.30	(min)
β	0.0096 ± 0.0002	0.0048 ± 0.0004	(1/min)
K_p	0.30 ± 0.04		
$K_{p,uu}$	0.18 ± 0.02		

UNIVERSITY of WISCONSIN
UWMILWAUKEE

Anxiolytic and antidepressant properties of the lead compound GL -II-73 compared to diazepam (DZP)



Statistical analysis for each test assessing emotionality in mice behavior

	GL-II-73			
Assay	Dose (mg/kg)	N	ANOVA values	p-value
Elevated Plus Maze	0 (i.p.)	13	F(2,37)=3	-
	5 (i.p.)	13	.7 ;	0.24
	10 (i.p.)	14	p=0.03	**0.009**
Forced Swim test	0 (i.p.)	8	F(3,26)=7	-
	1 (i.p.)	8	.2 ;	0.53
	5 (i.p.)	6	p=0.001	0.58
	10 (i.p.)	8		**0.0003**

UNIVERSITY of WISCONSIN
UWMILWAUKEE

In vitro microsomal stability

Entry	Microsomal stability (HLM) after 2 hr		Microsomal stability (MLM) after 2 hr	
	Half-life (min)	% remaining	Half-life (min)	% remaining
GL-I-54	100 ± 4.5	36.4± 2	53 ± 10	15 ± 3
GL-II-73	280 ± 31	73.34 ± 0.6	472.7 ± 56	81.6 ± 0.27

In vitro cytotoxicity

Entry	HEK293LD_{50}(μM)[a]	HEPG2 LD50 (μM)[a]
GL-I-54	>400	>400
GL-II-73	>200	>400

Result and Conclusion

Our promising lead compound, GL -II-73 shows stunning results in -vivo studies. In addition, the novel ligands GL -I-54 is metabolically stable in human and mouse liver microsomes and exhibit excellent cytotoxicity as well as GL -II-73. GL-I-54 results indicate good safety and metabolic profile for further in -vivo behavioral testing in animal models in both Schizophrenia and depression.

References

- *Li, G. et al. Arkivoc,* ***2018****, iv, 158-182*
- *Prevot, T. et al. Mol Neuropsychiatry,* ***2019****;5:84–97*

Acknowledgment

We wish to acknowledge the NIH for generous financial support (R01MH096463, R01NS076517, R01HL118561). We also thank the Milwaukee Institute for Drug Discovery

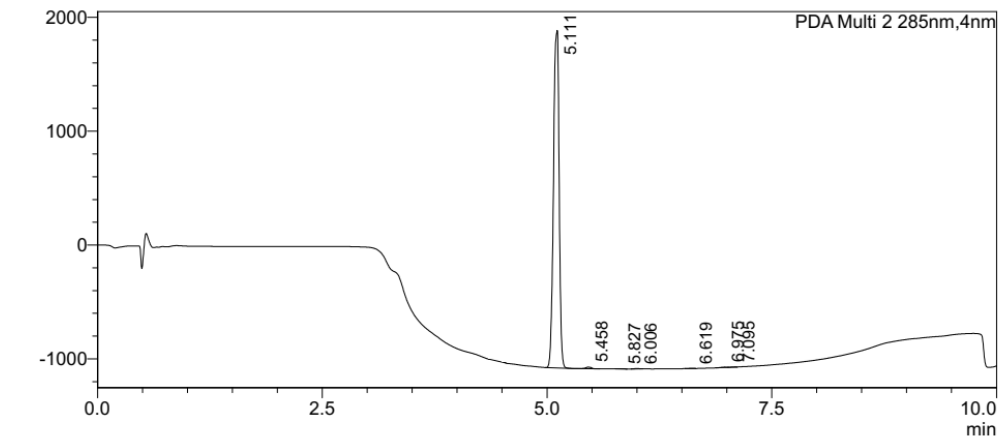
SHIMADZU LabSolutions

Analysis Report

<Sample Information>

Sample Name	: SRE		
Sample ID	:		
Data Filename	: SRE_Gradient 3 ABBA 40 short_10-24-2023a_004.lcd		
Method Filename	: Gradient 3 ABBA 40 short.lcm		
Batch Filename	: 10-24-2023a.lcb		
Vial #	: 4-38	Sample Type	: Unknown
Injection Volume	: 1 uL		
Date Acquired	: 10/24/2023 4:11:41 PM	Acquired by	: Anna M Benko
Date Processed	: 10/25/2023 9:49:50 AM	Processed by	: Anna M Benko

<Chromatogram>



<Peak Table>

SRE_Gradient 3 ABBA 40 short_10-24-2023a_004.lcd

PDA Ch2 285nm

Peak#	Ret. Time	Area	Area%
1	5.111	15314306	99.268
2	5.458	72427	0.469
3	5.827	8316	0.054
4	6.006	11543	0.075
5	6.619	5937	0.038
6	6.975	11045	0.072
7	7.095	3538	0.023
Total		15427112	100.000

Method SRE_Gradient 3 ABBA 40 short_10-24-2023a_004.lcd

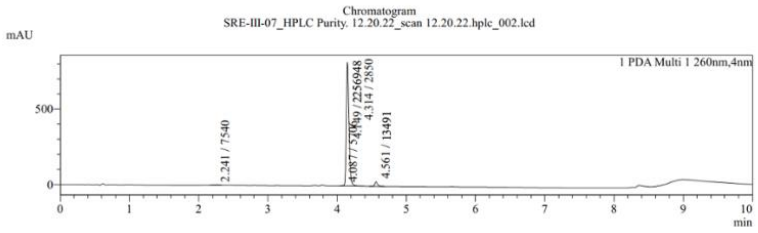
<<Header>>
Generated : 10/24/2023 3:36:04 PM

<<Pump>>
Mode : Binary gradient
Pump A : LC-30AD
Pump B : LC-30AD
Total Flow : 0.5000 mL/min
B Conc. : 2.0 %
B Curve : 0

Status:Manual Integration

Sample Information SRE-III-07_HPLC Purity. 12.20.22_scan 12.20.22.hplc_002.lcd

Acquired by	: sepideh rezvanian
Date Acquired	: 12/20/2022 10:50:03 AM
Sample Type	: Unknown
Level#	:0
Sample Name	: SRE-III-07
Sample ID	: SRE-III-07
ISTD Amount	: (Level1 Conc.)
Sample Amount	: 1
Dilution Factor	: 1
Tray#	: 3
Vial#	: 29
Injection Volume	: 0.5
Data File	: SRE-III-07_HPLC Purity. 12.20.22_scan 12.20.22.hplc_002.lcd
Method File	: HPLC Purity. 12.20.22.lcm
Original Method File	: HPLC Purity. 12.20.22.lcm
Report Format File	: DEFAULT.lsr
Tuning File	: 20220510_AT.lct
Processed by	: sepideh rezvanian
Date Processed.	: 12/20/2022 11:07:45 AM



Peak Table SRE-III-07_HPLC Purity. 12.20.22_scan 12.20.22.hplc_002.lcd

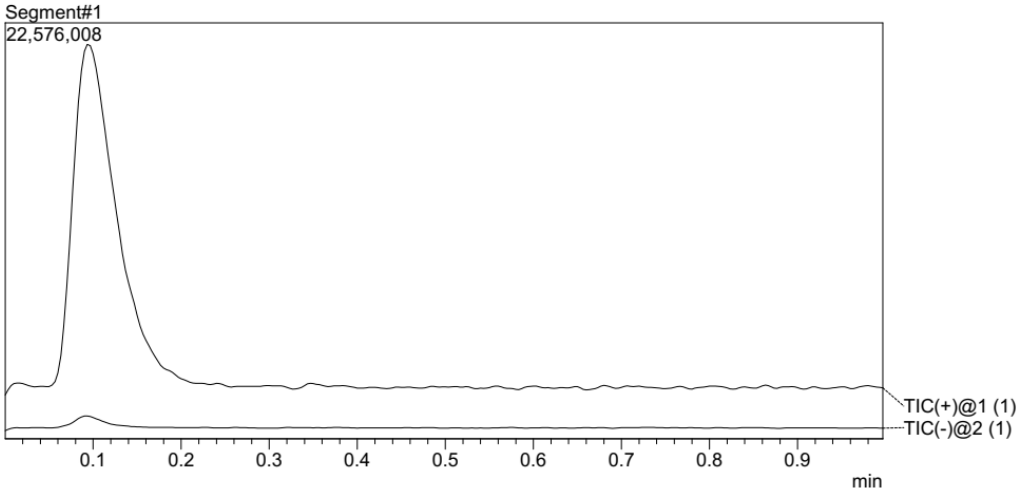
PDA Ch1 260nm

Peak#	Ret. Time	Area	Area%
1	2.241	7540	0.330
2	4.087	5706	0.250
3	4.149	2256948	98.706
4	4.314	2850	0.125
5	4.561	13491	0.589
Total		2286535	100.000

==== Shimadzu Labsolutions Data Report ====

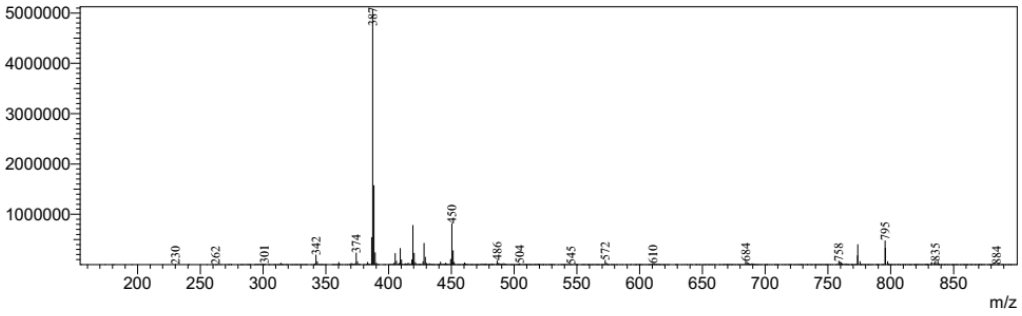
Sample ID : SRE-I-72 Date Acquired :3/19/2021 9:56:54 AM
Data Filename : scan 03.19.21 SRE-I-72 004.lcd

<Chromatogram>



<Spectrum>

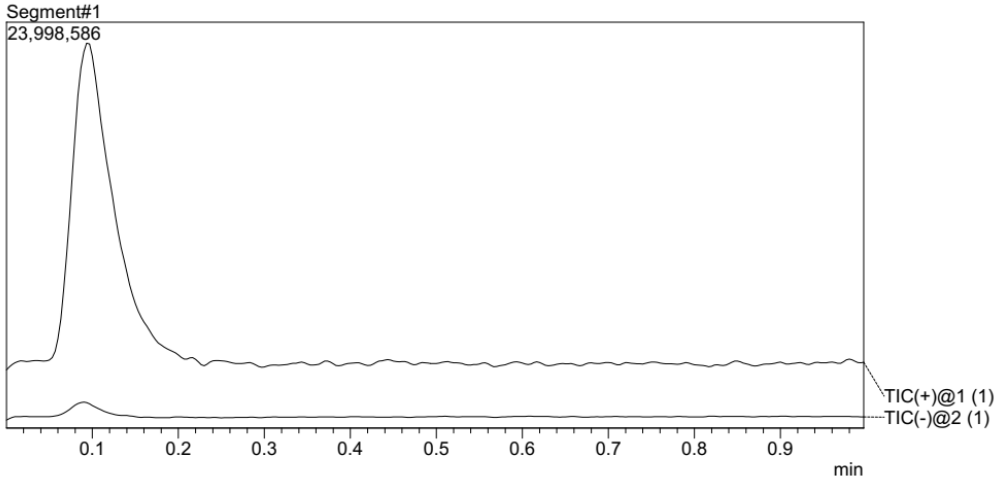
R.Time:----(Scan#:----)
MassPeaks:556 BasePeak:387(5072974)
Spectrum Mode:Averaged 0.070-0.110(43-67)
BG Mode:Averaged 0.747-0.910(449-547) Polarity:Positive Segment 1 - Event 1



==== Shimadzu Labsolutions Data Report ====

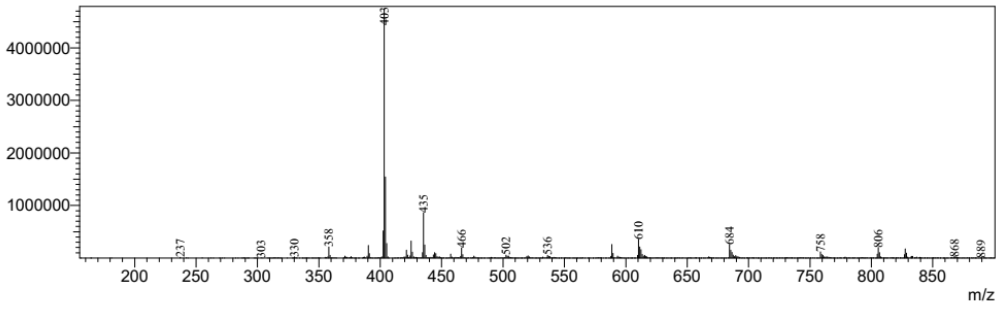
Sample ID : SRE-II-11 Date Acquired :3/19/2021 10:00:06 AM
Data Filename : scan 03.19.21 SRE-II-11 006.lcd

<Chromatogram>



<Spectrum>

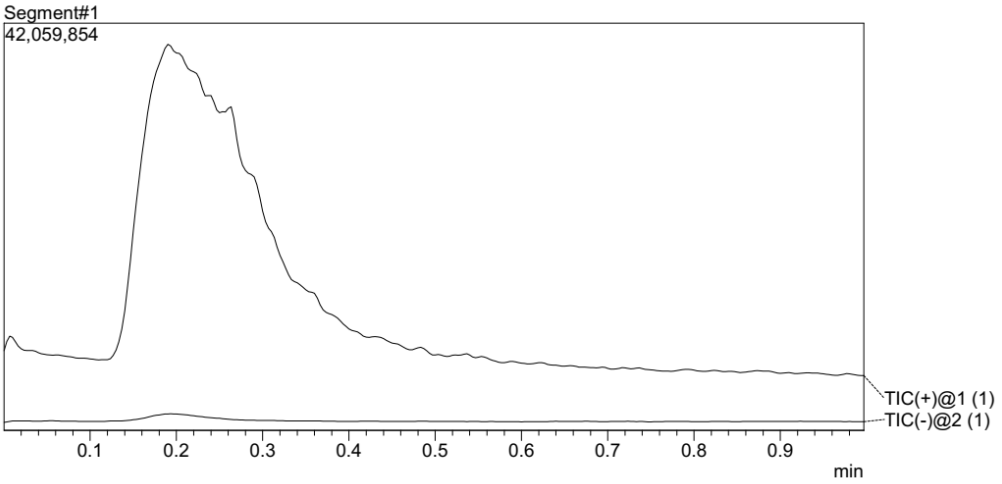
R.Time:----(Scan#:----)
MassPeaks:586 BasePeak:403(4742267)
Spectrum Mode:Averaged 0.070-0.113(43-69)
BG Mode:Averaged 0.783-0.917(471-551) Polarity:Positive Segment 1 - Event 1



==== Shimadzu Labsolutions Data Report ====

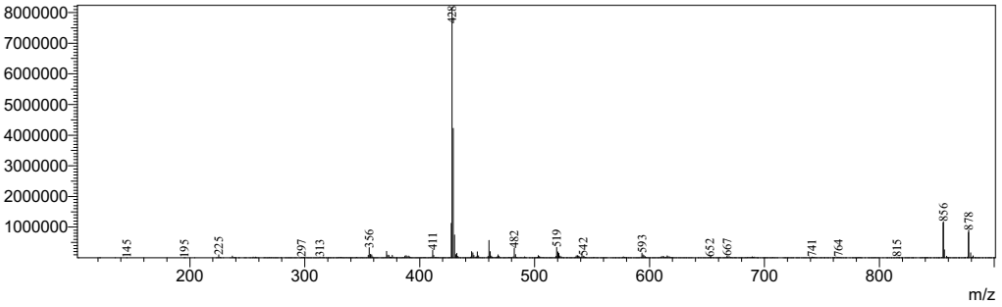
Sample ID : SRE-II-42 Date Acquired :6/14/2021 3:25:37 PM
Data Filename : SRE-II-42 scan 6.14.21 004.lcd

<Chromatogram>



<Spectrum>

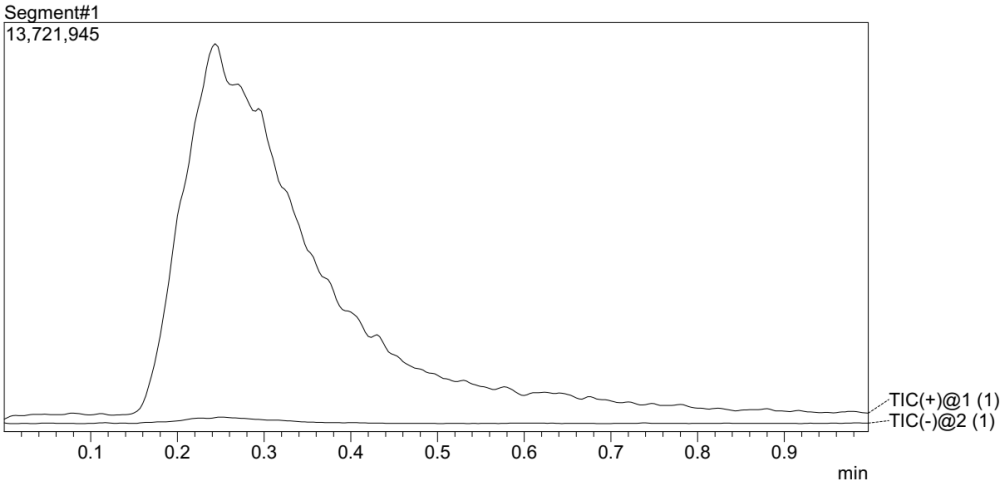
R.Time:----(Scan#:----)
MassPeaks:624 BasePeak:428(8153356)
Spectrum Mode:Averaged 0.143-0.210(87-127)
BG Mode:Averaged 0.840-0.927(505-557) Polarity:Positive Segment 1 - Event 1



==== Shimadzu Labsolutions Data Report ====

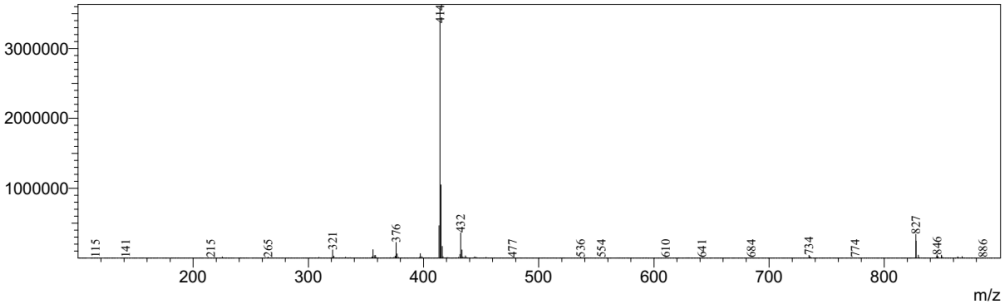
Sample ID : SRE-II-44,2 Date Acquired :8/5/2021 5:25:18 PM
Data Filename : SRE-II-44,2_scan 08.05.2021_010.lcd

<Chromatogram>



<Spectrum>

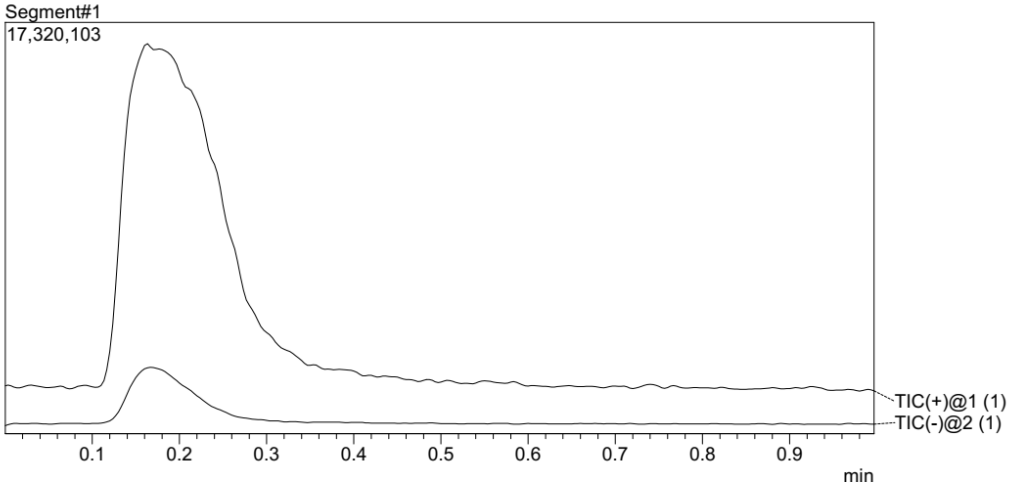
R.Time:----(Scan#:----)
MassPeaks:772 BasePeak:414(3596259)
Spectrum Mode:Averaged 0.177-0.273(107-165)
BG Mode:Averaged 0.837-0.950(503-571) Polarity:Positive Segment 1 - Event 1



==== Shimadzu Labsolutions Data Report ====

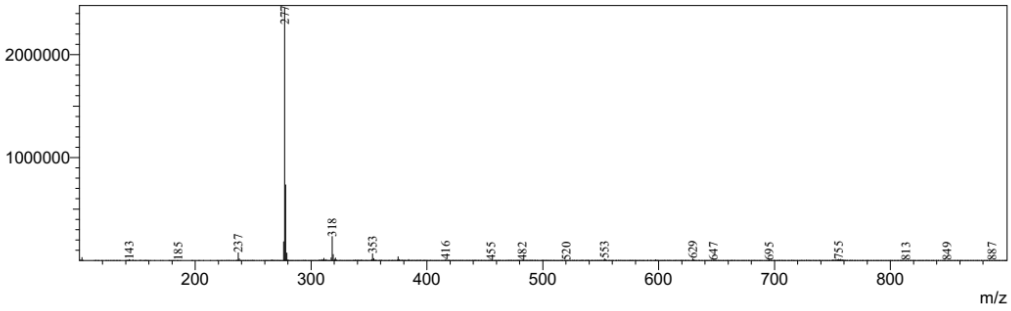
Sample ID : SRE-III-35 Date Acquired :10/31/2022 7:08:38 PM
Data Filename : SRE-III-35 scan 10.31.2022 004.lcd

<Chromatogram>



<Spectrum>

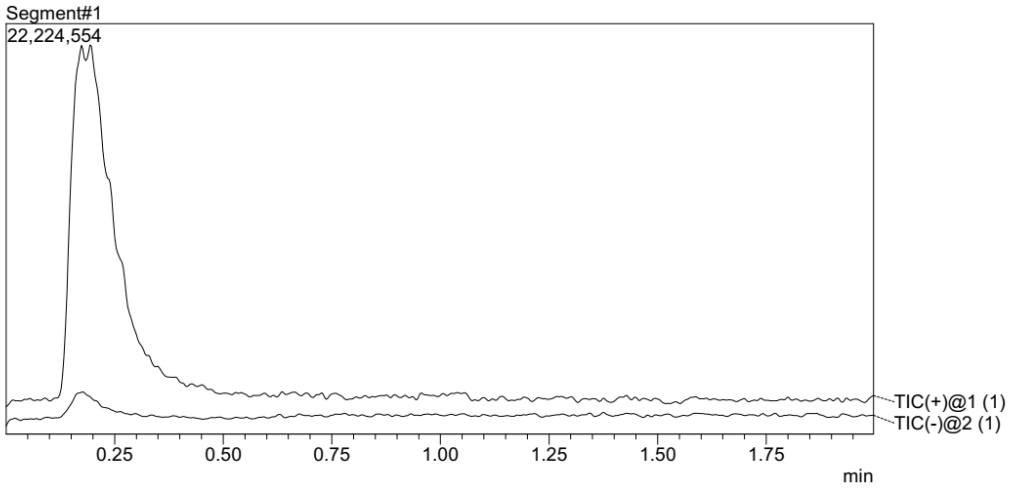
R.Time:----(Scan#:----)
MassPeaks:720 BasePeak:277(2452730)
Spectrum Mode:Averaged 0.077-0.160(47-97)
BG Mode:Averaged 0.817-0.937(491-563) Polarity:Positive Segment 1 - Event 1



==== Shimadzu Labsolutions Data Report ====

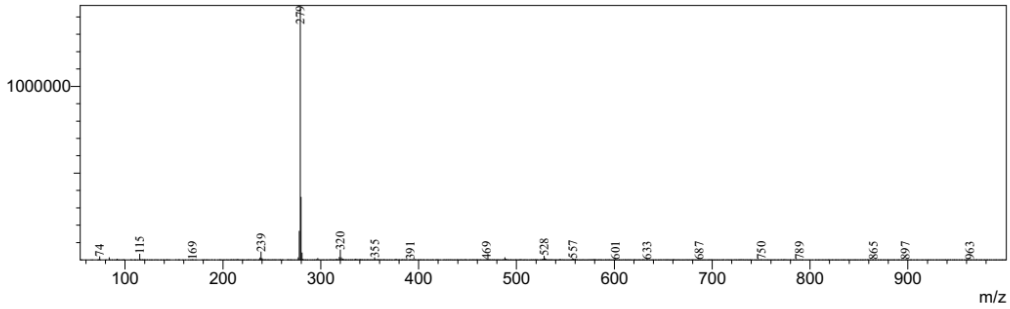
Sample ID : SRE-IV-11.After MeOH Date Acquired :9/15/2023 6:33:54 PM
Data Filename : SRE-IV-11.After MeOH scan 09.15.2023 006.lcd

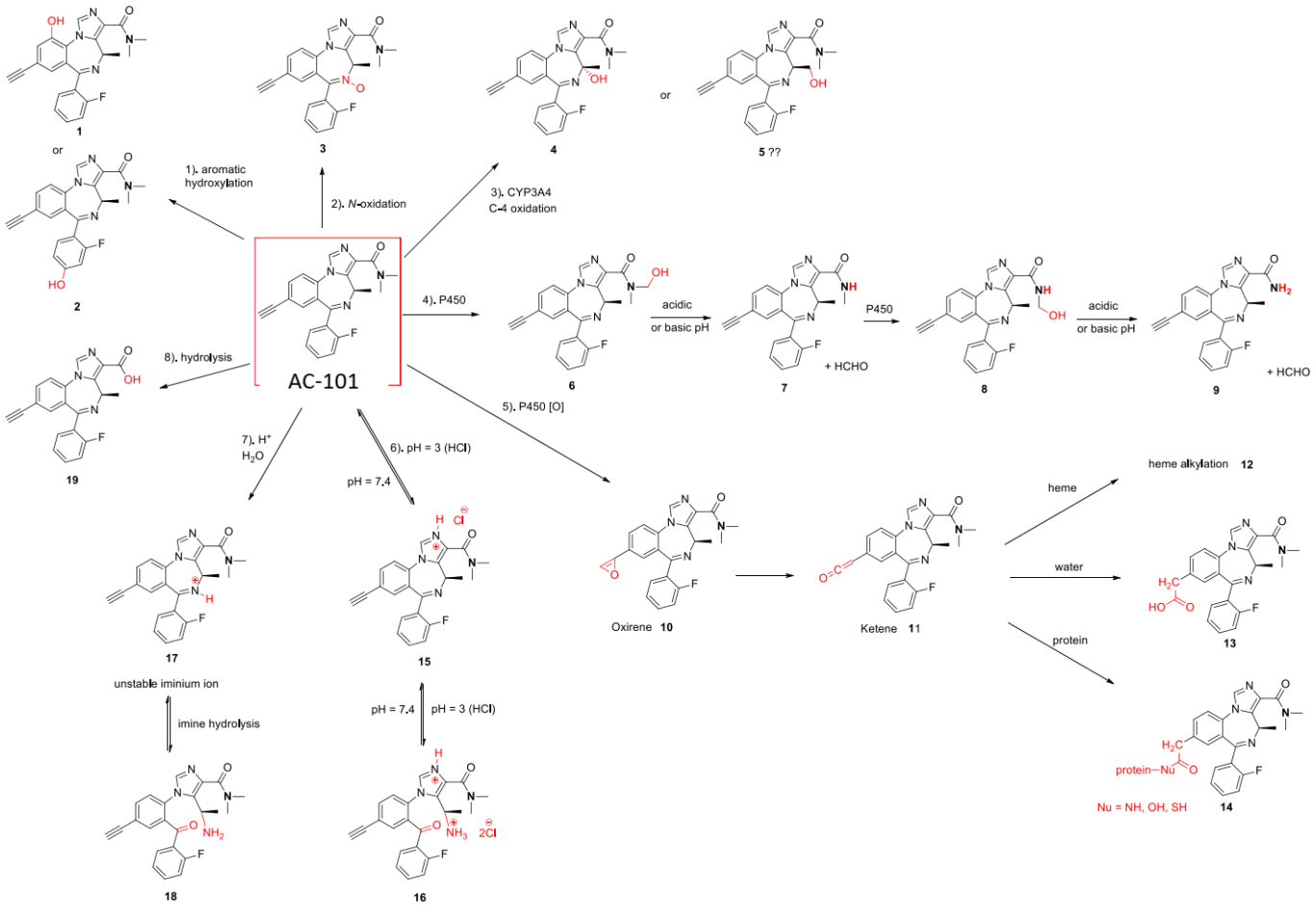
<Chromatogram>



<Spectrum>

R.Time:----(Scan#:----)
MassPeaks:845 BasePeak:279(1451650)
Spectrum Mode:Averaged 0.067-0.157(41-95)
BG Mode:Averaged 1.653-1.857(993-1115) Polarity:Positive Segment 1 - Event 1




AC-101
1
or
2
3
4
or
5 ??
1). aromatic hydroxylation
2). N-oxidation
3). CYP3A4 C-4 oxidation
4). P450
5). P450 [O]
6). pH = 3 (HCl)
pH = 7.4
7). H+ H2O
8). hydrolysis
19
6
acidic or basic pH
7
+ HCHO
P450
8
acidic or basic pH
9
+ HCHO
Oxirene 10
Ketene 11
heme
water
protein
heme alkylation 12
13
protein–Nu
Nu = NH, OH, SH
14
15
16
17
unstable iminium ion
imine hydrolysis
18
pH = 7.4
pH = 3 (HCl)

Description

As for the metabolites, I did some literature search on possible pathways of our compound, please see the second attachment. Here is a brief description of the possible pathways:

1. The compound can undergo aromatic hydrolysis and a hydroxyl group can be introduced at two positions (**1** or **2**)
2. *N*-oxidation (**3**)
3. C(4) oxidation by CYP3A4, a hydroxyl group added at C(4) position (**4**). Or maybe at the *R*-methyl group (**5**), this I'm not sure.
4. *N*-Dealkylation processes catalyzed by cytochrome P450s, leading to a carbinol-amide intermediate (**6**), which eliminates a molecule of aldehyde to produce a secondary amide (**7**). The same process can be applied to form another intermediate (**8**), and further form a primary amide (**9**).
5. The terminal acetylene can be metabolized by cytochrome P450 to form a reactive ketene intermediate (**11**). The ketene then proceeds to alkylate either the P450 heme moiety (**12**)and/or apoprotein. react with water to form a carboxylic acid metabolite (**13**). Or binds with proteins (**14**).
6. At acidic pHs (pH = 3), imine hydrolysis may occur (**16**) from the salts formed from the heterocyclic benzodiazepines (**15**), but the reaction does not proceed furthermore, and at physiologic pH (post-injection) reformation of the benzodiazepine ring is favored.
7. At acidic condition, iminium ion salts (**17**) can only be formed with strong acids, which are unstable and readily undergo sequential hydrolysis to form the inactive product (**18**).
8. Since GL-II-73 is an amide, it can be hydrolyzed to its carboxylic acid (**19**).

A new class of immune modulators

A particularly promising avenue for treatment of solid tumors is an immunotherapeutic approach in which the body's immune system is artificially stimulated to directly identify and attack the tumor cells. A variety of methods including immune checkpoint inhibition [1,2], T-cell transfer [3], vaccination [4], and viral approaches are being pursued (Fig. 1). Barriers such as tumor heterogeneity, the immunosuppressive nature of many cancers, and the limited number of identifiable targets has reduced the efficacy of these approaches. There is therefore a significant demand for agents that can turn tumors responsive to immunotherapy approaches.

An immunotherapy approach may involve either antagonizing the tumor's inherent immune suppressive properties or conversely inducing a cancer-specific immune response using either exogenous or endogenous agents. Immunotherapy has recently been popularized by impressive outcomes in hematogenous malignancies [5]. We have shown that treating a melanoma mouse model with a member of a benzodiazepine class of compounds, an 'activator' of the GABAA receptor, tumor regression is enhanced [6]. Molecular analysis of the treated tumors compared to untreated tumor bearing mice, revealed that tumor regression was commensurate with infiltration into the tumor microenvironment of polyfunctional CD8+ T-cells loaded with the cytokines interferon-gamma (IFN-g) and tumor necrosis factor alpha (TNF-a). This observation lead us to explore the infiltration of other immune cells into the tumor microenvironment.

We find that in the melanoma mouse model B16F10, tumors show relative to control (untreated) an enhanced presence of macrophages of the anti-tumor M1-phenotype (unpublished). This is based on immunohistochemical staining of control vs treated tumors. This result suggests that the benzodiazepine class of compounds elicit a phenotypic switching (or 'reprogramming') of immune cell populations.

We then explored whether one of our GABAA receptor 'activators' (AM1-1) can potentiate the response of immunotherapy. We also tested the effect of a member of this class of activators to enhance the effect of the immune checkpoint inhibitor anti-PDL1. To test this we employed the Lewis Lung cancer model which is considered a non-immunogenic model and poorly responsive to anti-PDL1 treatment. Indeed, we find that there is a minimal effect of anti-PDL1 alone on tumor volume in this mouse model (Fig. 2). Our activator alone shows an enhanced effect vs anti-PDL1. Importantly, combining anti-PDL1 with our activator we observe: (1) a significantly greater effect in reducing tumor volume as compared to either anti-PDL1 or our activator alone; (2) the effect is sustained i.e., tumor is kept under control (Fig. 2).

References

The following references are cited herein to support certain statements made with respect to the background of the subject matter. Citation should not be construed as relevant to patentability of the subject matter. The entire disclosures of the cited references are incorporated herein by reference.

1. Brahm, C.G.; van Linde, M.E.; Enting, R.H.; Schuur, M.; Otten, R.H.J.; Heymans, M.W.; Verheul, H.M.W.; Walenkamp, A.M.E. The Current Status of Immune Checkpoint Inhibitors in Neuro-Oncology: A Systematic Review. Cancers (Basel) 2020, 12, E586.

2. Majd, N.; Dasgupta, P.; de Groot, J. Immunotherapy for Neuro-Oncology. Adv Exp Med Biol 2020, 1244, 183–203.

3. Maggs, L.; Cattaneo, G.; Dal, A.E.; Moghaddam, A.S.; Ferrone, S. CAR T Cell-Based Immunotherapy for the Treatment of Glioblastoma. Front Neurosci 2021, 15, 662064.

4. Keskin, D.B.; Anandappa, A.J.; Sun, J.; Tirosh, I.; Mathewson, N.D.; Li, S.; Oliveira, G.; Giobbie-Hurder, A.; Felt, K.; Gjini, E.; et al. Neoantigen Vaccine Generates Intratumoral T Cell Responses in Phase Ib Glioblastoma Trial. Nature 2019, 565, 234–239.

5. Melenhorst, J.J.; Chen, G.M.; Wang, M.; Porter, D.L.; Chen, C.; Collins, M.A.; Gao, P.; Bandyopadhyay, S.; Sun, H.; Zhao, Z.; et al. Decade-Long Leukaemia Remissions with Persistence of CD4+ CAR T Cells. Nature 2022, 1–7.

6. Pomeranz Krummel, D.A., Nasti T.H., Kaluzova M., Kallay L., Bhattacharya D., Melms J.C., Izar B., Xu M., Burnham A., Ahmed T., Li G., Lawson D., Kowalski J., Cao Y., Switchenko J.M., Ionascu D., Cook J.M., Medvedovic M., Jenkins A., Khan M.K., Sengupta S. Melanoma Cell Intrinsic GABAA Receptor Enhancement Potentiates Radiation and Immune Checkpoint Inhibitor Response by Promoting Direct and T Cell-Mediated Antitumor Activity. Int J Radiat Oncol Biol Phys. 2021, 109(4), 1040-1053.

Figures

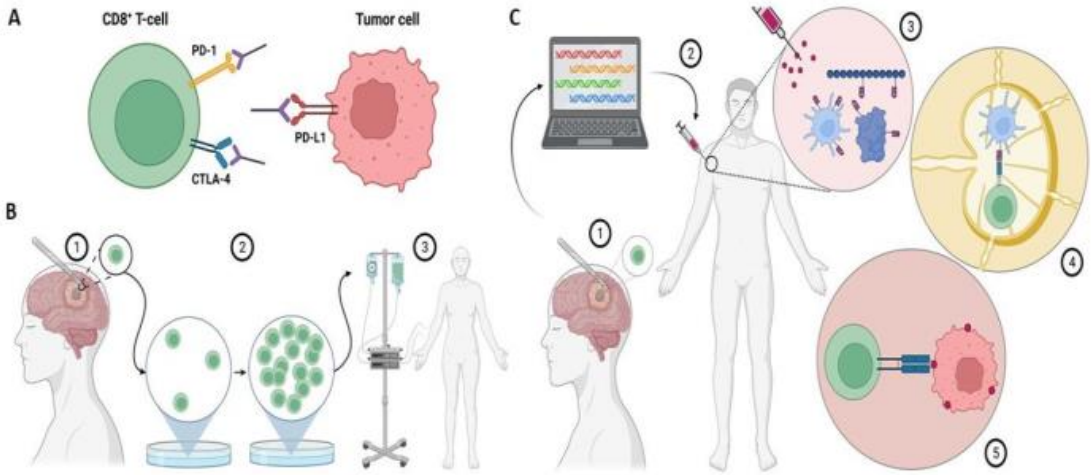


Figure 1. Immunotherapy approaches shown for treatment of brain tumors. (a) Immune checkpoint inhibitors bind to and inhibit immunosuppressive molecules on either T-cells or tumor cells. This dampens tumor cells' ability to evade the immune system. (b) (1) In tumor-infiltrating lymphocyte (TIL) therapy, T-cells from the tumor microenvironment are isolated following surgical resection. (2) Isolated T-cells are clonally expanded using IL-2 stimulation. (3) Expanded T-cells are reintroduced to patient. (c) (1) In the vaccine approach, resected tumor biopsy is taken from patient and sequenced to identify neoantigens. (2) Neoantigens are then delivered via vaccine. (3) At the site of injection, neoantigens stimulate antigen presenting cells (APCs). (4) In the lymph node, APCs present T-cells with neoantigens. (5) Activated T-cells at-tack cancer cells (from *Lechpammer M, et al. Advances in Immunotherapy for the Treatment of Adult Glioblastoma: Overcoming Chemical and Physical Barriers. Cancers (Basel). 2022;14(7):1627*).

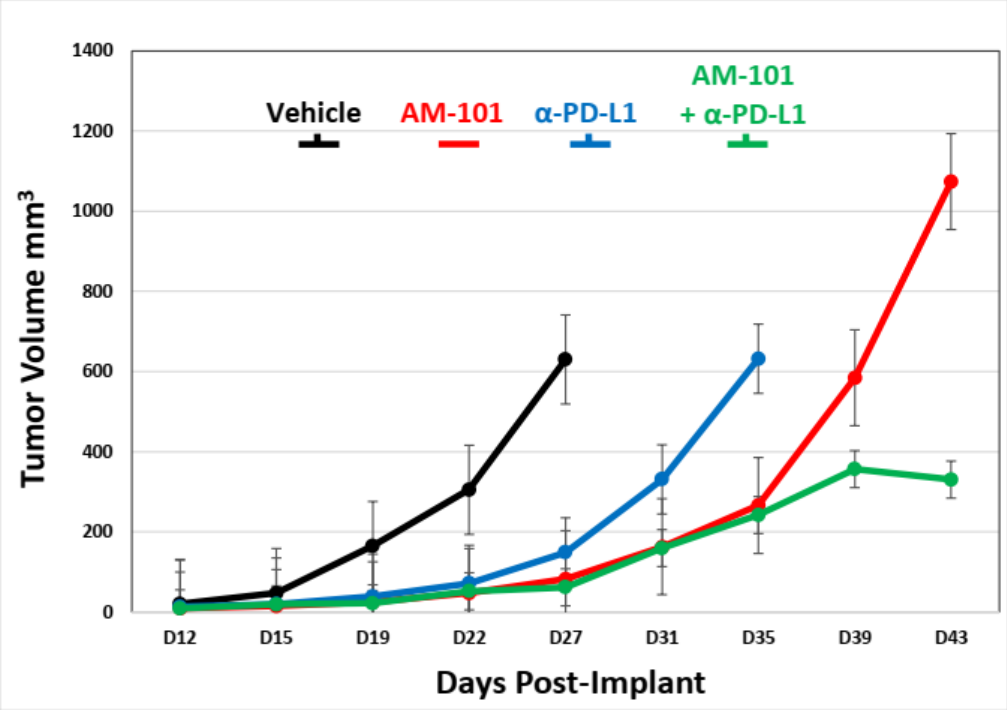
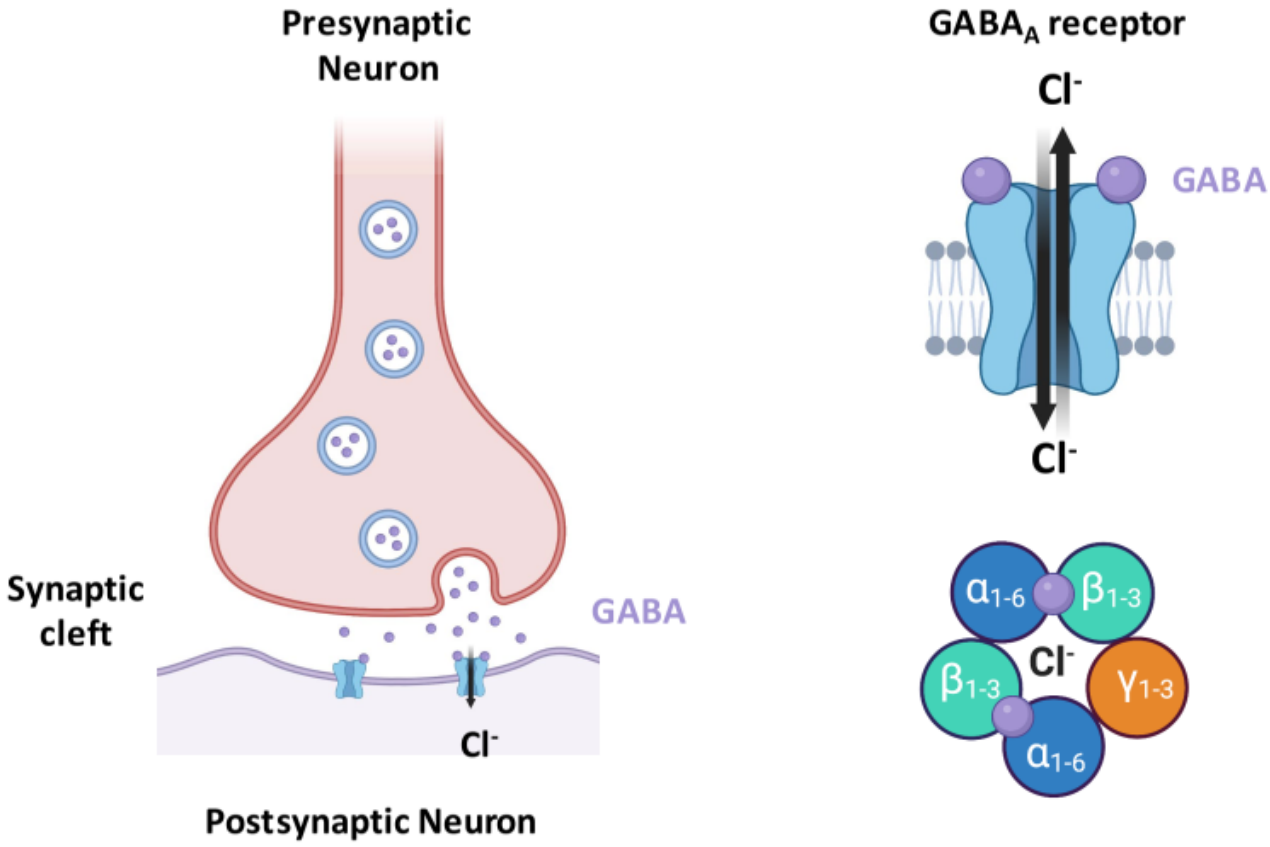


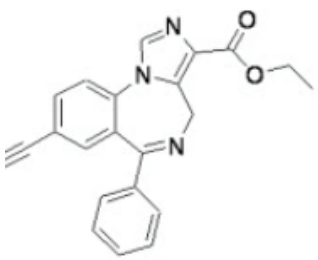
Figure 2. In vivo treatment of mice bearing Lewis Lung Cancer (LLC) flank tumors. Shown is effect of treating mice bearing tumors with our 'activator' (AM-101), an immune checkpoint inhibitor (anti-PDL1), and a combination of AM-101 and anti-PD-L1.

Signal transmission at a chemical synapse



Rao, et al. Ligand-gated ion channels as targets for treatment and management of cancers. Frontiers in Physiology, 2022.

c1990s, Development of $GABA_A$ receptor subtype-specific anticonvulsants-anxiolytics: nonsedating and devoid of side effects



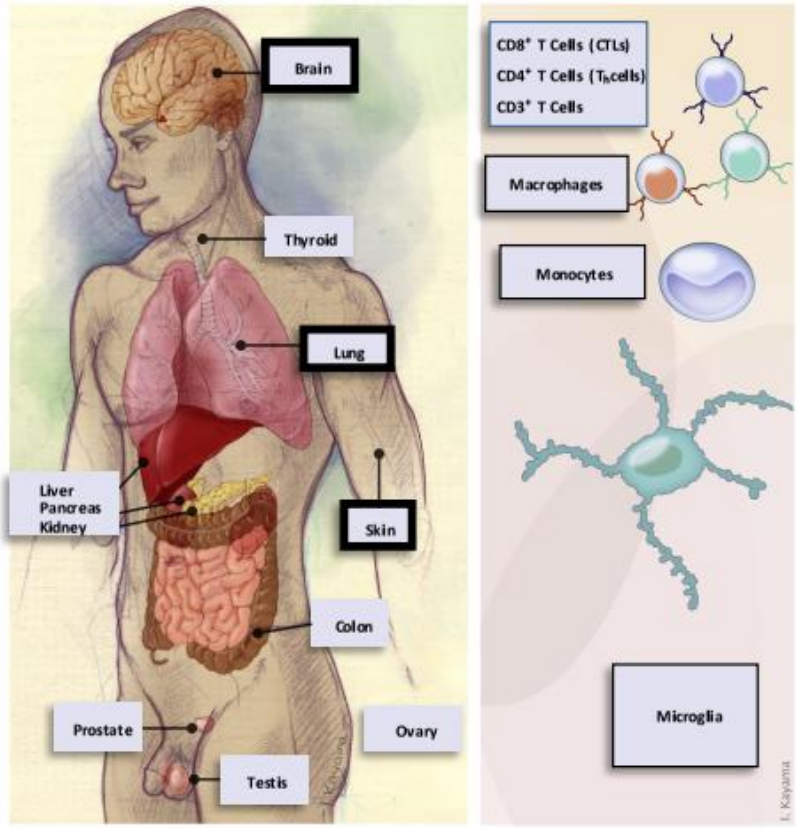
XHe-II-053

Lewter, L.; Fisher, J.; Siemian, J.; Methuku, K..; Poe, M.; Cook, J.M.; Li, Jun-Xu, Antinociceptive Effects of a Novel α2/α3 Subtype Selective GABA(A) Receptor Positive Allosteric Modulator, ACS *Chem Neurosci*, (2017).

Huang Q, Zhang W, Liu R, McKernan RM, Cook JM (1996). Benzo-fused benzodiazepines employed as topological probes for the study of benzodiazepine receptor

Witkin, J. M. The α2,3-Selective Potentiators of GABA(A) Receptors, KRM-II-81 and MP-III-80, Produce Anxiolytic Effects and Block Chemo Therapy – Induced Hyperalgesia in Mice without Tolerance Development. *Pharm.Biochem.Beha-v.* 196, 172996, 2020.

$GABA_A$ receptors are also present in cancer & immune cells



Tissue	Malignancy Type
Central nervous system	
Brain	Glioblastoma
	Medulloblastoma
	Neuroblastoma
Systemic	
Lung	NSCLC
Skin	Melanoma (Stage III/IV)
Liver	Hepatocellular carcinoma
Kidney	Renal cell carcinoma
Breast	Basal like
Pancreas	Ductal adenocarcinoma
Colon	Colorectal
Ovarian	Ovarian carcinoma
	Ovarian metastasis
Thyroid	Thyroid carcinomas
Prostate	Acinar adenocarcinoma
	Ductal adenocarcinoma

Bhattacharya, et al. Therapeutically leveraging $GABA_A$ receptors in cancer. Exp Biol Med. 2021.

c2014, Group 3 Medulloblastomas possess functional $GABA_A$ receptors

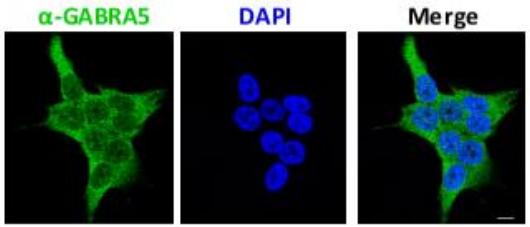
S. Sengupta, MD/PhD



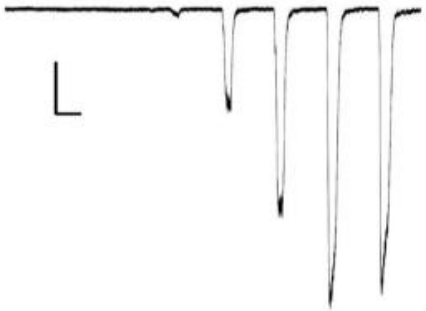
α5-GABAA receptors negatively regulate *MYC*-amplified medulloblastoma growth

Soma Sengupta[1,8,#], Shyamal Dilhan Weeraratne[1,#], Hongyu Sun[1,6], Jillian Phallen[3], Sundari K. Rallapalli[2], Natalia Teider[1], Bela Kosaras[1], Vladimir Amani[1], Jessica Pierre-Francois[1], Yujie Tang[4], Brian Nguyen[4], Furong Yu[4], Simone Schubert[4], Brianna Balansay[4], Dimitris Mathios[3], Mirna Lechpammer[1,9], Tenley C. Archer[1], Phuoc Tran[5], Richard J. Reimer[4], James M. Cook[2], Michael Lim[3], Frances E. Jensen[1,6,*], Scott L. Pomeroy[1,*], and Yoon-Jae Cho[4,7,@,*]

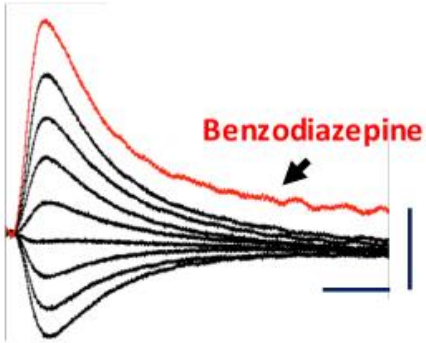
Staining shows $GABA_A$ receptor present in cancer cells



Electrophysiology shows receptor is function (GABA-responsive current)

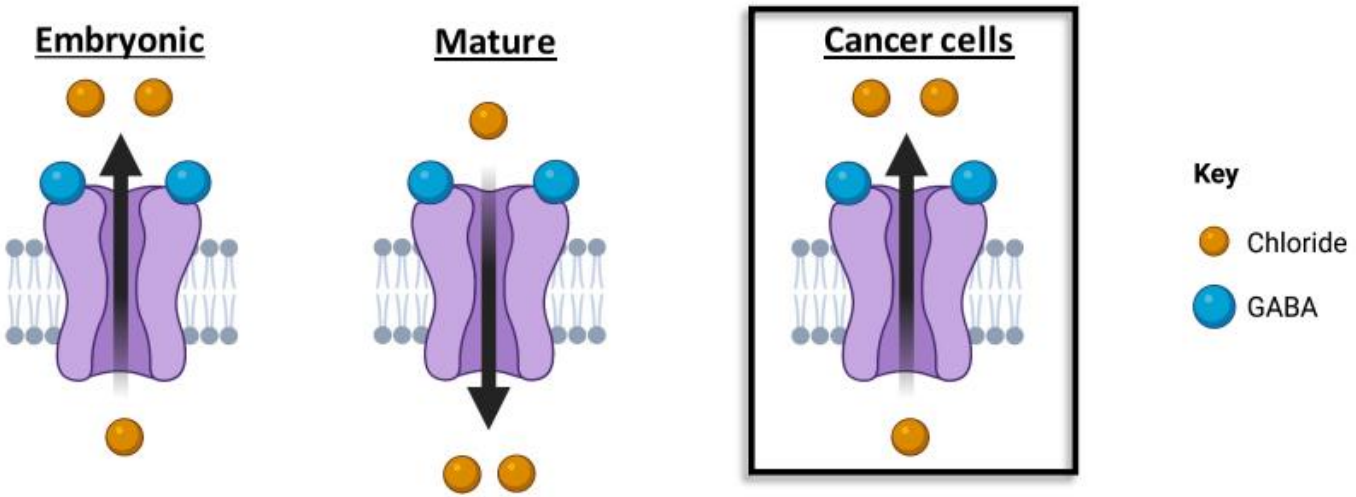


GABA-responsive current in tumor enhanced by benzodiazepines



$GABA_A$ receptors in cancer move chloride anions out, not in

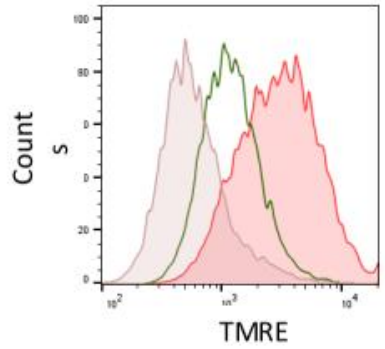
Receptor in cancer cells moves Cl- out, like the embryonic receptor.



Rao, et al. Ligand-gated ion channels as targets for treatment and management of cancers. Frontiers in Physiology, 2022.

GABA$_A$ receptor 'activators' depolarize cancer cells and induce apoptosis

Monitoring rapid (10 min) binding to cancer cells of positively charged dye (TMRE)



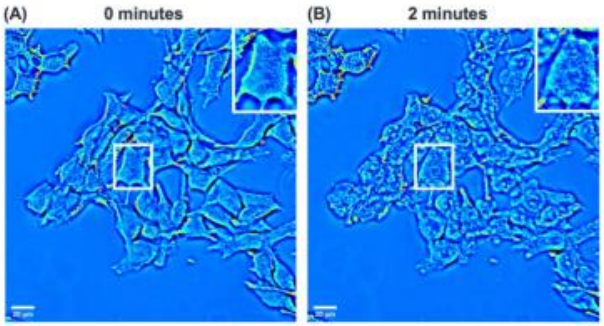
Key:

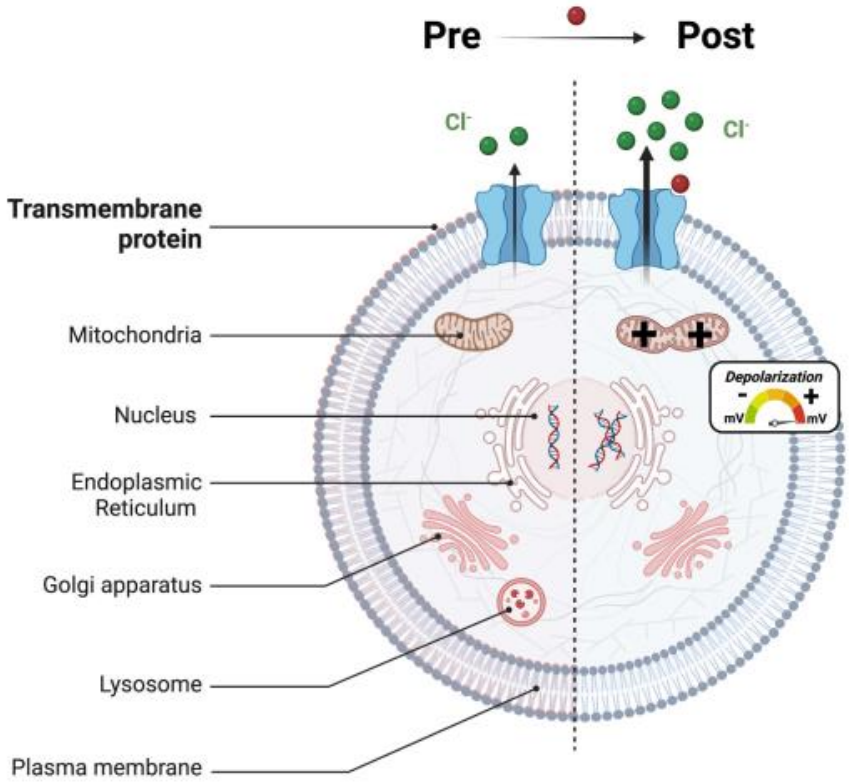
No Drug

AM-101

FCCP (Positive control)

Time-lapse Microscopy Images of cancer cells treated with AM-101 shows significant blebbing



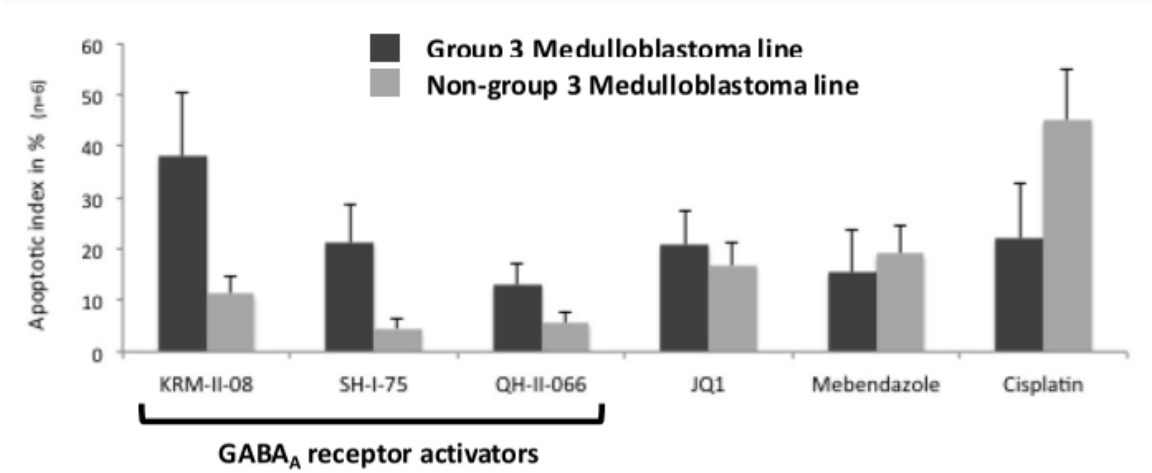


c2016, $GABA_A$ receptor 'activators' as effective as standard-of-care chemotherapy

First *in vivo* testing of compounds targeting Group 3 medulloblastomas using an implantable microdevice as a new paradigm for drug development

Oliver Jonas[1,*,†], David Calligaris[2,†], Kashi Reddy Methuku[3], Michael M. Poe[3], Jessica Pierre Francois[4], Frank Tranghese[4], Armen Changelian[2], Werner Sieghart[5], Margot Ernst[5], Daniel A. Pomeranz Krummel[6], James M. Cook[3], Scott L. Pomeroy[4], Michael Cima[1], Nathalie YR Agar[2,7,8], Robert Langer[1], and Soma Sengupta[9,*]

Data from Intratumor drug sensitivity assay, 'activators more effective and specific than chemo.



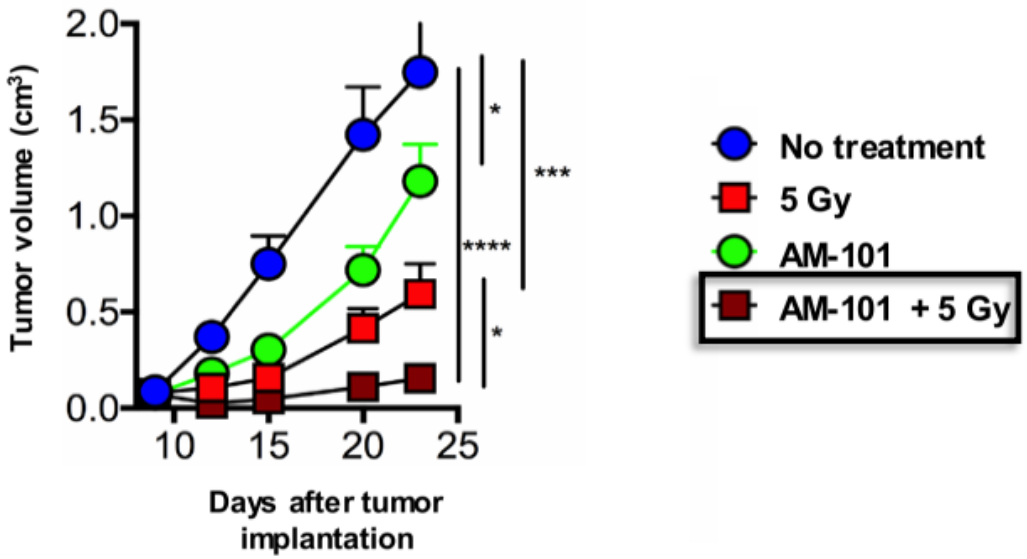
c2020, $GABA_A$ receptor 'activators' radiosensitize melanoma tumors

International Journal of Radiation Oncology biology • physics
www.redjournal.org

Biology Contribution

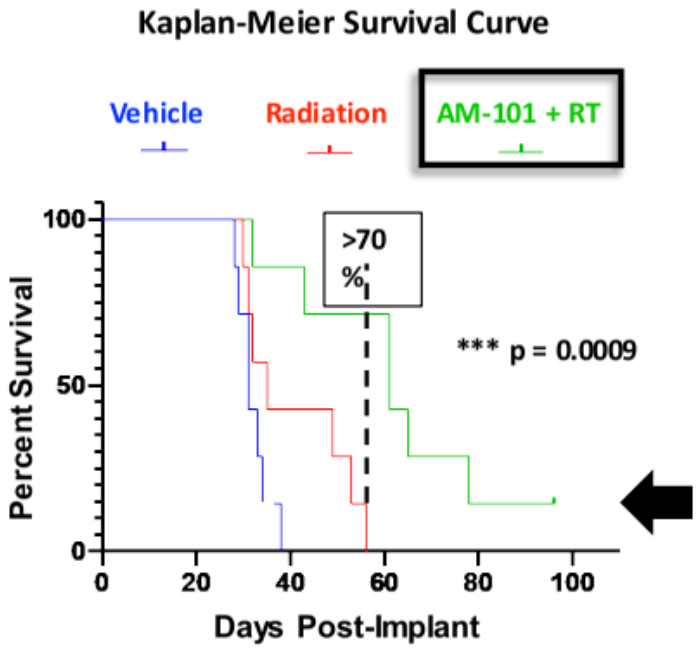
Melanoma Cell Intrinsic $GABA_A$ Receptor Enhancement Potentiates Radiation and Immune Checkpoint Inhibitor Response by Promoting Direct and T Cell–Mediated Antitumor Activity

Daniel A. Pomeranz Krummel, PhD,* Tahseen H. Nasti, PhD,† Milota Kaluzova, PhD,‡ Laura Kallay, PhD,* Debanjan Bhattacharya, PhD,* Johannes C. Melms, MD,§ Benjamin Izar, MD, PhD,§ Maxwell Xu, BS,‖ Andre Burnham, BS,‡ Taukir Ahmed, PhD,¶ Guanguan Li, PhD,¶ David Lawson, MD,# Jeanne Kowalski, PhD,** Yichun Cao, MPH,†† Jeffrey M. Switchenko, PhD,†† Dan Ionascu, PhD,§§ James M. Cook, PhD,¶ Mario Medvedovic, PhD,‖‖ Andrew Jenkins, PhD,¶¶ Mohammad K. Khan, MD, PhD,## and Soma Sengupta, MD, PhD*



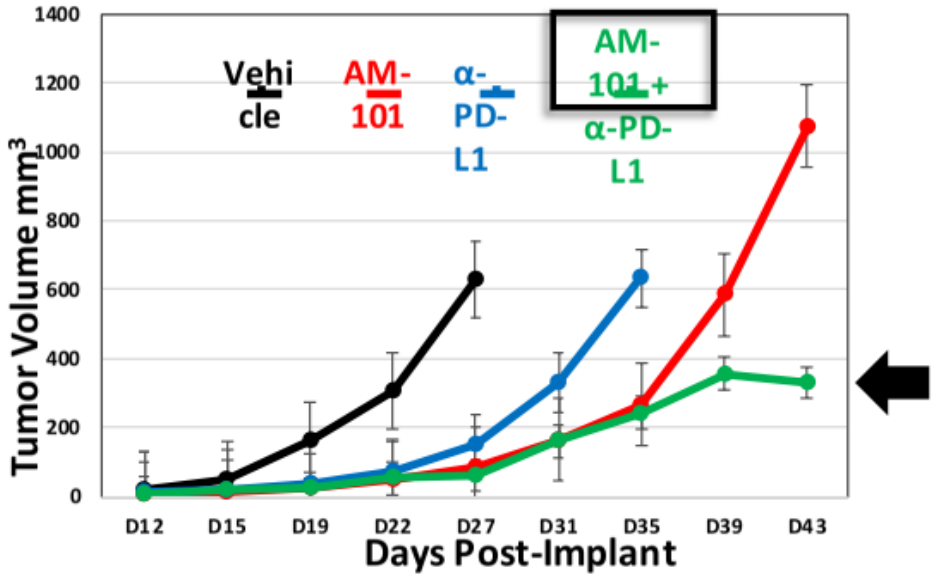
$GABA_A$ receptor 'activators' radiosensitize lung metastatic brain tumors

AM-101 significantly improves survival of mice with metastatic lung cancer.



$GABA_A$ receptor 'activators' modulate the immune system

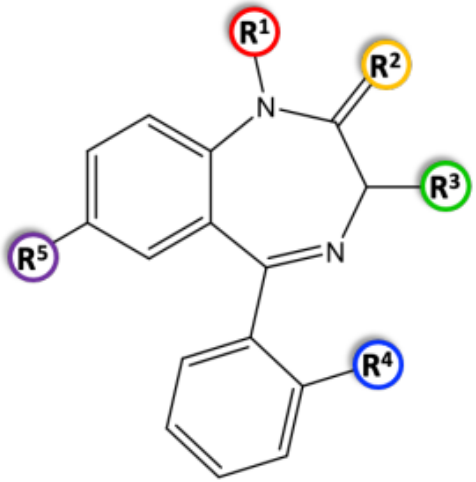
AM-101 sensitives tumor in a lung cancer mouse model to immune checkpoint inhibitor.



Potential for Translation

- Drug can potentially be used with various treatment modalities (radiation, chemotherapy, immunotherapy).
- Drug can be used to treat primary site and metastatic lesions (data shown for lung cancer).
- Drug is rapidly brain penetrant.
- Drug enhances anti-tumor immune cells (CD8+ T cell; M1-type macrophages) in the tumor microenvironment; turns a ‘cold’ tumor ‘hot’.

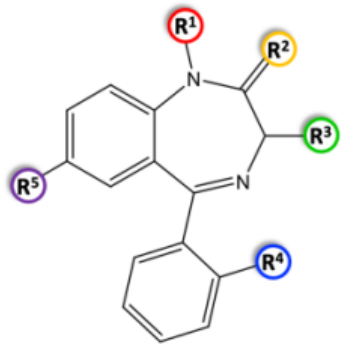
Compound scaffold



R(X)	Selected from the group consisting of:
1	Hydrogen, methyl, ethyl, trifluoromethyl, deuterated methyl (CD_3), tritiated methyl (CT_3), cyclopropyl, d(5)-cyclopropyl.
2	O, S, Se, CF2, CH2, or R^1 and R^2 together form a substituted or unsubstituted C_5 heteroaryl ring.
3	Hydrogen, methyl, hydroxyl, acetate, deuterated methyl. H , 2D, CH3, CD3, OH, OAc,2F, H, F ethyl, cyclopropyl.
4	Hydrogen, methyl, halo, deuterated methyl. H , 2D, CH3, CD3, OH, OAc, 2F, H, F ethyl, cyclopropyl.
5	***C2-C4 alkynyl, C3-C6 cycloalkyl, ethinyl (acetylene), alkynyl halide. ethinyl(acetylene), cyclopropyl, d(5)-cyclopropyl, C2-C4-alkynyl, methyl alkynyl, C3-C6 cycloalkyl, alkynyl-CD3, alkynyl-CF3.***

CLAIMS

1. A compound, or a pharmaceutically acceptable salt, racemate, or enantiomer thereof, according to the following structure:



Formula I

wherein:

R^1 is selected from the group consisting of hydrogen, methyl, ethyl, trifluoromethyl, deuterated methyl (CD_3), tritiated methyl (CT_3), cyclopropyl, and d(5)-cyclopropyl;

R^2 is selected from the group consisting of O, S, Se, CF_2, and SH_2; or R^1 and R^2 together form a substituted or unsubstituted C5 heteroaryl ring;

R^3 is selected from the group consisting of hydrogen, methyl, hydroxyl, acetate, deuterated methyl (CD_3), 2D, OAc, 2F, F ethyl, and cyclopropyl;

R^4 is selected from the group consisting of hydrogen, methyl, halo, deuterated methyl (CD_3), 2D, OAc, 2F, F ethyl, and cyclopropyl; and

R^5 is selected from the group consisting of C2-C4 alkynyl, C3-C6 cycloalkyl, ethinyl (acetylene), alkynyl halide, cyclopropyl, d(5)-cyclopropyl, methyl alkynyl, alkynyl-CD_3, and alkynyl-CF_3.

2. An immune modulator compound, substantially as shown and described in the appended disclosure.

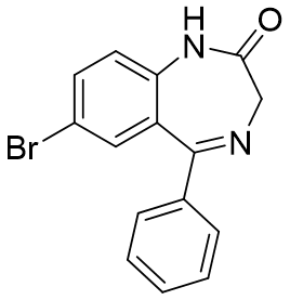
3. A method of modulating an immune response in a subject in need thereof, the method comprising administering to the subject an effective amount of the compound according to claim 1 or claim 2.

4. The method according to claim 3, further comprising administering an additional therapy selected from the group consisting of radiation, chemotherapy, immunotherapy, and combinations thereof.

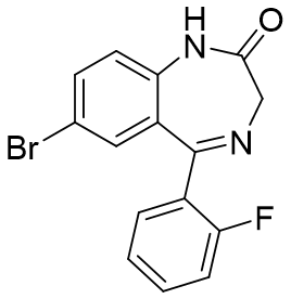
5. A method of enhancing the activity of anti-tumor cells in a tumor microenvironment, the method comprising treating the tumor microenvironment with the compound according to claim 1 or claim 2.

6. A method of treating cancer in a subject in need thereof, the method comprising administering to the subject an effective amount of the compound according to claim 1 or claim 2.

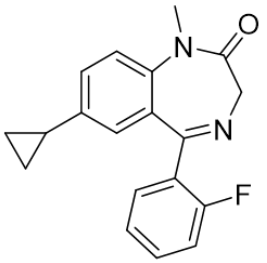
7. A method of treating cancer, substantially as shown and described in the appended disclosure.



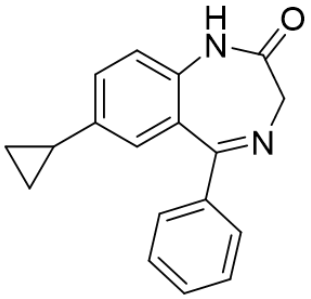
(5)



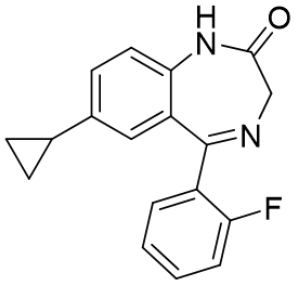
(6)



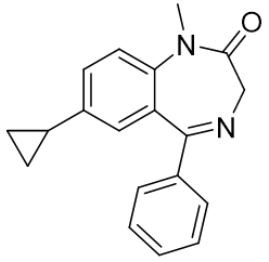
(12)



(7) SRE-III-35

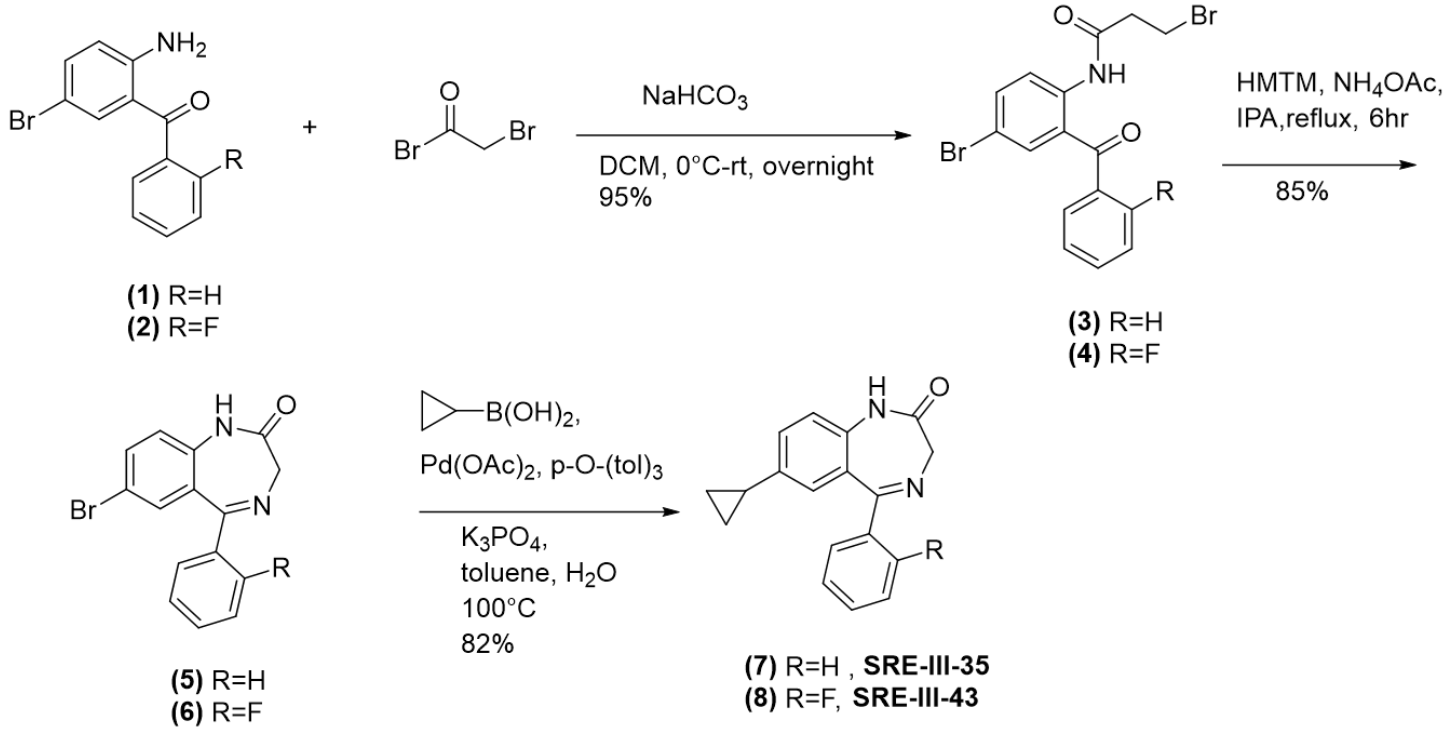


(8) SRE-III-43



(11)

Scheme 1



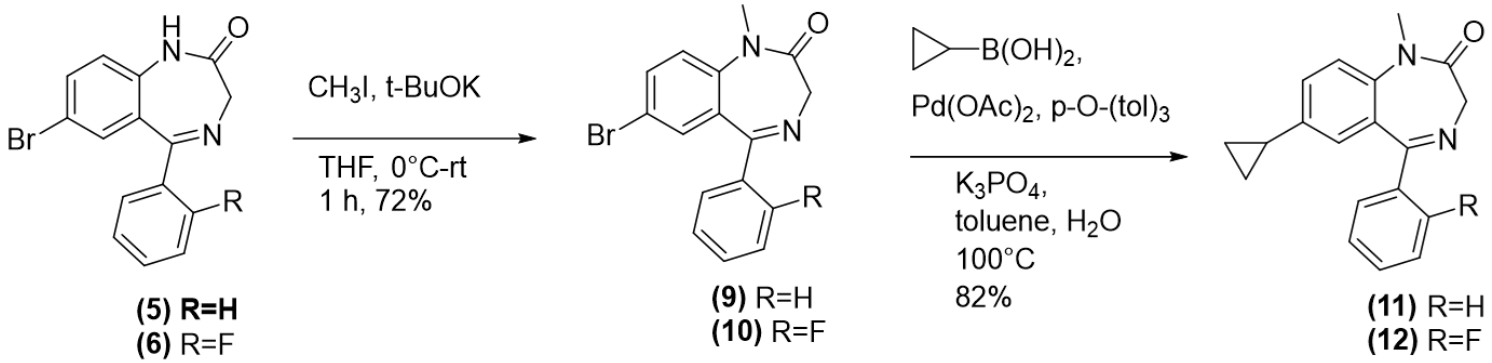
(1) R=H
(2) R=F

(3) R=H
(4) R=F

(5) R=H
(6) R=F

(7) R=H , **SRE-III-35**
(8) R=F, **SRE-III-43**

Scheme 2



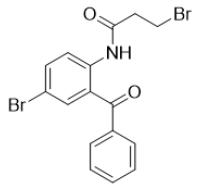
(5) R=H
(6) R=F

(9) R=H
(10) R=F

(11) R=H
(12) R=F

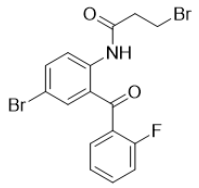
Experimental of scheme 1

The cyclized intermediate, diazepine core , was synthesized by employing a Délepine reaction invented by Stephane Marcel Délepine . The reaction mixture of the bromoacetamide , hexamethylene tetramine (HMTM, 2.2 equivalents), and ammonium acetate (2.2 equivalents) in IPA was heated to reflux at 80 ◦C for 4 hours to yield diazepine core **(5/6)** in 85% yield, The cyclopropyl ligand **(7/8)** was synthesized from cyclopropyl boronic acid *via* a Suzuki-coupling reaction with the aryl bromide (**5/6**). The coupling reaction was carried out in the presence of potassium phosphate, palladium (II) acetate and tri-o-tolyl phosphine in toluene at 100 ^{o}C for 12 hours. This process was executed in good yield (82%), as shown in Scheme 1.



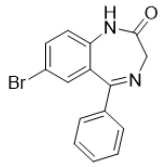
(3)

To a mixture of **(2-amino-5-bromophenyl) (phenyl) methanone** (1, 60 g, 217.29 mmol), sodium bicarbonate (36.50 g, 434.58 mmol), and DCM (600 mL), bromoacetyl bromide (24.61 mL, 282.48 mmol) was added dropwise over a 60-min period. The temperature was kept between -10°C – 0°C with continuous stirring. The white colored reaction mixture, which resulted, was then allowed to stir for longer than 3 h at rt. The completion of the reaction was verified by analysis by TLC (silica gel) and 50% ethyl acetate / hexanes. The reaction mixture was then slowly diluted over 30 min with water (300 mL) as carbon dioxide bubbles evolved. The biphasic mixture, which resulted, was allowed to stand for 15 min and the layers were separated. The aq layer was extracted with dichloromethane (300 mL) and the combined organic layers were washed with 5% aq sodium bicarbonate solution (300 mL) and then 10% aq sodium chloride solution (300 mL). The organic layer was dried (Na_2SO_4). The solvents were removed under reduced pressure and the residue was slurried with ethanol (300 mL) at 50 – 55°C for 30 min. Upon cooling to rt and after holding the temperature for 1 h, the solid, which formed, was filtered and washed with ethanol (60 mL x 3). The solid was dried under vacuum at 40°C to afford the product *N*-(2-benzoyl-4-bromophenyl)-2-bromoacetamide **3** as an off-white solid (82.6 g, 95.5%). ^{1}H NMR (500 MHz, $CDCl_3$): δ11.60 (s,1H) 7.66-7.64 (m, 2H, 2 xArH), 7.60-7.57 (m, 2H, 2 xArH), 7.52-7.49 (m, 2H, 2xArH), 7.38 (dd, 1H, J=8.5, 2.0Hz,H-4), 6.67(d, 1H, J=8.5Hz, H-3), 4.21 (s, 2H). 13C NMR (500 MHz, CDCl3): 198.2,165.21, 149.4, 139.5, 134.4, 133.4, 131.7, 129.3, 128.5, 120.3, 119.2, 118.8, 42.3



(4)

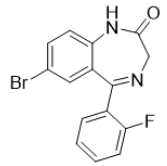
To a mixture of (2-amino-5-bromophenyl) (2' fluorophenyl) methanone (50 g, 169.99 mmol), sodium bicarbonate (28.56 g, 339.99 mmol), and dichloromethane (500 mL), bromoacetyl bromide (17.76 mL, 203.98 mmol) was added dropwise over a 60 min time period. The temperature was kept between -10°C – 0°C with continuous stirring. The white colored reaction mixture, which resulted, was then allowed to stir for longer than 3 h at rt. The completion of the reaction was verified by analysis by TLC (silica gel) and 50% ethyl acetate / hexanes. The reaction mixture was then slowly diluted over 30 min with water (300 mL) as carbon dioxide bubbles ocurred. The biphasic mixture, which resulted, was allowed to stand for 15 min and the layers were separated. The aq layer was extracted with dichloromethane (300 mL) and the combined organic layers were washed with 5% aq sodium bicarbonate solution (300 mL) and then 10% aq sodium chloride solution (300 mL). The organic layer was dried (Na2SO4). The solvents were removed under reduced pressure and the residue was slurried with ethanol (300 mL) at 50 – 55°C for 30 min. Upon cooling to rt and after holding the temperature for 1 h, the solid, which formed, was filtered, and washed with ethanol (60 mL x 3). The solid was dried under vacuum at 40°C to afford the product 2-bromo-*N*-[4-bromo-2-(2-fluorobenzoyl)phenyl] -acetamide **(4)** as an off-white solid (67.73 g, 96%). ^{1}H NMR (500 MHz, CDCl3): δ11.60 (s,1H) 7.66-7.64 (m, 2H, 2 x ArH), 7.60-7.57 (m, 2H, 2 x ArH), 7.52-7.49 (m, 2H, 2xArH), 7.38 (dd, 1H, J=8.5, 2.0Hz, H-4), 6.67(d, 1H, J=8.5Hz, H-3), 4.21 (s, 2H). 13C NMR (500 MHz, CDCl3): 198.2,165.21, 149.4, 139.5, 134.4, 133.4, 131.7, 129.3, 128.5, 120.3, 119.2, 118.8, 42.3



(5)

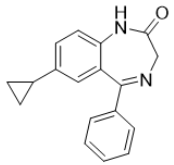
A mixture of *N*-(2-benzoyl-4-bromophenyl)-2-bromoacetamide **(3)** (70 g, 176.3 mmol), hexamethylenetetramine (HMTM, 54.38 g, 387.9 mmol), ammonium acetate (29.9 g, 387.9 mmol), and isopropanol (700 mL) was heated to reflux (82 °C). The reaction mixture was held at reflux for 6 h, at which point the reaction progress was deemed complete on analysis by TLC (silica gel and 1:1, ethyl acetate/hexanes). The reaction mixture was then cooled to 0 – 5°C using an ice bath. The solid, which resulted, was filtered, and washed with cold isopropanol (100 mL x 2) and then water (100mL x 4). The solid was dried under vacuum at 40 °C to afford 32 g of the benzodiazepine **5** as an off-white solid. The IPA was removed from the mother liquor under reduced pressure. The solid was then extracted with ethyl acetate. The ethyl acetate was removed under reduced pressure and the residue was purified by column chromatography using 1:4 ethyl acetate/hexanes to afford 7 -bromo-5-phenyl-1,3-dihydro-2*H*-1,4-benzodiazepin-2-one (**5**). (38.9 g, 70%)

^{1}H NMR (500 MHz, CDCl3): δ9.89 (s,1H), 7.82(d, 1H) 7.66-7.64 (m, 2H, 2 x ArH), 7.60-7.57 (m, 2H, 2 x ArH), 7.52-7.49 (m, 2H, 2xArH), 7.38 (dd, 1H, J=8.5, 2.0Hz,H4), 4.32 (s, 2H). 13C NMR (500 MHz, CDCl3): 170.2,165.21, 149.4, 139.5, 134.4, 133.4, 131.7, 129.3, 128.5, 120.3, 119.2, 118.8, 56.2.



(6)

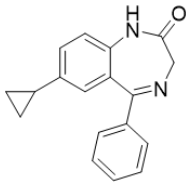
A mixture of **2-bromo-*N*-[4-bromo-2-(2-fluorobenzoyl)phenyl]-acetamide (4),** (50 g, 120.48 mmol), hexamethylenetetramine (HMTM, 35.47 g, 252.99 mmol), ammonium acetate (19.5 g, 252.99 mmol), and isopropanol (500 mL) was heated to reflux (82°C). The reaction mixture was held at reflux for 6 h, at which point the reaction progress was deemed complete on analysis by TLC (silica gel and 1:1, ethyl acetate/hexanes). The reaction mixture was then cooled to 0 – 5°C using an ice bath. The solid, which resulted, was filtered, and washed with cold isopropanol (100 mL x 2) and then water (100mL x 4). The solid was dried under vacuum at 40°C to afford 32 g of the benzodiazepine **6** as an off-white solid. The IPA was removed from the mother liquor under reduced pressure. The solid was then extracted with ethyl acetate. The ethyl acetate was removed under reduced pressure and the residue was purified by column chromatograpy using 1:4 etheyl acetate/hexanes to afford **7-Bromo-5-(2-fluorophenyl)-1,3-dihydrobenzo[e]-1,4-diazepin-2-one**. (**6)** (28.1 g, 70%) ^{1}H NMR (500 MHz, CDCl3): δ9.89 (s,1H), 7.82(d, 1H) 7.66-7.64 (m, 2H, 2 x ArH), 7.60-7.57 (m, 2H, 2 x ArH), 7.52-7.49 (m, 2H, 2xArH), 7.38 (dd, 1H, J=8.5, 2.0Hz,H-4), 4.32 (s, 2H). 13C NMR (500 MHz, CDCl3): 170.2,165.21, 149.4, 139.5, 134.4, 133.4, 131.7, 129.3, 128.5, 120.3, 119.2, 118.8, 56.2.



(7)

To a solution of palladium (II) acetate (0.099g, 0.44 mmol) and tri-o-tolyl phosphine (0.27 g, 0.88 mmol) in toluene, the 7-bromo-5-phenyl-1,3-dihydro-2H-benzo[e][1,4]diazepin-2-one **5** (2.0 g, 6.3 mmol) was added. Then in sequence, cyclopropyl boronic acid (2.45 g, 28.52 mmol), and bis(triphenylphosphine) (5.38g, 25.37 mmol) and water (0.5 mL) were added under argon. A reflux condenser was attached, and the reaction mixture was heated to reflux. The mixture was stirred and heated to 100 ° C. After 12 h the reaction was completed on analysis by mass spectroscopy, and it was then cooled to rt and silica gel (3 g) was added. After stirring for 30 minutes open to the air, the spent catalyst on silica gel was removed by filtration through a pad of celite and washed with EtOAc. Then the filtrate was concentrated under reduced pressure. The residue which resulted was purified by a wash column (silica gel, EtOAc) to afford the desired product as a white solid **7** (1.29g, 74 %)
^{1}H NMR (500 MHz, $CDCl_3$) δ 9.67 (s, 1H), 7.65 (d,*J* = 7.5 Hz, 1H), 7.55 (dd,*J* = 14.8, 7.3 Hz, 2H), 7.47 (t,*J* = 7.5 Hz, 2H), 7.25 (d,*J* = 7.6 Hz, 1H), 7.21 (d,*J* = 8.0 Hz, 1H), 7.02 (d,*J* = 1.7 Hz, 1H), 4.29 (s, 2H), 1.89– 1.82 (m, 1H), 0.98 – 0.94 (m, 2H), 0.64 – 0.57 (m, 2H). ^{13}C NMR (126 MHz, $CDCl_3$) δ170.3, 166.00, 139.66, 138.35, 137.24, 132.71, 131.34, 130.98, 130.68, 129.95, 129.57, 129.22, 121.85, 121.69, 47.10, 14.83, 9.32, 9.18

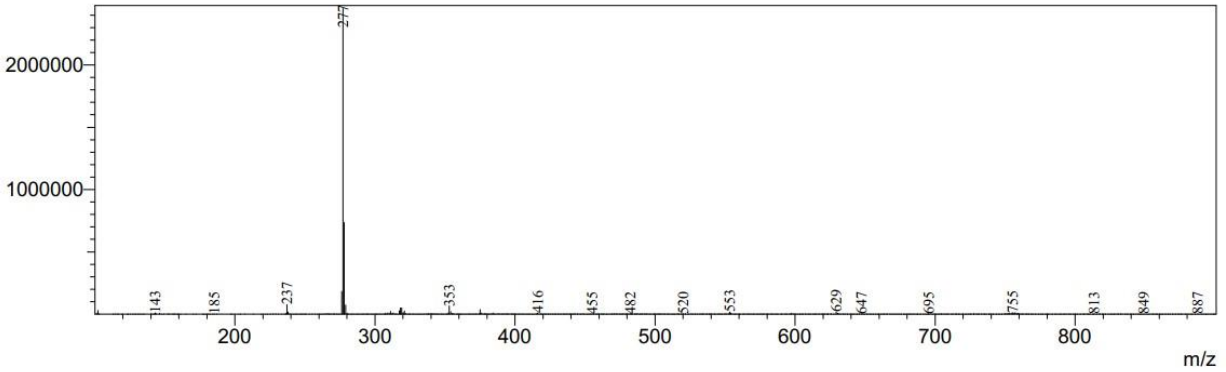
Molecular Weight: 276.34

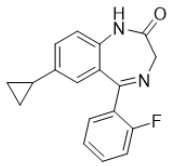


(7)

<Spectrum>

R.Time:----(Scan#:----)
MassPeaks:720 BasePeak:277(2452730)
Spectrum Mode:Averaged 0.077-0.160(47-97)
BG Mode:Averaged 0.817-0.937(491-563) Polarity:Positive Segment 1 - Event 1

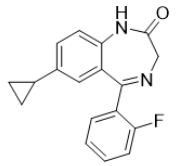




(8)

To a solution of palladium (II) acetate (0.07g, 0.31 mmol) and tri -o-tolyl phosphine (0.19g, 0.63 mmol) in toluene, the 7-bromo-5-(2-fluorophenyl)-1,3-dihydro-2H-benzo[e][1,4]diazepin-2-one **6**, X=F(1.5 g, 4.5 mmol) was added . Then in sequence, cyclopropyl boronic acid (1.74 g, 20.25 mmol), and bis(triphenylphosphine) (3.81g, 18 mmol) and water (0.36 mL) were added under argon. A reflux condenser was attached, and the reaction mixture was heated to reflux. The mixture was stirred and heated to 100 ° C. After 12 h the reaction was completed on analysis by mass spectroscopy, and it was then cooled to rt and silica gel (2.5 g) was added. After stirring for 30 minutes open to the air, the spent catalyst on silica gel was removed by filtration through a pad of celite and washed with EtOAc. Then the filtrate was concentrated under reduced pressure. The residue which resulted was purified by a wash column (silica gel, EtOAc) to afford the desired product as a white solid **8** (0.99 g, 75 %). ^{1}H NMR (500 MHz, $CDCl_3$) δ 9.66 (s, 1H), 7.62 (t, J = 7.2 Hz, 1H), 7.57 (t, J = 7.4 Hz, 1H), 7.31 (d, J = 8.2 Hz, 1H), 7.29 (s, 1H), 7.26 (d, J = 7.1 Hz, 1H), 7.24 (s, 1H), 6.95 (s, 1H), 4.36 (s, 2H), 1.86–1.80 (m, 1H), 0.94 (dt, J = 6.3, 3.1 Hz, 2H), 0.59 (dt, J = 10.0, 4.9 Hz, 2H). ^{13}C NMR (126 MHz, $CDCl_3$) δ 170.2, 165.27, 161.59, 159.57, 140.13, 139.0, 134.6, 132.61, 132.14, 124.40, 123.95, 121.72, 116.46, 116.40, 116.23, 14.80, 9.25, 9.05

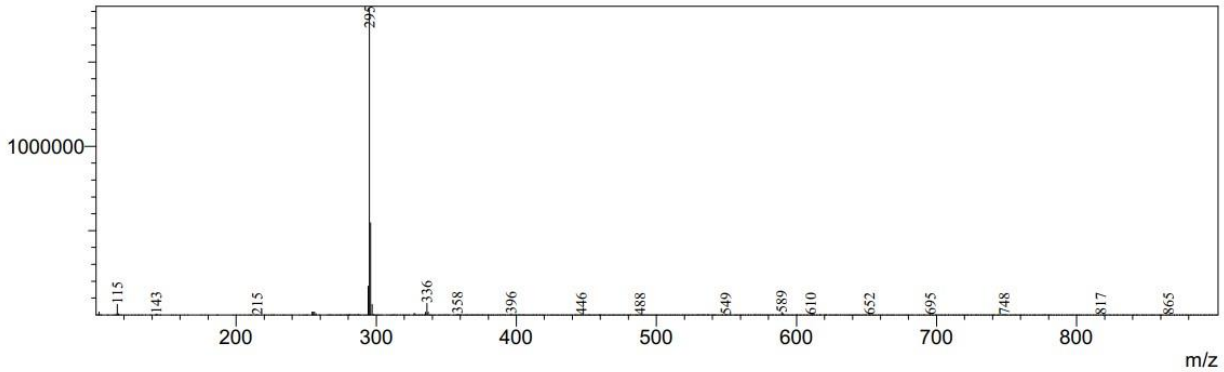
Molecular Weight: 294.33

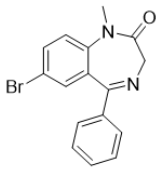


(8)

<Spectrum>

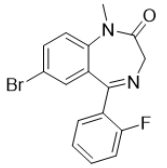
R.Time:----(Scan#:----)
MassPeaks:687 BasePeak:295(1811952)
Spectrum Mode:Averaged 0.067-0.153(41-93)
BG Mode:Averaged 0.850-0.927(511-557) Polarity:Positive Segment 1 - Event 1





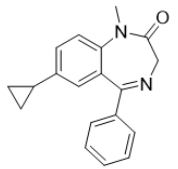
(9)

The 7-bromo-5-phenyl-1,3-dihydro-2H-1,4-benzodiazepin-2-one **5**, (38.0 g, 120.6 mmol) was dissolved in THF, (150 mL) and the solution was cooled to 0 ◦C using an ice bath. Then potassium tert butoxide (16.23 g, 144.7 mmol), which was dissolved in 100 mL of THF, was added dropwise by using an addition funnel. Then methyl iodide (8.26 mL, 132.7 mmol) was added dropwise to the reaction mixture over a 5 min period, while maintaining the temperature at 0 ◦C. Upon completion of the addition, the reaction mixture was allowed to warm to rt and stirred for 60 min, at which point the reaction was deemed complete on analysis by TLC (silica gel). The reaction mixture was then diluted with ethyl acetate (200 mL) and a solution of 10% aq sodium chloride (200 mL) was added. The biphasic mixture, which resulted, was allowed to stand for 15 min and the layers were separated. The aq layer was then extracted with ethyl acetate (100 mL) and the combined organic layers were washed with 10% aq sodium chloride solution (100 mL). The organic layer was dried (Na_2SO_4). The solvent was removed under reduced pressure. The brown solid, which was obtained, was purified by crystallization using 15:85(ethyl acetate/hexanes), to give 7 -bromo-1-methyl-5-phenyl-1,3-dihydro-2H-1,4- benzodiazepin-2-one **9** (29.76 g, 75%) as a brownish white solid. 1H NMR (500 MHz, CDCl3): 7.82(d, 1H) 7.66-7.64 (m, 2H, 2 x ArH), 7.60-7.57 (m, 2H, 2 xArH), 7.52-7.49 (m, 2H, 2xArH), 7.38 (dd, 1H, J=8.5, 2.0Hz,H4), 4.6 (D, 1H), 3.6(D,1H), 3.3(S,3H). 13C NMR (500 MHz, CDCl3): 171.2, 168.21, 149.4, 139.5, 134.4, 133.4, 131.7, 129.3, 128.5, 120.3, 119.2, 118.8, 82.3, 79.2, 56.2, 34.2.



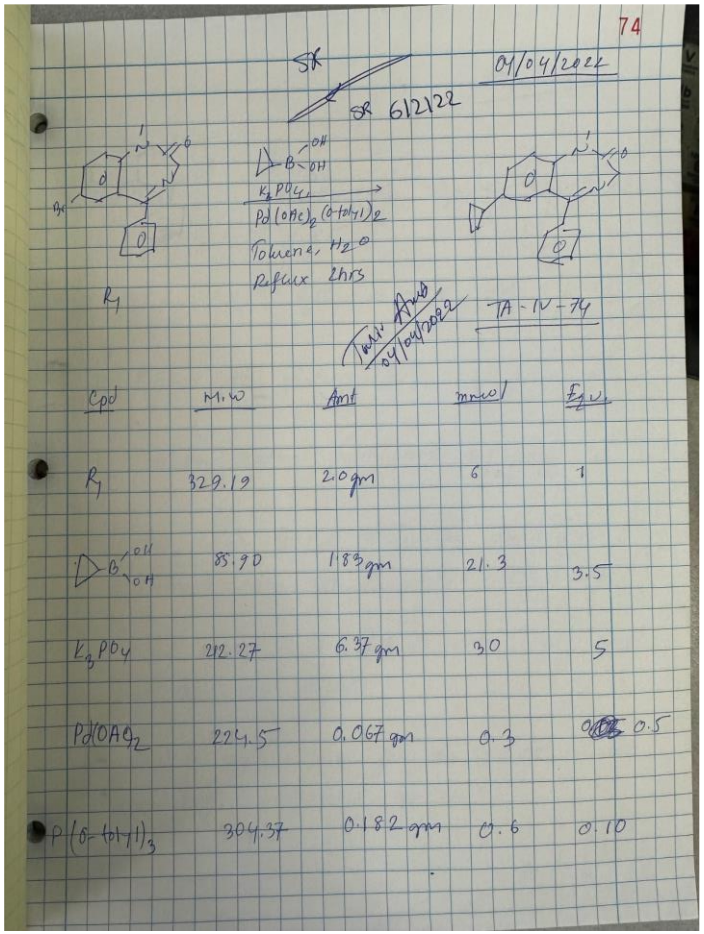
(10)

The 7-Bromo-5-(2-fluorophenyl)-1,3-dihydrobenzo[e]-1,4-diazepin-2-one **(6)** (25 g, 75.04 mmol) was dissolved in THF, (150 mL) and the solution was cooled to 0 ◦C using an ice bath. Then potassium tert butoxide (10.10 g, 90.00 mmol) which was dissolved in 100 mL of THF, was added dropwise by using an addition funnel. Then methyl iodide (5.14 mL, 82.54 mmol) was added dropwise to the reaction mixture over a 5 min period, while maintaining the temperature at 0oC. Upon completion of the addition, the reaction mixture was allowed to warm to rt and stir for 60 min, at which point the reaction was deemed complete on analysis by TLC (silica gel). The reaction mixture was then diluted with ethyl acetate (200 mL) and a solution of 10% aq sodium chloride (200 mL) was added. The biphasic mixture, which resulted, was allowed to stand for 15 min and the layers were separated. The aq layer was then extracted with ethyl acetate (100 mL) and the combined organic layers were washed with 10% aq sodium chloride solution (100 mL). The organic layer was dried (Na_2SO_4). The solvent was removed under reduced pressure. The brown solid which was obtained was purified by crystallization using 15:85(ethyl acetate/hexanes), to give 7 -Bromo-5-(2-fluorophenyl)-1,3-dihydro-1- methyl-2H-1,4-benzodiazepin-2-one **(10)** (18.75 g, 72%) as a brownish white solid. 1H NMR (500 MHz, CDCl3): 7.82(d, 1H) 7.66-7.64 (m, 2H, 2 x ArH), 7.60-7.57 (m, 2H, 2 x ArH), 7.52-7.49 (m, 2H, 2xArH), 7.38 (dd, 1H, J=8.5, 2.0Hz,H-4), 4.6 (D, 1H), 3.6(D,1H), 3.3(S,3H). 13C NMR (500 MHz, CDCl3): 171.2, 168.21, 149.4, 139.5, 134.4, 133.4, 131.7, 129.3, 128.5, 120.3, 119.2, 118.8, 82.3, 79.2, 56.2, 34.2.



(11)

To a solution of palladium (II) acetate (0.067g, 0.3 mmol) and tri -o-tolyl phosphine (0.182g, 0.6 mmol) in toluene, the 7-bromo-5-(2-fluorophenyl)-1,3-dihydro-2H-benzo[e][1,4]diazepin-2-one **9** (2.0 g, 6.0 mmol) was added . Then in sequence, cyclopropyl boronic acid (1.83 g, 21.3 mmol), and bis(triphenylphosphine) (6.37g, 30 mmol) and water (1.0 mL) were added under argon. A reflux condenser was attached, and the reaction mixture was heated to reflux. The mixture was stirred and heated to 100 ° C. After 12 h the reaction was completed on analysis by mass spectroscopy, and it was then cooled to rt and silica gel (2.5 g) was added. After stirring for 30 minutes open to the air, the spent catalyst on silica gel was removed by filtration through a pad of celite and washed with EtOAc. Then the filtrate was concentrated under reduced pressure. The residue which resulted was purified by a wash column (silica gel, EtOAc) to afford the desired product as a white solid (0.99 g, 75 %). ^{1}H NMR (500 MHz, $CDCl_3$) δ 7.66 – 7.62 (m, 2H), 7.50 – 7.45 (m, 1H), 7.43 – 7.39 (m, 2H), 7.25 – 7.23 (m, 2H), 7.01 (d, J = 1.8 Hz, 1H), 4.80 (d, J = 10.6 Hz, 1H), 3.80 (d, J = 10.6 Hz, 1H), 3.39 (s, 3H), 1.88 (ddd, J = 8.4, 6.7, 4.2 Hz, 1H), 1.00 – 0.95 (m, 2H), 0.66 – 0.62 (m, 2H). ^{13}C NMR (126 MHz, $CDCl_3$) δ 170.31, 170.15, 141.69, 139.86, 138.87, 130.36, 129.57, 128.54, 128.53, 128.22, 127.47, 120.97, 57.04, 34.77, 14.85, 9.48, 9.33.



74

SK

SK 612122

01/04/2022

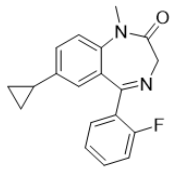
K_3PO_4
$Pd(OAc)_2$ (o-tolyl)$_2$
Toluene, H_2O
Reflux 2hrs

R_1

Toluene Azeo 04/04/2022

TA-IV-74

Cpd	M.W	Amt	mmol	Eq.
R_1	329.19	2.0 gm	6	1
	85.90	1.83 gm	21.3	3.5
K_3PO_4	212.27	6.37 gm	30	5
$Pd(OAc)_2$	224.5	0.067 gm	0.3	0.5
P(o-tolyl)$_3$	304.37	0.182 gm	0.6	0.10



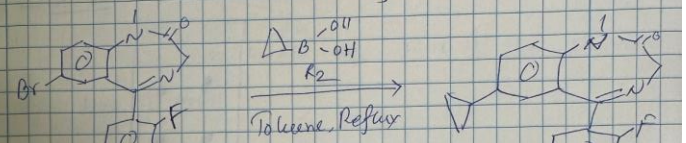
(12)

To a solution of palladium (II) acetate (0.016g, 0.072 mmol) and tri -o-tolyl phosphine (0.044g, 0.14 mmol) in toluene, the 7-bromo-5-(2-fluorophenyl)-1,3-dihydro-2H-benzo[e][1,4]diazepin-2-one **10** (0.5 g, 1.44 mmol) was added . Then in sequence, cyclopropyl boronic acid (0.433 g, 5.04 mmol), and bis(triphenylphosphine) (1.53g, 7.2 mmol) and water (0.33 mL) were added under argon. A reflux condenser was attached, and the reaction mixture was heated to reflux. The mixture was stirred and heated to 100 ° C. After 12 h the reaction was completed on analysis by mass spectroscopy, and it was then cooled to rt and silica gel (1.5 g) was added. After stirring for 30 minutes open to the air, the spent catalyst on silica gel was removed by filtration through a pad of celite and washed with EtOAc. Then the filtrate was concentrated under reduced pressure. The residue which resulted was purified by a wash column (silica gel, EtOAc) to afford the desired product as a white solid. ^{1}H NMR (500 MHz, $CDCl_3$) δ 7.66 (td, *J* = 7.5, 1.8 Hz, 1H), 7.50– 7.43 (m, 1H), 7.26 (ddd, *J* = 7.5, 6.3, 3.3 Hz, 2H), 7.20 (dd, *J* = 8.5, 2.1 Hz, 1H), 7.07 (ddd, *J* = 10.2, 8.3, 0.9 Hz, 1H), 6.91 (d, *J* = 1.9 Hz, 1H), 4.85 (d, *J* = 10.6 Hz, 1H), 3.82 (d, *J* = 10.6 Hz, 1H), 3.43 (s, 3H), 1.84 (tt, *J* = 8.4, 5.1 Hz, 1H), 0.98– 0.93 (m, 2H), 0.65 – 0.57 (m, 2H). ^{13}C NMR (126 MHz, $CDCl_3$) δ 169.73, 167.10, 161.57, 159.56, 140.54, 140.24, 131.96, 131.90, 131.43, 131.41, 129.70, 129.69, 128.45, 127.55, 127.45, 126.15, 126.14, 124.29, 124.27, 121.12, 116.20, 116.02, 57.04, 34.88, 14.82, 9.34, 9.28.

SR

6/12/22

04/14/2022



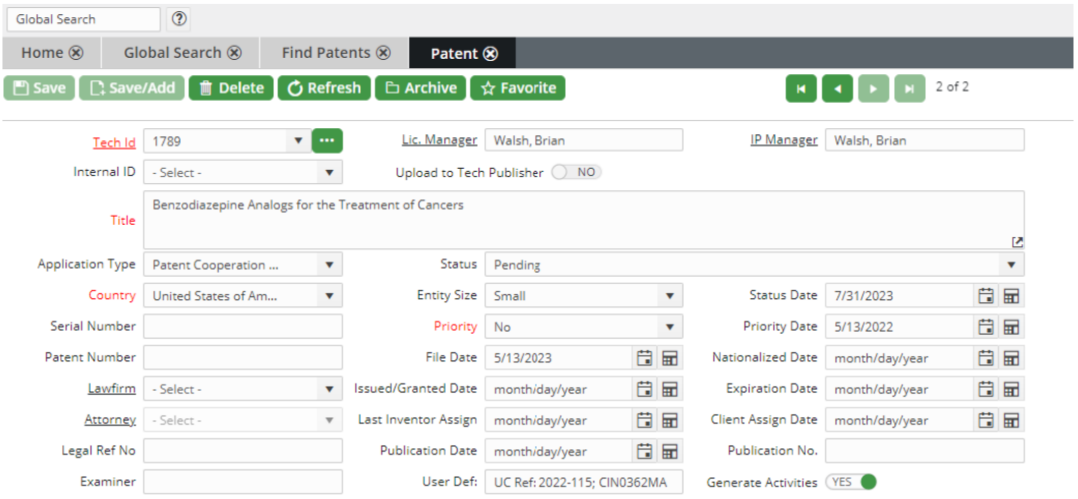
Toluene Dried 04/14/2022

IA-IV-77

Cpd	M.W	Amt	mmol	Eq.
R_1	347.21	0.500 gm	1.44 mmol	1.0
R_2	85.90	0.433 gm	5.04 mmol	3.5
$Pd(OAc)_2$	224.5	0.016 gm	0.072 mmol	0.05
$P(o\text{-}tol)_3$	304.37	0.044 gm		0.10
K_3PO_4	212.27	1.53 gm		5

University of Cincinnati (UC) Ref.	Title	Application No.	UWMRF Ref.
2021-139	Brain penetrant chemosensitizer to treat lung cancer	63/208,246 PCT/US2022/032163	OTT 1752
2021-140	Small brain penetrant molecule to potentiate TMZ for glioblastoma	63/196,459 PCT/US2022/032163	OTT 1753
2022-064 CIN0357WO	Novel Deuterated Benzodiazepine Analogs for Cancer Use	63/330,051 PCT filed by UC 04/12/2023	OTT1765
2022-087	Development of a New Class of Small Molecule Autophagy Modulators for Treatment of Cancers	63/330,143	OTT1783
2022-115 CIN0362WO	Benzodiazepine Analogs for the Treatment of Cancers	63/341,571 PCT filed by UC 05/13/2023	OTT1789
2023-073	A New Class of Immune Modulators	63/446,980 63/453,355 Provisional filed by UC 02/20/2023	OTT1811 & OTT1805

Emory Ref.	Title	UWMRF Ref.
	Uses of radiation and benzodiazepine derivatives in cancer therapies	OTT1572


Global Search
Home
Global Search
Find Patents
Patent
Save
Save/Add
Delete
Refresh
Archive
Favorite
2 of 2
Tech Id
1789
Lic. Manager
Walsh, Brian
IP Manager
Walsh, Brian
Internal ID
- Select -
Upload to Tech Publisher
NO
Title
Benzodiazepine Analogs for the Treatment of Cancers
Application Type
Patent Cooperation ...
Status
Pending
Country
United States of Am...
Entity Size
Small
Status Date
7/31/2023
Serial Number
Priority
No
Priority Date
5/13/2022
Patent Number
File Date
5/13/2023
Nationalized Date
month/day/year
Lawfirm
- Select -
Issued/Granted Date
month/day/year
Expiration Date
month/day/year
Attorney
- Select -
Last Inventor Assign
month/day/year
Client Assign Date
month/day/year
Legal Ref No
Publication Date
month/day/year
Publication No.
Examiner
User Def:
UC Ref: 2022-115; CIN0362MA
Generate Activities
YES

American College of Neuropsychopharmacology

www.nature.com/npp

ARTICLE

Check for updates

Symptomatic and neurotrophic effects of GABAA receptor positive allosteric modulation in a mouse model of chronic stress

Ashley Bernardo[1], Philip Lee[2], Michael Marcotte[1], Md Yeunus Mian[3], Sepideh Rezvanian[3], Dishary Sharmin[3], Aleksandra Kovačević[4], Miroslav M. Savić[4], James M. Cook[3], Etienne Sibille [1,2,5] ✉ and Thomas D. Prevot [1,5] ✉

© The Author(s), under exclusive licence to American College of Neuropsychopharmacology 2022

Chronic stress is a risk factor for Major Depressive Disorder (MDD), and in rodents, it recapitulates human behavioral, cellular and molecular changes. In MDD and after chronic stress, neuronal dysfunctions and deficits in GABAergic signaling are observed and responsible for symptom severity. GABA signals predominantly through GABAA receptors (GABAA-R) composed of various subunit types that relate to downstream outcomes. Activity at α2-GABAA-Rs contributes to anxiolytic properties, α5-GABAA-Rs to cognitive functions, and α1-GABAA-Rs to sedation. Therefore, a therapy aiming at increasing α2- and α5-GABAA-Rs activity, but devoid of α1-GABAA-R activity, has potential to address several symptomologies of depression while avoiding side-effects. This study investigated the activity profiles and behavioral efficacy of two enantiomers of each other (GL-II-73 and GL-I-54), separately and as a racemic mixture (GL-RM), and potential disease-modifying effects on neuronal morphology. Results confirm GL-I-54 and GL-II-73 exert positive allosteric modulation at the α2-, α3-, α5-GABAA-Rs and α5-containing GABAA-Rs, respectively, and separately reduces immobility in the forced swim test and improves stress-induced spatial working memory deficits. Using unpredictable chronic mild stress (UCMS), we show that acute and chronic administration of GL-RM provide pro-cognitive effects, with mild efficacy on mood symptoms, although at lower doses avoiding sedation. Morphology studies showed reversal of spine density loss caused by UCMS after chronic GL-RM treatment at apical and basal dendrites of the PFC and CA1. Together, these results support using a racemic mixture with combined α2-, α3-, α5-GABAA-R profile to reverse chronic stress-induced mood symptoms, cognitive deficits, and with anti-stress neurotrophic effects.

Neuropsychopharmacology; https://doi.org/10.1038/s41386-022-01360-y

INTRODUCTION

Chronic stress is a risk factor for psychiatric disorders including Major Depressive Disorder (MDD), displaying mood and cognitive symptoms [1–3]. Interventions to treat depression and other stress-related psychopathologies have focused on the monoaminergic system [4] with limited efficacy on mood symptoms and no efficacy on cognitive symptoms, highlighting unmet clinical needs. Recent studies have focused on the glutamatergic system [5], with promising effects on mood, cognition and cell structure [6, 7]. Similar efficacies were reported with compounds targeting the GABAergic system [8].

Mood and cognitive symptoms result from cellular dysfunctions, altered communication between cells and neuronal atrophy [9–13]. Transcranial magnetic stimulation in MDD patients shows reduced GABAergic function (i.e., cortical inhibition) [14, 15], contributing to impaired excitation/inhibition balance in MDD [16, 17]. Reduced GABA levels are reported in the occipital cortex [18–24], prefrontal cortex (PFC) [25] and anterior cingulate cortex [18, 25–27]. In the PFC, synaptic densities and expression of synaptic function-related genes are reduced [12, 28]. Chronic stress-related disorders [13, 29] and animal models report similar findings [30–32] and demonstrate critical links between prefrontal and hippocampal functions [33]. Chronic stress reduces dendritic length and spine density in the PFC and hippocampus (HPC), likely contributing to cognitive deficits. Of approved treatments, some monoamine-based interventions have reported structural plasticity and remodeling in chronic stress models [34–36], and more recently the NMDA receptor antagonist, ketamine, has shown efficacy at increasing spine density and dendritic complexity in mice, along with antidepressant properties [37]. The neurotrophic effects of ketamine are hypothesized to act through BDNF-TrkB signaling while its fast-acting antidepressant properties are suggested to be initially mediated by activity on GABAergic neurons followed by long-term GABA and glutamate changes [38], highlighting a potential role for GABA in these therapeutic effects.

GABA signals through ionotropic GABAA receptors (GABAA-Rs) and metabotropic GABAB receptors. GABAA-Rs are pentameric ion channels, formed by a combination of 19 subunit subtypes [39]. Drugs acting on GABAA-Rs exist (benzodiazepines or imidazodiazepines), but their use is limited because of side effects (sedation)

[1]Campbell Family Mental Health Research Institute of CAMH, Toronto, Canada. [2]Department of Pharmacology and Toxicology, University of Toronto, Toronto, Canada. [3]Department of Chemistry and Biochemistry, University of Wisconsin−Milwaukee, Milwaukee, USA. [4]Department of Pharmacology, Faculty of Pharmacy, University of Belgrade, Belgrade, Serbia. [5]Department of Psychiatry, University of Toronto, Toronto, Canada. ✉email: Etienne.sibille@camh.ca; thomas.prevot@camh.ca

Received: 23 February 2022 Revised: 17 May 2022 Accepted: 31 May 2022
Published online: 14 June 2022

SPRINGER NATURE

due to broad activity at several receptor subunits, including α1- GABAA-Rs [40–42]. Studies demonstrated α2-GABAA-Rs, strongly present in the amygdala [43–45] and HPC [43, 46, 47], are linked to regulation of anxious phenotypes [48–52]. The role of α3-GABAA- Rs are not fully characterized, but appear linked to behavioral despair in mice [53]. Other studies link α5-GABAA-Rs with cognitive performances [8, 54, 55], aligned with their preferential expression in cognitive processing regions (HPC and mPFC) [43, 56]. Our group and others showed targeting α5-GABAA-Rs with a positive allosteric modulator (PAM) reverses stress- [55] and age-[57, 58] related cognitive deficits, and chronically reverses age-related neuronal atrophy [8]. Potentiation of α2- and α5- GABAA-Rs, while limiting potentiation of α1-GABAA-R, is hypothe- sized to improve mood and cognitive symptoms while reducing side effects [40, 59], altogether suggesting potential for treatment of symptomatic and morphological alterations in chronic stress and MDD.

Previously, we showed the α5-PAM GL-II-73, has pro-cognitive and anxiolytic properties, and reduces immobility in the forced swim test (suggesting potential for antidepressant properties in human) at 10 mg/kg IP but not at 5 mg/kg IP [55], and neurotrophic effects at 30 mg/kg PO [58] in mice. However, it remained unknown if its enantiomer, GL-I-54, has similar or complementary properties. Here, we investigated the similarities and/or complementarities of receptor selectivity and behavioral efficacy profile of GL-I-54 and GL-II-73 in stressed mice. We then investigated the symptomatic and neurotrophic potentials of a racemic mixture of both compounds in a mouse model of chronic stress.

MATERIALS AND METHODS

Details provided in the supplementary material.

Compounds

GL-I-54 and GL-II-73 were synthesized as in [60], with >99% chemical and optical purity. GL-RM is a 1:1 mix of each compound.

Electrophysiology

Electrophysiological recordings used HEK-293T cell line transfected with full-length cDNAs for human GABAA-R subtypes α(1/2/3/4/5)β3γ2 [61, 62]. PubMed Protein Sequence repository for GABAA-R subunits reports the binding pocket formed by α1/2/3/5 and γ2 is 100% conserved between mouse and human, predicting similar activity and selectivity across species. Current recordings were performed in absence or presence (5 μM) of GABA. GL-I-54 or GL-II-73 was applied at 0.033–33.33 μM concentrations.

Animals

Seven independent cohorts of 8-week old C57BL/6 mice (50% female) were obtained from Military Medical Academy (Belgrade, Serbia) or Jackson Laboratories (Stock#000664; MA, USA), measuring: pharmacoki- netics (#1; n = 25), individual enantiomers on elevated plus maze and forced swim test (#2; n = 24), effect of GL-I-54 on Y-maze (#3; n = 42), GL-I- 54 side effects in the rotarod (#4, n = 18), and acute (#5; n = 36) and chronic (#6; n = 36) efficacy of GL-RM and supplementary maximum tolerated dose of GL-I-54 (#7; n = 18). Animals were individually housed and maintained on a 12 h light/dark cycle (7:00 ON, 19:00 OFF), with *ad libitum* food and water.

Ethical statement

All animal work was completed in accordance with Ontario Animals for Research Act (RSO 1990, Chapter A.22), Canadian Council on Animal Care (CCAC), Ethical Council for the Protection of Experimental Animals of the Ministry of Agriculture, Forestry and Water Management of the Republic of Serbia, and was approved by the Institutes' Animal Care Committees.

Drug administration

GL-I-54 (1, 3, 5, 10, 30 mg/kg), GL-II-73 (5 mg/kg) or GL-RM (10 mg/kg) were diluted in vehicle solution (85% distilled H_2O, 14% propylene glycol (Sigma Aldrich) and 1% Tween 80 (Sigma Aldrich)) and administered intraper- itoneal (IP), 30 min before testing. For oral administration, GL-RM was prepared in tap water (30 mg/kg) and given through drinking water, considering 6 mL average daily fluid intake/animal.

GL-I-54 pharmacokinetics

Mice were treated IP with 3 mg/kg GL-I-54 and euthanized at different time points (5–720 min post-injection) for brain and plasma quantification of ligand by ultraperformance LC-MS/MS (cassette dosing) [63]. In vitro hydrolytic plasma stability of GL-I-54 was tested in vitro at 37 °C, utilizing blank mouse plasma spiked with GL-I-54 and internal standard, as in [64].

Plasma protein and brain tissue binding studies

A rapid equilibrium dialysis assay determined the free fraction of GL-I-54 in mouse plasma and brain tissue as in [65]. GL-I-54-free brain concentrations were calculated by multiplying the total brain concentrations with the appropriate free fractions determined by rapid equilibrium dialysis.

Liver microsomal assay

Metabolic stability was tested in C57BL/6 mouse liver microsomes at 2 μM and 0.5 mg/mL of matrix concentration, as in [66]. NADPH solution, Microsomes/S9 and compounds were added to assay plates. Plates were quenched at T0, 30, 60, and 120 min and assessed in refrigerated LC-MS/MS autosampler. Intrinsic hepatic clearance calcula- tions used 45 mg microsomes/g of liver and 87.5 g liver/kg of body weight for mouse.

Stress paradigms

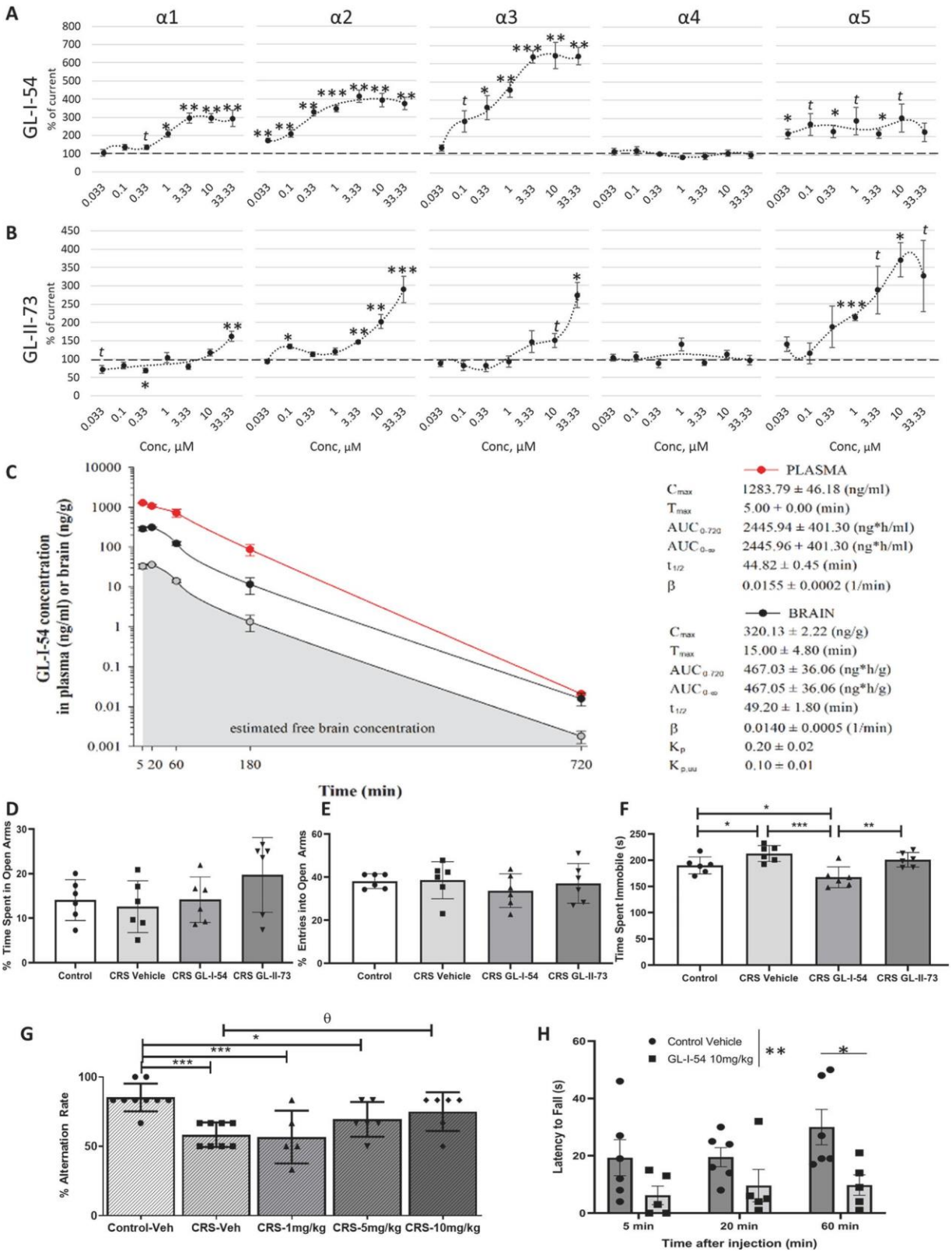
Two stress paradigms were utilized. The first, chronic restraint stress (CRS), was used with cohorts #2 and #3, consisting of placing mice in a 50 mL Falcon™ Tube for 1 hr twice daily for 1 week. This paradigm consists of a strong stressor that is commonly used for early drug screens. Due to the stress CRS applies, this test is not appropriate for longer (chronic) studies. Therefore, cohorts #5 and #6 were subjected to Unpredictable Chronic Mild Stress (UCMS), a stress paradigm that relies on milder stressors, has slower onset and typically better relates to disease state. These study designs also allow for replication between two different stress paradigms. We used randomized mild stressors (Light modification, cage tilt, predator odor, reduced space, reduce space with odor, restraint, wet bedding, new bedding, no bedding exchange mice or forced bath) twice daily over 6 weeks. Weeks with behavioral testing applied one stressor per day after the behavioral testing (2 weeks). CRS and UCMS animals were housed in a separate room from controls, without environmental enrichment to exacerbate effects of other stressors.

Behavioral tests

Side effects were measured in the rotarod test in cohort #4, assessing locomotor coordination on latency to fall off an accelerating rod over 6 trials and in a maximum tolerated dose-clinical observation study (Supplementary Materials Fig. 4). Mice in cohorts #2 were tested in the elevated plus maze (EPM), measuring avoidance of open arms for 10 min as a proxy of anxiety [67], and in the forced swim test (FST), measuring time spent immobile for 6 min. In cohort #3, mice were exposed to CRS to induce a working memory deficit in the Y maze test, and to test the capacity of reversal of GL-I-54. In cohorts #5 and #6, mice were subjected to UCMS, and each animal's coat state was scored (0 = well-groomed, smooth coat, 1=soiled coat or bald patches) weekly for seven coat regions, as in [68]. Behavioral screen included: anxiety-like avoidance behavior (EPM, open-field, OF; Novelty Suppressed Feeding, NSF; and the Phenotyper Test [67], PT), Sucrose Consumption; (SC), immobility in the FST and cognitive function (Y-maze alternation task [55, 58, 69]).

Tissue collection and golgi staining

Cohort #6 was euthanized by cervical dislocation 24 h after last behavioral test. Brains were immersed in Golgi-Cox staining solution, and assigned a unique identifier (4 brains/group). Brains were shipped to NeuroDigiTech (San Francisco CA, USA) for sectioning (100 μm thickness), mounting and blind quantification of basal and apical dendrites of PFC and CA1 pyramidal cells using NeuroLucida v10 software. Neurons (n = 6/animal) were analyzed for dendritic length, spine number and spine density [70].



Statistics

Statistical analyses used GraphPad Prism 9. Electrophysiology data and compounds activity at GABAA-R subunits were compared to 100% using t-tests. Other analyzes used two-way ANOVA with concentration and subunit as co-factors, and Bonferroni post-hoc tests. Behavioral analyzes used one-way or two-way ANOVA, and repeated measure ANOVA as relevant. Fishers PLSD tests were used for post-hoc analyses.

Z-scores were calculated to assess consistency of behavioral phenotypes across tests, referred to as z-emotionality using averaged z-scores of behavioral tests as in [71]. Full calculations in supplementary.

Fig. 1 Electrophysiological, pharmacokinetic and behavioral profiles of GL-II-73 and GL-I-54. Electrophysiological recordings were obtained from HEK-293T cells transfected with full-length cDNA for human GABAA receptor subtypes α1β3γ2, α2β3γ2, α3β3γ2, α4β3γ2 or α5β3γ2, in presence of GL-I-54 (A) or GL-II-73 (B), and in the presence of GABA in the medium (5 μM). Pharmacokinetic profile of GL-I-54 was also examined (C). Plasma, brain and free brain concentration-time profile of GL-I-54 after intraperitoneal cassette administration of 3 mg/kg dose in male C57BL/6 mice (n = 3 per time point). C_{max}, maximum concentration in plasma or brain; T_{max}, time of maximum concentration in plasma or brain; $AUC_{0–720}$, area under the plasma or brain concentration-time curve from 0 to 720 min; $AUC_{0-\infty}$, area under the plasma or brain concentration-time curve from 0 to extrapolated infinite time; $t_{1/2}$, elimination half-life from plasma or brain; β, elimination constant rate from plasma or brain; K_p, brain-to-plasma partition coefficient (K_p = $AUC_{0-\infty}$, brain/$AUC_{0-\infty}$, plasma); $K_{p,uu}$, ratio of unbound brain to unbound plasma drug concentrations ($K_{p,uu}$ = K_p × unbound fraction in brain/unbound fraction in plasma). GL-I-54 and GL-II-73 were then tested in the elevated plus maze and forced swim test at the dose of 5 mg/kg, in mice previously exposed to chronic restraint stress (CRS). Drugs were administered IP, 30 min prior to testing. Percent time spent in the open arms (D) and percent entries into open arm (E) showed no difference between groups. Time immobile (F) showed more time spent immobile in the CRS-Vehicle group, and less time immobile in animals receiving GL-I-54, compared to CRS-Vehicle. GL-II-73 did not show an effect. GL-I-54 was tested in the Y-maze task, assessing working memory (G). Animals subjected to CRS and receiving vehicle showed a significant decrease in alternation rate, suggesting a working memory deficit. Animal subjected to CRS and receiving the highest dose of GL-I-54 showed significant increase in alternation rate, suggesting reversal of working memory deficits induced by CRS. Finally, independent mice were tested in the rotarod (H; N = 5 Control Vehicle and N = 6 GL-I-54). Mice were trained to maintain themselves on a rotating rod (rotarod) for 3 trials. Then, they were injected with GL-I-54 at 10 mg/kg, and tested 5 min, 20 min and 60 min past injection time. Latency to fall from the rod was recorded, and showed significant reductions in latency to fall in mice receiving GL-I-54. All values are represented as mean ± standard error of the mean. *p < 0.05, **p < 0.01, ***p < 0.001 compared to 100% in A, B) or to Control, Control/Vehicle in D-G. $^{\theta}p$ < 0.05 compared to CRS-Vehicle.

RESULTS

Statistical significances are provided in Supplementary Tables.

GL-I-54 and GL-II-73 exhibit different GABAA-R potentiation profiles but similar metabolic stability

Both enantiomers were confirmed PAMs, not agonists (Supple- mentary Fig. 1 and Fig. 1A, B), acting only in the presence of GABA. GL-I-54 significantly increased potentiation at α2-GABAA-Rs (>0.03 μM), α3-GABAA-Rs (>0.33 μM), α1-GABAA-Rs (>1 μM) and α5-GABAA-Rs (0.03, 0.33 and 3.33 μM; Fig. 1A), with preferential activity at α3- and α2- over α1-, α4- and α5-GABAA-Rs (Supplementary Table 1A).

GL-II-73 significantly increased potentiation at α5-GABAA-Rs (>1 μM), α2-GABAA-Rs (3.33 μM), α3-GABAA-Rs (33.33 μM) and α1-GABAA-Rs (33.33 μM; Fig. 1B), with preferential activity at α5- GABAA-Rs over α1-GABAA-Rs (>0.3 μM), α2-GABAA-Rs (between 3.3 and 10 μM), α3-GABAA-Rs (between 1 and 10 μM) and α4- GABAA-Rs (>0.33 μM) (Supplementary Table 1B), confirming data previously published [55].

Pharmacokinetic profile, brain penetrance and stability

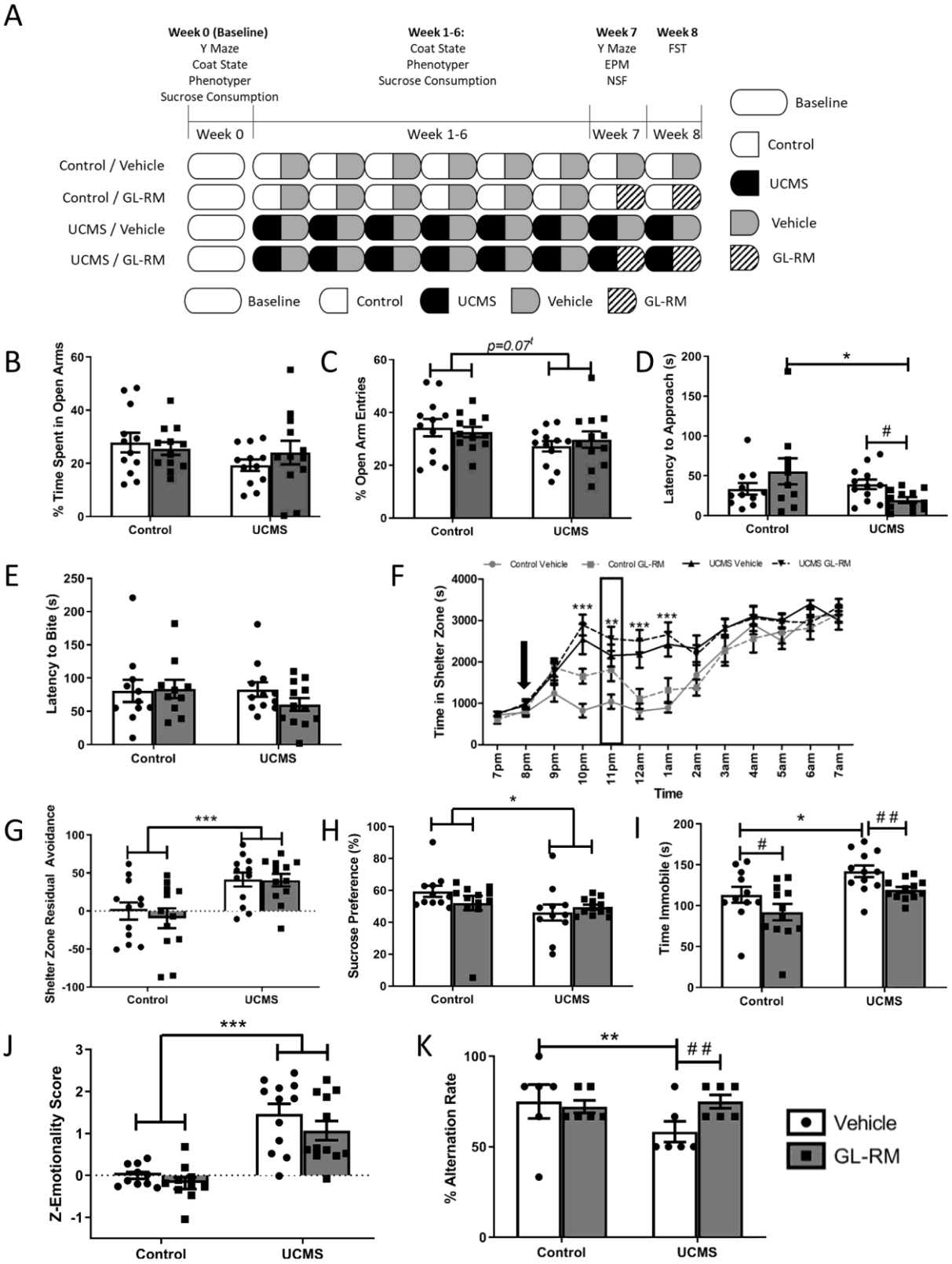
Pharmacokinetic profile of GL-I-54 dosed at 3 mg/kg in mice is represented in Fig. 1C (statistical analyses in Supplementary Table 2). Accounting for the doses administered in respective studies, GL-I-54 and GL-II-73 exhibit comparable pharmacokinetic patterns. As a representative example, 20 min after the 3 mg/kg dose, GL-I-54 achieved 311.75 ± 6.72 ng/g, while GL-II-73 reached 264.61 ± 38.22 ng/g (Supplementary Fig. 2). After appropriate adjustments (for the 5 mg/kg dose, free fraction, brain tissue density and unit), these close-to-maximum concentrations achiev- able in the mouse brain correspond to the 0.100–0.330 μM concentration range in electrophysiological recordings (calcula- tion in Supplementary Fig. 2). This implies that, in acute behavioral experiments with 5 mg/kg dose, GL-I-54 likely potentiates α_1, α_2, α_3 and α_5 GABAA-Rs, however, α_1 potentiation is mild. 5 mg/kg of GL-II-73, on the other hand, is fairly silent on all GABAA-Rs, with the potential to mildly activate α_2 and α_5 receptors; on α_1 and α_3 receptors, nevertheless, it behaves as a null modulator. Plasma and brain free fractions of GL-I-54 were 22.57% and 11.49%, respectively, while, as previously reported for GL-II-73 were 20.39% and 12.14% [55], respectively. Brain to plasma ratio (K_p) evaluates brain penetrance (penetrant when K_p > 0.04). GL-I-54 is brain penetrant (K_p = 0.20), similarly to GL-II-73 (K_p = 0.30), which is further supported by the ratio of unbound brain to unbound plasma ligand concentrations values, $K_{p,uu}$ (0.10 vs 0.18, respec- tively). GL-I-54 displayed high in vitro metabolic stability, although lower compared to GL-II-73; after 4 h of incubation in mouse plasma, the fraction of remaining intact ligand was 78.41% (vs 98.88% of GL-II-73 [55]). In the liver microsomal assay, GL-I-54 showed a 198 min half-life with 70% remaining after 2 h. Intrinsic hepatic clearance was 27.6 mL/min/kg. GL-II-73 showed a longer half-life, 256 min, with 75.6% remaining after 2 h. Intrinsic hepatic clearance was 21.3 mL/min/kg.

Acute administration of GL-I-54 displays anxiolytic effects and reverses spatial working memory deficits in the chronic restrain stress model with locomotor side effects at higher dose

In mice subjected to CRS, GL-I-54 (5 mg/kg) and GL-II-73 (5 mg/kg) were tested for their effects on anxiety-related avoidance in the elevated plus maze (EPM), and on immobility in the forced swim test (FST). Effects on spatial working memory were tested in the Y-maze (5 mg/kg and 10 mg/kg). After CRS, GL-I-54 and GL-II-73 had no effect on percent time in open arms of the EPM or percent entries into open arms (Fig. 1D, E; and Supplementary Table 2). In the FST, CRS increased time spent immobile, which was significantly reversed by GL-I-54 (Fig. 1F), suggesting GL-I-54 reverses stress- induced increase in immobility in this test. Interestingly, GL-I-54 given in non-stressed animals at the dose of 5 mg/kg showed a trend at increasing time in the open arm in the EPM, and significantly reduced time spent immobile in the FST (Supplemen- tary Fig. 3). In the Y-maze, CRS induced an alternation rate deficit that was reversed by GL-I-54 at 10 mg/kg but not 5 mg/kg (Fig. 1G), suggesting the capacity of reversing spatial working memory deficits. Locomotor side effects of GL-I-54 at 10 mg/kg were tested in the rotarod (Fig. 1H, and Supplementary Table 2) to support previous finding from a maximum tolerated dose-clinical observa- tion study demonstrating sedative properties of GL-I-54 (Supple- mentary Fig. 4). Decreasing latency to fall 60 min after injection was found, suggesting sedation at this dose.

Acute administration of GL-RM reverses spatial working memory deficits in the UCMS model

Based on the selective effects observed with acute administration of GL-I-54 or GL-II-73 alone at 5 mg/kg, we tested potential additive effects and low side effects using a 1:1 racemic mixture of 5 mg/kg each, called GL-RM, in the UCMS model (Fig. 2A; and Supplementary Table 3), with a final GL-RM dose of 10 mg/kg. Weekly monitoring showed UCMS deteriorated coat state, not reversed by acute treatment, weight gain remained unaffected (Supplementary Fig. 5). Using the Phenotyper, no locomotor activity differences were detected between groups with GL-RM injection supporting its lack of sedative effects (Supplementary Fig. 6).



In the EPM, there was no effect of UCMS or treatment on percent time in open arms (Fig. 2B). There was a trend level effect of stress reducing the percent of entries into open arms but no effect of treatment (Fig. 2C). NSF latency to approach found a significant interaction between UCMS and treatment, due to reduced latency in UCMS + GL-RM treated animals compared to Control+GL-RM and compared to UCMS + vehicle (Fig. 2D), suggesting anxiolytic properties through reduced avoidance. Latency to bite was unaffected by UCMS or treatment (Fig. 2E). Phenotyper test and associated measure of residual avoidance

Fig. 2 Effect of acute treatment of GL-RM on anxiety, emotionality and working memory deficits in mice subjected to chronic stress. Male and female mice were tested at baseline in the Y-maze, the phenotyper and the sucrose consumption test prior to being subjected to 6 weeks of UCMS (A). Weekly, mice were tested in the phenotyper test, the sucrose consumption and their weight and coat state were measured. After 6 weeks of UCMS, acute injections were performed 30 min prior to behavioral testing. In the elevated plus maze, time spent (B) and entries (C) in the open arms were measured, with no significant effect of UCMS, treatment or interaction. In the novelty suppressed feeding test, latency to approach (D) and latency to bite (E) were assessed. Statistical analyses showed that acute GL-RM treatment reduces latency to approach in mice subjected to UCMS. In the phenotyper test (F), mice were placed in the box overnight, where a stressful stimulus was applied at 11 pm, for 1 h. Time spent in the shelter zone showed that mice subjected to UCMS spent more time in the shelter than control mice. Calculating a residual avoidance score (G), statistical analyses showed a significant increase in residual avoidance in mice subjected to UCMS. In the sucrose consumption test (H), mice subjected to UCMS showed a significant decrease in preference to sucrose. In the forced swim test (I), mice subjected to UCMS showed increased immobility, while mice treated with GL-RM showed a reduction in immobility. Combining the individual score into a global z-score (J), statistical analyses confirmed a significant impact of UCMS, with reduced effect of GL-RM. Finally, mice were tested in the Y-maze (K), where statistical analyses showed altered alternation with UCMS, which is reversed by acute GL-RM treatment. $^{*}p < 0.05$, $^{**}p < 0.01$, $^{***}p < 0.001$ effect of UCMS, $^{\#}p < 0.05$, $^{\#\#}p < 0.01$ effect of GL-RM.

used in Prevot et al. [67] assess anxiety-related avoidance weekly. The residual avoidance score captures the time spent in the shelter, after a 1 h-light challenge, measuring residual avoidance of the previously-lit zone. Prior to UCMS, there was no group difference (Supplementary Fig. 7A, B). Upon UCMS, residual time spent in the shelter following an acute light challenge was increased (Fig. 2F, G; Supplementary Fig. 7C–G). On week 6, acute GL-RM treatment did not affect time in the shelter after the light challenge (Fig. 2F). Sex-dependent analyses showed males spent more time in the shelter than females (data not shown).

At week 6, sucrose preference was significantly reduced by UCMS but unaffected by GL-RM (Fig. 2H, and Supplementary Table 3), suggesting a lack of effect from treatment at reversing UCMS-induced reduced sucrose preference. In the FST, UCMS increased time immobile, which was reduced by GL-RM (Fig. 2I). Z-scoring of behavioral emotionality, integrating behavioral out- comes in a single readout confirmed the effect of UCMS, and a limited efficacy of acute GL-RM treatment (Fig. 2J). In contrast, the Y-maze spatial working memory deficit induced by UCMS was significantly reversed by acute GL-RM treatment (Fig. 2K).

Altogether, these results showed that acute administration of GL-RM mainly overcomes spatial working memory deficits induced by UCMS, while having reduced efficacy on emotionality.

Chronic GL-RM conserves spatial working memory benefits in the UCMS model

The effects of chronic GL-RM administration were investigated in mice subjected to UCMS (Fig. 3A). Altered coat state and reduced weight gain with UCMS was significant from week 1–6, with no effect on chronic GL-RM (Supplementary Fig. 8).

There was no effect of UCMS or treatment in the EPM, OF and NSF latency to approach (Fig. 3B–F, and Supplementary Table 4). Latency to bite found an effect of UCMS and treatment. Unexpectedly, UCMS + GL-RM mice compared to Control + GL- RM mice showed decreased latency to bite (Fig. 3G). In the Phenotyper test (Fig. 3H and Supplementary Fig. 9), UCMS increased residual avoidance in the shelter zone, while chronic GL-RM was trending to decrease it.

Sucrose preference was unaffected by UCMS, but chronic GL- RM increased preference (Fig. 3I). In the FST, the time spent immobile was unaffected by UCMS or treatment (Fig. 3J). UCMS significantly increased z-emotionality, with a trend level effect of chronic GL-RM reducing z-emotionality (Fig. 3K).

In the Y-maze, UCMS decreased percent alternation rate (Control + Vehicle vs UCMS + Vehicle) and chronic GL-RM sig- nificantly increased percent alternation rate between UCMS + vehicle and UCMS + GL-RM groups (Fig. 3L), confirming efficacy at reversing stress-induced spatial working memory deficits.

Results suggest that chronic GL-RM may contribute to reducing z-emotionality, with discrete effects on individual outcomes, and confirm its effect at reversing UCMS-induced spatial working memory deficits.

Chronic GL-RM administration reverses neuronal morphology deficits induced by UCMS

We quantified morphological changes in apical and basal dendrites of PFC pyramidal neurons (Fig. 4A–C, and Supplemen- tary Fig. 10). Dendritic length was not affected by UCMS or treatment, but spine count and spine density were significantly lower in UCMS compared to control mice (Fig. 4D, E, and Supplementary Fig. 10). Such decreases were reversed by chronic GL-RM in basal and apical segments, with spine density in apical PFC dendrites of GL-RM treated UCMS animals being significantly higher than UCMS animals and not significantly different from controls (Fig. 4D).

Similarly, significant UCMS effects on spine density and reversal by chronic GL-RM treatment were observed in CA1 pyramidal neurons (Fig. 4E, and Supplementary Fig. 11).

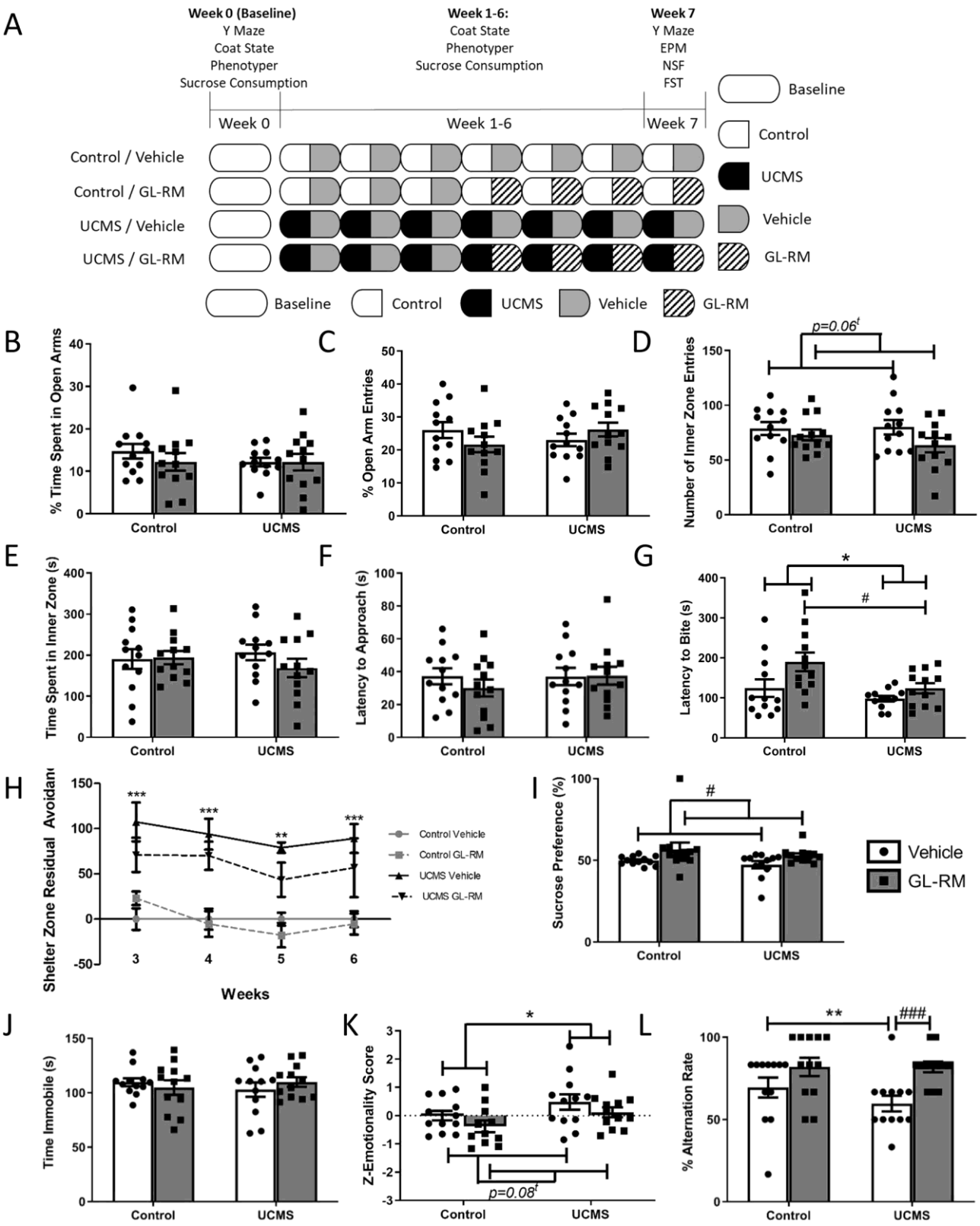
Improved cognitive functions might be related to improved spine density and overall neuronal morphology (Supplementary Table 5 and Supplementary Fig. 12), although studies with larger sample size are required to confirm this hypothesis.

DISCUSSION

This work is based on observations that patients with psycho-pathologies related to chronic stress exposure experience mood and cognitive deficits, while current treatments display moderate- to-no efficacy for mood and cognition [1–3, 9]. We investigated the efficacy of two enantiomers with activity at α3-, α2-, α5- GABAA-Rs (GL-I-54) and α5-GABAA-Rs (GL-II-73) separately, and in combination (GL-RM) at alleviating such symptoms and neuronal atrophy in CRS and UCMS models. GL-I-54 reduced immobility in the FST, did not show efficacy in the EPM, nor reversed stress- induced working memory deficits at low dose (5 mg/kg). GL-I-54 required a higher dose (10 mg/kg) to reverse working memory deficits though while causing slight sedation. GL-II-73 previously showed no effect on working memory at doses lower than 10 mg/ kg [55]. Acute and chronic treatment of a racemix combination of both enantiomers (GL-RM) improved stress-induced working memory deficits. Acute GL-RM only decreased immobility in the FST, suggesting inconclusive results on emotionality. Finally, chronic GL-RM treatment reversed the UCMS-induced reduction in spine densities in the PFC and CA1 of UCMS mice, with morphological measures correlating with improvement of emo-tionality and working memory.

Racemic mixtures have therapeutic relevance by harnessing different enantiomer GABAA-R specificities

Therapeutic development often favors pure substances over racemic mixtures due to superior selectivity and reduced off- target activities [72, 73]. Racemic development becomes justified if therapeutic benefits of each enantiomer are similar, complimen- tary or devoid of side-effects and toxicity [74]. GL-RM harnessed the similar, yet unique selectivity profiles of GL-I-54 and GL-II-73 to



target the GABAA-Rs known to be involved in anxiety, depression and cognition. GL-I-54 displays activity at α3-, α2-, α5-, α1-GABAA- Rs while GL-II-73 confirmed preferential activity at α5-GABAA-Rs [55], likely reflecting different interactions of each compound's conformation in the binding pocket.

Racemic mixtures are not uncommon in the treatment of MDD [75, 76]. Fluoxetine [75, 77], citalopram [78] or ketamine [37] are clinically used racemic antidepressants [75, 79, 80]. Racemic R,S-ketamine has more efficacy than non-racemic S-Ketamine [81]. Racemic therapies can harness broader selectivity profiles to

Fig. 3 Effect of chronic treatment of GL-RM on anxiety, emotionality and working memory deficits in mice subjected to chronic stress. Male and female mice were tested at baseline in the Y-maze, the phenotyper and the sucrose consumption test prior to being subjected to 6 weeks of UCMS (A). After 3 weeks of UCMS, chronic treatment with GL-RM in the drinking water was initiated, for a total of 4 weeks. Weekly, mice were tested in the phenotyper test, the sucrose consumption and their weight and coat state were measured. After 6 weeks of UCMS, and 3 weeks of treatment, mice were tested in the elevated plus maze. Time spent (B) and entries (C) in the open arms were measured, but did not show statistical differences. Mice were also tested in the open field for the time spent (D) and number of entries (E) in the inner zone. Again, statistical analyses did not reveal any effect of UCMS nor treatment. In the novelty suppressed feeding test, latency to approach (F) and latency to bite (G) were assessed. Mice were tested in the Phenotyper weekly, and the residual avoidance scores from week 3 to 6 were analyzed, since the treatment was onboard during these testing periods (H). In the sucrose consumption test (I), mice receiving chronic GL-RM showed a significant increase in preference to sucrose. In the forced swim test (J), statistical analyses did not reveal significant differences between groups. Combining the individual score into a global z-score (K), statistical analyses confirmed a significant impact of UCMS at increasing emotionality, with a trend level effect ofchronic GL-RM reducing emotionality. Finally, mice were tested in the Y-maze (L), where statistical analyses showed altered alternation with UCMS, which is reversed by acute GL-RM treatment. $^{*}p < 0.05$, $^{**}p < 0.01$, $^{***}p < 0.001$ effect of UCMS, $^{\#}p < 0.05$, $^{\#\#\#}p < 0.001$ effect of GL-RM.
◀

address multiple pathophysiological mechanisms but have the added risk of off-target side effects. In vivo, considering estimated free concentrations in the brain after a 5 mg/kg dose, we found that concentration is slightly above 100 nM. At this concentration, GL-I-54 may act as a PAM at non-α1 GABAARs, while GL-II-73 would mainly have only slight PAM activity at α2- and α5-GABAA- Rs, and be a null modulator at α1-GABAA-Rs. When combined together, low concentrations of GL-II-73 may be effective as an "on-site softener" of activity of GL-I-54, especially at α1-GABAA-Rs, limiting binding of GL-I-54 in the binding pocket and therefore limiting negative effects observed when potentiating this subunit, further suggesting GL-RM as an intervention for a more complete treatment of depression symptomatology.

Targeting α2-, α3-, α5-GABRA-Rs with GL-RM displays superior efficacy on spatial working memory at lower concentrations than individual enantiomers

Reconciling potentiation profiles with behavioral results, we compared GL-I-54 and GL-II-73 alone at 5 mg/kg or 10 mg/kg after CRS to GL-RM 10 mg/kg (each enantiomer at 5 mg/kg) after UCMS. At 5 mg/kg, GL-I-54 reduced immobility in the FST. Previously reported, GL-II-73 only reduced immobility at 10 not 5 mg/kg [55]. Acute GL-RM reduced UCMS-exposed animal immobility in the FST suggesting GL-RM retains this effect likely due to GL-I-54 activity. GL-RM also reduced immobility in non- stressed animals showing effects at baseline and in the absence of UCMS. Neither enantiomer showed significant efficacy on avoidance behavior, separately or in combination (GL-RM).

Interestingly, GL-RM combined the efficacy of both enantiomers for pro-cognitive effects, specifically spatial working memory. While neither enantiomer elicited pro-working memory effects at 5 mg/kg alone, their combined activity in GL-RM improved working memory deficits. This could be the result of an additive effect of the two compounds at GABAA-Rs, or a reduction of a putative amnestic effect caused by α1-GABAA-R null potentiation [82] with the use of a low GL-II-73 dose. Nevertheless, this finding demonstrates a clinical advantage for using GL-RM over either pure enantiomer at low concentrations, avoiding side effects and benefiting from combined profiles.

Chronic GL-RM administration has neurotrophic effects

As in MDD, chronic stress leads to reduced synchronicity between the PFC and HPC, and dysfunctional information processing within cortical and hippocampal structures [83]. Dendritic length and spine density are reduced in the PFC and HPC of MDD patients and stressed mice [84], contributing to cognitive deficits. Our findings are consistent with other UCMS studies reporting neuronal atrophy and working memory deficits [85–87]. We previously showed that chronic administration of GL-II-73 alone remedies age-related spine loss in pyramidal neurons, through α5-GABAA-R modulation was confined to apical dendrites [58], where α5-GABAA-Rs are primarily located [88–90], and consistent with GL-II-73 preferentially potentiating α5-GABAA-Rs. With GL-RM, neurotrophic effects were extended to basal segments in both PFC and HPC, suggesting a potential role of α2- and/or α3-GABAA- Rs in this neurotrophic effect. Previously, α5- and α2-GABAA-Rs have been implicated in dendritic outgrowth, spine maturation and synapse formation [91–93], thus their modulation by GL-RM may be responsible for spine density restoration at apical and basal dendrites.

While showing spine count improvements, it remains unclear whether spines are prevented from shrinking, or if they are generated *de novo*. Ketamine showed ability to overcome stress hormone-induced spine loss by a combination of restored spines and *de novo* spines, with some preference for *de novo* [94]. A similar combination may also be the case for GL-RM. Evidence that GL-RM has an effect at a pathophysiological level (not only symptomatic levels) is substantially valuable for translational efficacy within humans.

Limitations

In our primary drug screening, the lack of a non-stress group receiving GL-I-54 does not allow us to know baseline effects of GL- I-54 in the Y maze. However, non-stressed animals perform at 80% accuracy, which leaves very little room for improvement, so other tests should be considered for baseline testing. In the GL-RM studies, we see that GL-RM administered in non-stressed animals does not have an effect, and previous studies from our group showed that GL-II-73 alone does not have an effect in the Y maze [55]. Therefore, we can anticipate that GL-I-54 does not have an effect alone, in non-stressed mice, but testing or validation in other tests would confirm this. In addition, we tested GL-RM on a single cognitive domain, but cognitive deficits in depression extend beyond spatial working memory and exploring others is needed for future experiments. Regarding neurotrophic effects, we investigated the PFC and HPC for their regulation of stress- related and depressive symptoms. It could be valuable to investigate how GL-RM modulates connectivity in subnuclei of the amygdala, potentially decreasing the hyperactivity/increased connectivity reported after chronic stress [95, 96]. We used chronic stress models because they recapitulate behavioral and cellular changes observed in human depression [97–100]. While using the most commonly reported stressors [101], variability in anxiety- related outcomes limited clear conclusions on procedure and treatment, not uncommon in behavioral studies [67, 102]. The Phenotyper test measuring context anxiety [67] provided insight to anxiolytic properties of GL-RM with better consistency. The discrepancy between EPM/NSF and Phenotyper results highlight potential biases from hands-on behavioral assays versus auto- matized approaches [103].

To conclude, the therapeutic relevance of a targeted PAM approach at GABAA-Rs is reinforced and the role of α5-GABAA-Rs in cognition is supported. At low-to-moderate dose, both compounds, used together, show promising effects for the treatment of mood and cognitive symptoms, as well as morphological changes in disorders such as MDD.

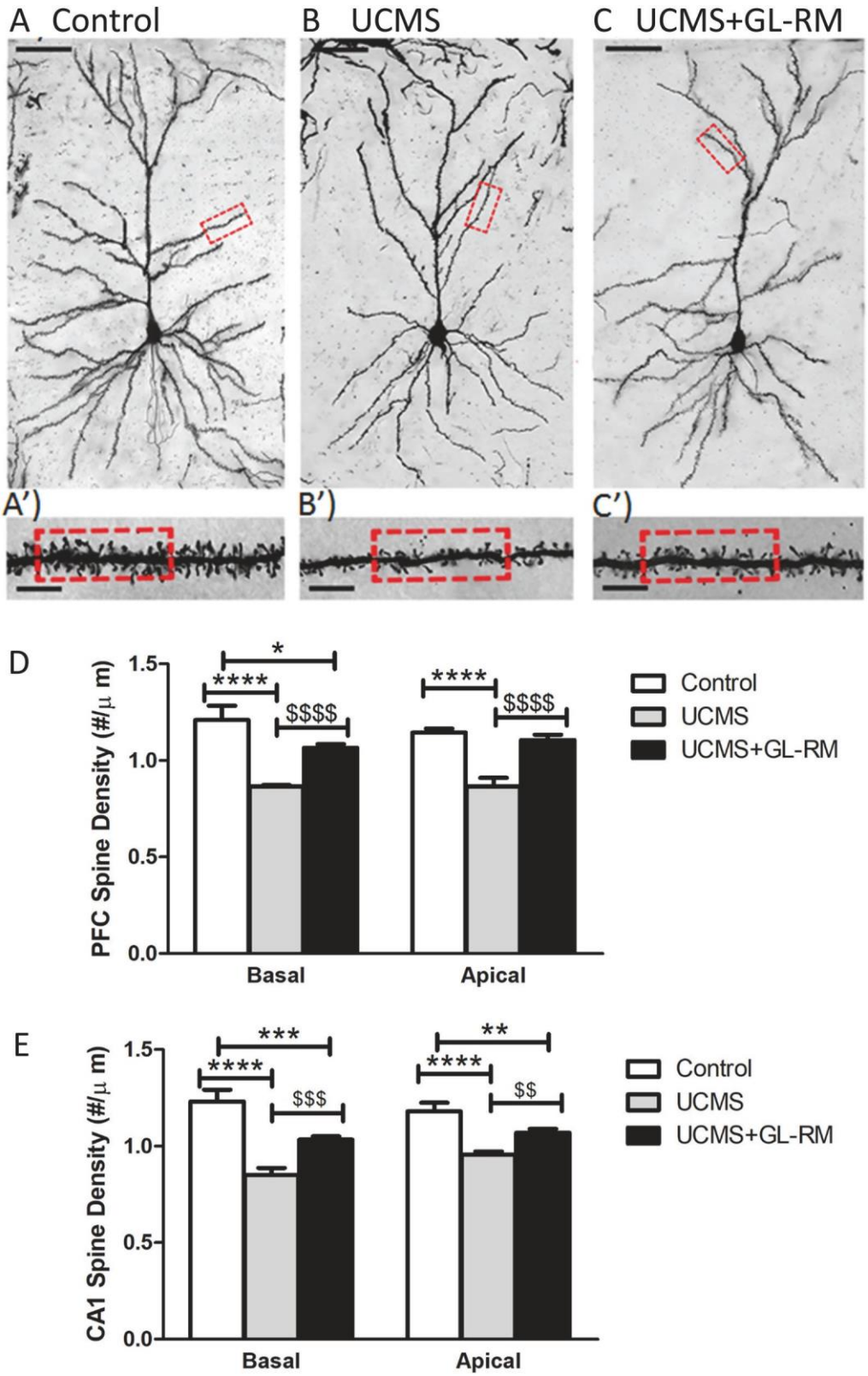


Fig. 4 Chronic treatment with GL-RM reverses chronic-stress induced spine density reduction in the PFC and the CA1. After completion of the behavioral screening, mice were euthanized and brains were stained with Golgi-Cox solution. Pyramidal neurons (N = 6 per mouse) from 4 mice per group (A–C) were analyzed for dendritic length, spine counts and spine density. Basal and apical spine densities were measured in the PFC (D) and the CA1 of the hippocampus (E). ANOVA in the basal and apical segments revealed significant differences between groups, in both brain regions. This difference was explained by a decrease in spine density in mice subjected to UCMS compared to Control mice that was partially reversed by chronic treatment with GL-RM. *$p < 0.05$, **$p < 0.01$, ***$p < 0.001$, ****$p < 0.0001$ compared to "Control"; $^{\$\$}p < 0.01$, $^{\$\$\$}p < 0.001$, $^{\$\$\$\$}p < 0.0001$ compared to "UCMS". Scale bar in (A–C) represents 50 μm.

REFERENCES

1. MacQueen GM, Memedovich KA. Cognitive dysfunction in major depression and bipolar disorder: Assessment and treatment options. Psychiatry Clin Neurosci. 2017;71:18–27.
2. Malhi GS, Mann JJ. Depression. Lancet. 2018;392:2299–312.
3. Gartlehner G, et al. Pharmacological and non-pharmacological treatments for major depressive disorder: review of systematic reviews. BMJ Open. 2017;7: e014912.
4. Hirschfeld RMA. History and evolution of the monoamine hypothesis of depression. J Clin Psychiatry. 2000;61(Suppl 6):4–6.
5. Xia C-Y, et al. Targeting the dysfunction of glutamate receptors for the development of novel antidepressants. Pharmacol Therapeutics. 2021;226:107875.
6. Davis MT, et al. Acute cognitive effects of single-dose intravenous ketamine in major depressive and posttraumatic stress disorder. Transl Psychiatry. 2021;11:205.
7. Gill H, et al. The effects of ketamine on cognition in treatment-resistant depression: A systematic review and priority avenues for future research. Neurosci Biobehav Rev. 2021;120:78–85.
8. Prevot T, Sibille E. Altered GABA-mediated information processing and cognitive dysfunctions in depression and other brain disorders. Mol Psychiatry. 2021;26:151–67.
9. Duman CH, Duman RS. Spine synapse remodeling in the pathophysiology and treatment of depression. Neurosci Lett. 2015;601:20–9.
10. Williams LM. Precision psychiatry: A neural circuit taxonomy for depression and anxiety. Lancet Psychiatry. 2016;3:472–80.
11. Banasr M, Dwyer JM, Duman RS. Cell atrophy and loss in depression: Reversal by antidepressant treatment. Curr Opin Cell Biol. 2011;23:730–7.
12. Kang HJ, et al. Decreased expression of synapse-related genes and loss of synapses in major depressive disorder. Nat Med. 2012;18:1413–7.
13. Holmes SE, et al. Lower synaptic density is associated with depression severity and network alterations. Nat Commun. 2019;10:1529.
14. Lissemore JI, et al. Reduced GABAergic cortical inhibition in aging and depression. Neuropsychopharmacology. 2018;43:2277–84.
15. Lee JC, et al. The role of transcranial magnetic stimulation in treatment-resistant depression: A review. Curr Pharm Des. 2012;18:5846–52.
16. Fogaca MV, Duman RS. Cortical GABAergic dysfunction in stress and depression: New insights for therapeutic interventions. Front Cell Neurosci. 2019;13:87.
17. Newton, DF, et al. Chapter 28 - Altered GABAergic Function, Cortical Microcircuitry, and Information Processing in Depression, in Neurobiology of Depression, J Quevedo, AF Carvalho, and CA Zarate, Editors. 2019, Academic Press. p. 315–29.
18. Bhagwagar Z, et al. Low GABA concentrations in occipital cortex and anterior cingulate cortex in medication-free, recovered depressed patients. Int J Neuropsychopharmacol/Off Sci J Collegium Int Neuropsychopharmacologicum (CINP). 2008;11:255–60.
19. Goddard AW, et al. Reductions in occipital Cortex GABA levels in panic disorder detected with 1H-Magnetic resonance spectroscopy. Arch Gen Psychiatry. 2001;58:556–556.
20. Price RB, et al. Amino acid neurotransmitters assessed by proton magnetic resonance spectroscopy: Relationship to treatment resistance in major depressive disorder. Biol Psychiatry. 2009;65:792–800.
21. Sanacora G, et al. Subtype-specific alterations of gamma-aminobutyric acid and glutamate in patients with major depression. Arch Gen Psychiatry. 2004;61:705–13.
22. Sanacora G, et al. Increased occipital cortex GABA concentrations in depressed patients after therapy with selective serotonin reuptake inhibitors. Am J Psychiatry. 2002;159:663–5.
23. Sanacora G, et al. Subtype-specific alterations of gamma-aminobutyric acid and glutamate in patients with major depression. Arch Gen Psychiatry. 2004;61:705–13.
24. Sanacora G, et al. Reduced cortical γ-Aminobutyric acid levels in depressed patients determined by proton magnetic resonance spectroscopy. Arch Gen Psychiatry. 1999;56:1043–1043.
25. Hasler G, et al. Reduced prefrontal glutamate/glutamine and gamma-aminobutyric acid levels in major depression determined using proton magnetic resonance spectroscopy. Arch Gen Psychiatry. 2007;64:193–200.
26. Gabbay V, et al. Anterior cingulate Cortexγ-Aminobutyric acid in depressed adolescents. Arch Gen Psychiatry. 2012;69:139–139.
27. Plante DT, et al. Reduced gamma-aminobutyric acid in occipital and anterior cingulate cortices in primary insomnia: A link to major depressive disorder? Neuropsychopharmacology. 2012;37:1548–57.
28. Feyissa AM, et al. Reduced levels of NR2A and NR2B subunits of NMDA receptor and PSD-95 in the prefrontal cortex in major depression. Prog Neuro-Psychopharmacol Biol Psychiatry. 2009;33:70–75.
29. Christoffel DJ, Golden SA, Russo SJ. Structural and synaptic plasticity in stress-related disorders. Rev Neurosci. 2011;22:535–49.
30. Izquierdo A, Wellman CL, Holmes A. Brief uncontrollable stress causes dendritic retraction in infralimbic cortex and resistance to fear extinction in mice. J Neurosci. 2006;26:5733–8.
31. Liston C, et al. Stress-induced alterations in prefrontal cortical dendritic morphology predict selective impairments in perceptual attentional set-shifting. J Neurosci. 2006;26:7870–4.
32. Shansky RM, et al. Stress-induced dendritic remodeling in the prefrontal cortex is circuit specific. Cereb Cortex. 2009;19:2479–84.
33. Abdallah CG, et al. Prefrontal cortical GABA abnormalities are associated with reduced hippocampal volume in major depressive disorder. Eur Neuropsychopharmacol. 2015;25:1082–90.
34. Bessa JM, et al. The mood-improving actions of antidepressants do not depend on neurogenesis but are associated with neuronal remodeling. Mol Psychiatry. 2009;14:764–73.
35. Ampuero E, et al. Chronic fluoxetine treatment induces structural plasticity and selective changes in glutamate receptor subunits in the rat cerebral cortex. Neuroscience. 2010;169:98–108.
36. Lyttle K, et al. Repeated fluvoxamine treatment recovers juvenile stress-induced morphological changes and depressive-like behavior in rats. Brain Res. 2015;1616:88–100.
37. Phoumthipphavong, V, et al., Longitudinal effects of ketamine on dendritic architecture in vivo in the mouse medial frontal cortex. eNeuro, 2016. 3: p. *ENEURO*.0133-15.2016.
38. Gerhard DM, et al. GABA interneurons are the cellular trigger for ketamine's rapid antidepressant actions. J Clin Invest. 2020;130:1336–49.
39. Mohler H. GABA(A) receptor diversity and pharmacology. Cell Tissue Res. 2006;326:505–16.
40. Sigel E, Ernst M. The Benzodiazepine binding sites of GABAA receptors. Trends Pharmacol Sci. 2018;39:659–71.
41. Pariente A, et al. The Benzodiazepine–dementia disorders link: Current state of knowledge. CNS Drugs. 2016;30:1–7.
42. Sieghart W, Savić MM. International Union of basic and clinical pharmacology. CVI: GABA(A) Receptor subtype- and function-selective ligands: Key issues in translation to humans. Pharm Rev. 2018;70:836–78.
43. Fritschy JM, Mohler H. GABAA-receptor heterogeneity in the adult rat brain: differential regional and cellular distribution of seven major subunits. J Comp Neurol. 1995;359:154–94.
44. Geracitano R, et al. Functional expression of the GABA(A) receptor α2 and α3 subunits at synapses between intercalated medial paracapsular neurons of mouse amygdala. Front Neural Circuits. 2012;6:32.
45. Stefanits H, et al. GABAA receptor subunits in the human amygdala and hippocampus: Immunohistochemical distribution of 7 subunits. J Comp Neurol. 2018;526:324–48.
46. Marowsky A, Fritschy JM, Vogt KE. Functional mapping of GABA A receptor subtypes in the amygdala. Eur J Neurosci. 2004;20:1281–9.
47. Heldt SA, Ressler KJ. Training-induced changes in the expression of GABAA-associated genes in the amygdala after the acquisition and extinction of Pavlovian fear. Eur J Neurosci. 2007;26:3631–44.
48. Dias R, et al. Evidence for a significant role of alpha 3-containing GABAA receptors in mediating the anxiolytic effects of benzodiazepines. J Neurosci. 2005;25:10682–8.
49. Möhler H. The GABA system in anxiety and depression and its therapeutic potential. Neuropharmacology. 2012;62:42–53.
50. Atack JR. GABAA receptor alpha2/alpha3 subtype-selective modulators as potential nonsedating anxiolytics. Curr Top Behav Neurosci. 2010;2:331–60.
51. Engin E, Liu J, Rudolph U. α2-containing GABA(A) receptors: a target for the development of novel treatment strategies for CNS disorders. Pharmacol therapeutics. 2012;136:142–52.
52. Collins I, et al. 3-Heteroaryl-2-pyridones: Benzodiazepine site ligands with functional delectivity for alpha 2/alpha 3-subtypes of human GABA(A) receptor-ion channels. J Med Chem. 2002;45:1887–900.
53. Miller BH, et al. Quantitative trait locus analysis identifies Gabra3 as a regulator of behavioral despair in mice. Mammalian genome: official journal of the International Mammalian Genome. Society. 2010;21:247–57.
54. Koh MT, Rosenzweig-Lipson S, Gallagher M. Selective GABA(A) alpha5 positive allosteric modulators improve cognitive function in aged rats with memory impairment. Neuropharmacology. 2013;64:145–52.
55. Prevot T, et al. Novel Benzodiazepine-like ligands with various anxiolytic, antidepressant, or pro-cognitive profiles. Molecular. Mol Neuropsychiatry. 2019;5:84–97.
56. Sigurdsson T, Duvarci S. Hippocampal-prefrontal interactions in cognition. Behav Psychiatr Dis Front Syst Neurosci. 2016;9:190–190.

57. Koh MT, Rosenzweig-Lipson S, Gallagher M. Selective GABA(A) α5 positive allosteric modulators improve cognitive function in aged rats with memory impairment. Neuropharmacology. 2013;64:145–52.
58. Prevot, TD, et al. Reversal of Age-Related Neuronal Atrophy by α5-GABAA Receptor Positive Allosteric Modulation. Cereb Cortex, 2020;31:1395–1408.
59. Rudolph U, et al. Benzodiazepine actions mediated by specific gamma-aminobutyric acid(A) receptor subtypes. Nature. 1999;401:796–800.
60. Li G, et al. Synthesis of chiral GABA(A) receptor subtype selective ligands as potential agents to treat schizophrenia as well as depression. Arkivoc. 2018;2018:158–82.
61. Billakota S, et al. Personalized medicine: Vinpocetine to reverse effects of GABRB3 mutation. Epilepsia. 2019;60:2459–65.
62. Kirsch GE, et al. Electrophysiology-based assays to detect subtype-selective modulation of human nicotinic acetylcholine receptors. ASSAY Drug Dev Technol. 2016;14:333–44.
63. Bayliss MK, Frick LW. High-throughput pharmacokinetics: Cassette dosing. Curr Opin Drug Disco Devel. 1999;2:20–5.
64. Stamenic TT, et al. Ester to amide substitution improves selectivity, efficacy and kinetic behavior of a benzodiazepine positive modulator of GABAA receptors containing the alpha5 subunit. Eur J Pharm. 2016;791:433–43.
65. Obradovic A, et al. Sh-I-048A, an in vitro non-selective super-agonist at the benzodiazepine site of GABAA receptors: The approximated activation of receptor subtypes may explain behavioral effects. Brain Res. 2014;1554:36–48.
66. Di L, et al. Optimization of a higher throughput microsomal stability screening assay for profiling drug discovery candidates. J Biomolecular Screen. 2003;8:453–62.
67. Prevot TD, et al. Residual avoidance: A new, consistent and repeatable readout of chronic stress-induced conflict anxiety reversible by antidepressant treatment. Neuropharmacology. 2019;153:98–110.
68. Nollet, M, Guisquet AM Le, Belzung C. Models of depression: unpredictable chronic mild stress in mice. Curr Protoc Pharmacol. 2013;5:Unit 5.65.
69. Faucher P, et al. Hippocampal injections of Oligomeric Amyloid β-peptide (1-42) induce selective working memory deficits and long-lasting alterations of ERK signaling pathway. Front Aging Neurosci. 2015;7:245.
70. Wu CC, et al. Selective vulnerability of dentate granule cells prior to amyloid deposition in PDAPP mice: digital morphometric analyses. Proc Natl Acad Sci USA. 2004;101:7141–6.
71. Guilloux J-P, et al. Integrated behavioral z-scoring increases the sensitivity and reliability of behavioral phenotyping in mice: Relevance to emotionality and sex. J Neurosci Methods. 2011;197:21–31.
72. Sekhon BS. Exploiting the power of stereochemistry in drugs: An overview of racemic and enantiopure drugs. J Mod Med Chem. 2013;1:10–36.
73. Nguyen LA, He H, Pham-Huy C. Chiral drugs: An overview. Int J Biomed Sci: IJBS. 2006;2:85–100.
74. Srinivas NR, Barbhaiya RH, Midha KK. Enantiomeric drug development: Issues, considerations, and regulatory requirements. J Pharm Sci. 2001;90: 1205–15.
75. Budău M, et al. Chirality of modern antidepressants: An overview. Adv Pharm Bull. 2017;7:495–500.
76. Zarate, CA, Commentary on the Canadian Network for Mood and Anxiety Treatments (CANMAT) Task Force Recommendations for the Use of Racemic Ketamine in Adults with Major Depressive Disorder. Canadian J Psychiatry. 2021:66:573–539.
77. Henry ME, et al. A comparison of brain and serum pharmacokinetics of R-fluoxetine and racemic fluoxetine: A 19-F MRS study. Neuropsychopharmacology. 2005;30:1576–83.
78. Gorman JM, Korotzer A, Su G. Efficacy comparison of escitalopram and citalopram in the treatment of major depressive disorder: pooled analysis of placebo-controlled trials. CNS Spectr. 2002;7:40–4.
79. Perez-Caballero L, et al. Fluoxetine: a case history of its discovery and preclinical development. Expert Opin Drug Disco. 2014;9:567–78.
80. Bezchlibnyk-Butler K, Aleksic I, Kennedy SH. Citalopram-a review of pharmacological and clinical effects. J Psychiatry Neurosci. 2000;25:241–54.
81. Bahji A, Vazquez GH, Zarate CA Jr. Comparative efficacy of racemic ketamine and esketamine for depression: A systematic review and meta-analysis. J Affect Disord. 2021;278:542–55.
82. Möhler H. Pathophysiological aspects of diversity in neuronal inhibition: A new benzodiazepine pharmacology. Dialogues Clin Neurosci. 2002;4:261–9.
83. Abbas AI, et al. Somatostatin interneurons facilitate hippocampal-prefrontal synchrony and prefrontal spatial encoding. Neuron. 2018;100:926–939.
84. Duman CH, Duman RS. Spine synapse remodeling in the pathophysiology and treatment of depression. Neurosci Lett. 2015;601:20–29.
85. Prévôt TD, et al. sst(2)-receptor gene deletion exacerbates chronic stress-induced deficits: Consequences for emotional and cognitive ageing. Prog Neuropsychopharmacol Biol Psychiatry. 2018;86:390–400.
86. Gumuslu E, et al. The antidepressant agomelatine improves memory deterioration and upregulates CREB and BDNF gene expression levels in unpredictable chronic mild stress (UCMS)-exposed mice. Drug Target Insights. 2014;8:11–21.
87. Fee C, et al. Chronic stress-induced behaviors correlate with exacerbated acute stress-induced cingulate cortex and ventral hippocampus activation. Neuroscience. 2020;440:113–29.
88. Hörtnagl H, et al. Patterns of mRNA and protein expression for 12 GABAA receptor subunits in the mouse brain. Neuroscience. 2013;236:345–72.
89. Schulz JM, et al. Dendrite-targeting interneurons control synaptic NMDA-receptor activation via nonlinear α5-GABA(A) receptors. Nat Commun. 2018;9:3576.
90. Serwanski DR, et al. Synaptic and nonsynaptic localization of GABAA receptors containing the alpha5 subunit in the rat brain. J Comp Neurol. 2006;499:458–70.
91. Duveau V, et al. Spatiotemporal specificity of GABAA receptor-mediated regulation of adult hippocampal neurogenesis. Eur J Neurosci. 2011;34:362–73.
92. Deprez F, et al. Partial inactivation of GABAA receptors containing the α5 subunit affects the development of adult-born dentate gyrus granule cells. Eur J Neurosci. 2016;44:2258–71.
93. Brady ML, Jacob TC. Synaptic localization of α5 GABA (A) receptors via gephyrin interaction regulates dendritic outgrowth and spine maturation. Dev Neurobiol. 2015;75:1241–51.
94. Moda-Sava RN, et al. Sustained rescue of prefrontal circuit dysfunction by antidepressant-induced spine formation. Science. 2019;364;eaat8078.
95. Nikolova YS, et al. Shifting priorities: highly conserved behavioral and brain network adaptations to chronic stress across species. Transl Psychiatry. 2018;8:26.
96. Zhang X, et al. Stress-Induced Functional Alterations in Amygdala: Implications for Neuropsychiatric Diseases. Front Neurosci. 2018;12:367–367.
97. Luscher B, Shen Q, Sahir N. The GABAergic deficit hypothesis of major depressive disorder. Mol Psychiatry. 2011;16:383–406.
98. Karolewicz B, et al. Reduced level of glutamic acid decarboxylase-67 kDa in the prefrontal cortex in major depression. Int J Neuropsychopharmacol. 2010;13:411–20.
99. Romeo B, et al. Meta-analysis of central and peripheral γ-aminobutyric acid levels in patients with unipolar and bipolar depression. J Psychiatry Neurosci. 2018;43:58–66.
100. Hasler G, et al. Reduced prefrontal glutamate/glutamine and gamma-aminobutyric acid levels in major depression determined using proton magnetic resonance spectroscopy. Arch Gen Psychiatry. 2007;64:193–200.
101. Antoniuk S, et al. Chronic unpredictable mild stress for modeling depression in rodents: Meta-analysis of model reliability. Neurosci Biobehav Rev. 2019;99:101–16.
102. Mineur YS, Belzung C, Crusio WE. Effects of unpredictable chronic mild stress on anxiety and depression-like behavior in mice. Behav Brain Res. 2006; 175:43–50.
103. Aarts E, et al. The light spot test: Measuring anxiety in mice in an automated home-cage environment. Behav Brain Res. 2015;294:123–30.

ACKNOWLEDGEMENTS

Authors thank Mehrab Ali and Netta Ussyshkin for support with administrative tasks throughout the study. They thank CAMH animal facility staff for the caring for our animals over the study duration. Authors further thank the members from Charles River Laboratories and NeuroDigitech for their contribution to data generation. We also thank Milwaukee Institute for Drug Discovery and University of Wisconsin-Milwaukee's Shimadzu Laboratory for Advanced and Applied Analytical Chemistry for help with spectroscopy and National Science Foundation, Division of Chemistry [CHE-1625735].

AUTHOR CONTRIBUTIONS

TP and ES designed the study. MYM, SR, DS and JMC synthesized the compounds tested in this study. TP and PL performed the behavioral piece. AK and MMS performed the pharmacokinetic piece. Electrophysiology was outsourced to Charles River Laboratories. TP, AB and MM analyzed the data. TP and AB wrote the manuscript.

FUNDING

CAMH Internal Fund (Discovery Fund), awarded to TP at the time of study execution, and the Campbell Family Mental Health Research Institute of CAMH. Chemistry synthesis funded by NIH (DA-043204, R01NS076517) to JMC. The Science Fund of the Republic of Serbia funded the pharmacokinetic study through Grant No. 7749108 NanoCellEmoCog. JMC, MMS, ES and TP are listed inventors on patents covering syntheses and use of the compounds. ES is Founder of Damona Pharmaceuticals, a biopharma dedicated to bring novel GABAergic compounds to the clinic. AB, PL, MM, MYM, SR, DS, and AK report no conflict of interest.

COMPETING INTERESTS

The authors declare no competing interests.

ADDITIONAL INFORMATION

Supplementary information The online version contains supplementary material available at https://doi.org/10.1038/s41386-022-01360-y.

Correspondence and requests for materials should be addressed to Etienne Sibille or Thomas D. Prevot.

Reprints and permission information is available at http://www.nature.com/ reprints

Publisher's note Springer Nature remains neutral with regard to jurisdictional claims in published maps and institutional affiliations.

A Platinum Open Access Journal for Organic Chemistry

Paper

Free to Authors and Readers DOAJ Seal

Arkivoc **2021**, part v, 171-188

An efficient debromination technique using PMHS with a number of ligands containing different functional groups

Md Yeunus Mian,[a] Prithu Mondal,[a] Dishary Sharmin,[a] Kamal P. Pandey,[a] Farjana Rashid,[a] Sepideh Rezvanian,[a] Lalit K. Golani,[a] V.V.N. Phani Babu Tiruveedhula,[a] Vilashini Rajaratnam[1], Shama P. Mirza[1], John D. Chan[2], Jeffrey M. Witkin[1], and James M. Cook*[1]

[1]Department of Chemistry and Biochemistry, Milwaukee Institute of Drug Discovery, University of Wisconsin-Milwaukee, Milwaukee, WI-53211

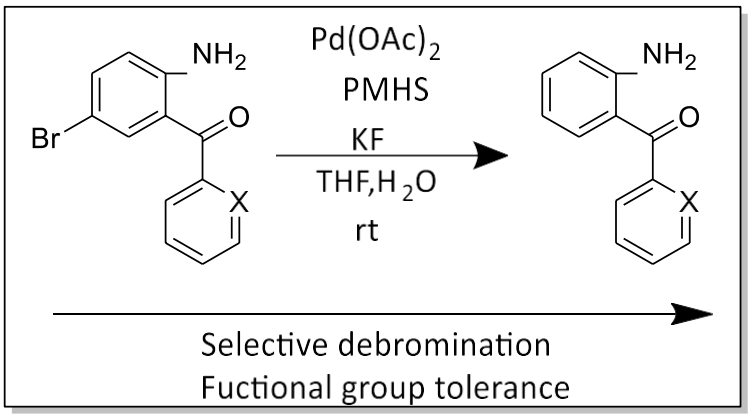
[2]Department of Chemistry, University of Wisconsin-Oshkosh, Oshkosh, WI-54901 E-mail: capncook@uwm.edu

This paper is dedicated to Professor Peter Alan Jacobi for his many important contributions to Organic Chemistry

Received 12-22-2021 **Accepted Manuscript** 03-21-2022 **Published on line** 04-07-2022

Abstract

Herein is described the strategy to debrominate different aryl bromides selectively, using polymethylhydrosiloxane (PMHS) which tolerates a variety of functional groups. Key elements of this approach include the use of catalytic $Pd(OAc)_2$ and the correct equivalents of polymethylhydrosiloxane (PMHS), in conjunction with aqueous KF. The present reaction process provides a strategic tool for the synthesis of a number of medicinally important molecules.



Keywords: debromination, polymethylhydrosiloxane, benzodiazepines, palladium acetate

DOI: https://doi.org/10.24820/ark.5550190.p011.712 **Page 171** ©**AUTHOR(S)**

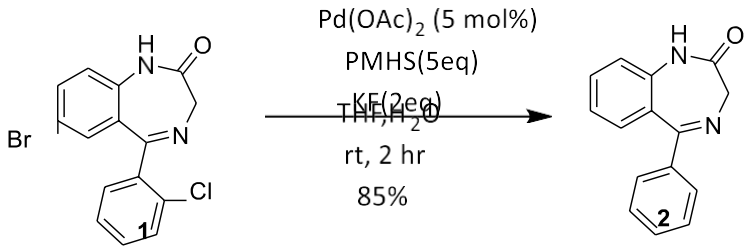
Introduction

Bromine-substituted aryl halides are important targets for further functionalization catalyzed by palladium catalysts or other chemical strategies.[1]Often times a cheap starting aryl bromide can be the lynch pin in the synthesis of new heterocyclic compounds. Replacement of bromine by hydrogen can be carried out using Polymethylhydrosiloxane (PMHS) reported earlier by Ronald *et al*.[2] It is a mild reducing agent, cost-effective, non-toxic and an easily handled chemical. It can be stored for long periods of time since it is more air and moisture stable than any other silanes.[3] PMHS is relatively inert but can transfer the hydride to participate in different metal catalyzed reductions.[4]Hydrosilanes are mild reducing agents with a variety of applications.[25,26]In addition, some hydrosilanes are compatible with some oxidizing agents and act as selective reducing agents in a one-pot redox cocktail.[27]

PMHS hydrodehalogenates aryl halides when using a palladium catalyst.[2] A method to debrominate aryl bromides in the presence of a number of functional groups such as ketones, amides, imines, and esters was developed. We debrominated bromo-benzodiazepines using this method and then nitrated the resulting product to synthesize pharmaceutically active potential drug candidates.[15]

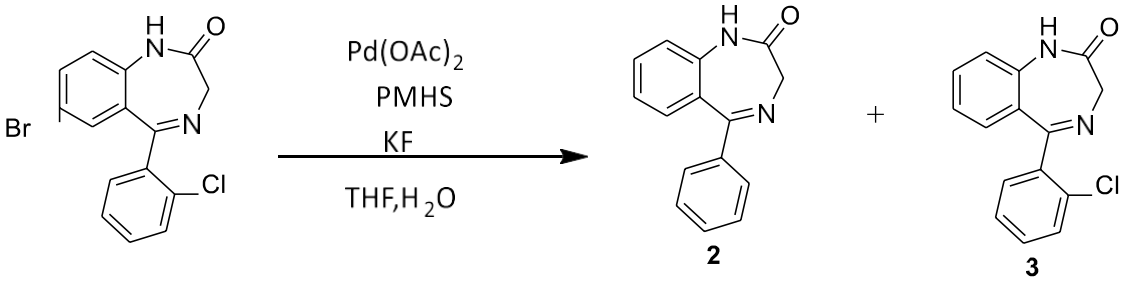
Results and Discussion

Recently, phosphine free palladium catalysts have enjoyed considerable success in different reductive dehalogenations.[6-13] We required a suitable system to debrominate different benzodiazepine compounds. The investigation initially revealed $Pd(OAc)_2$ with PMHS in the presence of potassium fluoride reduced chlorobenzene to benzene,[2] and this transformation took place at room temperature. We followed the conditions to debrominate a benzodiazepine which bears a bromo and a chloro functionality. The benzodiazepine **1** was synthesized according to the literature procedure.[14] As expected both halogens were reduced by PMHS (Scheme 1).



Scheme 1. Dehalogenation of benzodiazepine.

Based on this result, we started to explore this system to find a better method to selectively debrominate the aryl halide without affecting other functional groups. Initially we investigated conditions to determine the correct equivalents of PMHS and reaction time for selective debromination. We used the substrate **1** for our initial investigation (Scheme 2). Different equivalents of PMHS and different mole% of Pd catalyst were used to identify the best conditions. It was found that bromide **1** could be debrominated chemoselectively by reducing the amount of PMHS in the presence of 5 mole% $Pd(OAc)_2$; although the reaction time was longer, as expected, and the reaction also gave the byproduct **2** in minor amounts. (Table 1, entry 10**;** 5:95).



1 **2** **3**

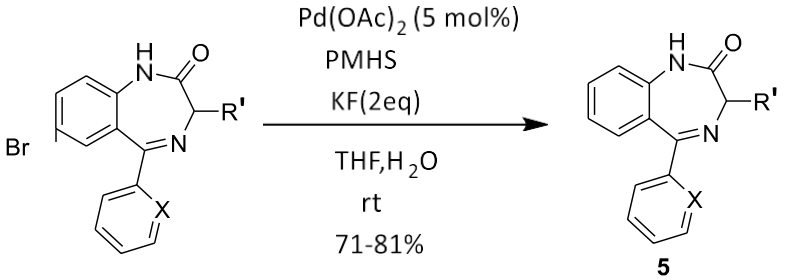
Scheme 2

Table 1. Effect of different equivalents of PMHS on selective debromination

Entry	Substrate	$Pd(OAc)_2$	PMHS(eq)	KF (eq)	Time	Temperature	*Ratio of Product (**2**:**3**)	[a]Yield
1	**1**	5 mol%	4	2	1 hr	r.t.	90:10	75%
2	**1**	1 mol%	4	2	2 hr	r.t.	83:17	79%
3	**1**	2 mol%	4	2	2 hr	r.t.	80:20	69%
4	**1**	3 mol%	4	2	1.5 hr	r.t.	71:29	73%
5	**1**	4 mol%	4	2	1.3 hr	r.t.	65:35	75%
6	**1**	5 mol%	3	2	2.2 hr	r.t	60:40	71%
7	**1**	5 mol%	2.5	2	2.5 hr	r.t	60:40	71%
8	**1**	5 mol%	1.05	2	3 hr	r.t	51:49[b]	65%[C]
9	**1**	5 mol%	1.05	2	4.0 hr	r.t	22:78 [b]	84%[C]
10	**1**	5 mol%	1.05	2	6.0 hr	r.t.	5:95	79%

*From HPLC (Pinnacle -C18 (2.1 mm × 50 mm, 1.8 µm particle size) column, flow rate of 0.5 mL/min, mobile phase-acetonitrile and water (containing 0.1% formic acid)) ;[a]Isolated combined yield of (**2** and **3**); [b] Ratio of **1** and **3**; [C] Combined yield of (**1** and **3**)

The debromination reaction was also investigated with different benzodiazepines, as shown in Table 2. Benzodiazepine derivatives (**4a-h**) were subjected to debromination under the same conditions (Scheme 3**,** Table 2) to furnish the products **5a-h** (71%-81%), respectively. We also increased the amount of PMHS to debrominate the substrate **4e** to produce **5e** (Table 2, entry 5). The debromination occurred smoothly in less reaction time without affecting the amide and imine functionality of the benzodiazepine substrates. A similar trend was also observed in the case of substrate **4h**. Here an interesting observation was found. Although the acetate is a labile protecting group to reduction, it survived the debromination reaction process by PMHS. The hydride source did not interfere with the acetate moiety.



4

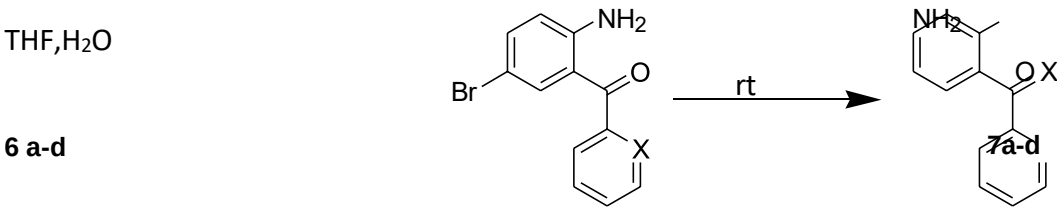
Scheme 3

Table 2. Debromination strategy on different benzodiazepines

Entry	Substrate	X	R'	PMHS (eq)	Time	Product	[a]Yield (%)
1	**4a**	C-H	H	1.05	3.5 hr	**5a**	71%
2	**4b**	C-H	CH_3(R)	1.05	4 hr	**5b**	73%
3	**4c**	C-H	CH_3(S)	1.05	3.5 hr	**5c**	79%
4	**4d**	C-F	CH_3(R)	1.05	4 hr	**5d**	78%
5	**4e**	C-F	CH_3(S)	3.0	2.0 hr	**5e**	79%
6	**4f**	C-Cl	CH_3(S)	1.05	4.5 hr	**5f**	75%
7	**4g**	N	CH_3(S)	1.05	2 hr	**5g**	81%
8	**4h**	C-F	$OCOCH_3$	4	45 min	**5h**	73%

[a]Isolated yield

We, then identified conditions in different benzophenone substrates, as shown in Table 3 (Scheme 4). The treatment of other benzophenone substrates afforded debrominated product **7a-d** in good to high yields (Table 3). We also observed that increasing the amounts of PMHS decreased the reaction time in some benzophenone substrates (**6a-b**), as expected. PMHS did not affect the ketone functionality in any benzophenone substrate (Table 3, entry 1-8), as we hypothesized. Selective debromination over chlorination was also observed in this case (Table 3, entry 3), which is also as expected and, gratifyingly, took place.



6 a-d

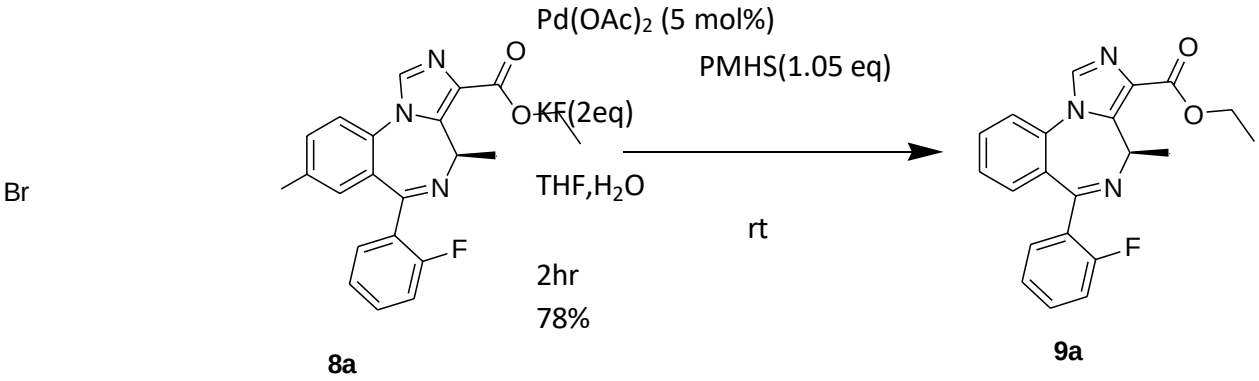
Scheme 4

Table 3. Selective debromination of benzophenone substrate

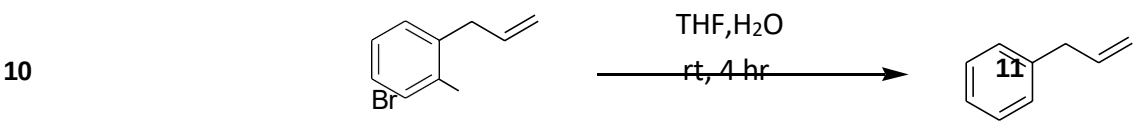
Entry	Substrate	X	$Pd(OAc)_2$	PMHS(eq)	KF (eq)	Time	Product	[a]Yield
1	**6a**	C-H	5 mol%	1.05	2	3.5 hr	**7a**	78%
2	**6b**	C-F	5 mol%	1.05	2	3.0 hr	**7b**	73%
3	**6c**	C-Cl	5 mol%	1.05	2	3.0 hr	**7c**	71%
4	**6d**	N	5 mol%	1.05	2	2.5 hr	**7d**	69%
5	**6a**	C-H	5 mol%	2	2	2.0 hr	**7a**	69%
6	**6a**	C-H	5 mol%	3	2	1.0 hr	**7a**	75%
7	**6a**	C-H	5 mol%	4	2	30 min	**7a**	70%
8	**6b**	C-F	5 mol%	4	2	45 min	**7b**	73%

[a]Isolated yield

Furthermore, we attempted the debromination on an imidazodiazepine substrate possessing an ester function (Scheme 5). The imidazodiazepine **8a** gave the debrominated product **9a** in good yield. The imidazodazepine ester was well tolerated under these reaction conditions confirming the mildness of the PMHS process. Also, upon investigation on a double bond containing aryl substrate, PHMS debrominated the bromine group selectively without interfering with the double bond (Scheme 6, preliminary data, SI)



Scheme 5. Effect of the debromination reaction on imidazodiazepine substrate **8a.**

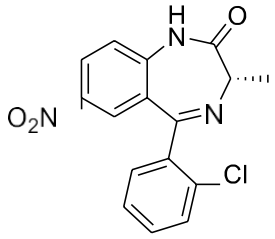


Scheme 6. Selective debromination by PMHS on a double bond containing substrate.

Anti-schistosomal activity of 8-*H* benzodiazepines

Schistosomiasis, a neglected tropical disease is one of the most dominant infectious diseases worldwide that has serious public health consequences [16-19]and is characterized by chronic helminthic infection with residual morbidity. Over 240 million people are infected, with 800 million at risk of infection and more than 90% of infections occurring in sub-Saharan Africa where the death rate is approximately 280,000 persons per year.[15] Schistosomiasis is caused by parasitic blood flukes (trematode worms) of the genus *Schistosoma*, of which *Schistosoma mansoni*, *Schistosoma japonicum and Schistosoma haematobium* cause infections in humans.[20]

The treatment of schistosomiasis relies only on one broad spectrum drug, praziquantel which is associated with several drawbacks including PZQ's lack of efficacy against immature parasites. Meclonazepam, a benzodiazepine was found to be effective in treatment of schistosomiasis[15]and was able to cure both mature and immature infections. But the curative dose of meclonazepam causes dose-limiting sedation in human trials and the development of this lead was dropped.[21-24]



meclonazepam

Figure 1. Structure of meclonazepam.

The chemical name of meclonazepam is (S)-5-(2-chlorophenyl)-3-methyl-7-nitro-1,3-dihydro-2*H*-benzo[*e*][1,4]diazepin-2-one and the structure bears a nitro group in one of the benzene rings (Figure 1). We synthesized different benzodiazepines (most of them in this manuscript) which contained 8-H instead of 8-nitro groups and assessed the synthesized compounds in schistosome mobility assays. This assay was done in order to identify the importance of the nitro group in the structure of the benzodiazepines in regard to activity. The results are summarized in Table 4.

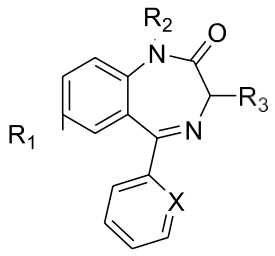
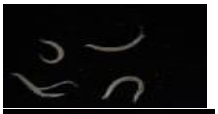
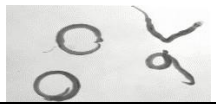


Figure 2. General structure of meclonazepam derivatives.

Table 4. Anti-schistosomal effect of C-7 H benzodiazepines

SL	R_1	R_2	R_3	X	Code	Activity	
1	NO_2	H	S-CH_3	C-Cl	MCLZ		Coiled ,dead IC_{50} 160nm
2	H	H	S-CH_3	C-Cl	MYM-V-03		alive, 30µM
3	H	H	S-CH_3	C-F	MYM-I-84		alive, 30µM
4	H	H	R-CH_3	C-F	MYM-I-94		alive, 30µM
5	H	H	S-CH_3	C-H	MYM-I-85		alive, 30µM
6	H	H	R-CH_3	C-H	MYM-I-86		alive, 30µM
7	H	H	S-CH_2CH_3	C-Cl	MYM-V-18		alive, 30µM
8	CN	H	S-CH_3	C-Cl	MYM-IV-12		alive, 30µM

The IC_{50} value of meclonazepam is 160 nM and it causes contractile paralysis of the parasites. The parasites were coiled, dead upon the exposure to the meclonazepam (Table 4). But changing the nitro group to hydrogen resulted in total loss of activity (entry 2, Table 4). Changing the nitro group to a hydrogen atom along with other modifications demonstrated no activity at all (entry 3-7, Table 4). Consequently, a hydrogen atom at the 8- position in place of a nitro group is not suitable for anti-schistosomal activity. In order to identify whether the electronic effects of the nitro group or the structure of nitro group itself was responsible for schistocidal activity, we replaced the nitro group with a cyano group and assessed the compound's activity in the schistosome mobility assay. This resulted in total loss of activity. This would argue, although not prove, against a pi stacking interaction with the ring-A aromatic ring in meclonazepam. Modification of different positions without changing the nitro group show various degrees of anti-schistosomal activity and some of these results are described in McCusker P. *et al*. 2019.[15] The nitro group in the structure of meclonazepam is crucial for the damage to the parasite.

Conclusions

It was demonstrated that ketones, amides, esters and imines were all well tolerated under the reduction conditions of PMHS employed here with catalytic $Pd(OAc)_2$ in THF. This is an efficient system for the

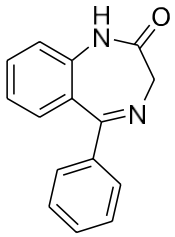
debromination of benzodiazepines, benzophenones and imidazodiazepines at room temperature. The debromination can be done with a small amount of Pd catalyst but 5 mol % still represents a general catalyst loading. It was also shown that debromination occurred selectively in the presence of a chloro functional group, which is key for the synthesis of some novel potential drug candidates.[15]

Experimental Section

General. All reactions were performed in round-bottom flasks with magnetic stir bars under an argon atmosphere. Organic solvents were purified when necessary by standard methods or purchased from Sigma- Aldrich Chemicals. The reagents and other chemicals were purchased from either Sigma-Aldrich, Oakwood Chemical, Alfa Aesar, Matrix Scientific, Admiral Chemical Company, or Acros Organic. The progress of reactions was visualized with TLC plates from Dynamic Adsorbents, Inc. under a UV light. The flash column chromatography was done for purification of some analogs on silica gel (230-400 mesh, Dynamic Adsorbents). An Agilent HPLC was used to determine the ratio of some debrominated products. The ^{1}H NMR and ^{13}C NMR spectra were obtained on Bruker Spectrospin 500 MHz instrument in $CDCl_3$ and chemical shifts were reported in δ (ppm). Multiplicities are represented as follows: singlet (s), broad signal (br), doublet (d), triplet (t), quartet (q), dd (doublet of doublets), and multiplet (m). The technique employed for HRMS was carried out on a LCMS- IT-TOF at the Milwaukee Institute for Drug Discovery in the Shimadzu Laboratory for Advanced and Applied Analytical Chemistry.

General procedure for the debromination: A three neck round bottom flask was charged with the aromatic halide. Then THF was added and the flask was purged with argon. Palladium acetate was then added under an argon atmosphere, followed by the addition of aq potassium fluoride solution. Then PMHS was added dropwise to the reaction mixture, which resulted in a deep greenish solution. The reaction mixture was then stirred for the required time by monitoring by TLC (see Tables for data). The consumption of starting material was confirmed on a LCMS 2020. The round bottom flask was open to the air at the end of the reaction. 2 Grams of alumina was added to the reaction flask and this was allowed to stir for 5 min. The reaction mixture was filtered through a pad of celite to removethe Pd salts; water and ethyl acetate was added to the filtrate. The layers were separated and the aq layer was extracted with ethyl acetate and the combined organic layer was washed with aq 10% NaCl solution (2x), dried over sodium sulfate, concentrated under reduced pressure and purified via silica gel column chromatography. The gradient elution was effected by ethyl acetate and hexane. The purified compounds were characterized by NMR spectroscopy, LCMS and HRMS (individually).

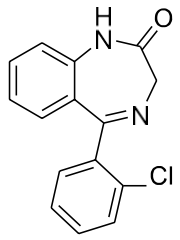
5-Phenyl-1,3-dihydro-2*H*-benzo[*e*][1,4]diazepin-2-one (2)



2

The $Pd(OAc)_2$ (0.04 g, 0.12 mmol) was added to a stirred solution of 7-bromo-5-phenyl-1,3-dihydro-2H-benzo[e][1,4]diazepin-2-one (**4**) (0.8 g, 2.53 mmol) in THF (10 mL) under argon. This was followed by addition of aq potassium fluoride (0.293 g, 5 mmol in 2 mL water) solution and PMHS (0.16 mL, 2.65 mmol). The flask was opened to air after the required reaction time (table 2), stirred with alumina and then filtered through celite. The aq layer was extracted with ethyl acetate (2x10mL) and the combined organic layer was washed with aq 10% sodium chloride solution (2x10mL), dried over Na_2SO_4 and, concentrated under reduced pressure. The residue was purified by silica gel column chromatography using EtOAc: hexane (35:65). The appropriate fractions were pooled, the solvents were removed under reduced pressure and the residue was dried under vacuum to obtain a white powder **5** (0.49 g, 81% yield). ^{1}H NMR (500 MHz, CDCl3) δ 9.66 (s, 1H), 7.56 (d, J 7.8 Hz, 2H), 7.52 (dd, J 11.3, 4.1 Hz, 1H), 7.48 – 7.44 (m, 1H), 7.39 (dd, J 11.0, 3.9 Hz, 2H), 7.34 (d, J 7.9 Hz, 1H), 7.22
(dd, J 7.9, 4.2 Hz, 1H), 7.19 – 7.14 (m, 1H), 4.36 (s, 2H). ^{13}C NMR (126 MHz, CDCl3) δ 172.33 (s), 171.13 (s), 139.47 (s), 138.82 (s), 131.71 (s), 131.36 (s), 130.30 (s), 129.70 (s), 128.18 (s), 127.26 (s), 123.33 (s), 121.21 (s), 56.71 (s). HRMS (ESI/ITTOF) *m/z*: $[M + H]^+$Calcd for $C_{15}H_{12}N_2O$ 237.1022; found 237.1007.

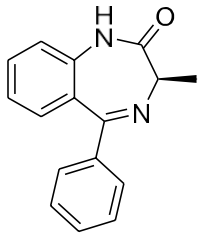
5-(2-Chlorophenyl)-1,3-dihydro-2*H*-benzo[*e*][1,4]diazepin-2-one (3)



3

7-Bromo-5-(2-chlorophenyl)-1,3-dihydro-2H-benzo[e][1,4]diazepin-2-one (**1**) (0.8 g, 2.28 mmol) was dissolved in THF (10 mL) under argon and then $Pd(OAc)_2$ (0.051 g, 0.114 mmol), and an aq potassium fluoride (0.264 g, 4.56 mmol in 2 mL water) solution was added under a positive flow of argon and this was followed by dropwise addition of PMHS (0.14 mL, 2.39 mmol). The reaction mixture, which resulted, was stirred the appropriate time (see Table 2) at rt and the flask was opened to the air to form more black palladium oxide and stirred with alumina, and then filtered through celite. The aq layer was extracted with ethyl acetate (3x10 mL); and the combined organic layer was washed with aq 10% sodium chloride solution (2x10 mL). It was then dried (Na_2SO_4) and concentrated under reduced pressure. The residue was purified by silica gelchromatography using EtOAc: hexane (40:60). The desired fractions were collected, evaporated and dried under vacuum to obtain a white powder **3** (0.51 g, 75% yield). ^{1}H NMR (500 MHz, CDCl3) δ 9.39 (s, 1H), 7.55 (ddd, J 7.6, 4.7, 2.3 Hz, 1H), 7.49
(ddd, J 8.7, 6.1, 2.8 Hz, 1H), 7.41 – 7.37 (m, 3H), 7.19 (d, J 8.3 Hz, 1H), 7.11 (ddd, 2H), 4.42 (s, 2H).^{13}C NMR (126 MHz, CDCl3) δ 171.57 (s), 170.57 (s), 139.10 (s), 137.96 (s), 133.27 (s), 131.85 (s), 131.03 (s), 130.63 (s), 130.03 (s), 129.90 (s), 127.91 (s), 126.84 (s), 123.85 (s), 121.04 (s), 56.59 (s). HRMS (ESI/ITTOF) *m/z*: $[M + H]^+$Calcd for $C_{15}H_{11}N_2OCl$ 271.0633; found 271.0608.

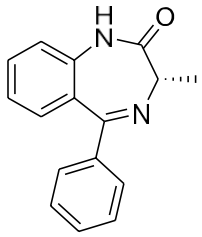
(*R*)-7-Bromo-3-methyl-5-phenyl-1,3-dihydro-2*H*-benzo[*e*][1,4]diazepin-2-one (5b)



5b

The (*R*)-7-bromo-3-methyl-5-phenyl-1,3-dihydro-2*H*-benzo[*e*][1,4]diazepin-2-one **4b** (1g, 3.03 mmol), tetrahydrofuran (10 mL) and $Pd(OAc)_2$ (0.04 g, 0.15 mmol) were charged to a round bottom flask under argon. Then aq potassium fluoride (0.351g, 6 mmol in 2 mL water) solution and PMHS (0.16 mL, 2.65 mmol) were added to the mixture and it was stirred for the time mentioned in Table 2. The flask was then opened to the air, stirred with alumina, and filtered through celite. The aq layer was extracted with ethyl acetate (3x10 mL) and the combined organic layer was washed with aq 10% sodium chloride solution (2x10mL), dried over Na_2SO_4 and concentrated under reduced pressure. The residue, which resulted, was purified with silica gel chromatography using EtOAc: hexane (35:65). The appropriate fractions were pooled, and the solvents were removed under reduced pressure. The residue was then dried under vacuum to obtain a white powder **5b** (0.55g, 73%). ^{1}H NMR (500 MHz, CDCl3) δ 9.40 (s, 1H), 7.55 – 7.50 (m, 3H), 7.43 (ddd, 1H), 7.39 – 7.32 (m, 3H), 7.22 (d, J 8.2 Hz, 1H), 7.15 (t, J 7.6 Hz, 1H), 3.79 (q, J 6.5 Hz, 1H), 1.79 (d, J 6.5 Hz, 3H). ^{13}C NMR (126 MHz, CDCl3) δ 173.04 (s), 169.09 (s), 139.35 (s), 138.50 (s), 131.58 (s), 131.06 (s), 130.13 (s), 129.80 (s, 2C), 128.15 (s, 2C), 127.73 (s), 123.19 (s), 121.15 (s), 58.69 (s), 17.09 (s). HRMS (ESI/ITTOF) *m/z*: $[M + H]^+$Calcd for $C_{16}H_{14}N_2O$ 251.1179; found 251.1155.

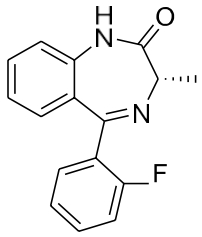
(*S*)-3-Methyl-5-phenyl-1,3-dihydro-2*H*-benzo[*e*][1,4]diazepin-2-one(5c)



5c

The desbromochiral compound **5c** (0.58g, 78%) was synthesized according to the procedure employed for **5b** maintaining the same scale. The yield was 78%.^{1}H NMR (500 MHz, $CDCl_3$) δ 9.74 (s, 1H), 7.53 (ddd, 2H), 7.50 (d, J 7.4 Hz, 1H), 7.42 (t, J 6.9 Hz, 1H), 7.38 – 7.31 (m, 3H), 7.24 (ddd, 1H), 7.14 (t, J 7.5 Hz, 1H), 3.79 (q, J 6.4 Hz, 1H), 1.80 (d, J 6.4 Hz, 3H). ^{13}C NMR (126 MHz, $CDCl_3$) δ 173.16 (s), 169.13 (s), 139.36 (s), 138.58 (s), 131.57 (s), 131.03 (s), 130.12 (s), 129.82 (s), 128.14 (s), 127.70 (s), 123.15 (s), 121.24 (s), 58.71 (s), 17.10 (s). HRMS (ESI/ITTOF) *m/z*: $[M + H]^+$Calcd for $C_{16}H_{14}N_2O$ 251.1179; found 251.1155.

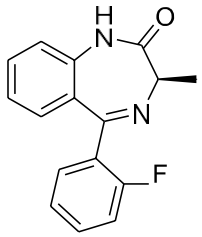
(*S*)-5-(2-Fluorophenyl)-3-methyl-1,3-dihydro-2*H*-benzo[*e*][1,4]diazepin-2-one (5e)



5e

The $Pd(OAc)_2$ (0.064 g, 0.144 mmol) was added to a stirred solution of (*S*)-7-bromo-5-(2-fluorophenyl)-3-methyl-1,3-dihydro-2*H*-benzo[*e*][1,4]diazepin-2-one **4e** (1 g, 2.88 mmol) in THF (10 mL) under argon. This was followed by addition of aq potassium fluoride (0.334 g, 5.76 mmol in 2 mL water) solution and PMHS (0.51 mL, 8.64 mmol). At the end of the reaction (TLC), the flask was opened to the air, stirred with alumina, and filtered through a pad of celite. The mixture was diluted with water and the aq layer was extracted with ethyl acetate (2x10 mL). The combined organic layer was washed with aq 10% sodium chloride solution (2x10 mL), dried ($Na_2SO_{4)}$ and concentrated under reduced pressure. The residue was purified with silica gel chromatography using EtOAc: hexane (35:65). The appropriate fractions were pooled, and the solvents were removed under reduced pressure. The solid, which remained, was dried under vacuum to obtain a white powder **5e** (0.61 g, 79% yield).^{1}H NMR (500 MHz, CDCl3) δ 8.91 (s, 1H), 7.65 – 7.56 (m, 1H), 7.51 (t, J 7.7 Hz, 1H), 7.44 (ddd, 1H),
7.25 (dd, J 12.3, 7.7 Hz, 2H), 7.20 – 7.16 (m, 1H), 7.14 (t, J 7.6 Hz, 1H), 7.05 (dd, J 9.6, 8.9 Hz, 1H), 3.81 (q, J 6.5 Hz, 1H), 1.79 (d, J 6.5 Hz, 3H). ^{13}C NMR (126 MHz, CDCl3) δ 172.26 (s), 165.77 (s), 160.49 (d, J 251.5 Hz), 137.27 (s), 131.78 (s), 131.73 (s), 131.59 (d, J 2.0 Hz), 129.77 (s), 128.59 (s), 127.85 (d, J 12.5 Hz), 124.28 (d, J 3.4 Hz), 123.73 (s), 121.03 (d, J 1.4 Hz), 116.08 (d, J 21.7 Hz), 58.72 (s), 17.01 (s). HRMS (ESI/ITTOF) *m/z*: $[M + H]^+$Calcd for $C_{16}H_{13}N_2OF$ 269.1085; found 269.1062.

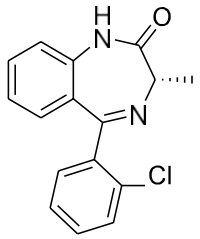
(*R*)-5-(2-Fluorophenyl)-3-methyl-1,3-dihydro-2*H*-benzo[*e*][1,4]diazepin-2-one(5d)



5d

The fluoro analog **5d** (0.6 g, 78%) was synthesized, according to the procedure employed for the synthesis of **5e** maintaining the identical scale. This process took a longer reaction time since less PMHS was employed. ^{1}H NMR (500 MHz, CDCl3) δ 9.15 (s, 1H), 7.60 (td, J 7.5, 1.3 Hz, 1H), 7.50 (ddd, 1H), 7.43 (ddt, 1H), 7.25 (t, J 7.3 Hz, 2H), 7.22 – 7.17 (m, 1H), 7.13 (t, J 7.6 Hz, 1H), 7.08 – 7.01 (m, 1H), 3.82 (q, J 6.5 Hz, 1H), 1.80 (d, J 6.5 Hz, 3H). ^{13}C NMR (126 MHz, CDCl3) δ 172.34 (s), 165.77 (s), 160.48 (d, J 251.6 Hz), 137.32 (s), 131.72 (s), 131.68 (s), 131.60 (d, J 2.4 Hz), 129.78 (s), 128.55 (s), 127.86 (d, J 12.5 Hz), 124.24 (d, J 3.6 Hz), 123.68 (s), 121.05 (s), 116.08 (d, J 21.6 Hz), 58.73 (s), 17.03 (s). HRMS (ESI/ITTOF) *m/z*: [M + H]+ Calcd for C16H13N2OF 269.1085; found 269.1062.

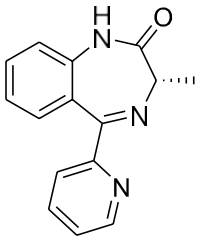
(*S*)-5-(2-Chlorophenyl)-3-methyl-1,3-dihydro-2*H*-benzo[*e*][1,4]diazepin-2-one (5f)



5f

(*S)*-7-Bromo-5-(2-chlorophenyl)-3-methyl-1,3-dihydro-2*H*-benzo[*e*][1,4]diazepin-2-one **4f** (0.9g, 2.47 mmol), THF (10 mL)was charged to a round bottom flask,after which,$Pd(OAc)_2$ (0.027 g, 0.123 mmol) was added to the stirred solution under a positive flow of argon. Then aq potassium fluoride (0.287g, 4.94 mmol in 2 mL water) solution and PMHS (0.16 mL, 2.65 mmol) were added, after which, the mixture was stirred for the time depicted in Table 2. The flask was then opened to the air upon the consumption of starting material. It was then stirred with alumina and filtered through a pad of celite. The organic layer was diluted with water and the aq layer was extracted with ethyl acetate (3x10 mL). The combined organic layer was washed with aq 10% sodium chloride solution (2x10 mL), dried (Na_2SO_4)and then concentrated under reduced pressure. The residue was purified by silica gel chromatography using EtOAc: hexane (40:60). The desired fractions were collectedand the solvent was evaporated under reduced pressure. The solid was dried under vacuum to obtain a light yellow powder **5f** (0.52g, 75%).^{1}H NMR (500 MHz, CDCl3) δ 8.98 (s, 1H), 7.53 (s, 1H), 7.50 (td, 1H), 7.37 (d, J 3.0 Hz, 3H), 7.17 (t, J 7.6 Hz, 1H), 7.12 (dd, 2H), 3.86 (q, J 6.5 Hz, 1H), 1.79 (d, J 6.5 Hz, 3H). ^{13}C NMR (126 MHz, CDCl3) δ 168.52 (s), 138.99 (s), 137.64 (s), 133.37 (s), 131.77 (s), 131.13 (s), 130.54 (s), 130.02 (s), 129.68 (s), 128.32 (s), 128.19 (s), 126.86 (s), 123.76 (s), 120.90 (s), 58.63 (s), 16.96 (s). HRMS (ESI/ITTOF) *m/z*: [M + H]+ Calcd for C16H13N2OCl 285.0789; found 285.0767.

(*S*)-3-Methyl-5-(pyridin-2-yl)-1,3-dihydro-2*H*-benzo[*e*][1,4]diazepin-2-one(5g)

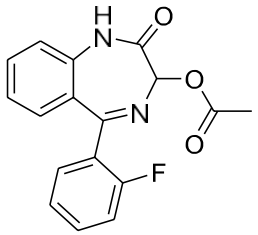


5g

To a stirred solution of (*S*)-7-bromo-5-(2-chlorophenyl)-3-methyl-1,3-dihydro-2*H*-benzo[*e*][1,4]diazepin-2-one **4g** (1 g, 3 mmol) in THF (10 mL), $Pd(OAc)_2$ (0.033 g, 0.15 mmol) was added under a positive flow of argon.This was followed by addition of aq potassium fluoride (0.348 g, 6 mmol in 3 mL water) solution and PMHS (0.19 mL, 3.15 mmol) and the reaction mixture was stirred for the appropriate time (Table 2). The flask was opened to the air and upon the consumption of starting material, it was stirred with alumina, and filtered through a pad of celite. The organic layer was diluted with water and the aq layer was extracted with ethyl acetate (3x10mL). The combined organic layer was washed with aq 10% sodium chloride solution (2x10 mL), dried (Na_2SO_4) and concentrated under reduced pressure. The residue was purified by silica gel chromatography using EtOAc: hexane (40:60). The expected fractions were pooled, the solvent was evaporated under reduced pressure,and

dried under vacuum to obtain a white powder **5g** (0.62g, 82%). ^{1}H NMR (500 MHz, $CDCl_3$) δ 8.64 (dt, 1H), 8.24 (s, 1H), 8.03 (d, J 7.9 Hz, 1H), 7.82 (td, J 7.7, 1.8 Hz, 1H), 7.51 (t, J 7.8 Hz, 1H), 7.41 – 7.36 (m, 2H), 7.20 (t, J 7.6 Hz, 1H), 7.10 (dd, J 8.2, 0.8 Hz, 1H), 3.86 (q, J 6.5 Hz, 1H), 1.79 (d, J 6.5 Hz, 3H). ^{13}C NMR (126 MHz, $CDCl_3$) δ 172.09 (s), 167.82 (s), 156.78 (s), 148.88 (s), 138.18 (s), 136.72 (s), 131.72 (s), 131.43 (s), 126.88 (s), 124.40 (s), 124.22 (s), 123.29 (s), 121.00 (s), 58.93 (s), 17.00 (s). HRMS (ESI/ITTOF) *m/z*: [M + H]+ Calcd for $C_{16}H_{13}N_3O$ 252.1131; found 252.1113.

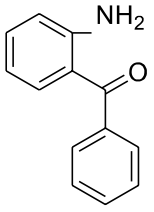
5-(2-Fluorophenyl)-2-oxo-2,3-dihydro-1*H*-benzo[*e*][1,4]diazepin-3-yl acetate(5h)



5h

A round bottom flask was charged with 7-bromo-5-(2-fluorophenyl)-2-oxo-2,3-dihydro-1*H*- benzo[*e*][1,4]diazepin-3-yl acetate **4h** (1g, 2.5 mmol), THF (10 mL), and the $Pd(OAc)_2$ (0.028 g, 0.125 mmol) was added to the stirred solution under a positive flow of argon. Then aq potassium fluoride (0.291g, 5 mmol in 2mL water) solution and PMHS (0.16 mL, 2.65 mmol) were added.The mixture, which resulted, was stirred for the time mentioned in Table 2. The flask was opened to the air upon the consumption of starting material, and stirred with alumina. It was then filtered through a pad of celite. The organic layer was diluted with water and the aq layer was extracted with ethyl acetate (3x10 mL). The combined organic layers were washed with an aq 10% sodium chloride solution (2x10 mL), dried (Na_2SO_4),and concentrated under reduced pressure. The residue was purified by silica gel chromatography using EtOAc: hexane (40:60). The expected fractions were collected, evaporated, and dried under vacuum to obtain a light yellow powder **5h** (0.58g, 73%). ^{1}H NMR (500 MHz, CDCl3) δ 8.92 (s, 1H), 7.68 (td, J 7.5, 1.4 Hz, 1H), 7.56 (t, J 7.7 Hz, 1H), 7.51 – 7.46 (m, 1H), 7.29 (t, J 5.2 Hz, 2H), 7.25 –
7.17 (m, 2H), 7.08 (t, 1H), 6.04 (s, 1H), 2.36 (s, 3H). ^{13}C NMR (126 MHz, CDCl3) δ 170.40 (s), 164.11 (s), 160.56 (d, J 252.6 Hz), 136.35 (s), 132.60 (s), 132.51 (s), 132.44 (s), 131.84 (d, J 1.6 Hz), 129.82 (s), 128.29 (s), 126.74 (d, J 12.0 Hz), 124.47 (s), 124.37 (d, J 3.6 Hz), 121.72 (s), 116.17 (d, J 21.5 Hz), 84.54 (s), 21.20 (s).). HRMS (ESI/ITTOF) *m/z*: [M + H]+ Calcd for $C_{17}H_{13}N_2O_3F$ 313.0983; found 313.0964.

(2-Aminophenyl)(phenyl)methanone (7a)

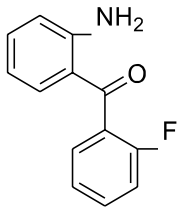


7a

To a solution of (2-amino-5-bromophenyl)(phenyl)methanone **6a**, (1g, 3.62 mmol) in THF (10 mL), $Pd(OAc)_2$ (0.04 g, 0.18 mmol) and aq potassium fluoride(0.42g, 7.25 mmol in 3mL water) solution were added under a positive flow of argon. Then PMHS (0.8 mL, 14.4 mmol) was added dropwise and the mixture was then stirred for the required time (see Table 3). At the end of the reaction the flask was open to the air; then the reaction

mixture was stirred with alumina and filtered through celite. The aq layer was extracted with ethyl acetate (2x 10 mL); and the combined organic layer was washed with an aq 10 % NaCl solution (3x10 mL). The organic layer was dried (Na_2SO_4) and concentrated under reduced pressure. The gummy greenish mass, which resulted, was then purified on silica gel (25g) chromatography using EtOAc: hexane (10:90). The appropriate fractions were collected, and the solvents were removed under reduced pressure.Then the residue was dried under vacuum at 35-40^oC for 2-3 hours to provide a white powder **7a** (0.63g, 88% yield). ^1H NMR (500 MHz, CDCl3) 1H NMR (500 MHz, CDCl3) δ 7.67 (d, J 7.3 Hz, 2H), 7.55 (t, J 7.3 Hz, 1H), 7.48 (t, J 6.7 Hz, 3H), 7.32 (t, J 7.5 Hz, 1H), 6.77 (d, J 8.2 Hz, 1H), 6.63 (t, J 7.5 Hz, 1H), 6.10 (s, 2H). ^{13}C NMR (126 MHz, CDCl3) δ 199.09 (s), 150.86 (s), 140.11 (s), 134.59 (s), 134.24 (s), 131.06 (s), 129.13 (s), 128.09 (s), 118.22 (s), 117.05 (s), 115.57 (s). HRMS (ESI/ITTOF) *m/z*: $[M + H]^+$Calcd for $C_{13}H_{11}NO$ 198.0913; found 198.0903.

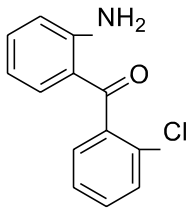
(2-Aminophenyl)(2-fluorophenyl)methanone (7b)



7b

The (2-amino-5-bromophenyl)(2-fluorophenyl) methanone **6b** (1g, 3.34 mmol), and tetrahydrofuran (8 mL) were charged to a round bottom flask. To this solution $Pd(OAc)_2$ (0.04 g, 0.18 mmol) was added under a positive pressure of argon. Then addition of aq. potassium fluoride (0.357g, 6.68mmol in 2mL water) solution was added to the mixture and this was followed by dropwise addition of PMHS (0.21 mL, 3.5mmol), which resulted in a greenish color. The reaction mixture was opened to the air after consumption of starting material. The reaction mixture was then stirred with alumina and filtered through celite. The aq layer was extracted with ethyl acetate (3x10 mL) and the combined organic layer was washed with aq10% NaCl (2x20 mL) solution. It was then dried (Na_2SO_4) and purified on a silica gel column using EtOAc: hexane (10:90). The solvents were removed and the solid residue was dried under high vacuum to afford a yellow powder **7b**(0.54g, 73% yield). ^1H NMR (500 MHz, CDCl3) δ 7.51 – 7.46 (m, 1H), 7.44 (ddd, 1H), 7.37 – 7.30 (m, 2H), 7.26 (t, J 7.5 Hz, 1H), 7.17 (t, J 9.0 Hz, 1H), 6.74 (d, J 8.3 Hz, 1H), 6.60 (t, J 7.6 Hz, 1H), 6.41 (s, 2H). ^{13}C NMR (126 MHz, CDCl3) δ 195.34 (s), 159.04 (d, $^1J_{C-F}$ = 249.6 Hz), 151.15 (s), 135.07 (s), 134.55 (d, $^5J_{C-F}$ = 1.6 Hz), 131.71 (d, $^3J_{C-F}$ = 8.1 Hz), 129.71 (d, $^3J_{C-F}$= 3.5 Hz), 128.71 (d, $^2J_{C-F}$ = 16.6 Hz), 124.13 (d, $^4J_{C-F}$= 3.4 Hz), 118.07 (s), 116.95 (s), 116.04 (d, $^2J_{C-F}$ = 21.6 Hz), 115.78 (s).). HRMS (ESI/ITTOF) *m/z*: $[M + H]^+$Calcd for $C_{13}H_{10}NOF$ 216.0819; found 216.0798.

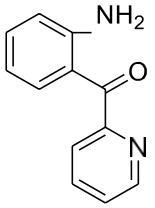
(2-Aminophenyl)(2-chlorophenyl)methanone (7c)



7c

The (2-amino-5-bromophenyl)(2-chlorophenyl)methanone **6c** (1g, 3.21 mmol) was dissolved in THF (10mL) and $Pd(OAc)_2$ (0.036 g, 0.161 mmol) was added under a positive pressure of argon to the solution with vigorous stirring. Then an aq potassium fluoride (0.372g, 6.42mmol in 3mL water) solution was added and this was followed by addition of PMHS (0.2mL, 3.37mmol). This process resulted in a bluish colored solution. At the end of the reaction (TLC) the flask was opened to the air, and stirred with alumina and filtered through celite. The aq layer was extracted with ethyl acetate(3x10 mL) and the combined organic layer was washed with a 10% aq NaCl solution (2x20mL). It was then dried (Na_2SO_4) and purified by silica gel chromatography using EtOAc: hexane (10:90). The solvents were removedunder reduced pressure and the residue was dried under high vacuum to afford a yellow powder **7c**(0.53g, 71% yield).^{1}H NMR (500 MHz, $CDCl_3$) δ 7.47 (dd, J 7.9, 1.0 Hz, 1H),
7.41 (td, J 7.6, 2.0 Hz, 1H), 7.37 (td, J 7.3, 1.3 Hz, 1H), 7.34 (dd, J 7.5, 1.8 Hz, 1H), 7.30 (dt, J 12.9, 3.6 Hz, 1H), 7.19 (dd, J 8.1, 1.4 Hz, 1H), 6.74 (dd, J 8.3, 0.5 Hz, 1H), 6.56 (td, 1H), 6.48 (s, 2H). ^{13}C NMR (126 MHz, $CDCl_3$) δ 197.28 (s), 151.42 (s), 139.85 (s), 135.23 (s), 134.68 (s), 130.71 (s), 130.33 (s), 129.85 (s), 128.42 (s), 126.63 (s), 117.43 (s), 117.00 (s), 115.78 (s). HRMS (ESI/ITTOF) *m/z*: $[M + H]^+$Calcd for $C_{13}H_{10}NOF$ 232.0524; found 232.0506.

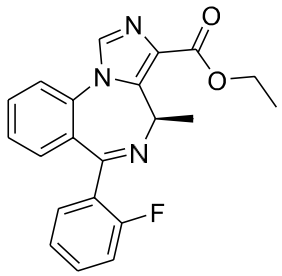
(2-Aminophenyl)(pyridin-2-yl)methanone (7d)



7d

A round bottom flask was charged with (2-amino-5-bromophenyl) (pyridin-2-yl) methanone **6d**(1g, 3.6mmol), as well as THF (10mL), and the flask was purged with argon. Palladium acetate (0.04 g, 0.18 mmol) was then added under an argon atmosphere and this was followed by the addition of aq potassium fluoride (0.419g, 7.2mmol in 4mL of water) solution. Then PMHS (0.23mL, 3.78mmol) was added dropwise to the reaction mixture, which resulted in a deep greenish colored solution. The reaction mixture was then stirred for the required time(see Table 3), and the round bottom flask was opened to the air at the end of the reaction. Then 2 g of alumina was added to the reaction flask and it was stirred for 5 min. The reaction mixture was then filtered through a pad of celite.Water and ethyl acetate was added to the filtrate. The layers were separated, and the aq layer was extracted with ethyl acetate (3x10mL) and the combined organic layer was washed with an aq 10% NaCl solution (2x10mL). It was then dried (Na_2SO_4) and purified by silica gel chromatography using EtOAc: hexane (10:90). The solvents were removed under reduced pressure and the solid residue was dried under high vacuum to afford a yellow powder**7d** (0.50g, 69% yield).^{1}H NMR (500 MHz, $CDCl_3$) δ 8.70 (ddd, J 4.8, 1.7, 0.9 Hz, 1H), 7.86 (td, J 7.7, 1.7 Hz, 1H), 7.76 (dt, J 7.8, 1.1 Hz, 1H), 7.65 (dd, J 8.2, 1.5 Hz, 1H), 7.43 (ddd, J 7.6, 4.8, 1.2
Hz, 1H), 7.30 (ddd, J 8.5, 7.0, 1.6 Hz, 1H), 6.73 (dd, J 8.4, 0.8 Hz, 1H), 6.61 (ddd, J 8.1, 7.1, 1.1 Hz, 1H), 6.32 (s, 1H).^{13}C NMR (126 MHz, $CDCl_3$) δ 196.04 (s), 157.52 (s), 151.83 (s), 148.46 (s), 136.89 (s), 135.03 (s), 134.81 (s), 124.95 (s), 123.88 (s), 117.03 (s), 116.78 (s), 115.57 (s).). HRMS (ESI/ITTOF) *m/z*: $[M + H]^+$Calcd for $C_{12}H_{10}N_2O$ 199.0866; found 199.0844.

Ethyl (*R*)-6-(2-fluorophenyl)-4-methyl-4*H*-benzo[*f*]imidazo[1,5-*a*][1,4]diazepine-3-carboxylate(9a)



9a

The $Pd(OAc)_2$ (0.029 g, 0.13 mmol) was added under a positive flow of argon to a stirred solution of (ethyl(R)-8-bromo-6-(2-fluorophenyl)-4-methyl-4*H*-benzo[*f*]imidazo[1,5-*a*][1,4]diazepine-3 carboxylate **8a** (1g, 2.26 mmol) in THF (10 mL). This addition was followed by addition of aqpotassium fluoride (0.262g, 4.52 mmol in 3mL water) solution and PMHS (0.14 mL, 2.37 mmol). This reaction mixture was stirred for 2hr at rt, and then the flask was opened to the air upon the consumption of starting material (TLC). The mixture was stirred with alumina, and filtered through a pad of celite. The organic layer, which resulted, was diluted with water and the aq layer was extracted with ethyl acetate (3x10 mL). The combined organic layer was washed with an aq 10% sodium chloride solution (2x10 mL), dried (Na_2SO_4),and concentrated under reduced pressure. The residue was purified on a silica gel column using EtOAc: hexane (50:50).^{1}H NMR (500 MHz, CDCl3) δ 7.93 (d, J 14.8 Hz, 1H),
7.72 (d, J 7.9 Hz, 1H), 7.60 (s, 2H), 7.47 (dd, J 11.8, 8.1 Hz, 1H), 7.44 – 7.30 (m, 2H), 7.25 (dt, J 11.6, 7.6 Hz, 1H), 7.04 (dt, J 14.7, 9.5 Hz, 1H), 6.71 (q, J 13.8, 6.8 Hz, 1H), 4.41 (q, J 15.9, 7.4 Hz, 2H), 1.42 (t, J 7.1, 1.4 Hz, 3H), 1.29 (d, J 7.5 Hz,3H). HRMS (ESI/ITTOF) *m/z*: $[M + H]^+$Calcd for $C_{12}H_{10}N_2O$ 364.1456; found 364.1437.

Adult schistosome mobility assays

S. mansoni cercariae (NMRI strain) infected Swiss Webster mice (female) were sacrificed after 49 days of infection by CO_2 euthanasia. The mesenteric vasculature of mice was dissected to recover adult schistosomes. The schistosomes were harvested and washed in DMEM (ThermoFisher cat. # 11995123) supplemented with HEPES (25mM), 5% v/v heat inactivated FCS (Sigma Aldrich cat. # 12133C) and Penicillin-Streptomycin (100 units/mL). 6 well dishes (4–5 male worms in 3mL media per well) were used to culture worms in the presence of various test compounds or DMSO (vehicle control) overnight (37 ˚C / 5% CO_2). Worms were imaged the following day to record movement phenotypes using a Zeiss Stemi 504 stereomicroscope and a CCD camera. 1 minute recordings were acquired at 4 frames per second and saved as a .TIFF stack, which was imported into ImageJ for analysis. All animal work was approved by IACUC committees at University of Wisconsin – Oshkosh and Madison (protocol numbers 000324-07-14-20 and V006353, respectively).

Acknowledgements

We wish to acknowledge the NIH for generous financial support (DA-043204, R01NS076517, R21AI146540). We also thank the Milwaukee Institute for Drug Discovery and the University of Wisconsin-Milwaukee's Shimadzu Laboratory for Advanced and Applied Analytical Chemistry for help with spectroscopy and the National ScienceFoundation, Division of Chemistry [CHE-1625735].

Supplementary Material

^{1}H NMR, ^{13}C NMR and HRMS spectra for all compounds are available in the Supplementary material file accompanying this paper.

References

1. Choi, H.Y. ; Chi., D.Y. *J. Am. Chem. Soc.* **2001**, *123*, 9202–9203. https://doi.org/10.1021/ja0164374
2. Ronald J.; RahaimJr.; Robert E.; MaleczkaJr. *Tetrahedron Lett.***2002,** *43*, 8823–8826. https://doi.org/10.1016/S0040-4039(02)02212-8
3. Nayal, O.S. ;Vinod Bhatt, V.; Sharma,S. ; Kumar, N. *J. Org. Chem.*, **2015**, *80*, 5912-5918. https://doi.org/10.1021/acs.joc.5b00156
4. Lawrence, N. J.; Drew, M. D.; Bushell, S. M. *J. Chem. Soc., Perkin Trans*. 1 **1999**, 3381–3391; https://doi.org/10.1039/A903662H
5. Pri-Bar, I.; Buchman, O. *J. Org. Chem*. **1986**, *51*, 734–735. https://doi.org/10.1021/jo00355a029
6. Viciu, M. S.; Grasa, G. A.; Nolan, S. P. *Organometallics* **2001**, *20*, 3607–3612. https://pubs.acs.org/doi/10.1021/om010332s
7. Viciu, M. S.; Kissling, R. M.; Stevens, E. D.; Nolan, S. P. *Org. Lett.* **2002**, *4*, 2229–2231. https://doi.org/10.1021/ol0260831
8. Grasa, G. A.; Viciu, M. S.; Huang, J.; Zhang, C.; Trudell, M. L.; Nolan, S. P. *Organometallics***2002**, *21*, 2866–2873 https://doi.org/10.1021/om020178p
9. Huang, T. H.; Chang, H. M.; Wu, M. Y.; Cheng, C. H. *J. Org. Chem*. **2002**, *67*, 99–105 https://doi.org/10.1021/jo010637g
10. Botella, L.; Najera, C. *Angew. Chem., Int. Ed.* **2002**, *41*, 179–181 https://doi.org/10.1002/1521-3757(20020104)114:1<187::AID-ANGE187>3.0.CO;2-A
11. Heidenreich, R. G.; Kohler, K.; Krauter, J. G. E.; Pietsch, J. *Synlett.* **2002**, 1118–1122 https://doi.org/10.1055/s-2002-32589
12. Kabalka, G. W.; Namboodiri, V.; Wang, L. *Chem.Commun.* **2001**, 775 https://doi.org/10.1039/B101470F
13. LeBlond, C. R.; Andrews, A. T.; Sun, Y.; Sowa, J. R., Jr. *Org. Lett.* **2001**, *3*, 1555–1557 https://doi.org/10.1021/ol015850d
14. Knutson, D.E.; Smith, J.L.; Ping, X. Jin, X.; Golani, L.K, Li, G. Rashid,F.; Mian, M.Y., Jahan,R., Sharmin, D., Cerne,R.; Cook, J.M.; Witkin, J. *ACS Chem. Neurosci.* **2020**, *11*, 2624−2637. https://doi.org/10.1021/acschemneuro.0c00295
15. McCusker, P.; Mian, M.Y.; Li, G., Olp, M.D.; Tiruveedhula, V.V.N.P.B.; Rashid, F.; Golani, L. K.; Verma, R. S.; Smith, B. C.; Cook, J. M.; Chan, J. D. *PLoS Negl Trop Dis* 13e0007826. https://doi.org/10.1371/journal. pntd.0007826
16. Chitsulo L, Engels D, Montresor A, Savioli L. *Acta Trop.* **2000**, *77*, 41–51 https://doi.org/10.1016/S0001-706X(00)00122-4
17. Engels D, Chitsulo L, Montresor A, Savioli L. *Acta Trop.* **2002**, *82*, 139–146.

https://doi.org/10.1016/S0001-706X(02)00045-1

18. Steinmann P, Keiser J, Bos R, Tanner M, Utzinger J. *Lancet Infect. Dis.***2006**, *6*, 411–425 https://doi.org/10.1016/S1473-3099(06)70521-7
19. King CH, Dickman K, Tisch DJ. *Lancet* **2005**, *365*, 1561–1569 https://doi.org/10.1016/S0140-6736(05)66457-4
20. Raso G, Vounatsou P, McManus DP, N'Goran EK, Utzinger J. *Int. J.Parasitol.* **2007**, *37*, 1491–1500. https://doi.org/10.1016/j.ijpara.2007.05.004
21. Baard AP, Sommers DK, Honiball PJ, Fourie ED, du Toit LE. *S. Afr. Med. J*. **1979**,*55*, 617–8. PMID: 380021.
22. Darragh A, Lambe R, Brick I, Downie WW. *Lancet*. **1981,***318*, 1042. https://doi.org/10.1016/S0140-6736(81)91233-2
23. Darragh A, Lambe R, Brick I, O'Boyle C. *Br. J. Clin. Pharmacol.***1982**,*14*, 871–2. https://doi.org/10.1111/j.1365-2125.1982.tb02052.x
24. O'Boyle C, Lambe R, Darragh A. *Eur J. Clin. Pharmacol*. **1985**, *29*, 105–8. https://doi.org/10.1007/bf00547377
25. Chandrasekhar S, Chandraiah L , Reddy R , Reddy MV. *Chemistry Letters*. **2000**, 29(7): 780–781 https://doi.org/10.1246/cl.2000.780
26. Nishiyama H, Park S, Itoh K. *Tetrahedron: Asymmetry*. **1992**, *3*, 1029–1034. https://doi.org/10.1016/S0957-4166(00)86036-X
27. Panda B, Sarker TK. *Tetrahedron Lett*., **2008**, 49, 6701-6703. https://doi.org/10.1016/j.tetlet.2008.09.071

This paper is an open access article distributed under the terms of the Creative Commons Attribution (CC BY) license (http://creativecommons.org/licenses/by/4.0/)

A Platinum Open Access Journal for Organic Chemistry

Paper

Free to Authors and Readers DOAJ Seal

Arkivoc **2021**, part v, 171-188

An efficient debromination technique using PMHS with a number of ligands containing different functional groups

Md Yeunus Mian,[a] Prithu Mondal,[a] Dishary Sharmin,[a] Kamal P. Pandey,[a] Farjana Rashid,[a] Sepideh Rezvanian,[a] Lalit K. Golani,[a] V.V.N. Phani Babu Tiruveedhula,[a] Vilashini Rajaratnam[1], Shama P. Mirza[1], John D. Chan[2], Jeffrey M. Witkin[1], and James M. Cook*[1]

[1]Department of Chemistry and Biochemistry, Milwaukee Institute of Drug Discovery, University of Wisconsin-Milwaukee, Milwaukee, WI-53211

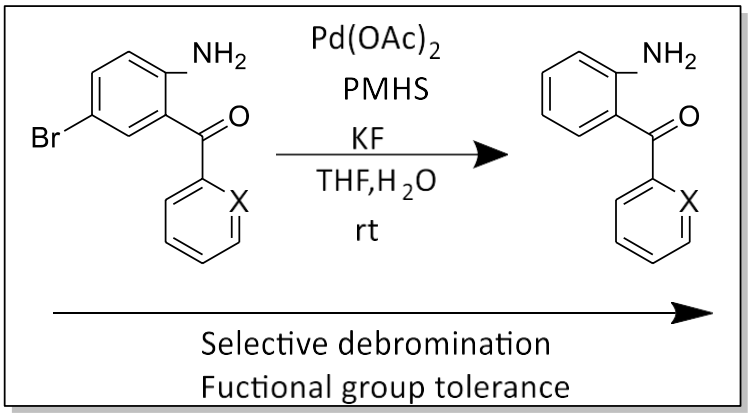
[2]Department of Chemistry, University of Wisconsin-Oshkosh, Oshkosh, WI-54901 E-mail: capncook@uwm.edu

This paper is dedicated to Professor Peter Alan Jacobi for his many important contributions to Organic Chemistry

Received 12-22-2021 **Accepted Manuscript** 03-21-2022 **Published on line** 04-07-2022

Abstract

Herein is described the strategy to debrominate different aryl bromides selectively, using polymethylhydrosiloxane (PMHS) which tolerates a variety of functional groups. Key elements of this approach include the use of catalytic $Pd(OAc)_2$ and the correct equivalents of polymethylhydrosiloxane (PMHS), in conjunction with aqueous KF. The present reaction process provides a strategic tool for the synthesis of a number of medicinally important molecules.



Keywords: debromination, polymethylhydrosiloxane, benzodiazepines, palladium acetate

DOI: https://doi.org/10.24820/ark.5550190.p011.712 ©**AUTHOR(S)**

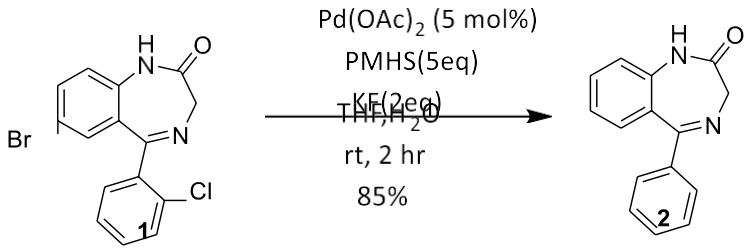
Introduction

Bromine-substituted aryl halides are important targets for further functionalization catalyzed by palladium catalysts or other chemical strategies.[1]Often times a cheap starting aryl bromide can be the lynch pin in the synthesis of new heterocyclic compounds. Replacement of bromine by hydrogen can be carried out using Polymethylhydrosiloxane (PMHS) reported earlier by Ronald *et al*.[2] It is a mild reducing agent, cost-effective, non-toxic and an easily handled chemical. It can be stored for long periods of time since it is more air and moisture stable than any other silanes.[3] PMHS is relatively inert but can transfer the hydride to participate in different metal catalyzed reductions.[4]Hydrosilanes are mild reducing agents with a variety of applications.[25,26]In addition, some hydrosilanes are compatible with some oxidizing agents and act as selective reducing agents in a one-pot redox cocktail.[27]

PMHS hydrodehalogenates aryl halides when using a palladium catalyst.[2] A method to debrominate aryl bromides in the presence of a number of functional groups such as ketones, amides, imines, and esters was developed. We debrominated bromo-benzodiazepines using this method and then nitrated the resulting product to synthesize pharmaceutically active potential drug candidates.[15]

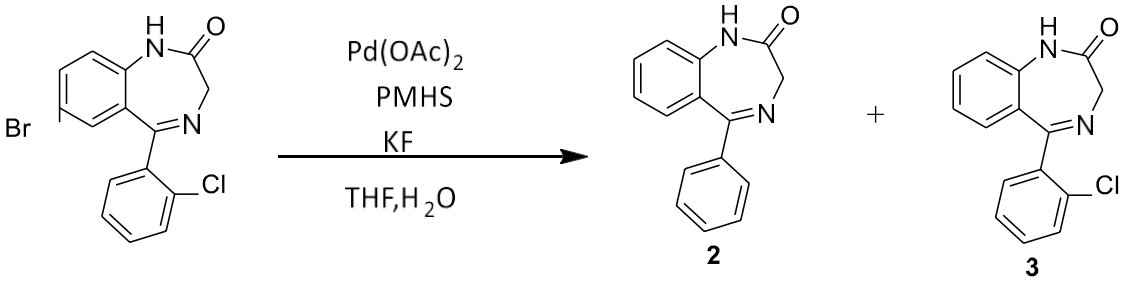
Results and Discussion

Recently, phosphine free palladium catalysts have enjoyed considerable success in different reductive dehalogenations.[6-13] We required a suitable system to debrominate different benzodiazepine compounds. The investigation initially revealed $Pd(OAc)_2$ with PMHS in the presence of potassium fluoride reduced chlorobenzene to benzene,[2] and this transformation took place at room temperature. We followed the conditions to debrominate a benzodiazepine which bears a bromo and a chloro functionality. The benzodiazepine **1** was synthesized according to the literature procedure.[14] As expected both halogens were reduced by PMHS (Scheme 1).



Scheme 1. Dehalogenation of benzodiazepine.

Based on this result, we started to explore this system to find a better method to selectively debrominate the aryl halide without affecting other functional groups. Initially we investigated conditions to determine the correct equivalents of PMHS and reaction time for selective debromination. We used the substrate **1** for our initial investigation (Scheme 2). Different equivalents of PMHS and different mole% of Pd catalyst were used to identify the best conditions. It was found that bromide **1** could be debrominated chemoselectively by reducing the amount of PMHS in the presence of 5 mole% $Pd(OAc)_2$; although the reaction time was longer, as expected, and the reaction also gave the byproduct **2** in minor amounts. (Table 1, entry 10**;** 5:95).



1 **2** **3**

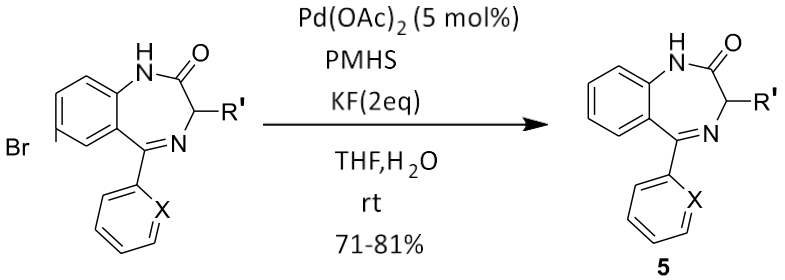
Scheme 2

Table 1. Effect of different equivalents of PMHS on selective debromination

Entry	Substrate	$Pd(OAc)_2$	PMHS(eq)	KF (eq)	Time	Temperature	*Ratio of Product (**2**:**3**)	[a]Yield
1	**1**	5 mol%	4	2	1 hr	r.t.	90:10	75%
2	**1**	1 mol%	4	2	2 hr	r.t.	83:17	79%
3	**1**	2 mol%	4	2	2 hr	r.t.	80:20	69%
4	**1**	3 mol%	4	2	1.5 hr	r.t.	71:29	73%
5	**1**	4 mol%	4	2	1.3 hr	r.t.	65:35	75%
6	**1**	5 mol%	3	2	2.2 hr	r.t	60:40	71%
7	**1**	5 mol%	2.5	2	2.5 hr	r.t	60:40	71%
8	**1**	5 mol%	1.05	2	3 hr	r.t	51:49[b]	65%[C]
9	**1**	5 mol%	1.05	2	4.0 hr	r.t	22:78 [b]	84%[C]
10	**1**	5 mol%	1.05	2	6.0 hr	r.t.	5:95	79%

*From HPLC (Pinnacle -C18 (2.1 mm × 50 mm, 1.8 µm particle size) column, flow rate of 0.5 mL/min, mobile phase-acetonitrile and water (containing 0.1% formic acid)) ;[a]Isolated combined yield of (**2** and **3**); [b] Ratio of **1** and **3**; [C] Combined yield of (**1** and **3**)

The debromination reaction was also investigated with different benzodiazepines, as shown in Table 2. Benzodiazepine derivatives (**4a-h**) were subjected to debromination under the same conditions (Scheme 3**,** Table 2) to furnish the products **5a-h** (71%-81%), respectively. We also increased the amount of PMHS to debrominate the substrate **4e** to produce **5e** (Table 2, entry 5). The debromination occurred smoothly in less reaction time without affecting the amide and imine functionality of the benzodiazepine substrates. A similar trend was also observed in the case of substrate **4h**. Here an interesting observation was found. Although the acetate is a labile protecting group to reduction, it survived the debromination reaction process by PMHS. The hydride source did not interfere with the acetate moiety.



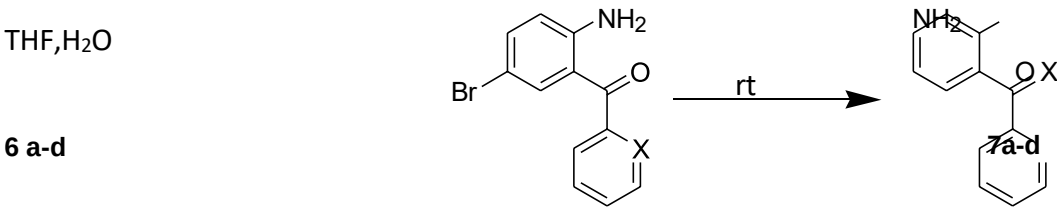
Scheme 3

Table 2. Debromination strategy on different benzodiazepines

Entry	Substrate	X	R'	PMHS (eq)	Time	Product	[a]Yield (%)
1	**4a**	C-H	H	1.05	3.5 hr	**5a**	71%
2	**4b**	C-H	CH_3(R)	1.05	4 hr	**5b**	73%
3	**4c**	C-H	CH_3(S)	1.05	3.5 hr	**5c**	79%
4	**4d**	C-F	CH_3(R)	1.05	4 hr	**5d**	78%
5	**4e**	C-F	CH_3(S)	3.0	2.0 hr	**5e**	79%
6	**4f**	C-Cl	CH_3(S)	1.05	4.5 hr	**5f**	75%
7	**4g**	N	CH_3(S)	1.05	2 hr	**5g**	81%
8	**4h**	C-F	$OCOCH_3$	4	45 min	**5h**	73%

[a]Isolated yield

We, then identified conditions in different benzophenone substrates, as shown in Table 3 (Scheme 4). The treatment of other benzophenone substrates afforded debrominated product **7a-d** in good to high yields (Table 3). We also observed that increasing the amounts of PMHS decreased the reaction time in some benzophenone substrates (**6a-b**), as expected. PMHS did not affect the ketone functionality in any benzophenone substrate (Table 3, entry 1-8), as we hypothesized. Selective debromination over chlorination was also observed in this case (Table 3, entry 3), which is also as expected and, gratifyingly, took place.



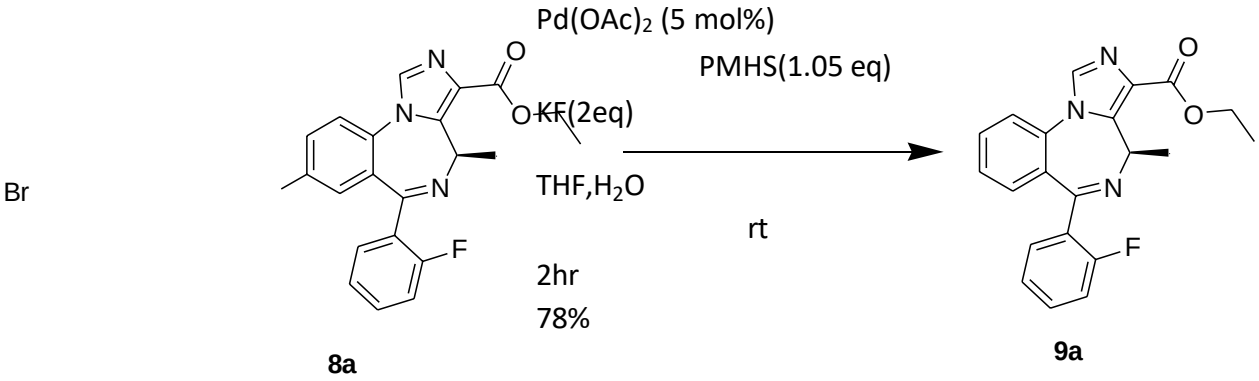
Scheme 4

Table 3. Selective debromination of benzophenone substrate

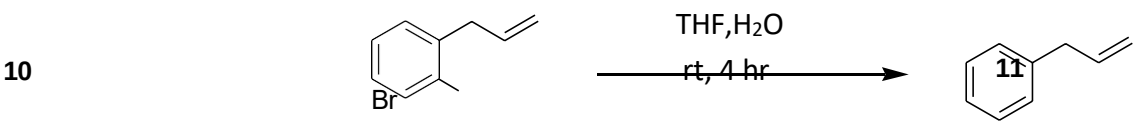
Entry	Substrate	X	$Pd(OAc)_2$	PMHS(eq)	KF (eq)	Time	Product	[a]Yield
1	**6a**	C-H	5 mol%	1.05	2	3.5 hr	**7a**	78%
2	**6b**	C-F	5 mol%	1.05	2	3.0 hr	**7b**	73%
3	**6c**	C-Cl	5 mol%	1.05	2	3.0 hr	**7c**	71%
4	**6d**	N	5 mol%	1.05	2	2.5 hr	**7d**	69%
5	**6a**	C-H	5 mol%	2	2	2.0 hr	**7a**	69%
6	**6a**	C-H	5 mol%	3	2	1.0 hr	**7a**	75%
7	**6a**	C-H	5 mol%	4	2	30 min	**7a**	70%
8	**6b**	C-F	5 mol%	4	2	45 min	**7b**	73%

[a]Isolated yield

Furthermore, we attempted the debromination on an imidazodiazepine substrate possessing an ester function (Scheme 5). The imidazodiazepine **8a** gave the debrominated product **9a** in good yield. The imidazodazepine ester was well tolerated under these reaction conditions confirming the mildness of the PMHS process. Also, upon investigation on a double bond containing aryl substrate, PHMS debrominated the bromine group selectively without interfering with the double bond (Scheme 6, preliminary data, SI)



Scheme 5. Effect of the debromination reaction on imidazodiazepine substrate **8a.**

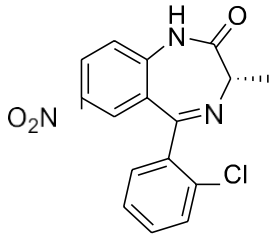


Scheme 6. Selective debromination by PMHS on a double bond containing substrate.

Anti-schistosomal activity of 8-*H* benzodiazepines

Schistosomiasis, a neglected tropical disease is one of the most dominant infectious diseases worldwide that has serious public health consequences [16-19]and is characterized by chronic helminthic infection with residual morbidity. Over 240 million people are infected, with 800 million at risk of infection and more than 90% of infections occurring in sub-Saharan Africa where the death rate is approximately 280,000 persons per year.[15] Schistosomiasis is caused by parasitic blood flukes (trematode worms) of the genus *Schistosoma*, of which *Schistosoma mansoni*, *Schistosoma japonicum and Schistosoma haematobium* cause infections in humans.[20]

The treatment of schistosomiasis relies only on one broad spectrum drug, praziquantel which is associated with several drawbacks including PZQ's lack of efficacy against immature parasites. Meclonazepam, a benzodiazepine was found to be effective in treatment of schistosomiasis[15]and was able to cure both mature and immature infections. But the curative dose of meclonazepam causes dose-limiting sedation in human trials and the development of this lead was dropped.[21-24]



meclonazepam

Figure 1. Structure of meclonazepam.

The chemical name of meclonazepam is (S)-5-(2-chlorophenyl)-3-methyl-7-nitro-1,3-dihydro-2*H*-benzo[*e*][1,4]diazepin-2-one and the structure bears a nitro group in one of the benzene rings (Figure 1). We synthesized different benzodiazepines (most of them in this manuscript) which contained 8-H instead of 8-nitro groups and assessed the synthesized compounds in schistosome mobility assays. This assay was done in order to identify the importance of the nitro group in the structure of the benzodiazepines in regard to activity. The results are summarized in Table 4.

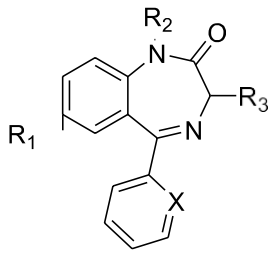
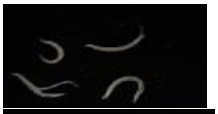
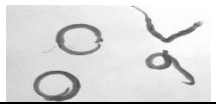


Figure 2. General structure of meclonazepam derivatives.

Table 4. Anti-schistosomal effect of C-7 H benzodiazepines

SL	R_1	R_2	R_3	X	Code	Activity	
1	NO_2	H	S-CH_3	C-Cl	MCLZ		Coiled ,dead IC_{50} 160nm
2	H	H	S-CH_3	C-Cl	MYM-V-03		alive, 30µM
3	H	H	S-CH_3	C-F	MYM-I-84		alive, 30µM
4	H	H	R-CH_3	C-F	MYM-I-94		alive, 30µM
5	H	H	S-CH_3	C-H	MYM-I-85		alive, 30µM
6	H	H	R-CH_3	C-H	MYM-I-86		alive, 30µM
7	H	H	S-CH_2CH_3	C-Cl	MYM-V-18		alive, 30µM
8	CN	H	S-CH_3	C-Cl	MYM-IV-12		alive, 30µM

The IC_{50} value of meclonazepam is 160 nM and it causes contractile paralysis of the parasites. The parasites were coiled, dead upon the exposure to the meclonazepam (Table 4). But changing the nitro group to hydrogen resulted in total loss of activity (entry 2, Table 4). Changing the nitro group to a hydrogen atom along with other modifications demonstrated no activity at all (entry 3-7, Table 4). Consequently, a hydrogen atom at the 8- position in place of a nitro group is not suitable for anti-schistosomal activity. In order to identify whether the electronic effects of the nitro group or the structure of nitro group itself was responsible for schistocidal activity, we replaced the nitro group with a cyano group and assessed the compound's activity in the schistosome mobility assay. This resulted in total loss of activity. This would argue, although not prove, against a pi stacking interaction with the ring-A aromatic ring in meclonazepam. Modification of different positions without changing the nitro group show various degrees of anti-schistosomal activity and some of these results are described in McCusker P. *et al*. 2019.[15] The nitro group in the structure of meclonazepam is crucial for the damage to the parasite.

Conclusions

It was demonstrated that ketones, amides, esters and imines were all well tolerated under the reduction conditions of PMHS employed here with catalytic $Pd(OAc)_2$ in THF. This is an efficient system for the

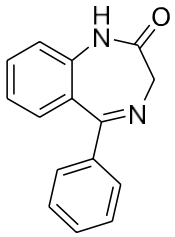
debromination of benzodiazepines, benzophenones and imidazodiazepines at room temperature. The debromination can be done with a small amount of Pd catalyst but 5 mol % still represents a general catalyst loading. It was also shown that debromination occurred selectively in the presence of a chloro functional group, which is key for the synthesis of some novel potential drug candidates.[15]

Experimental Section

General. All reactions were performed in round-bottom flasks with magnetic stir bars under an argon atmosphere. Organic solvents were purified when necessary by standard methods or purchased from Sigma- Aldrich Chemicals. The reagents and other chemicals were purchased from either Sigma-Aldrich, Oakwood Chemical, Alfa Aesar, Matrix Scientific, Admiral Chemical Company, or Acros Organic. The progress of reactions was visualized with TLC plates from Dynamic Adsorbents, Inc. under a UV light. The flash column chromatography was done for purification of some analogs on silica gel (230-400 mesh, Dynamic Adsorbents). An Agilent HPLC was used to determine the ratio of some debrominated products. The ^{1}H NMR and ^{13}C NMR spectra were obtained on Bruker Spectrospin 500 MHz instrument in $CDCl_3$ and chemical shifts were reported in δ (ppm). Multiplicities are represented as follows: singlet (s), broad signal (br), doublet (d), triplet (t), quartet (q), dd (doublet of doublets), and multiplet (m). The technique employed for HRMS was carried out on a LCMS- IT-TOF at the Milwaukee Institute for Drug Discovery in the Shimadzu Laboratory for Advanced and Applied Analytical Chemistry.

General procedure for the debromination: A three neck round bottom flask was charged with the aromatic halide. Then THF was added and the flask was purged with argon. Palladium acetate was then added under an argon atmosphere, followed by the addition of aq potassium fluoride solution. Then PMHS was added dropwise to the reaction mixture, which resulted in a deep greenish solution. The reaction mixture was then stirred for the required time by monitoring by TLC (see Tables for data). The consumption of starting material was confirmed on a LCMS 2020. The round bottom flask was open to the air at the end of the reaction. 2 Grams of alumina was added to the reaction flask and this was allowed to stir for 5 min. The reaction mixture was filtered through a pad of celite to removethe Pd salts; water and ethyl acetate was added to the filtrate. The layers were separated and the aq layer was extracted with ethyl acetate and the combined organic layer was washed with aq 10% NaCl solution (2x), dried over sodium sulfate, concentrated under reduced pressure and purified via silica gel column chromatography. The gradient elution was effected by ethyl acetate and hexane. The purified compounds were characterized by NMR spectroscopy, LCMS and HRMS (individually).

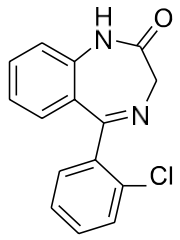
5-Phenyl-1,3-dihydro-2*H*-benzo[*e*][1,4]diazepin-2-one (2)



2

The $Pd(OAc)_2$ (0.04 g, 0.12 mmol) was added to a stirred solution of 7-bromo-5-phenyl-1,3-dihydro-2H-benzo[e][1,4]diazepin-2-one (**4**) (0.8 g, 2.53 mmol) in THF (10 mL) under argon. This was followed by addition of aq potassium fluoride (0.293 g, 5 mmol in 2 mL water) solution and PMHS (0.16 mL, 2.65 mmol). The flask was opened to air after the required reaction time (table 2), stirred with alumina and then filtered through celite. The aq layer was extracted with ethyl acetate (2x10mL) and the combined organic layer was washed with aq 10% sodium chloride solution (2x10mL), dried over Na_2SO_4 and, concentrated under reduced pressure. The residue was purified by silica gel column chromatography using EtOAc: hexane (35:65). The appropriate fractions were pooled, the solvents were removed under reduced pressure and the residue was dried under vacuum to obtain a white powder **5** (0.49 g, 81% yield). ^{1}H NMR (500 MHz, CDCl3) δ 9.66 (s, 1H), 7.56 (d, J 7.8 Hz, 2H), 7.52 (dd, J 11.3, 4.1 Hz, 1H), 7.48 – 7.44 (m, 1H), 7.39 (dd, J 11.0, 3.9 Hz, 2H), 7.34 (d, J 7.9 Hz, 1H), 7.22
(dd, J 7.9, 4.2 Hz, 1H), 7.19 – 7.14 (m, 1H), 4.36 (s, 2H). ^{13}C NMR (126 MHz, CDCl3) δ 172.33 (s), 171.13 (s), 139.47 (s), 138.82 (s), 131.71 (s), 131.36 (s), 130.30 (s), 129.70 (s), 128.18 (s), 127.26 (s), 123.33 (s), 121.21 (s), 56.71 (s). HRMS (ESI/ITTOF) *m/z*: $[M + H]^+$Calcd for $C_{15}H_{12}N_2O$ 237.1022; found 237.1007.

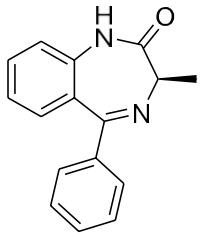
5-(2-Chlorophenyl)-1,3-dihydro-2*H*-benzo[*e*][1,4]diazepin-2-one (3)



3

7-Bromo-5-(2-chlorophenyl)-1,3-dihydro-2H-benzo[e][1,4]diazepin-2-one (**1**) (0.8 g, 2.28 mmol) was dissolved in THF (10 mL) under argon and then $Pd(OAc)_2$ (0.051 g, 0.114 mmol), and an aq potassium fluoride (0.264 g, 4.56 mmol in 2 mL water) solution was added under a positive flow of argon and this was followed by dropwise addition of PMHS (0.14 mL, 2.39 mmol). The reaction mixture, which resulted, was stirred the appropriate time (see Table 2) at rt and the flask was opened to the air to form more black palladium oxide and stirred with alumina, and then filtered through celite. The aq layer was extracted with ethyl acetate (3x10 mL); and the combined organic layer was washed with aq 10% sodium chloride solution (2x10 mL). It was then dried (Na_2SO_4) and concentrated under reduced pressure. The residue was purified by silica gelchromatography using EtOAc: hexane (40:60). The desired fractions were collected, evaporated and dried under vacuum to obtain a white powder **3** (0.51 g, 75% yield). ^{1}H NMR (500 MHz, CDCl3) δ 9.39 (s, 1H), 7.55 (ddd, J 7.6, 4.7, 2.3 Hz, 1H), 7.49
(ddd, J 8.7, 6.1, 2.8 Hz, 1H), 7.41 – 7.37 (m, 3H), 7.19 (d, J 8.3 Hz, 1H), 7.11 (ddd, 2H), 4.42 (s, 2H).^{13}C NMR (126 MHz, CDCl3) δ 171.57 (s), 170.57 (s), 139.10 (s), 137.96 (s), 133.27 (s), 131.85 (s), 131.03 (s), 130.63 (s), 130.03 (s), 129.90 (s), 127.91 (s), 126.84 (s), 123.85 (s), 121.04 (s), 56.59 (s). HRMS (ESI/ITTOF) *m/z*: $[M + H]^+$Calcd for $C_{15}H_{11}N_2OCl$ 271.0633; found 271.0608.

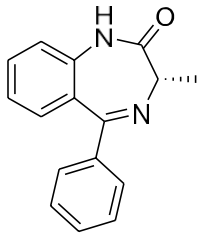
(*R*)-7-Bromo-3-methyl-5-phenyl-1,3-dihydro-2*H*-benzo[*e*][1,4]diazepin-2-one (5b)



5b

The (*R*)-7-bromo-3-methyl-5-phenyl-1,3-dihydro-2*H*-benzo[*e*][1,4]diazepin-2-one **4b** (1g, 3.03 mmol), tetrahydrofuran (10 mL) and $Pd(OAc)_2$ (0.04 g, 0.15 mmol) were charged to a round bottom flask under argon. Then aq potassium fluoride (0.351g, 6 mmol in 2 mL water) solution and PMHS (0.16 mL, 2.65 mmol) were added to the mixture and it was stirred for the time mentioned in Table 2. The flask was then opened to the air, stirred with alumina, and filtered through celite. The aq layer was extracted with ethyl acetate (3x10 mL) and the combined organic layer was washed with aq 10% sodium chloride solution (2x10mL), dried over Na_2SO_4 and concentrated under reduced pressure. The residue, which resulted, was purified with silica gel chromatography using EtOAc: hexane (35:65). The appropriate fractions were pooled, and the solvents were removed under reduced pressure. The residue was then dried under vacuum to obtain a white powder **5b** (0.55g, 73%). ^{1}H NMR (500 MHz, CDCl3) δ 9.40 (s, 1H), 7.55 – 7.50 (m, 3H), 7.43 (ddd, 1H), 7.39 – 7.32 (m, 3H), 7.22 (d, J 8.2 Hz, 1H), 7.15 (t, J 7.6 Hz, 1H), 3.79 (q, J 6.5 Hz, 1H), 1.79 (d, J 6.5 Hz, 3H). ^{13}C NMR (126 MHz, CDCl3) δ 173.04 (s), 169.09 (s), 139.35 (s), 138.50 (s), 131.58 (s), 131.06 (s), 130.13 (s), 129.80 (s, 2C), 128.15 (s, 2C), 127.73 (s), 123.19 (s), 121.15 (s), 58.69 (s), 17.09 (s). HRMS (ESI/ITTOF) *m/z*: $[M + H]^+$Calcd for $C_{16}H_{14}N_2O$ 251.1179; found 251.1155.

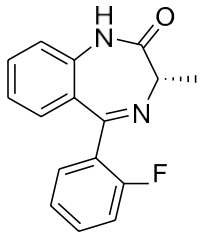
(*S*)-3-Methyl-5-phenyl-1,3-dihydro-2*H*-benzo[*e*][1,4]diazepin-2-one(5c)



5c

The desbromochiral compound **5c** (0.58g, 78%) was synthesized according to the procedure employed for **5b** maintaining the same scale. The yield was 78%.^{1}H NMR (500 MHz, $CDCl_3$) δ 9.74 (s, 1H), 7.53 (ddd, 2H), 7.50 (d, J 7.4 Hz, 1H), 7.42 (t, J 6.9 Hz, 1H), 7.38 – 7.31 (m, 3H), 7.24 (ddd, 1H), 7.14 (t, J 7.5 Hz, 1H), 3.79 (q, J 6.4 Hz, 1H), 1.80 (d, J 6.4 Hz, 3H). ^{13}C NMR (126 MHz, $CDCl_3$) δ 173.16 (s), 169.13 (s), 139.36 (s), 138.58 (s), 131.57 (s), 131.03 (s), 130.12 (s), 129.82 (s), 128.14 (s), 127.70 (s), 123.15 (s), 121.24 (s), 58.71 (s), 17.10 (s). HRMS (ESI/ITTOF) *m/z*: $[M + H]^+$Calcd for $C_{16}H_{14}N_2O$ 251.1179; found 251.1155.

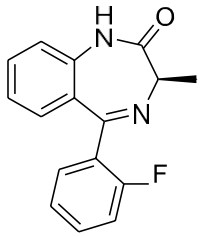
(*S*)-5-(2-Fluorophenyl)-3-methyl-1,3-dihydro-2*H*-benzo[*e*][1,4]diazepin-2-one (5e)



5e

The $Pd(OAc)_2$ (0.064 g, 0.144 mmol) was added to a stirred solution of (*S*)-7-bromo-5-(2-fluorophenyl)-3-methyl-1,3-dihydro-2*H*-benzo[*e*][1,4]diazepin-2-one **4e** (1 g, 2.88 mmol) in THF (10 mL) under argon. This was followed by addition of aq potassium fluoride (0.334 g, 5.76 mmol in 2 mL water) solution and PMHS (0.51 mL, 8.64 mmol). At the end of the reaction (TLC), the flask was opened to the air, stirred with alumina, and filtered through a pad of celite. The mixture was diluted with water and the aq layer was extracted with ethyl acetate (2x10 mL). The combined organic layer was washed with aq 10% sodium chloride solution (2x10 mL), dried ($Na_2SO_{4)}$ and concentrated under reduced pressure. The residue was purified with silica gel chromatography using EtOAc: hexane (35:65). The appropriate fractions were pooled, and the solvents were removed under reduced pressure. The solid, which remained, was dried under vacuum to obtain a white powder **5e** (0.61 g, 79% yield).^{1}H NMR (500 MHz, CDCl3) δ 8.91 (s, 1H), 7.65 – 7.56 (m, 1H), 7.51 (t, J 7.7 Hz, 1H), 7.44 (ddd, 1H),
7.25 (dd, J 12.3, 7.7 Hz, 2H), 7.20 – 7.16 (m, 1H), 7.14 (t, J 7.6 Hz, 1H), 7.05 (dd, J 9.6, 8.9 Hz, 1H), 3.81 (q, J 6.5 Hz, 1H), 1.79 (d, J 6.5 Hz, 3H). ^{13}C NMR (126 MHz, CDCl3) δ 172.26 (s), 165.77 (s), 160.49 (d, J 251.5 Hz), 137.27 (s), 131.78 (s), 131.73 (s), 131.59 (d, J 2.0 Hz), 129.77 (s), 128.59 (s), 127.85 (d, J 12.5 Hz), 124.28 (d, J 3.4 Hz), 123.73 (s), 121.03 (d, J 1.4 Hz), 116.08 (d, J 21.7 Hz), 58.72 (s), 17.01 (s). HRMS (ESI/ITTOF) *m/z*: $[M + H]^+$Calcd for $C_{16}H_{13}N_2OF$ 269.1085; found 269.1062.

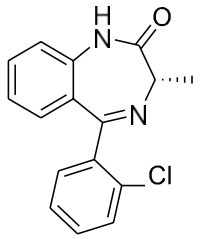
(*R*)-5-(2-Fluorophenyl)-3-methyl-1,3-dihydro-2*H*-benzo[*e*][1,4]diazepin-2-one(5d)



5d

The fluoro analog **5d** (0.6 g, 78%) was synthesized, according to the procedure employed for the synthesis of **5e** maintaining the identical scale. This process took a longer reaction time since less PMHS was employed. ^{1}H NMR (500 MHz, CDCl3) δ 9.15 (s, 1H), 7.60 (td, J 7.5, 1.3 Hz, 1H), 7.50 (ddd, 1H), 7.43 (ddt, 1H), 7.25 (t, J 7.3 Hz, 2H), 7.22 – 7.17 (m, 1H), 7.13 (t, J 7.6 Hz, 1H), 7.08 – 7.01 (m, 1H), 3.82 (q, J 6.5 Hz, 1H), 1.80 (d, J 6.5 Hz, 3H). ^{13}C NMR (126 MHz, CDCl3) δ 172.34 (s), 165.77 (s), 160.48 (d, J 251.6 Hz), 137.32 (s), 131.72 (s), 131.68 (s), 131.60 (d, J 2.4 Hz), 129.78 (s), 128.55 (s), 127.86 (d, J 12.5 Hz), 124.24 (d, J 3.6 Hz), 123.68 (s), 121.05 (s), 116.08 (d, J 21.6 Hz), 58.73 (s), 17.03 (s). HRMS (ESI/ITTOF) *m/z*: [M + H]+ Calcd for C16H13N2OF 269.1085; found 269.1062.

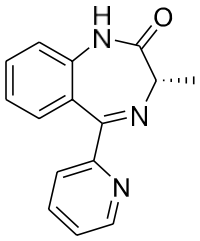
(*S*)-5-(2-Chlorophenyl)-3-methyl-1,3-dihydro-2*H*-benzo[*e*][1,4]diazepin-2-one (5f)



5f

(*S)*-7-Bromo-5-(2-chlorophenyl)-3-methyl-1,3-dihydro-2*H*-benzo[*e*][1,4]diazepin-2-one **4f** (0.9g, 2.47 mmol), THF (10 mL)was charged to a round bottom flask,after which,$Pd(OAc)_2$ (0.027 g, 0.123 mmol) was added to the stirred solution under a positive flow of argon. Then aq potassium fluoride (0.287g, 4.94 mmol in 2 mL water) solution and PMHS (0.16 mL, 2.65 mmol) were added, after which, the mixture was stirred for the time depicted in Table 2. The flask was then opened to the air upon the consumption of starting material. It was then stirred with alumina and filtered through a pad of celite. The organic layer was diluted with water and the aq layer was extracted with ethyl acetate (3x10 mL). The combined organic layer was washed with aq 10% sodium chloride solution (2x10 mL), dried (Na_2SO_4)and then concentrated under reduced pressure. The residue was purified by silica gel chromatography using EtOAc: hexane (40:60). The desired fractions were collectedand the solvent was evaporated under reduced pressure. The solid was dried under vacuum to obtain a light yellow powder **5f** (0.52g, 75%).^{1}H NMR (500 MHz, CDCl3) δ 8.98 (s, 1H), 7.53 (s, 1H), 7.50 (td, 1H), 7.37 (d, J 3.0 Hz, 3H), 7.17 (t, J 7.6 Hz, 1H), 7.12 (dd, 2H), 3.86 (q, J 6.5 Hz, 1H), 1.79 (d, J 6.5 Hz, 3H). ^{13}C NMR (126 MHz, CDCl3) δ 168.52 (s), 138.99 (s), 137.64 (s), 133.37 (s), 131.77 (s), 131.13 (s), 130.54 (s), 130.02 (s), 129.68 (s), 128.32 (s), 128.19 (s), 126.86 (s), 123.76 (s), 120.90 (s), 58.63 (s), 16.96 (s). HRMS (ESI/ITTOF) *m/z*: [M + H]+ Calcd for C16H13N2OCl 285.0789; found 285.0767.

(*S*)-3-Methyl-5-(pyridin-2-yl)-1,3-dihydro-2*H*-benzo[*e*][1,4]diazepin-2-one(5g)

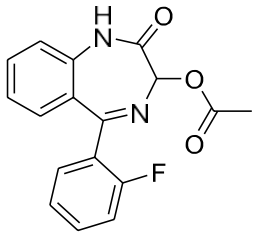


5g

To a stirred solution of (*S*)-7-bromo-5-(2-chlorophenyl)-3-methyl-1,3-dihydro-2*H*-benzo[*e*][1,4]diazepin-2-one **4g** (1 g, 3 mmol) in THF (10 mL), $Pd(OAc)_2$ (0.033 g, 0.15 mmol) was added under a positive flow of argon.This was followed by addition of aq potassium fluoride (0.348 g, 6 mmol in 3 mL water) solution and PMHS (0.19 mL, 3.15 mmol) and the reaction mixture was stirred for the appropriate time (Table 2). The flask was opened to the air and upon the consumption of starting material, it was stirred with alumina, and filtered through a pad of celite. The organic layer was diluted with water and the aq layer was extracted with ethyl acetate (3x10mL). The combined organic layer was washed with aq 10% sodium chloride solution (2x10 mL), dried (Na_2SO_4) and concentrated under reduced pressure. The residue was purified by silica gel chromatography using EtOAc: hexane (40:60). The expected fractions were pooled, the solvent was evaporated under reduced pressure,and

dried under vacuum to obtain a white powder **5g** (0.62g, 82%). ^{1}H NMR (500 MHz, $CDCl_3$) δ 8.64 (dt, 1H), 8.24 (s, 1H), 8.03 (d, J 7.9 Hz, 1H), 7.82 (td, J 7.7, 1.8 Hz, 1H), 7.51 (t, J 7.8 Hz, 1H), 7.41 – 7.36 (m, 2H), 7.20 (t, J 7.6 Hz, 1H), 7.10 (dd, J 8.2, 0.8 Hz, 1H), 3.86 (q, J 6.5 Hz, 1H), 1.79 (d, J 6.5 Hz, 3H). ^{13}C NMR (126 MHz, $CDCl_3$) δ 172.09 (s), 167.82 (s), 156.78 (s), 148.88 (s), 138.18 (s), 136.72 (s), 131.72 (s), 131.43 (s), 126.88 (s), 124.40 (s), 124.22 (s), 123.29 (s), 121.00 (s), 58.93 (s), 17.00 (s). HRMS (ESI/ITTOF) *m/z*: [M + H]+ Calcd for $C_{16}H_{13}N_3O$ 252.1131; found 252.1113.

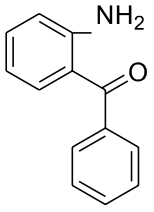
5-(2-Fluorophenyl)-2-oxo-2,3-dihydro-1*H*-benzo[*e*][1,4]diazepin-3-yl acetate(5h)



5h

A round bottom flask was charged with 7-bromo-5-(2-fluorophenyl)-2-oxo-2,3-dihydro-1*H*- benzo[*e*][1,4]diazepin-3-yl acetate **4h** (1g, 2.5 mmol), THF (10 mL), and the $Pd(OAc)_2$ (0.028 g, 0.125 mmol) was added to the stirred solution under a positive flow of argon. Then aq potassium fluoride (0.291g, 5 mmol in 2mL water) solution and PMHS (0.16 mL, 2.65 mmol) were added.The mixture, which resulted, was stirred for the time mentioned in Table 2. The flask was opened to the air upon the consumption of starting material, and stirred with alumina. It was then filtered through a pad of celite. The organic layer was diluted with water and the aq layer was extracted with ethyl acetate (3x10 mL). The combined organic layers were washed with an aq 10% sodium chloride solution (2x10 mL), dried (Na_2SO_4),and concentrated under reduced pressure. The residue was purified by silica gel chromatography using EtOAc: hexane (40:60). The expected fractions were collected, evaporated, and dried under vacuum to obtain a light yellow powder **5h** (0.58g, 73%). ^{1}H NMR (500 MHz, CDCl3) δ 8.92 (s, 1H), 7.68 (td, J 7.5, 1.4 Hz, 1H), 7.56 (t, J 7.7 Hz, 1H), 7.51 – 7.46 (m, 1H), 7.29 (t, J 5.2 Hz, 2H), 7.25 –
7.17 (m, 2H), 7.08 (t, 1H), 6.04 (s, 1H), 2.36 (s, 3H). ^{13}C NMR (126 MHz, CDCl3) δ 170.40 (s), 164.11 (s), 160.56 (d, J 252.6 Hz), 136.35 (s), 132.60 (s), 132.51 (s), 132.44 (s), 131.84 (d, J 1.6 Hz), 129.82 (s), 128.29 (s), 126.74 (d, J 12.0 Hz), 124.47 (s), 124.37 (d, J 3.6 Hz), 121.72 (s), 116.17 (d, J 21.5 Hz), 84.54 (s), 21.20 (s).). HRMS (ESI/ITTOF) *m/z*: [M + H]+ Calcd for $C_{17}H_{13}N_2O_3F$ 313.0983; found 313.0964.

(2-Aminophenyl)(phenyl)methanone (7a)

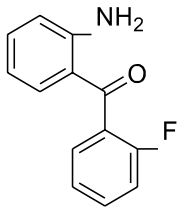


7a

To a solution of (2-amino-5-bromophenyl)(phenyl)methanone **6a**, (1g, 3.62 mmol) in THF (10 mL), $Pd(OAc)_2$ (0.04 g, 0.18 mmol) and aq potassium fluoride(0.42g, 7.25 mmol in 3mL water) solution were added under a positive flow of argon. Then PMHS (0.8 mL, 14.4 mmol) was added dropwise and the mixture was then stirred for the required time (see Table 3). At the end of the reaction the flask was open to the air; then the reaction

mixture was stirred with alumina and filtered through celite. The aq layer was extracted with ethyl acetate (2x 10 mL); and the combined organic layer was washed with an aq 10 % NaCl solution (3x10 mL). The organic layer was dried (Na_2SO_4) and concentrated under reduced pressure. The gummy greenish mass, which resulted, was then purified on silica gel (25g) chromatography using EtOAc: hexane (10:90). The appropriate fractions were collected, and the solvents were removed under reduced pressure.Then the residue was dried under vacuum at 35-40^oC for 2-3 hours to provide a white powder **7a** (0.63g, 88% yield). ^1H NMR (500 MHz, CDCl3) 1H NMR (500 MHz, CDCl3) δ 7.67 (d, J 7.3 Hz, 2H), 7.55 (t, J 7.3 Hz, 1H), 7.48 (t, J 6.7 Hz, 3H), 7.32 (t, J 7.5 Hz, 1H), 6.77 (d, J 8.2 Hz, 1H), 6.63 (t, J 7.5 Hz, 1H), 6.10 (s, 2H). ^{13}C NMR (126 MHz, CDCl3) δ 199.09 (s), 150.86 (s), 140.11 (s), 134.59 (s), 134.24 (s), 131.06 (s), 129.13 (s), 128.09 (s), 118.22 (s), 117.05 (s), 115.57 (s). HRMS (ESI/ITTOF) *m/z*: $[M + H]^+$Calcd for $C_{13}H_{11}NO$ 198.0913; found 198.0903.

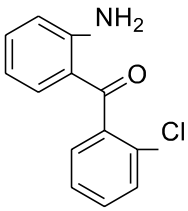
(2-Aminophenyl)(2-fluorophenyl)methanone (7b)



7b

The (2-amino-5-bromophenyl)(2-fluorophenyl) methanone **6b** (1g, 3.34 mmol), and tetrahydrofuran (8 mL) were charged to a round bottom flask. To this solution $Pd(OAc)_2$ (0.04 g, 0.18 mmol) was added under a positive pressure of argon. Then addition of aq. potassium fluoride (0.357g, 6.68mmol in 2mL water) solution was added to the mixture and this was followed by dropwise addition of PMHS (0.21 mL, 3.5mmol), which resulted in a greenish color. The reaction mixture was opened to the air after consumption of starting material. The reaction mixture was then stirred with alumina and filtered through celite. The aq layer was extracted with ethyl acetate (3x10 mL) and the combined organic layer was washed with aq10% NaCl (2x20 mL) solution. It was then dried (Na_2SO_4) and purified on a silica gel column using EtOAc: hexane (10:90). The solvents were removed and the solid residue was dried under high vacuum to afford a yellow powder **7b**(0.54g, 73% yield). ^1H NMR (500 MHz, CDCl3) δ 7.51 – 7.46 (m, 1H), 7.44 (ddd, 1H), 7.37 – 7.30 (m, 2H), 7.26 (t, J 7.5 Hz, 1H), 7.17 (t, J 9.0 Hz, 1H), 6.74 (d, J 8.3 Hz, 1H), 6.60 (t, J 7.6 Hz, 1H), 6.41 (s, 2H). ^{13}C NMR (126 MHz, CDCl3) δ 195.34 (s), 159.04 (d, $^1J_{C-F}$ = 249.6 Hz), 151.15 (s), 135.07 (s), 134.55 (d, $^5J_{C-F}$ = 1.6 Hz), 131.71 (d, $^3J_{C-F}$ = 8.1 Hz), 129.71 (d, $^3J_{C-F}$= 3.5 Hz), 128.71 (d, $^2J_{C-F}$ = 16.6 Hz), 124.13 (d, $^4J_{C-F}$= 3.4 Hz), 118.07 (s), 116.95 (s), 116.04 (d, $^2J_{C-F}$ = 21.6 Hz), 115.78 (s).). HRMS (ESI/ITTOF) *m/z*: $[M + H]^+$Calcd for $C_{13}H_{10}NOF$ 216.0819; found 216.0798.

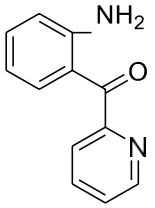
(2-Aminophenyl)(2-chlorophenyl)methanone (7c)



7c

The (2-amino-5-bromophenyl)(2-chlorophenyl)methanone **6c** (1g, 3.21 mmol) was dissolved in THF (10mL) and $Pd(OAc)_2$ (0.036 g, 0.161 mmol) was added under a positive pressure of argon to the solution with vigorous stirring. Then an aq potassium fluoride (0.372g, 6.42mmol in 3mL water) solution was added and this was followed by addition of PMHS (0.2mL, 3.37mmol). This process resulted in a bluish colored solution. At the end of the reaction (TLC) the flask was opened to the air, and stirred with alumina and filtered through celite. The aq layer was extracted with ethyl acetate(3x10 mL) and the combined organic layer was washed with a 10% aq NaCl solution (2x20mL). It was then dried (Na_2SO_4) and purified by silica gel chromatography using EtOAc: hexane (10:90). The solvents were removedunder reduced pressure and the residue was dried under high vacuum to afford a yellow powder **7c**(0.53g, 71% yield).^{1}H NMR (500 MHz, $CDCl_3$) δ 7.47 (dd, J 7.9, 1.0 Hz, 1H),
7.41 (td, J 7.6, 2.0 Hz, 1H), 7.37 (td, J 7.3, 1.3 Hz, 1H), 7.34 (dd, J 7.5, 1.8 Hz, 1H), 7.30 (dt, J 12.9, 3.6 Hz, 1H), 7.19 (dd, J 8.1, 1.4 Hz, 1H), 6.74 (dd, J 8.3, 0.5 Hz, 1H), 6.56 (td, 1H), 6.48 (s, 2H). ^{13}C NMR (126 MHz, $CDCl_3$) δ 197.28 (s), 151.42 (s), 139.85 (s), 135.23 (s), 134.68 (s), 130.71 (s), 130.33 (s), 129.85 (s), 128.42 (s), 126.63 (s), 117.43 (s), 117.00 (s), 115.78 (s). HRMS (ESI/ITTOF) *m/z*: $[M + H]^+$Calcd for $C_{13}H_{10}NOF$ 232.0524; found 232.0506.

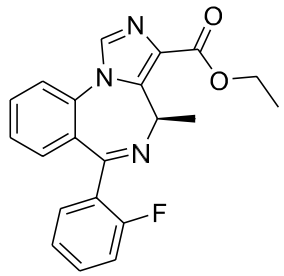
(2-Aminophenyl)(pyridin-2-yl)methanone (7d)



7d

A round bottom flask was charged with (2-amino-5-bromophenyl) (pyridin-2-yl) methanone **6d**(1g, 3.6mmol), as well as THF (10mL), and the flask was purged with argon. Palladium acetate (0.04 g, 0.18 mmol) was then added under an argon atmosphere and this was followed by the addition of aq potassium fluoride (0.419g, 7.2mmol in 4mL of water) solution. Then PMHS (0.23mL, 3.78mmol) was added dropwise to the reaction mixture, which resulted in a deep greenish colored solution. The reaction mixture was then stirred for the required time(see Table 3), and the round bottom flask was opened to the air at the end of the reaction. Then 2 g of alumina was added to the reaction flask and it was stirred for 5 min. The reaction mixture was then filtered through a pad of celite.Water and ethyl acetate was added to the filtrate. The layers were separated, and the aq layer was extracted with ethyl acetate (3x10mL) and the combined organic layer was washed with an aq 10% NaCl solution (2x10mL). It was then dried (Na_2SO_4) and purified by silica gel chromatography using EtOAc: hexane (10:90). The solvents were removed under reduced pressure and the solid residue was dried under high vacuum to afford a yellow powder**7d** (0.50g, 69% yield).^{1}H NMR (500 MHz, $CDCl_3$) δ 8.70 (ddd, J 4.8, 1.7, 0.9 Hz, 1H), 7.86 (td, J 7.7, 1.7 Hz, 1H), 7.76 (dt, J 7.8, 1.1 Hz, 1H), 7.65 (dd, J 8.2, 1.5 Hz, 1H), 7.43 (ddd, J 7.6, 4.8, 1.2
Hz, 1H), 7.30 (ddd, J 8.5, 7.0, 1.6 Hz, 1H), 6.73 (dd, J 8.4, 0.8 Hz, 1H), 6.61 (ddd, J 8.1, 7.1, 1.1 Hz, 1H), 6.32 (s, 1H).^{13}C NMR (126 MHz, $CDCl_3$) δ 196.04 (s), 157.52 (s), 151.83 (s), 148.46 (s), 136.89 (s), 135.03 (s), 134.81 (s), 124.95 (s), 123.88 (s), 117.03 (s), 116.78 (s), 115.57 (s).). HRMS (ESI/ITTOF) *m/z*: $[M + H]^+$Calcd for $C_{12}H_{10}N_2O$ 199.0866; found 199.0844.

Ethyl (*R*)-6-(2-fluorophenyl)-4-methyl-4*H*-benzo[*f*]imidazo[1,5-*a*][1,4]diazepine-3-carboxylate(9a)



9a

The $Pd(OAc)_2$ (0.029 g, 0.13 mmol) was added under a positive flow of argon to a stirred solution of (ethyl(R)-8-bromo-6-(2-fluorophenyl)-4-methyl-4*H*-benzo[*f*]imidazo[1,5-*a*][1,4]diazepine-3 carboxylate **8a** (1g, 2.26 mmol) in THF (10 mL). This addition was followed by addition of aqpotassium fluoride (0.262g, 4.52 mmol in 3mL water) solution and PMHS (0.14 mL, 2.37 mmol). This reaction mixture was stirred for 2hr at rt, and then the flask was opened to the air upon the consumption of starting material (TLC). The mixture was stirred with alumina, and filtered through a pad of celite. The organic layer, which resulted, was diluted with water and the aq layer was extracted with ethyl acetate (3x10 mL). The combined organic layer was washed with an aq 10% sodium chloride solution (2x10 mL), dried (Na_2SO_4),and concentrated under reduced pressure. The residue was purified on a silica gel column using EtOAc: hexane (50:50).^{1}H NMR (500 MHz, CDCl3) δ 7.93 (d, J 14.8 Hz, 1H),
7.72 (d, J 7.9 Hz, 1H), 7.60 (s, 2H), 7.47 (dd, J 11.8, 8.1 Hz, 1H), 7.44 – 7.30 (m, 2H), 7.25 (dt, J 11.6, 7.6 Hz, 1H),
7.04 (dt, J 14.7, 9.5 Hz, 1H), 6.71 (q, J 13.8, 6.8 Hz, 1H), 4.41 (q, J 15.9, 7.4 Hz, 2H), 1.42 (t, J 7.1, 1.4 Hz, 3H), 1.29 (d, J 7.5 Hz,3H). HRMS (ESI/ITTOF) *m/z*: $[M + H]^+$Calcd for $C_{12}H_{10}N_2O$ 364.1456; found 364.1437.

Adult schistosome mobility assays

S. mansoni cercariae (NMRI strain) infected Swiss Webster mice (female) were sacrificed after 49 days of infection by CO_2 euthanasia. The mesenteric vasculature of mice was dissected to recover adult schistosomes. The schistosomes were harvested and washed in DMEM (ThermoFisher cat. # 11995123) supplemented with HEPES (25mM), 5% v/v heat inactivated FCS (Sigma Aldrich cat. # 12133C) and Penicillin-Streptomycin (100 units/mL). 6 well dishes (4–5 male worms in 3mL media per well) were used to culture worms in the presence of various test compounds or DMSO (vehicle control) overnight (37 ˚C / 5% CO_2). Worms were imaged the following day to record movement phenotypes using a Zeiss Stemi 504 stereomicroscope and a CCD camera. 1 minute recordings were acquired at 4 frames per second and saved as a .TIFF stack, which was imported into ImageJ for analysis. All animal work was approved by IACUC committees at University of Wisconsin – Oshkosh and Madison (protocol numbers 000324-07-14-20 and V006353, respectively).

Acknowledgements

We wish to acknowledge the NIH for generous financial support (DA-043204, R01NS076517, R21AI146540). We also thank the Milwaukee Institute for Drug Discovery and the University of Wisconsin-Milwaukee's Shimadzu Laboratory for Advanced and Applied Analytical Chemistry for help with spectroscopy and the National ScienceFoundation, Division of Chemistry [CHE-1625735].

Supplementary Material

^{1}H NMR, ^{13}C NMR and HRMS spectra for all compounds are available in the Supplementary material file accompanying this paper.

References

1. Choi, H.Y. ; Chi., D.Y. *J. Am. Chem. Soc.* **2001**, *123*, 9202–9203. https://doi.org/10.1021/ja0164374
2. Ronald J.; RahaimJr.; Robert E.; MaleczkaJr. *Tetrahedron Lett.***2002,** *43*, 8823–8826. https://doi.org/10.1016/S0040-4039(02)02212-8
3. Nayal, O.S. ;Vinod Bhatt, V.; Sharma,S. ; Kumar, N. *J. Org. Chem.*, **2015**, *80*, 5912-5918. https://doi.org/10.1021/acs.joc.5b00156
4. Lawrence, N. J.; Drew, M. D.; Bushell, S. M. *J. Chem. Soc., Perkin Trans*. 1 **1999**, 3381–3391; https://doi.org/10.1039/A903662H
5. Pri-Bar, I.; Buchman, O. *J. Org. Chem*. **1986**, *51*, 734–735. https://doi.org/10.1021/jo00355a029
6. Viciu, M. S.; Grasa, G. A.; Nolan, S. P. *Organometallics* **2001**, *20*, 3607–3612. https://pubs.acs.org/doi/10.1021/om010332s
7. Viciu, M. S.; Kissling, R. M.; Stevens, E. D.; Nolan, S. P. *Org. Lett.* **2002**, *4*, 2229–2231. https://doi.org/10.1021/ol0260831
8. Grasa, G. A.; Viciu, M. S.; Huang, J.; Zhang, C.; Trudell, M. L.; Nolan, S. P. *Organometallics***2002**, *21*, 2866–2873 https://doi.org/10.1021/om020178p
9. Huang, T. H.; Chang, H. M.; Wu, M. Y.; Cheng, C. H. *J. Org. Chem*. **2002**, *67*, 99–105 https://doi.org/10.1021/jo010637g
10. Botella, L.; Najera, C. *Angew. Chem., Int. Ed.* **2002**, *41*, 179–181 https://doi.org/10.1002/1521-3757(20020104)114:1<187::AID-ANGE187>3.0.CO;2-A
11. Heidenreich, R. G.; Kohler, K.; Krauter, J. G. E.; Pietsch, J. *Synlett.* **2002**, 1118–1122 https://doi.org/10.1055/s-2002-32589
12. Kabalka, G. W.; Namboodiri, V.; Wang, L. *Chem.Commun.* **2001**, 775 https://doi.org/10.1039/B101470F
13. LeBlond, C. R.; Andrews, A. T.; Sun, Y.; Sowa, J. R., Jr. *Org. Lett.* **2001**, *3*, 1555–1557 https://doi.org/10.1021/ol015850d
14. Knutson, D.E.; Smith, J.L.; Ping, X. Jin, X.; Golani, L.K, Li, G. Rashid,F.; Mian, M.Y., Jahan,R., Sharmin, D., Cerne,R.; Cook, J.M.; Witkin, J. *ACS Chem. Neurosci.* **2020**, *11*, 2624−2637. https://doi.org/10.1021/acschemneuro.0c00295
15. McCusker, P.; Mian, M.Y.; Li, G., Olp, M.D.; Tiruveedhula, V.V.N.P.B.; Rashid, F.; Golani, L. K.; Verma, R. S.; Smith, B. C.; Cook, J. M.; Chan, J. D. *PLoS Negl Trop Dis* 13e0007826. https://doi.org/10.1371/journal. pntd.0007826
16. Chitsulo L, Engels D, Montresor A, Savioli L. *Acta Trop.* **2000**, *77*, 41–51 https://doi.org/10.1016/S0001-706X(00)00122-4
17. Engels D, Chitsulo L, Montresor A, Savioli L. *Acta Trop.* **2002**, *82*, 139–146.

https://doi.org/10.1016/S0001-706X(02)00045-1
18. Steinmann P, Keiser J, Bos R, Tanner M, Utzinger J. *Lancet Infect. Dis.***2006**, *6*, 411–425 https://doi.org/10.1016/S1473-3099(06)70521-7
19. King CH, Dickman K, Tisch DJ. *Lancet* **2005**, *365*, 1561–1569 https://doi.org/10.1016/S0140-6736(05)66457-4
20. Raso G, Vounatsou P, McManus DP, N'Goran EK, Utzinger J. *Int. J.Parasitol.* **2007**, *37*, 1491–1500. https://doi.org/10.1016/j.ijpara.2007.05.004
21. Baard AP, Sommers DK, Honiball PJ, Fourie ED, du Toit LE. *S. Afr. Med. J*. **1979**,*55*, 617–8. PMID: 380021.
22. Darragh A, Lambe R, Brick I, Downie WW. *Lancet*. **1981,***318*, 1042. https://doi.org/10.1016/S0140-6736(81)91233-2
23. Darragh A, Lambe R, Brick I, O'Boyle C. *Br. J. Clin. Pharmacol.***1982**,*14*, 871–2. https://doi.org/10.1111/j.1365-2125.1982.tb02052.x
24. O'Boyle C, Lambe R, Darragh A. *Eur J. Clin. Pharmacol*. **1985**, *29*, 105–8. https://doi.org/10.1007/bf00547377
25. Chandrasekhar S, Chandraiah L , Reddy R , Reddy MV. *Chemistry Letters*. **2000**, 29(7): 780–781 https://doi.org/10.1246/cl.2000.780
26. Nishiyama H, Park S, Itoh K. *Tetrahedron: Asymmetry*. **1992**, *3*, 1029–1034. https://doi.org/10.1016/S0957-4166(00)86036-X
27. Panda B, Sarker TK. *Tetrahedron Lett*., **2008**, 49, 6701-6703. https://doi.org/10.1016/j.tetlet.2008.09.071

This paper is an open access article distributed under the terms of the Creative Commons Attribution (CC BY) license (http://creativecommons.org/licenses/by/4.0/)

The Free Internet Journal for Organic Chemistry

Paper

Archive for Organic Chemistry

Arkivoc **2020**, part vii, 242-256

Design, synthesis and characterization of novel gamma-aminobutyric acid type A receptor ligands

Kamal P. Pandey,[#] Md Zubair Ahmed Khan,[#] Lalit K. Golani,[#] Prithu Mondal, Md Yeunus Mian, Farjana Rashid, V. V. N. Phani Babu Tiruveedhula, Daniel E. Knutson, Dishary Sharmin, Taukir Ahmed, Sepideh Rezvanian, Nicolas M. Zahn, Leggy A. Arnold, Jeffrey M. Witkin, and James M. Cook[*]

Department of Chemistry and Biochemistry, Milwaukee Institute for Drug Discovery, University of Wisconsin-Milwaukee, Milwaukee, Wisconsin 53211, USA

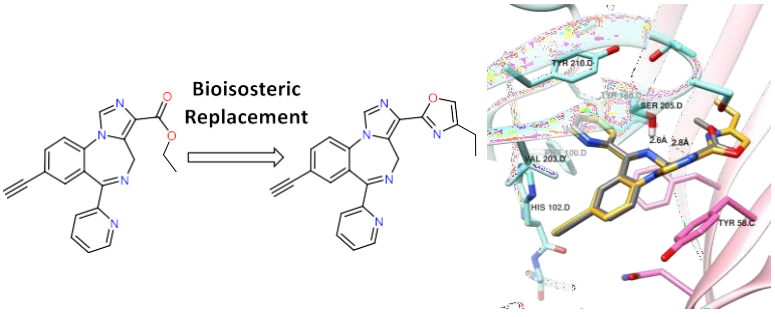
E-mail: capncook@uwm.edu

We dedicate this work to Professor Jan Bergman for his outstanding contributions to heterocyclic and organic chemistry as a whole

Received 10-15-2020 **Accepted** 11-11-2020 **Published on line** 12-02-2020

Abstract

Antinociceptive ligand HZ-166 is a $GABA_A$ $\alpha2/\alpha3$ receptor subtype-selective potentiator. It has been shown to exhibit anxiolytic-like effects in rodent and rhesus monkeys, as well as reduced sedative/ataxic liabilities. In order to improve the metabolic stability of HZ-166, the ethyl ester moiety was bioisosterically replaced with 2,4-disubstituted oxazoles and oxazolines. The new analogs of HZ-166 were synthesized, characterized, and evalutated for their biological activity and docked in the human full-length heteromeric $\alpha1\beta3\gamma2L$ $GABA_A$ receptor subtype CyroEM structure (6HUO). Importantly no sedation nor ataxia was observed on the rotorod for LKG-I-70 (**6**) or KPP-III-51 (**6c**) at 100 and 120 mg/kg, respectively. There was also no loss of righting response for either ligand.



Keywords: $GABA_A$ receptor, bioisosteres, subtype selectivity, metabolism, docking

Introduction

Benzodiazepines (BDZs) act on gamma-amino-butyric acid A ($GABA_A$) receptor ion channels and allosterically potentiate the influx of chloride ions through the channel, imparting a hyperpolarized state to the neuron. The pharmacological action exerted by a BZD is dependent on the discrete subunits of the receptor complex. Convergent evidence from transgenic animals and molecules with selectivity for the proteins required for ligand gating has suggested that $\alpha_1\beta_{2/3}\gamma_2$ comprised $GABA_A$ receptors mediate the tolerance and sedative/ataxic effects of the drugs, whereas the α2 and α3 $GABA_A$ receptors mediate the anticonvulsant anxiolytic and antinociceptive effects of ligands distinct from sedative/ataxic effects.[1-3] A compelling clinical opportunity exists in the development of selective α1-sparing subtype $GABA_A$ receptor ligands. These new ligands are expected to result in superior treatments for seizures and anxiety without causing amnesia, sedation, ataxia, or the propensity for addiction/dependence.

The ligand HZ-166 (ethyl 8-ethynyl-6-(pyridin-2-yl)-4*H*-benzo[*f*]imidazo[1,5-*a*][1,4]diazepine-3-carboxylate) is an α2/α3-subtype selective imidazodiazepine that has been reported to produce anticonvulsant activity at non-motor-impairing doses in both mice (maximal electroshock, and PTZ) and rats (maximal electroshock, PTZ, and hippocampal kindling).[4-9] Imidazodiazepines have very different structures as compared to BZDs diazepam, alprazolam and chlorodiazepoxide. However, the ester functionality of HZ-166 is metabolically labile creating reduced bioavailability when compare to the oxazole KRM-II-81 (5-(8-ethynyl-6-(pyridin-2-yl)- 4*H*-benzo[*f*]imidazo[1,5-*a*][1,4]diazepin-3-yl)oxazole).[6] It is well known that molecules which contain ester functional groups are susceptible to hydrolysis. Hydrolysis of the ester function results in the formation of the corresponding carboxylic acid and alcohol. Ester bioisosteres have been utilized commonly in drug design in order to render the ester topology metabolically stable with less adverse effects and provide better clinical candidates. Prior results indicated that replacement of ester functions by a five membered ring (oxazole or oxadiazole) significantly increased the *in vitro* and *in vivo* stability.[6, 10-12] Moreover, the efficacy at $GABA_A$ BZ receptors was enhanced, as compared to the corresponding ester ligands. Encouraged by the previous results, the substituted novel oxazoles and oxazolines were designed, synthesized and characterized.

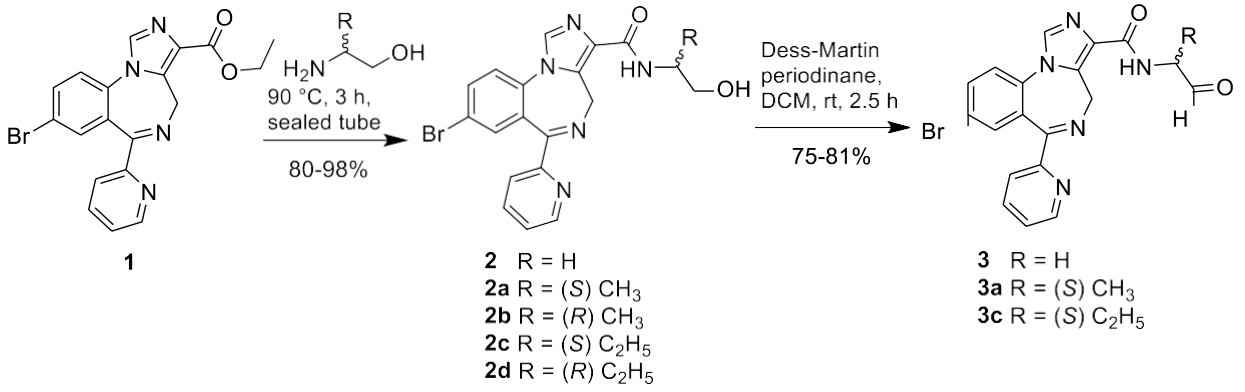
Results and Discussion

Chemistry

Recently our research group published an improved large-scale synthesis of the ethyl ester **1**.[13] The ester **1** was then heated to 90 °C with substituted ethanolamines (individually) in a sealed tube to afford α-hydroxy amides **2a-2d** that were purified by chromatography and in 80-98% yield. The α-hydroxy amides **2**, **2a** and **2c** were then oxidized by treatment with the Dess-Martin reagent to provide the corresponding α- acylaminoaldehydes **3**, **3a** and **3c**, which were purified by crystallization, in 75-81% yield (Scheme 1).

To afford oxazoles **4**, **4a** and **4c** from α-acylaminoaldehydes **3**, **3a** and **3c**, a cyclodehydration reaction (Robinson–Gabriel synthesis) was employed. At first, the Burgess reagent was employed to dehydrate analog **3**. The aldehyde **3** was dissolved in anhydrous THF and then the Burgess reagent was added after which the mixture was heated to reflux for 1.5 hours. The above reaction resulted in poor yields (20-24%, entries 1 and 2). The yield of the reaction was highest with newly purchased Burgess reagent and decreased with storage over time, as expected. The Wipf group had reported the Burgess reagent was oxidative but moisture sensitive; they also

obtained the best yields with freshly prepared Burgess reagent.[14] This group also demonstrated that 5-unsubtituted oxazoles can be synthesized from α-acylaminoaldehydes by using triphenylphosphine and iodine.[15] Unfortunately, reaction of triphenylphosphine and iodine gave a poor yield of the oxazole **4** (entry 3) from **3**. Examination of a publication by Morwick, T., *et. al*. indicated modified reaction conditions, in which triphenylphosphine and hexachloroethane were employed, to synthesize 5- unsubtituted oxazoles from α-acylaminoaldehydes looked promising.[16] Fortunately, the triphenylphosphine and hexachloroethane-mediated reaction conditions gave better yields of the oxazole **4** (entries 4 and 5, Scheme 2).

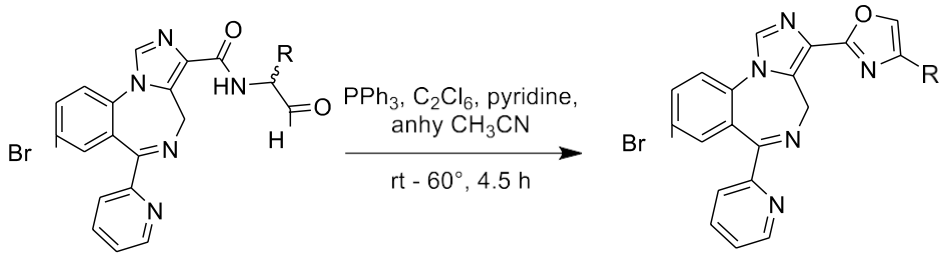


1

2 R = H
2a R = (*S*) CH_3
2b R = (*R*) CH_3
2c R = (*S*) C_2H_5
2d R = (*R*) C_2H_5

3 R = H
3a R = (*S*) CH_3
3c R = (*S*) C_2H_5

Scheme 1. Synthesis of α-acylaminoaldehydes **3**, **3a** and **3c**.



3 R = H
3a R = (*S*) CH_3
3c R = (*S*) C_2H_5

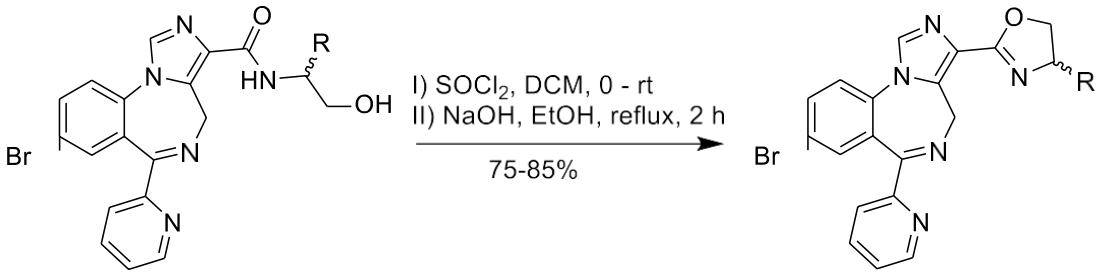
4 R = H
4a R = CH_3
4c R = C_2H_5

Entry	Reagents and conditions	Yield
1	Burgess reagent (2 eq), THF (anhyd), 1.5 h, reflux	20%
2	Burgess reagent (3 eq), THF (anhyd), 1.5 h, reflux	24%
3[15]	PPh_3 (2 eq), I_2 (2 eq), CH_3CN (anhyd), Et_3N (4.5 eq), 1.5 h, rt	28%
4[16]	PPh_3 (2 eq), C_2Cl_6 (2 eq), CH_3CN (anhyd), pyridine (4 eq), 2 h, 60 °C	55%
5[16]	PPh_3 (3 eq), C_2Cl_6 (3 eq), CH_3CN (anhyd), Et_3N (6 eq), 2 h, 0 °C-rt	71-74%

Scheme 2. Synthesis of oxazoles **4**, **4a** and **4c**.

The five membered heterocyclic oxazolines **5-5d** were also employed as bioisosteric replacement of carboxylic acid esters.[17] The α-hydroxy amides **2a-2d** reacted with thionyl chloride in dichloromethane to provide α-halo amides (not shown). The crude α-halo amides were then heated with sodium hydroxide in ethanol to afford the cyclized five-membered oxazolines **5-5d** in 75-85% yield (Scheme 3).[18-19] The optical rotation of the chiral oxazolines **5a-5d** were measured. The chiral oxazolines **5c** and **5d** were also evaluated by

chiral HPLC to detect any racemization. Examination of the data obtain indicated that there was no racemization (Supplementary material).

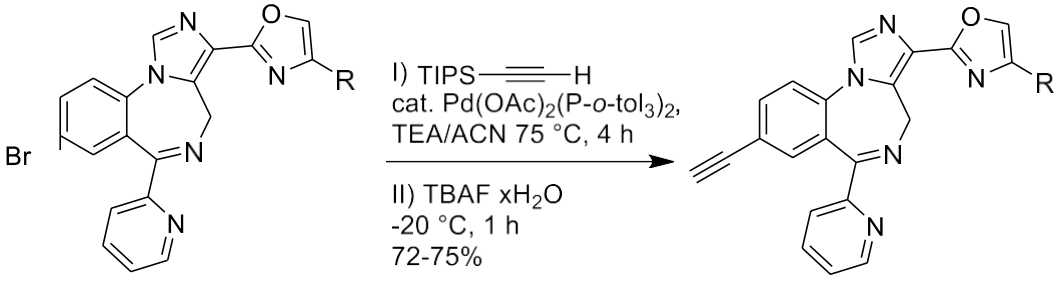


2 R = H
2a R = (*S*) CH_3
2b R = (*R*) CH_3
2c R = (*S*) C_2H_5
2d R = (*R*) C_2H_5

5 R = H
5a R = (*S*) CH_3
5b R = (*R*) CH_3
5c R = (*S*) C_2H_5
5d R = (*R*) C_2H_5

Scheme 3. Synthesis of oxazolines **5-5d.**

The aryl bromide moiety in imidazodiazepines **4** and **4c** was subjected to a copper-free Sonogashira coupling[20-21] to afford the triisopropylsilyl (TIPS) protected acetylenes (not shown). Finally, deprotection of the TIPS group with fluoride anion provided the 8-ethinyl imidazodiazepines **6** and **6c** in 72-75% yield (Scheme 4).



4 R = H
4c R = C_2H_5

6 R = H
6c R = C_2H_5

Scheme 4. Synthesis of 8-ethinyl imidazodiazepines **6** and **6c.**

Molecular modeling

To determine if the ester replacement in **4**, **4a**, **4c**, **5-5d**, **6** and **6c** could undergo a similar binding pose as HZ- 166, molecular docking was performed using AutoDock Vina 1.5.6.[22] A recently published CryoEM structure of the human full-length α1β3γ2L $GABA_A$ receptor ion complex with alprazolam (PDB: 6HUO) by Masiulis S. *et al*[23] was used. The molecular docking scores (binding affinity) of the designed ligands were determined and noted (Table 1). The binding poses of all ligands described here was found to be similar to HZ-166 (not shown). Illustrated in Figure 1 is the overlay of the binding pose of oxazole **6c** and HZ-166. The binding affinities (based on docking scores) of all ligands was found to be within ±1 kcal/mol difference from the lead compound HZ- 166 (-9 kcal/mol), which suggested all bioisosteres would bind with the receptor complex with a similar affinity to the lead compound ester HZ-166. The halogen substituted benzodiazepines e.g. diazepam and alprazolam undergo a halogen bond interaction with the carbonyl oxygen of the backbone of the α1His102 amino acid in the CryoEM structure (Figure

S1 in Supplementary material). Examination of the docking of 8-bromo substituted bioisosteres **4**, **4a**, **4c** and **5-5d** shows a similar halogen bond interaction with the carbonyl oxygen of the backbone of the α1His102 amino acid, but most of the docking software (including AutoDock Vina)[24] does not include halogen bonding in their scoring functions and, therefore, are unable to successfully predict the correct docking score of such complexes. Therefore, it was expected the ligands with bromine at position 8 would bind stronger with the α1β3γ2L $GABA_A$ receptor complex, as compared to the 8-ethinyl substituted ligands (**6** and **6c**) and would exert increased motor side effect. A general method for the molecular modeling is provided in the Supplementary material.

Table 1. Docking score (binding affinity) of bioisosteric ligands

Comp	Binding affinity kcal/mol	Comp	Binding affinity kcal/mol
4	-9	**5b**	-9.8
4a	-9.8	**5c**	-9.3
4c	-9.1	**5d**	-9.5
5	-9.6	**6**	-9.9
5a	-10	**6c**	-9.6

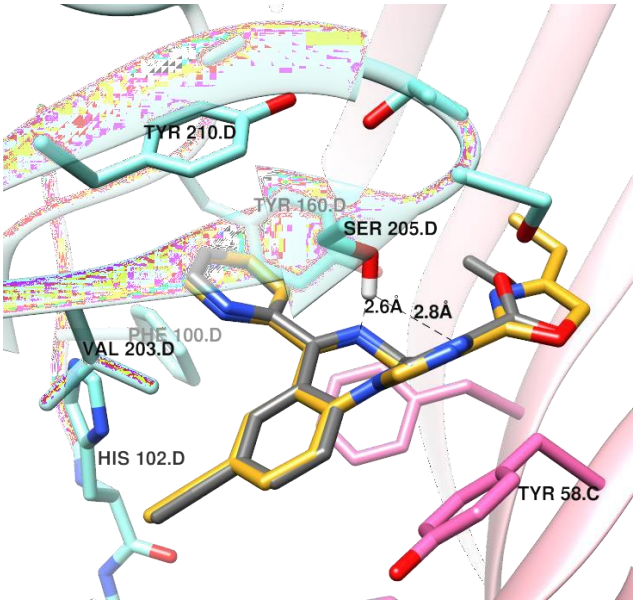


Figure 1. Overlay of the docked conformations of HZ-166 (gray) and **6c** (gold), in the complex with the α1β3γ2L $GABA_A$ receptor 6HUO at the $\alpha^+\gamma^-$ interface BZ binding site [α1 (represented as chain D, color: aquamriane) and γ2 ((represented as chain C, color: orchid)], dashed lines indicate hydrogen bonds.

Rotarod study

The ethinyl analog **6c** was evaluated for potential motor side effects. The motor/sensory study was carried out in CFW mice on a rotating rod (rotarod). The experiment was conducted by placing mice on the rotarod for a maximum of 3 minutes after oral administration of **6c** at doses of 40, 80 and 120 mg/kg. The mice were also observed for loss of righting reflex, an indication of undesired CNS effects. The mice exhibited no sedation nor ataxia, or loss of righting reflex; in contrast diazepam (5mg/kg) significantly impaired rotarod performance (Figure 2). The ligand (**6c**) exhibited sensorimotor steadiness at all three time-points, which indicated no sedative/ataxic effects (Figure 2). The rotarod experiment was performed according to the previously

published protocol.[25] In addition, **LKG-I-70** (**6**) was assayed on the rotarod and no sign of sedation nor ataxia was observed even up to 100 mg/kg. There was also no loss of righting response. Based on this early data both 1,3-oxazoles have potential clinical use. There is much work to be done to determine if this holds up in other cases.

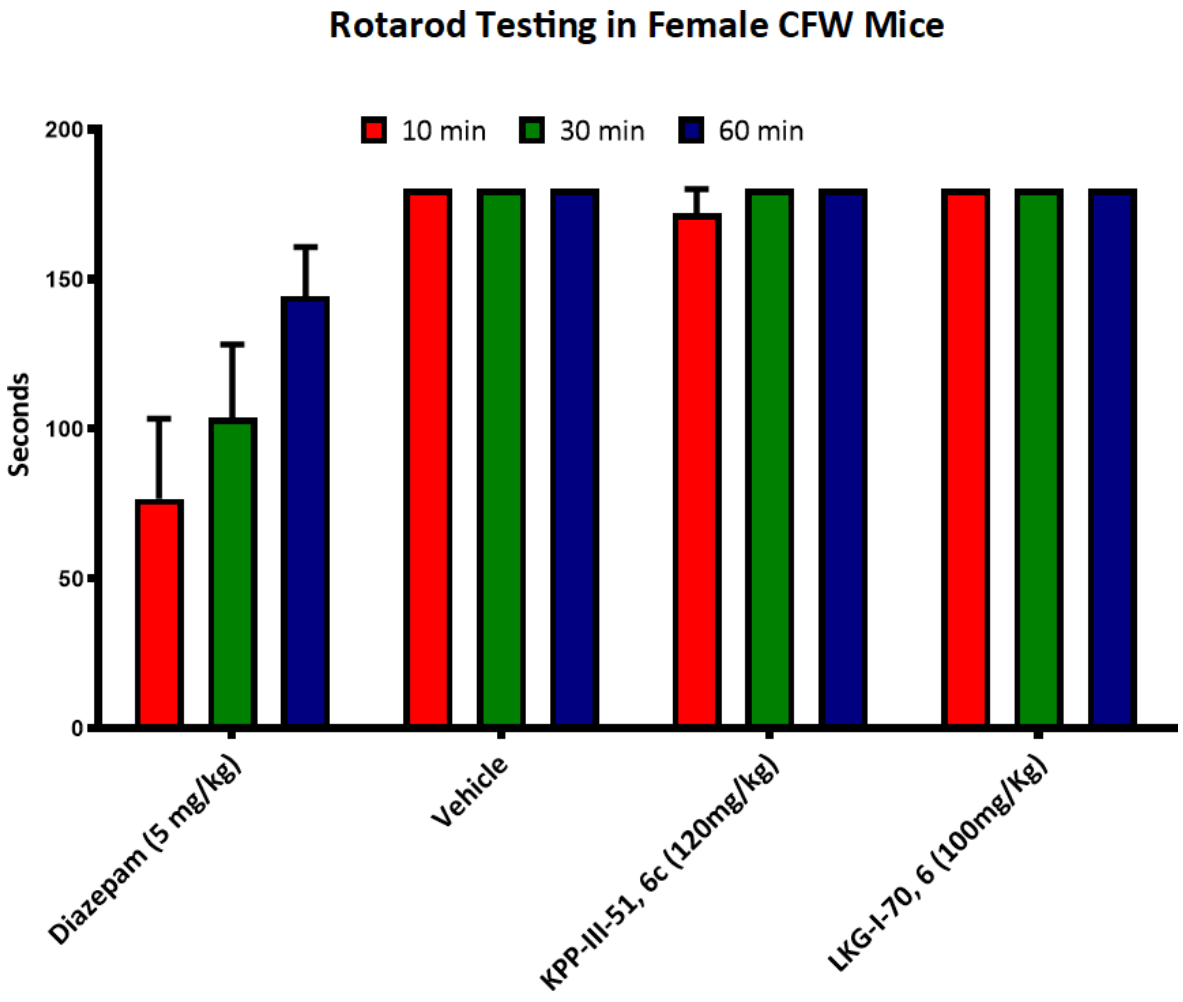


Figure 2. The rotarod study in CFW mice.

Conclusion

The 2-substituted novel oxazole and oxazoline analogs of α2/α3-subtype selective imidazodiazepine HZ-166 were synthesized and characterized. The new chiral oxazolines were analyzed for any racemization by measuring the optical rotation, as well as chiral HPLC; no racemization was detected. These new analogs (especially **6** and **6c**) should be more metabolically stable than HZ-166 with potentially less adverse effects and provide better clinical candidates. Examination of the molecular docking study suggests these molecules can bind with the α1β3γ2L $GABA_A$ receptor in a similar pose as HZ-166 but not as tightly. Ligands **6** and **6c"** were also evaluated for motor side effects (rotarod) and neither exhibited sedative nor ataxic effects. Therefore, 2- substituted oxazole and oxazoline bioisosteres of ethyl ester HZ-166 appear to be novel targets for the potential treatment of epilepsy, anxiety and neuropathic pain, by acting via selective positive allosteric

amplification of $GABA_A$ signaling via α2/α3-containing $GABA_A$ receptors. From examination of the data further modification of 8-bromo oxazolines **5-5d** to 8-ethinyl oxazolines is suggested and ongoing. We are also in the process of analyzing these new analogs in various animal models (anxiolytic, anticonvulsant and antinociception).

Experimental Section

General: For all reactions oven-dried round-bottom flasks or screw-cap test tubes were used, unless otherwise specified. All chemicals were purchased from commercial suppliers and purified by standard methods, if required. For all organic reactions anhydrous solvents were employed unless specified. The progress of reactions was visualized with TLC plates from Dynamic Adsorbents, Inc. under a UV light. The flash column chromatography was done for purification of some analogs on silica gel (230-400 mesh, Dynamic Adsorbents). The melting points were determined on a Stuart melting point SMP3 apparatus manufactured by Barloworld Scientific US Ltd. The CHIRALPAK® IB-N3 HPLC Column from Daicel Corporation was used for confirmation of enantiomeric excess. The ^{1}H and ^{13}C NMR spectra were obtained on Bruker Spectrospin 500 MHz or 300 MHz instruments in $CDCl_3$ and chemical shifts were reported in δ (ppm). Multiplicities are represented as follows: singlet (s), broad signal (br), doublet (d), triplet (t), quartet (q), dd (doublet of doublets), dt (doublet of triplets), td (triplet of doublets) and multiplet (m). The technique employed for HRMS was carried out on a LCMS-IT-TOF at the Milwaukee Institute for Drug Discovery in the Shimadzu Laboratory for Advanced and Applied Analytical Chemistry.

8-Bromo-*N*-(2-hydroxyethyl)-6-(pyridin-2-yl)-4*H*-benzo[*f*]imidazo[1,5-*a*][1,4]diazepine-3-carboxamide (2). The mixture of **1** (2 g, 4.8 mmol) and excess 2-aminoethan-1-ol (8 mL) was heated in a sealed tube at 90 °C for 20 h. Analysis by TLC (silica gel, EtOAc/hexane/methanol 2:1:0.5 and a few drops of 14% aq NH_4OH) indicated the disappearance of starting material and the appearance of a new spot (R_f = 0.3). After which the reaction mixture was cooled to rt and diluted by addition of EtOAC (30 mL) and water (20 mL). The organic layer was separated, and the aq layer was extracted with EtOAc (20 mL x 3). The combined organic layer was washed with brine (20 mL) and dried (Na_2SO_4). The solvent was removed under reduced pressure and the residue was purified by crystallization (20% MeOH in EtOAc) to afford **2** as light-yellow colored needle shape crystals (1.94 g, 94%). mp 265-266 °C (20% MeOH in EtOAc). ^{1}H NMR (500 MHz, $CDCl_3$): δ_H 8.61 – 8.56 (m, 1H), 8.09 (d, *J* 7.9 Hz, 1H), 7.92 (s, 1H), 7.83 – 7.76 (m, 2H), 7.57 (d, *J* 2.2 Hz, 1H), 7.48 (d, *J* 8.6 Hz, 1H), 7.39-7 (m, *J* 7.5, 4.8, 1.1 Hz, 1H), 6.07 (d, *J* 12.2 Hz, 1H), 4.47 – 4.43 (m, 2H), 4.17 (d, *J* 12.2 Hz, 1H), 4.11 (t, *J* 19.0, 6.0 Hz, 2H). ^{13}C NMR (126 MHz, $CDCl_3$): δc 167.0 (s), 160.1 (s), 156.3 (s), 148.7 (s), 136.9 (s), 135.4 (s),135.3 (s) 134.9 (s), 134.6 (s), 128.5 (S), 127.3 (s), 124.8 (s), 124.3 (s), 124.2 (s), 124.2 (s), 120.3(s), 64.9 (s), 54.7 (s), 45.0 (s). HRMS (ESI/IT-TOF) *m/z*: $[M + H]^+$ Calcd for $C_{19}H_{16}BrN_5O_2$ 426.0566; found 426.0543.

(*S*)-8-Bromo-*N*-(1-hydroxypropan-2-yl)-6-(pyridin-2-yl)-4*H*-benzo[*f*]imidazo[1,5-*a*][1,4]diazepine-3- carboxamide (2a). The carboxamide **2a** was prepared from **1** by following the same procedure described for synthesis of **2** from **1**. The (*S*)-2-aminopropan-1-ol (8 mL) was used instead of 2-aminoethan-1-ol. The crude residue was purified by crystallization from 15% MeOH in EtOAc to provide **2a** as light-yellow colored needle shape crystals (1.64g, 98%). mp 259-260 °C (20% MeOH in EtOAc). ^{1}H NMR (300 MHz, $CDCl_3$): δ_H 8.55 (d, *J* 4.7 Hz, 1H), 8.14 (d, *J* 7.9 Hz, 1H), 7.90 – 7.81 (m, 1H), 7.77 (dd, *J* 8.6, 2.7 Hz, 2H), 7.59 (d, *J* 2.3 Hz, 1H), 7.50 – 7.39 (m, 1H), 7.39 – 7.32 (m, 1H), 7.24 (d, *J* 7.2 Hz, 1H), 6.24 (d, *J* 10.8 Hz, 1H), 4.22 (qd, *J* 6.7, 3.2 Hz, 1H), 4.12 (s, 1H), 3.75 (d, *J* 9.3 Hz, 1H), 3.64 (dd, *J* 11.0, 6.4 Hz, 1H), 1.98 (s, 1H), 1.28 (d, *J* 6.8 Hz, 3H). ^{13}C NMR (75 MHz,

$CDCl_3$): δ_C 166.8 (s), 163.4 (s), 156.3 (s), 148.5 (s), 136.9 (s), 135.9 (s), 135.4 (s), 134.9 (s), 134.6 (s), 133.2 (s), 131.2 (s), 128.6 (s), 124.8 (s), 124.2 (s), 124.0 (s), 120.4 (s), 67.6 (s), 48.0 (s), 44.8 (s), 17.1(s). HRMS (ESI/IT-TOF) *m/z*: $[M + H]^+$ Calcd for $C_{20}H_{18}BrN_5O_2$ 440.0722; found 440.0694.

(*R*)-8-Bromo-*N*-(1-hydroxypropan-2-yl)-6-(pyridin-2-yl)-4*H*-benzo[*f*]imidazo[1,5-*a*][1,4]diazepine-3- carboxamide (2b). The carboxamide **2b** was prepared from **1** by following the same procedure described for synthesis of **2** from **1**. The (*R*)-2-aminopropan-1-ol (8 mL) was used instead of 2-aminoethan-1-ol. The crude residue was purified by crystallization from 15% MeOH in EtOAc to provide **2b** as light-yellow colored needle shape crystals (1.53 g, 85%). mp 261-262 °C (20% MeOH in EtOAc). ^{1}H NMR (300 MHz, $CDCl_3$): δ_H 8.56 (d, *J* 4.4 Hz, 1H), 8.15 (d, *J* 7.9 Hz, 1H), 7.83 (dd, *J* 7.7, 1.8 Hz, 1H), 7.77 (dd, *J* 8.5, 2.3 Hz, 2H), 7.59 (d, *J* 2.2 Hz, 1H), 7.43 (d, *J* 8.6 Hz, 1H), 7.39 – 7.32 (m, 1H), 7.23 (d, *J* 7.2 Hz, 1H), 6.26 (d, *J* 12.6 Hz, 1H), 4.22 (qd, *J* 6.9, 3.4 Hz, 1H), 4.13 (d, *J* 13.2 Hz, 1H), 3.75 (d, *J* 10.9 Hz, 1H), 3.64 (dd, *J* 11.1, 6.5 Hz, 1H), 1.87 (s, 1H), 1.28 (d, *J* 6.6 Hz, 3H). ^{13}C NMR (75 MHz, $CDCl_3$): δ_C 166.8 (s), 163.5 (s), 156.3 (s), 148.5 (s), 136.9 (s), 136.0 (s), 135.4 (s), 134.9 (s), 134.6 (s), 133.2 (s), 131.2 (s), 128.6 (s), 124.8 (s), 124.2 (s), 124.0 (s), 120.5 (s), 67.7 (s), 48.1 (s), 44.8 (s), 17.1 (s). HRMS (ESI/IT-TOF) *m/z*: $[M + H]^+$ Calcd for $C_{20}H_{18}BrN_5O_2$ 440.0722; found 440.0699.

(*S*)-8-Bromo-*N*-(1-hydroxybutan-2-yl)-6-(pyridin-2-yl)-4*H*-benzo[*f*]imidazo[1,5-*a*][1,4]diazepine-3- carboxamide (2c). The carboxamide **2c** was prepared from **1** by following the same procedure described for synthesis of **2** from **1**. The (*S)*-2-amino-1-butanol (8 mL) was used instead of 2-aminoethan-1-ol. The crude residue was purified by crystallization from 15% MeOH in EtOAc to provide **2c** as light-yellow colored needle shape crystals (1.35 g, 83%). mp 255-256 °C (20% MeOH in EtOAc). ^{1}H NMR (500 MHz, $CDCl_3$): δ_H 8.54 (d, *J* 3.6 Hz, 1H), 8.11 (d, *J* 7.9 Hz, 1H), 7.79 – 7.71 (m, 3H), 7.53 (s, 1H), 7.36 – 7.33 (m, 2H), 7.21 (d, *J* 7.8 Hz, 1H), 6.21 (t, *J* 12.5 Hz, 1H), 4.10 – 3.96 (m, 2H), 3.7 (1H), 3.65 – 3.62 (m, 1H), 1.66 (s, 1H), 1.59 – 1.53 (m, 1H), 0.98 (br, 3H). ^{13}C NMR (126 MHz, $CDCl_3$): δ_C 166.8 (s), 163.3 (s), 156.3 (s), 148.5 (s), 137.0 (s), 135.8 (s), 135.3 (s), 134.9 (s), 134.6 (s), 133.2 (s), 131.2 (s), 128.5 (s), 124.8 (s), 124.2 (s), 124.0 (s), 120.4 (s), 65.4 (s), 53.4 (s), 44.7 (s), 24.3 (s), 10.7 (s). HRMS (ESI/IT-TOF) *m/z*: $[M + H]^+$ Calcd for $C_{21}H_{20}BrN_5O_2$ 454.0879; found 454.0866.

(*R*)-8-Bromo-*N*-(1-hydroxybutan-2-yl)-6-(pyridin-2-yl)-4*H*-benzo[*f*]imidazo[1,5-*a*][1,4]diazepine-3- carboxamide (2d). The carboxamide **2d** was prepared from **1** by following the same procedure described for synthesis of **2** from **1**. The (*R*)-2-amino-1-butanol (8 mL) was used instead of 2-aminoethan-1-ol. The crude residue was purified by crystallization from 15% MeOH in EtOAc to provide **2d** as light yellow-colored needle shaped crystals (1.35 g, 80%). mp 250-251 °C (20% MeOH in EtOAc). ^{1}H NMR (500 MHz, $CDCl_3$): δ_H 8.56 – 8.51 (m, 1H), 8.11 (d, *J* 8.0 Hz, 1H), 7.83 – 7.70 (m, 3H), 7.55 (d, *J* 2.3 Hz, 1H), 7.34 (m, 2H), 7.23 (d, *J* 7.9 Hz, 1H), 6.23 (t, *J* 11.1 Hz, 1H), 4.10 (dd, *J* 9.3, 4.9 Hz, 1H), 4.03 – 3.92 (m, 1H), 3.76 (t, *J* 8.5 Hz, 1H), 3.66 (s, 1H), 3.46 (s, 1H), 1.68 (s, 1H), 1.59 (m, 1H), 0.98 (br, 3H). ^{13}C NMR (126 MHz, $CDCl_3$): δ_C 166.8 (s), 163.5 (s), 156.3 (s), 148.5 (s), 137.0 (s), 135.9 (s), 135.3 (s), 134.9 (s), 134.6 (s), 133.2 (s), 131.2 (s), 128.5 (s), 124.8 (s), 124.2 (s), 124.0 (s), 120.5 (s), 65.7 (s), 53.6 (s), 44.7 (s), 24.3 (s), 10.7(s). HRMS (ESI/IT-TOF) *m/z*: $[M + H]^+$ Calcd for $C_{21}H_{20}BrN_5O_2$ 454.0879; found 454.0861.

8-Bromo-*N*-(2-oxoethyl)-6-(pyridin-2-yl)-4*H*-benzo[*f*]imidazo[1,5-*a*][1,4]diazepine-3-carboxamide (3). To a solution of **2** (3 g, 7.04 mmol) in CH_2Cl_2 (70 mL), the Dess-Martin periodinane (3.5 g, 8.4 mmol) was added in one portion and the mixture was stirred at rt for 4 h. The reaction mixture was analyzed by TLC (silica gel, EtOAc/hexane/MeOH 2:1:0.5). After the completion of the reaction by TLC, the mixture was diluted with CH_2Cl_2 (100 mL) and quenched by addition of a sat. aq $NaHCO_3$ solution (80 mL) and a sat. solution of aq $Na_2S_2O_3$ (80 mL). The mixture was stirred for 20 min and the layers were separated. The aq layer was extracted with CH_2Cl_2 (100 mL x 2) and the combined organic layer was washed with brine (100 mL) and dried (Na_2SO_4). The solvent was removed under reduced pressure and the residue was purified by flash chromatography

(silica gel, 5% MeOH in CH_2Cl_2) to provide amide **3** as a yellow powder (2.4 g, 81%), which was employed directly in the next step without further characterization.

(*S*)-8-Bromo-*N*-(1-oxopropan-2-yl)-6-(pyridin-2-yl)-4*H*-benzo[*f*]imidazo[1,5-*a*][1,4]diazepine-3-carboxamide (3a). The carboxamide **3a** was prepared from **2a** by following the same procedure described for the synthesis of **3** from **2**. The carboxamide **3a**, so obtained, was purified by flash chromatography (silica gel, 5% MeOH in DCM) to afford **3a** as a white powder (2.83 g, 79%). ^{1}H NMR (500 MHz, $CDCl_3$): δ_H 9.67 (s, 1H), 8.57 (ddd, *J* 4.8, 1.8, 0.9 Hz, 1H), 8.15 (dt, *J* 7.9, 1.1 Hz, 1H), 7.87 – 7.80 (m, 2H), 7.78 (dd, *J* 8.6, 2.2 Hz, 1H), 7.61 (t, *J* 4.5 Hz, 2H), 7.45 (d, *J* 8.5 Hz, 1H), 7.37 (ddd, *J* 7.6, 4.8, 1.2 Hz, 1H), 6.25 (d, *J* 12.5 Hz, 1H), 4.63 (m, 1H), 4.14 (d, *J* 12.7 Hz, 1H)), 1.46 (d, *J* 7.4 Hz, 3H). ^{13}C NMR (75 MHz, $CDCl_3$): δ_C 199.5 (s), 166.8 (s), 162.7 (s), 156.3 (s), 148.6 (s), 136.9 (s), 136.1 (s), 135.4 (s), 134.9 (s), 134.6 (s), 133.3 (s), 130.7 (s), 128.6 (s), 124.8 (s), 124.2 (s), 124.0 (s), 120.5 (s), 54.0 (s), 44.8 (s), 14.6 (s). HRMS (ESI/IT-TOF) *m/z*: $[M + H]^+$ Calcd for $C_{20}H_{16}BrN_5O_2$ 438.0566; found 438.0549.

(*S*)-8-Bromo-*N*-(1-oxobutan-2-yl)-6-(pyridin-2-yl)-4*H*-benzo[*f*]imidazo[1,5-*a*][1,4]diazepine-3-carboxamide (3c). The carboxamide **3c** was prepared from **2c** by following the same procedure described for the synthesis of **3** from **2**. The carboxamide **3c**, so obtained, was purified by flash chromatography (silica gel, 5% MeOH in DCM) to afford **3c** as a white powder (2.67 g, 75%). ^{1}H NMR (500 MHz, $CDCl_3$): δ_H 9.68 – 9.62 (m, 1H), 8.54 (dt, *J* 4.7, 1.3 Hz, 1H), 8.15 – 8.09 (m, 1H), 7.88 – 7.71 (m, 3H), 7.63 – 7.55 (m, 2H), 7.43 (d, *J* 8.6 Hz, 1H), 7.34 (ddd, *J* 7.5, 4.8, 1.2 Hz, 1H), 6.22 (d, *J* 12.5 Hz, 1H), 4.57 (s, 1H), 4.11 (q, *J* 7.2 Hz, 2H), 1.78 (dt, *J* 14.4, 7.3 Hz, 1H), 1.05 – 0.96 (m, 3H). ^{13}C NMR (126 MHz, $CDCl_3$): δ_C 199.6 (s), 166.8 (s), 162.9 (s), 156.3 (s), 148.6 (s), 137.0 (s), 136.2 (s), 135.4 (s), 134.9 (s), 134.6 (s), 133.4 (s), 130.9 (s), 128.6 (s), 124.9 (s), 124.2 (s), 124.0 (s), 120.5 (s), 59.5 (s), 44.8 (s), 22.6 (s), 9.8 (s). HRMS (ESI/IT-TOF) *m/z*: $[M + H]^+$ Calcd for $C_{21}H_{18}BrN_5O_2$ 452.0722; found 452.0705.

2-(8-Bromo-6-(pyridin-2-yl)-4*H*-benzo[*f*]imidazo[1,5-*a*][1,4]diazepin-3-yl)oxazole (4). The hexachloroethane (2.4 g, 10.5 mmol) was dissolved in anhydrous acetonitrile (20 mL). The carboxamide **3** (1.5 g, 3.5 mmol) was dissolved in anhydrous acetonitrile (12 mL) and added to the above solution. The reaction mixture was cooled to 0 °C, and triethylamine (2.1 g, 21.2 mmol) was added dropwise. Triphenylphosphine (2.76 g, 10.5 mmol) was then added to the above solution in three portions. The ice bath was removed, and the reaction mixture was allowed to stir for 2 h at rt. The reaction progress was monitored by TLC (silica gel, EtOAc/hexane/ methanol 2:1:0.5 and a few drops of 14% aq. NH_4OH). After completion of reaction, water (20 mL) was added.

The aq layer was extracted with ethyl acetate (25 mL x 2). The combined organic layer was washed with brine (20 mL) and dried (Na_2SO_4). The solvents were removed under reduced pressure and the residue was purified by flash chromatography (silica gel, EtOAc/hexane 2:1, and 3% triethylamine) to afford oxazole **4** as a light yellow colored solid (1.0 g, 72%). A small amount of oxazole **4** crystallized in EtoAc for a melting point (white needle shaped crystals). mp 247-248 °C (crystallized from EtoAc). ^{1}H NMR (300 MHz, $CDCl_3$): δ_H 8.59 (d, *J* 4.1 Hz, 1H), 8.12 (d, *J* 7.9 Hz, 1H), 7.96 (s, 1H), 7.81 (t, *J* 8.7 Hz, 2H), 7.73 (s, 1H), 7.60 (s, 1H), 7.51 (d, *J* 8.6 Hz, 1H), 7.42 – 7.32 (m, 1H), 7.27 (s, 1H), 6.17 (d, *J* 12.7 Hz, 1H), 4.31 (d, *J* 12.7 Hz, 1H), 1.63 (s, 2H). ^{13}C NMR (126 MHz, $CDCl_3$): δ_C 165.8 (s), 156.9.0 (s), 155.1 (s), 148.3 (s), 143.7 (s), 137.6 (s), 136.5 (s), 135.8 (s), 136.2 (s), 134.6 (s), 134.1 (s), 133.9 (s), 130.1 (s), 127.2.0 (s), 125.9 (s), 125.1 (s), 122.9 (s), 119.6 (s), 44.2 (s). HRMS (ESI/IT-TOF) *m/z*: $[M + H]^+$ Calcd for $C_{19}H_{12}BrN_5O$ 406.0303; found 406.0296.

2-(8-Bromo-6-(pyridin-2-yl)-4*H*-benzo[*f*]imidazo[1,5-*a*][1,4]diazepin-3-yl)-4-methyloxazole (4a). The methyl oxazole **4a** was prepared from **3a** following the same procedure described for the synthesis of **4** from **3**. The methyl oxazole **4a**, so obtained, was purified by flash chromatography (silica gel, 2:1 EtOAc/ hexane, and 3% triethylamine) to afford **4a** as a light yellow colored solid (1.6 g, 71%). A small amount of oxazole **4a** crystallized in EtoAc for a melting point (white needle shaped crystals). mp 241-242 °C (crystallized from

EtoAc). ^{1}H NMR (500 MHz, $CDCl_3$): δ_H 8.57 (q, *J* 2.7 Hz, 1H), 8.08 (d, *J* 6.9 Hz, 1H), 7.95 (s, 1H), 7.82 (d, *J* 2.4 Hz, 1H), 7.79 (q, *J* 1.8 Hz, 1H), 7.77 (p, *J* 2.3 Hz, 1H), 7.72 – 7.65 (m, 1H), 7.57 (d, *J* 2.1 Hz, 1H), 7.50 (d, *J* 8.5 Hz, 1H), 7.36 (ddt, *J* 7.3, 4.9, 1.2 Hz, 2H), 6.14 (d, *J* 12.7 Hz, 1H), 4.27 (d, *J* 12.7 Hz, 1H), 2.25 (d, *J* 1.3 Hz, 3H). ^{13}C NMR (126 MHz, $CDCl_3$): δ_C δ 167.1 (s), 162.7 (s), 156.8 (s), 156.4 (s), 148.7 (s), 137.4 (s), 136.9 (s), 136.2 (s), 135.4 (s), 134.9 (s), 134.6 (s), 133.5 (s), 130.9 (s), 128.5 (s), 124.8 (s), 124.2 (s), 124.0 (s), 120.3 (s), 45.0 (s), 14.6(s). HRMS (ESI/IT-TOF) *m/z*: $[M + H]^+$ Calcd for $C_{20}H_{14}BrN_5O$ 420.0460; found 420.0444.

2-(8-Bromo-6-(pyridin-2-yl)-4H-benzo[f]imidazo[1,5-*a*][1,4]diazepin-3-yl)-4-ethyloxazole (KPP-III-34, 4c). The ethyl oxazole **4c** was prepared from **3c** following the same procedure described for the synthesis of **4** from **3**. The ethyl oxazole **4c**, so obtained, was purified by flash chromatography (silica gel, EtOAc/hexanes 2:1 and 3% triethylamine) to afford **4c** as a light-yellow colored powder (1.0 g, 74%). A small amount of oxazole **4c** was crystallized in EtOAc for a melting point (white needle shaped crystals). mp 246-247 °C (crystallized from EtoAc). ^{1}H NMR (500 MHz, $CDCl_3$): δ_H 8.59 – 8.52 (m, 1H), 8.06 (d, *J* 7.9 Hz, 1H), 7.96 (s, 1H), 7.86 – 7.73 (m, 2H), 7.55 (d, *J* 2.2 Hz, 1H), 7.48 (d, *J* 8.6 Hz, 1H), 7.40 (s, 1H), 7.37-7.32 (m, 1H), 6.14 (d, *J* 12.7 Hz, 1H), 4.25 (d, *J* 13.1 Hz, 1H), 2.62 (q, *J* 7.5 Hz, 2H), 1.27 (t, *J* 7.5 Hz, 3H). ^{13}C NMR (126 MHz, $CDCl_3$): δ_C 167.5 (s), 157.0 (s), 156.7 (s), 149.0 (s), 144.1 (s), 137.3 (s), 135.7 (s), 135.4 (s), 135.3 (s), 135.2 (s), 133.2 (s), 133.1 (s), 128.9 (s), 128.0 (s), 125.3 (s), 124.6 (s), 124.4 (s), 120.7 (s), 45.4 (s), 20.3 (s), 13.0 (s). HRMS (ESI/IT-TOF) *m/z*: $[M + H]^+$ Calcd for $C_{21}H_{16}N_5OBr$ 434.0616; found 434.0596.

2-(8-Bromo-6-(pyridin-2-yl)-4*H*-benzo[*f*]imidazo[1,5-*a*][1,4]diazepin-3-yl)-4,5-dihydrooxazole (5). The carboxamide **2** (500 mg, 1.2 mmol,) was dissolved in CH_2Cl_2 (50 mL) and the solution was cooled to 0 °C. Thionyl chloride (837 mg, 7.2 mmol) was added to the solution dropwise and then the reaction mixture was allowed to stir at rt for 16 h. After completion of the process the reaction mixture was cooled to 0 °C and a sat. aq solution of $NaHCO_3$ (100 mL) was added dropwise. The solution was allowed to stir for 30 min at 0 °C. The organic layer was separated and the aq layer was extracted with CH_2Cl_2 (3 × 10 mL). The combined organic layer was dried (Na_2SO_4). The solvent was evaporated, and a white solid was obtained directly for the next step without further purification. The white solid was dissolved in in ethanol (25 mL) and NaOH (300 mg, 7.5 mmol) was added. The solution obtained was refluxed for 2 hours. The reaction mixture was cool to rt and ethanol was removed under reduced pressure to afford a solid residue. The solid residue was dissolved in CH_2Cl_2 (100 mL) and washed with a saturated aq solution of $NaHCO_3$ (100 mL). The organic layer was separated and an aq layer was extracted with CH_2Cl_2 (3 × 100 mL). The combined organic layer was dried (Na_2SO_4). The organic solvent was removed and the solid residue obtained was purified by crystallization (5% MeOH in EtOAc) to afford compound **5** as white colored needle shaped crystals (407 mg, 85%). mp 230-231 °C (crystallized from 5% MeOH in EtOAc). ^{1}H NMR (300 MHz, $CDCl_3$): δ_H 8.61 – 8.56 (m, 1H), 8.09 (d, *J* 7.9 Hz, 1H),
7.92 (s, 1H), 7.83 – 7.76 (m, 2H), 7.57 (d, *J* 2.2 Hz, 1H), 7.48 (d, *J* 8.6 Hz, 1H), 7.39-7.35 (m, *J* 7.5, 4.8, 1.1 Hz, 1H), 6.07 (d, *J* 12.2 Hz, 1H), 4.47 – 4.43 (m, 2H), 4.18 (d, *J* 12.2 Hz, 1H), 4.11 (t, *J* 19.0, 6.0 Hz, 2H). ^{13}C NMR (126 MHz, $CDCl_3$): δ_C 167.0 (s), 160.1 (s), 156.3 (s), 148.6 (s), 136.9 (s), 135.5 (s), 135.3 (s), 134.9 (s), 134.8 (s), 134.6 (s), 128.5 (s), 127.2 (s), 124.8 (s), 124.2 (s), 124.0 (s), 120.3 (s), 67.3 (s), 54.7 (s), 45.0 (s). HRMS (ESI/IT-TOF) *m/z*: $[M + H]^+$ Calcd for $C_{19}H_{14}N_5OBr$ 435.0695; found 435.0691.

(*S*)-2-(8-Bromo-6-(pyridin-2-yl)-4*H*-benzo[*f*]imidazo[1,5-*a*][1,4]diazepin-3-yl)-4-methyl-4,5-dihydrooxazole 5a. The oxazoline **5a** was prepared from **2a** by following the same procedure described for **5** from **2**. The chloroalkane intermediate was purified by crystallization (15% DCM and hexane). The chloroalkane obtained was a light yellow colored solid. The ethyl oxazoline **5a**, so obtained, was purified by crystallization using 5% MeOH in EtOAc to afford compound **5a** as white colored needle shaped crystals (230 mg, 82%).

The characterization of chloroalkane intermediate: ^{1}H NMR (300 MHz, $CDCl_3$): δ_H 8.56 (d, *J* 4.5 Hz, 1H), 8.15 (d, *J* 7.9 Hz, 1H), 7.83 (dd, *J* 7.7, 1.7 Hz, 1H), 7.81 (s, 1H), 7.78 (dd, *J* 8.5, 2.2 Hz, 1H), 7.60 (d, *J* 2.2 Hz, 1H), 7.44 (d, *J*

8.6 Hz, 1H), 7.37 (dd, *J* 7.6, 4.9 Hz, 1H), 7.27 (d, *J* 10.2 Hz, 1H), 6.27 (d, *J* 12.4 Hz, 1H), 4.56 – 4.48 (m, 1H), 4.15 (d, *J* 12.5 Hz, 1H), 3.68 (dd, *J* 10.8, 3.9 Hz, 2H), 1.37 (d, *J* 6.7 Hz, 3H). ^{13}C NMR (75 MHz, $CDCl_3$): δ_C 166.8 (s), 162.1 (s), 156.3 (s), 148.6 (s), 136.9 (s), 136.0 (s), 135.4 (s), 134.9 (s), 134.6 (s), 133.2 (s), 131.3 (s), 128.6 (s), 124.8 (s), 124.2 (s), 124.0 (s), 120.4 (s), 49.2 (s), 45.1 (s), 44.8 (s), 18.1 (s). HRMS (ESI/IT-TOF) *m/z*: $[M + H]^+$ Calcd for $C_{20}H_{17}BrClN_5O$ 458.0383; found 458.0363.

The characterization of oxazoline **5a**: mp 199-200 °C (crystallized from 5% MeOH in EtOAc). $[\alpha]_D^{25}$ -40 (*c* 1.0, $CHCl_3$). ^{1}H NMR (300 MHz, $CDCl_3$): δ_H ^{1}H NMR (300 MHz, $CDCl_3$) δ 8.58 (d, *J* 4.9 Hz, 1H), 8.08 (d, *J* 7.9 Hz, 1H), 7.91 (d, *J* 1.0 Hz, 1H), 7.83 (d, *J* 7.6 Hz, 1H), 7.78 (ddd, *J* 8.5, 2.3, 1.0 Hz, 1H), 7.57 (dd, *J* 2.2, 1.0 Hz, 1H), 7.51 – 7.44 (m, 1H), 7.41 – 7.33 (m, 1H), 6.05 (d, *J* 12.6 Hz, 1H), 4.53 (s, 1H), 4.40 (h, *J* 6.9 Hz, 1H), 4.18 (d, *J* 12.7 Hz, 1H), 3.97 (t, *J* 7.7 Hz, 1H), 1.38 (d, *J* 6.5 Hz, 3H). ^{13}C NMR (75 MHz, $CDCl_3$): δ_C 167.1 (s), 159.0 (s), 156.4 (s), 148.8 (s), 136.9 (s), 135.3 (s), 135.2 (s), 135.0 (s), 134.9 (s), 134.6 (s), 128.5 (s), 127.4 (s), 124.8 (s), 124.2 (s), 124.0 (s), 120.3 (s), 73.9 (s), 61.9 (s), 45.1 (s), 21.5 (s). HRMS (ESI/IT-TOF) *m/z*: $[M + H]^+$ Calcd for $C_{20}H_{16}BrN_5O$ 422.0616; found 422.0608.

(*R*)-8-Bromo-*N*-(1-chloropropan-2-yl)-6-(pyridin-2-yl)-4*H*-benzo[*f*]imidazo[1,5-*a*][1,4]diazepine-3- carboxamide 5b. The oxazoline **5b** was prepared from **2b** by following the same procedure described for **5** from **2**. The chloroalkane intermediate was purified by crystallization (15% DCM and hexane). The chloroalkane obtained was a light yellow colored solid. The ethyl oxazoline **5b**, so obtained, was purified by crystallization using 5% MeOH in EtOAc to afford compound **5b** as white colored needle shaped crystals (224 mg, 80%).

The characterization of chloroalkane intermediate: ^{1}H NMR (300 MHz, $CDCl_3$): δ_H 8.56 (d, *J* 4.5 Hz, 1H), 8.15 (d, *J* 7.9 Hz, 1H), 7.83 (dd, *J* 7.7, 1.7 Hz, 1H), 7.81 (s, 1H), 7.76 (dd, *J* 8.5, 2.2 Hz, 1H), 7.60 (d, *J* 2.2 Hz, 1H), 7.44 (d, *J* 8.5 Hz, 1H), 7.37 (ddd, *J* 7.7, 4.8, 1.2 Hz, 1H), 7.27 (d, J 10.2 Hz, 1H), 6.28 (d, *J* 12.4 Hz, 1H), 4.52 (s, 1H), 4.15 (d, *J* 13.0 Hz, 1H), 3.68 (dd, *J* 10.8, 3.9 Hz, 2H), 1.37 (d, *J* 6.6 Hz, 3H). ^{13}C NMR (75 MHz, $CDCl_3$): δ_C 166.8 (s), 162.1 (s), 156.3 (s), 148.6 (s), 136.9 (s), 136.0 (s), 135.4 (s), 134.9 (s), 134.6 (s), 133.2 (s), 131.3 (s), 128.6 (s), 124.8 (s), 124.2 (s), 124.0 (s), 120.5 (s), 49.2 (s), 45.1 (s), 44.8 (s), 18.0 (s). HRMS (ESI/IT-TOF) *m/z*: $[M + H]^+$ Calcd for $C_{20}H_{17}BrClN_5O$ 458.0383; found 458.0367.

The characterization of oxazoline **5b**: mp 201-202 °C (crystallized from 5% MeOH in EtOAc). $[\alpha]_D^{25}$ +44 (*c* 1.0, $CHCl_3$). ^{1}H NMR (500 MHz, $CDCl_3$): δ_H 8.58 (d, *J* 4.0 Hz, 1H), 8.07 (d, *J* 7.9 Hz, 1H), 7.91 (s, 1H), 7.81 (td, *J* 7.8, 1.8 Hz, 1H), 7.77 (dd, *J* 8.6, 2.2 Hz, 1H), 7.56 (d, *J* 2.3 Hz, 1H), 7.47 (d, *J* 8.6 Hz, 1H), 7.37 (ddd, *J* 7.6, 4.8, 1.2 Hz, 1H), 6.05 (d, *J* 11.1 Hz, 1H), 4.53 (dd, *J* 7.2, 2.1 Hz, 1H), 4.45 – 4.35 (m, 1H), 4.17 (d, *J* 12.7 Hz, 1H), 4.00 – 3.91 (m, 1H), 1.37 (d, *J* 6.6 Hz, 3H). ^{13}C NMR (126 MHz, $CDCl_3$): δ_C 167.1 (s), 159.0 (s), 156.4 (s), 148.8 (s), 136.9 (s), 135.3 (s), 135.2 (s), 135.0 (s), 134.9 (s), 134.7 (s), 128.5 (s), 127.4 (s), 124.8 (s), 124.3 (s), 124.0 (s), 120.3 (s), 73.9 (s), 61.9 (s), 45.1 (s), 21.5 (s). HRMS (ESI/IT-TOF) *m/z*: $[M + H]^+$ Calcd for $C_{20}H_{16}BrN_5O$ 422.0616; found 422.0594.

(*S*)-2-(8-Bromo-6-(pyridin-2-yl)-4*H*-benzo[*f*]imidazo[1,5-*a*][1,4]diazepin-3-yl)-4-ethyl-4,5-dihydrooxazole (KPP-III-96B, 5c). The oxazoline **5c** was prepared from **2c** by following the same procedure described for **5** from **2**. The chloroalkane intermediate was purified by crystallization (15% DCM and hexane). The chloroalkane obtained was a light yellow colored solid. The ethyl oxazoline **5c**, so obtained, was purified by crystallization using 5% MeOH in EtOAc to afford compound **5c** as white colored needle shaped crystals (235 mg, 78%).

The characterization of chloroalkane intermediate: ^{1}H NMR (500 MHz, $CDCl_3$): δ_H 8.55 (dd, *J* 4.8, 1.8, 1H), 8.14 (dt, *J* 8.0, 1.1 Hz, 1H), 7.92 – 7.73 (m, 3H), 7.59 (d, *J* 2.2 Hz, 1H), 7.37-7.32 (m, 2H), 7.31 – 7.25 (m, 1H), 6.27 (d, *J* 12.2 Hz, 1H), 4.47 – 3.98 (m, 2H), 3.78 – 3.69 (m, 2H), 1.97 – 1.51 (m, 2H), 1.00 (d, *J* 9.4 Hz, 3H). ^{13}C NMR (126 MHz, $CDCl_3$): δ_C 166.8 (s), 162.4 (s), 156.2 (s), 148.5 (s), 137.0 (s), 136.0 (s), 135.4 (s), 134.9 (s), 134.6 (s), 133.2

(s), 131.2 (s), 128.5 (s), 124.9 (s), 124.23 (s) 124.0 (s), 120.5 (s), 50.5, 47.7 (s), 44.8 (s), 24.9 (s), 10.45 (s). HRMS (ESI/IT-TOF) *m/z*: [M+H] $^+$ Calcd for $C_{21}H_{19}N_5OClBr$ 472.0540; found 472.0531.

The characterization of oxazoline **5c:** mp 247-248 °C (crystallized from 5% MeOH in EtOAc). $[\alpha]_D^{25}$ -13.6 (*c* 1.0, $CHCl_3$). ^{1}H NMR (500 MHz, $CDCl_3$): δ_H 8.55 (d, *J* 4.1 Hz, 1H), 8.04 (d, *J* 6.4 Hz, 1H), 7.89 (s, 1H), 7.79 (td, *J* 7.7, 1.2 Hz, 1H), 7.74 (dd, *J* 8.6, 2.0 Hz, 1H), 7.53 (d, *J* 1.9 Hz, 1H), 7.44 (d, *J* 8.6 Hz, 1H), 7.34 (dd, *J* 6.8, 5.1 Hz, 1H), 6.03 (s, 1H), 4.47 (s, 1H), 4.22 (dd, *J* 15.5, 7.4 Hz, 1H), 4.15 (d, *J* 11.6 Hz, 1H), 4.03 (t, *J* 7.9 Hz, 1H), 1.82 – 1.73 (m, 1H), 1.59 (dt, *J* 13.8, 7.1 Hz, 1H), 1.01 (s, 3H). ^{13}C NMR (126 MHz, $CDCl_3$): δ_C 167.0 (s), 158.9 (s), 156.4 (s), 148.7 (s), 136.9 (s), 135.3 (s), 135.2 (s), 134.9 (s), 134.8 (s), 134.6 (s), 128.5 (s), 127.4 (s), 124.8 (s), 124.2 (s), 124.0 (s), 120.2 (s), 72.0 (s), 68.0 (s), 45.1 (s), 28.7 (s), 10.3 (s). HRMS (ESI/IT-TOF) *m/z*: [M + H]$^+$ Calcd for $C_{21}H_{18}BrN_5O$ 436.0773; found 436.0756.

(*R*)-2-(8-Bromo-6-(pyridin-2-yl)-4*H*-benzo[*f*]imidazo[1,5-*a*][1,4]diazepin-3-yl)-4-ethyl-4,5-dihydrooxazole (KPP-IV-09, 5d). The oxazoline **5d** was prepared from **2d** by following the same procedure described for **5** from **2**. The chloroalkane intermediate was purified by crystallization (15% DCM and hexane). The chloroalkane obtained was a light yellow colored solid. The ethyl oxazoline **5d**, so obtained, was purified by crystallization using 5% MeOH in EtOAc to afford compound **5d** as white colored needle shaped crystals (213 mg, 75%).

The characterization of chloroalkane intermediate: ^{1}H NMR (500 MHz, $CDCl_3$): δ_H 8.57 (dd, *J* 4.9, 1.7 Hz, 1H), 8.16 (d, *J* 7.9 Hz, 1H), 7.93 – 7.74 (m, 3H), 7.60 (d, *J* 2.2 Hz, 1H), 7.44 (d, *J* 8.6 Hz, 1H), 7.37 (dd, *J* 7.5, 4.8 Hz, 1H), 7.27 (d, *J* 13.5 Hz, 1H), 6.29 (d, *J* 12.5 Hz, 1H), 4.32 (m, 1H), 4.16 (d, *J* 12.1 Hz, 1H), 3.79 – 3.70 (m, 2H), 2.05 – 1.37 (m, 2H), 1.02 (t, *J* 7.0 Hz, 3H). ^{13}C NMR (126 MHz, $CDCl_3$): δ_C 166.7 (s), 162.4 (s), 156.2 (s), 148.5 (s), 137.0 (s), 136.0 (s), 135.4 (s), 134.9 (s), 134.6 (s), 133.2 (s), 131.4 (s), 128.8 (s), 124.6 (s), 124.2 (s), 124.0 (s), 120.5 (s), 50.5 (s), 47.7 (s), 44.81(s), 24.1 (s), 10.5 (s). HRMS (ESI/IT-TOF) *m/z*: [M+H] $^+$ Calcd for $C_{21}H_{19}N_5OClBr$ 472.0540; found 472.0538.

The characterization of oxazoline **5d**: mp 248-249 °C (crystallized from 5% MeOH in EtOAc). $[\alpha]_D^{25}$ -10.5 (*c* 1.0, $CHCl_3$). ^{1}H NMR (500 MHz, $CDCl_3$): δ_H 8.54 (d, *J* 4.7 Hz, 1H), 8.03 (d, *J* 7.8 Hz, 1H), 7.89 (s, 1H), 7.78 (td, *J* 7.8, 1.8 Hz, 1H), 7.73 (dd, *J* 8.7, 2.3 Hz, 1H), 7.53 (d, *J* 2.2 Hz, 1H), 7.44 (d, *J* 8.6 Hz, 1H), 7.33 (dd, *J* 7.6, 4.8 Hz, 1H), 6.03 (t, *J* 11.4 Hz, 1H), 4.46 (d, *J* 10.4 Hz, 1H), 4.25 – 4.12 (m, 2H), 4.01 (t, *J* 8.0 Hz, 1H), 1.76 (dt, *J* 14.4, 7.0 Hz, 1H), 1.59 (dt, *J* 13.9, 7.2 Hz, 1H), 1.00 (t, *J* 7.4 Hz, 3H). ^{13}C NMR (126 MHz, $CDCl_3$): δ_C 167.0 (s), 158.9 (s), 156.4 (s), 148.1 (s), 136.9 (s), 135.2 (s), 135.2 (s), 134.9 (s), 134.8 (s), 134.6 (s), 128.5 (s), 127.4 (s), 124.8 (s), 124.3 (s), 124.0 (s), 120.2 (s), 72.0 (s), 68.0 (s), 45.1 (s), 28.5 (s), 10.4 (s). HRMS (ESI/IT-TOF) *m/z*: [M + H]$^+$ Calcd for $C_{21}H_{18}BrN_5O$ 436.0773; found 436.0757.

2-(8-Ethynyl-6-(pyridin-2-yl)-4*H*-benzo[*f*]imidazo[1,5-*a*][1,4]diazepin-3-yl)oxazole (LKG-I-70, 6). A mixture of paladium (II) acetate (27.6 mg, 0.12 mmol), tri-*o*-tolylphosphine (75.2 mg, 0.25 mmol) and anhydrous acetonitrile (15 mL) was allowed to stir at rt for 15 min. The bromide **4** (1 g, 2.47 mmol), triisopropylsilylacetylene (541 mg, 1.97 mmol), triethylamine (724 mg, 7.15 mmol), and acetonitrile (10 mL) were added to the mixture. The reaction mixture was monitored by TLC (silica gel, EtOAc/hexane/methanol 2:1:0.5 and a few drops of triethylamine). The solvent was removed under reduced pressure and the residue was dissolved in CH_2Cl_2 (40 mL) and filtered through a bed of celite. The filtrate was washed with brine (20 mL) and dried (Na_2SO_4). The solvent was removed under reduced pressure and the residue was passed through a short pad of silica gel (silica gel, EtOAc/hexanes 3:1 with 3% triethylamine) to afford a light yellow colored solid (1.3 g, 93%), which was used for the next step without further purification. To the mixture of this solid (1.3 g, 2.9 mmol), THF (25 mL) and water (0.15 mL), TBAF xH_2O (0.9 g, 3.4 mmol, 1M in THF) was added dropwise at -10 °C and the mixture was allowed to stir at rt for 1 h. Analysis by TLC (Silica gel, EtOAc/hexane/MeOH 2:1:0.5 and a few drops of 14% aq. NH_4OH) indicated the disappearance of starting material. The reaction mixture was then quenched with water and diluted with EtOAc (30 mL). The organic

layer was separated and washed with brine (20mL) and dried (Na_2SO_4). The solvents were removed under reduced pressure and the residue was purified using flash column chromatography (silica gel, EtOAc/hexane 2:1 and 3% triethylamine) to yield a light yellow colored solid **LKG-I-70** or **6** (650 mg, 75%). Small amount of oxazole **6** was crystalize from EtoAc for melting point (white needle shape crystals). mp 215-216 °C (crystallized from EtOAc). ^{1}H NMR (500 MHz, $CDCl_3$): δ_H 8.57 (dd, *J* 5.0, 1.7 Hz, 1H), 8.08 (d, *J* 7.9 Hz, 1H), 8.01 (s, 1H), 7.81 (td, *J* 7.8, 1.8 Hz, 1H), 7.75 (dd, *J* 8.4, 1.9 Hz, 1H), 7.70 (s, 1H), 7.59 (d, *J* 8.4 Hz, 1H), 7.54 (d, *J* 1.8 Hz, 1H), 7.40-7.32 (m, 1H), 7.24 (s, 1H), 6.16 (s, 1H), 4.27 (s, 1H), 3.15 (s, 1H). ^{13}C NMR (126 MHz, $CDCl_3$): δ_C 167.6 (s), 157.2 (s), 156.3 (s), 148.6 (s), 137.9 (s), 137.1 (s), 136.3 (s), 135.6 (s), 135.4 (s), 135.0 (s), 133.1 (s), 128.1 (s), 127.3 (s), 127.0 (s), 124.9 (s), 124.2 (s), 122.9 (s), 121.1 (s), 81.7 (s), 79.5 (s), 44.9 (s). HRMS (ESI/IT- TOF) *m/z*: $[M + H]^+$ Calcd for $C_{21}H_{13}N_5O$ 352.1198; found 352.1169.

4-Ethyl-2-(8-ethynyl-6-(pyridin-2-yl)-4*H*-benzo[*f*]imidazo[1,5-*a*][1,4]diazepin-3-yl)oxazole (KPP-III-51, 6c). The ethinyl **6c** was prepared from **4c** by following the same procedure described for the synthesis of **4** from **3**. The ethinyl **6c**, so obtained was purified using flash column chromatography (silica gel, EtOAc/hexane 2:1 and 3% triethylamine) to yield a light yellow colored solid **6c** (382 mg, 72%). A small amount of oxazole **6c** was crystallized from EtOAc for a melting point (white needle shaped crystals).

The characterization of the TIPS protected **6c**: ^{1}H NMR (500 MHz, $CDCl_3$): δ_H 8.60 – 8.56 (m, 1H), 8.07 – 8.03 (m, 1H), 7.80 (td, *J* 7.7, 1.8 Hz, 2H), 7.72 (dd, *J* 8.3, 1.9 Hz, 1H), 7.53 (d, *J* 8.3 Hz, 1H), 7.47 (d, *J* 1.8 Hz, 1H), 7.40 (d, *J* 1.4 Hz, 1H), 7.36 (ddd, *J* 7.5, 4.8, 1.3 Hz, 1H), 6.21 – 6.04 (m, 1H), 4.25 (s, 1H), 2.62 (dd, *J* 7.5, 1.3 Hz, 2H), 1.27 (t, *J* 7.5 Hz, 3H), 1.10 (d, *J* 3.5 Hz, 21H). ^{13}C NMR (126 MHz, $CDCl_3$): δ_C 167.8 (s), 156.7 (s), 156.5 (s), 148.7 (s), 143.7 (s), 136.9 (s), 135.8 (s), 135.5 (s), 135 (s), 134.9 (s), 132.9 (s), 132.7 (s), 127.6 (s), 126.9 (s), 124.8 (s), 124.1 (s), 122.7 (s), 122.5 (s), 104.9 (s), 93.7 (s), 45.0 (s), 19.9 (s), 18.6 (s), 12.7 (s), 11.24 (s). HRMS (ESI/IT-TOF) *m/z*: $[M + H]^+$ Calcd for $C_{32}H_{37}N_5OSi$ 536.2846; found 536.2855.

The characterization of 8-ethinyl imidazodiazepine **6c**: mp 240-241 °C (crystallized from EtoAc). ^{1}H NMR (500 MHz, $CDCl_3$): δ_H 8.60 (d, *J* 4.8, 1.3 Hz, 1H), 8.08 (d, 1H), 8.01 (s, 1H), 7.83 (td, *J* 7.7, 1.8 Hz, 1H), 7.77 (dd, *J* 8.4, 1.9 Hz, 1H), 7.61 (d, 1H), 7.78 – 7.76 (dd, 1H), 7.43 (s, 1H), 7.4-7.32 (m, 1H), 6.18 (br, 1H), 4.29 (br, 1H), 3.17 (s, 1H), 2.65 (m, *J* 7.5, 1.2 Hz, 2H), 1.42 – 1.26 (t, 3H). ^{13}C NMR (126 MHz, $CDCl_3$): δ_C 167.0 (s), 156.0 (s), 156.4 (s), 148.0 (s), 143.1 (s), 137.7 (s), 136.2 (s), 135.7 (s), 135.4 (s), 134.9 (s), 132.8 (s), 132.7 (s), 127.5 (s), 126.9 (s), 124.8 (s), 123.1 (s), 122.8 (s), 121 (s), 81.1 (s), 78.8 (s), 45.0 (s), 19.9 (s), 12.6 (s). HRMS (ESI/IT-TOF) *m/z*: $[M + H]^+$ Calcd for $C_{23}H_{17}N_5O$ 380.1506; found 380.1478.

Acknowledgements

We wish to acknowledge the NIH for generous financial support (DA-043204, R01NS076517). We also thank the Milwaukee Institute for Drug Discovery and the University of Wisconsin-Milwaukee's Shimadzu Laboratory for Advanced and Applied Analytical Chemistry for help with spectroscopy and the National Science Foundation, Division of Chemistry [CHE-1625735].

Supplementary Material

Figure S1, Chiral column data of oxazolines **5c** and **5d**, ^{1}H NMR and ^{13}C NMR spectra for all new compounds are available in the Supplementary material file accompanying this paper.

References

[#] These authors contributed equally to this research

1. Rudolph, U.; Crestani, F.; Benke, D.; Brunig, I.; Benson, J. A.; Fritschy, J. M.; Martin, J. R.; Bluethmann, H.; Mohler, H. *Nature* **1999,** *401*, 796-800.
http://dx.doi.org/10.1038/44579.
2. McKernan, R. M.; Rosahl, T. W.; Reynolds, D. S.; Sur, C.; Wafford, K. A.; Atack, J. R.; Farrar, S.; Myers, J.; Cook, G.; Ferris, P.; Garrett, L.; Bristow, L.; Marshall, G.; Macaulay, A.; Brown, N.; Howell, O.; Moore, K. W.; Carling, R. W.; Street, L. J.; Castro, J. L.; Ragan, C. I.; Dawson, G. R.; Whiting, P. J. *Nature Neuroscience* **2000,** *3*, 587-592.
http://dx.doi.org/10.1038/75761.
3. Collinson, N.; Kuenzi, F. M.; Jarolimek, W.; Maubach, K. A.; Cothliff, R.; Sur, C.; Smith, A.; Otu, F. M.; Howell, O.; Atack, J. R.; McKernan, R. M.; Seabrook, G. R.; Dawson, G. R.; Whiting, P. J.; Rosahl, T. W. *J. Neurosci.* **2002,** *22*, 5572-5580.
https://dx.doi.org/10.1523/JNEUROSCI.22-13-05572.2002.
4. Witkin, J. M.; Smith, J. L.; Ping, X.; Gleason, S. D.; Poe, M. M.; Li, G.; Jin, X.; Hobbs, J.; Schkeryantz, J. M.; McDermott, J. S.; Alatorre, A. I.; Siemian, J. N.; Cramer, J. W.; Airey, D. C.; Methuku, K. R.; Tiruveedhula, V. V. N. P. B.; Jones, T. M.; Crawford, J.; Krambis, M. J.; Fisher, J. L.; Cook, J. M.; Cerne, R. *Neuropharmacology* **2018,** *137*, 332-343.
http://dx.doi.org/10.1016/j.neuropharm.2018.05.006.
5. Duke, A. N.; Meng, Z.; Platt, D. M.; Atack, J. R.; Dawson, G. R.; Reynolds, D. S.; Tiruveedhula, V. V. N. P. B.; Li, G.; Stephen, M. R.; Sieghart, W.; Cook, J. M.; Rowlett, J. K. *J. Pharmacol. Exp. Ther.* **2018,** *366*, 145-157. http://dx.doi.org/10.1124/jpet.118.249250.
6. Poe, M. M.; Methuku, K. R.; Li, G.; Verma, A. R.; Teske, K. A.; Stafford, D. C.; Arnold, L. A.; Cramer, J. W.; Jones, T. M.; Cerne, R.; Krambis, M. J.; Witkin, J. M.; Jambrina, E.; Rehman, S.; Ernst, M.; Cook, J. M.; Schkeryantz, J. M. *J. Med. Chem.* **2016,** *59*, 10800-10806. http://dx.doi.org/10.1021/acs.jmedchem.6b01332.
7. Li, G.; Golani, L. K.; Jahan, R.; Rashid, F.; Cook, J. M. *Synthesis* **2018,** *50*, 4124-4132. http://dx.doi.org/10.1055/s-0037-1610211.
8. Fischer, B. D.; Licata, S. C.; Edwankar, R. V.; Wang, Z. J.; Huang, S.; He, X.; Yu, J.; Zhou, H.; Johnson, E. M., Jr.; Cook, J. M.; Furtmüller, R.; Ramerstorfer, J.; Sieghart, W.; Roth, B. L.; Majumder, S.; Rowlett, J. K. *Neuropharmacology* **2010,** *59*, 612-618.
http://dx.doi.org/10.1016/j.neuropharm.2010.08.011.
9. Di Lio, A.; Benke, D.; Besson, M.; Desmeules, J.; Daali, Y.; Wang, Z. J.; Edwankar, R.; Cook, J. M.; Zeilhofer, H. U. *Neuropharmacology* **2011,** *60*, 626-632.
http://dx.doi.org/10.1016/j.neuropharm.2010.11.026.
10. Witkin, J. M.; Cerne, R.; Davis, P. G.; Freeman, K. B.; do Carmo, J. M.; Rowlett, J. K.; Methuku, K. R.; Okun, A.; Gleason, S. D.; Li, X.; Krambis, M. J.; Poe, M.; Li, G.; Schkeryantz, J. M.; Jahan, R.; Yang, L.; Guo, W.; Golani, L. K.; Anderson, W. H.; Catlow, J. T.; Jones, T. M.; Porreca, F.; Smith, J. L.; Knopp, K. L.; Cook, J. M. *Pharmacol. Biochem. Behav.* **2019,** *180*, 22-31. http://dx.doi.org/10.1016/j.pbb.2019.02.013.
11. Moerke, M. J.; Li, G.; Golani, L. K.; Cook, J.; Negus, S. S. *Behav. Pharmacol.* **2019,** *30*, 452-461. http://dx.doi.org/10.1097/fbp.0000000000000464.

12. Witkin, J. M.; Li, G.; Golani, L. K.; Xiong, W.; Smith, J. L.; Ping, X.; Rashid, F.; Jahan, R.; Cerne, R.; Cook, J. M.; Jin, X. *J. Pharmacol. Exp. Ther.* **2020,** *372*, 83-94. http://dx.doi.org/10.1124/jpet.119.260968.
13. Knutson, D. E.; Smith, J. L.; Ping, X.; Jin, X.; Golani, L. K.; Li, G.; Tiruveedhula, V.; Rashid, F.; Mian, M. Y.; Jahan, R.; Sharmin, D.; Cerne, R.; Cook, J. M.; Witkin, J. M. *ACS Chem. Neurosci.* **2020,** *11*, 2624-2637. http://dx.doi.org/10.1021/acschemneuro.0c00295.
14. Wipf, P.; Venkatraman, S. *Tetrahedron Lett.* **1996,** *37*, 4659-4662. http://dx.doi.org/10.1016/0040-4039(96)00918-5.
15. Wipf, P.; Miller, C. P. *J. Org. Chem.* **1993,** *58*, 3604-3606. http://dx.doi.org/10.1021/jo00066a004.
16. Morwick, T.; Hrapchak, M.; DeTuri, M.; Campbell, S. *Org. Lett.* **2002,** *4*, 2665-2668. http://dx.doi.org/10.1021/ol020092s.
17. Zhang, Y.-K.; Plattner, J. J.; Easom, E. E.; Jacobs, R. T.; Guo, D.; Sanders, V.; Freund, Y. R.; Campo, B.; Rosenthal, P. J.; Bu, W.; Gamo, F.-J.; Sanz, L. M.; Ge, M.; Li, L.; Ding, J.; Yang, Y. *J. Med. Chem.* **2015,** *58*, 5344-5354. http://dx.doi.org/10.1021/acs.jmedchem.5b00678.
18. Tosaki, S.-y.; Tsuji, R.; Ohshima, T.; Shibasaki, M. *J. Am. Chem. Soc.* **2005,** *127*, 2147-2155. http://dx.doi.org/10.1021/ja043770.
19. Gou, D. M.; Liu, Y. C.; Chen, C. S. *J. Org. Chem.* **1993,** *58*, 1287-1289. http://dx.doi.org/10.1021/jo00057a054.
20. Cassar, L. *Journal of Organometallic Chemistry* **1975,** *93*, 253-257. https://dx.doi.org/10.1016/S0022-328X(00)94048-8.
21. Dieck, H. A.; Heck, F. R. *J. of Organomet. Chem.* **1975,** *93*, 259-263. http://dx.doi.org/10.1016/S0022-328X(00)94049-X.
22. Trott, O.; Olson, A. J. *J. Comput. Chem.* **2010,** *31*, 455-461. http://dx.doi.org/10.1002/jcc.21334.
23. Masiulis, S.; Desai, R.; Uchański, T.; Serna Martin, I.; Laverty, D.; Karia, D.; Malinauskas, T.; Zivanov, J.; Pardon, E.; Kotecha, A.; Steyaert, J.; Miller, K. W.; Aricescu, A. R. *Nature* **2019,** *565*, 454-459. http://dx.doi.org/10.1038/s41586-018-0832-5.
24. Koebel, M. R.; Schmadeke, G.; Posner, R. G.; Sirimulla, S. *J. Cheminform.* **2016,** *8*, 27. http://dx.doi.org/10.1186/s13321-016-0139-1.
25. Li, G.; Stephen, M. R.; Kodali, R.; Zahn, N. M.; Poe, M. M.; Tiruveedhula, V. V. N. P. B.; Huber, A. T.; Schussman, M. K.; Qualmann, K.; Panhans, C. M.; Raddatz, N. J.; Baker, D. A.; Prevot, T. D.; Banasr, M.; Sibille, E.; Arnold, L. A.; Cook, J. M. *Arkivoc* **2018**, 158-182. http://dx.doi.org/10.24820/ark.5550190.p010.460.

This paper is an open access article distributed under the terms of the Creative Commons Attribution (CC BY) license (http://creativecommons.org/licenses/by/4.0/)

Contents lists available at ScienceDirect

Bioorganic & Medicinal Chemistry Letters

Rationalizing the binding and α subtype selectivity of synthesized imidazodiazepines and benzodiazepines at GABAA receptors by using molecular docking studies

Lalit K Golani [a,1], Md Yeunus Mian [a,1], Taukir Ahmed [a], Kamal P Pandey [a], Prithu Mondal [a], Dishary Sharmin [a], Sepideh Rezvanian [a], Jeffrey M Witkin [a,b], James M Cook [a,*]

[a] Department of Chemistry and Biochemistry, Milwaukee Institute of Drug Discovery, University of Wisconsin-Milwaukee, Milwaukee, WI, USA
[b] Laboratory of Antiepileptic Drug Discovery, St. Vincent's Hospital, Indianapolis, IN USA

ARTICLE INFO

Keywords:
γ-Aminobutyric acid type A receptor
Benzodiazepines
Halogen bond
Bioisostere Molecular docking
Protein ligand interactions

ABSTRACT

The pharmacological actions exerted by benzodiazepines are dependent on the discrete α protein subunits of the γ-aminobutyric acid type A receptor ($GABA_A$ R). Recent developments *via* a cryo-EM structure of the α1β3γ2L $GABA_A$ R ion channel provide crucial insights into ligand efficacy and binding affinity at this subtype. We investigated the molecular interactions of diazepam and alprazolam bound $GABA_A$ R structures (6HUP and 6HUO) to determine key binding interaction domains. A halogen bond between the chlorine atoms of diazepam and alprazolam with the group on the backbone of the α1 histidine amino acid 102 is important to the positive allosteric modulatory actions of diazepam and alprazolam in the α1β3γ2L $GABA_A$ R ion channel. In order to gain insight into α subtype selectivity we designed and synthesized close structural analogs of diazepam and alprazolam. These compounds were then docked into the recently publish cryo-EM structures of $GABA_A$ Rs (6HUP and 6HUO). This modeling along with radio-ligand binding data resulted in the conclusion that the non-classical bioisosteric replacement of the chlorine atom at C7 with an ethinyl group (compound **5**) resulted in an 11-fold gain in α5 binding selectivity over the α1 subtype. Moreover, the potency of compound **5** resulted in a ligand with less sedation than diazepam, while still maintaining the same anxiolytic potency. These modeling data extend our understanding of the structural requirements for α-subtype-selective compounds that can be utilized to achieve improved medical treatments. It is clear that the ethinyl group in place of a halogen atom decreases the affinity and efficacy of benzodiazepines and imidazodiazepines at α1 subtypes, which results in less sedation and ataxia.

The γ-aminobutyric acid type A receptor ($GABA_A$ R) is an ionotropic receptor and ligand-gated chloride ion channel that is regulated by the endogenous ligand γ-aminobutyric acid (GABA). [1–2] Activation of $GABA_A$ Rs leads to the inhibition of neurotransmission by hyperpolarization of the neuron. $GABA_A$ Rs are heteropentameric ligand-gated membrane bound ion channels and are composed of different subunits (six α, three β, three γ, one δ, one ε, one θ, one π, and three ρ subunits). [3] The majority of $GABA_A$ Rs, however, are composed of two α, two β, and one γ2 subunits. The subunit composition of $GABA_A$ R is thought to control the different pharmacological and biological effects of GABA and exogenous ligands. Benzodiazepines (BZDs) are a general class of drugs known to bind to the $GABA_A$ R at an allosteric site. A large set of data has been assembled indicating that α and γ subunits are necessary for the pharmacological actions of BZDs. Classical 1,4-BZDs, such as diazepam (DZP), bind non-selectively to α1-3 and 5βγ2 $GABA_A$ Rs at the well-documented BZD binding site located at the $\alpha^+\gamma^-$ interface. [4–5] The pharmacological actions exerted by a BZD are dependent on the discrete subunits of the $GABA_A$ R complex. The BZDs exert sedative, hypnotic, anxiolytic, antinociceptive muscle relaxant and anticonvulsant actions. From a therapeutic perspective, it has been the goal of drug discovery efforts to design compounds that can specifically modulate selective biological actions that can translate into directed therapeutic effects. Precise knowledge of the structure of the binding site of action enables rational approaches to chemical design for this purpose. Much effort has

* Corresponding author.
E-mail address: capncook@uwm.edu (J.M. Cook).
[1] Both authors contributed equally.

https://doi.org/10.1016/j.bmcl.2022.128637
Received 15 July 2021; Received in revised form 18 February 2022; Accepted 20 February 2022
Available online 23 February 2022

been directed toward developing α subtype-selective molecules since these subunits have such a remarkable impact on pharmacological activity linked to specific therapeutic endpoints and side-effect profiles. [6–11] Knowledge of key binding domains within $GABA_A$ Rs is a prerequisite for rational structure-based drug design that could accelerate the discovery of novel subtype selective drugs of therapeutic use.

Recently, several cryo-EM independent studies have provided crucial insights into the structure of heteropentameric $GABA_A$ Rs. [12–16] These structures not only yielded unprecedented insights into the overall architecture of heteropentameric $GABA_A$ Rs, but also into the protein interactions of diverse ligands including the agonist GABA and positive allosteric modulator (PAM) BZDs (diazepam and alprazolam). [17]

The $GABA_A$ receptor-signaling mechanism is described by a "lock and pull" mechanism. Binding of GABA at the $\beta3^+/\alpha1^-$ interface leads to the movement of loop-C, which initiates a concerted global anti- clockwise motion in the extra cellular domain (ECD). The BZDs facili- tate this motion by binding at the $\alpha1^+/\gamma2^-$ ECD interface. [17] Exami- nation of cryo-ER structures of the α1β3γ2L $GABA_A$ R (6HUP and 6HUO) clearly illustrates what is believed to be the active conformations of diazepam (DZP) and alprazolam (ALP). These cryo-ER structures reveal three of the most important interactions which are important for BZDs to function as a PAM, i) bifurcated hydrogen bonding with α1Ser205, ii) halogen bonding with the backbone of α1His102, note that flunitrazepam and clonazepam contain nitro groups at C7 which likely are involved in a hydrogen bond with the histidine side chain and compensate for the lack of the C7 halogen bond interaction of diazepam and, iii) pi-pi stacking with α1Tyr210 and α1Phe100 (Figs. 1 and 2). In the case of diazepam the α subunit is in dispensable because diazepam does have other binding sites in this complex, however in this article we are only focused on the BZP binding site. [18] DZP and ALP interact with the α1His102 *via* halogen bonding interactions with the backbone carbonyl group, as shown in Figs. 1 and 2. The distance between the chlorine atom and carbonyl oxygen of α1His102 was 3.8 Å in the DZP bound cryo-EM structure (6HUP) and 2.9 Å in the case of ALP (6HUO).

The σ-hole angle is 165-167° in both cryo-EM structures. The bifurcated hydrogen bond formed by ALP with α1Ser205 is shorter than that configured with bound DZP. The shorter halogen bond and bifurcated hydrogen bond interactions are consistent with the more potent affinity

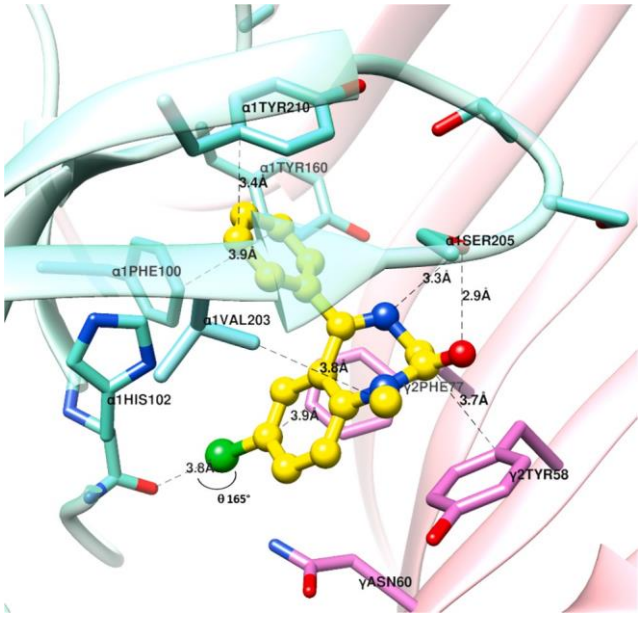


Fig. 1. Diazepam (yellow) in complex with α1 (aquamarine) and γ2 (orchid) subunits of α1β3γ2L $GABA_A$ receptor 6HUP. Dashed lines indicate π–π interactions, hydrogen bonds and a halogen bond.

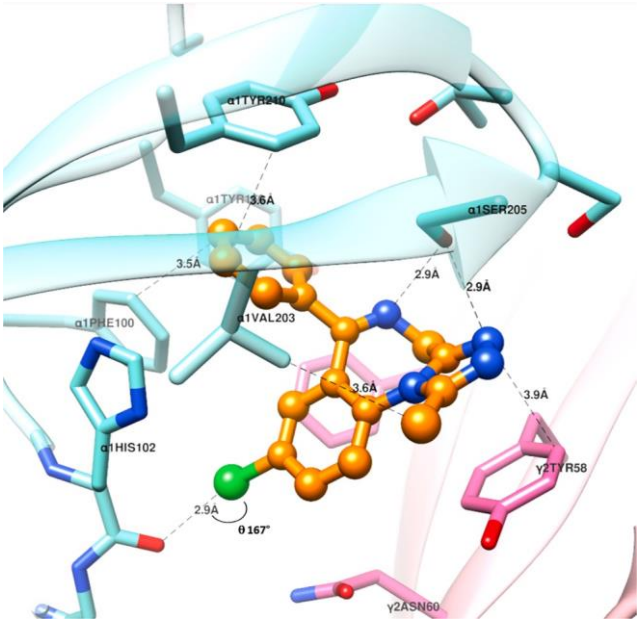


Fig. 2. Alprazolam (orange) in the complex with α1 (aquamarine) and γ2 (orchid) subunits of α1β3γ2L $GABA_A$ receptor 6HUO. Dashed lines indicate π–π interactions, hydrogen bonds and a halogen bond.

of ALP toward α1 as compared to DZP (Tables 1 and 2), which results in enhanced sedation for the former.

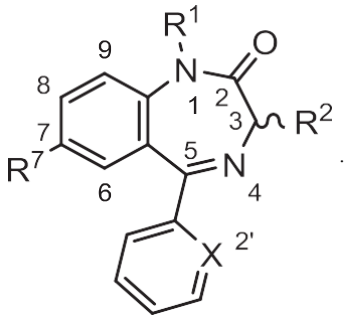
The active conformation of BZDs is unique at the $\alpha^+\gamma^-$ interface of $GABA_A$ R and enables the ligands to function as PAMs. The movement of loop-C at the $\alpha^+\gamma^-$ interface during $GABA_A$ channel opening is facilitated by BZD binding in this unique conformation. The unique active conformation of BZDs is further evident from two cryo-EM structures (6HUP and 6HUO), both structures of which have similar active conformations of DZP and ALP (Figs. 1 and 2). [17] Flumazenil is a competitive antagonist of BZDs and it is used as an antidote in the treatment of benzodiazepine overdose. [19] Examination of the cryo-ER structure of flumazenil (6D6U) with the $GABA_A$ R illustrates that flumazenil binds at the $\alpha^+\gamma^-$ interface in a completely different conformation compared to DZP or ALP (Fig. 3). [16] Examination of the cryo-EM structure (6D6U) also indicates that flumazenil does not form the two key interactions of the bifurcated hydrogen bond and the halogen bond interaction with the protein. The lack of these interactions is responsible for the inability of flumazenil to facilitate the loop-C movement at the $\alpha^+\gamma^-$ interface of the $GABA_A$ R. Therefore, flumazenil acts as a competitive antagonist at this site (Figure 3) where it overlaps with only part of the structure of the BZDs.

Examination of the sequence alignment of α1-6 subunits indicates that in the α4 and α6 peptides the α1His102 is replaced with an arginine residue (Table S1), the larger side chain of which sterically clashes with ALP and DZP. This could explain why classical BZDs such as DZP and ALP do not act on $GABA_A$ R subtypes containing α4 or α6 subunits [5]. The His102 is conserved in α1-3 and α5 subunits. The amino acid resi- dues involved in the interaction with the pendant ring of DZP and ALP are conserved in α1-3 and α5 subunits (Table S1). Examination of the loop-C region of the α subunits shows subtle differences in amino acid residues inside the BZD binding site (Table S1). The Ser205 residue in the α1 subunit is replaced in α5 subunits with Thr205. Moreover, the Val203 residue in the α1 subunit is replaced with Ile203 in α2-3 and α5 subunits. These subtle differences in amino acids provides unique 3- dimensional shapes of BZD R binding pockets.

We have developed several novel subtype selective PAMs and have been exploring ligand-receptor interactions of these compounds and other BZD-like molecules at $GABA_A$ Rs. [11,20–25] To further

Table 1

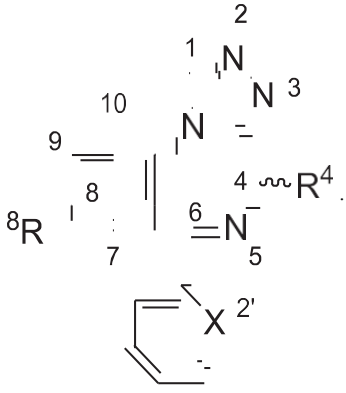
Binding affinities at α1-3 and α5 human $GABA_A$ R subtypes



Comp	Code	R^1	R^2	R^7	X	K_i (nM)			
						α1	α2	α3	α5
	Diazepam	CH_3	H	Cl	C—H	14	20	15	11
	QH-II-059	CH_3	H	H	C—H	81	138	318	98
	QH-II-063	CH_3	H	Br	C—H	9.4	9.3	31	7.7
	QH-II-058b	H	H	H	C—H	288	233	350	140
3	QH-II-066	CH	H	C≡CH	C—H	76.3	42.1	47.4	6.8
3	XLi-352	CH	H	C≡CH	C-Cl	1.6	0.99	ND	1.96
3	KRM-II-08	CH	H	C≡CH	C-F	3.9	1.2	3.4	0.8
	XLI-286	H	H	Br	C-Cl	0.05	0.06	0.12	0.68
	JYI-42	H	H	Br	C-F	0.26	0.15	0.28	0.26
	flunitrazepam[36]	CH_3	H	NO_2	C-F	2.2	2.5	4.5	2.1
	SH-I-030	H	*S*-CH_3	Br	C—H	14.4	11	19.1	1.89
	SH-I-035B	H	*R*-CH_3	Br	C—H	>3000	>3000	>3000	>3000

Table 2

Binding affinities at α1-3 and α5 human $GABA_A$ R subtypes



Comp.	Code	R^4	R^8	X	K_i (nM)			
					α1	α2	α3	α5
13.	alprazolam[36]	H	Cl	C—H	0.8	0.6	1.4	1.5
14.	Xli-2TC	H	Br	C—H	2.8	0.7	ND	0.6
15.	DM-II-90	H	Br	C-Cl	0.5	1	0.6	0.4
16.	SH-I-04	H	Br	N	7.3	6.1	5.1	7.7
17.	XLi-270	H	C≡CH	C—H	36.4	25.8	ND	5.3
18.	XLi-296	H	C≡CH	C-Cl	3.3	0.6	1.9	4.4
19.	JYI-70	H	C≡CH	C-F	6.3	2.1	ND	0.6
20.	SH-TRI-108	H	C≡CH	N	143.9	81.3	103.9	45.6
3 21.	SH-TS-CH3	*S*-CH	C≡CH	C—H	107.2	50.1	20.9	8.1

investigate the molecular interactions and binding affinities at the $\alpha_{1-3}{}^{+}\gamma^{-}$ and $\alpha_5{}^{+}\gamma^{-}$ interfaces of $GABA_A$ Rs, we designed and synthesized close analogs of DZP and ALP **1**–**21**. In this article we used recently published cryo-EM structure data on α1β3γ2L $GABA_A$ Rs (6HUP and 6HUO) to investigate the differences in the molecular interactions. [17] Compounds **2, 3** and **5** were designed to investigate the role of the halogen atom at C7. Ligands **6**–**9** were designed to investigate the molecular interactions of 2-substitution on the pendent phenyl ring of DZP. Ligands **11** and **12** were designed to investigate the role of a chiral methyl group in the seven-membered ring of DZP. To further investigate the role of these substitutions in different chemical scaffolds, we also synthesized analogs of ALP **13**–**21** with a benzo[f][1,2,4]triazolo [4,3–a1,4]diazepine scaffold.

We studied the cryo-ER structure of DZP and ALP bound at α1β3γ2L $GABA_A$ R (6HUP and 6HUO) and docked them with the synthesized ligands (Figures 1, 2 and 4). A halogen bond with the backbone of the α1His102 group is important for binding of DZP and ALP, as well as movement of the loop-C (acting as a PAM) to hold the chlorine ion channel open longer, which results in more sedation and more ataxia. An ethinyl group is an interesting bioisosteric replacement of a halogen (Cl, Br or I) executed by our group, especially where halogens at C7 (Cl, Br or I) are involved in a halogen bond interaction with the protein.[26–29]

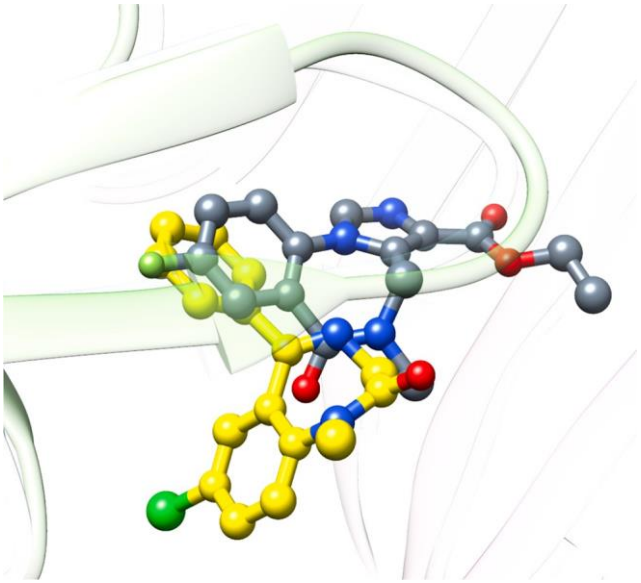


Fig. 3. Overlap of diazepam (yellow) and flumazenil (grey) in the ion complex with α1 (aquamarine) and γ2 (orchid) subunits of α1β3γ2L $GABA_A$ receptor 6HUP and 6D6U.

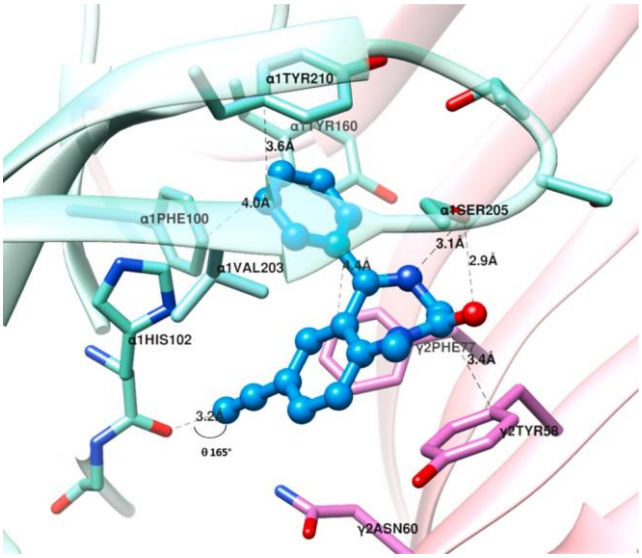


Fig. 4. Docked pose of QH-II-066 **5** (deep sky blue) with the α1 (aquamarine) and γ2 (orchid) subunits of α1β3γ2L $GABA_A$ receptor 6HUP. Dashed lines indicate π–π interactions and hydrogen bonds. There is no halogen bond.

Halobenzenes (Cl, Br or I) and phenylacetylene have similar molecular electrostatic potentials. Phenylacetylene like halobenzene creates an area of positive charge at the tip of the C—H bond and an area of negative charge perpendicular to the C— H bond. [30] More recently there has been a bioisoteric replacement of a chlorine atom with an ethinyl group for the two-marketed anti-cancer drugs gefitinib (iressa) and erlotinib (tarceva). [26] Synthetically an ethinyl moiety can be easily introduced into a precursor molecule bearing a bromine atom *via* Sonogashira cross-coupling, which makes comparisons of bromine and acetylene a straightforward task to tune affinities and physicochemical properties. Intrigued by the different size but similar molecular electrostatic potentials of acetylene compared to halogens (Cl, Br or I) we replaced chlorine at C7 of DZP with the ethinyl group (see ligand **5**). Illustrated in Figure 4 is the docking pose of ligand **5** (QH-II-066) in the α1β3γ2L cryo-EM structure 6HUP. **Examination of the docking in** Figure 4 **clearly shows that ligand 5 can adopt a similar conformation as DZP, consequently, it can act as a PAM at the α1 $GABA_A$ R subtype, although it exerts much less sedation and ataxia than diazepam** [33]. We also replaced the chlorine atom at C7 with a nitro group (**10** or flunitrazepam). Ligand **10** was docked in the cryo-EM structure 6HUP. Examination of the docked pose of **10** indicates that it also adopts a similar conformation to DZP. The nitro group at C7 forms two hydrogen bond interactions, one with the side chain of α1His102 and the second with the side chain of γ21Asn60 (not shown). Again, this ligand **10** is strongly sedating. We were also interested in the N1- desmethyl compounds (**4**, **8** and **9**) because the N1-methyl group of DZP forms a hydrophobic interaction with α1Val203. The subtle dif- ferences in the amino acids on the loop-C of the α subunits provide different 3-dimensional shape requirements for ligands. This idea pro- vides increased interest in chiral compounds such **11** and **12**. Docking studies of compound **11** and **12** show that the α1β3γ2L $GABA_A$ R (6HUP and 6HUO) has space for the (*S*)-methyl group but not enough space for the (*R*)-methyl group (compound **12**) hence the subtype selectivity of the (*R*) enantiomers is much different than the (*S*) enantiomers, as re- ported. [31–32] The synthesis of all the analogs **1**–**21** are described in the literature. [33–35]

Affinity of compounds at $GABA_A$ recombinant subtypes was measured by competition of [^{3}H]flunitrazepam binding to HEK cell membranes expressing human αxβ2γ2 receptors. The concentrations resulting in half-maximal inhibition of radioligand binding were converted into K_i values by using the Cheng-Prusoff relationship. Data represent the average of at least three determinations with a SEM of ± 5%. NDnot determined.

Affinity of compounds at $GABA_A$ recombinant subtypes was measured by competition for [^{3}H]flunitrazepam binding to HEK cell membranes expressing human αxβ2γ2 receptors. The concentrations resulting in half-maximal inhibition of radioligand binding were con- verted into K_i values by using the Cheng-Prusoff relationship. Data represent the average of at least three determinations with a SEM of ± 5%. NDnot determined.

We performed radioligand displacement studies and compared the potencies of the BZD ligands at α1-3β2γ2 and α5β2γ2 human $GABA_A$ R subtypes (Tables 1 and 2), as described previously. [37–38,42] Ligand **2** with no substitution at C7 shows a 6–20 fold decrease in binding affinity at BZD R (α1-3 and α5) as compared to DZP. The demethylated analog of compound **2** displays a further decrease in binding affinity (compound **4**) indicating that the halogen atoms at the C7 position are involved in an important interaction with $GABA_A$ Rs impacting biological activity. Replacing the chlorine atom with a bromine at the C7 position of DZP (compound **3**) did not modify binding affinity at α1-3 and α5 receptors. These data illustrate that the larger bromine atom can form a similar halogen bond with the α1His102 residue. The replacement of the chlorine atom with an ethinyl group (QH-II-066 **5**) resulted in a 3 to 6-fold decrease in binding affinity at α1-3 receptors, while binding affinity at α5 was increased. The binding affinity of ligand **5** indicates that it is 11- fold more selective toward α5 receptors, as compared to α1 receptors. The α1His102 residue is present in α1-3 and α5, however a difference in the binding affinity of compound **5** with α1-3 vs α5 suggest that binding pocket within the α5 $GABA_A$ R can be selectively targeted. The substitution at the 2′-position with a chlorine atom (compounds **6** and **8**) increased the binding affinity at α1-3 and α5 $GABA_A$ R. However, compound **6** and **8** lost the selectivity toward α5 $GABA_A$ R. The 2′-F substituted compounds **7** and **9** demonstrated increased binding affinity at α1-3 and α5 $GABA_A$ R. However, compound **7** was 5-fold more selective for α5 receptors, as compared to α1 receptors. This finding illustrates that the bulky halogen atom at the 2-position is detrimental towards α5 selectivity. The replacement of an acetylene with nitro at C7 in compound **10** (flunitrazepam) led to the loss of α5 selectivity. Ligand **7** exerted similar binding affinity at α1-3 and α5 $GABA_A$ R. The chiral ligand **11** with the (*S*)-methyl function at C3 exerted an increased binding affinity when compared to the non-chiral ligand **4**. Ligand **11**

shows 7-fold more selectivity towards α5 $GABA_A$ Rs, as compared to α1receptors while ligand **4** was only 2 to 3-fold more selective towards α5 $GABA_A$ Rs, as compared to α1 receptors. The chiral ligand **12** with (*R*)-methyl at C3 with a bromine atom at C7 did not show any binding selectivity with α1-3 and α5 $GABA_A$ Rs. A similar SAR trend was observed in the ALP scaffold. For example, replacing the chlorine atom with ethinyl yielded compound **17** with 6 to 7-fold selectivity for α5 $GABA_A$ Rs, as compared to α1 R's. The 2'-Cl substitution (compound **18**) resulted in loss in α5 $GABA_A$ R selectivity relative to α1. In contrast, the 2'-F (compound **19**) maintained α5 $GABA_A$ R selectivity. A chiral analog of ALP (compound **21**) with (*S*)-methyl at C4 was 13-fold more selective towards α5 $GABA_A$ Rs, as compared to α1 subtypes.

In summary, we designed and synthesized new α subtype-selective BZDs. These compounds were evaluated for their molecular interactions at the $\alpha^+\gamma^-$ interface of $GABA_A$ R in 6HUP and 6HUO protein cryo-ER structures. We believe this is the first report that identifies a halogen bond between the chlorine atom of DZP or ALP with the carbonyl oxygen backbone of the α1His102 at the $\alpha^+\gamma^-$ interface of $GABA_A$ Rs. Non classical bioisosteric replacement of halogens (Cl or Br) with an ethinyl moiety in DZP yielded QH-II-066 **5** which exhibited an 11-fold increase in binding affinity towards α5 over α1 containing $GABA_A$ Rs and the affinity and efficacy at α1 subtypes decreased with the ethinyl substitution, which resulted in decreased sedation, a key in design of new anxiolytics[33]. We hypothesize that the difference in shapes of the binding pockets of α1 and α5 that result from the different amino acids in the two sequences, confer compound **5** with enhanced selectivity for α5 over α1. The chiral analogs bearing the (*S*)-methyl group in the seven membered ring yielded compounds with 7- and 13-fold selectivity towards α5 over α1 $GABA_A$ Rs (compounds **11** and **21**, respectively). In a previous report, we tested ligands **5** and **7** in group 3 meduloblastoma cells which have high expression of GABRA5 (γ-aminobutyric acid type A receptor α5 subunit) (GABRA5 codes for the α5 subunit of the $GABA_A$ R) and found both of these compound were efficacious against cancer. [39–40] Moreover, the potency of compound **5** resulted in a ligand with less sedation than diazepam, while still maintaining the same anxiolytic potency. [33,41]

Declaration of Competing Interest

The authors declare that they have no known competing financial interests or personal relationships that could have appeared to influence the work reported in this paper.

Acknowledgements

We wish to acknowledge the NIH for generous financial support (DA-043204, AA14617 R01NS076517). We also thank the Milwaukee Institute for Drug Discovery and the University of Wisconsin-Milwaukee's Shimadzu Laboratory for Advanced and Applied Analytical Chemistry for help with spectroscopy and the National Science Foundation, Divi- sion of Chemistry [CHE-1625735].

Appendix A. Supplementary data

Supplementary data to this article can be found online at https://doi.org/10.1016/j.bmcl.2022.128637.

References

[1] Cromer BA, Morton CJ, Parker MW. Anxiety over GABA(A) receptor structure relieved by AChBP. *Trends Biochem Sci.* 2002;27:280. https://doi.org/10.1016/S0968-0004(02)02092-3.

[2] Sieghart W, Sperk G. Subunit composition, distribution and function of GABA(A) receptor subtypes. *Curr Top Med Chem.* 2002;2:795. https://doi.org/10.2174/1568026023393507.

[3] Sieghart W, Fuchs K, Tretter V, et al. Structure and subunit composition of GABA (A) receptors. *Neurochem Int.* 1999;34:379. https://doi.org/10.1016/S0197-0186(99)00045-5.

[4] Sieghart W, Ernst M. Heterogeneity of GABAA receptorsrevived interest in the development of subtype-selective drugs. *Curr Med Chem.* 2005;5:217. https://doi.org/10.2174/1568015054863837.

[5] Clayton T, Chen JL, Ernst M, Richter L, Cromer BA, Morton CJNgH, Kaczorowski CC, Helmstetter FJ, Furtmuller R, Ecker G, Parker MW, Sieghart W, Cook JM. An updated unified pharmacophore model of the benzodiazepine binding site on gamma-aminobutyric acid(a) receptorscorrelation with comparative models. *Curr Med Chem.* 2007;142755. 10.2174/092986707782360097.

[6] Neutel CI. Risk of traffic accident injury after a prescription for a benzodiazepine. *Ann Epidemiol.* 1995;5:239. https://doi.org/10.1016/1047-2797(94)00112-7.

[7] Engeland A, Skurtveit S, Morland J. Risk of road traffic accidents associated with the prescription of drugsa registry-based cohort study. *Ann Epidemiol.* 2007;17:597. https://doi.org/10.1016/j.annepidem.2007.03.009.

[8] Atack JR. GABAA receptor subtype-selective modulators. I. alpha2/alpha3-selective agonists as non-sedating anxiolytics. *Curr Top Med Chem.*. 2011;11:1176. https://doi.org/10.2174/156802611795371350.

[9] Gurrell R, Gorman D, Whitlock M, et al. Photosensitive epilepsyRobust clinical efficacy of a selective GABA potentiator. *Neurology*. 2019;92:1786. https://doi.org/10.1212/WNL.0000000000007271.

[10] Poe MM, Methuku KR, Li G, et al. Synthesis and characterization of a novel γ-aminobutyric acid type A (GABAA) receptor ligand that combines outstanding metabolic stability, pharmacokinetics, and anxiolytic efficacy. *J Med Chem.* 2016;9: 10800. https://doi.org/10.1021/acs.jmedchem.6b01332.

[11] Witkin JM, Cerne R, Davis PG, Freeman KB, do Carmo JM, Rowlett JK, Methuku KR, Okun A, Gleason S. Li X, Krambis MJ, Poe M, Li G, Schkeryantz JM, Jahan R, Yang L, Guo W, Golani LK, Anderson WH, Catlow JT, Jones TM, Porreca F, Smith JL, Knopp KL, Cook JM. The alpha2,3-selective potentiator of GABAA receptors, KRM-II-81, reduces nociceptive-associated behaviors induced by formalin and spinal nerve ligation in rats. *Pharmacol Biochem Behav.* 2019;180:22. 10.1016/j.pbb.2019.02.013.

[12] García-Nafría J, Tate CG. Cryo-electron microscopymoving beyond x-ray crystal structures for drug receptors and drug development. *Annu Rev Pharmacol.* 2020;60. https://doi.org/10.1146/annurev-pharmtox-010919-023545.

[13] Laverty D, Desai R, Uchanski T, et al. Cryo-EM structure of the human alpha1beta3gamma2 GABAA receptor in a lipid bilayer. *Nature*. 2019;565:516. https://doi.org/10.1038/s41586-018-0833-4.

[14] Liu S, Xu L, Guan F, et al. Cryo-EM structure of the human alpha5beta3 GABAA receptor. *Cell Res.* 2018;28:958. https://doi.org/10.1038/s41422-018-0077-8.

[15] Phulera S, Zhu H, Yu J, et al. Cryo-EM structure of the benzodiazepine-sensitive alpha1beta1gamma2S tri-heteromeric GABAA receptor in complex with GABA. *Elife*. 2018;7. https://doi.org/10.7554/eLife.39383.001.

[16] Zhu S, Noviello CM, Teng J, Walsh RM, Hibbs KJJRe. Structure of a human synaptic GABA A receptor. *Nature*. 2018;55967. https://doi.org/10.1038/s41586-018-0255-3.

[17] Masiulis S, Desai R, Uchanski T, et al. GABAA receptor signalling mechanisms revealed by structural pharmacology. *Nature*. 2019;565454. https://doi.org/10.1038/s41586-018-0832-5.

[18] Wongsamitkul N, Maldifassi MC, Simeone X, Baur R, Ernst M, Sigel E. α subunits in GABAA receptors are dispensable for GABA and diazepam action. *Sci Rep.* 2017;7 15498. 10.1038/s41598-017-15628-7.

[19] Weinbroum A, Rudick V, Sorkine P, et al. Use of flumazenil in the treatment of drug overdosea double-blind and open clinical study in 110 patients. *Crit Care Med.* 1996;24:199. https://doi.org/10.1097/00003246-199602000-00004.

[20] Smith JL, Ping X, Jin X, Golani LK, Li G, Rashid F, Jahan R, Cook JM, Witkin JM. The positive allosteric modulator of alpha-2/3-containing γ-aminobutyric acid type a receptors, KRM-II-81, is active in pharmacoresistant models of epilepsy and in human epileptic tissue. *Neurosurgery* 2019;66 (Supplement_1). 10.1093/neuros/nyz310_697.

[21] Methuku KR, Li X, Cerne R, et al. An antidepressant-related pharmacological signature for positive allosteric modulators of alpha2/3-containing GABAA receptors. *Pharmacol Biochem Behav.*. 2018;170:9. https://doi.org/10.1016/j.pbb.2018.04.009.

[22] Berro LF, Rüedi-Bettschen D, Cook JE, et al. GABAA receptor subtypes and the abuse-related effects of ethanol in rhesus monkeysexperiments with selective positive allosteric modulators. *Alcohol Clin Exp Res.* 2019;43:791. https://doi.org/10.1111/acer.14000.

[23] Moerke MJ, Li G, Golani LK, Cook JM, Negus SS. Effects of the α2/α3-subtype-selective GABAA receptor positive allosteric modulator KRM-II-81 on pain-depressed behavior in ratscomparison with ketorolac and diazepam. *Behav Pharmacol*. 2019;30:452. https://doi.org/10.1097/FBP.0000000000000464.

[24] Witkin JM, Li G, Golani LK, et al. The positive allosteric modulator of alpha2/3-containing GABAA receptors, KRM-II-81, is active in pharmaco-resistant models of epilepsy and reduces hyperexcitability after traumatic brain injury. *J Pharmacol Exp Ther.*. 2019 https://doi.org/10.1124/jpet.119.260968.

[25] Golani L, Witkin J, Cook J. Novel imidazobenzodiazepine GABAA receptor alpha 2/alpha 3 selective PAM for the treatment of refractory/resistance epilepsy. *In Abstrt Pap Am Chem S. American Chemical SocietyOrlando, Florida*. 2019:257.

[26] Ciardiello F, Tortora G. A novel approach in the treatment of cancertargeting the epidermal growth factor receptor. *Clin Cancer Res.* 2001;72958. PMID11595683.

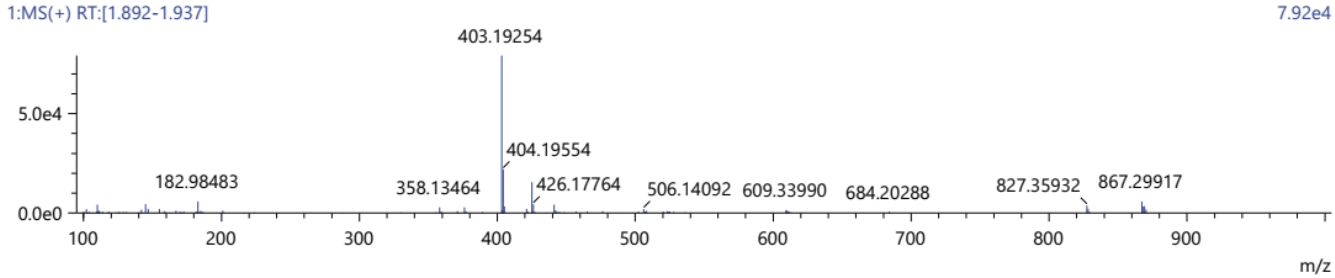
[27] Yun CH, Boggon TJ, Li Y, et al. Structures of lung cancer-derived EGFR mutants and inhibitor complexesmechanism of activation and insights into differential inhibitor sensitivity. *Cancer Cell*. 2007;11217. https://doi.org/10.1016/j.ccr.2006.12.017.

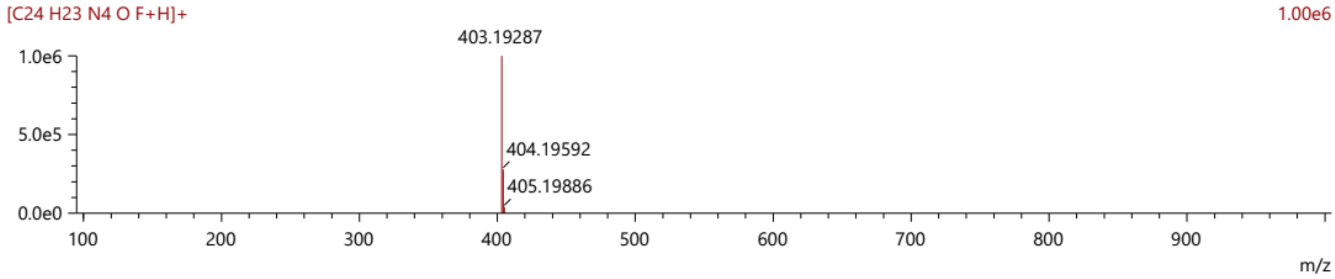
[28] Park JH, Liu Y, Lemmon MA, Radhakrishnan R. Erlotinib binds both inactive and active conformations of the EGFR tyrosine kinase domain. *Biochem J.* 2012;448:417. https://doi.org/10.1042/BJ20121513.

[29] Parks DJ, Lafrance LV, Calvo RR, et al. Lu T.1,4-Benzodiazepine-2,5-diones as small molecule antagonists of the HDM2-p53 interactiondiscovery and SAR. *Bioorg Med Chem Lett.*. 2005;15:765. https://doi.org/10.1016/j.bmcl.2004.11.009.
[30] Wilcken R, Zimmermann MO, Bauer MR, et al. experimental and theoretical evaluation of the ethynyl moiety as a halogen bioisostere. *ACS Chem Biol.* 2015;10: 2725. https://doi.org/10.1021/acschembio.5b00515.
[31] Cook JM, Li G, Poe MM, Savic M, Sibille E. Preparation of substituted benzo[f] imidazo[1,5-a][1,4]diazepine-3-carboxamides as α5-containing GABAA receptor agonists for treatment of cognitive and mood symptoms in neurodegenerative and neuropsychiatric disorders. *WO.* 2017:2017161370:A1.
[32] Obradovic A, Joksimovic S, Poe MM, et al. Sh-I-048A, an in vitro non-selective super-agonist at the benzodiazepine site of GABAA receptorsthe approximated activation of receptor subtypes may explain behavioral effects. *Brain Res.* 2014; 1554:36. https://doi.org/10.1016/j.brainres.2014.01.036.
[33] Cook JM, Huang Q, He X, et al. Anxiolytic agents with reduced sedative and ataxic effects. *US.* 2006:7119196:B2.
[34] Cook JM, Huang S, Edwankar R, Namjoshi OA, Wang ZJ. Selective agents for pain suppression. US8835424 B2, 2014.
[35] Li G, Golani LK, Jahan R, Rashid F, Cook JM. Improved synthesis of anxiolytic, anticonvulsant, and antinociceptive α2/α3-gaba(a)-ergic receptor subtype selective ligands as promising agents to treat anxiety, epilepsy, and neuropathic pain. *Synthesis.* 2018;50:4124. https://doi.org/10.1055/s-0037-1610211.
[36] Clayton T, Poe MM, Rallapalli S, et al. A review of the updated pharmacophore for the alpha 5 gaba(a) benzodiazepine receptor model. *Int. J Med Chem.* 2015;430248. https://doi.org/10.1155/2015/430248.

Formula Predictor Result	**C24 H23 N4 O F**
Mass	403.19254
Error Margin	5 ppm
DBE Range	0 - 1000
Electron Ions	Both configurations
HC Ratio	Not Used
Nitrogen Rule	Used

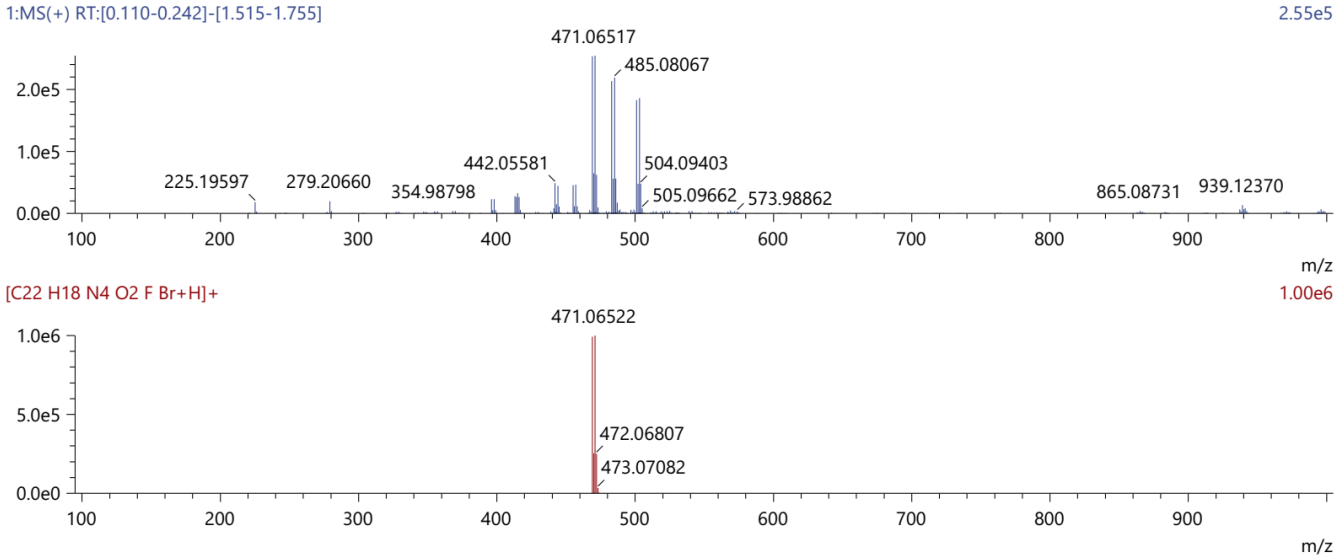
Score	Pred. (M)	Pred. m/z	Meas. m/z	Diff. (mDa)	Formulae (M)	Ion	Diff. (ppm)	Iso Score	DBE
98.28	402.18559	403.19287	403.19254	-0.33	C24 H23 N4 O F	[M+H]+	-0.818	98.49	15.0





Formula Predictor Result	**C22 H18 N4 O2 F Br**
Mass	469.06689
Error Margin	5 ppm
DBE Range	0 - 1000
Electron Ions	Both configurations
HC Ratio	Not Used
Nitrogen Rule	Used

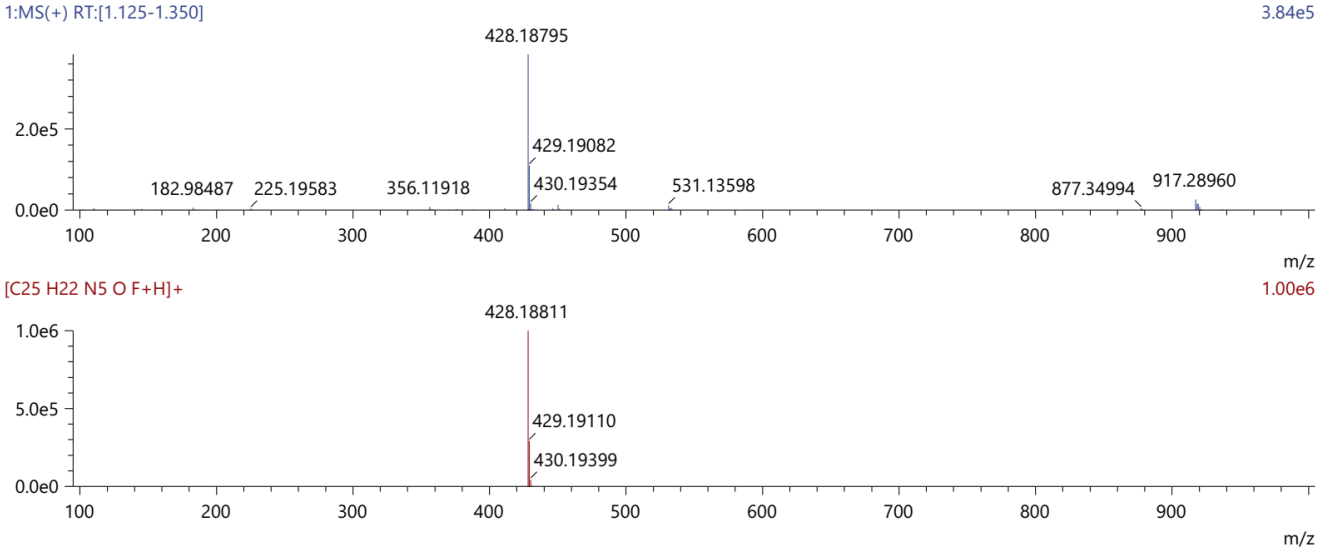
Score	Pred. (M)	Pred. m/z	Meas. m/z	Diff. (mDa)	Formulae (M)	Ion	Diff. (ppm)	Iso Score	DBE
99.67	468.05972	469.06699	469.06689	-0.10	C22 H18 N4 O2 F Br	[M+H]+	-0.213	99.72	15.0



Scan positive no column.lcm

Formula Predictor Result	**C25 H22 N5 O F**
Mass	428.18795
Error Margin	5 ppm
DBE Range	0 - 1000
Electron Ions	Both configurations
HC Ratio	Not Used
Nitrogen Rule	Used

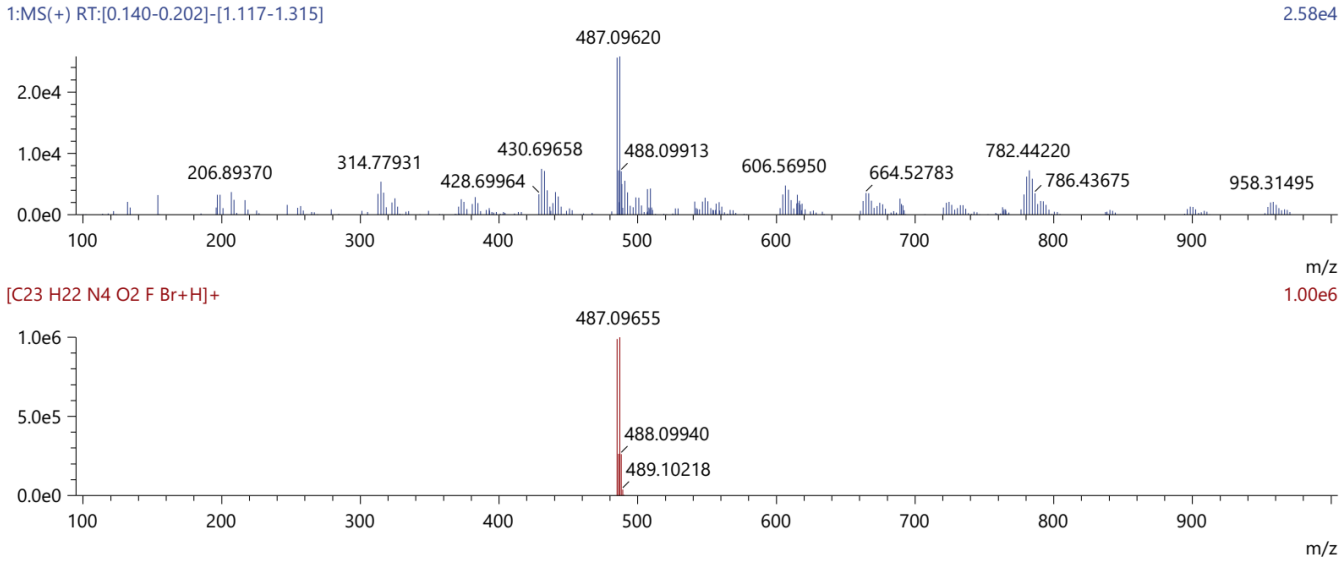
Score	Pred. (M)	Pred. m/z	Meas. m/z	Diff. (mDa)	Formulae (M)	Ion	Diff. (ppm)	Iso Score	DBE
98.81	427.18084	428.18811	428.18795	-0.16	C25 H22 N5 O F	[M+H]+	-0.374	98.84	17.0



lkll

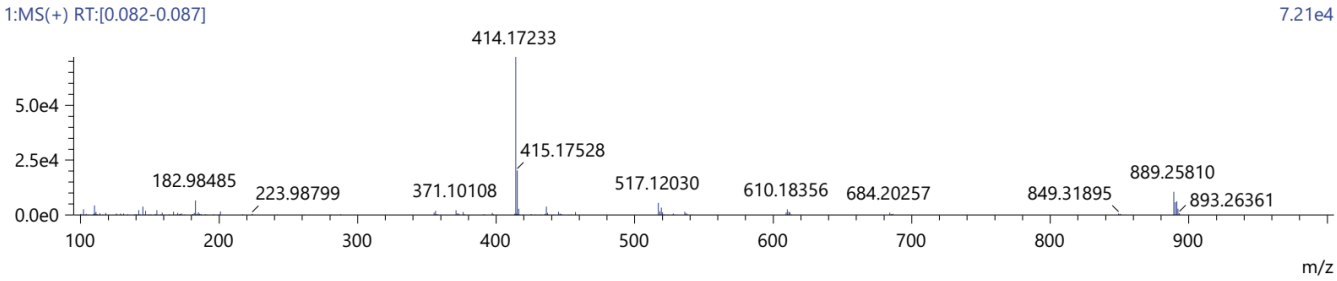
Formula Predictor Result	**C23 H22 N4 O2 F Br**
Mass	485.09819
Error Margin	5 ppm
DBE Range	0 - 1000
Electron Ions	Both configurations
HC Ratio	Not Used
Nitrogen Rule	Used

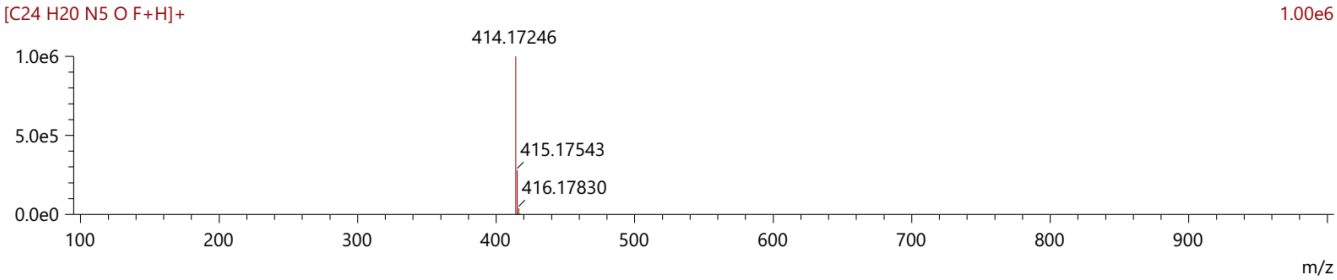
Score	Pred. (M)	Pred. m/z	Meas. m/z	Diff. (mDa)	Formulae (M)	Ion	Diff. (ppm)	Iso Score	DBE
99.25	484.09102	485.09829	485.09819	-0.10	C23 H22 N4 O2 F Br	[M+H]+	-0.206	99.24	14.0



Formula Predictor Result	**C24 H20 N5 O F**
Mass	414.17233
Error Margin	5 ppm
DBE Range	0 - 1000
Electron Ions	Both configurations
HC Ratio	Not Used
Nitrogen Rule	Used

Score	Pred. (M)	Pred. m/z	Meas. m/z	Diff. (mDa)	Formulae (M)	Ion	Diff. (ppm)	Iso Score	DBE
99.79	413.16519	414.17246	414.17233	-0.13	C24 H20 N5 O F	[M+H]+	-0.314	99.90	17.0





Formula Predictor Result	**C22 H18 N3 O2 F**
Mass	376.1455
Error Margin	5 ppm
DBE Range	0 - 1000
Electron Ions	Both configurations
HC Ratio	Not Used
Nitrogen Rule	Used

Score	Pred. (M)	Pred. m/z	Meas. m/z	Diff. (mDa)	Formulae (M)	Ion	Diff. (ppm)	Iso Score	DBE
69.85	375.13830	376.14558	376.14550	-0.08	C22 H18 N3 O2 F	[M+H]+	-0.213	66.58	15.0

